MEASUREMENTS OF FILM COOLING PERFORMANCE IN A TRANSONIC SINGLE PASSAGE MODEL

by
Paul M. Kodzwa, Jr. and John K. Eaton

Prepared with support from
General Electric Aircraft Engines

Report No. TF 93

June 2005

Flow Physics and Computation Division
Department of Mechanical Engineering
Stanford University
Stanford, CA 94305-3035

Abstract

Film cooling is an essential technology for the development of high performance gas turbine engines. A well-designed film cooling strategy allows higher turbine inlet temperatures, improving the engine thermodynamic efficiency. A poorly designed strategy can cause high local temperature gradients, leading to component failures and costly repairs. Hence accurate prediction tools are vital for designers. With the increasing complexity of cooling designs, correlations and incremental design approaches have become outdated, signaling the urgent need for "physics-based" tools that can be coupled to standard modern computational tools, such as commercial computational fluid dynamics (CFD) codes. A glaring problem with the development of this new technology is the lack of well-resolved data with well-defined boundary conditions. Thus, a frequent problem facing model developers is elucidating if differences between experimental data and predictions are due to the experimental data, the applied model, or the applied boundary conditions.

The purpose of this experiment to provide highly resolved film cooling performance and heat transfer coefficient measurements of compound angle round holes coupled with realistic gas turbine engine blade geometry and flow conditions. The ultimate goals are: 1) to develop an experimental procedure than can provide timely data for film cooling design; 2) provide full-field surface film cooling data for developing computational models in realistic flows. An experimental two-dimensional representation of the flow field between two modern, transonic turbine airfoil surfaces was used in these tests. This facility, termed as a single passage model, was carefully designed using a heuristic CFD-driven process to match that of an infinite cascade, the most common domain used for performing 2-D CFD simulations of film cooling on modern gas turbine blade geometries. By achieving this goal, the facility provided the identical flow conditions to multi-passage linear cascade, but with substantially reduced costs. Additionally, the simpler overall construction of the single passage allowed the use of steady state, constant heat flux boundary conditions which are more amenable to comparisons with standard CFD prediction techniques.

Thermochromic liquid crystals (TLCs) are used to provide full-field surface temperature measurements that can subsequently be used to collect heat transfer coefficient and film cooling effectiveness data. This technique has been proven to be valuable as an evaluation and measurement tool in linear cascades and is thus implemented here. Tiny periscopes

(borescopes) are used for optical access to image the measurement surfaces.

Finally, film-cooling effectiveness and heat transfer coefficient results for compound angle round holes inserted in the pressure side surface of a modern blade geometry are presented for various film-cooling flow conditions and hole geometries. This included a range of blowing conditions, density ratios and inlet turbulence ratios.

The uncooled heat transfer measurements revealed two interesting results. First, the thermal boundary layer on the aft portion of the airfoil, where the flow accelerates to supersonic conditions, is unaffected by the turbulence intensity at the inlet of the passage. Additionally, these data also suggest that the heat transfer coefficient can depend on the local surface heat flux boundary condition. This observation was supported by additional numerical and theoretical analysis. This, if true, would be an extremely important observation: it would mean that standard transient heat transfer measurement techniques for transonic flow would have an inherent error, possibly corrupting the subsequent measurements. Furthermore, it raises the importance of carefully matching numerical and experimental boundary conditions, to ensure that the accuracy of numerical models are directly tested.

The measured film cooling results indicated two regimes for jet-in-crossflow interaction: one where the jet is rapidly entrained into the local boundary layer, the other where the jet blows straight through the boundary layer. It was determined that the mass flux or momentum flux rate of the jet versus the mainstream flow determines which regime the film cooling jet lies. The effect of varying density ratio and turbulence intensity on film cooling performance was found to be highly dependent on the jet regime.

Acknowledgements

We wish to earnestly acknowledge our collaborators and supporters at General Electric Aircraft Engines, without whom this project would not have been possible. Dr. Frederick A. Buck, Dr. Robert Bergholz and Dr. David C. Wisler provided essential insight into the frustrating challenges that affect their business and their desire for better heat transfer prediction tools.

We would also like to thank Professors M. Godfrey Mungal and Juan G. Santiago and Dr. Gorazd Medic for their valuable technical advice and expertise during various stages of this project, specifically in the development of the flow facility.

Much of the work shown in this thesis would not have been possible without the consistent technical advice and effort from Dr. Christopher J. Elkins. Dr. Elkins always had the ability to appear at crucial stages in this project and bring precious sanity from chaos.

Dr. Creigh Y. McNeil, Dr. Xiaohua Wu and Dr. Gregory M. Laskowski provided immeasurable technical during the design phases of this project. Their frequent frank analysis of our research was instrumental to the completion of this project.

Many of the components built in the course of this experiment required an extremely high level of machining and fabrication expertise. This was amply provided by Mr. Tom Carver, Mr. Jonathan Glassman, Mr. James Hammer, Mr. Tom Hasler, Mr. Lakbhir Johal and Mr. Scott Sutton. These gentlemen spent an inordinate amount of time, well beyond what they were required, to assist a naive and inexperienced graduate student. We are deeply indebted to their blood and sweat, without which this experiment would have never left the drawing board.

During the evolution of this project, several procedural and bureaucratic roadblocks were encountered. Mrs. Amy E. Osugi and Mrs. Marlene Lomuljo-Bautista were invaluable in resolving these issues, and we gratefully acknowledge their support.

We wish to express my sincere gratitude and appreciation to the National Science Foundation for their award of a three-year fellowship that initially supported Paul Kodzwa's tenure at Stanford.

Contents

Abstract **iii**

Acknowledgements **v**

List of Tables **xi**

List of Figures **xiii**

Nomenclature **xxviii**

1 Introduction **1**

1.1 Introduction to Film Cooling and Thesis Objectives 1
1.2 Approaches to Film Cooling Design and Implementation 2
1.3 Thesis Objectives Restated 8
1.4 Introduction to Film Cooling Physics 9
1.5 General Characteristics of the Jet-In-Crossflow Interaction 11
1.5.1 Blowing/Momentum Ratio Effects on Jet-Mainstream Interaction . . 12
1.5.2 Effect of Hole Inclination 15
1.5.3 Hole Spacing and Pattern Effects on Film Cooling Performance . . . 18
1.5.4 Compound Angle Hole Orientation Effects on Film Cooling Performance 21
1.5.5 Hole Exit Shape Effects on Film Cooling Performance 24
1.5.6 Characteristics of the Effects of Hole Length and Plenum Conditions on Film Cooling Performance 28
1.5.7 Effect of Freestream and Jet-Cross-stream Generated Turbulence . . 31
1.5.8 Importance of Density Ratio on Film Cooling Performance 33
1.5.9 Effects of Pressure Gradient and Boundary Layer Thickness on Film Cooling Performance 36
1.5.10 Streamwise Curvature Effects on Film Cooling Performance 39
1.5.11 Effect of Miscellaneous Conditions 42
1.5.12 Combined Parameter Effects on Film Cooling 43
1.6 Numerical Modeling Efforts for Film Cooling Design 46
1.6.1 The Navier-Stokes Equations and Reynolds Averaging 48

1.6.2 LES and DNS Efforts . . . 50
1.6.3 RANS Simulation Efforts . . . 51
1.6.4 Macro-model or Parametric Simulations . . . 54
1.6.5 Boundary-Layer Equation Simulations and Correlations . . . 56
1.7 Experimental Approximations for Turbine Flow Conditions . . . 57
1.8 Experimental Measurement Techniques for Measuring Film Cooling Performance . . . 66
1.8.1 Transient Heat Transfer Measurement Techniques . . . 66
1.8.2 Steady State Heat Transfer Measurement Techniques . . . 71
1.8.3 Mass Transfer Analogy Technique . . . 71

2 Single Passage Apparatus **75**
2.1 Overview of Single Passage Design Concept . . . 75
2.1.1 Infinite Cascade Simulation . . . 80
2.1.2 Buck and Prakash Methodology . . . 86
2.1.3 Revised Design Procedure for Transonic Single Passage Models . . . 92
2.1.4 2-D Simulation Sensitivity and Comparative Studies . . . 106
2.1.5 3-D Simulation Results . . . 107
2.2 Physical Single Passage Model Design and Fabrication . . . 114
2.3 Experimental Test Facility . . . 123
2.3.1 Supply System . . . 123
2.3.2 Exhaust System . . . 125
2.3.3 Film Cooling Supply System . . . 130
2.3.4 Orifice Plate Implementation . . . 132
2.4 Flow Validation and Conditions . . . 137
2.4.1 Atmospheric Pressure Measurement . . . 137
2.4.2 Temperature Measurement . . . 137
2.4.3 Pressure Measurement . . . 138
2.4.4 Pitot and Kiel Probes . . . 138
2.4.5 Hotwire Calibration and Measurement Procedures . . . 141
2.4.6 Validation Experiment Results . . . 149

3 Heat Transfer Experiment Methodology **168**
3.1 Optical Access Apparatus and Implementation . . . 168

3.1.1 Implementation of Borescopes to the Single Passage Model 170
3.1.2 Geometry Correction Algorithms 177
3.2 General Aspects of Thermochromic Liquid Crystal Application 181
3.2.1 Introduction to Thermochromic Liquid Crystals and Their Properties 181
3.2.2 Introduction to TLC Thermography 187
3.3 In-situ TLC Calibration System 190
3.3.1 In-situ Calibration Apparatus 191
3.3.2 Sample Preparation 195
3.3.3 TLC System Light Source 200
3.4 TLC Calibration and Measurement Algorithms 205
3.4.1 Borescope Adjustment Settings and Image Manipulation 205
3.4.2 Imaging System Settings 206
3.4.3 Calibration Grid Algorithm 208
3.4.4 Black and White Reference Setting 210
3.4.5 TLC Calibration Procedure 213
3.4.6 Borescope Re-positioning Error 220
3.4.7 Temperature Measurement 222
3.4.8 Measurement System Validation 225
3.5 Heat Transfer Measurement Techniques and Implementation 231
3.5.1 Heat Transfer Surface Design and Construction 235

4 Uncooled Heat Transfer Experiments: Results and Analysis 244
4.1 Experimental Results 244
4.1.1 Recovery Temperature Measurements 245
4.1.2 Heat Transfer Coefficient Data Acquisition Process and Uncertainty Analysis 250
4.1.3 Heat Transfer Coefficient Measurements 251
4.2 Discussion 266

5 Cooled Heat Transfer Experiments: Results and Discussion 268
5.1 Data Reduction and Measurement Uncertainty 269
5.2 Flow Conditions for Experimental Cases 274
5.3 Flow Conditions for CFD and Literature Comparisons 275
5.4 Isoenergetic Temperature Distributions 278

5.4.1 Effects of Blowing Ratio 284
5.4.2 Density Ratio effects 287
5.4.3 Turbulence effects on isoenergetic temperature distribution 287
5.4.4 Discussion 291
5.5 Film-Cooling Effectiveness Results 292
5.5.1 Effects of blowing ratio on film-effectiveness 292
5.5.2 Density Ratio Effects 300
5.5.3 Turbulence effects on film effectiveness 302
5.5.4 Discussion of Film Cooling Results 310
5.6 Heat Transfer Coefficient Results 310
5.6.1 Baseline Comparison 310
5.6.2 Effects of Blowing Ratio on Heat Transfer Coefficient 311
5.6.3 Effects of Density Ratio in Heat Transfer Coefficient 318
5.6.4 Effects of Turbulence on Heat Transfer Coefficient 325
5.6.5 Discussion of Heat Transfer Coefficient Measurements 330
5.7 Overall Discussion of Results 330

6 Conclusions and Future Work 334

A Detailed Uncertainty Analyses 338

A.1 Pressure Measurement Uncertainty 338
A.2 Isentropic Mach Number (M_{is}) Measurement Uncertainty 342
A.3 Mass Flow Rate Measurement Uncertainty 343
A.4 Hotwire Measurement Uncertainty 346
A.5 Adiabatic Film Effectiveness Measurement Uncertainty 348
A.6 Heat Transfer Coefficient Measurement Uncertainty 349

B Humidity Measurement Methodology 352

C Calibration and Sensitivity Study of RANS Heat Transfer Predictions 356

C.1 Compressible Flow Over a Flat Plate 356
C.1.1 Numerical Preliminaries 358
C.1.2 Laminar Flow 359
C.1.3 Turbulent Flow 371

List of Tables

2.1 Comparison of engine conditions to experimental conditions. 79

2.2 Comparison of computed stagnation point locations using various turbulence models and conditions for infinite two-dimensional cascade. 83

2.3 Comparison of computed stagnation point axial locations for Buck and Prakash single passage versus infinite cascade. 88

2.4 Comparison of computed stagnation point axial locations for new design versus infinite cascade and Buck and Prakash design. 95

2.5 Comparison of computed bleed mass flow rates for different designs. 95

2.6 Comparison of computed total mass flow rates for different designs. 101

2.7 Exhaust manifold design parameters. 106

2.8 Discharge coefficients for film cooling runs. 135

2.9 Nominal uncertainties for orifice plate runs. 137

2.10 Flow facility coefficients for single passage. 143

2.11 Operating conditions. 150

2.12 Sensitivity test for integral length scale – low turbulence condition 163

2.13 Sensitivity test for integral length scale – high turbulence condition 163

3.1 Pressure side calibrator TEC configuration. 192

3.2 Suction side calibrator TEC configuration. 192

3.3 Candidate light source and halogen bulb combinations. 201

3.4 Borescope settings to observe pressure side wall. 206

3.5 Sony XC-003 Camera settings for measurements. 207

3.6 Imaging system settings for measurement. 208

3.7 Film cooling hole geometry. 233

3.8 Parameter matrix for uncooled surface. 234

3.9 Parameter matrix for film-cooled surface. 235

3.10 Backloss thermocouple locations. 236

3.11 Definitions of compound angle round hole definition angles (derived from Buck (2000)). 241

4.1 Sample backloss evaluation for uncooled heat transfer experiment ($T_\circ = 33.1°$).247

4.2 Heating film conditions for low turbulence flow condition. 251
4.3 Estimated locations and values of $\overline{h}(s_c/c_{blade})$ maxima for low turbulence flow condition. 254
4.4 Heating film conditions for high turbulence flow condition. 258
4.5 Estimated locations and values of $\overline{T}(s_c/c_{blade})$ maxima. 258
4.6 Estimated locations and values of $\overline{h}(s_c/c_{blade})$ maxima for high turbulence flow condition. 260

5.1 Nominal heating film conditions for film cooling experiments. 274
5.2 Nominal Dimensionless Parameters Values for T_{iso} measurements. 275
5.3 Nominal Dimensionless Parameters Values for $T_{aw,c}$ Measurements. 276
5.4 Nominal Dimensionless Parameters Values for T_w Measurements. 277
5.5 $T_{\circ,fc}$ and $P_{\circ,fc}$ for T_{iso} measurements. 279
5.6 $T_{\circ,fc}$ and $P_{\circ,fc}$ for $T_{aw,c}$ measurements. 280
5.7 $T_{\circ,fc}$ and $P_{\circ,fc}$ for T_w measurements. 281
5.8 Comparison of studied film cooling parameters for various experiments. . . 282

A.1 Pressure transducer elemental uncertainties. 340
A.2 Pressure transducer error propagation. 341
A.3 Estimated Uncertainty for Various Values of M_{is}. 344
A.4 Estimated Uncertainty for Main Air Supply Mass Flow Rate $\dot{m}$ (kg/s). . . . 345
A.5 Estimated Uncertainty for Boundary Layer Bleed Mass Flow Rate $\dot{m}(\frac{\mathrm{kg}}{\mathrm{s}})$. . 345
A.6 Estimated Uncertainty for Film Cooling Orifice Plate Run #1 $\dot{m}(\frac{\mathrm{kg}}{\mathrm{s}})$. . . . 345
A.7 Estimated Uncertainty for Film Cooling Orifice Plate Run #2 $\dot{m}(\frac{\mathrm{kg}}{\mathrm{s}})$. . . . 346
A.8 Estimated Uncertainty for Hotwire Calibration Coefficients. 348
A.9 Estimated Uncertainty for Hotwire Measurements of ρu. 348
A.10 Estimated Uncertainty for Film Cooling Effectiveness Measurements. 350
A.11 Estimated Uncertainty for Heat Transfer Coefficient Measurements. 351

C.1 Boundary condition values for flat plate simulations. 358

List of Figures

1.1 Example of a compound angle round (CARH) film cooling hole. 4
1.2 Example of a diffuser exit (DEH) film cooling hole. 5
1.3 Comparison of Rolls Royce ACE trailing edge film cooling tests by Abhari and Epstein (1994) with 3-D RANS simulation of Garg and Gaugler (1996). 7
1.4 Schematic of the four types of vortical structures found in the jet-in-crossflow interaction flow field (from Fric and Roshko (1994)). 11
1.5 Figure of flow characteristics for normal injection with low blowing ratios (from Andreopoulos and Rodi (1984)). 14
1.6 Figure of flow characteristics for normal injection with high blowing ratios (from Andreopoulos and Rodi (1984)). 14
1.7 Definition of row spacing S relative to the stagnation point of a turbine airfoil. 19
1.8 Schematic of an annular rotating cascade (from Atassi et al. (2004)). 57
1.9 Layout of housing for space shuttle main engine turbopump turbine shock-tube test (from Dunn et al. (1994)). 59
1.10 Layout of shock-tube facility (from Dunn et al. (1994)). 59
1.11 Comparison of predictions and measurements of time-averaged Stanton numbers for GE Aircraft Engine turbine vane geometry (from Haldeman and Dunn (2004)). 60
1.12 Layout of typical linear cascade (from Häring et al. (1995)). 61
1.13 Schlieren image from Rolls Royce linear cascade (from Bryanston Cross et al. (1983)). 62
1.14 Layout of four-passage linear cascade (from Abuaf et al. (1997)). 64
1.15 Layout of double passage cascade (from Radomsky and Thole (2000)). . . . 64
1.16 Layout of single passage linear cascade (from Buck and Prakash (1995)). . . 65
1.17 Button gages installed in rotating rig blade geometry (from Dunn (1986)). . 68

2.1 Three arbitrary blades from an idealized, 2-D infinite cascade with representative computational domains. 76
2.2 Single arbitrary blade with periodic boundary conditions at mid-pitch. . . . 76
2.3 Blade passage with inlet and outlet periodic boundary conditions. 77
2.4 Idealized Single Passage Model. 77

2.5 Experimental single passage model. 79
2.6 Grid and flow conditions for GEAE Inviscid Simulation. 81
2.7 Grid and flow conditions for 2-D RANS Simulation. 82
2.8 Computed isentropic Mach number distributions for experimental turbine blade geometry using standard k-ε turbulence model (courtesy of Athans (2000) and Laskowski (2000)). 83
2.9 Computed isentropic Mach number distributions for experimental turbine blade geometry using Chen and Kim variant of the k-ε turbulence model (courtesy of Athans (2000) and Laskowski (2000)). 84
2.10 Definition of axial location. 84
2.11 Mach number contours for 2-D infinite cascade viscous simulation (courtesy of Laskowski (2000)) 85
2.12 Streamlines from infinite cascade simulation as calculated and rotated by the inlet angle for implementation in the single passage model (courtesy of Laskowski (2000)) 85
2.13 Sample grid and boundary conditions for single passage model design. . . . 87
2.14 Example of a bleed separation bubble near the stagnation point on the suction side wall. 89
2.15 Isentropic Mach number distribution comparison for geometry using Buck-Prakash Method. 89
2.16 Comparison of Mach number contours for ideal and Buck and Prakash design single passage models. 90
2.17 Contour plot of Mach number difference between infinite cascade and Buck and Prakash single passage ($\epsilon_{M_{ic}} = \frac{M_{IC}}{M_{B-P}} - 1$). 91
2.18 Demonstration of the effect of rotation of pressure side straight tailboard. . 92
2.19 Comparison of inlet walls defined by Buck and Prakash and new single passage design approaches. 94
2.20 Comparison of M_{is} distributions for Buck and Prakash and new single passage design approaches. 94
2.21 Comparison of $C_f = \frac{\tau_w}{\frac{1}{2}\rho\tilde{u}_\infty^2}$ distributions for Buck and Prakash and new single passage design approaches. ($\rho = \frac{P(s)}{RT(s)}$, $\tilde{u}_\infty = M_{is}\sqrt{\gamma RT(s)}$) 96
2.22 Comparison of Mach number contours for ideal single passage model and single passage with periodic tailboards. 97

2.23 Contour plot of error in Mach number between infinite cascade and 2-D RANS of single passage with periodic boundary conditions ($\epsilon_{M_{IC}} = \frac{M_{IC}}{M_{2DRANS}} - 1$). 98
2.24 Computed trailing edge streamlines from single passage calculation with periodic exit boundaries. These are used to design the tailboards. 99
2.25 Definition of rotation angles for pressure and suction side blade surfaces. Complete blades are shown in this figure for ease of identification. 99
2.26 Comparison of M_{is} distributions for various pressure tailboard angles. . . . 100
2.27 Contour plots of Mach number for infinite cascade and 2-D RANS-design single passage with $\phi_{\delta,ps} = 1.90°$. 101
2.28 Contour plot of error in Mach number between infinite cascade and 2-D RANS-design single passage with $\phi_{\delta,ps} = 1.90°$ ($\epsilon_{M_{IC}} = \frac{M_{IC}}{M_{2DRANS}} - 1$). . . . 103
2.29 Contour plot of error in Mach number between infinite cascade and 2-D RANS-design single passage with $\phi_{\delta,ps} = 0.3°$ ($\epsilon_{M_{IC}} = \frac{M_{IC}}{M_{2DRANS}} - 1$). 103
2.30 Contour plot of error in TKE between infinite cascade and 2-D RANS-design single passage with $\phi_{\delta,ps} = 0.3°$ ($\epsilon_{TKE_{IC}} = \frac{TKE_{IC}}{TKE_{2DRANS}} - 1$). 104
2.31 Generic form of supersonic diffuser for model exit. 105
2.32 Examination of effect of grid resolution on M_{is} distribution. 107
2.33 Contour plot of error in Mach number between coarse (57600 cells) and fine (230400 cells) 2-D RANS simulations of full geometry single passage ($\epsilon_{M_{GR}} = \frac{M_{2DRANS,fine}}{M_{2DRANS,coarse}} - 1$). 108
2.34 Full and truncated computational domains with applied boundary conditions. 109
2.35 Examination of effect of bellmouth truncation on M_{is} distribution. 110
2.36 Simplified 3D computational grid with applied boundary conditions. 111
2.37 Comparison of M_{is} distribution at $Z' = 0.0$ (centerline) to 2-D simulation and infinite cascade results. 112
2.38 Comparison of M_{is} distributions at $Z' = 0.0$ (centerline), $Z' = -0.25$ and $Z' = -0.5$ (endwall). 112
2.39 Comparison of M_{is} distributions at $Z' = 0.0$ (centerline), $Z' = -0.375$ and $Z' = -0.5$ (endwall). 113
2.40 Comparison of M_{is} distributions at $Z' = 0.0$, $Z' = -0.4375$ and $Z' = -0.5$. 113
2.41 $\mathcal{Q} = 1(10)^8$ isosurface showing formation of vortical structures due to endwall boundary layer-stagnation point interaction. 115

2.42 Reverse angle view of $\mathcal{Q} = 1(10)^8$ isosurface showing formation of vortical structures due to endwall boundary layer-stagnation point interaction. . . . 116
2.43 Three-dimensional separation of a boundary layer entering a turbine cascade (from Langston (1980)). 117
2.44 3-D plot of isosurface $\mathcal{S} = 0.10$. 118
2.45 Schematic of single passage experiment. 119
2.46 Figure of various views of exhaust manifold. 120
2.47 Figure of pressure side bleed fitting installed on pressure side measurement surface. 121
2.48 Picture of pressure side bleed fitting. 122
2.49 Picture of suction side bleed fittings. 122
2.50 Flow system preceding single passage model (from Mukerji and Eaton (2002)). 124
2.51 Schematic of integrated diffuser and plenum for the single passage model designed by Mukerji and Eaton (2002). 126
2.52 Pictures of turbulence grid designed by DeGraaff (2000). 127
2.53 Figure of the overall flow system, showing the exhaust system for the experiment. 128
2.54 Orifice plate runs for measuring boundary layer bleed mass flow rates. . . . 128
2.55 Orifice fitting from Miller (1983). 129
2.56 Picture showing installed boundary layer bleed orifice plate runs. 129
2.57 Picture of liquid CO_2 dewar system. 130
2.58 Picture of Plexiglas tools for ensuring concentricity between orifice plate bore and pipe. 131
2.59 Picture heat exchanger bath, consisting of five gallon container, immersion heater and copper tube coil. 132
2.60 Plot of ideal and measured mass flow rates as a function of pipe ID Reynolds number ($Re_{D_{pipe}}$) for orifice plate run #1. 134
2.61 Plot of ideal and measured mass flow rates as a function of pipe ID Reynolds number ($Re_{D_{pipe}}$) for orifice plate run #2. 135
2.62 Plot of directly computed and fitted discharge coefficients as a function of pipe ID Reynolds number ($Re_{D_{pipe}}$) for orifice plate run #1. 136
2.63 Plot of directly computed and fitted discharge coefficients as a function of pipe ID Reynolds number ($Re_{D_{pipe}}$) for orifice plate run #2. 136

2.64 Picture of single passage traverse holding Pitot probe, inserted through pressure side inlet wall. 140
2.65 Schematic of profile directions for single passage inlet. 140
2.66 Plot calibration curve for ρu vs. $\dot{m}$ at the center of the single passage inlet without the turbulence grid installed. 144
2.67 Plot calibration curve for ρu vs. $\dot{m}$ at the center of the single passage inlet with the turbulence grid installed. 144
2.68 Plot of Mach number from pressure side to suction side inlet wall along centerline of channel. 151
2.69 Plot of Mach number from endwall to endwall wall along centerline of channel. 152
2.70 Plot of static temperature profile expressed as $\frac{T(Y')}{T_{o,plenum}}$ from pressure side to suction side inlet wall along centerline of channel. 152
2.71 Plot of static temperature profile expressed as $\frac{T(Y')}{T_{o,plenum}}$ from endwall to endwall wall along centerline of channel. 153
2.72 Plot of velocity profile expressed as $\frac{\overline{u}}{u_{nom}}$ from pressure side to suction side inlet wall along centerline of channel. 153
2.73 Plot of velocity profile expressed as $\frac{\overline{u}}{u_{nom}}$ from endwall to endwall wall along centerline of channel. 154
2.74 Plot of total pressure profile expressed as $\frac{P_\circ(Y')}{P_{\circ,plenum}}$ from pressure side to suction side inlet wall along centerline of channel. 155
2.75 Plot of total pressure profile expressed as $\frac{P_\circ(Y')}{P_{\circ,plenum}}$ from endwall to endwall wall along centerline of channel. 155
2.76 Plot of $\frac{P(Y')}{P_{o,plenum}}$ from pressure side to suction side inlet wall along centerline of channel. 156
2.77 Plot of $\frac{P(Y')}{P_{o,plenum}}$ from endwall to endwall wall along centerline of channel. . 156
2.78 Plot of static density profile expressed as $\frac{\rho(Y')}{\rho_{\circ,plenum}}$ from pressure side to suction side inlet wall along centerline of channel. 157
2.79 Plot of static density profile expressed as $\frac{\rho(Y')}{\rho_{\circ,plenum}}$ from endwall to endwall wall along centerline of channel. 157
2.80 Measurements of turbulence intensity $TI\%$ from pressure inlet wall to suction side inlet wall. 158
2.81 Measurements of turbulence intensity $TI\%$ from pressure inlet wall to suction side inlet wall. 159

2.82 Power spectrum at various inlet velocities and low turbulence condition. . . 160
2.83 Power spectrum at various inlet velocities and high turbulence condition. . 161
2.84 Autocorrelation function f_{xx} at various inlet velocities and low turbulence condition. 162
2.85 Autocorrelation function f_{xx} at various inlet velocities and high turbulence condition. 162
2.86 Measurements of integral length scale ℓ from pressure inlet wall to suction side inlet wall for low turbulence condition. 164
2.87 Measurements of integral length scale ℓ from endwall to endwall for low turbulence condition. 164
2.88 Measurements of $\frac{T_E}{t_\circ}$ from pressure inlet wall to suction side inlet wall for low turbulence condition. 165
2.89 Measurements of turbulence intensity $TI\%$ from pressure inlet wall to suction side inlet wall for low turbulence condition. 165
2.90 Measurements of M_{is} for low turbulence condition. 166
2.91 Measurements of M_{is} for high turbulence condition 166

3.1 Picture of ITI Borescope with single-chip $\frac{1}{4}$" CCD camera attached and detailed view of the rotary mirror sleeve assembly. 169
3.2 Picture of a fiberscope (Imaging Products Group (2004)). 169
3.3 Single passage model viewing wells. 171
3.4 Borescope window pieces. 174
3.5 Suction side window piece. 175
3.6 Schematic of borescope illumination and viewing optical system. 176
3.7 Picture of lighting and viewing borescope positioning systems. 176
3.8 Measured M_{is} distribution along pressure side wall with suction side window installed – low turbulence case. 177
3.9 Measured M_{is} distribution along pressure side wall with suction side window installed – high turbulence case. 178
3.10 Pressure side geometry calibration piece. 181
3.11 Probable organization of the cholesteric phase (from Fergason (1966a)). . . 183

3.12 Variation of wavelength of maximum reflectance and molecular state as a function of temperature for a typical TLC mixture (from Anderson and Baughn (2004) and Parsley (1991a)). 184
3.13 Definition of angles $\phi_{TLC,i}$ and $\phi_{TLC,s}$ with respect to a TLC-coated surface. 185
3.14 Lighting and viewing angle effects on wavelength of maximum reflectance (derived from Fergason (1968)). 186
3.15 Schematic of pressure and suction side copper calibrator pieces. 194
3.16 Pressure side copper calibrator installed in single passage model. 195
3.17 Calibrator thermoelectric cooler power circuit (modeled after Elkins et al. (2001)). 196
3.18 Simplified thermistor circuit. 197
3.19 Maxim ICL7663 Voltage regulator for thermistor measurement circuit. . . . 197
3.20 Maxim DG406 16-channel CMOS analog multiplexer for thermistor circuit. 197
3.21 Overall multi-thermistor circuit. 198
3.22 Initial and aged HLX tungsten halogen lamps. 201
3.23 $\overline{R}$, $\overline{G}$, $\overline{B}$ curves showing degradation effects of HLX lamp illumination. . . . 202
3.24 Q curves showing degradation effects of HLX lamp illumination. 202
3.25 Eiko and Ushio EKE lamps. 203
3.26 $\overline{\overline{R}}$, $\overline{\overline{G}}$, $\overline{\overline{B}}$ curves for EKE EIKO lamps, showing negligible illumination degradation. 204
3.27 Q curves for EKE EIKO lamps, showing negligible illumination degradation. 204
3.28 Linear transformation operations accounting for borescope mirroring and rotation effects. 206
3.29 Linear transformation operations accounting for borescope mirroring and rotation effects. 209
3.30 Calibration grid for zone #1. 211
3.31 Calibration grid for zone #4. 212
3.32 Effect of reference value on $Q = f(\overline{R}$, $\overline{G}$, and $\overline{B})$ curve. 214
3.33 Effect of reference value on $\overline{R}$, $\overline{G}$, and $\overline{B}$ curves. 214
3.34 $\overline{\overline{R}}$, $\overline{\overline{G}}$ and $\overline{\overline{B}}$ curves for two calibration cells in zone #1. 216
3.35 Q, S and I curves for two calibration cells in zone #1. 216
3.36 $\overline{\overline{R}}$, $\overline{\overline{G}}$ and $\overline{\overline{B}}$ curves for three calibration cells in zones #1 and #2. 217
3.37 Q curves for three calibration cells in zones #1 and #2. 217

3.38 Calibration grid for zone #2. 218
3.39 Histograms of calibration cell temperatures for zone # 1 imaging system setting. 220
3.40 Effect of borescope repositioning on $\overline{\overline{R}}$, $\overline{\overline{G}}$ and $\overline{\overline{B}}$ curves. 221
3.41 Effect of borescope repositioning on $Q = f(\overline{\overline{R}}, \overline{\overline{G}}, \overline{\overline{B}})$. 221
3.42 Zone #1 spatial grid, mapping image pixels to spatial coordinates. 223
3.43 Overview of background grid interpolation process. 224
3.44 Spanwise-averaged calibrator surface temperatures ($\overline{T}(s_c)$) at various set temperatures. 225
3.45 Plot of difference between spanwise-averaged and set temperatures ($\overline{T}(s_c) - T_{set}$) at $T_{set} = 26.2$°C. 226
3.46 Plot of difference between spanwise-averaged and set temperatures ($\overline{T}(s_c) - T_{set}$) at $T_{set} = 28.1$°C. 226
3.47 Plot of difference between spanwise-averaged and set temperatures ($\overline{T}(s_c) - T_{set}$) at $T_{set} = 30.0$°C. 226
3.48 Plot of difference between spanwise-averaged and set temperatures ($\overline{T}(s_c) - T_{set}$) at $T_{set} = 34.0$°C. 227
3.49 Sample spatially-resolved temperature map and TLC-painted copper calibrator surface for comparison. 228
3.50 Plot comparing spanwise-averaged recovery temperature measurements versus prediction suggested from Deissler and Loeffler (1958). 229
3.51 Plot showing the difference $T_{rec,TLC} - T_{rec,Predicted}$ with $T_o = 27.6$°C. . . . 229
3.52 Plot showing the difference $T_{rec,TLC} - T_{rec,Predicted}$ with $T_o = 31.5$°C. . . . 230
3.53 Plot showing the difference $T_{rec,TLC} - T_{rec,Predicted}$ with $T_o = 33.6$°C. . . . 230
3.54 Picture of Ren Shape 450 pressure side wall substrate for heat flux film. . . 236
3.55 Cross-sectional view of heating film. 237
3.56 Masks for the heat flux surface. 238
3.57 Clamping arrangement for heat flux surface. 238
3.58 Pictures of uncooled and cooled heat flux surfaces. 240
3.59 Schematic of compound angle round hole film cooling definition angles. . . . 241
3.60 Picture of Plexiglas fixtures for heat flux surface film cooling holes. 242
3.61 Schematic of assembled heat flux surface. 242
3.62 Schematic of current sense resistor circuit. 243

4.1 Measured spatially-resolved maps of $T_{rec}(Z', s_c/c_{blade})$ with $T_{\circ} = 31.0°$ for low and high turbulence cases (in $°C$). 246
4.2 Measured spanwise-averaged $\overline{T_{rec}}$ distributions for low and high turbulence cases with $T_{\circ} = 31.0°$C. 247
4.3 Computed $T_{rec}(s_c/c_{blade})$ distributions for airfoil pressure side surface using a range of turbulence models with varying inlet $TI\%$, $\frac{\ell}{c_{blade}}$ and Prandtl numbers. 248
4.4 Computed $T_{rec}(s_c/c_{blade})$ distributions for airfoil pressure side surface using Chen and Kim 1987 variant of k-ε with varying values of Pr_t. 249
4.5 Computed $T_{rec}(s_c/c_{blade})$ distributions for airfoil pressure side surface using Medic and Durbin 2002a implementation of k-ω with varying values of Pr_t. 249
4.6 Measured spanwise-averaged $\overline{T_w}(s_c/c_{blade})$ distributions for low turbulence cases with various heat fluxes applied. 252
4.7 Measured spatially-resolved maps of $T_w(Z', s_c/c_{blade})$ at various heat flux settings (in $°C$). 253
4.8 Measured spatially-resolved maps of $h(Z', s_c/c_{blade})$ at various heat flux settings (in $\frac{W}{m^2 \cdot K}$). 255
4.9 Measured spanwise-averaged $\overline{h}(s_c/c_{blade})$ distributions for low turbulence case with heat fluxes $q'' = 6.12\frac{kW}{m^2}$ and $q'' = 7.60\frac{kW}{m^2}$ applied. 256
4.10 Measured spanwise-averaged $\overline{h}(s_c/c_{blade})$ distributions for low turbulence case with heat fluxes $q'' = 7.60\frac{kW}{m^2}$ and $q'' = 8.91\frac{kW}{m^2}$ applied. 256
4.11 Measured spanwise-averaged $\overline{h}(s_c/c_{blade})$ distributions for low turbulence case with heat fluxes $q'' = 8.91\frac{kW}{m^2}$ and $q'' = 8.97\frac{kW}{m^2}$ applied. 257
4.12 Measured spanwise-averaged $\overline{h}(s_c/c_{blade})$ distributions for low turbulence case with heat fluxes $q'' = 8.97\frac{kW}{m^2}$ and $q'' = 12.70\frac{kW}{m^2}$ applied. 257
4.13 Measured spanwise-averaged $\overline{T_w}(s_c/c_{blade})$ distributions for low and high turbulence cases with heat fluxes $q'' = 31.0°$. 259
4.14 Measured spanwise-averaged $\overline{T_w}(s_c/c_{blade})$ distributions for low and high turbulence cases with various heat fluxes applied. 260
4.15 Measured spatially-resolved maps of $T_w(Z', s_c/c_{blade})$ at various heat flux settings with high turbulence flow conditions (in $°C$). 261
4.16 Measured spatially-resolved maps of $h(Z', s_c/c_{blade})$ at various heat flux settings (in $\frac{W}{m^2 \cdot K}$). 262

4.17 Measured spanwise-averaged $\overline{h}(s_c/c_{blade})$ distributions for low and high turbulence cases at various heat flux settings. 263
4.18 Measured spanwise-averaged $\overline{h}(s_c/c_{blade})$ distributions for low and high turbulence cases at various heat flux settings. 263
4.19 Measured spanwise-averaged $\overline{h}(s_c/c_{blade})$ distributions for low and high turbulence cases at various heat flux settings. 264
4.20 Computed and measured spanwise-averaged $\overline{h}(s_c/c_{blade})$ distributions at various heat flux settings. 265
4.21 Comparison of baseline M_{is} distribution with measured suction side M_{is} with $q'' = 12.9\frac{kW}{m^2}$. 267

5.1 Difference between measured and predicted spanwise-averaged isoenergetic condition temperature distribution ($\overline{T_{iso}} - T_{rec}(M_{is})$). 283
5.2 Plots of measured ($\overline{T_{iso}}$) and predicted spanwise-averaged isoenergetic condition temperature distributions ($T_{rec}(M_{is})$). 284
5.3 Plots of measured ($\overline{T_{iso}}$) and predicted spanwise-averaged isoenergetic condition temperature distributions ($T_{rec}(M_{is})$) for experimental cases 3, 4, 5, and 7. 285
5.4 Difference between measured and predicted spanwise-averaged isoenergetic condition temperature distribution ($\overline{T_{iso}} - T_{rec}(M_{is})$) for experimental cases 3, 4, 5, and 7. 285
5.5 Plots of measured ($\overline{T_{iso}}$) and predicted spanwise-averaged isoenergetic condition temperature distributions ($T_{rec}(M_{is})$) for experimental cases 10, 11, and 12. 286
5.6 Difference between measured and predicted spanwise-averaged isoenergetic condition temperature distribution ($\overline{T_{iso}} - T_{rec}(M_{is})$) for experimental cases 10, 11, and 12. 286
5.7 Plots of measured ($\overline{T_{iso}}$ and predicted spanwise-averaged isoenergetic condition temperature distributions ($T_{rec}(M_{is})$) for experimental cases 10, 9, and 18. 287
5.8 Difference between measured and predicted spanwise-averaged isoenergetic condition temperature distribution ($\overline{T_{iso}} - T_{rec}(M_{is})$) for experimental cases 10, 9, and 18. 288

5.9 Plots of measured ($\overline{T_{iso}}$) and predicted spanwise-averaged isoenergetic condition temperature distributions ($T_{rec}(M_{is})$) for experimental cases 11, 14, 12 and 15. 288
5.10 Difference between measured and predicted spanwise-averaged isoenergetic condition temperature distribution ($\overline{T_{iso}} - T_{rec}(M_{is})$) for experimental cases 11, 14, 12 and 15. 289
5.11 Plots of measured ($\overline{T_{iso}}$) and predicted spanwise-averaged isoenergetic condition temperature distributions ($T_{rec}(M_{is})$) for experimental cases 7, 6, 12 and 13. 289
5.12 Difference between measured and predicted spanwise-averaged isoenergetic condition temperature distribution ($\overline{T_{iso}} - T_{rec}(M_{is})$) for experimental cases 7, 6, 12 and 13. 290
5.13 Plots of measured ($\overline{T_{iso}}(s_c/c_{blade})$) and predicted spanwise-averaged isoenergetic condition temperature distributions ($T_{rec}(M_{is})$) for experimental cases 9, 8, 16 and 18. 290
5.14 Difference between measured and predicted spanwise-averaged isoenergetic condition temperature distribution ($\overline{T_{iso}} - T_{rec}(M_{is})$) for experimental cases 9, 8, 16 and 18. 291
5.15 Spatially-resolved maps of η_T showing effects of blowing ratio for cases 3, 4, 5 and 7. 294
5.16 Spatially-resolved maps of η_T showing effects of blowing ratio for cases 10, 11 and 12. 295
5.17 Plots of $\overline{\eta_T}(s_c/c_{blade})$ showing the effect of blowing ratio for cases 3, 4, 5 and 7. 296
5.18 Plots of $\overline{\eta_T}(s_c/c_{blade})$ showing the effect of blowing ratio for cases 7, 10, 11 and 12. 296
5.19 Spatially-resolved maps of $\eta_{T,iso}$ showing effects of blowing ratio for cases 3, 4, 5 and 7. 297
5.20 Spatially-resolved maps of $\eta_{T,iso}$ showing effects of blowing ratio for cases 10, 11 and 12. 298
5.21 Plots of $\overline{\eta_{T,iso}}$ showing the effect of blowing ratio for cases 3, 4, 5 and 7. . . 299
5.22 Plots of $\overline{\eta_{T,iso}}$ showing the effect of blowing ratio for cases 7, 10, 11 and 12. 299
5.23 Plots of $\overline{\eta}$ showing the effect of blowing ratio for cases 3, 4, 5 and 7. 300
5.24 Plots of $\overline{\eta}$ showing the effect of blowing ratio for cases 7, 10, 11 and 12. . . 301

5.25 Plots of $\overline{\eta_{iso}}$ showing the effect of blowing ratio for cases 3, 4, 5 and 7. . . . 301
5.26 Plots of $\overline{\eta_{iso}}$ showing the effect of blowing ratio for cases 7, 10, 11 and 12. . 302
5.27 Spatially-resolved maps of η_T showing effects of density ratio for cases 9, 18, 14 and 17. 303
5.28 Plots of $\overline{\eta_T}$ showing the effect of injectant for cases 7, 9, 10 and 18. 304
5.29 Plots of $\overline{\eta_{iso}}$ showing the effect of injectant for cases 11, 14, 12 and 17. . . . 304
5.30 Plots of $\overline{\eta_{T,iso}}$ showing the effect of injectant for cases 7, 9, 10 and 18. . . . 305
5.31 Plots of $\overline{\eta_{T,iso}}$ showing the effect of injectant for cases 11, 14, 12 and 17. . . 305
5.32 Plots of $\overline{\eta}$ showing the effect of injectant for cases 7, 9, 10 and 18. 306
5.33 Plots of $\overline{\eta}$ showing the effect of injectant for cases 11, 14, 12 and 17. 306
5.34 Plots of $\overline{\eta}$ showing the effect of injectant for cases 7, 9, 10 and 18. 307
5.35 Plots of $\overline{\eta_{iso}}$ showing the effect of injectant for cases 11, 14, 12 and 17. . . . 307
5.36 Spatially-resolved maps of η_T showing effects of turbulence level for cases 3, 4, 5 and 7. 308
5.37 Plots of $\overline{\eta_T}$ showing the effect of turbulence for cases 10, 6, 11 and 13. . . . 309
5.38 Plots of $\overline{\eta_T}$ showing the effect of turbulence for cases 8, 6, 17 and 16. 309
5.39 Spatially-resolved maps of h_{iso}, h and $h_{ratio} = \frac{h}{h_{no\ fc}}$. 312
5.40 Plots of $\overline{h}$, $\overline{h_{iso}}$ and $\overline{h_{no\ fc}}$and compared to the uncooled results from section 4.1.3 showing the effect of distortion of heat flux boundary condition. . . . 313
5.41 Spatially-resolved maps of $h_{ratio,2} = \frac{h}{h_{BL=0}}$ showing the effects of blowing ratio for cases 3, 4, 5, and 7. 314
5.42 Spatially-resolved maps of $h_{ratio,2} = \frac{h}{h_{BL=0}}$ showing the effects of blowing ratio for cases 10, 11 and 12. 315
5.43 Plots of $\overline{h}_{ratio,2} = \frac{\overline{h}}{h_{BL=0}}$ showing the effect of blowing ratio for cases 3 and 4. 316
5.44 Plots of $\overline{h}_{ratio,2} = \frac{\overline{h}}{h_{BL=0}}$ showing the effect of blowing ratio for cases 5 and 7. 316
5.45 Plots of $\overline{h}_{ratio,2} = \frac{\overline{h}}{h_{BL=0}}$ showing the effect of blowing ratio for cases 10 and 11. 317
5.46 Plots of $\overline{h}_{ratio,2} = \frac{\overline{h}}{h_{BL=0}}$ showing the effect of blowing ratio for cases 11 and 12. 317
5.47 Spatially-resolved maps of $h_{iso,ratio,2} = \frac{h_{iso}}{h_{iso,BL=0}}$ showing the effects of blowing ratio for cases 3, 4, 5, and 7. 319
5.48 Spatially-resolved maps of $h_{iso,ratio,2} = \frac{h_{iso}}{h_{iso,BL=0}}$ showing the effects of blowing ratio for cases 10, 11 and 12. 320

5.49 Plots of $\overline{h}_{iso,ratio,2} = \frac{\overline{h}_{iso}}{h_{iso,BL=0}}$ showing the effect of blowing ratio for cases 3 and 4. 321
5.50 Plots of $\overline{h}_{iso,ratio,2} = \frac{\overline{h}_{iso}}{h_{iso,BL=0}}$ showing the effect of blowing ratio for cases 5 and 7. 321
5.51 Plots of $\overline{h}_{iso,ratio,2} = \frac{\overline{h}_{iso}}{h_{iso,BL=0}}$ showing the effect of blowing ratio for cases 10 and 11. 322
5.52 Plots of $\overline{h}_{iso,ratio,2} = \frac{\overline{h}_{iso}}{h_{iso,BL=0}}$ showing the effect of blowing ratio for cases 11 and 12. 322
5.53 Spatially-resolved maps of $h_{ratio,2} = \frac{h}{h_{BL=0}}$ showing the effects of density ratio for cases 9, 18, 14, and 17. 323
5.54 Plots of $\overline{h}_{ratio,2} = \frac{\overline{h}}{h_{BL=0}}$ showing the effect of density ratio for cases 9 and 18. 324
5.55 Plots of $\overline{h}_{ratio,2} = \frac{\overline{h}}{h_{BL=0}}$ showing the effect of density ratio for cases 18, 14 and 17. 324
5.56 Spatially-resolved maps of $h_{iso,ratio,2} = \frac{h_{iso}}{h_{iso,BL=0}}$ showing the effects of density ratio for cases 9, 18, 14, and 17. 326
5.57 Plots of $\overline{h}_{iso,ratio,2} = \frac{\overline{h}_{iso}}{h_{iso,BL=0}}$ showing the effect of density ratio for cases 9 and 18. 327
5.58 Plots of $\overline{h}_{iso,ratio,2} = \frac{\overline{h}}{h_{iso,BL=0}}$ showing the effect of density ratio for cases 18, 14 and 17. 327
5.59 Spatially-resolved maps of $h_{ratio,2} = \frac{h}{h_{BL=0}}$ showing the effects of turbulence for cases 6, 13, 8, and 16. 328
5.60 Plots of $\overline{h}_{ratio,2} = \frac{\overline{h}}{h_{BL=0}}$ showing the effect of turbulence for cases 6 and 13. 329
5.61 Plots of $\overline{h}_{ratio,2} = \frac{\overline{h}}{h_{BL=0}}$ showing the effect of density ratio for cases 8 and 16. 329
5.62 Spatially-resolved maps of $h_{iso,ratio,2} = \frac{h}{h_{BL=0}}$ showing the effects of turbulence for cases 6, 13, 8, and 16. 331
5.63 Plots of $\overline{h}_{iso,ratio,2} = \frac{\overline{h}_{iso}}{h_{iso,BL=0}}$ showing the effect of turbulence for cases 6 and 13. 332
5.64 Plots of $\overline{h}_{iso,ratio,2} = \frac{\overline{h}_{iso}}{h_{iso,BL=0}}$ showing the effect of density ratio for cases 8 and 16. 332

B.1 Schematic of wet-bulb humidity sensor. 352

C.1 Flat plate computational domain. 359

C.2 Computed laminar flow, flat plate recovery factors (r_∞) with $Pr = 1.0$, $c_p = 1.0\frac{kJ}{kg \cdot K}$. 360
C.3 Computed freestream Mach number distributions (M_{cntrl}) with $Pr = 1.0$, $c_p = 1.0\frac{kJ}{kg \cdot K}$. 360
C.4 Computed pressure distributions ($\frac{P}{P_\circ}$) with $Pr = 1.0$, $c_p = 1.0\frac{kJ}{kg \cdot K}$. 361
C.5 Computed and predicted flat plate skin friction coefficients (C_f) with $Pr = 1.0$, $c_p = 1.0\frac{kJ}{kg \cdot K}$. 362
C.6 Computed flat plate skin friction coefficients (C_f) with $Pr = 0.71$, $c_p = 1.0\frac{kJ}{kg \cdot K}$. 362
C.7 Computed laminar flow, flat plate recovery factors (r_∞) with $Pr = 0.71$, $c_p = 1.0\frac{kJ}{kg \cdot K}$. 363
C.8 Computed $\frac{T_w}{T_\circ}$ profiles for various flow conditions and applied heat fluxes with $Pr = 0.71$, $c_p = 1.0\frac{kJ}{kg \cdot K}$. 364
C.9 Computed h distributions with $Pr = 0.71$, $c_p = 1.0\frac{kJ}{kg \cdot K}$ with $M = 0.8$ and $M = 1.7$. 364
C.10 Computed flat plate skin friction coefficients (C_f) with $Pr = 0.71$, $c_p = 1.0\frac{kJ}{kg \cdot K}$ at two heat flux settings with $M = 0.8$. 365
C.11 Computed flat plate skin friction coefficients (C_f) with $Pr = 0.71$, $c_p = 1.0\frac{kJ}{kg \cdot K}$ at two heat flux settings with $M = 1.7$. 365
C.12 Computed pressure distributions ($\frac{P}{P_\circ}$) with $Pr = 0.71$, $c_p = 1.0\frac{kJ}{kg \cdot K}$ at two heat flux settings with $M = 0.8$ and $M = 1.7$. 366
C.13 Computed M_{is} distributions ($\frac{P}{P_\circ}$) with $Pr = 0.71$, $c_p = 1.0\frac{kJ}{kg \cdot K}$ at two heat flux settings with $M = 0.8$ and $M = 1.7$. 366
C.14 Computed $h_{ratio} = \frac{h_{q_1''}}{h_{q_2''}}$ distributions with $Pr = 0.71$, $c_p = 1.0\frac{kJ}{kg \cdot K}$ with $M = 0.8$ and $M = 1.7$. 367
C.15 Computed Nu_x distributions with $Pr = 0.71$, $c_p = 1.0\frac{kJ}{kg \cdot K}$ with q_1'' and q_2'' surface heat fluxes applied and $M = 0.8$ and $M = 1.7$. 368
C.16 Computed flat plate recovery factors (r_∞) with $Pr = 0.71$, $c_p = 1.0\frac{kJ}{kgK}$ and $k = 0.026\frac{W}{m \cdot K}$. 369
C.17 Computed h distributions with $Pr = 0.71$, $c_p = 1.0\frac{kJ}{kg \cdot K}$ and $k = 0.026\frac{W}{m \cdot K}$ with $M = 0.8$. 370
C.18 Computed $h_{ratio} = \frac{h_{q_1''}}{h_{q_2''}}$ distributions with $Pr = 0.71$, $c_p = 1.0\frac{kJ}{kg \cdot K}$ and $k = 0.026\frac{W}{m \cdot K}$ with $M = 0.8$. 370

C.19 Computed $\frac{T_w}{T_\circ}$ profiles for various flow conditions and applied heat fluxes with $Pr = 0.71$, $c_p = 1.0\frac{kJ}{kg \cdot K}$ and $k = 0.026\frac{W}{m \cdot K}$ with $M = 0.8$. 371
C.20 Computed Nu_x distributions with $Pr = 0.71$, $c_p = 1.0\frac{kJ}{kg \cdot K}$ and $k = 0.026\frac{W}{m \cdot K}$ with q_1'' and q_2'' surface heat fluxes applied and $M = 0.8$. 372
C.21 Computed recovery factors r_∞ distributions using k-ε Chen and k-ω turbulence models with $Pr = 1.0$, $Pr_t = 1.0$ and $c_p = 1.0\frac{kJ}{kg \cdot K}$ and $M = 0.8$ and $M = 1.7$. 373
C.22 Computed flat plate skin friction coefficients (C_f) using k-ε Chen and k-ω turbulence models $Pr = 1.0$, $Pr_t = 1.0$ and $c_p = 1.0\frac{kJ}{kg \cdot K}$. 373
C.23 Computed turbulent flat plate boundary layer recovery factors r_∞ using k-ε as proposed by Chen and Kim (1987) with $Pr = 0.71$ and various values of Pr_t specified. 374
C.24 Computed turbulent flat plate boundary layer recovery factors r_∞ using k-ω as implemented by Medic and Durbin (2002a) with $Pr = 0.71$ and various values of Pr_t specified. 375

Nomenclature

Roman Symbols

A_{ij}	Local velocity tensor	$[\frac{1}{\mathrm{s}}]$
A_H	Heater area	$[\mathrm{m}^2]$
AP	Blade pitch spacing	[m]
AS	Passage aspect ratio	[-]
BL	Blowing or mass flux ratio $= \frac{\rho_j u_j}{\rho_\infty u_\infty}$	[-]
C_f	Skin friction coefficient	[-]
c_p	Specific heat	$[\frac{\mathrm{J}}{\mathrm{kg \cdot K}}]$
c_{blade}	Blade chord length	[m]
d	Film cooling hole diameter	[m]
D	Internal hole diameter	[m]
DR	Density ratio $= \frac{\rho_j}{\rho_\infty}$	[-]
e	Total energy	$[\frac{\mathrm{J}}{\mathrm{kg \cdot K}}]$
h	Heat transfer coefficient	$[\frac{\mathrm{W}}{\mathrm{m^2 \cdot K}}]$
h^i	Enthalpy	$[\frac{\mathrm{J}}{\mathrm{kg \cdot K}}]$
H	Model height	[m]
I	Momentum flux ratio $= \frac{\rho_j u_j^2}{\rho_\infty u_\infty^2}$	[-]
K	Acceleration parameter	[-]
K_p	Proportional control constant	[-]
K_d	Differential control constant	[-]
K_i	Integral control constant	[-]
k	Thermal conductivity	$[\frac{\mathrm{W}}{\mathrm{m \cdot K}}]$
ℓ	Turbulence length scale	[m]

L	Film cooling hole length	[m]
M	Mach number	[-]
$\dot{m}$	Mass flow rate	$[\frac{\mathrm{kg}}{\mathrm{s}}]$
p	Pitch spacing of film cooling holes	[m]
P	Static pressure	[Pa]
$P_\circ$	Stagnation (total) Temperature	[K]
P_H	Heater power	[W]
ΔP	Pressure differential	[Pa]
Pr	Prandtl number	[-]
r	Recovery factor	[-]
s	Surface distance	[-]
s_c	Distance relative to the stagnation point along airfoil surface	[m]
T	Static temperature	[°C]
$T_\circ$	Stagnation (total) temperature	[°C]
TKE	Turbulent kinetic energy	[]
$TI\%$	Turbulence intensity	[-]
V	Voltage	[V]
Re_D	Reynolds number based on hole diameter $= \frac{uD}{\nu}$	[-]

Calligraphic Letters

$\mathcal{D}$	Total diffusion coefficient	$[\frac{\mathrm{m}^2}{\mathrm{s}}]$
$\mathcal{P}$	Perpendicular distance for backloss thermocouples	[m]
$\mathcal{Q}$	Vortical structure visualization parameter	$[\frac{1}{\mathrm{s}^2}]$
$\mathcal{R}$	Radius of curvature	[m]
$\mathcal{S}$	Two dimensionality parameter $(= \frac{\tilde{w}}{\sqrt{\tilde{u}^2+\tilde{v}^2+\tilde{w}^2}})$	[-]

Acronyms

BLE	Boundary Layer Equations
CARH	Compound Angle Round Holes
CRVP	Counter-Rotating Vortex Pair
DAC	Digital-Analog Control
DAQ	Digital Acquisition
DEH	Diffuser-Exit Holes
DNS	Direct Numerical Simulation
DSSN	Downstream Spiral Separation Node Vortices
LES	Large Eddy Simulation
MM	Macro-model for Film Cooling
RANS	Reynolds-Averaged Navier-Stokes
RSM	Reynolds Stress Model
SMC	Second Moment Closure
SGS	Sub-grid Scales
TEC	Thermoelectric Cooler
TLC	Thermochromic Liquid Crystal

Greek Symbols

δ	Uncertainty, or differential element	[]
δ_1	Displacement boundary layer thickness	[m]
η	Adiabatic film cooling effectiveness	[]
γ	Ratio of specific heats $(= \frac{c_v}{c_p})$	[]
ν	Fluid kinematic viscosity	$[\frac{\mathrm{m}^2}{\mathrm{s}}]$
μ	Fluid viscosity	$[\mathrm{Pa} \cdot \mathrm{s}]$
ρ	Density	$[\frac{\mathrm{kg}}{\mathrm{m}^3}]$

τ	Shear stress	[Pa]
θ	Dimensionless temperature	[-]
ζ	Thermal diffusivity	$[\frac{m^2}{s}]$

Subcripts/Superscripts

$()'$	Reynolds-averaged fluctuating value
$()''$	Favre-averaged fluctuating value
$()^+$	Denotes value in wall coordinates or positive perturbation
$()^-$	Denotes negative perturbation
$\tilde{()}$	Mass-averaged value
$\bar{()}$	Time-averaged value
$\circ$	Stagnation (total) condition value
∞	Freestream condition value
c	Coolant condition
i	Row index
iso	Isoenergetic condition
j	Column index, film cooling jet
l	Laminar/molecular value
$MODEL$	Model dimension
$plenum$	Single passage plenum condition value
psb	Pressure side bleed
m	Mass transfer
w	Value at wall
rec	Recovery value
ssb	Suction side bleed

t	Turbulent value
τ	Relating to wall shear stress
$w2$	Hole exit condition

Chapter 1

Introduction

1.1 Introduction to Film Cooling and Thesis Objectives

Film cooling is one technique to protect key gas turbine engine components during operation. The fundamental concept behind this strategy can be presented using the following idealized situation: a cool secondary flow is ejected through a series of holes in a given component. Under the appropriate conditions, the flow from the holes coalesces to form a blanket, or film of cooler air that "insulates" the component from an extremely hot mainstream flow. Another expectation is that the addition of "thermal mass" near the wall via blowing thickens the boundary layer and acts as a heat sink, consequently reducing heat transfer to the wall (Moffat (1987)). This technique may also be used to protect a surface from large radiative heat loads as well. In comparison to other strategies – such as ceramic thermal barrier coatings (TBC) – the general purpose of film cooling is not to protect the surface in the immediate vicinity of the film cooling holes, but the surface downstream of the injection location.

Film cooling has grown in prominence as gas turbine engine operators continually demand improvements in engine performance. As a consequence of the air Brayton cycle, the idealized thermodynamic cycle upon which the gas turbine engine is designed, the most direct manner to improve engine efficiency is to raise the combustor exit temperature. Thus, in many gas turbine engines, the turbine inlet temperature is either at or above the melting point of many of the materials used in construction. This approach, however, reduces the durability of the engine – increasing the turbine inlet temperature increases the likelihood of component failure due to thermal stress. The primary design objective for a given film cooling strategy is to provide the most effective protection for a given component using the least amount of film cooling flow. The more air that is used for film cooling, the less that is available for generating thrust, degrading the efficiency of the engine. Additionally, film cooling may cause aerodynamic losses which would also limit engine efficiency. This overarching constraint affects how designers implement a given film cooling strategy especially with respect to: the delivery mechanism, specifically the shape and location of the film cooling holes for an arbitrary blade design and the desired amount of flow at various operating conditions.

Clearly, to develop the most effective film cooling designs, it would be ideal if designers had the computational capability to accurately model the thermal boundary condition for conjugate models that predict thermal stresses on engine components. This would enable "numerical experiments" without having to build costly facilities and allowing the design of optimal cooling systems, while at the same time providing data for durability analyses. Furthermore, simulations generally have faster turn-around times than experiments, and can easily fit into the aggressive design time frame of gas turbine manufacturers. However, there is currently no computational tool that can perform this task, so designers often have to perform extrapolations or estimates based on limited experimental data.

This thesis presents an experiment to provide highly detailed film cooling performance data for a transonic rotor blade geometry. The ultimate objective of this work is twofold: to further the efforts in computational models for film cooling by providing data suitable for comparison to spatially resolved computations, and to provide an evaluation tool for film cooling designers.

The following sections provide additional background to various film cooling implementation schemes, experimental techniques to evaluate film cooling performance and an overview of current knowledge about film cooling physics and modeling techniques for estimating film cooling performance. Having established this baseline, the specific thesis objectives will be stated.

1.2 Approaches to Film Cooling Design and Implementation

References such as Hill and Petersen (1992) or Lakshiminarayana (1993) give thorough outlines of the overall design procedure for a new aircraft engine. Typically engine designers will have a target overall cycle efficiency, thrust-to-weight ratio and fuel consumption rate. These will be based on consumer requirements for a given aircraft class and the expected usage frequency and duration. An overall engine configuration is then developed, specifying the bypass ratio, the number of compressor and turbine stages, the required pressure ratio per stage, and other necessary parameters. Aerodynamic designers then design blade shapes for both rotor and stator components to achieve the desired pressure rise or drop across each stage of the compressor or turbine, respectively. This process has been well developed over several years and integrates the advanced use of inviscid and viscous simulation techniques to accurately design these components from an aerodynamics perspective (Dunn (2001)).

The focus of the film cooling designer is primarily on the turbine and to a lesser extent, the combustor. Generally, film cooling designers for a commercial aircraft engine company will receive a turbine rotor or stator blade or other component geometry after the aerodynamics design is complete. The flow conditions entering the given stage would have been estimated, such as: flow angle, inlet Mach number, flow stagnation temperature and pressure, and the pressure ratio across the rotor stage (Buck (1999)). The total amount of bypass air available for film cooling would be also specified. This will be of the order of a few percent of the mainstream flow rate (Lakshiminarayana (1993)). However, there would still be significant uncertainty of the level of inlet turbulence, and the flow temperature profile exiting the combustor section. Frequently, large-scale structures of burning fuel (termed as “hot streaks”) exit the combustor and impact the turbine, affecting the heat transfer rates to key engine components (Khalatov et al. (1993)). Such phenomena are extremely difficult, if not impossible, to predict with current combustion modeling techniques. Thus, such an issue can only be diagnosed once the engine has been built and put into service.

Figures 1.1 and 1.2 show the two primary classes of film cooling holes described in the open literature used on real engine blades, compound angle round and diffuser-shaped exit holes. In actuality, these two classes can be combined, i.e. a diffuser-shaped exit may be placed on a compound round hole, if there is believed to be benefits of such an implementation in a given situation.

For compound angle holes, two angles define the orientation of the simplest film cooling hole: the first angle α defines the hole inclination with respect to the wall and the second angle β defines the hole axis orientation with respect to the freestream direction. Diffuser-shaped exit holes come in a variety of shapes, specified by experience and manufacturing capabilities. The one presented in figure 1.2 displays the common features of these holes. Φ is the streamwise diffusion angle, while Ψ is the lateral diffusion angle. Goldstein et al. (1974) was the first paper in the open literature to document the primary differences and benefits of holes with a diffuser-shaped exit. The seminal observation from this work was that for given flow conditions such holes give better film cooling performance by limiting the penetration of the film cooling jet into the mainstream and promoting a jet trajectory which was nearly tangential to the cooled surface.

An obvious question that can be asked is “Why use discrete film cooling holes and not

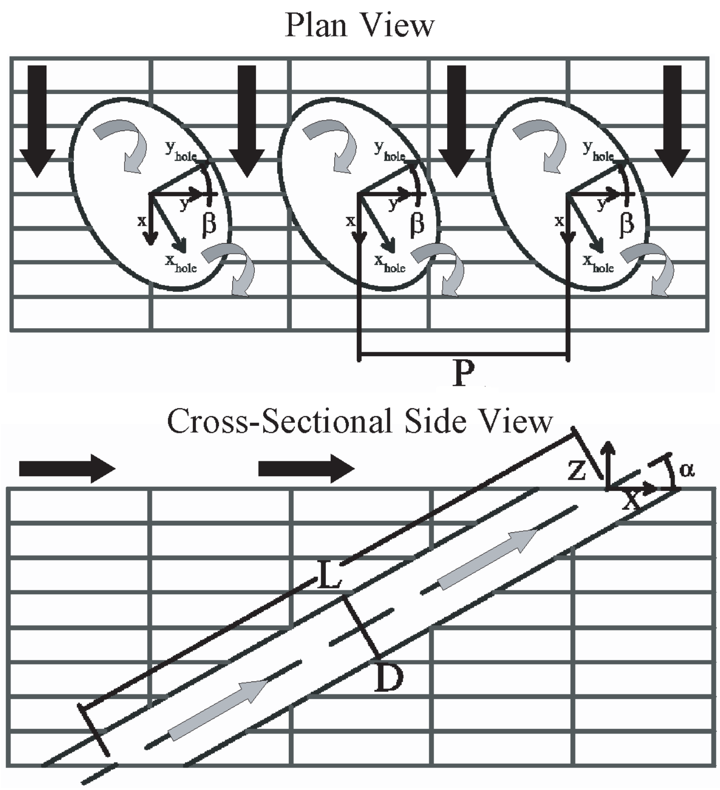

Figure 1.1: Example of a compound angle round (CARH) film cooling hole.

slots?". First, there are substantial modeling advantages to using slots, Goldstein (1971) documents that slots traditionally give higher effectiveness and are much easier to model. Secondly, Goldstein (1971) presents several well established, and successful models and correlations for slot film cooling. However, design considerations, such as maintaining the structural integrity of the cooled component, make using such an approach in actual turbine components impractical.

Two parameters are used to identify the film cooling performance for a given design, the adiabatic film cooling effectiveness (other terms that are used in the literature are the film cooling effectiveness or film effectiveness, these are used interchangeably in this thesis), η and the convective heat transfer coefficient, h. These parameters are defined as in Goldstein (1971) as:

$$\eta = \frac{T_{aw} - T_{rec}}{T_{w_2} - T_{rec}} \tag{1.1}$$

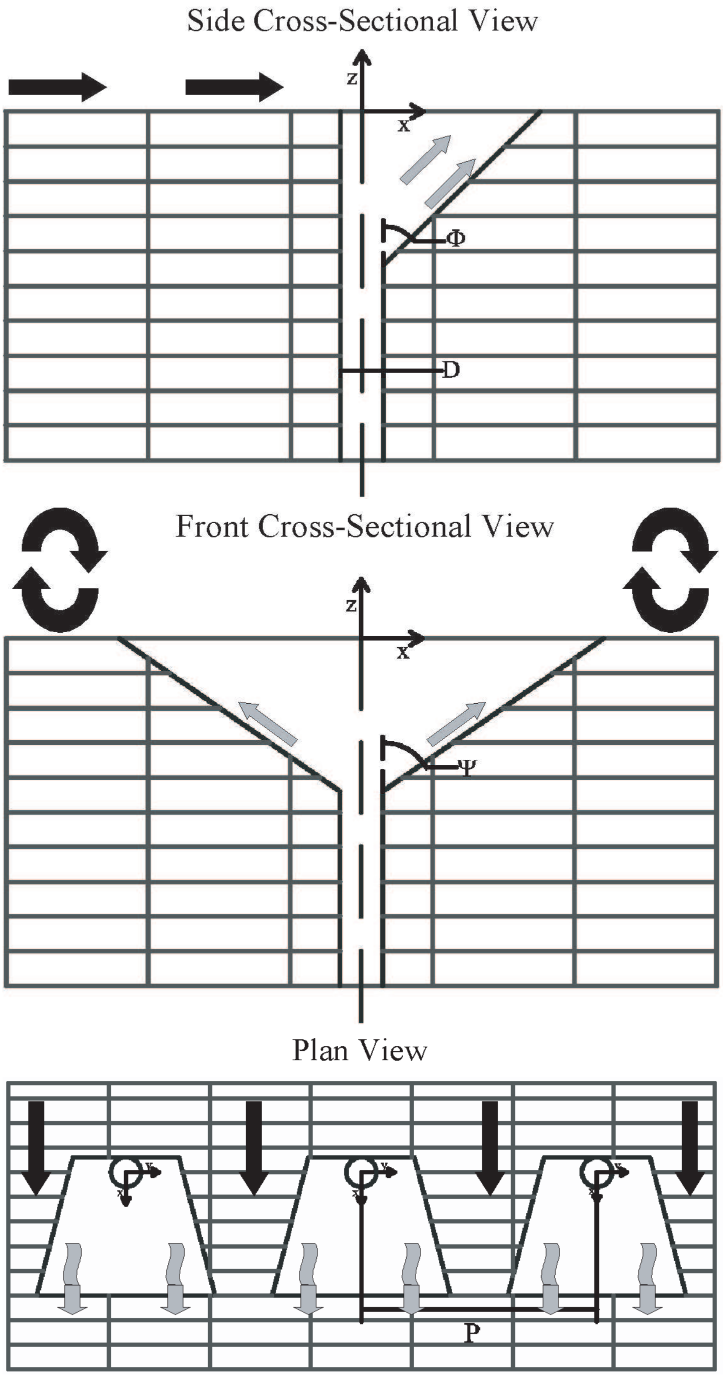

Figure 1.2: Example of a diffuser exit (DEH) film cooling hole.

$$q'' = h(T_{aw} - T_w) \tag{1.2}$$

where T_{aw} is the adiabatic wall temperature distribution of the film cooled surface, T_{rec} is the recovery temperature of the adiabatic surface without any film cooling and T_{w2} is the temperature of the secondary flow at the exit of the film cooling hole. T_w is the temperature along the surface with a constant heat flux applied and equal coolant and mainstream total temperatures ($T_{o,c} = T_{o,\infty}$). The first parameter, the adiabatic film effectiveness, gives designers a measure of the coverage performance of a given film cooling strategy. The heat transfer coefficient is typically estimated using the component geometry in question without film cooling. This is because is it is far easier to obtain this parameter using thoroughly developed boundary layer codes such as STAN7 (Crawford and Kays (1976)). Luo and Lakshminarayana (1997) demonstrated the general accuracy of this approach using a range of computational models to predict surface heat transfer and skin friction on gas turbine engine components. Nevertheless, it has been documented that under certain conditions, film cooling can dramatically increase the heat transfer coefficient, increasing the heat transfer rate to the blade. The significant dilemma facing those in the film cooling community is to develop tools that accurately calculate the adiabatic film cooling effectiveness and heat transfer coefficient with film cooling for arbitrary blade geometries and conditions. Both these values are important as they are used for the implementation of thermal boundary conditions to estimate the metal temperature distribution of a component during operation and to develop durability predictions. The heat flux boundary conditions for these calculations is constructed by first inserting equation 1.1 into equation 1.2, solving for T_{aw} in terms of η which gives (Buck (1999)):

$$q'' = h(\eta T_{w_2} - T_{rec}(1 - \eta) - T_w) \tag{1.3}$$

Garg and Gaugler (1996) demonstrated current deficiencies in techniques used to compute the heat transfer coefficient for a modern, transonic rotor blade. These authors applied 3-D RANS (Reynolds-Averaged Navier-Stokes) calculations with rotation to a Rolls Royce ACE engine turbine blade geometry with several rows of film cooling holes and a trailing edge film cooling slot installed on the upstream nozzle guide vane. These results were compared to measurements from a short duration, transient rotating annular cascade presented by Abhari and Epstein (1994). Several turbulence models were implemented in the RANS calculations, the k-ω model presented by Wilcox (1994), the q-ω model developed by Coakley

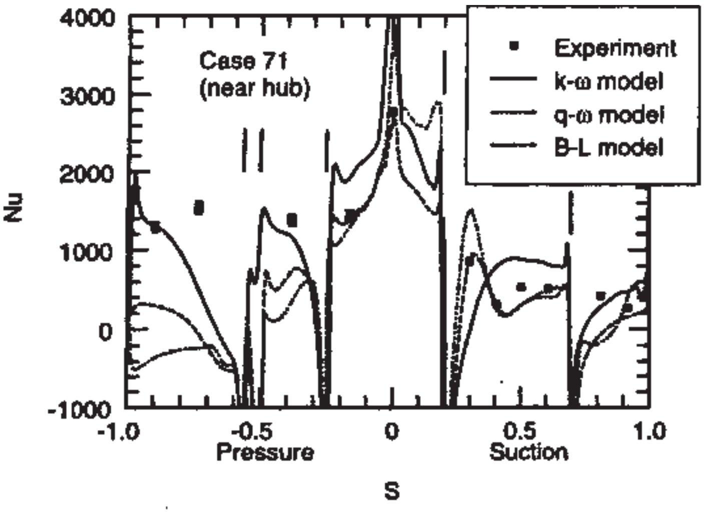

Figure 1.3: Comparison of Rolls Royce ACE trailing edge film cooling tests by Abhari and Epstein (1994) with 3-D RANS simulation of Garg and Gaugler (1996).

(1983) and the zero-equation *B-L* model developed by Baldwin and Lomax (1978). Figure 1.3 displays the experimental results, presented as symbols, and the 3-D RANS simulation results, represented as solid lines. Three issues are apparent from these data and subsequent observations by Garg and Gaugler (1996):

1. There appears to be significant disagreement between the predicted computational and experimental results at some locations, which in some cases exceeds 100 % based on the experimental value and a specific turbulence model.

2. It is unclear if the differences between experimental and simulation results is due to modeling issues, or the inability to specify boundary conditions for the simulation with low-uncertainty.

3. The harsh conditions in the rotating cascade limits the fidelity and resolution of the resulting heat transfer data especially in areas of large spatial gradients in the heat transfer coefficient distribution.

As a result of these shortcomings, designers are left with an incremental design approach, using field experience to refine film cooling design strategies in newer engines. The parameters that the designer can normally modify are: the location of the film cooling holes, the shape of the film cooling holes, and how much combustor bypass air should be ejected from the holes. This approach is based on only a partial understanding of film cooling physics and often leads to unexpected results. This is because film cooling performance depends on a wide variety of mainstream flow parameters, any of which may dominate under differing circumstances. Eckert (1984) argues that such a parameter space requires studies varying only single parameters at one time, and observing its effect. Unfortunately, this approach does not coincide with the design and upgrade time frames for engine companies. Additionally, the complexity of this problem, eliminates the utility of standard correlation techniques, and calls for the use of numerical schemes to directly model the flow physics. Yet it is extremely difficult to construct computational models, or evaluate film cooling hole performance, without obtaining detailed measurements in a flow field that closely represents characteristics of that in an operating engine turbine. Moreover, film cooling can add substantial aerodynamic losses to the performance of the turbine stage as documented by Haller and Camus (1984), Yamamoto et al. (1991) and Lee et al. (1997). In other words, a poorly designed cooling system may protect engine components, but adversely affect the overall performance of the engine.

An examination of experimental studies from the open literature reveals an additional reason that magnifies the continuing need for high-quality data with well-defined boundary conditions, is the presence of conflicting data sets. Such a conflict may be due to one of the three general issues: the flow conditions, the experimental flow and heat transfer boundary conditions or the measurement technique utilized. Accordingly, the subsequent sections will discuss film cooling jet parameters that may affect performance, but also external flow conditions and measurement techniques that may corrupt the result and give misleading trends.

1.3 Thesis Objectives Restated

The subsequent sections present a detailed review of previous literature to further demonstrate that film cooling is an extremely complex problem, and the ability to accurately predict the performance of different cooling systems is vital to advancing turbine designs. Some of these referenced works provide a detailed review of the science of the jet-in-crossflow interaction. This was done to elucidate the individual effects of various parameters on the film cooling performance of various cooling strategies. This information was used as a basis to explain and verify many of the results obtained in this experiment. Furthermore, subsequent sections will also emphasize that the critical roadblock to improving turbomachinery heat transfer modeling is the lack of data collected at engine representative conditions with high-resolution and low-uncertainty. With these problems in mind, the objectives of this thesis are:

1. Develop an experimental facility that can obtain spatially-resolved film cooling performance measurements on a transonic rotor blade geometry. This facility should be equivalent to a linear cascade, but with substantially reduced flow requirements.

2. Develop a measurement system that uses steady state thermochromic liquid crystal techniques to measure the heat transfer coefficient and film cooling effectiveness. The data should have low-uncertainty and well-defined boundary conditions that are easily reproducible numerically. This would allow the measured data to serve as a test-bed for RANS modeling efforts as well as for design purposes.

3. Measure the constant heat flux heat transfer coefficient and film cooling effectiveness under a variety of conditions for compound-angle round holes installed on the pressure side of modern, highly curved, transonic airfoil. The examined conditions will involve adjusting the blowing ratio, density ratio, momentum ratio, and turbulence intensity and length scale.

1.4 Introduction to Film Cooling Physics

The key phenomenon affecting film cooling performance is the interaction between the vorticity contained in the boundary layers of the film cooling hole and mainstream boundary layer. The resulting flow structures are dependent on a large number of parameters, including:

1. Film cooling hole geometry.

2. Properties of the coolant and mainstream (Buck (2000) states that in real engines, the film cooling flow has an absolute total temperature in excess of 800K, while the mainstream has an absolute total temperature in excess of 1500K). A possible modeling parameter for this flow feature is the density ratio, $DR = \frac{\rho_j}{\rho_\infty}$.

3. Local streamwise curvature.

4. Local turbulence properties.

5. Mass flux of film cooling flow, versus mass flux of mainstream flow (i.e. the blowing ratio, $BL = \frac{\rho_j u_j}{\rho_\infty u_\infty}$).

6. Momentum flux of film cooling flow, versus momentum flux of mainstream flow (i.e. the momentum ratio, $I = \frac{\rho_j u_j^2}{\rho_\infty u_\infty^2}$).

Typical blowing ratios for film cooling range from $BL = 0$–5, depending on the geometry and flow conditions. Contrasting studies by Andreopoulos and Rodi (1984) and Smith and Mungal (1998) for blowing ratio ranges of $BL = 0$–5 and $BL = 5$–25 respectively suggest that the primary feature of film cooling jets is that they are re-entrained into the boundary layer far downstream. The mean properties of the boundary layer recover to their initial state, as if the jet never existed. This distinguishes them from jets for other industrial applications with much higher blowing ratios. Therefore, all observations presented from the literature and in this thesis are characteristic of film cooling jets, rather than jets in applications such as vertical short take-off and landing (V/STOL) aircraft.

Despite apparent contradictions in data sets, and the general complexity of the film cooling jet-mainstream interaction, there are some general rules of thumb that designers use for an initial guess for a film cooling strategy. Gartshore et al. (2001) provided a sample summary of these concepts, a modified version of which is presented below:

1. Compound-angle round (cylindrical) holes, in general, provide better performance than holes with either streamwise ($\beta = 0°$) or normal ($\alpha = 90°$) injection.

2. Low values of α are best, but values between 25° to 45° are the smallest practical angles, based on the ease of machining.

3. Holes with a diffuser-exit, i.e. a flared exit, can dramatically improve film cooling performance, by promoting a flow which exits near tangential to the surface.

4. Spanwise hole spacing has a significant effect on film cooling performance, and values of $\frac{p}{d}$ of about 3 are common. Smaller values of this ratio are difficult to use in practice.

5. Low values of BL, or I provide better film cooling performance. Very low blowing ratio values are impractical as they will have unavoidable fluctuations near the hole exit limiting their utility.

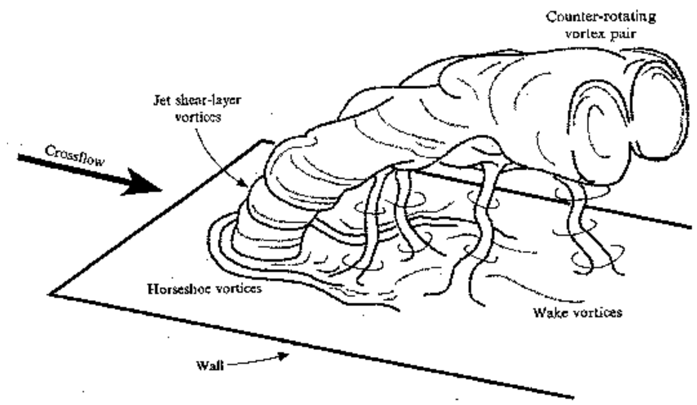

Figure 1.4: Schematic of the four types of vortical structures found in the jet-in-crossflow interaction flow field (from Fric and Roshko (1994)).

6. Holes with large $\frac{L}{d}$ values give better film cooling performance. It has been suggested that the effect of this parameter is most pronounced when $\frac{L}{d} \leq 5.0$.

These observations are based on experimental evidence collected at primarily incompressible, flat plate boundary layer flow conditions. The following sections provide additional background on the nature of the interaction of discrete film cooling jets and the mainstream flow as well as effects of various parameters.

1.5 General Characteristics of the Jet-In-Crossflow Interaction

Figure 1.4 shows the various vortical structures that develop from the interaction of a normal jet with crossflow. Fric and Roshko (1994) suggest that all of these structures, except for the counter-rotating vortex pair (CRVP) are not shed from the jet, but are formed from the vorticity that is contained in the crossflow boundary layer. These authors argue, from a combination of single-wire hotwire data and flow visualizations of a normal jet, that the CRVP is entirely made up of film cooling fluid. This contention is supported by Haven and Kurosaka (1997), who also argue that this vortex pair has a sense of rotation that can promote jet lift-off and cause entrainment of crossflow towards the wall. These two flow features that result from the CRVP can lead to serious degradation of the film cooling layer and augment heat transfer to the wall. Thus, the pivotal objective to improve film cooling performance is to contain the jet-lift off phenomenon and minimize the entrainment of mainstream fluid near the wall. There are several variables which effect the flow structure in the vicinity of the hole, each of which can have varying degrees of effect depending on the implementation. The following sections attempt to present research on each of the major parameters that affect the complexity of the interaction of the film cooling flow with the mainstream. It should be emphasized that the effect of each of these parameters in isolation appear to be of the same order of magnitude with respect to each other. In other words, depending on the flow situation, one parameter may have slightly more dominance over another. These observations are derived primarily from flat plate incompressible boundary layer experiments. Nevertheless, such data can be used to give general direction on possible design trends. However, it will become clear that the only way to develop highly accurate predictive tools that generate advanced cooling designs that use less air and provide greater performance is the execution of well-controlled experiments that simulate real hardware at realistic flow conditions.

1.5.1 Blowing/Momentum Ratio Effects on Jet-Mainstream Interaction

Bergeles et al. (1976) and Ramsey and Goldstein (1971) examined a normal jet with a turbulent boundary layer and blowing ratios that ranged from $BL = 0.046$–2.0. The boundary layer displacement thickness was of the same order of magnitude for both experiments ($\delta_1 \approx 0.05d$). Surface visualizations presented by Bergeles et al. (1976) demonstrated that the mainstream is swept under the film cooling jet immediately downstream of the film cooling hole, effectively forming a "blister" of reversing mainstream fluid on the surface. As the blowing ratio is increased from $BL = 0$ to $BL = 0.5$, this "blister" grows in size and lengthens in the downstream direction. Peterson and Plesniak (2004), also studied normal injection holes, although of a particularly short length ($\frac{L}{d} \approx 0.66$), and found that this recirculating region becomes smaller as BL increases above 0.5. These authors determined that this flow feature consisted of a pair of vortices, which they termed as "downstream spiral separation node" vortices (DSSN).

Cross-sectional flow visualizations, by Bergeles et al. (1976), showed that the film cooling jet at relatively low blowing ratios ($BL < 1$) is rapidly bent into the boundary layer by the mainstream flow. Detailed 3-D hotwire measurements of a normal jet performed by Andreopoulos and Rodi (1984) support this observation, and suggest that as the blowing ratio is increased the effective radius of curvature around which the jet bends increases. These results suggest that the near field of strong jets (i.e. with high blowing ratio values) is a function of complex inviscid dynamics. In contrast, at lower blowing ratios, where the jets are much weaker, the flow characteristics are dominated by turbulent diffusion. These flow attributes are further supported by Kelso et al. (1996) who performed comprehensive flow visualizations using a water tunnel to identify different vortical structure regimes as a function of blowing ratio.

At lower blowing ratios, all these experiments found that the crossflow dramatically effects the efflux from the film cooling hole, lowering the velocity of fluid in the upstream half of the film cooling hole. With increasing blowing ratio, this effect weakens and the exiting velocity profile becomes more independent of the crossflow conditions.

Baldauf et al. (2002a), using an extensive set of open-literature data, argue that as blowing ratio increases, the film cooling jet penetrates further into the cross-stream, initially improving film cooling effectiveness immediately downstream of the film cooling hole. Beyond this optimum point, the effectiveness begins to decline. Ramsey and Goldstein (1971) observed that as the blowing ratio increases further, the CRVP begins to lift away from the wall, causing a gradual reduction in film cooling effectiveness. Eventually blow-off occurs, the CRVP completely separates from the wall – leading to a precipitous drop in effectiveness. Depending on the flow conditions, the jet may reattach, leading to an increase in effectiveness downstream (Kruse (1984)). Fric and Roshko (1994) detail the flow structures when the normal jet passes straight through, in their case, a laminar boundary layer into the freestream. The blowing ratios used in this work ranged from $BL = 2$–10. Thus the flow field that is described is more applicable to those with a high blowing ratio (i.e. $BL \geq 5$). Figures 1.5 and 1.6 compare the observed flow structures for low and high blowing ratio cases.

Baldauf et al. (2002b) documents the augmentation in the heat transfer coefficient as the blowing ratio increases. An interesting feature of the data presented by Baldauf et al. (2002b) is an apparent augmentation of heat transfer coefficient at low blowing ratios several diameters downstream, in spite of the fact that at the same conditions there is a slight reduction in the heat transfer coefficient immediately downstream of the injection location. Andreopoulos and Rodi (1984) suggest that a possible cause of this apparent anomaly is the presence of a secondary longitudinal vortex motion in the form of bound vortices that entrain mainstream fluid. At low blowing ratios, this is primarily from the vorticity contained in the hole sidewall boundary layer. In contrast, at higher blowing ratios, these vortices are due to the shearing at the interface of the film cooling jet and the mainstream flow.

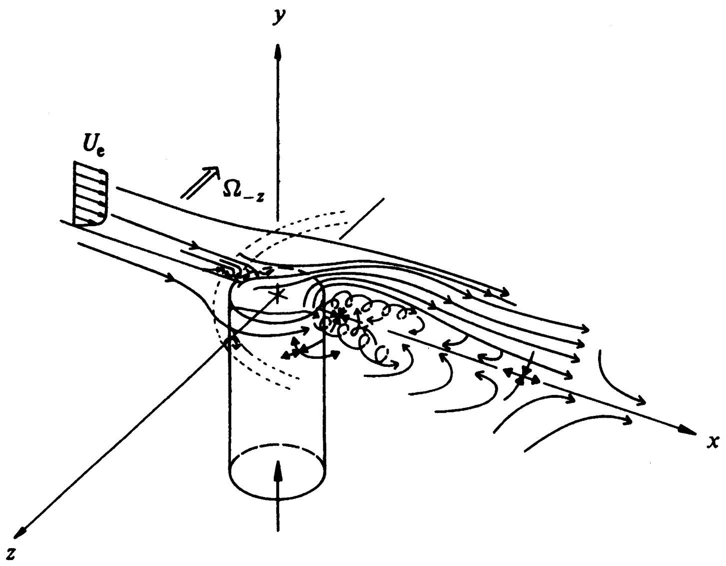

Figure 1.5: Figure of flow characteristics for normal injection with low blowing ratios (from Andreopoulos and Rodi (1984)).

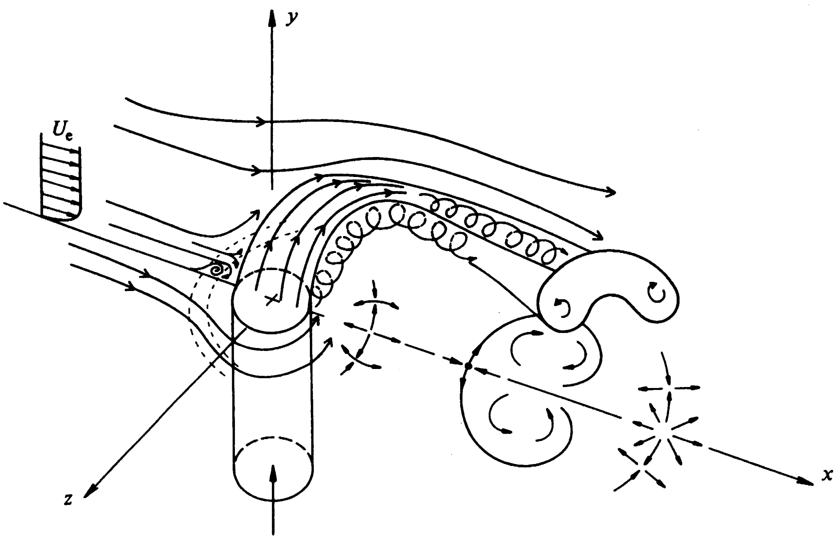

Figure 1.6: Figure of flow characteristics for normal injection with high blowing ratios (from Andreopoulos and Rodi (1984)).

Yavuzkurt et al. (1980) suggested that the entrainment of the mainstream fluid is more important in the augmentation of heat transfer, rather than turbulent mixing.

There is a debate in the film cooling community about the appropriateness of using the blowing ratio to correlate the behavior of film cooling performance. Abramovich (1963), citing numerous early studies argues that the behavior of a three-dimensional film cooling jet, as implemented in gas turbine engines, is correlated better using the momentum ratio, I, rather than the blowing ratio BL. This is in contrast to two-dimensional film cooling – where a slot rather than a row of holes is used. Goldstein (1971) demonstrated that performance data for film cooling slots can be adequately correlated using the blowing ratio, BL, hence the expectation for discrete hole film cooling. As the great majority of all film cooling performance data have been taken in incompressible flow, these two parameters, BL and I cannot be decoupled unless the density ratio is adjusted. This masks the effective difference between these two parameters. Studies by Sinha et al. (1991a) and Etheridge et al. (2001) where the density ratio was independently varied revealed that at low blowing ratios, where the jet remains attached to the surface, the film cooling performance can be correlated with the blowing ratio. Once the jet detaches, the data are better correlated by the momentum ratio.

1.5.2 Effect of Hole Inclination

Effective film cooling strategies produce jets with trajectories that are tangential with respect to the cooled surface. Based on this argument, one would expect that the smaller the inclination angle (α) becomes, the more effective the cooling scheme. However, measurements by Kruse (1984) appear to contradict this hypothesis. Several experiments are documented in this work for a variety of hole inclinations, ranging from $\alpha = 90°$ to $\alpha = 10°$. Judging from plots of adiabatic film cooling effectiveness, there appears to be an optimal hole inclination. Furthermore, Kruse suggested that decreasing the angle of inclination, increases the sensitivity of heat transfer coefficient augmentation to the blowing ratio. In other words, small values of α give the largest marginal increase of heat transfer coefficient as more film cooling flow is applied. Measurements by Hay et al. (1985) taken on a flat plate with a row of holes with an inclination angle of $\alpha = 90°$ and $\alpha = 35°$ disagree with this conclusion. They found that the more the more normal the injection, the greater the sensitivity of the heat transfer coefficient to the blowing ratio. Results presented by Baldauf et al. (2002b) appear to agree with the latter set of conclusions.

In addition to normal injection, Ramsey and Goldstein (1971) investigated the effect of hole inclination for a single hole. Measurements of velocity, turbulence intensity and temperature using a hole with $\alpha = 35°$ were reported in this study. Given the same mainstream flow conditions, it was observed that the inclined jet exhibited less penetration and less spreading in the vertical and lateral directions. This indicates that shallower angles provide less lateral mixing than steeper injection holes. Bergeles et al. (1977) performed measurements of the flow field formed by a jet inclined $\alpha = 30°$ to a flat plate. It was noted that the maximum effectiveness and coverage occurs at a blowing ratio $BL \approx 0.5$, after which the jet begins to lift off the wall. Furthermore, it was observed that the "blister" of recirculating mainstream flow that forms immediately downstream of the film cooling hole is much smaller with the inclined that with normal injection. Lee et al. (1994) performed flow visualization experiments using Schlieren photographs for normal and inclined ($\alpha = 35°$) jets. These authors also performed 3-D velocity measurements with a five-hole directional probe. These experiments revealed that inclined jets maintain their structure further downstream than normal jets, and there is very little interaction with the crossflow in comparison to normal injection. Interestingly, the "blister" was not observed in these data, which is not altogether unexpected as their lowest blowing ratio was $BL \approx 0.8$.

Pietrzyk et al. (1989) used 2-D Laser-Doppler anemometry to measure vertical and streamwise components of velocity using a row of holes with $\alpha = 35°$. These measurements indicated that the downstream flowfield eventually approaches that of a standard turbulent boundary layer. Furthermore, it was observed in these data, as well as that of Burd and Simon (1997), that jetting occurs on the upside edge of the hole, rather than the downside edge. In contrast to the results by Lee et al. (1994), a separation region or "blister" was observed immediately downstream of the film cooling holes. Peterson and Plesniak (2004) point out that this area of recirculating flow is due to the mainstream flow wrapping around the film cooling jet. Mass transfer measurements by Goldstein et al. (1999) using a single row of holes, inclined with $\alpha = 35°$, indicate that this region is an area of high mass transfer (and by inference high heat transfer).

Foster and Lampard (1980), using mass transfer tests, found that the spanwise-averaged film cooling effectiveness far downstream (i.e. $\frac{x}{d} > 40$) becomes independent of injection angle. The point at which this occurs is sensitive to the blowing ratio applied, with higher blowing ratios pushing this point further downstream. At higher blowing ratios, when the jet lifts off the cooled surface, holes with a steeper injection angle perform better. These authors argue that although holes with normal injection ($\alpha = 90°$) give jets with a higher trajectory, they generate a higher degree of spanwise mixing, allowing the jets to coalesce and reattach to the surface sooner than shallower injection holes. This effect becomes more apparent at higher blowing ratios when the film cooling jet completely lifts off from the cooled surface. This observation could explain the greater enhancement of the heat transfer coefficient with normal injection: the increased spanwise mixing entrains more mainstream fluid, increasing heat transfer.

Goldstein and Stone (1997) performed additional measurements on concave and convex surfaces, using a row of holes at a variety of injection angles ($\alpha = 15°$, $25°$ and $45°$). Two density ratios were applied, $DR = 1.0$ and $DR = 2.0$. A range of blowing ratios were tested to identify the characteristics of the jet-mainstream interaction as the blowing ratio was increased with a given injection angle. Data from this study indicated that at very low blowing ratios, $BL < 0.3$, the resulting film cooling effectiveness is primarily determined by mainstream parameters (e.g. $\frac{\delta_1}{d}$, $TI\%$). As the blowing ratio increases, and jet-lift off approaches, shallower injection angles perform better as these produce jet trajectories which are more tangential to the cooled surface. At high blowing ratios, just as reported by Foster and Lampard (1980), steeper injection holes were found to produce better overall performance.

Kohli and Bogard (1997) examined holes with $\alpha = 35°$ and $\alpha = 55°$ on a flat plate. They reported that the overall film cooling effectiveness with holes inclined at $\alpha = 55°$ is very comparable to 35° at low blowing/momentum ratios. As the blowing ratio is increased, the 55° holes showed only a slight reduction in centerline effectiveness. The maximum effectiveness for both types of holes occurred at momentum flux ratio of $I \approx 0.1$. This study reports turbulence measurements that show greater spanwise mixing for 55° holes, which apparently results in greater lateral diffusion. There is some confusion about these data, however, as the desired blowing ratios were achieved by lowering or raising the mainstream flow velocity. This subsequently changes the local boundary layer properties. Nevertheless, the overall conclusion supports that argued by Foster and Lampard (1980) and Goldstein and Stone (1997).

1.5.3 Hole Spacing and Pattern Effects on Film Cooling Performance

Slots have been shown to provide the most effective film cooling strategy; however, discrete holes are used in practice to maintain the structural integrity of the cooled component. Turbine blade cooling designers have two strategies for cooling, one is using single, or double rows of holes (film cooling) and the other is full-coverage film cooling where an array of rows is used. The difference between these two strategies is described by Kays and Crawford (1993) who state that the purpose of the latter strategy is to cool the surface in between holes, while the former is to cool the downstream surface. Full-coverage film cooling would be used primarily at the leading edge of turbine blades where extremely high temperatures are encountered. Obviously the downstream impermeable surface of such an array would be cooled in the same manner as film cooling. Two geometrical parameters have been investigated with respect to hole spacing: the lateral hole spacing, $\frac{p}{d}$ and the row spacing in the streamwise direction, $\frac{s}{d}$. Figure 1.7 defines the row spacing parameter, s relative to the stagnation point of a turbine airfoil. Figures 1.1 and 1.2 define the lateral hole spacing, p. In a typical installation, the row spacing is $\frac{s}{d} \approx 3$ at the leading edge, while additional downstream rows are $\frac{s}{d} \approx 17$ from the leading edge (Muska et al. (1975)).

The key flow feature that changes between slots and discrete holes is the presence of the CRVP from each hole. The question then becomes how row-row and inter-row hole-to-hole spacings affect the interaction of adjacent CRVP's. If this interaction is constructive, it would be expected that there would be increased entrainment of mainstream fluid near the wall, augmenting the heat transfer coefficient. Measurements performed by Kruse (1984) indicated a monotonic increase in film effectiveness the smaller the spacing between adjacent film cooling holes. Sterland and Hollingsworth (1975) contradicted this, with mean velocity and flow visualization data measured downstream of an insert with variable hole spacing installed on the suction surface of an airfoil geometry. These data strongly indicated that given a specific blowing ratio and angle of injection there is an optimal hole spacing. Bergeles et al. (1977) suggests that to achieve maximum spanwise coverage, a hole spacing of $1.4d$ should be specified for a row of holes. This was based on the examination of the cooled "footprint" downstream of a single hole. The minimum lateral spacing for film cooling holes is typically $\frac{p}{d} \approx 3.0$ to maintain component structural integrity (Lander et al. (1972)).

Sellars (1963) presented a model that assumed that the overall film cooling effectiveness from several rows can be computed from data or correlations for a single row of holes. The

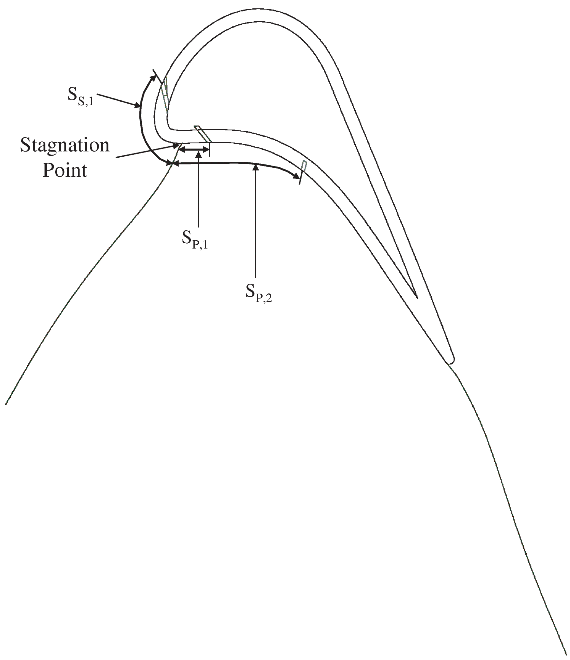

Figure 1.7: Definition of row spacing S relative to the stagnation point of a turbine airfoil.

crucial assumption in this model is that a downstream group of holes cools as if the mainstream was cooled by the upstream row. In other words, the adiabatic wall temperature downstream of a row of holes, can be used as the recovery temperature for the next row of holes ($T_{r_2} = T_{aw_1}$). By inference, it is expected that there is a maximum blowing ratio where this model totally fails, especially when the jets begin to detach from the wall. Muska et al. (1975) demonstrated the utility of this model for blowing ratios $0.1 \leq BL \leq 1.3$ and row spacings $16.7 \leq \frac{s}{d} \leq 25.0$ for both a flat plate and the suction side surface of a turbine rotor blade geometry.

Mayle and Camarata (1975) performed measurements of adiabatic film effectiveness and heat transfer coefficient over a two-dimensional, full-coverage array of staggered compound angle holes. These results suggested that the improvements in film effectiveness with decreasing hole spacing are not monotonic, that is there is an optimum spacing after which jet coalescence occurs. Le Brocq et al. (1973) using inline full-coverage film cooling flow injection showed that jet coalescence is detrimental to the film cooling layer. Afejuku et al. (1980) found that staggered arrangement of two rows of holes gave far better results when compared to in-line injection for practically all conditions; including shallow injection angles, high blowing rates, and small row spacings. Additionally, Stanton number data presented by Mayle and Camarata (1975) suggested that smaller hole spacings lead to increased heat transfer augmentation, especially at higher blowing ratios. Kruse (1984) displays data which suggest that the augmentation increases monotonically with decreasing hole spacing. This is supported by Eriksen and Goldstein (1974) who presented measurements of heat transfer coefficient for air injection through either a single hole or a row of holes into a turbulent boundary layer on a flat plate. These results show that along the centerline, the downstream heat transfer coefficient for the single and multiple hole cases agree; however, there is significant augmentation of the heat transfer coefficient laterally due to the interaction of adjacent jets.

Jabbari and Goldstein (1978) examined two staggered rows of inclined holes ($\frac{s}{d} = 2.6$). Results from this work indicated improved film cooling performance at the same blowing ratio when compared to a single row. This benefit was especially apparent at higher blowing ratios and at distances far downstream of the film cooling holes. Part of this improvement is due to the increased injection of coolant into the mainstream flow; but these data at a variety of blowing conditions demonstrated that the interaction of the staggered jets is the primary cause of the improvement. In contrast, the effect of the blowing on the heat transfer coefficient followed the same trends as that with a single row of holes. Bergeles et al. (1980), using staggered rows spaced $\frac{s}{d} = 3.0$ apart, suggested that the upstream jets may delay blow-off for the downstream jets at high blowing rates. Mass concentration measurements collected by Afejuku et al. (1983) indicate that the jet structure can persist as far as 40 diameters downstream of the injection location. Furthermore, these data inferred that the distribution of momentum flux in the upstream film can dramatically affect the trajectory of the downstream film cooling jets. By adjusting the momentum flux of the upstream jets, areas of momentum excess or deficit may be created in the inter-row boundary layer. This phenomenon will determine how far the downstream film cooling jet will penetrate into the mainstream; if there is a substantial deficit – the jets will penetrate further into the mainstream, if there is an excess the jets will move closer to the wall for higher blowing ratios. Sinha et al. (1991b) endorsed these conclusions with mean and fluctuating velocity measurements.

Ligrani et al. (1994c) and Ligrani et al. (1994d) examined the effect of hole spacing on film cooling performance for two staggered rows (spaced $\frac{s}{d} = 3.0$ apart) and a single row of holes installed on a flat plate with $\alpha = 35°$, $\beta = 30°$. The blowing ratio was varied in the range $0.5 \leq BL \leq 1.5$. In these experiments, the hole spacing for each row was reduced from $\frac{p}{d} = 3.9$ to 3.0 in the first study, and from $\frac{p}{d} = 7.8$ to 6 in the second test. In both cases, the reduction in hole spacing was found to improve film cooling effectiveness in the range $\frac{x}{d} < 60$. Measurements of the heat transfer coefficient from these two configurations revealed a higher degree of heat transfer coefficient augmentation with two rows of film cooling holes. This suggested that the dual row configuration had a higher degree of turbulent mixing, in spite of the large spanwise hole spacing. The augmentation effect was found to be consistent at all values of $\frac{x}{d}$.

1.5.4 Compound Angle Hole Orientation Effects on Film Cooling Performance

One parameter that can affect distribution of coolant is the shape and orientation of a row of film cooling holes. Adjusting the injection geometry relative to the flow direction can change the amount of lateral mixing and augmentation of heat transfer rates to the cooled wall. Unfortunately, the effects of these parameters are hardly monotonic, and are often coupled with other parameters.

Considerable study has been devoted to the trajectory and flow characteristics downstream of a variety of hole shapes. Haven and Kurosaka (1997) used PIV (particle image velocimetry) and PLIF (planar laser induced fluorescence) to establish the effect of hole geometry on the structure of the CRVP (or kidney vortices) downstream of a normal jet injected into a cross-stream. They identified a “double-decked” flow structure, with the lower deck consisting of a steady vortex pair consistent with the CRVP. They argue that the origin of this pair of vortices is the sidewall boundary layers rolled up by the mainstream. The important consequence of this conclusion is that it suggests that the spacing between the two vortices is a direct function of the hole width in the direction perpendicular to the mainstream flow direction. The closer these two vortices are to each other, the greater the propensity the jet will have to lift-off due to the induced upward velocity from the kidney pair. The upper deck consists of an unsteady pair of vortices whose structure is also direct function of the aspect ratio of the hole from which the jet issued. Low-aspect ratio holes (where the hole has a much larger projected length in the streamwise direction in comparison to the spanwise direction) appear to produce intermittent vortices that rotate in the same sense as the lower deck vortices. This serves to add an additional induced upward velocity. High-aspect ratio holes (where the hole has a much larger projected length in the spanwise rather than the streamwise direction) on the contrary, appear to produce intermittent anti-kidney vortices which induce a downward velocity preventing jet lift-off. This suggests that such holes give improved film cooling performance. The drawback of these observations with respect to the behavior of the CRVP is that under certain conditions, this flow feature can collapse into a single vortex. However, film cooling performance data presented by Watanabe et al. (1999) and Takahashi et al. (2000) confirm that holes with increasing aspect ratio have improved performance.

Generally, two hole geometry aspects are modified: the injection angles (α and β), and/or the amount of diffusion at the hole exit. Round (also termed as cylindrical) holes where the injection angles are adjusted are called compound angle round holes (CARH), while holes with a shaped exits are called diffuser-exit holes (DEH). Examples of these hole configurations were shown in figures 1.1 and 1.2.

Goldstein et al. (1970) examined a single hole with lateral injection ($\beta = 15°$, $35°$, $\alpha = 0°$) and found an increase in the peak film cooling effectiveness and improved lateral protection when compared to normal ($\alpha = 90°$, $\beta = 0°$) or inclined $\alpha = 35°$, $\beta = 0°$) injection. As the blowing ratio was increased ($BL \approx 1$), the authors observed that the lateral injection scheme retards jet lift-off, i.e. such holes have jet trajectories which are more tangential to the cooled surface. Honami et al. (1994) performed simultaneous velocity and temperature measurements downstream of a row of lateral injection holes ($\alpha = 30°, \beta = 90°$). Results from this study documented the formation of single vortex structures rather than CRVP's. These structures form in an asymmetrical fashion relative to the hole center as they depart each film cooling hole. As blowing ratio was increased, these vortices were found to lift-off the injection surface, consistent with when a CRVP was present. This single vortex structure was found to draw freestream fluid towards the wall, which suggests that this geometry would cause an augmentation of heat transfer levels. Additional examination revealed that these vortical structures have a large-scale motion that moves the vortex in a spanwise direction as it progresses downstream, confluent with the injection angle. The exiting vortical structure was found to interact with the surface on the side concurrent with the injection angle, this means that the downstream surface film effectiveness is highly asymmetric. Comparison of these results with that of Compton and Johnston (1992) suggested that the maximum vorticity was a function of the blowing ratio and the orientation angle, β. These observations strongly suggest that when lateral injection is used, the hole-to-hole spacing is as small as possible. This is because the asymmetric downstream coolant distribution can produce localized areas of high thermal gradients, despite the improved lateral mixing. Such gradients can cause thermal stresses, which could lead to component failure.

Kaszeta et al. (1998) used triple-hotwire anemometry to examine the mean velocity, turbulence intensity and turbulent shear stress fields downstream of row of film cooling holes inclined $\alpha = 35°$ to the surface, with lateral injection ($\beta = 90°$), a pitch spacing of $\frac{p}{d} = 3.0$ and a hole length of $\frac{L}{d} = 2.3$. The investigators compared their results for lateral injection with those for a row of holes with streamwise injection ($\beta = 0°$). This comparison confirmed that lateral injection generally enhances turbulent mixing in the spanwise and wall normal directions, as measured by the turbulence intensity. The level of turbulence intensity was found to be relatively uniform in the spanwise direction. 3-D LDV measurements presented by Khan and Johnston (2000) provide additional insight into the flowfield downstream of a single compound angle round hole ($\alpha = 30°$, $\beta = 60°$, $\frac{L}{d} = 3.5$). The authors found that the exiting skewed vortex has the ability to affect the local boundary layer thickness, thinning it on the downwash side of the vortex, and thickening it on the upwash side. Furthermore, their data suggested the applicability of a standard turbulent diffusion model, except in the vortex core.

Lee et al. (1997) presented oil-film visualizations and 3-D flow measurements for compound angle orientations of cylindrical holes. Several important observations were retained from this work: as the orientation angle increases the CRVP collapses into a single one, increasing the orientation angle limits the lift-off tendency of the film cooling jet at high blowing ratios, and that the aerodynamic penalty increases with increasing orientation angle. For a row of holes at this inclination, results from this study indicated that the transition from a pair of vortices to a single one occurs when $\beta \geq 15°$.

Another drawback of the compound angle injection approach, as indicated previously, is its augmentation effect on the heat transfer coefficient due to the subsequent high level of turbulent mixing. Cho et al. (1998) reported mass transfer measurements that confirm that as the orientation angle and blowing ratio increase, the level of heat transfer coefficient augmentation also increases. This means that for effective implementation a moderate blowing ratio and orientation angle must be selected to maximize lateral mixing of coolant, but contain increases in the heat transfer coefficient. Studies presented by Jubran and Brown (1985), Ligrani and Ramsey (1997a), Ligrani and Ramsey (1997b), Ligrani et al. (1992), Jung and Lee (2000), Goldstein and Jin (2001), Ekkad et al. (1997b), Ekkad et al. (1997a), Sen et al. (1996) and Schmidt et al. (1996) examine single rows and dual staggered rows of film cooling holes. Results from these studies provide conclusive evidence that increasing the orientation angle improves film effectiveness, with the disadvantage of consistently augmenting heat transfer coefficients. This effect is particularly dramatic at higher blowing ratio conditions as indicated by the previously mentioned studies.

1.5.5 Hole Exit Shape Effects on Film Cooling Performance

Given the primary disadvantage of compound angle round holes, i.e. under certain conditions they can dramatically augment the heat transfer coefficient and give relatively high aerodynamic losses, effort has been placed on the investigation of other hole geometries for film cooling. Quinn and Militzer (1989), Quinn (1990) and Quinn (1992) performed detailed turbulence and mean flow measurements in the near field of normal-injection square, triangular and round turbulent free jets issuing into quiescent air. Comparisons between these data sets revealed that square and triangular jets more effectively mix with the surrounding air. Further work presented by Haven and Kurosaka (1997) showed that normally-injected square jets do not penetrate as far into an applied crossflow, when compared to round jets. Makki and Jakubowski (1986) examined trapezoidal holes that were diffused in the direction of the mainstream flow and demonstrated that this configuration showed improved performance when compared to round holes.

Findlay et al. (1999) conducted film cooling effectiveness, mean velocity and turbulence measurements for single rows of three different geometries of square jets in crossflow. A mass transfer procedure was used for the film effectiveness measurements and a three-component LDV system was used for the flowfield measurements. Jets with blowing ratios of $BL = 0.5$, 1.0 and 1.5 with a density ratio of $DR = 1$ were injected through normal ($\alpha = 90°$), streamwise-inclined ($\alpha = 30°$, $\beta = 0°$) and spanwise-inclined ($\alpha = 30°$, $\beta = 90°$) square holes. Of the three, the spanwise-inclined were found to provide the least sensitivity to jet blow-off, and thus the best overall performance. This observation agrees with data from Haven and Kurosaka (1997) that showed holes that offer larger aspect ratios perpendicular to the flow provide better overall film effectiveness. Thole et al. (1998) conducted PIV measurements detailing the mean velocity and turbulence field downstream of simple-inclined holes, two of which had diffuser-exits. One had a laterally-diffused exit (fan-shaped), and one had a forward-laterally diffused exit (laid-back fan shaped). These data confirm that diffuser-exit holes produce less jet penetration, but also produce reduced velocity gradients and lower turbulence production relative to round holes.

Gartshore et al. (2001) examined the film cooling effectiveness of square and cylindrical holes with identical aspect ratios, but with a compound orientations ($\alpha = 30°$, $\beta = 45°$). Blowing ratios of $BL = 0.5$, $BL = 1.0$ and $BL = 1.5$ were applied in this test. The results from this study agreed with previous observations suggested that square holes have increased mixing with the freestream compared to round holes, thus providing lower performance. Heat transfer data from Licu et al. (2000) and Cho et al. (2001) for square and rectangular holes suggest that the mixing dynamics between the coolant jet and the mainstream are a highly complex. The results in these two studies were not compared to that from round holes, so it is unclear if the levels of augmentation are higher than that found in cylindrical holes. The higher levels of turbulent mixing with square holes suggest increased augmentation of the heat transfer coefficient in comparison to round holes, but evidence to support this is limited.

As mentioned previously, Goldstein et al. (1974) was the first in the open literature to demonstrate effectiveness of cooling hole diffused-exits in reducing the jet momentum flux near the wall, which limited the penetration of jet into the crossflow boundary layer. The injection holes consisted of circular holes with a shaped exit with both lateral and forward diffusion ($\Psi = 10°$, $\Phi = 10°$). These authors presented surface film cooling performance measurements and carbon fog visualization images to confirm this effect for a flat plate boundary layer. An added benefit of diffused exit holes, if designed correctly, is the reduction of aerodynamic losses and a reduction of heat transfer coefficient augmentation. Haller and Camus (1984) demonstrated that improvements in film cooling effectiveness can be achieved without any additional aerodynamic loss penalty, using holes with a spanwise flare angle of 25°. This introduces tremendous flexibility in the exit design of a film cooling hole. Unfortunately, the implementation of such holes requires an extended design and manufacturing effort, and thus they are used sparingly. The standard techniques for producing such geometries are electrical discharge machining (EDM) or spark erosion.

Hay and Lampard (1995), using measurements of discharge coefficients for holes with diffused exits reported that entry cylindrical section should have a length of at least $2d$. They argue that the flow separates at the entry and that a long enough development length will allow the flow to reattach before passing into the diffused exit section. This is vital to improving the diffusion of the flow and enhancing the lateral coverage of the film layer. It is very possible if the diffusion angle is too large, the coolant flow will separate in the exit region.

Gritsch et al. (1998b) examined the film-cooling effectiveness in the near-field region ($\frac{x}{d} < 10$) downstream of a single, inclined cylindrical hole, and two holes with diffused exits: a fan-shaped exit and a laid-back fan-shaped exit. The crossflow Mach number was varied up to $M = 0.6$, while the applied blowing ratio was adjusted in the range $0 < BL < 2$. Results from this study confirmed that the diffused exit holes provide improved lateral spreading of coolant when compared to the cylindrical hole, particularly at higher blowing ratios, where jet lift-off occurred for the cylindrical hole. The hole with the largest diffused exit (i.e. the laid-back diffuser exit) provided the best lateral coverage. Gritsch et al. (2001) expanded this study to examine impact of diffused-hole exits on the heat transfer coefficient. Using exactly the same geometry and flow conditions, these authors reported that compared to the cylindrical hole both expanded exit holes limited the amount of heat transfer coefficient augmentation. This amelioration effect was particularly distinct at higher blowing ratios with the laid-back hole exit.

Yu et al. (2002) measured the film cooling effectiveness and heat transfer coefficient downstream of a single inclined hole ($\alpha = 30°$) with different types of diffuser-exits. The baseline case ("termed Shape A", by the authors) was a straight cylindrical hole. This was first modified by adding a forward-diffuser exit (Shape B, $\alpha = 30°$, $\beta = 0°$, $\Psi = 0°$, $\Phi = 10°$), and then a lateral-diffuser exit was added (Shape C, $\alpha = 30°$, $\beta = 0°$, $\Psi = 10°$, $\Phi = 10°$). The blowing ratios tested were $BL = 0.5$ and $BL = 1.0$ with the density ratio set to $DR \approx 1$. The greatest improvement in film effectiveness was achieved when both forward and lateral diffusion was applied to the film cooling hole. When only forward diffusion was applied, there was only limited improvement in film effectiveness. At the blowing ratios tested, the diffused-exit holes reduce the heat transfer coefficient. Flow visualizations using a pulsed laser sheet revealed that the flow structure of the injected coolant appeared to be virtually unchanged with a forward-diffused exit. When both forward and lateral diffusion were applied, the downstream coolant flow structure changed dramatically, showing behavior similar to that observed by Goldstein et al. (1974). The jet trajectory was much lower in this case, with flow structures characteristic of energetic turbulent mixing.

One question is the performance of holes where a diffused exit is placed on a compound-angled hole. Bell et al. (2000) conducted an extensive study, measuring the film cooling effectiveness and heat transfer coefficient for a wide range of holes with shaped exits. The hole geometries examined in this study were: simple-inclined round holes ($\alpha = 35°$, $\beta = 0°$), laterally-diffused, simple-inclined holes ($\alpha = 35°$, $\beta = 0°$, $\Psi = 12°$, $\Phi = 0°$), forward-diffused, simple-inclined holes ($\alpha = 35°$, $\beta = 0°$, $\Psi = 0°$, $\Phi = 15°$), laterally-diffused, compound angle holes ($\alpha = 35°$, $\beta = 60°$, $\Psi = 0$, $\Phi = 12°$) and forward-diffused, compound angle holes ($\alpha = 35°$, $\beta = 60°$, $\Psi = 15°$, $\Phi = 0°$). The blowing ratio, momentum ratio and density ratio were varied in the ranges $0.4 < BL < 1.8$, $0.17 < I < 3.5$ and $0.9 < DR < 1.4$, respectively. Data presented in this report showed that holes with a diffused-exit and compound-angle orientation provide the highest effectiveness. Furthermore, in contradiction to Gritsch et al. (1998b), results from this study showed little difference in the spanwise-averaged performance of the simple-inclined holes, regardless if a diffused-exit was implemented. With respect to heat transfer, the simple-inclined holes with diffusion were found to have a very limited effect on augmenting the heat transfer coefficient, a conclusion in-line with that of Gritsch et al. (2001). In comparison, compound angle holes were found to raise the heat transfer coefficient, an observation that becomes more apparent as the blowing ratio increases ($BL > 0.5$). Additional examination of these data revealed that compound-angle round holes with forward-diffusion augment the heat transfer to a greater degree in the blowing ratio range $0.4 < BL < 1$. As the blowing ratio increases outside this range, compound angle holes with lateral-diffusion provide the most amplification.

Sen et al. (1996) and Schmidt et al. (1996) performed heat transfer coefficient and adiabatic film cooling effectiveness measurements for three single-row, inclined hole geometries. The first was a single row of inclined holes with $\alpha = 35°$, the second was a row of compound-angled holes ($\alpha = 35°$, $\beta = 60°$) and the last was a row of compound angle holes with a $\Phi = 15°$ forward expansion. Schmidt et al. (1996) reported that at low momentum ratio conditions ($I < 0.5$) the compound-angled hole with a diffused exit provided the best lateral coverage. As the momentum ratio was increased, the compound-angle film cooling holes were found to provide better coverage than the round holes. However, the film effectiveness was found to have a fairly narrow optimal range, beyond which the film cooling performance dropped off markedly. In comparison, the compound-angled holes with a diffuser exit were found to improve almost monotonically over the range examined ($0.16 < I < 3.9$). Lateral measurements of the heat transfer coefficient presented by Sen et al. (1996) suggested that the diffuser-exit further augments the heat transfer coefficient for a compound angle round hole at a momentum ratio of $I = 1.0$. The diffused exit became the superior arrangement with increasing momentum ratio. Nevertheless, there appear to be additional factors which affect this observation. Dittmar et al. (2003), using measurements of film cooling effectiveness and heat transfer coefficient for a variety of hole geometries and configurations, argued that if there is coolant separation in the diffused-exit portion of the cooling hole, the high levels of turbulent kinetic energy are convected into mainstream, which could increase the heat transfer coefficient.

1.5.6 Characteristics of the Effects of Hole Length and Plenum Conditions on Film Cooling Performance

The major effect of hole length is on the thickness of the sidewall boundary layers and development of the velocity profile for the film cooling fluid. The typical film cooling hole length is $\frac{L}{d} \approx 3.5$. This is set by the internal serpentine passage configuration of a given turbine engine component. Historically, film cooling studies have used unrealistic long-hole deliveries ($\frac{L}{d} \gg 4$), raising the issue of the effect of this parameter on the interaction of the film cooling flow and the mainstream. Harrington et al. (2001) presented film cooling effectiveness results for a flat plate with full-coverage film cooling applied. A staggered hole pattern with holes of length $\frac{L}{d} = 1$, row-to-row spacing of $\frac{s}{d} = 7.14$, and hole-to-hole spacing of $\frac{p}{d} = 7.14$ was used. A comparison of the resulting data from similar tests, such as Metzger et al. (1973) who developed a full-coverage film cooling experiment with $\frac{s}{d} = 4.8$, $\frac{p}{d} = 4.8$ and $\frac{L}{d} > 10$, revealed a substantial reduction in film cooling performance with decreasing hole length.

Burd and Simon (1997) documented the sensitivity of film cooling to the injection hole length and the geometry of the supply plenum. In this experiment, the film effectiveness and mean centerline velocity were measured downstream of rows of holes by with $\frac{L}{d} = 3.0$ and $\frac{L}{d} = 7.0$. Two plena were examined in this study, an "unrestricted" plenum and one of height $\frac{H}{d} \approx 2$. These authors argued that flow characteristics of short versus long film cooling holes have a larger effect on the downstream film cooling performance than the plenum geometry. Nevertheless, film cooling effectiveness data for a short hole demonstrated that flow conditions in the plenum do have an effect on the jet-in-crossflow interaction. This effect was apparently amplified as the blowing ratio increased. This work was supplemented by additional measurements of discharge coefficients by Burd and Simon (1999). Data from these reports suggested that as the hole length was reduced, the effective angle of injection (α) appears to increase, i.e. becomes steeper. This was attributed to jetting of coolant flow on the upstream edge of the film cooling hole, due to the formation of a recirculation region at the entrance of the hole.

Lutum and Johnson (1999) refined this study, examining hole lengths that ranged from $\frac{L}{d} = 1.75$ to $\frac{L}{d} = 18.0$. Data from this report indicated an improvement in film cooling performance as the hole is lengthened, given the flow conditions used. The authors argued that longer holes allow the coolant flow to become fully developed. The rise in film effectiveness is particularly sensitive to hole lengths in the range $0.0 \leq \frac{L}{d} \leq 5.0$. As the length of the hole increases outside this range, the marginal gain in film cooling performance diminishes greatly.

As discussed earlier, in real engine components film cooling holes are supplied by a serpentine passage (or channel) that winds through the blade. In contrast, the vast majority of experiments on film cooling use large, stagnation condition reservoirs to feed the film cooling holes. A serpentine channel distributes flow unevenly across sets of film cooling holes and may even have an outlet. Plena have no outlet and output all flow through a single set of holes. This raises the issue of how supply system flow conditions affect film cooling performance. Channels will not only have a non-negligible mean velocity (which is also characteristic of narrow plenum geometries), but also inherently large flow structures which may affect the film cooling jet-in-crossflow interaction. Wittig et al. (1996) was the first paper in the open literature to present results for a single film cooling hole fed by a narrow channel ($\frac{H}{d} \approx 2$). Hale et al. (2000a) explored the effect of various flow conditions in a narrow plenum with short ($0.66 \leq \frac{L}{d} \leq 3$), inclined ($\alpha = 30°$, $90°$) film cooling holes. The flow in the narrow plenum ($\frac{H}{d} \approx 1$) is oriented in the same (co-flow) and opposite (counter-flow) direction as the mainstream flow. Results from these experiments indicated that better film cooling performance was obtained with inclined holes if co-flow plenum conditions, rather than counter-flow, were implemented with longer holes. This could be due to the increased amount of separation at the inlet of the inclined hole when a counter-flow plenum condition is applied. This would lead to a steeper injection angle, as discussed previously. When the coolant is injected normally to the freestream flow, longer holes produce improved film cooling performance if a counter-flow condition is present in the plenum. If a co-flow condition is applied, shorter normal injection holes produce better performance.

To further this investigation, Peterson and Plesniak (2002, 2004) performed detailed particle-image velocimetry measurements to study the development of the film cooling jet passing through a short, normal hole ($\frac{L}{d} \approx 0.66d$). The supply system consisted of a narrow plenum, identical to that of Hale et al. (2000a) ($\frac{H}{d} \approx 1$). These data demonstrated that flow structures in the supply system can affect the strength of the vortical structures (in this case the CRVP) that exit the film cooling hole. This consequently affects the trajectory and spreading of the film cooling jet. The authors confirmed that the effects of supply flow structure become more significant as the hole is shortened. The measurements also showed that in the case of normal injection, where there is limited separation at the hole inlet, a pair of counter-rotating in-hole vortices form as a result of the flow entering the hole from the supply channel. These are termed as an in-hole counter-rotating vortex pair (INCRVP). The structure of the INCRVP was found to be sensitive to the flow conditions in the supply system, such as pre-existing vortices. Co-flow conditions in the plenum result in a INCRVP that constructively interacts with the CRVP, resulting in a higher jet trajectory and less spanwise mixing when compared to the counterflow conditions.

Complimentary measurements of discharge coefficients presented by Gritsch et al. (2001), Hay et al. (1983), Bunker and Bailey (2001) and Hay et al. (1994) combined the effects of cooling hole inlet crossflow and hole inclination. As previously stated, hole inclination, under certain conditions, will cause a separation bubble at the hole inlet. Data from these studies showed that interaction of inlet crossflow and hole inclination has significant, albeit inconsistent, effects on the coolant as it is injected into the mainstream flow.

Wang et al. (1996) and Kaszeta and Simon (2000) measured the eddy diffusivity distribution downstream of inclined holes ($\alpha = 35°$) with hole lengths of $\frac{L}{d} = 7.0$ and $\frac{L}{d} = 2.3$. Blowing ratios of $BL = 0.5$ and $BL = 1.0$ were applied. Results from these reports indicated, regardless of hole length, there was greater eddy transport in the spanwise direction compared to the wall normal or streamwise directions. This observation was found to be more pronounced with longer holes. From a film cooling performance perspective, elevated levels of eddy diffusivity infers increased mixing. Hale et al. (2000a) observed that this strong turbulent mixing anisotropy raises the film cooling effectiveness between holes and reduces the downstream laterally-averaged effectiveness.

Hale et al. (2000b) conducted a range of studies on short ($\frac{L}{d} = 0.66$), normal injection film cooling holes with varying plenum conditions, including surface convective heat transfer measurements, flow visualization experiments and numerical simulations. This work supported conjecture that if INCRVPs form and strengthen the vortical structures that are ejected, the increased lateral mixing raises the heat transfer coefficient. Goldstein et al. (1997), using a naphthalene sublimation technique, presented mass transfer coefficients in the entry region of film cooling holes using various plenum geometries. Not surprisingly, data from this study indicated that secondary flow structures in the supply system enhance heat transfer. Another mass transfer study by Cho and Goldstein (1995) demonstrated that the mass transfer coefficients in the film cooling hole, and at the hole entrance are fairly insensitive to crossflow at the hole exit.

1.5.7 Effect of Freestream and Jet-Cross-stream Generated Turbulence

The flow in aircraft engine turbine stages is characterized by elevated levels of turbulence. This can be linked to several sources, including:

1. The highly complex exiting flow conditions from the combustor.
2. Wakes from upstream stages.
3. The interaction between film cooling jets and the mainstream flow.

The amplification effect of elevated levels of freestream turbulence on heat transfer and skin friction has been well documented by several researchers (Simonich and Bradshaw (1978), Blair and Werle (1980), Blair (1983), Hancock (1980) and Maciejewski and Moffat (1992)). Goebel et al. (1993) reported that the ranges of axial and swirl combustor exit turbulence intensities to range between 5% and 20%. It should be emphasized that these values will vary spatially, especially with newer combustors which are believed in the design community to have more severe exit turbulence. The presence of upstream wakes and rotation has been demonstrated by several researchers, such as Du et al. (1997, 1998, 1999), to cause high turbulence intensity levels ($\approx 12\%$).

It is important to distinguish between elevated turbulence levels due to film cooling jets and mainstream flow conditions. A well-documented flow in which turbulence can develop is the case of a jet emerging into quiescent air. Heuristically, it can be hypothesized that similar behavior would result from film cooling jets. That is, an augmentation of turbulence due to interaction of the film cooling flow and a cross-stream. Experiments performed by Pietrzyk et al. (1989) with inclined holes with $\frac{\delta_1}{d} \ll 1$ showed that turbulence intensity levels as high as 26% can be achieved immediately downstream of a row of film cooling holes. This turbulence augmentation effect persists far downstream, even after the strong velocity gradients of the film cooling jet have dissipated. Andreopoulos (1985) using hot-wire measurements also concluded that when $\frac{\delta_1}{d} \ll 1$, the jet-turbulent fluid will dominate the boundary layer downstream. MacMullin et al. (1989) demonstrated the effect of circular wall jets on the downstream turbulence field and consequential increases in skin friction and heat transfer coefficients for a flat plate.

Yavuzkurt (1997) proposed that long length scales in the cross-stream direction is one of the mechanisms through which the mainstream turbulence augments the diffusion of momentum and energy. However, Wang et al. (1999), using a linear cascade of blades (an experimental facility described in section 1.7), found that the augmentation of heat transfer was not a monotonic function of both length scale and turbulence intensity, as the most augmentation occurred with moderate turbulence intensity levels and relatively small length scales.

Kadotani and Goldstein (1979b and 1979c) examined the effect of mainstream turbulence intensity and length scale on the film cooling jet-mainstream interaction and the resulting downstream film cooling effectiveness. In these experiments, the turbulence intensity was varied from 0.3% to 20.6%, while the length scale was varied from 0.06D to 0.33D. Both parameters were found to have significant effects on the structure of the jet-mainstream interaction. Contrary to the previously mentioned study by Wang et al. (1999), the data from this report indicates that when the mainstream turbulence scale is large, the jets are thoroughly mixed with the freestream. Jumper et al. (1991), using a circular wall jet to raise the freestream turbulence intensity to the same level as that expected in the film, argued that the increased turbulence level in the freestream gives increased mixing that quickly dissipates the film layer. This conclusion was arrived upon comparison with other data sets by Han and Mehendale (1986) and Goldstein et al. (1968). However, the hole geometry utilized was significantly different from the compared papers, making conclusions difficult. Bons et al. (1996) studied the effect of freestream turbulence intensity levels up to 17.4%. The authors reported that free-stream turbulence decreases film effectiveness directly downstream of the injection hole and increases film effectiveness between injection holes due to enhanced mixing.

An examination of the previously mentioned work suggests two contradicting effects of increased turbulence intensity level, i.e. increased mixing of momentum which effectively thins the boundary layer, and increased disintegration of the structure of the film cooling layer. The first effect would tend to increase the film cooling effectiveness downstream, the second would reduce the film cooling effectiveness. In general, based on the reviewed literature, a key parameter in determining which scenario dominates is the blowing ratio.

At higher blowing ratios with cylindrical film cooling holes, the downstream effectiveness is raised as the jet is deflected closer to the wall. Asymmetrically, with low blowing ratios, the increased dispersion of the film cooling layer dominates, lowering the downstream effectiveness. This latter result is consistently observed with diffuser-exit holes as the flow is generally more tangential to the surface at higher blowing ratios. Hence, the effect of increased dispersion dominates. To add to the confusion, the increased turbulent mixing due to freestream turbulence leads to improved spanwise mixing and thus better between-hole film cooling performance. This hypothesis appears to be supported by Saumweber et al. (2003) who presented film cooling effectiveness data for both inclined and diffuser-shaped holes exposed to varying turbulence intensity levels.

A vital situation when full-coverage film cooling is applied is at the leading edges of turbine blades, which are usually exposed to the highest total temperatures in an operating engine. Hence, several studies have focused on the effects of increased turbulence intensity on film cooling performance and heat transfer augmentation near the leading edge. Mehendale and Han (1992), Ou et al. (1992), and Ou and Han (1992) examined the effects of increasing turbulence intensity on film cooling performance for a leading edge geometry. The effects of hole location and a cylindrical leading-edge geometry were investigated to develop a database for further simulation studies. The trends observed are in-line with previously observed behavior, i.e. the effects of increased turbulence intensity are strongly coupled to the blowing ratio. Film layers with low blowing ratios were found to be rapidly dispersed by increased turbulence intensity, while increasing the local heat transfer coefficient. High blowing ratio film layers were found to be relatively insensitive to increases in the turbulence intensity, consistent with previous studies with flat plates.

1.5.8 Importance of Density Ratio on Film Cooling Performance

Recall that in operational gas turbine engines, combustor bypass air is used for cooling. Consequently, the total temperature of the film cooling flow ($T_{o,c}$) is typically 50% of the total temperature of the mainstream flow ($T_{o,\infty}$), on an absolute scale. This raises the issue of density gradients between the film cooling and mainstream flows. Often experimenters simulate high density film cooling flows with foreign gas injection. Teekaram et al. (1989) demonstrated the suitability this technique using CO_2. Nevertheless, it is difficult to isolate the effect of this parameter as it is coupled to the blowing ratio (BL) and momentum ratio (I). Intuitively, it can be argued that increasing the density ratio, maintaining the same blowing ratio, would delay jet lift-off and improve film cooling performance.

Le Brocq et al. (1973) presented measurements on a flat plate with full-coverage film cooling. Three configurations were examined: one consisted of multiple rows of staggered holes with an angle of inclination of $\alpha = 45°$ or $\alpha = 90°$, the other had rows of holes arranged in an in-line configuration with an angle of inclination of $\alpha = 90°$. A variety of conditions were explored in this study, but one of key interest was the utilization of freon as the film coolant to provide a density ratio of $DR \approx 4.2$. The report presented pitot probe measurements that describe the streamwise development of mean velocity profiles. Furthermore, mass transfer measurements were performed at the wall to measure film effectiveness. When these data were compared to measurements with a density ratio of $DR \approx 1$, holding the blowing ratio constant, it was apparent that denser coolant gave superior performance. Launder and York (1974) continued these tests reporting film cooling effectiveness and mean velocity profile data using CO_2 as coolant, giving a density ratio of $DR \approx 1.5$. Foster and Lampard (1980) reported pitot probe measurements of mean velocity profiles at locations $\frac{x}{d} = 4$, 11, 24, and 61 downstream of a row of holes with $BL = 1.4$. A mixture of freon and air was used as the coolant to achieve a density ratio of $DR \approx 2$. The focus of this study was not on examining the effect of density ratio, but the effect of other parameters such as injection angle and boundary layer thickness.

Pedersen et al. (1977) was the first paper in the open-literature to isolate the effects of variable density ratio. A flat plate with a row of inclined holes ($\alpha = 30°$) was used in this study. The density ratio was varied in the range $0.7 \leq DR \leq 4.2$ while the blowing ratio was set to $BL \approx 0.213$, 0.5, 1 and 2. Data from this study indicated that the effect of varying density ratio on the centerline film cooling effectiveness was more pronounced at higher blowing ratios ($BL > 0.5$), improving centerline effectiveness. Not surprisingly, these data demonstrated that increasing the density ratio increases the blowing ratio at which jet lift-off occurs. Furthermore, as the density ratio is increased, additional experimental data reported in this study suggested increased lateral spreading of the film cooling jet. As a consequence, the laterally averaged film cooling effectiveness is raised as the density ratio is increased. This improvement is more evident as the blowing ratio is increased. The only exception to this trend was once the jet completely detaches; film cooling jets with less dense coolant appeared to reattach at a shorter distance downstream. As a result the downstream laterally-averaged film effectiveness is better for lower density ratio jets far downstream – holding the blowing ratio constant for different cases.

Pietrzyk et al. (1990) performed two-component Laser-Doppler velocimetry measurements of the mean and turbulence characteristics of a single jet from a row of holes with an angle of inclination of $\alpha = 35°$ and hole length of $\frac{L}{d} = 3.5$. Liquid nitrogen cooled film cooling air was ejected through these holes with a nominal density ratio of $DR = 2$, blowing ratio of $BL = 0.5$ and momentum ratio of $I = 0.125$ (this will be referred to as the high-density jet). These results were then compared to previous measurements conducted by Pietrzyk et al. (1989) with a density ratio of $DR = 1$, blowing ratios of $M = 0.5$ and $M = 0.25$ and momentum ratios of $I = 0.125$ and $I = 0.062$. This examination revealed that immediately downstream of a given film cooling hole, a lower mean velocity was observed with the high-density jet compared to either of the unit density ratio cases. More precisely, even though the high-density jet has a higher momentum ratio than the lowest unit density ratio case, it produces a higher film effectiveness. This is consistent with film cooling effectiveness measurements performed by Foster and Lampard (1975). However, the mean velocity vectors indicated that the high-density jet penetration was bounded by the two unit density ratio jets. Furthermore, these data showed that as the high-density jet proceeded downstream, the mean velocity profile approached that obtained for a unit density jets at the same mass flux ratio. Turbulence measurements showed a lower decay rate for the high-density jet as it proceeded downstream.

Sinha et al. (1991b) conducted film cooling effectiveness measurements on an inclined row of holes ($\alpha = 35°, \frac{L}{d} = 1.75$) installed in a flat plate. The density ratio of the cooling jets was varied from $1.2 \leq DR \leq 2.0$. The blowing ratio varied between $0.25 \leq BL \leq 1$, and the momentum ratio ranged between $0.05 \leq I \leq 0.83$. The density ratio was varied keeping either the blowing ratio or the momentum ratio constant. Experimental data from this investigation confirmed that decreasing the density ratio, maintaining a constant blowing ratio, degrades the film cooling effectiveness by raising the momentum ratio, increasing the propensity of the jets to lift-off from the surface. When the momentum ratio was held constant and the density ratio was increased, the film cooling performance generally improves as a higher blowing ratio is applied; the exception occurring once the jets lift-off the surface. Laterally-averaged film cooling effectiveness data confirmed that increasing density ratio increases the lateral spreading of the film cooling jets.

Etheridge et al. (2001) examined film cooling on the pressure side surface (concave surface) of a first stage turbine vane in a double passage cascade (an experimental facility described in Section 1.7). A row of film cooling holes with an angle of inclination of

$\alpha = 50°$ was inserted near the leading edge, which corresponds to a location of high concave curvature and substantial pressure gradient effects. Density ratios of $DR = 1.1$ and 1.6 were applied over a range of blowing ratios, $0.2 \leq BL \leq 1.5$, and momentum ratios, $0.05 \leq I \leq 1.2$. The trends in this data were consistent with those obtained on flat plates, i.e. increases in the density ratio improve lateral mixing, and generally improve the downstream film cooling performance.

In contrast, there are relatively few studies that examine the effect of density ratio on the heat transfer coefficient. Based on observations of the behavior of the film effectiveness, the presence of increased lateral mixing and slower decay rates for injection-generated turbulence suggests that there would be increased augmentation of the heat transfer coefficient as the density ratio is increased. However, Ammari et al. (1990) presented heat transfer measurements using a mass transfer analogy technique that appear to contradict this hypothesis. Density ratios of $DR = 1$, 1.38 and 1.52 were utilized with a flat plate geometry with a single row of holes and angles of inclination of $\alpha = 90°$ and 35°. The applied blowing ratio ranged from $0.5 \leq BL \leq 2.0$. The density ratio was varied holding the blowing ratio constant. Heat transfer data for normal injection showed that this condition was relatively insensitive to the change in density ratio. However, increasing the density ratio was found to reduce the heat transfer augmentation for inclined holes.

1.5.9 Effects of Pressure Gradient and Boundary Layer Thickness on Film Cooling Performance

Pressure gradient and boundary layer thickness are inextricably linked in the modern gas turbine engine so they have been grouped in this subsection. Typical turbine engine components have high curvature and corresponding severe acceleration which dramatically affects the boundary layer growth on the blade surface. Experiments have been performed that attempt to isolate the effect of each of these parameters on the nature of the film cooling jet-mainstream flow interaction using flat plate and curved duct experiments. The essential result of this research indicates that each of these parameters, holding the others constant, have subtle differences in how they affect the development of the film cooling layer.

Eriksen and Goldstein (1974) argue that the thicker the local boundary layer is, the easier it is for the film cooling jet to lift off from the surface. This is because the jet is most effectively bent over when the crossflow has the highest possible velocity. This suggests that, holding everything else constant, increased boundary layer thickness reduces film cooling effectiveness. This agrees with film effectiveness measurements by Liess (1975) that showed injected jets penetrate further into the crossflow the thicker the boundary layer. However, Foster and Lampard (1980) suggests that this could also be due to increased mixing within the thicker boundary layer that leads to reduced effectiveness. Andreopoulos (1985) points out that a key parameter that affects the nature the interaction of the film cooling jet and the freestream is the relative size of the boundary layer and the hole diameter ($\frac{\delta_1}{d}$). Three regimes are identified in this study: $\frac{\delta_1}{d} \ll 1$, $\frac{\delta_1}{d} \approx 1$ and $\frac{\delta_1}{d} \gg 1$. Andreopoulos (1985) argued that this parameter determines if the eddy diffusivity in the boundary layer or in the film cooling jet dictates the resulting flow field. In the extreme cases where either the hole diameter or the boundary layer thickness is much larger, the nature of the turbulence from the hole or the boundary layer will dictate the mixing phenomena between the film cooling jet and the mainstream flow.

A frequently observed feature of the jet-mainstream interaction is the presence of the downstream spiral separation node vortices (DSSNV's). Peterson and Plesniak (2004) showed that these form as mainstream fluid wraps around the CRVP of the film cooling hole. Kadotani and Goldstein (1979a) reported that the presence and size of this backflow region is highly dependent on the momentum deficit at the wall downstream of the hole. In other words, thicker boundary layers are expected to have larger backflow regions.

Another question is the effect of boundary layer thickness on the behavior of the heat transfer coefficient in the presence of film cooling. Hay et al. (1985) examined the effect of the condition of the boundary layer at the point of injection under negligible streamwise pressure gradient conditions. Two displacement thicknesses were investigated: $\frac{\delta_1}{d} = 0.63$ and $\frac{\delta_1}{d} = 0.16$. The first was a fully turbulent boundary layer and the other was transitional. Mass transfer results from this investigation revealed that the boundary layer condition has little effect on the heat transfer coefficient for this situation.

With respect to the effect of streamwise pressure gradient on film cooling, experimental results have been contradictory. Using previous experience with the effect of boundary layer thickness on film effectiveness, one may expect to see improved performance in the presence of favorable gradients. What may add additional confusion when examining experimental studies is whether the effect of the applied pressure gradient has a greater impact by adjusting the thickness of the local boundary layer or changing the nature of the flow exiting the film cooling hole. A key parameter presented in research that isolates the effect of pressure gradient is the dimensionless acceleration parameter, $K = \frac{\nu}{U_{\inf}} \frac{dU_{\inf}}{dx}$.

For a flat plate boundary layer, Jones and Launder (1972) found that favorable pressure gradients reduce heat transfer to the wall, and further demonstrated that flow with $K \geq 4.0(10)^{-6}$ can cause relaminarization of the boundary layer. Launder and York (1974) examined the effects of pressure gradient on film cooling performance using carbon dioxide with a full-coverage film cooling strategy. Results from this study indicated reductions in turbulent mixing due to the application of a strong favorable pressure gradient. This observation was characterized by concentration contours downstream of each hole which indicated a lengthening and narrowing of the film cooling footprint. The one drawback of this work is the unusually low blowing ratios ($2.4(10)^{-3} \leq BL \leq 1.1(10)^{-2}$) which gave laminar flow through the film cooling holes, which is not the case in most modern turbine engines. Furthermore, the thickness of the local boundary layer is unclear in this study.

Schmidt and Bogard (1995) used a flat plate test facility with a top wall contour to generate a pressure distribution representative of that on the suction side of a generic gas turbine blade. With such a setup, acceleration parameter values of $K = 1.5(10)^{-6}$ at the injection location and $K = -0.5(10)^{-6}$ $50d$ downstream of the film cooling holes were achieved . Data from this experiment, in contrast to Launder and York (1974), indicated that the overall effect of pressure gradient on the film cooling effectiveness was small. Once film cooling jets completely detached from the surface, the pressure gradient had virtually no effect on the film cooling effectiveness. When the jets were attached to the cooled wall, however, the presence of the pressure gradient slightly improved the lateral spread of the film cooling footprints and increased the decay of the spanwise-averaged effectiveness. Teekaram et al. (1991) contradicts these results using a flow facility where the acceleration parameter was varied from $-0.22(10)^{-4} \leq K \leq 2.62(10)^{-6}$. Spanwise-averaged data suggest that the effect of mainstream pressure gradient is minimal when the film cooling jets are attached, and the effect becomes pronounced with the jets detach, primarily near the point on injection.

The effect of pressure gradient on heat transfer coefficient appears to be more distinct than its effect on the film cooling effectiveness, especially in the case of a favorable pressure gradient. Hay et al. (1985) found an adverse mainstream pressure gradient had a negligible effect on the heat transfer coefficient with film cooling applied. In contrast, they found that a favorable pressure gradient produced large reductions in the heat transfer irrespective of film cooling hole geometry. Ammari et al. (1991) generally supports these conclusions, but points out that these trends are highly sensitive to the flow conditions of the injected film cooling fluid, i.e. the applied blowing ratio and injection geometry. Changes in these parameters can affect the response of the film cooling layer to the applied pressure gradient. Results from Teekaram et al. (1991), using a transient heat transfer measurement technique modeling an isothermal wall, contradict these trends. One difference between these tests is the presence of compressibility effects; Hay et al. (1985) and Ammari et al. (1991) use relatively low-speed, incompressible flow conditions while Teekaram et al. (1991) used transonic flow conditions. Another is the measurement technique, Hay et al. (1985) and Ammari et al. (1991) used a mass transfer analogy to infer heat transfer coefficients.

1.5.10 Streamwise Curvature Effects on Film Cooling Performance

Modern gas turbine engine blades possess tremendous amounts of streamwise and spanwise curvature. Curvature imposes a pressure gradient in the direction of the radius of curvature of the surface. Two key situations are examined in the literature to isolate the effect of curvature on film cooling performance: 1) mid-span streamwise curvature, 2) leading edge curvature. On typical turbine blades, leading edges are cooled with full-coverage film cooling with rows positioned within $\frac{s}{d} \leq 4.0$ from the stagnation point. Mid-span cooling rows are usually placed $\frac{s}{d} \approx 16.0$ from the leading edge (Muska et al. (1975)).

Before proceeding with the interaction of streamwise curvature with film cooling flows, it is useful to examine the effect of curvature on the undisturbed boundary layer. The key difference between flows over curved surfaces and flat plates can be found in the normal pressure gradient applied by centrifugal force. White (1991) and Schlichting and Gersten (2000) suggest that the effect of wall curvature for laminar boundary layers is small if $\frac{\delta_1}{|\mathcal{R}|} \ll 1$, where $\mathcal{R}$ is the radius of curvature. $\mathcal{R} > 0$ for convex walls and $\mathcal{R} < 0$ for concave walls. However, this is not the case for turbulent boundary layers, as shown by Bradshaw (1973). Further measurements performed by So and Mellor (1973), So and Mellor (1975) and Meroney (1974) confirm that streamwise curvature not only has a tremendous effect on the mainstream flow, but also on the Reynolds stresses which clearly affects the structure of the near-wall turbulent boundary layer. These experiments along with those presented by Eskinazi and Yeh (1956) show that the Reynolds stresses are reduced on convex surfaces and increased on concave surfaces when compared to a flat plate. Furthermore, these studies demonstrated the effect of curvature is an order of magnitude larger than $\frac{\delta_1}{|\mathcal{R}|}$. Mayle et al. (1977) points out that in the case of $\frac{\delta_1}{|\mathcal{R}|} \ll 1$, the production of $\overline{v'^2}$ and $\overline{u'v'}$ are directly affected by curvature. As one might infer, the reduction of Reynolds stresses on a convex surface would result in a corresponding reduction in surface heat transfer, and vice versa for a concave surface. Heat transfer measurements presented by Thomann (1968) confirmed these hypotheses, reflecting the effects of curvature on the Reynolds stresses.

A stability analysis performed by Görtler (1940) revealed that centrifugal force on concave walls causes instabilities that manifest themselves as streamwise vortices, which are often called Taylor-Görtler vortices. Tani (1962) was credited as the first to investigate and confirm this phenomenon experimentally. Barlow and Johnston (1985) performed further flow visualization and velocimetry measurements, using planar-laser induced fluorescence and laser-doppler velocimetry. Results from this study found that these vortices arrange themselves as roll cells, with a diameter of the order of a boundary layer thickness. Furthermore, observations reported in these studies show that the roll cells, in their unperturbed state, move randomly about, appearing, disappearing, merging, and separating. This suggests that such vortices can act to enhance mixing on a concave surface and obviously affect film cooling performance and heat transfer behavior. Observations by Blair (1974), Langston et al. (1977), Langston (1980) and Goldstein and Chen (1985) that indicated that similar vortices are also common near endwalls in blade passages, bringing further importance to studies examining the impact of roll cells on heat transfer augmentation. Furthermore, Eibeck and Eaton (1987) demonstrated that these vortices can maintain their coherence over large streamwise distances (100 boundary layer thicknesses for a flat plate) and augment heat transfer coefficient as much as 24%. Ligrani et al. (1989), Ligrani and Williams (1990), Ligrani et al. (1991), Ligrani and Mitchell (1994a and 1994b) examined the effects of embedded longitudinal vortices on film cooling jets. The "bottom line" of these studies is such vortices can dramatically affect the trajectory and spreading of film cooling jets and consequently degrade the effectiveness of the film cooling layer.

Returning to the general effects of curvature on film cooling effectiveness; from Euler's equation in streamline coordinates (Fay (1994)) it can be observed that the wall-normal pressure gradient would act to keep film cooling jets closer to a convex surface and vice versa for concave surfaces. Thus, at conditions where the condition of the mainstream dominates the jet-in-crossflow interaction (i.e. at very low blowing rates, $BL \ll 1$), it is expected that convex surfaces have better film cooling performance, compared to concave surfaces, holding everything else constant. At such flow conditions the presence of greater turbulent mixing and streamwise vortices would act to degrade film cooling performance on concave surfaces. Ito et al. (1978) developed a simplified model, based on inviscid fluid dynamics, to predict the trends for curvature effects on film cooling performance. The seminal result of this analysis was that the pivotal parameter that affects the trajectory of the film cooling jet and subsequently the film effectiveness is the momentum ratio, I. From this analysis, Ito et al. (1978) postulated for a convex wall ($\mathcal{R} > 0$) that the film cooling performance deteriorates as I increases above 1, and would be better than that on a flat plate or concave wall under the same conditions if $I < 1$. On a concave wall, this analysis predicts that the film cooling performance deteriorates as I decreases below 1, and would be better than on a flat plate or convex surface if $I > 1$. This analysis presupposed that the coolant was injected normally into the mainstream flow; however, it can be extended by multiplying the momentum ratio by $cos^2\alpha$. Ito et al. (1978) presented data from concave surfaces of turbine rotor blades in a low-speed linear cascade (a facility presented in section 1.7). These data verify the validity of this inviscid model and confirm the increased lateral spreading of the film cooling layer on concave surfaces. Data for laterally-averaged effectiveness indicated enhanced spanwise mixing on concave surfaces, causing increased film cooling jet spreading. Ko et al. (1986), using a constant radius of curvature concave surface, observed this phenomenon as well. Schwarz and Goldstein (1989) performed flow visualizations of film cooling on a concave surface that further demonstrated that lateral mixing is very strong. Data from Schwarz et al. (1991) indicated a limited inverse proportional relationship on the severity of curvature ($\frac{R}{d}$). Nevertheless, comparison of effectiveness data reported in this study with data for the pressure side of the turbine blade geometry used by Ito et al. (1978) showed distinctly different behavior. This was attributed to the continuously varying radii of curvature on the turbine blade. Schwarz and Goldstein (1989) also presented data that showed that the downstream lateral averaged effectiveness is a monotonically increasing function of momentum ratio for a concave surface. This was found to be primarily because of the large amount of added thermal mass; especially at higher blowing ratios.

In comparison, Ito et al. (1978) also presented data from convex surfaces of 2-D turbine blades and found considerably less lateral mixing than would be found on either a flat plate or concave surface. This was further supported by Ko et al. (1983) who presented data on a convex surface with a single radius of curvature. Schwarz and Goldstein (1989) demonstrated that an optimum laterally-averaged effectiveness occurs at momentum ratio below 1, using a constant radius surface. Such an optimum was also observed by Ito et al. (1978). Beyond this point, the spanwise-averaged effectiveness drops off, increasing again due to the sheer amount of thermal mass added to the flow. The latter effect is not predicted by the model presented by Ito et al. (1978), primarily due to the assumptions used in formulating this model do not account for this feature.

With respect to film cooling of curved leading edges, Görtler (1955) presented calculations and analysis that demonstrated that streamwise vortices can also form near stagnation points, as the nearby streamlines develop a concave curvature as they pass around the stagnation point. This behavior is further confirmed by the direct numerical simulations of Kalitzin et al. (2003). These vortical structures not only affect the local heat transfer coefficients, but the distribution of coolant from leading edge film cooling holes. Tillman and Jen (1984) and Tillman et al. (1984) measured discharge coefficients at a range of blowing ratios for several configurations of hole geometries subjected to a stagnation point flow. Mee et al. (1999), Salcudean et al. (1994), Mick (1988), Luckey et al. (1977) and Luckey and L'Ecuyer (1981) examine a variety of leading edge geometries, film cooling hole geometries and blowing conditions and report the effects on the film cooling effectiveness and heat transfer coefficient.

1.5.11 Effect of Miscellaneous Conditions

All the results presented earlier assume a hydrodynamically smooth surface for measurements. In operational gas turbine engines, surfaces of cooled components have a initial roughness from a ceramic thermal barrier coating (TBC) and become progressively rougher due to corrosion, or deposits of a variety of contaminants. This raises the issue of how these practical issues affect film cooling performance. Goldstein et al. (1985) examined the effect of surface roughness on film cooling effectiveness using staggered cylindrical roughness elements with a diameter of $0.5d$ and a characteristics heights of $0.5d$ or $0.25d$. The elements were arranged in three configurations: upstream only, downstream only and upstream and downstream. The primary effect of the roughness elements is the greater amount of turbulent mixing that occurs in the boundary layer as a direct result of the roughness elements. Hence, the observed behavior mirrors that of a increased turbulence levels on film cooling. At low blowing rates, roughness appears to reduce film cooling performance by increasing the amount of turbulent mixing. At high blowing ratios, increased surface roughness improves the film cooling effectiveness by limiting the penetration of the film cooling jet into the mainstream. In both cases, the presence of roughness increases the lateral mixing of the coolant flow, reducing spanwise variations. Results from this study indicated that generally the presence of roughness causes a decrease in the spanwise-averaged effectiveness.

In modern gas turbine engines, the flow around turbine components is often transonic; this introduces the interaction of shock waves and film cooling flow. Shock waves can form at the trailing edges of rotor and stator blades, these are often called “fishtail” shocks. An example of such shock structures can be seen in Figure 1.13 on the trailing edges of the 2-D turbine stator blades arranged as a linear cascade of blades. Shocks may also be produced from the interaction of a supersonic flow interacting with a row of film cooling holes. Wittig et al. (1996) demonstrated that the blockage from exiting coolant from a row of holes can cause a bow shock when exposed to supersonic flow. This can have ramifications on the downstream film cooling performance. Gritsch et al. (1998a) reported that bow shocks that form at the upstream interface of the injected coolant and the mainstream flow can improve film cooling performance. Ligrani et al. (2001) explored a range of blowing ratios, film cooling plenum configurations and their effects on resulting shock structure that forms at the interface of the film cooling jet and a supersonic mainstream flow. This study demonstrated that the presence of film cooling in a supersonic flow can cause the formation of complex oblique shock structures that affect the essential features of the jet-mainstream interaction.

1.5.12 Combined Parameter Effects on Film Cooling

The previous sections presented results from experiments that attempted to isolate one or two parameters at a time and examine the resulting effect on the film cooling jet-mainstream interaction. The drawback with this approach is that in operating engines, all these parameters are combined at the same time and it is often unclear which parameter dominates or the manner in which these parameters interact. Furthermore, a key factor in film cooling performance is the very nature of the mainstream flow itself. The vast majority of experiments cited in the previous sections are for an incompressible flow, while in modern turbine engines the flow is more often than not, compressible. Thus, to advance the science of film cooling modeling it is necessary to develop experiments that include as many mainstream flow features as possible that are consistent with expected turbine conditions. However, it is just as important that the boundary conditions and data are as accurate and well-resolved as possible. Section 1.7 describes standard approaches to achieving experimental conditions consistent with an actual engine. This section presents some results from some of these facilities. In the majority of experiments presented here, measurement blade components are constructed from a variety of metals. This means that the wall boundary condition is certainly not adiabatic for performing film cooling effectiveness measurements. Nevertheless, it is often assumed that any conduction errors are negligible – an assumption that is often invalid.

Gauntner (1977) compared the film cooling performance of a set of compound angle holes ($\alpha = 30°$ and $\beta = 45°$) with simple-inclined holes. An annular sector cascade (described in Section 1.7), at conditions representative of that of an advanced turbofan engine at takeoff and cruise, was utilized in these tests. Measurements were performed with thermocouples embedded at various locations in the flow facility.

Nirmalan and Hylton (1990), using a three-vane, two dimensional linear cascade, performed steady state measurements of the heat transfer coefficient with both leading edge and downstream film cooling injection. The cascade was fitted with an internally cooled measurement airfoil and a relatively high density of thermocouples. The heat transfer coefficient distribution was obtained via finite element analysis, solving for the internal temperature distribution.

Takeishi et al. (1992), using the mass transfer analogy, conducted film cooling effectiveness measurements in a low-speed linear cascade and a rotating annular cascade. Comparison of these two data sets showed good agreement on the suction sides of the airfoils in question, but lower effectiveness on the pressure side when rotation is present. These observations are in line with those of Dring et al. (1980) who measured film cooling effectiveness on the rotor blade of a low speed turbine stage using a mass transfer analogy in a linear cascade. Abuaf et al. (1997) reported film cooling effectiveness and heat transfer coefficient measurements of a five-vane linear cascade. This facility was designed to operate in two modes: in steady state mode to obtain film cooling effectiveness measurements and in transient mode for heat transfer coefficient measurements.

Camci and Arts (1985a) performed measurements of the heat transfer coefficient on the suction side of a turbine airfoil in a six rotor blade linear cascade both with and without film cooling. The measurement blade was constructed of a low-thermal conductivity material. A short-duration transient technique was utilized with embedded thermocouples. This study was expanded by Camci and Arts (1985b) who performed additional measurements with leading edge full-coverage film cooling. Camci (1989) used data from these experiments to calculate the temperature gradients inside the measurement turbine blade and determined areas susceptible to thermal fatigue. Camci and Arts (1990) extended these tests with a more intricate film cooling injection system, involving leading edge and mid-chord cooling rows. Thin film gages were used in all these tests to measure the heat transfer coefficient based on the free-stream recovery temperature. Lastly, Camci and Arts (1991) investigated the effects of flow incidence on the interaction of film cooling and the resulting heat transfer coefficient distribution.

Ekkad et al. (1997) examined the combined effect of grid turbulence and unsteady upstream wakes on a turbine blade. In this study, an incompressible linear cascade was utilized with a varying density ratio, modified with air and CO_2 as coolant. A rotating spoked wheel with 32 rods simulated the upstream stage wakes in this test. Results from this study found that the film coolant injection augmented the heat transfer coefficient. Furthermore, increasing the turbulence intensity led to additional augmentation of the heat transfer coefficient.

Du et al. (1997, 1998, 1999) performed a series of low-speed linear cascade tests that mimic characteristic situations found in operational turbine engines. In the first test, velocity and heat transfer measurements were performed to quantify the effect of trailing edge injection on the downstream velocity field and heat transfer on a linear cascade consisting of five uncooled blades. These results showed that trailing edge injection augments the heat transfer coefficient, especially near the leading edges of the blade row. In the next test, the authors explored the separate effects of unsteady upstream wakes on blade surface heat transfer and film cooling performance. The final test examined the combined effects of unsteady upstream wakes, grid-generated turbulence and upstream trailing edge film cooling injection on the heat transfer coefficient and film cooling effectiveness of a downstream row.

Arts and Bourguignon (1990) examined the film cooling performance of a double row of film cooling holes on the pressure side of a turbine nozzle guide vane. Drost and Bölcs (1999) examined the film cooling effectiveness and heat transfer coefficient on a turbine nozzle guide vane (NGV) using a five-blade linear cascade. Film cooling rows were installed on both pressure and suction surfaces of the tested airfoil. A range of blowing ratios, density ratios, inlet Mach numbers and Reynolds numbers based on blade chord were examined.

Abhari and Epstein (1994) conducted time-resolved measurements of heat transfer coefficient on a fully cooled transonic turbine stage. In these tests, a rotating, short-duration (0.3s), transient test facility was utilized with high frequency response thin film heat flux gages. The focus of this study was to experimentally quantify the influence of flow three-dimensionality and unsteadiness on film cooling performance on a transonic, rotating turbine stage. The measurement blade geometry in this test, a Rolls Royce ACE high pressure turbine stage geometry, was fitted with several film cooling rows which injected coolant 27% cooler than the mainstream total temperature (on an absolute scale). Additionally, there was upstream coolant injection, to simulate the trailing edge injection of an upstream stator row. Results from this experiment suggested that the flow over the central part of the airfoil geometry is primarily two-dimensional. Additionally, the film cooling performance was found to be much poorer on the pressure side than the suction side. These data compared favorably to two-dimensional linear cascade data from Rigby et al. (1990), who also simulated the effect of upstream passing wakes. Abhari (1996) used data from these two studies to develop additional numerical analysis to investigate the effect of rotor-stator interaction on film cooling performance.

Cutbirth and Bogard (2002a and 2002b) present film cooling effectiveness data on the pressure side of a turbine vane installed in a double passage cascade. In the first series of tests, the authors examine the interaction of film cooling holes at the leading edge (termed in the literature as “showerhead” film cooling) with downstream film coolant injection. The authors argue with mean velocity and turbulence measurements, conducted with a LDV system, that showerhead cooling introduces high turbulence levels that augment mixing of the downstream injected coolant. This results in lowering the effectiveness of the downstream row in this particular case. The subsequent report examines the effect of increasing the turbulence levels with and without showerhead cooling. The turbulence levels chosen included one that was higher than the level caused by showerhead injection ($Tu\% = 20\%$). In spite of this, the authors found that showerhead injection still has a significant effect on the downstream film cooling performance.

1.6 Numerical Modeling Efforts for Film Cooling Design

Several efforts have been presented in the open literature that attempt to simulate the complex characteristics of the interaction of a film cooling jet and a mainstream flow. These efforts can be divided into the following classes, sorted by order of computational expense from highest to lowest:

1. Direct Numerical Simulation (DNS)

2. Large-Eddy Simulations (LES).

3. Full Reynolds-Averaged Navier Stokes (RANS) Simulations.

4. Macro-model or Parametric Simulations (MM).
5. Boundary Layer Equation Simulations (BLE).
6. Correlations.

Computational expense of these techniques is closely linked to the intricacies of simulation approach. The more directly the flow physics of the jet-in-crossflow are simulated, the more expensive the procedure. Presumably, the more "physics-based" the simulation technique, the more robust the resulting predictions are when extrapolations are required for new designs. More precisely, one would expect that correlations which are directly fit to experimental data would have increased uncertainty when new designs are developed outside the parameter ranges of the base data. Nevertheless, a critical issue in film cooling design is that any optimization procedure must have an extremely short turnaround time (1–2 days) to fit in the design time frame for a new engine. This constraint, along with the fact that the flow conditions are almost always compressible, with strong streamwise curvature limits the use of higher accuracy simulation schemes. However, the value of LES or DNS is greater understanding of the inherent complex flow structures in the jet-in-crossflow interaction which can be used to improve modeling efforts. Lakehal (2002) demonstrated the value of this approach in providing data for improved RANS simulations. Although these numerical tools can provide a greater volume of high-resolution data in comparison to experiments, there is always a question of their accuracy.

Another quandary in numerical modeling efforts using RANS, MM or BLE is the dependence on high-resolution, low uncertainty experimental data with well-defined boundary conditions. Unfortunately, the vast majority of experimental data that meets these requirements utilize a low-speed, flat plate boundary layer flow condition. This is useful for initial validation of film cooling simulation techniques and examining the complex flow structures and turbulence characteristics downstream of a row of film cooling holes. The deficiency of this general approach is that it does not incorporate enough of the flow characteristics of a gas turbine engine, i.e. compressibility and complex curvature. On the other hand, experiments that accurately model real gas turbine engine conditions, practically by default, do not have accurately known boundary conditions (Dunn (2001)). Hence, the problem for the modeler is often whether the difference in predictions are because of the models or differences in the applied boundary conditions. Thus the transition of lower-order accuracy simulation techniques to their implementation as design tools is limited by the availability of high-quality experimental data, with well-defined boundary conditions at comparable flow conditions to operational turbine engines.

1.6.1 The Navier-Stokes Equations and Reynolds Averaging

Before delving into the application of various solution techniques, it is useful to recount the appropriate describing equations. Often incompressible flow conditions are assumed in numerical analyses and the cardinal computed variables are ρ and u_i. These are termed primitive variables. For compressible flows, the primary computed variables are ρ, ρu_i and e, which are termed conservative variables. In tensorial notation the Navier-Stokes equations (for mass, momentum and energy) for a compressible, variable property flow are (from MacCormack (1995)):

Continuity

$$\frac{\partial \rho}{\partial t} + \frac{\partial(\rho u_j)}{\partial x_j} = 0 \tag{1.4}$$

Momentum

$$\frac{\partial \rho u_i}{\partial t} + \frac{\partial(\rho u_i u_j)}{\partial x_j} = -\frac{\partial P}{\partial x_i} + \frac{\partial \tau_{ij}}{\partial x_j} \tag{1.5}$$

Energy

$$\frac{\partial e}{\partial t} + \frac{\partial(e u_j)}{\partial x_j} = -\frac{\partial P u_j}{\partial x_j} + \frac{\partial \tau_{ij} u_i}{\partial x_j} + \frac{\partial q_j}{\partial x_j} \tag{1.6}$$

where the total energy is defined as:

$$e = \rho(\epsilon + 0.5 u_i u_i) \tag{1.7}$$

the perfect gas equation of state is:

$$P = P(\rho, \epsilon) = (\gamma - 1)\rho\epsilon \tag{1.8}$$

the viscous stress tensor is defined as:

$$\tau_{ij} = \mu\left(\frac{\partial u_i}{\partial x_j} + \frac{\partial u_j}{\partial x_i}\right) + \delta_{ij}\lambda\frac{\partial u_k}{\partial x_k} \tag{1.9}$$

assuming a Newtonian fluid:

$$\lambda = -\frac{2}{3}\mu,\ \mu = \mu(T),\ q_j = k\frac{\partial T}{\partial x_j},\ k = \frac{\mu c_p}{Pr},\ \epsilon = c_v T \tag{1.10}$$

Farve (1965) suggested a density-weighted averaging procedure that, when applied to the compressible Navier-Stokes equations, gives a compact result. The instantaneous value is decomposed into a mass-averaged term and a fluctuating term:

$$u_i = \tilde{u}_i + u_i'' \tag{1.11}$$

Where $\tilde{u}_i$ is defined as:

$$\tilde{u}_i = \frac{1}{\overline{\rho}} \lim_{\tau_s \to \infty} \frac{1}{\tau_s} \int_t^{\tau_s + t} \rho(\mathbf{x}, \tau) u_i(\mathbf{x}, \tau) \mathrm{d}\tau \tag{1.12}$$

Whereas instantaneous variables that are decomposed using standard Reynolds averaging are simply decomposed into a time-averaged and a fluctuating term:

$$u_i = \overline{u}_i + u_i' \tag{1.13}$$

Where $\overline{u}_i$ is defined as:

$$\overline{u}_i = \lim_{\tau_s \to \infty} \frac{1}{\tau_s} \int_t^{\tau_s + t} u_i(\mathbf{x}, \tau) \mathrm{d}\tau \tag{1.14}$$

Applying Farve averaging to the flow variables:

$$\begin{aligned}
\rho &= \overline{\rho} + \rho' \\
P &= \overline{P} + P' \\
u_i &= \tilde{u}_i + u_i'' \\
h^i &= \tilde{h}^i + h'' \\
e &= \tilde{e} + e'' \\
T &= \tilde{T} + T'' \\
q_j &= \overline{q}_j + q_j'' \\
\tau_{ij} &= \overline{\tau_{ij}} + \tau_{ij}'
\end{aligned} \tag{1.15}$$

The Farve-averaged equations for a compressible, turbulent flow become (from MacCormack (1995)):

Continuity

$$\frac{\partial \overline{\rho}}{\partial t} + \frac{\partial (\overline{\rho} \tilde{u}_j)}{\partial x_j} = 0 \tag{1.16}$$

Momentum

$$\frac{\partial \overline{\rho}\tilde{u}_i}{\partial t} + \frac{\partial(\overline{\rho}\tilde{u}_i\tilde{u}_j)}{\partial x_j} = -\frac{\partial \overline{p}}{\partial x_i} + \frac{\partial}{\partial x_j}(\tau_{ij} - \overline{\rho u_i'' u_j''}) \tag{1.17}$$

Energy

$$\frac{\partial \overline{e}}{\partial t} + \frac{\partial(\overline{e}\tilde{u}_j)}{\partial x_j} = -\frac{\partial \overline{p}\tilde{u}_j}{\partial x_j} - \frac{\partial \overline{\rho u_j'' h''}}{\partial x_j} + \frac{\partial}{\partial x_j}\left[\tilde{u}_i(\overline{\tau_{ij}} - \overline{\rho u_i'' u_j''}) - \overline{u_i''(\tau_{ij}' - \rho u_i'' u_j''/2)}\right] + \frac{\partial \overline{q}_j}{\partial x_j} \tag{1.18}$$

Where $\frac{\partial \overline{\rho u_j'' h''}}{\partial x_j}$ represents the Reynolds heat flux terms and $-\frac{\partial}{\partial x_j}\overline{u_i''(\tau_{ij} - \rho u_i'' u_j''/2)}$ represents the Reynolds dissipation terms.

1.6.2 LES and DNS Efforts

Direct Numerical Simulation (DNS) is a technique that provides the solution for the three-dimensional, unsteady Navier-Stokes and continuity equations with specified boundary and initial conditions. All the scales of the flow are numerically resolved, from large-scale coherent structures to the smallest turbulent eddies. In spite of the tremendous advances in computational capabilities, the necessary numerical requirements limit the application of this technique to relatively simple geometries and low Reynolds numbers. Nevertheless, Hahn and Choi (1997) presented such a simulation for a slot issuing into a laminar crossflow and a row of circular, normal holes injecting a turbulent jet into a turbulent crossflow. For the circular jet injection case, $14.6(10)^6$ grid points were used. Due to limitations of resources and computation time, the flow velocities were much lower than comparable experiments. In this simulation, a relatively low mainstream displacement thickness-based Reynolds number ($Re_{\delta_1} = 500$) and a representative boundary layer displacement ($\frac{\delta_1}{d} = 0.143$) were implemented. A parabolic profile was imposed at the injection location with a blowing ratio of $BL = 0.5$. Muldoon and Acharya (1999) performed a direct numerical simulation of a row of normally inclined, square jets at blowing ratio of $BL = 0.5$. This mirrored an experimental setup presented by Ajersch et al. (1997). A comparison of the numerical and experimental data showed good agreement for the mean velocity profiles in the near-field of the injection point. In both numerical studies, turbulent statistics were not presented. Hence, there is little knowledge of the behavior of Reynolds stresses in these flows.

Large Eddy Simulation is computational technique where only the large-scale, time-dependent flow structures are directly computed. These large-scale structures are dependent on the flow boundary conditions and contain the majority of the kinetic energy in the flow. The smaller scales or subgrid scales (SGS) are expected to be weaker and are relatively insensitive to the boundary conditions, and thus are modeled. This simplification allows high-accuracy simulations of injected jets at typical experimental conditions. One of the primary issues inherent to LES is the implementation of accurate and reliable wall boundary conditions. Considering the objective of any film cooling simulation is to obtain the wall temperature distribution, wall boundary conditions are clearly critical. Yuan et al. (1999) reported on a set of LES performed on a single round jet injecting normally into a turbulent crossflow. The focus of this work was the jet entrainment and trajectory characteristics for a range of flow conditions. For this case, a domain size of approximately $1.34(10)^6$ grid points was utilized. Blowing ratios of $BL = 2$ and $BL = 3$, with displacement thickness-based Reynolds numbers of $Re_{\delta_1} = 182$ and $Re_{\delta_1} = 363$ were investigated in this study. Tyagi and Acharya (2003) compared the results of LES simulation performed on a row of inclined holes ($\alpha = 35°$) at blowing ratios of $BL = 0.5$ and $BL = 1$ to velocity measurements of Lavrich and Chiappetta (1990) and the film cooling effectiveness measurements of Sinha et al. (1991b). This comparison demonstrated the feasibility of using LES to accurately model the complex fluid dynamical processes that occur in the jet-in-crossflow interaction. The results from this simulation were then used to examine the various flow structures present in the flowfield and their effects on entrainment rates and mixing processes in the wake region.

1.6.3 RANS Simulation Efforts

The popularity of using simulation techniques that solve the Reynolds-Averaged Navier Stokes (RANS) equations has grown dramatically over the last 25 years. This is generally because of the dramatic improvements in cost-effective numerical resources, both from computational and storage perspectives. This approach presents almost the ideal combination of relative speed and robustness that can fit into the design procedure of many gas turbine engine companies. However, there are significant issues about the reliability and accuracy of such models for film cooling.

The RANS equations for a compressible turbulent flow (Equations 1.16, 1.17 and 1.18) include Reynolds stress terms ($-\overline{\rho u_i'' u_j''}$) that must be represented using a turbulence model. The simplest approach to calculating these stresses rests upon the Boussinesq eddy viscosity approximation, which models these stresses as:

$$-\overline{\rho u_i'' u_j''} = \mu_t \left(\frac{\partial \tilde{u}_i}{\partial x_j} + \frac{\partial \tilde{u}_i}{\partial x_j} \right) + \delta_{ij} \lambda_t \frac{\partial \tilde{u}_k}{\partial x_k}, \ \lambda_t = -\frac{2}{3} \mu_t \tag{1.19}$$

Where the subscript t refers to turbulent flow and μ_t is called the eddy viscosity. With this assumption the total effective viscosity, μ can be computed as:

$$\mu = \mu_l + \mu_t \tag{1.20}$$

where μ_l is the molecular viscosity. The Reynolds heat flux and dissipation terms are similarly modeled as:

$$-\overline{\rho u_j'' h''} + \overline{u_i''(\tau_{ij}' - \rho u_i'' u_j''/2)} = k_t \frac{\partial T}{\partial x_j} \tag{1.21}$$

Again, with this assumption, the total effective thermal conductivity, k is:

$$k = k_l + k_t \tag{1.22}$$

The turbulent thermal conductivity is related to the eddy viscosity using the turbulent Prandtl number, (Pr_t) using the relation:

$$k_t = \frac{\gamma\mu}{Pr_t} c_v \tag{1.23}$$

Pr_t is assumed to have a value of 0.9, this assumption is considered somewhat dubious and alternative models have been proposed (Kays and Crawford (1993)). Nevertheless, the vast majority of RANS calculations use this assumption.

This overall approach is one of the most popular techniques to predict film cooling effectiveness for a wide range of mainstream conditions and injection geometries, as well as other flows of engineering interest. One further assumption which is implicit in this presentation is that the turbulent viscosity is isotropic. Such an assumption has been experimentally and numerically shown to be inadequate. Wang et al. (1996) and Kaszeta and Simon (2000) directly measured and verified the anisotropy of the eddy diffusivity downstream of different hole geometries. Turbulence measurements by Andreopoulos and Rodi (1984) present the variation of Reynolds stresses as the film cooling jet interacts with and the mainstream. These measurements indicated that generally the primary shear stress, $\overline{uv}$, can be described using an eddy viscosity model. The important exceptions where there is streamline convergence or divergence, which frequently occurs in the immediate vicinity of the hole, and in the lateral spreading in the jet. These observations are matched by the LES of Tyagi and Acharya (2003), that has been previously described. Bergeles et al. (1978) was the first to suggest a linear relationship to model the anisotropy of the eddy viscosity for extremely low blowing rates ($BL < 0.1$). Demuren et al. (1986) demonstrated that these recommended modifications to the standard two-equation $k-\varepsilon$ can improve predictions for film cooling effectiveness for a wide variety of hole geometries. Data presented by Ajersch et al. (1997) demonstrated the inability of the two layer $k-\varepsilon$ model to predict the near hole velocity and turbulence fields (specifically TKE and $\overline{u'w'}$) at higher blowing ratios, despite this correction for the eddy viscosity for a row of square jets. However, these authors found that the prediction does improve further downstream as the flow recovers to a standard turbulent boundary layer. Hoda and Acharya (2000) furthered this effort, testing seven different eddy-viscosity based, two-equation turbulence models. They found close agreement right at the jet exit and far downstream, but showed that these models incorrectly captured the wake region immediately downstream of the injection point.

Lakehal (2002) used channel and boundary layer DNS data to improve the near wall modeling and variation of the eddy viscosity and turbulent Prandtl number, with vastly improved results especially with increasing blowing rate. This is a important development considering that Walters and Leylek (1997) showed that models without these modifications produced worse results as the blowing ratio is increased.

Another issue with standard two-equation turbulence models is the overprediction of turbulent kinetic energy in regions of high irrotational strains. Such a deficiency leads to over predictions of turbulent mixing. Durbin (1996) presented one strategy to account for this problem that he proved to be successful for a high-Reynolds number, incompressible flow. Medic and Durbin (2002a and 2002b) demonstrated how the spurious production of turbulent kinetic energy can dramatically affect the prediction of heat transfer and film cooling effectiveness on transonic turbine blade geometries, specifically the cases presented by Camci and Arts (1985a and 1985b). The authors further show how the implementation of limiters for the production of turbulent kinetic energy can substantially improve the heat transfer predictive capability of RANS.

In spite of these well-documented deficiencies, considerable research has been conducted using RANS to develop insight into the complex fluid dynamics characteristic of the film cooling jet-in-crossflow mixing process. Leylek and Zerkle (1994) and Walters and Leylek (2000a) demonstrated the importance of including the supply channel and conditions on film cooling predictions using RANS. Furthermore, they suggested practices to keep numerical errors to a minimum. This work was followed by studies by Walters and Leylek (2000a), McGovern and Leylek (2000), Hyams and Leylek (2000) and Brittingham and Leylek (2000) that examined the effect of hole geometry on the downstream film cooling effectiveness and flow field characteristics. Walters and Leylek (2000b) examined the resulting aerodynamic losses due to film cooling on a turbine blade geometry. Garg and Gaugler (1996) and Theodoridis et al. (2001) conducted RANS simulations on the effects of leading edge film cooling on the calculated heat transfer coefficient on a transonic turbine blade geometry (C3X vane). As discussed in Section 1.2, Garg (1999) applied two-equation turbulence models and a zero-equation turbulence model to a film-cooled rotor blade operating at representative engine conditions. Garg and Gaugler (1997a) and Garg and Gaugler (1997b) examined the effect of coolant-to-mainstream temperature ratios and the velocity distribution from rows of cooling holes on the overall film cooling performance for a variety of blade geometries and cooling configurations.

Another approach to closing the RANS equations is to model the Reynolds stresses using stress transport models. These models are called Reynolds Stress Models (RSM) or Second Moment Closure models (SMC). Such an approach allows for the expected anisotropy in complex turbulent flows. However, the results of applying this solution approach to heat transfer and film cooling predictions have been mixed. Garg and Ameri (2001) compared the results from a RSM applied to the uncooled heat transfer experimental measurements of Giel et al. (1999). This was found to provide significant improvement over $k-\omega$, except in areas of large adverse pressure gradients. Azzi and Lakehal (2002) compared results of two-equation turbulence models modified as suggested by Lakehal (2002) to a variety of RSMs and also found no distinct improvement in film cooling effectiveness predictions.

A pressing issue with the application of RANS with film cooling has been the excessive number of grid points required to minimize numerical error and capture the spreading phenomena from the film cooling jets. Davis (2000) estimated grid point counts of a minimum of 700,000 for single row of film cooling holes installed on a transonic blade geometry. Given the complexity of cooling systems installed in modern turbine blade, the current time investment required to obtain a solution with limited error, and the fact that these calculations still produce results that deviate as much as 50% relative to experimental measurements makes large-scale design applications of RANS effectively impractical.

1.6.4 Macro-model or Parametric Simulations

An impediment to the implementation of RANS for film cooling optimization is the time required to generate a computational grid for new designs. Often this takes longer and causes more difficulties than the actual simulation. Considering the number of variables that can affect film cooling performance, it is vital that as many cooling strategies as possible are accurately tested before the final design is complete. As a consequence, effort has been placed to developing parametric models that add source terms to the Reynolds-averaged Navier-Stokes equations that impose the effects of film cooling on the flow field. Such an approach has the advantage that once a grid is generated for the blade components, no other grids need be generated. The optimization proceeds until the best cooling system is achieved. Higher accuracy simulations can then be implemented to verify the design.

Ziegler and Wooler (1971) and Le Grivès (1978) following a theoretical model for jet trajectory and mixing processes, developed a set of closed form equations for the vortex strength and spacing for the CRVP. However, this model was developed for $BL \approx 8$, where the jet passes straight-through the boundary layer. Such a situation is more appropriate for V/STOL or smokestack jet injection, rather than film cooling. Subramanya and Porey (1984) presents an alternative model formulated along similar lines as Le Grivès (1978), except at blowing ratios more representative of film cooling designs.

Kim (1985) reported on an analytical mixing model for a buoyant jet injected into a pipe. The premise of this technique is based on jet trajectory, diffusion layer, and flow establishment models based on “fitting” experimental data. The distinction of this model in comparison to previous such analyses was inclusion of the injection angle and the applicable range of blowing ratios in the model parameters. In this model, the switch-over with increasing blowing ratio from the turbulent diffusion dominated mixing processes for weak jets to the inviscid jet dynamics of strong jets is modeled.

Kulisa et al. (1992) and LeBœuf et al. (1991) presented a jet injection model based an integral solution of the three-dimensional jet equations. This technique avoids the use of previous analytical methods and is coupled with the main solver for the RANS equations. However, to close the set of equations for the jet model, several “educated guesses” are made about the shape of the jet cross-section and its interaction with the mainstream flow.

The critical deficiency with all these models is their current inability to correctly account for the changes in the hole geometry. Of these models that use a vorticity model for the jet evolution, virtually all these assume a CRVP leaves the injection hole, but experimental data has shown that this is definitely not the case for specific hole geometries, such as compound angle holes. The model presented by LeBœuf et al. (1991) can be easily corrected to account for this, but this requires a high degree of experimental data on the jet velocity and temperature field evolution for a range of cases. Clearly this limits the predictive capability to conditions that are within the domain of collected data, but it is expected to be an improvement over lower-order techniques.

1.6.5 Boundary-Layer Equation Simulations and Correlations

Instead of applying the RANS equation to an entire domain, a combination of the boundary layer equations (also called the thin-layer Navier-Stokes equations) and the Euler equations can be used. This approach has advantages over solving the full RANS equations where the flow solver is fully coupled for the entire flow domain. The boundary layer equations are parabolic so they can be solved in a single sweep of a numerical scheme, meaning highly-resolved solutions can be obtained virtually instantaneously with modern computers. The use of the boundary-layer equations requires detailed *a priori* understanding of the flow field because the equations are typically only valid for attached, shock-free flows. Schönung and Rodi (1987) documented predictions for a row of holes with a modified two-dimensional boundary layer code that attempted to account for the complex mixing process inherent in the jet-in-crossflow interaction. Haas et al. (1992) extended this to explore the effect of temperature gradients between the coolant and the mainstream. In both these studies the wall shape was either a flat plate or the suction side of a turbine blade. The results from both these studies are generally poor in comparison to experiments. Furthermore, considering that this model implicitly precludes the possibility of cooling jet lift-off, it is of limited utility as a prediction tool.

In spite of the massive computational capabilities available, the most used tool by film cooling designers is still correlations. In comparison to RANS simulations, this is considered a more robust, and certainly more efficient design path for turbine manufacturers. As mentioned earlier, Goldstein (1971) documented a set of successful correlations for slot injection film cooling. Such correlations were based on control volume analyses to develop their functional forms, and then data was used to "tune" various constants. In the case, of three-dimensional film cooling, the number of variables that affect performance made the use of correlations a highly approximate science. Hence, there are very few papers in the open-literature that present new correlations for film cooling. Brown and Saluja (1979) used analyses based on an energy balance to correlate film cooling effectiveness to hole spacing ($\frac{s}{d}$). Jubran (1989) developed a correlation extending an approach based on the momentum ratio, I, for two rows of inclined holes. Baldauf et al. (2002a, 2002b, 2001b and 2001a) presented a set of correlations for heat transfer augmentation and film cooling effectiveness

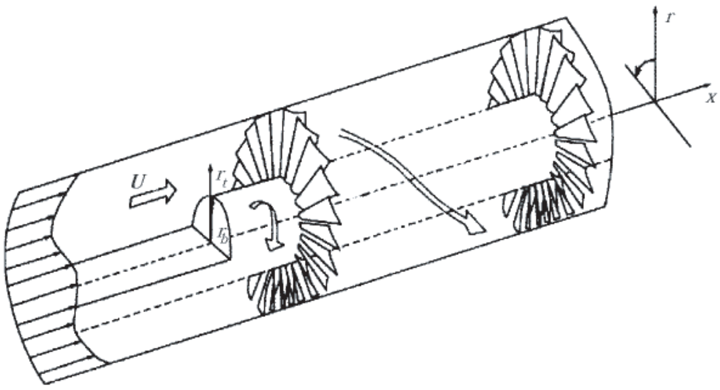

Figure 1.8: Schematic of an annular rotating cascade (from Atassi et al. (2004)).

with blowing ratio (BL), density ratio (DR), injection angle (α) and hole spacing ($\frac{s}{d}$). The form of the correlations was achieved by taking multiple data sets and intelligently choosing constants and functional forms to collapse the data, rather than using control volume analyses. The assumed geometry for both these approaches was a flat plate with inclined holes, this raises the obvious question of how to extend this to more complicated geometries. Nevertheless, such correlations give an important "first guess" for film cooling design.

1.7 Experimental Approximations for Turbine Flow Conditions

There are several approaches presented in the open literature to experimentally simulate the flow field around a given gas turbine engine rotor or stator blade geometry. The flow facility selection effectively decides the appropriate measurement technique. Clearly the best facility for simulating engine conditions would be a full mock up of the engine. However, the costs involved in pursuing such a course are only warranted once all engine subsystems, including film cooling have been designed. Furthermore, the better the facility is at simulating engine conditions, the more uncertain the flow boundary conditions are for each stage due to the complexity of the flow. The classes of facilities can, in general, be divided into two main subsets: non-rotating cascades (linear and annular) and rotating facilities. These subsets can further be divided into transient and steady state experiments.

The first simplification is a steady state, annular rotating cascade, an example of one is shown in Figure 1.8. This approach is primarily used for compressor geometries as demonstrated by Schulz and Gallus (1988) and Wisler et al. (1987). Blair (1994) using an incompressible, steady, ambient temperature, large-scale turbine rotor passage, obtained highly-resolved maps of heat transfer coefficient without film cooling. The only complexity lacking from this work was the matching of inlet Mach number for a typical rotor stage. The extreme costs and flow requirements make building a new engine preferable than building such a cascade that matches typical engine Mach numbers. As a compromise, transient rotating annular cascades, such as that introduced earlier by Abhari and Epstein (1994) are utilized. This particular facility operates in blowdown mode, where a large tank is filled with compressed air, and a shutter valve is suddenly opened at the commencement of the test. Such a facility offers tremendous savings in comparison to steady state facilities. Furthermore, the short measurement times limit conduction effects. This is an important issue because real engine hardware (i.e. metal) is used in these experiments. Another approach is a shock-tube driven transient rotating facility, as pioneered by Dunn and Stoddard (1979) and Dunn (1986) who presented heat transfer data for an uncooled Garrett TFE (turbofan engine) 731-2 high-pressure full stage rotating turbine. The same shock tube facility was used with different turbine housings, modeling several different turbine stages. Dunn and Chupp (1988) presented time-averaged heat-flux data for an uncooled Teledyne 702 high-pressure turbine stage and Dunn et al. (1994) conducted time-averaged heat transfer and pressure measurements for the uncooled first-stage vane and blade rows of the Space Shuttle Main Engine (SSME) fuel turbine. These housings are designed for a specific class of blade geometries. This means that for every new class of blade, a whole new housing with instrumentation is required. Figure 1.9 shows the device housing for the SSME test, as an example of the range of instrumentation required for each test and Figure 1.10 shows an overall view of the shock-tube facility.

These experiments can be designed to run at a wide variety of conditions, from engine takeoff to cruise conditions for a specific engine. The primary drawbacks of this approach are linked to the extreme nature of the flow conditions; such as, high inlet temperatures, on the order of 500 K and highly stressed experimental components due to rotation rates as high as 10,000 rpm. Such tests often have a duration of a few hundred milliseconds, requiring the use of complex transient measurement techniques to extract heat transfer and pressure data on the test engine component. This is discussed in more detail later in this chapter. These techniques typically only allow for low spatial resolution measurements of desired quantities, which effectively limits their usefulness to modeling efforts, unless there

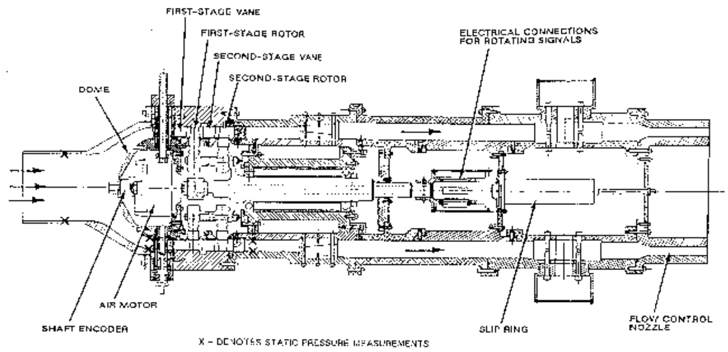

Figure 1.9: Layout of housing for space shuttle main engine turbopump turbine shock-tube test (from Dunn et al. (1994)).

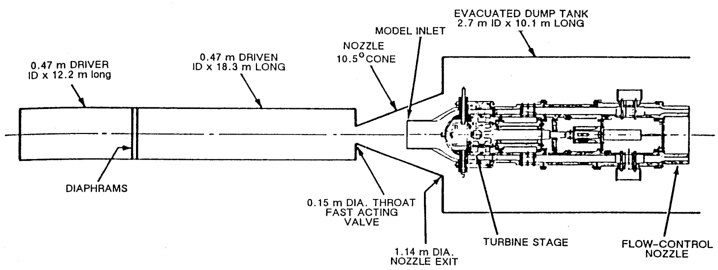

Figure 1.10: Layout of shock-tube facility (from Dunn et al. (1994)).

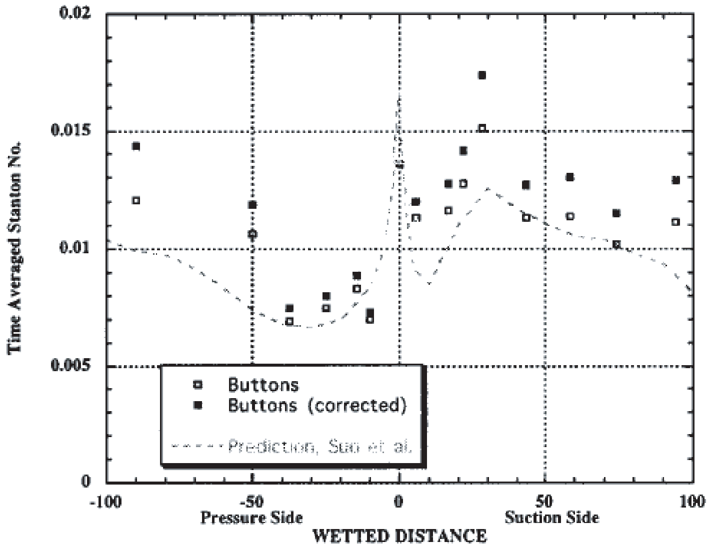

Figure 1.11: Comparison of predictions and measurements of time-averaged Stanton numbers for GE Aircraft Engine turbine vane geometry (from Haldeman and Dunn (2004)).

is a high density of sensors in regions where the measured parameters have high gradients, a situation which rarely happens. This observation is clearly shown in Figure 1.3. Furthermore, the harsh conditions in these experiments cause these sensors to have a relatively high mortality rate. This does not obviate the usefulness of rotating facilities. However, it suggests that to obtain higher measurement fidelity it is practical to simplify the flowfield, especially if the blade midspan behavior is of primary interest. Furthermore, as Dunn (2001) and Haldeman and Dunn (2004) suggest, transient annular cascades provide high uncertainty in the measurements for computational boundary conditions, thus complicating the evaluation of modeling techniques utilized in various flow solvers. The effect of this is presented in Figure 1.11, which compared heat transfer coefficient RANS predictions to measurements for a modern uncooled turbine vane at midspan. The differences between computed and measured values are significant. Another issue with these experiments is the necessary lead time: typically there is a 3–4 year evolution from "drawing board" to data collection.

A further simplification of the flow field is a non-rotating annular cascade which can either consist of a full annulus or a 60° sector, based on the flow requirements. Martinez-Botas et al. (1995) presented uncooled heat transfer results in an annular cascade. Thermochromic liquid crystal paint was used to obtain spatially-resolved measurements. However, the time

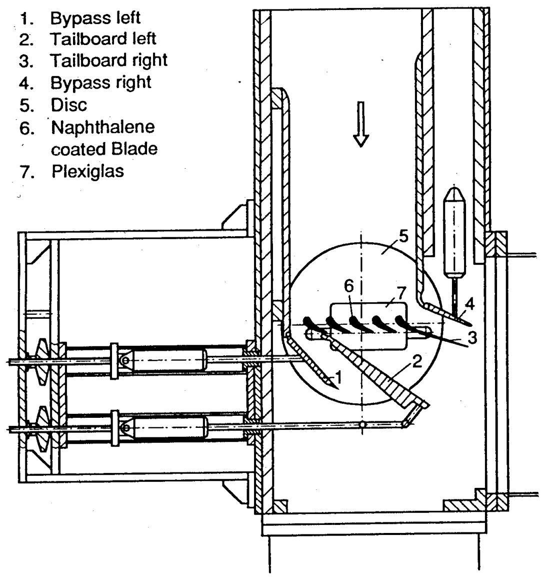

Figure 1.12: Layout of typical linear cascade (from Häring et al. (1995)).

and expense required to build such a facility gives them no real advantage over linear cascades.

To advance the suite of computational tools and augment understanding of heat transfer and flow physics it is necessary to design experiments that can provide high-resolution data, while retaining as many of the key characteristics of the flow field as possible. Linear cascades, a non-rotating, 2-D simplification of a given turbine stage are often used for this purpose. Essentially, this an "unwrapping" of a disk of blades. Linear cascades were initially used to develop means for reducing endwall losses by contouring, as presented by Armstrong (1955). Figure 1.12 shows the typical layout of such a flow facility. In this setup, a row of 5 blades is used. As shown in the figure, there is an entry duct leading up to the blade row. This is to set ensure the flow is well-conditioned and perform inlet measurements such as turbulence intensity and length scale. However, this also introduces boundary layers that grow along the inlet walls. This can affect the observed flow structures in the linear cascade, affecting the two-dimensionality of flow conditions in the passage and consequently measurements of the heat transfer coefficient, skin friction and film effectiveness. To limit this effect, bypass or suction slots are installed near the blade row to remove the approaching boundary layer.

Figure 1.13: Schlieren image from Rolls Royce linear cascade (from Bryanston Cross et al. (1983)).

Figure 1.13 shows a Schlieren image from a linear cascade (Bryanston Cross et al. (1983)). The inlet Mach number for this class of blade geometry is approximately 0.4, the flow accelerates to a peak Mach number of approximately 1.7. Due to the high streamwise curvature on the blade geometry, there is a complex oblique shock structure with several reflections that can be observed in this figure. This shock structure has been found to be extremely sensitive to the local flow conditions and nearby geometry. This means that the number of blades in the linear cascade, the tailboard angles and the amount of bypass suction have substantial effects on how faithful the experimental flow conditions are to the design intent. Baughn (1995) and Guenette et al. (1989) suggest that the flow around the center airfoil of a two-dimensional linear cascade presents nearly identical flow characteristics as that found along the mid-span position of a blade in a rotating annular cascade. This suggests that such facilities, if cost effective can give a reasonable representation of the flow conditions in a real turbine stage. Regardless of the effect of rotation, linear cascades are clearly a much closer approximation of the flow field around real engine turbine blade geometries than a flat plate. Furthermore, well-resolved film cooling performance data from such experiments can be used in point-to-point comparisons with results from RANS or other simulation techniques to improve modeling efforts. In other words, linear cascades are an acceptable compromise that can provide data for both design and modeling improvement purposes. They provide tremendous flexibility in investigating a variety of conditions, including endwall heat transfer (Giel et al. (1996)), incidence effects on film cooling performance (Camci and Arts (1991)) and film cooling-generated aerodynamics losses (Yamamoto et al. (1991)).

Linear cascade experiments are very amenable to optical fluid mechanics and heat transfer measurement techniques such as LDV (Hobson et al. (2003)), infrared thermography (Gottlich et al. (2002)) and thermochromic liquid crystals (Drost and Bölcs (1999)). However, these experiments are, like rotating rigs, expensive to build and maintain. These facilities can be run in either steady state or transient modes, the latter of which is clearly more cost effective. Typically, to obtain a periodic flow field around the center measurement blade in the linear cascade requires at least nine other "dummy" blades. As the typical mass flow rate through a passage in between two blades is approximately 1 kg/s, the requirement for so many passages places the need for a substantial flow requirement for the facility. In the case of Giel et al. (2004) the required flow rate was 26 kg/s at steady state conditions, in comparison the necessary flow rate for the experiment presented by Abhari and Epstein (1994) was 16.6 kg/s. Usually, the blade row is installed on a disk which can be replaced for each new test (c.f. Giel et al. (1999) and Drost and Bölcs (1999)). This means every time a new blade geometry is tested, at least nine blades must be manufactured. These limitations result in linear cascades being very expensive to run so they are a shared resource for turbine blade design teams, effectively limiting their usefulness as a design tool.

To further reduce the cost of performing heat transfer measurements on real turbine blade geometries, the restriction on the number of blades to achieve periodic flow conditions has been relaxed, as shown by Abuaf et al. (1997) who used a transonic four-passage cascade (shown in figure 1.14). A further simplification is a double passage cascade, where a single blade is bounded by two shaped outer walls, as presented by Goldstein and Spores (1988) and Radomsky and Thole (2000) for low speed flow. Priddy and Bayley (1988) presented LDV mean and turbulence measurements from such an experimental setup, again operating at incompressible flow conditions. Laskowski et al. (2005) extended this approach using a RANS-based inverse design procedure for transonic flow conditions to achieve periodic flow conditions around the central airfoil by adjusting the shapes of the outer two walls. Figure 1.15 shows cross-sectional views of such a facility.

Single passage models are the simplest form of a linear cascade. Figure 1.16 presents the salient features of a single passage model. They consist of a single passage bounded by two

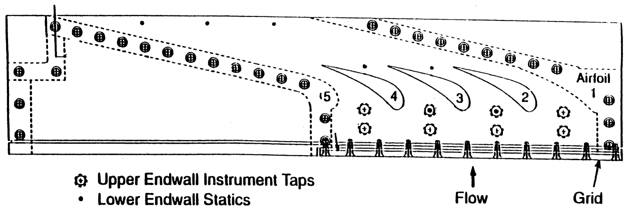

Figure 1.14: Layout of four-passage linear cascade (from Abuaf et al. (1997)).

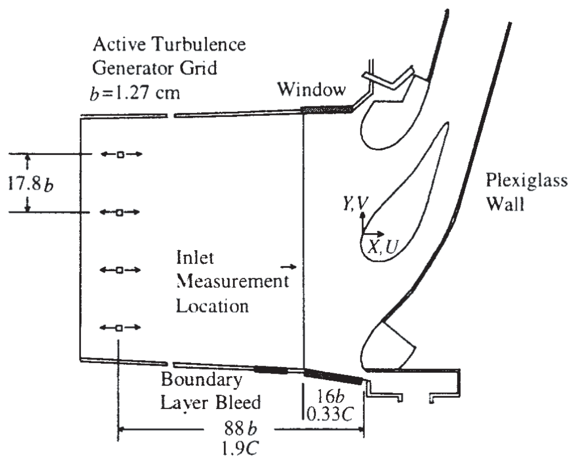

Figure 1.15: Layout of double passage cascade (from Radomsky and Thole (2000)).

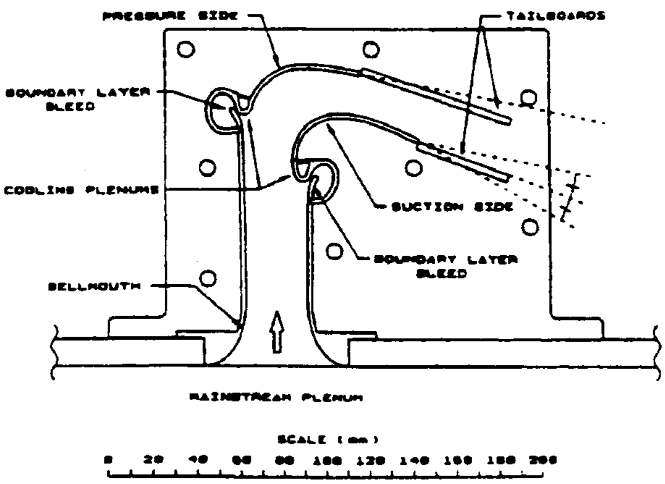

Figure 1.16: Layout of single passage linear cascade (from Buck and Prakash (1995)).

walls which are shaped by the blade geometry under examination. Blair (1974) first utilized a single passage model to perform endwall heat transfer and film cooling measurements. Bailey (1980), Chung and Simon (1991) and Chung et al. (1991) extended this approach to study airfoil aerodynamics. Buck and Prakash (1995) combined a single passage model with a mass transfer analogy technique to perform film cooling performance measurements. All these approaches were for blade geometries where the flow is entirely subsonic. Thus to extend this technique to more modern blade geometries where the flow reaches supersonic conditions, additional refinements are required.

Another approach involves the use of a flat plate, but with a contoured upper wall to develop similar pressure gradients as seen around specific engine components. Teekaram et al. (1989), Teekaram et al. (1991) and Schmidt and Bogard (1995) mimicked a representative pressure distribution found on the suction side surface of a turbine airfoil on a flat plate using a contoured top wall. As the effect of curvature is, by default, not included in such an approach, it is considered of limited value for design and modeling purposes.

1.8 Experimental Measurement Techniques for Measuring Film Cooling Performance

There are two main classifications of the methods used for film cooling performance measurements: transient and steady state techniques. The choice of flow facility for obtaining film cooling performance data often dictates the appropriate measurement technique. However, there is also the question of how the resulting data will be used. When using measurements for validation of numerical models the thermal boundary conditions imposed in the experiment must be considered. In simulations, it is relatively trivial to impose perfect adiabatic surfaces, or constant heat flux surfaces. However, such ideal conditions can rarely be achieved in experiments. Hence, in designing an experiment, it is vital to examine how accurately the thermal boundary conditions will be defined. Additionally, the measurement technique obviously determines the measurable film cooling parameters: the heat transfer coefficient, the film cooling effectiveness or both.

1.8.1 Transient Heat Transfer Measurement Techniques

The operating principle of transient heat transfer measurements is about the same regardless of the technique used to measure the surface temperature, be it thermocouples, thin-film gauges or thermochromic liquid crystals. A step change in temperature is abruptly imposed on the measurement surface, either by the rapid insertion of the surface into a preheated flow (Abuaf et al. (1997)), opening a diaphragm that suddenly exposes the surface to preheated flow (Abhari and Epstein (1994)), impulsive injection of coolant at a different temperature along with mainstream exposure (Yu et al. (2002)) or suddenly applying a heat flux to the measurement surface (Vogel et al. (2003)). The primary benefit of using transient facilities is that they can limit experimental test times, reducing expenses associated with steady state experiments.

Experiments such as those conducted by Camci and Arts (1985a), Teekaram et al. (1989), and Arts and Bourguignon (1990) use isentropic light piston compression tube facilities, an approach introduced by Jones and Schultz (1970) and Schultz and Jones (1973). The measurement surfaces, either a flat plate, or blades installed in a linear cascade, are made of ceramic. Thin-film resistance sensors are painted on the measurement surfaces to record the temperature history. A short measurement period of steady state flow conditions is achieved during the test as the piston drives the expanding air through the experiment. A

1-D, semi-infinite conduction analysis is used to obtain the heat flux from the time-resolved temperature data. The heat transfer coefficient is determined using the measured heat flux, the measured wall temperature and the known freestream temperature. It is important to note that the thermal boundary condition (i.e. surface temperature distribution) changes over the course of the experiment. This is a common problem of all transient techniques.

In rotating experiments where either a blowdown or shock-tube is used a high-pressure air source, thin-film heat flux gages with a high frequency response are needed to provide time-accurate measurements of unsteady convective heat transfer rates. Several experiments conducted by Dunn and Stoddard (1979), Dunn (1986), Dunn and Hause (1982), Dunn and Chupp (1988) and Dunn et al. (1994) use a method presented by Vidal (1956), again using a thin-film resistance sensor. These sensors provide a time record of the surface temperature and a quasi 1-D conduction model is used to calculate the surface heat flux. The gages used in this series of experiments are constructed from a thin (≈ 100Å) platinum strip, as a resistance thermometer, attached to a low thermal diffusivity material, such as Pyrex. The completed gage is then embedded in the desired component which has a much larger thermal diffusivity. Figure 1.17 shows examples of the gages installed on experimental turbine blade geometries, Dunn et al. (1986) presents the typical analyses used to extract time-resolved heat flux data from these gages. Epstein et al. (1986) presented an alternative gage used by Abhari and Epstein (1994). This type of sensor consists of a thin layer of polyamide, rather than Pyrex as the substrate. Two metal film resistance thermometers are sputtered on both sides. This approach does not require drilling small holes, as insert gages require, instead these gages can be directly deposited on the surface, minimizing any flow disruptions.

The thin-film resistance sensor approach presents several problems that can make the measurements difficult to interpret. Mukerji et al. (1999) demonstrated that such sensors can corrupt the heat transfer measurement by as much as 30%, by changing the thermal boundary condition on the blade, if it is constructed out of a high thermal diffusivity material. This error is linked to the low thermal diffusivity substrate that is used to augment the signal to noise ratio of the measured temperature over the short test time. This substrate causes a local temperature rise over the gage, producing a wall temperature step. This has been termed as the "heat island effect" by Dunn et al. (1997). Corrections for this problem have been proposed by Moffat et al. (2000). Furthermore, Diller (1993) argued that the flow conditions in blade passages are highly sensitive to local perturbations: i.e. a

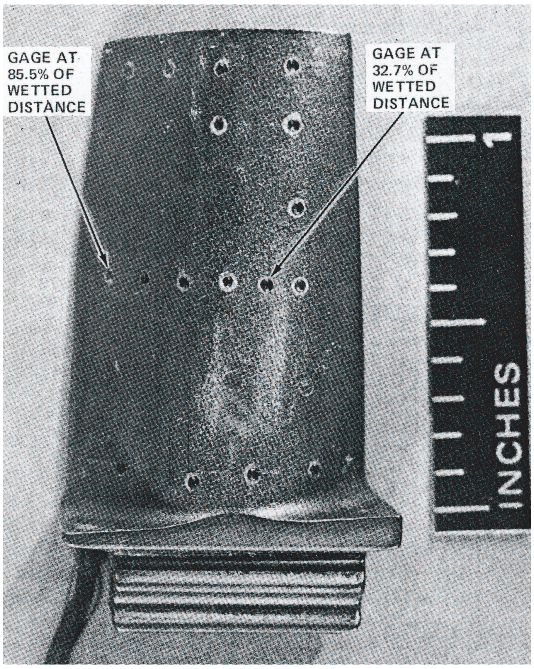

Figure 1.17: Button gages installed in rotating rig blade geometry (from Dunn (1986)).

poorly installed gage can cause physical disruptions of the boundary layer, also affecting the measurements. This point was supported by data presented by Peabody and Diller (1998) who directly examined the effect of steps around insert gage on the measured heat transfer coefficient. Under certain circumstances this error can be as large as 75% when compared to a gage directly deposited on the component surface.

In experiments where the overall test time is much longer, over several seconds rather than milliseconds, thermocouples or thermochromic liquid crystal paint can be used to performed time-resolved surface temperature measurements. Different transient models, incorporating this temperature history can then be used to compute the parameters of interest: the heat transfer coefficient and the film cooling effectiveness. Lander et al. (1972) developed a lumped capacitance model with thin-walled airfoils ($\approx$ 0.03 inches in thickness). The heat transfer coefficient was obtained from the transient heating of a three-vane linear cascade, suddenly exposed to hot mainstream flow downstream of a combustor. Two cascades were used in these tests: a “dummy” one that was used to set the flow conditions, and an instrumented cascade that was quickly inserted into the flow. An exponential curve was fitted to the each thermocouple-recorded time history to obtain the heat transfer coefficient. The subsequent steady state operation was used to obtain the film effectiveness, as it assumed that the thin metal wall may be approximated as adiabatic. This is the general approach followed by Abuaf et al. (1997), which was discussed earlier.

To improve the spatial resolution of the measurement technique, temperature-sensitive paints, such as thermochromic liquid crystals are used in transient experiments. Ireland and Jones (2000) discuss the growing popularity of this technique. The techniques for applying, calibrating and preparing surfaces with this paint along with some of the history of this approach are covered in Chapter 3. The critical assumption of this technique is that changes in the thermal conditions of the surface have negligible effects on the flow conditions (Vedula and Metzger (1991)). A semi-infinite 1-D analysis of thermal conduction in the measurement surface is used with the following partial differential equation and boundary conditions:

$$k\frac{\partial^2 T}{\partial y^2} = \zeta\frac{\partial T}{\partial t} \tag{1.24}$$

$$T(0,0) = T_i$$

$$-k\frac{\partial T}{\partial y}\bigg|_{y=0} = h(T(0,t) - T_{rec})$$

$$\lim_{y\to\infty} T(y,t) = T_i$$

Solving this set of equations gives the following relationship that describes the surface temperature history:

$$\frac{T(0,t) - T_i}{T_{rec} - T_i} = 1 - e^{\frac{h^2\zeta t}{k^2}} erfc\left(\frac{h\sqrt{\zeta t}}{k}\right) \tag{1.25}$$

The recovery temperature is related to the mainstream total temperature:

$$\frac{T_{rec}}{T_\infty} = 1 + \frac{1}{2}r_\infty(\gamma - 1)M^2 \tag{1.26}$$

$$\frac{T_\circ}{T_\infty} = 1 + \frac{\gamma - 1}{2}M^2$$

Where r_∞ is termed the recovery factor, which has a typical value of $r_\infty = Pr^{\frac{1}{3}}$ as recommended by Kays and Crawford (1993). Ideally, if the mainstream temperature and flow conditions were changed with minimal transients, equations 1.25 and 1.26 could be used directly to compute the local heat transfer coefficient based on the measured wall temperature traces. However, in reality this is difficult to achieve and there are often transients while the mainstream temperature adjusts. Metzger and Larson (1986) demonstrated how

Duhamel's Theorem may be used to incorporate this effect in the analysis. Another solution is to preheat the test section to some large temperature and shuttle it quickly into the flow. Martinez-Botas et al. (1995) followed the latter approach for obtaining spatially-resolved heat transfer coefficient measurements in an annular cascade. In this experiment, narrow-band thermochromic liquid crystals were used since they have a known narrow temperature range over which they change color. As the blades cool, the time at which the crystals change color at each location is recorded. The local heat transfer coefficient is computed using equation 1.25. This is also known as the single isotherm technique.

To extend this technique to measure film cooling performance (η and h), the recovery temperature is replaced using the definition of the film effectiveness. Thus, the problem becomes a "three-temperature problem", as discussed by Vedula and Metzger (1991). To close the resulting equation set, two similar transient tests are run to generate independent conditions. Ekkad and Han (2000) and Yu et al. (2002) provide additional information on the application of this technique, Ekkad et al. (1997 and 1997b) applied this technique for compound-angle injection. Yu and Chyu (1998) extended this to a "four-temperature problem" when there is injection from different rows at different temperatures. Drost et al. (1997) uses a series of steps to model the coolant total temperature ($T_{o,c}$) time history for a case where a step change in coolant temperature could not be effected. Duhamel's theorem was used to develop the functional form of the surface temperature history. A regression analysis was performed using 6 to 8 tests at identical aerodynamic conditions to obtain the film effectiveness and heat transfer coefficient. This method was used in a linear cascade by Drost and Bölcs (1999). Vogel et al. (2003) suggested another technique where a heat flux is suddenly applied rather than affecting a step change in the mainstream or film coolant total temperatures. Again, a regression scheme is used to solve for the heat transfer coefficient and film cooling effectiveness. The quoted uncertainty of these techniques from their proponents ranges from 6% to 10%.

Depending on the method applied, the comparative numerical model of the experiment will apply an isothermal or constant heat flux boundary condition to the equivalent measurement surfaces. Considering that heat transfer measurements are inherently sensitive to the thermal boundary conditions, there is the issue of properly "matching" the numerical and experimental boundary conditions. If there is a discrepancy, the difference between the prediction and the experimental data could be due to the difference in boundary conditions, rather than numerical modeling.

1.8.2 Steady State Heat Transfer Measurement Techniques

Virtually all the flat plate data discussed above were collected at steady state conditions. The primary drawbacks with extending state steady state measurements to transonic flow conditions are linked to the expense of a constantly running facility and conduction losses, which corrupt the measurement. The primary advantage of using steady state facilities, if conduction losses can be minimized, is that there can be one-to-one matching of experimental boundary conditions to numerical boundary conditions. As there are now more options for building real geometry experiments out of very low thermal conductivity materials which can withstand typical aerodynamic forces during operation, this approach is being revisited. Considering the continuing disparity between the predictive capability of numerical models for full engine geometries and conditions, the importance of developing controlled experiments, with well-defined boundary conditions which closely model typical engine conditions is becoming more apparent.

1.8.3 Mass Transfer Analogy Technique

One technique to avoid the issue of conduction losses is to rely on mass transfer as an analog. Several of the experiments presented previously that examine film cooling performance use this approach. The compressible species continuity equation, with Γ_m defined as the mass fraction of species m is:

$$\frac{\partial \rho \Gamma_m}{\partial t} + \frac{\partial}{\partial x_j}(\rho u_j \Gamma_m) = \frac{\partial n''_m}{\partial x_j} \tag{1.27}$$

Assuming the validity of Fick's Law:

$$n''_m = \rho \mathcal{D}_m \frac{\partial \Gamma_m}{\partial x_j},\ \mathcal{D}_m = \frac{\Gamma \mu}{Sc_m} c_v \tag{1.28}$$

Performing Farve-averaging as previously done on the mass fraction, Γ_m:

$$\Gamma_m = \tilde{\Gamma}_m + \Gamma''_m \tag{1.29}$$

Which gives the Reynolds averaged equation for the species continuity equation:

$$\frac{\partial \overline{\rho} \tilde{\Gamma}_m}{\partial t} + \frac{\partial (\overline{\rho} \tilde{u}_i \tilde{\Gamma}_m)}{\partial x_j} = \frac{\partial}{\partial x_j}(n''_m - \overline{\rho u''_j \Gamma''_m}) \tag{1.30}$$

If a Boussinesq approximation is assumed, the Reynolds mass flux term $-\overline{\rho u''_j \Gamma''_m}$ may be modeled as:

$$-\overline{\rho u''_j \Gamma''_m} = \overline{\rho} \mathcal{D}_{t,m} \frac{\partial \Gamma_m}{\partial x_j} \tag{1.31}$$

With this assumption, the total diffusion coefficient per species is computed as:

$$\mathcal{D}_m = \mathcal{D}_{l,m} + \mathcal{D}_{t,m} \tag{1.32}$$

The turbulent diffusion coefficient is related to the eddy viscosity using the turbulent Schmidt number, Sc_t, via the relation:

$$\mathcal{D}_{t,m} = \frac{\Gamma \mu}{Sc_{t,m}} c_v \tag{1.33}$$

Eckert and Drake (1972) demonstrated, under the conditions of constant properties and low velocities (i.e. small Eckert numbers, $Ec \ll 1$), that the energy equation collapses to the form of equation 1.27. Furthermore, under these assumptions, the continuity and momentum equations can be decoupled from the energy and mass diffusion equations. Thence, for laminar flow the mass transfer and energy equations are analogous to each other if $Pr = Sc$, that is the Lewis number is unity, $Le = 1$. For turbulent flow the RANS forms of these equations are analogous if the turbulent Schmidt and Prandtl numbers are equal, $Pr_t = Sc_t$ (which also implies that the turbulent Lewis number is unity, $Le_t = 1$). Eckert (1976) argues that all experimental evidence points to this indeed being the case. Additionally, Goldstein (1971) pointed out that if the flow is sufficiently turbulent the requirement of $Le_t = 1$ may also be relaxed somewhat. This means that mass transfer measurements can be used to directly measure heat transfer data, provided the boundary conditions are consistent. When variable properties are present, Eckert (1976) argues that the mass/heat transfer analogy should still hold as a “good” approximation, provided the density ratio is consistent between the mass transfer experiment and the equivalent heat transfer experiment.

Pedersen et al. (1977) performed a range of film cooling measurements in a low-speed flow using various mixtures of helium, carbon dioxide or refrigerant F-12 with air as coolant. As walls are impermeable to mass transfer, this situation is completely analogous to an adiabatic wall condition, with the foreign gas injection equivalent to coolant at a different temperature. Hence, the film cooling effectiveness is defined as the following ratio of mass fractions:

$$\eta = \frac{\Gamma_w - \Gamma_\infty}{\Gamma_2 - \Gamma_\infty} \tag{1.34}$$

If the injected coolant is made of a single constituent, not contained in the mainstream, $\Gamma_\infty = 0$ and $\Gamma_2 = 1$. Thence,

$$\eta = \Gamma_w \tag{1.35}$$

An alternative formulation to measuring the heat transfer coefficient on a film cooled surface with an isothermal boundary condition is presented by Choe et al. (1976). In this method, the heat flux q" is defined as:

$$q" = h'(T_{w'} - T_\infty) \tag{1.36}$$

and a dimensionless temperature, θ, is used:

$$\theta = \frac{T_2 - T_\infty}{T_{w'} - T_\infty} \tag{1.37}$$

Using these definitions the heat transfer coefficient at arbitrary wall and film coolant temperatures, h', can be found using superposition – defining h'_0 as the heat transfer coefficient measured with $T_2 = T_\infty$, or $\theta = 0$, h' can be computed as:

$$\frac{h'}{h'_0} = 1 + \mathcal{K}\theta \tag{1.38}$$

where the constant, $\mathcal{K}$ is defined as:

$$\mathcal{K} = \frac{h'_1 - h'_0}{h'_0} \tag{1.39}$$

In this equation h'_1 is the heat transfer coefficient measured on an isothermal surface measured when $\theta = 1$. Experience with flat plate turbulent boundary layers indicates that the isothermal heat transfer coefficient measured with $\theta = 1$ and incompressible conditions may be assumed to meet the condition:

$$h'_0 \approx h \tag{1.40}$$

Where h is the heat transfer coefficient measured on a constant heat flux surface with the film coolant total temperature the same as the mainstream total temperature ($T_{\circ,c} = T_{\circ,\infty}$). This is also termed the isoenergetic flow condition. Goldstein and Cho (1995), using analysis and experimental data, showed that a naphthalene sublimation technique can be used as an analogy to an isothermal boundary condition for measurement of the heat transfer coefficient (h'). A surface coated with or cast out of naphthalene is exposed to a pure air mainstream flow for a set length of time. The local surface depth is measured with a precision depth gage or by weighing the measurement surface, allowing the computation of the mass transfer coefficient. The local heat transfer coefficient is then calculated using the equation:

$$h'_m = \frac{\dot{m}}{\rho_{v,w} - \rho_{v,\infty}} \tag{1.41}$$

Where h'_m represents the mass transfer coefficient with an iso-concentration boundary condition. If $\rho_{v,\infty} = 0$, this equation may be simplified to:

$$h'_m = \frac{\rho \delta z / \delta \tau}{\rho_{v,w}} \tag{1.42}$$

where the mass flow rate is estimated, given the density of solid naphthalene, ρ and experimental run time of τ, as:

$$\dot{m} = \rho \delta z / \delta \tau \tag{1.43}$$

Following Goldstein et al. (1999) and Goldstein and Jin (2001), the ratio of dimensionless mass transfer coefficients with pure air injection ($h'_{m,0}$) and no film cooling applied (h'_m), is approximately equal to the ratio of heat transfer coefficients measured with an isothermal boundary condition applied. That is:

$$\frac{h'_{m,0}}{h'_m} \approx \frac{h'_0}{h'} \tag{1.44}$$

Eckert (1984) demonstrated that the adiabatic film effectiveness can be estimated knowing the isothermal heat transfer coefficients, h'_0 and h'_1 as shown in the equation below:

$$\eta = 1 - \frac{h'_1}{h'_0} \tag{1.45}$$

Using equation 1.44 and defining $h'_{m,1}$ as the mass transfer coefficient measured with naphthalene-vapor-saturated air injection, equation 1.45 can be reformulated as:

$$\eta = 1 - \frac{h'_{m,1}}{h'_{m,0}} \tag{1.46}$$

Goldstein and Cho (1995) documented some of the major limitations of the naphthalene sublimation technique, specifically that it cannot be used in high velocity flows where recovery temperature effects are present, and that the shape of the surface changes during measurement. Nevertheless, these authors do present a substantial number of low-speed cases, including flows over cylinders and flat plate flows where this approach agrees well with heat transfer data.

Chapter 2

Single Passage Apparatus

The design of the single passage facility can be divided into two major components: the aerodynamic design of the model and its subsequent modification for heat transfer tests. This chapter details the first component — the development of a facility that has a flowfield identical to that of a two-dimensional linear cascade. This setup could then be used for any of the heat transfer or fluid mechanics measurement techniques presented in Section 1.6.1. The blade geometry used in these designs was an advanced blade geometry provided by General Electric Aircraft Engines (GEAE). This blade is used for the first stage rotor of the next generation of CFM56 class commercial aircraft turbines. This is highly curved airfoil operating at transonic conditions, with meanflow Mach numbers as high as 1.5.

2.1 Overview of Single Passage Design Concept

There are two-well accepted computational domains for non-rotating, two-dimensional turbine blade geometries. Both these approaches simulate an infinite row of blades, as shown in figure 2.1. Incoming and departing streamlines have been included in this figure for discussion purposes. One approach is a single blade with periodic boundary conditions at mid-pitch, as shown in figure 2.2: the other uses two blade surfaces, the pressure side of the upper blade and the suction side of the lower blade with periodic boundaries leading up to and departing from the two blade surfaces, as presented in figure 2.3.

The single passage experimental technique under study mimics the latter approach, although the inlet and exit periodic boundary condition surfaces have been replaced with walls. This introduces the need for boundary layer bleed suction and appropriately shaping the exit walls of the passage to develop a flow-field that closely matches that around the center airfoil of a linear cascade. Figure 2.4 presents the general features of the single passage, for comparison to the numerical approach. The ultimate design objective of the single passage model is to shape the walls and control the suction rates, such that the flowfield is identical to that in an infinite cascade.

The aerodynamic design procedure incorporated 2-D and 3-D full-geometry simulations

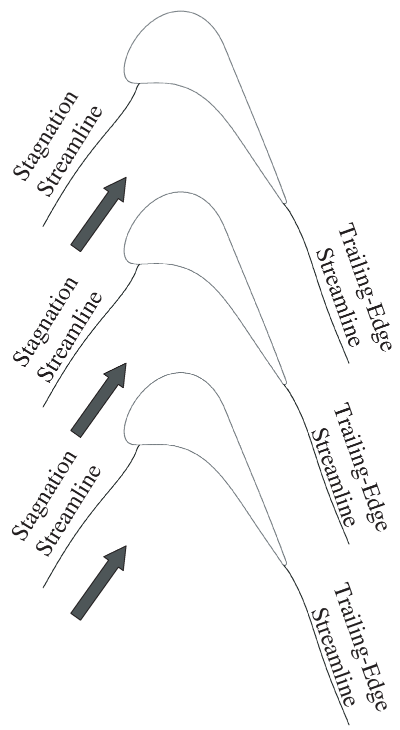

Figure 2.1: Three arbitrary blades from an idealized, 2-D infinite cascade with representative computational domains.

The blade shape has been distorted to ensure protection of proprietary information.

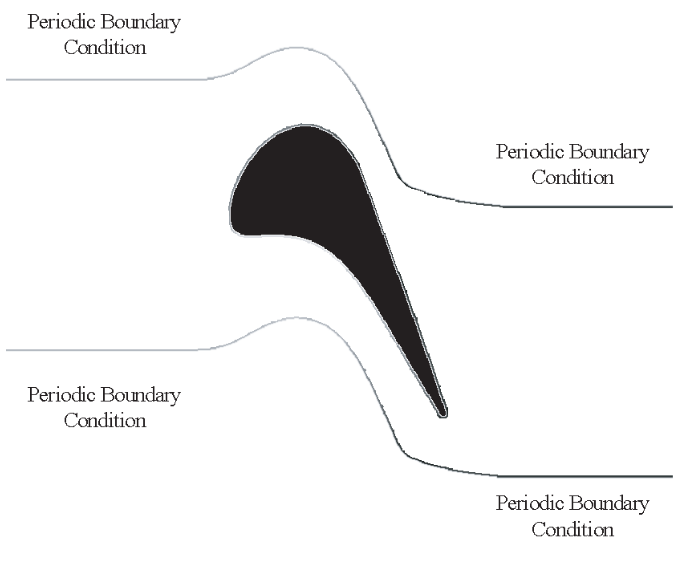

Figure 2.2: Single arbitrary blade with periodic boundary conditions at mid-pitch.

The blade shape has been distorted to ensure protection of proprietary information.

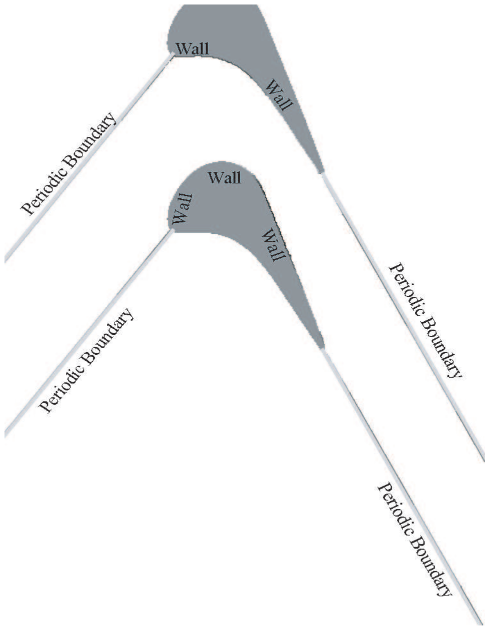

Figure 2.3: Blade passage with inlet and outlet periodic boundary conditions.
The blade shape has been distorted to ensure protection of proprietary information.

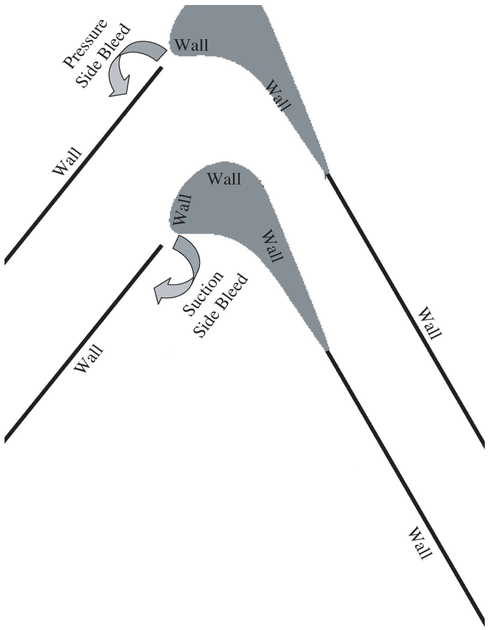

Figure 2.4: Idealized Single Passage Model.
The blade shape has been distorted to ensure protection of proprietary information.

at various steps. The RANS equations were solved using a commercial CFD package, STAR-CD. This solver uses an implicit, finite-volume, cell-centered algorithm that solves the RANS equations in primitive variable form with the flow equations decoupled. A modified version of the SIMPLE (Semi-Implicit Method for Pressure-Linked Equations) algorithm is used to solve for the static pressure field and the corresponding velocity field (see Issa (1986), Issa et al. (1986), and Patankar and Spalding (1972)). In all the simulations for the aerodynamics design, a two-layer, two-equation k-ε turbulence model was implemented. This model incorporated a modification proposed by Chen and Kim (1987) which limits the production of spurious levels of turbulent kinetic energy. These equations were decoupled from the mean flow solver and solved sequentially to compute the turbulent viscosity (μ_t) at each iteration. Convergence for each calculation was achieved when the value of the residuals for each variable equation dropped at least three orders of magnitude. A second-order accurate differencing scheme, termed the Monotone Advection and Reconstruction Scheme (MARS) was used on all variables in almost all these simulations. Due to numerical stability issues, central-differencing rather than MARS was used for density in some cases. As this is also a spatial second-order accurate scheme the results were expected to have comparable accuracy to those where MARS was used on all variables. The STAR-CD Methodology Manual (2001) contains further details on the implementation of the mean flow solver and turbulence models.

Table 2.1 summarizes the expected flow conditions for the given blade geometry at typical engine and test conditions (from Buck (2000)). The model scale was selected based on instrumentation concerns and flow supply limitations. The experiment was designed to run at ambient conditions with the model back pressure assumed to be at atmospheric pressure. The first step in the design process was to perform an infinite cascade simulation with identical flow conditions as that expected in the experiment. This was to provide a comparative baseline for subsequent design approaches.

Figure 2.5 shows a schematic of the experimental single passage model with its salient features identified. The model is designed to be placed on top of a plenum with flow passing upwards into the bellmouth. The inlet duct length was chosen to be long enough such there would be adequate clearance between the exhaust flow and the top of the plenum, and also to provide probe access to an inlet measurement station one-chord length upstream of the blade leading edge. The downstream duct length was chosen to be long enough such that the exhaust manifold shape would have minimal effect on the flow in the test region. The

Table 2.1: Comparison of engine conditions to experimental conditions.

Parameter	Engine Condition	Test Condition
Scale	1	1.3
Chord Length, c_{blade} (m)	redacted	redacted
Airfoil Pitch Spacing, AP (m)	1.205	1.567
$\gamma_{inlet} = \frac{c_v}{c_p}$	redacted	1.4
Inlet Angle	29.2°	29.2°
Exit Angle	-68.6°	-68.6°
$\frac{P_{o,inlet}}{P_{exit}}$	2.57	2.57
$P_{o,inlet}$ (Pa)	$1.59(10)^6$	$2.60(10)^5$
$T_{o,inlet}$ (K)	1490	300
Inlet Mach Number	≈ 0.340	≈ 0.340
Reynolds Number, $Re_c = \frac{\rho \tilde{u}_{inlet} c_{blade}}{\mu}$	$4.70(10)^5$	$6.62(10)^5$

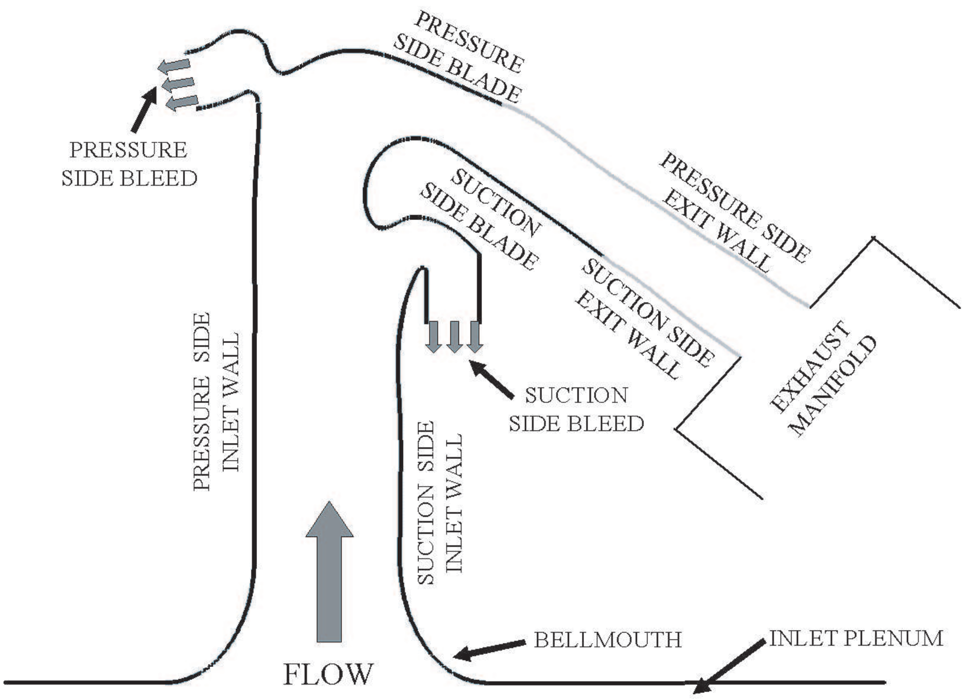

Figure 2.5: Experimental single passage model.

design process determines the shape of the inlet pressure and suction walls, the amount of boundary layer bleed suction and the shape of the outlet walls, achieving the desired flow field in between the blade surfaces. There are two design procedures that are contrasted in the following subsections: one is based on inviscid flow analysis (as presented by Buck and Prakash (1995)), the other is an iterative 2-D RANS-based simulation approach. The first was used to develop the initial prototype of the single passage model and was found to be inadequate. The second was found to produce a model design which met the stated objectives.

The model was developed using two-dimensional flow computations. Nevertheless, in the actual experimental facility, the flow is inherently three-dimensional, in part due to presence of flat endwalls that enclose the model. Researchers such as Langston (1980) and Chung and Simon (1991) have demonstrated that the boundary layers that develop along the endwalls include highly complex three-dimensional flow features. With this in mind, the aspect ratio of the model was chosen to be $AS = 1.276$, where AS is defined as:

$$AS = \frac{H_{MODEL}}{AP} \tag{2.1}$$

Where AP is the blade pitch spacing. This value was based on GEAE practice and flow supply limitations. Ideally, this aspect ratio is large enough such that the three-dimensional effects are limited to the near-endwall regions. This would result in a highly two-dimensional flow field over a wide-band encompassing the midspan region of the blade. The 3-D RANS simulations were used to verify this assumption.

The computational design of the experimental facility required assumptions for the inlet flow boundary conditions. To verify the validity of these assumptions, these computations were repeated after the model was built using measured values for the inlet turbulence intensity, integral length scale and mean flow quantities. The effect of these small changes to the inlet boundary conditions on the computed pressure distribution was found to be negligible.

2.1.1 Infinite Cascade Simulation

Inviscid and viscous periodic cascade simulations were conducted by Athans (2000) and Laskowski (2000), respectively, to develop comparative baselines and provide vital data to complete the single passage model design. In the inviscid calculations, a GEAE finite-volume, cell-centered, propriety solver (NOVAK) was used with a single passage grid

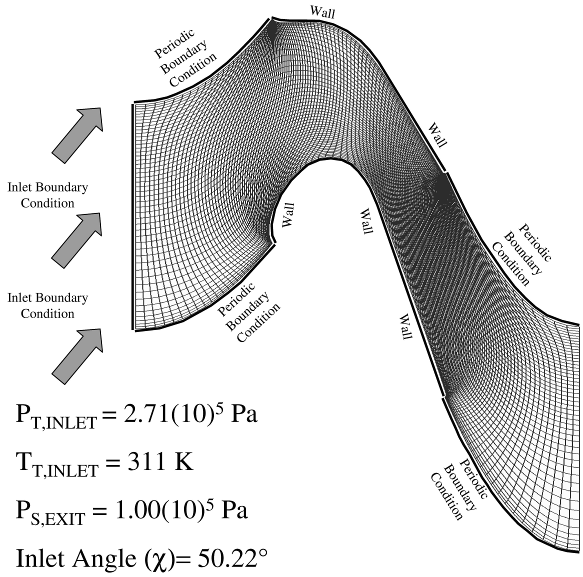

Figure 2.6: Grid and flow conditions for GEAE Inviscid Simulation.
The blade shape has been distorted to ensure protection of proprietary information.

with inlet and exit periodic boundary conditions. The computational grid, consisting of approximately 7,000 cells in a H-mesh, and the flow conditions are shown in figure 2.6. The design applications of this simulation will be presented shortly. Figure 2.7 presents grid and flow conditions used in the 2-D RANS simulations. The mesh consisted of three distinctive blocks with point-to-point matching at interfaces. H-mesh grids were used at inlet and exit portions of the domain, while an O-mesh was used around the blade (Durbin (1998)). The inlet boundary condition was specified one-chord length upstream of the airfoil leading edge and the exit boundary condition was specified 1.25 chord-lengths downstream of the trailing edge. Periodic boundary conditions were implemented along lines half-pitch between adjacent blades. This is standard practice for such simulations. A grid refinement study was conducted using grids that ranged in size up to 100,000 cells. For the results shown here, a grid of approximately 30,000 cells was used. The cells around the blade were set to achieve cell heights where $y^+ = \frac{yu_\tau}{\nu}$ ranged between $0.1 < y^+ < 1.33$. The inlet values for turbulence intensity and integral length scale were assumed to be $TI\% \approx 5\%$ and $\frac{\ell}{c_{blade}} \approx 0.277$, based on previous experience in similar facilities. The integral length scale was estimated by multiplying the turbine blade pitch spacing by 0.05. Laskowski (2000) found by varying these parameters in the ranges $10\% < TI\% < 15\%$ and $0.028 < \frac{\ell}{c_{blade}} < 0.277$ that the two-equation k-ε model proposed by Chen and Kim (1987) produced the most reasonable results

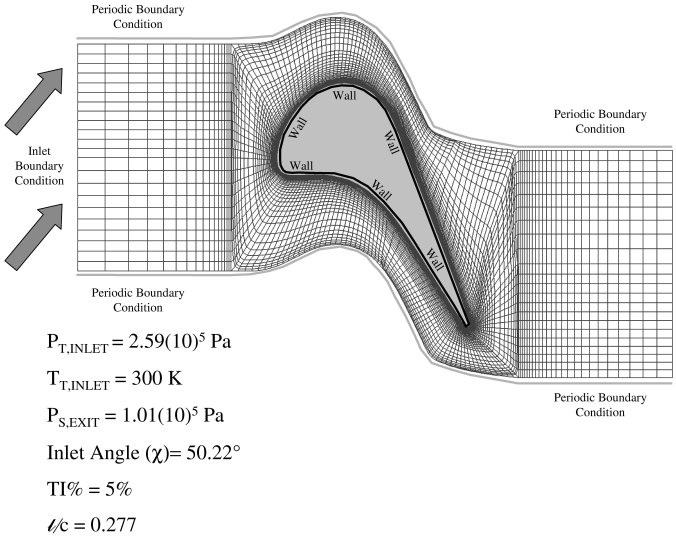

Figure 2.7: Grid and flow conditions for 2-D RANS Simulation.
The blade shape has been distorted to ensure protection of proprietary information.

based on the stagnation point location. This flow feature should be determined only by the inlet flow angle and flow conditions, i.e. the stagnation points for the inviscid and RANS simulations should be identical. The standard k-ε turbulence model was found to move the stagnation point as these parameters were varied, effectively changing the angle of incidence which was deemed to be un-physical. The Chen and Kim variant of the k-ε model has the advantage of "desensitizing" some of the main characteristics of the numerical solution to uncertainty in the inlet turbulence intensity and integral length scale. This observation is apparent from an examination of table 2.2 that presents the calculated stagnation point axial location using various turbulence models. Figures 2.8 and 2.9 display the calculated pressure distribution using these approaches, presented as the isentropic Mach number, M_{is} versus the surface coordinate $\frac{s_c}{c_{blade}}$. This is a reformulation of the pressure distribution, using the inlet stagnation pressure to compute a Mach number as shown in equation 2.2.

$$M_{is} = \sqrt{\frac{2}{\gamma - 1}\left(\left(\frac{P_{\circ,inlet}}{P}\right)^{\frac{\gamma-1}{\gamma}} - 1\right)} \tag{2.2}$$

The negative surface distance positions shown in figures 2.8 and 2.9 correspond to locations on the pressure side of the airfoil, while the positive surface positions correspond to the

Table 2.2: Comparison of computed stagnation point locations using various turbulence models and conditions for infinite two-dimensional cascade.

Turbulence Model	$M_{is} = 0$ ($\frac{x}{c_{blade}}$)
k-ε Standard (TI% = 10%, $\frac{\ell}{c_{blade}} = 0.028$)	$2.28(10)^{-3}$
k-ε Standard (TI% = 10%, $\frac{\ell}{c_{blade}} = 0.28$)	$1.37(10)^{-3}$
k-ε Chen (TI% = 10%, $\frac{\ell}{c_{blade}} = 0.028$)	$2.76(10)^{-3}$
k-ε Chen (TI% = 10%, $\frac{\ell}{c_{blade}} = 0.28$)	$2.28(10)^{-3}$
GEAE Inviscid Calculation (NOVAK)	$2.76(10)^{-3}$

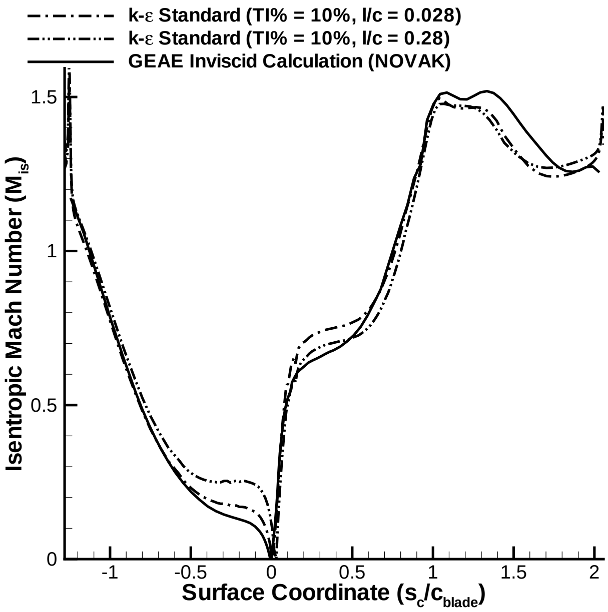

Figure 2.8: Computed isentropic Mach number distributions for experimental turbine blade geometry using standard k-ε turbulence model (courtesy of Athans (2000) and Laskowski (2000)).

suction side surface.

Figure 2.10 provides a visual description of these surface coordinate positions, along with a definition of the axial location along the blade. Figure 2.11 shows Mach number contours for the 2-D RANS calculation using the Chen and Kim variant of the k-ε turbulence model.

To design the shape of the inlet and outlet walls, and the amount of boundary layer bleed suction, streamlines were constructed from the 2-D RANS and inviscid infinite cascade simulations. Figure 2.12 presents the streamlines in the initial orientation of the blade geometry, and the streamlines after the domain was rotated to fix the inlet angle.

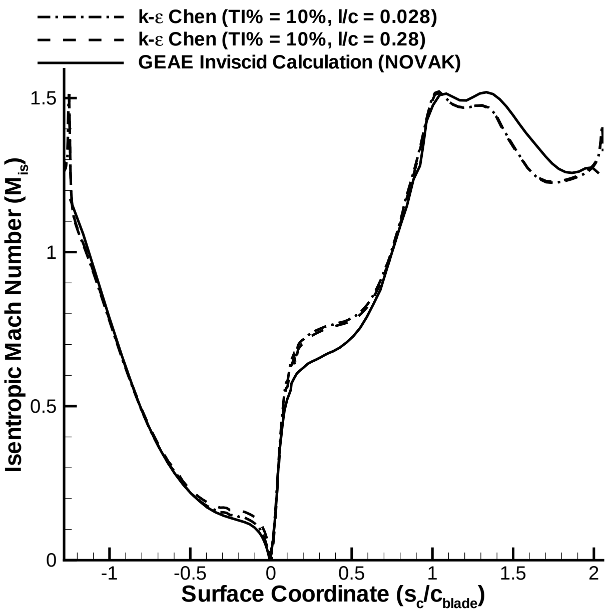

Figure 2.9: Computed isentropic Mach number distributions for experimental turbine blade geometry using Chen and Kim variant of the k-ε turbulence model (courtesy of Athans (2000) and Laskowski (2000)).

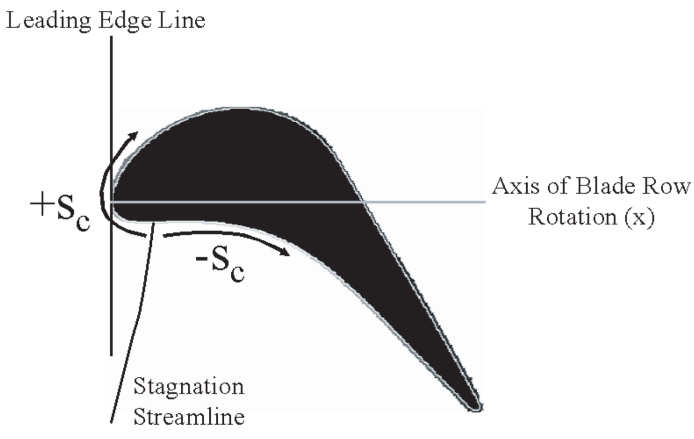

Figure 2.10: Definition of axial location.
The blade shape has been distorted to ensure protection of proprietary information.

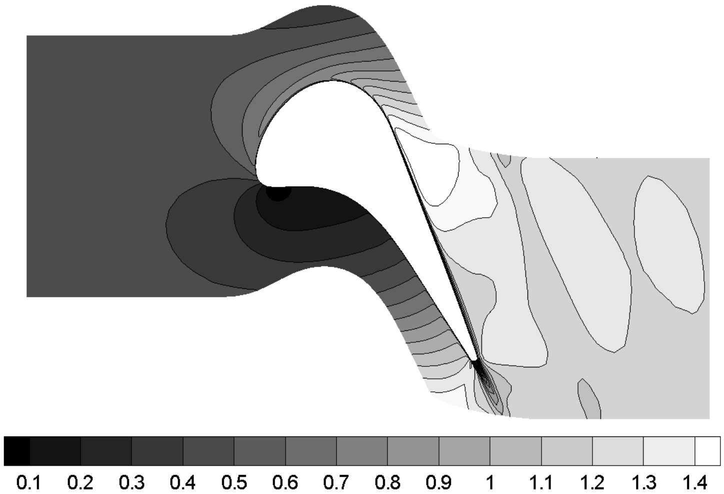

Figure 2.11: Mach number contours for 2-D infinite cascade viscous simulation (courtesy of Laskowski (2000))

The blade shape has been distorted to ensure protection of proprietary information.

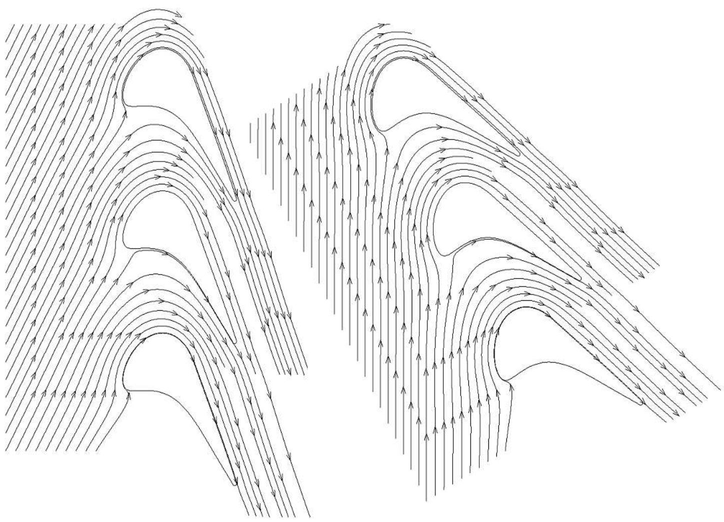

Figure 2.12: Streamlines from infinite cascade simulation as calculated and rotated by the inlet angle for implementation in the single passage model (courtesy of Laskowski (2000))

The blade shape has been distorted to ensure protection of proprietary information.

2.1.2 Buck and Prakash Methodology

Buck and Prakash (1995) presented a design procedure that was implemented in a single passage model for a 1970-era first stage rotor blade geometry. This particular blade geometry was designed to operate at subsonic compressible flow conditions ($M_{is,max} \approx 0.95$). Following the procedure of these authors, an estimate of the 99% boundary layer thickness is calculated assuming that the shape of the inlet wall could be represented as a flat plate with zero pressure gradient, and the boundary layer velocity profile could be modeled as a $\frac{1}{7}^{th}$-power profile (Kays and Crawford (1993)). This boundary layer thickness estimate is then used to estimate the amount of mass flow that must be bled off through both the suction and pressure side bleeds. One deficiency of this technique is the fact that the inlet wall boundary layers are exposed to adverse pressure gradients as they approach the two blade stagnation points. Clearly, this invalidates the zero pressure gradient assumption used to develop the boundary layer thickness estimate. The shape of the inlet walls was then found by using streamlines from the inviscid calculation that define a streamtube that passes the necessary mass flow. The wall shapes followed these streamlines up to an axial distance of one-chord length upstream of the blade surfaces. The shape of the bellmouth was defined with two ellipses with major and minor axes chosen to achieve a 3-to-1 contraction. The exit duct walls (hereafter referred to as tailboards) were assumed to be straight, with an angle tangential to the trailing edge angle of streamlines from the inviscid calculations.

A first generation model was deigned using this methodology. Model construction details are omitted here for brevity. However, measurements showed that the pressure distribution was far from the infinite cascade solution. Changes to the suction rates and tailboard angles were not sufficient to obtain the desired pressure profiles. Apparently, this inviscid design methodology that had previously worked for a subsonic cascade, was inadequate for the highly-loaded transonic stage under investigation here.

The pressure data from this “first-cut” model did serve a useful purpose: they were used to validate the 2-D RANS simulation method prior to the design of the second-generation model. Figure 2.13 presents a subset of the computational grid with typical boundary condition values used in these simulations. This grid was generated in a multi-block fashion utilizing an in-house structured iterative elliptic grid generator developed by Wu (2000) using a methodology presented by Hsu and Lee (1991). This approach ensures grid line orthogonality on all the boundaries of the domain. Three H-grid blocks were used in constructing the domain; two blocks were used for each bleed section, and one for the main

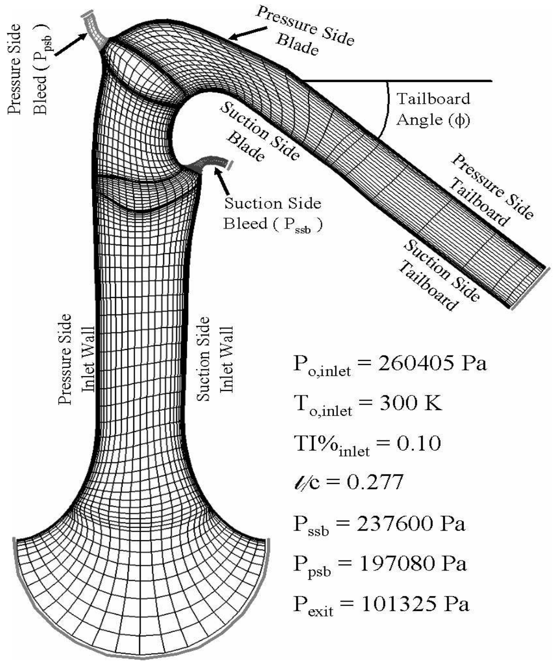

Figure 2.13: Sample grid and boundary conditions for single passage model design. *The blade shape has been distorted to ensure protection of proprietary information.*

passage. The cell heights near the walls were stretched to achieve y^+ values ranging from 0.14 to 3.7. A grid refinement study was performed to determine the smallest possible grid size that could be run while maintaining satisfactory accuracy: this resulted in a mesh size of approximately 60,000 cells for the majority of results presented here. The largest two-dimensional grid during the design process contained approximately 150,000 cells. Two forms for inlet boundary geometries were explored in this work: one with a horizontal line across the entrance, the other was a semi-circular boundary (as shown in Figure 2.13). A stagnation boundary condition was applied in both cases, specifying the stagnation pressure and temperature, turbulence intensity and integral length scale. Virtually identical results were achieved using these two approaches. Constant pressure boundary conditions were implemented on the bleed exit boundaries. Additionally, on these boundaries, a zeroth-order extrapolation was used for the other flow parameters (MacCormack (1995)). The set pressures were adjusted to achieve the necessary mass flow rate. Initial guesses for these pressures were calculated assuming one-dimensional isentropic flow between the model inlet and the bleed exit. Using this basis, appropriate compressible flow functions (Zucrow and Hoffman (1976)) as exemplified for the suction side bleed in equations 2.3 and 2.4 were

Table 2.3: Comparison of computed stagnation point axial locations for Buck and Prakash single passage versus infinite cascade.

Configuration	$M_{is} = 0$ ($\frac{x}{c_{blade}}$)
k-ε Chen (TI% = 10%, $\frac{\ell}{c_{blade}} = 0.28$)	$2.28(10)^{-3}$
Suction Side Blade, k-ε Chen (TI% = 10%, $\frac{\ell}{c_{blade}} = 0.28$)	$1.24(10)^{-3}$
Pressure Side Blade, k-ε Chen (TI% = 10%, $\frac{\ell}{c_{blade}} = 0.28$)	$3.71(10)^{-3}$

solved simultaneously to estimate the bleed exit pressure.

$$\dot{m}_{ssb} = P_{\circ,inlet} A_{ssb} M_{ssb} \left(\frac{\gamma}{RT_{\circ,inlet}}\right)^{\frac{1}{2}} \left(1 + \frac{\gamma-1}{2} M^2\right)^{-\frac{\gamma+1}{2(\gamma-1)}} \tag{2.3}$$

$$\frac{P_{ssb}}{P_{\circ,inlet}} = \left(1 + \frac{\gamma-1}{2} M^2\right)^{-\frac{\gamma}{\gamma-1}} \tag{2.4}$$

These pressures are then “fine tuned” based on the subsequent simulation results. A parametric study conducted on this test case revealed that the more mass flow that passed through the bleeds, the further the stagnation point would move away from the desired location in the flow direction. In other words in the case of the suction side blade wall, as the mass flow was increased the stagnation point would move towards the blade leading edge. Consequently, the bleed pressures were raised to move the stagnation points on the pressure and suction surfaces to their correct locations. This gave rise to separation regions at the inlet of the two bleeds. Figure 2.14 presents an exaggerated example of this phenomenon occurring in the suction side bleed.

Figure 2.15 shows the isentropic Mach number results obtained with the “first-cut” geometry experimentally and numerically, operating at optimum conditions. The ordinate axis is the surface coordinate relative to the stagnation point. Table 2.3 presents the axial position of the stagnation points relative to the leading edge of the blade, in the flow path direction through the engine. Figure 2.16 compares Mach number contours for the idealized single passage and the computed behavior following this design approach. Two observations were made at this point:

1. The 2-D computational model of the single passage model does an adequate job of predicting the surface pressure distribution.

2. The data suggest that the design procedure leads to significant departures in the desired locations of the stagnation points on the two blade surfaces and the location

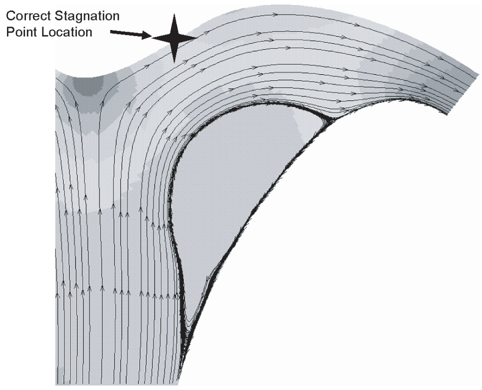

Figure 2.14: Example of a bleed separation bubble near the stagnation point on the suction side wall.

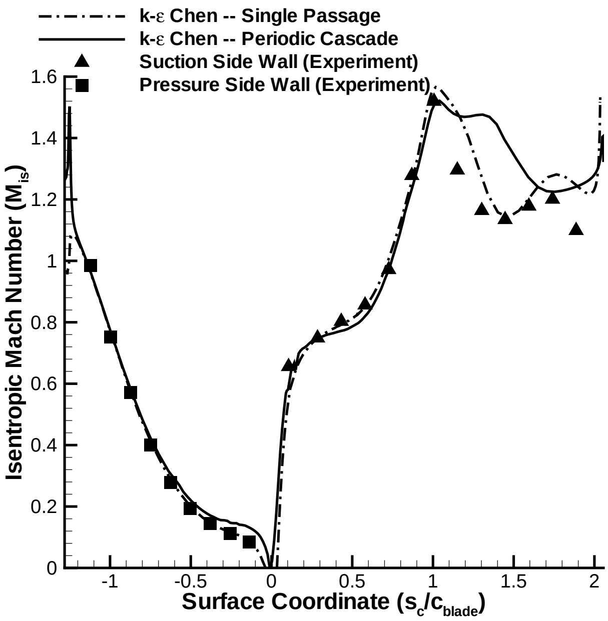

Figure 2.15: Isentropic Mach number distribution comparison for geometry using Buck-Prakash Method.

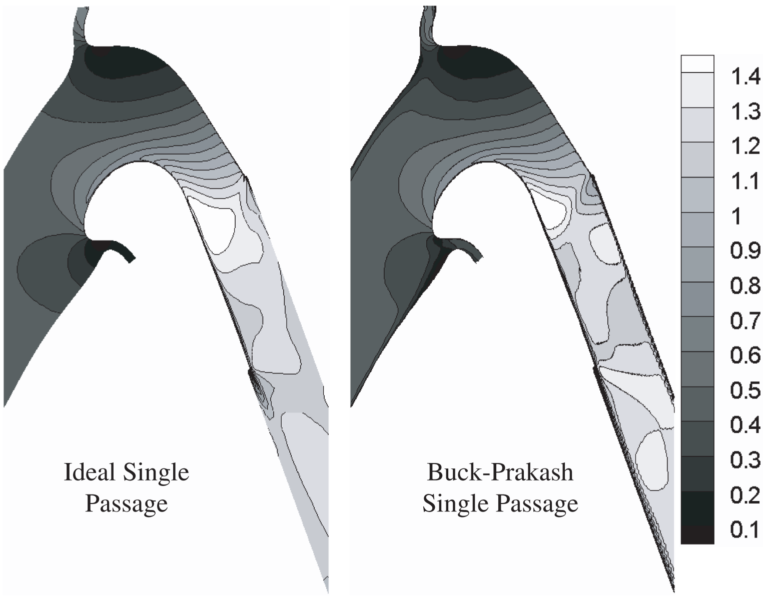

Figure 2.16: Comparison of Mach number contours for ideal and Buck and Prakash design single passage models.
This figure was generated by interpolating the infinite cascade calculation onto the grid used for the Buck-Prakash geometry calculation.
The blade shape has been distorted to ensure protection of proprietary information.

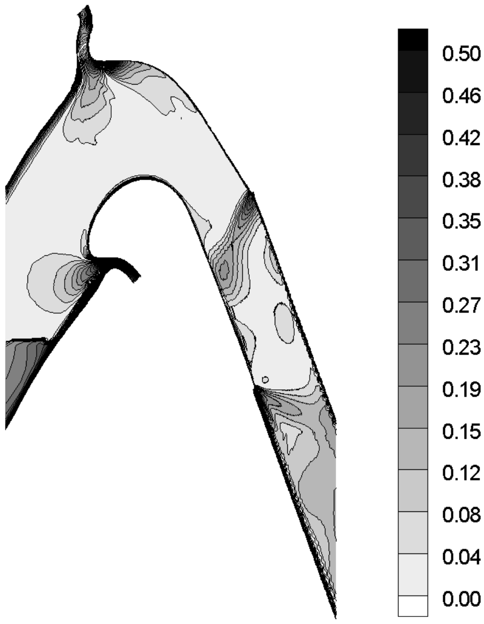

Figure 2.17: Contour plot of Mach number difference between infinite cascade and Buck and Prakash single passage ($\epsilon_{M_{ic}} = \frac{M_{IC}}{M_{B-P}} - 1$).
The blade shape has been distorted to ensure protection of proprietary information.

and strength of the shocks in the passage.

The latter critique is made even more apparent in figure 2.17 which shows contours of the difference in computed Mach number between the Buck and Prakash design single passage and the infinite cascade, expressed as $\epsilon_{M_{ic}} = \frac{M_{IC}}{M_{B-P}} - 1$. This figure shows a computed error as high as 50% near the stagnation points and in the shock region.

Before proceeding with the redesign of the single passage geometry, the viability of straight tailboards in providing the appropriate shock structure was explored. Figure 2.18 shows the isentropic Mach number distribution where the pressure side tailboard angle was rotated counter-clockwise by 7.35° (i.e. $\phi_{ps,new} = 32.2°$) compared to the baseline case ($\phi_{ss} = \phi_{ps} = 39.6°$). It is evident from this figure that "opening up" the pressure side tailboard wall allows the flow in the passage to speed up. As the suction side M_{is} distribution demonstrates, the strong normal shock totally disappears. However, instead of following the desired distribution after the initial oblique shock, the flow continues to accelerate well above it. These results suggested that the shock structure is heavily dependent on the shape of the pressure side exit wall. Additionally, these results suggested that curved, rather than straight, exit walls would generate the correct shock structure.

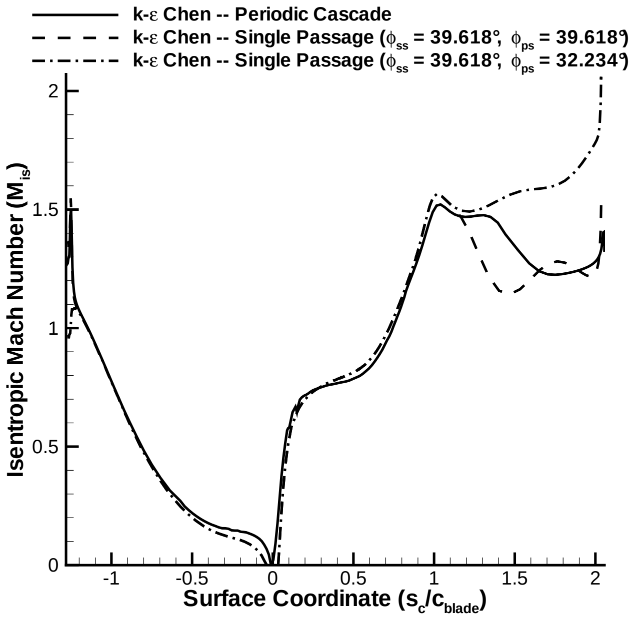

Figure 2.18: Demonstration of the effect of rotation of pressure side straight tailboard.

2.1.3 Revised Design Procedure for Transonic Single Passage Models

Based on this experience, it was decided to develop a heuristic, iterative approach coupled with CFD to redesign the inlet and exit duct walls to obtain better agreement with the infinite cascade result. The problem was decoupled into two issues:

1. Correctly position the stagnation point on the suction and pressure side surfaces by adjusting the shape of the inlet walls using streamlines from the RANS infinite cascade calculation. To decouple this from any effect from the shape of the exit passage, enforce periodic boundary conditions, instead of wall boundary conditions along the trailing edge surfaces of the domain.

2. Correctly position and set-up the shock structure on the aft side of the airfoil geometry by shaping the exit duct walls again using streamlines from the RANS simulation produced from step 1. This is done after satisfactory agreement is achieved with respect to the location of the stagnation point on the two measurement surfaces.

Bleed Design

The underlying rationale of this new technique is that the streamline one-displacement-thickness (δ^*) away from a properly-designed inlet wall should correspond to a streamline in the infinite cascade flow condition. Under this assumption, the boundary layer must remain attached for the bleed to function correctly. To ensure this occurs, the chosen wall shape must have streamwise pressure gradients that ensure attached, thin boundary layers. This was achieved by taking successive streamlines from the infinite cascade simulation and performing a 2-D RANS calculation to determine the predicted M_{is} distribution. The streamlines were chosen consistent with the desired direction of movement for the predicted stagnation point.

The straight tailboards are replaced with periodic boundary conditions which extended one-chord length in the axial direction downstream of the trailing edges of the airfoils. The boundaries upon which periodicity was imposed were straight lines with angles consistent with the straight tailboards used in Section 2.1.2 ($\phi_{ss} = \phi_{ps} = 39.6°$). One-to-one boundary face matching was used along these boundaries. This equated the values of all flow variables along the boundaries. One deficiency of this approach is that it forced the resulting grid to have a high level of skewness downstream of the airfoil trailing edges, due to the high turning angle. For ease of implementation, the same grid was used for the case with periodic boundary conditions and with tailboards. The resulting level of skewness in the grid was found to be acceptable for both cases.

Figure 2.19 compares the inlet wall shapes first using the Buck and Prakash method and the final result of the new design procedure. The bellmouth was redesigned to provide a 2.2-to-1 contraction consistent with the wider inlet. The values for the constant pressure boundary conditions on the two bleeds were set using periodic arguments, rather than to achieve a specific mass flow. In other words, these values were set to have the pressure distribution along the blade surface into the bleed match the equivalent location on the opposite blade. Figure 2.20 compares the M_{is} distribution using these two approaches and the target distribution. Table 2.4 confirms the agreement between the stagnation point locations on both surfaces and the infinite cascade. The figure verifies the assertion that the effect of the bleed conditions has a relatively small effect on the downstream shock structure. The peak isentropic Mach number is slightly higher than the infinite cascade simulation result. It is unclear if this difference is due to a geometry difference or another numerical issue. This figure also demonstrates that the mass flow approach for setting the

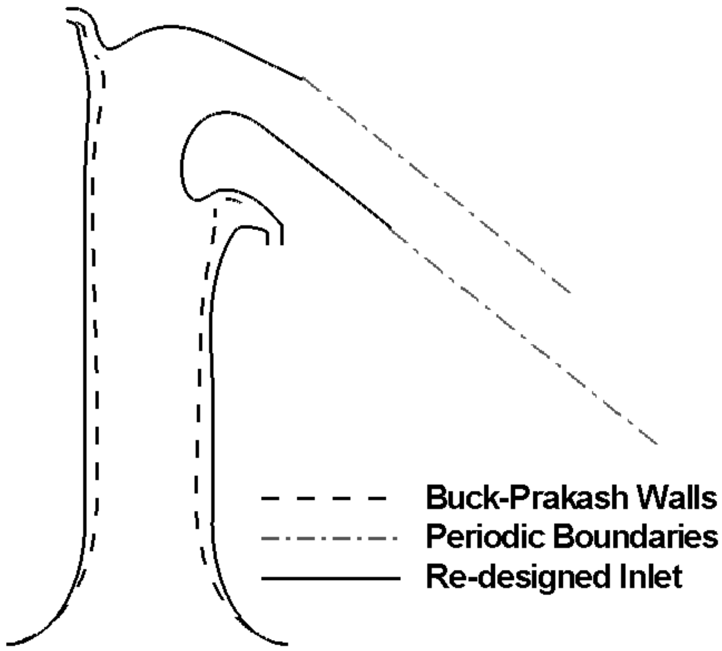

Figure 2.19: Comparison of inlet walls defined by Buck and Prakash and new single passage design approaches.

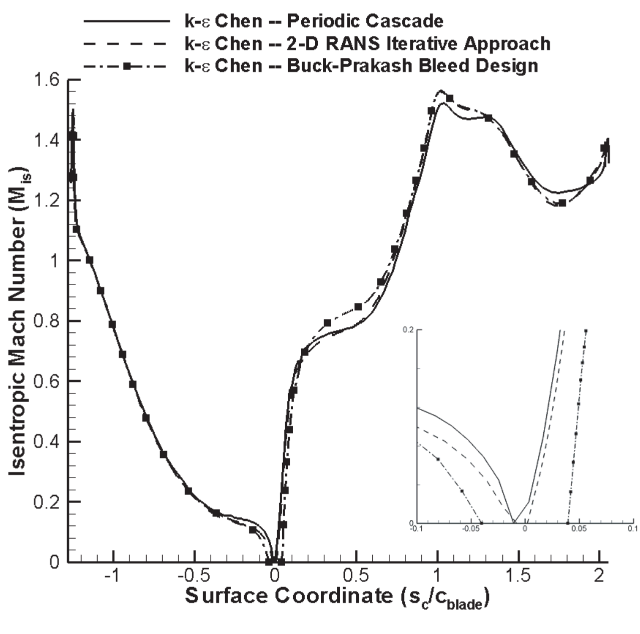

Figure 2.20: Comparison of M_{is} distributions for Buck and Prakash and new single passage design approaches.

Table 2.4: Comparison of computed stagnation point axial locations for new design versus infinite cascade and Buck and Prakash design.

Configuration	$M_{is} = 0$ ($\frac{x}{c_{blade}}$)
k-ε Chen (TI% = 10%, $\frac{\ell}{c_{blade}} = 0.28$)	$2.28(10)^{-3}$
Suction Side Blade, k-ε Chen (TI% = 10%, $\frac{\ell}{c_{blade}} = 0.28$)	$2.64(10)^{-3}$
Pressure Side Blade, k-ε Chen (TI% = 10%, $\frac{\ell}{c_{blade}} = 0.28$)	$2.64(10)^{-3}$
Suction Side Blade (BP), k-ε Chen (TI% = 10%, $\frac{\ell}{c_{blade}} = 0.28$)	$1.24(10)^{-3}$
Pressure Side Blade (BP), k-ε Chen (TI% = 10%, $\frac{\ell}{c_{blade}} = 0.28$)	$3.71(10)^{-3}$

Table 2.5: Comparison of computed bleed mass flow rates for different designs.

Parameter	Buck and Prakash Design	New Design
Suction Side Bleed ($\dot{m}_{ssb}$, $\frac{\text{kg}}{\text{s}}$)	$6.24(10)^{-2}$	$8.93(10)^{-2}$
Pressure Side Bleed ($\dot{m}_{psb}$, $\frac{\text{kg}}{\text{s}}$)	$7.22(10)^{-2}$	$9.29(10)^{-2}$

inlet wall shape is inappropriate as it does not incorporate any constraint on the periodicity of the airfoil surface pressure distributions leading to the bleeds. It should be added that attempting to raise the bleed exit pressures to enforce periodicity (and further reduce the mass flow rates on the bleeds) led to large separation regions developing in the Buck and Prakash design. An examination of the wall skin friction coefficient distribution on the suction side inlet wall, shown in figure 2.21 clearly demonstrates that the new bleed wall shapes produce little or no separation. This observation is demonstrated by the "dip" at $\frac{S}{S_{max}} \approx 0.9$ where C_f goes to zero on the Buck and Prakash-designed suction side inlet wall. Table 2.5 compares the mass flow rates for the two design results. It is important to note that the mass flow through the newly-designed bleeds is considerably higher than that in the original design. If the Buck and Prakash design was adjusted to have the same bleed mass flow rates, the stagnation points would be further away from their desired locations. This means that the inlet wall shape is the determinant factor in fixing the stagnation point location, and by association the necessary mass flow rate for the bleed to function correctly.

Tailboard Design

Results presented in Section 2.1.2 demonstrated the necessity of curved tailboards in achieving the desired shock structure. By extension from the design process for the inlet walls, the desired exit wall designs should be those that produce streamlines one-δ^* away

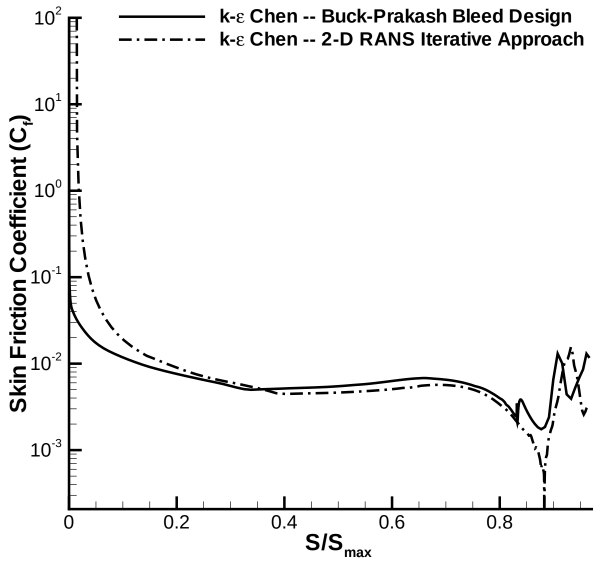

Figure 2.21: Comparison of $C_f = \frac{\tau_w}{\frac{1}{2}\rho\tilde{u}_\infty^2}$ distributions for Buck and Prakash and new single passage design approaches. ($\rho = \frac{P(s)}{RT(s)}$, $\tilde{u}_\infty = M_{is}\sqrt{\gamma RT(s)}$)

from the wall that closely follow those of an infinite cascade. Laskowski et al. (2005) pointed out that the downstream shock structure is highly sensitive to small changes in the exit wall shapes. Furthermore, considering that the displacement thicknesses of the boundary layers on the exit walls are strongly coupled to the shock structure, it is virtually impossible to determine *a priori* the optimal wall shape. Thus some form of iterative scheme must be used to design the exit walls. Laskowski et al. (2005) presented a computation-intensive technique using a cost function minimization routine to optimize the shapes of the exit walls for a double passage model, reducing the difference between computed infinite cascade and double passage M_{is} distributions. Another approach, which is followed in this work, uses heuristic arguments to ascertain the appropriate exit wall shapes.

Figure 2.22 evinces the similarities in the shock structure between the idealized single passage and one with periodic tailboards and properly designed bleeds. Figure 2.23 presents contours of the error ($\epsilon_{M_{IC}} = \frac{M_{IC}}{M_{2DRANS}} - 1$) between the two cases. The maximum error between the flowfields was estimated to be approximately 8%.

Figure 2.24 displays computed trailing edge streamlines from the single passage com-

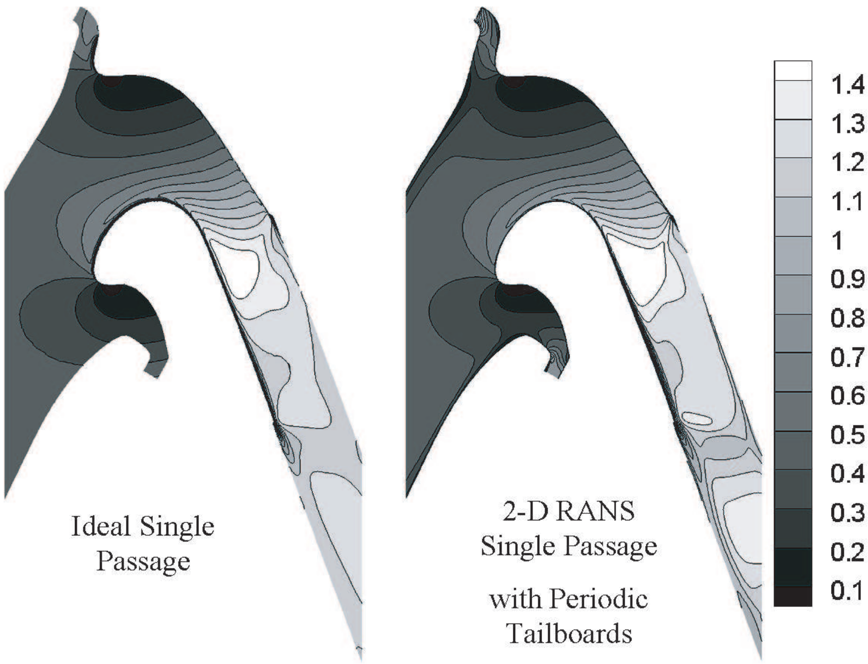

Figure 2.22: Comparison of Mach number contours for ideal single passage model and single passage with periodic tailboards.

The blade shape has been distorted to ensure protection of proprietary information.

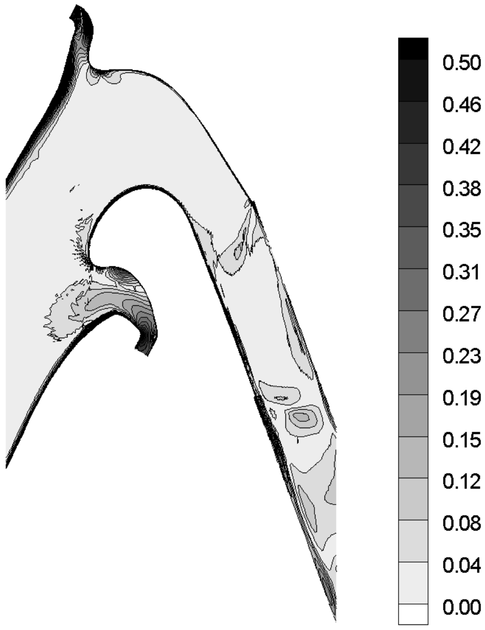

Figure 2.23: Contour plot of error in Mach number between infinite cascade and 2-D RANS of single passage with periodic boundary conditions ($\epsilon_{M_{IC}} = \frac{M_{IC}}{M_{2DRANS}} - 1$).
The blade shape has been distorted to ensure protection of proprietary information.

putation with periodic exit boundaries. This figure emphasizes the point that the ideally-designed tailboard would produce a streamline one-δ^* from the wall that curves slightly in select locations. The design procedure for the exit wall is based on the postulate that the ideal wall shape consists of the closest streamline to the trailing edge, rotated to account for the growing boundary layer along the wall. The pivot point for this rotation was assumed to be at the trailing edge of each blade, as shown in figure 2.25. Based on previous results, it was conjectured that it was only necessary to adjust the pressure side wall. Thus, the pressure side wall was rotated counter-clockwise by a defined angle, $\phi_{\delta,ps}$. A rotation angle for the suction side wall also was defined ($\phi_{\delta,ss}$). However, this was found to be unnecessary.

Figure 2.26 presents the evolution of the single passage M_{is} distribution with increasing angle of rotation for the pressure side wall. When $\phi_{\delta,ps} \approx 0°$, the interference of the boundary layer with the mainstream flow causes an strong initial shock to form, evidenced by the dramatic drop in the suction side M_{is} distribution. As $\phi_{\delta,ps}$ increases, the M_{is} distribution along the suction side blade wall approaches that of the infinite cascade simulation. The difference between these two results are minimized at a particular angle, in these simulations it was at $\phi_{\delta,ps} = 0.3°$. Beyond this value, the oblique shocks continue to weaken, resulting in

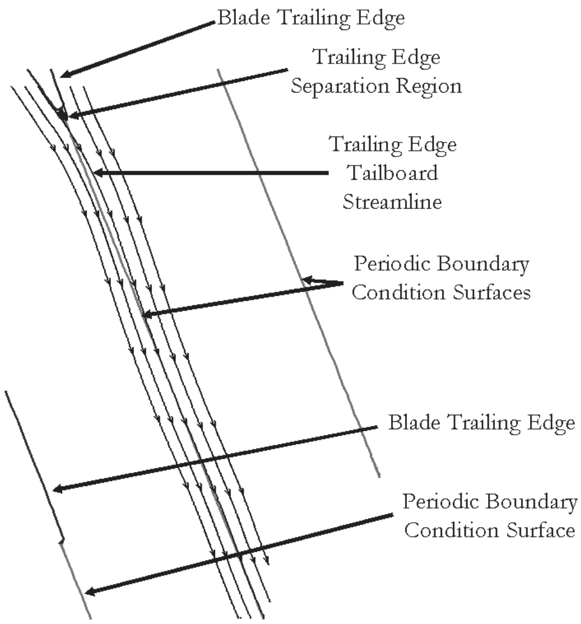

Figure 2.24: Computed trailing edge streamlines from single passage calculation with periodic exit boundaries. These are used to design the tailboards.

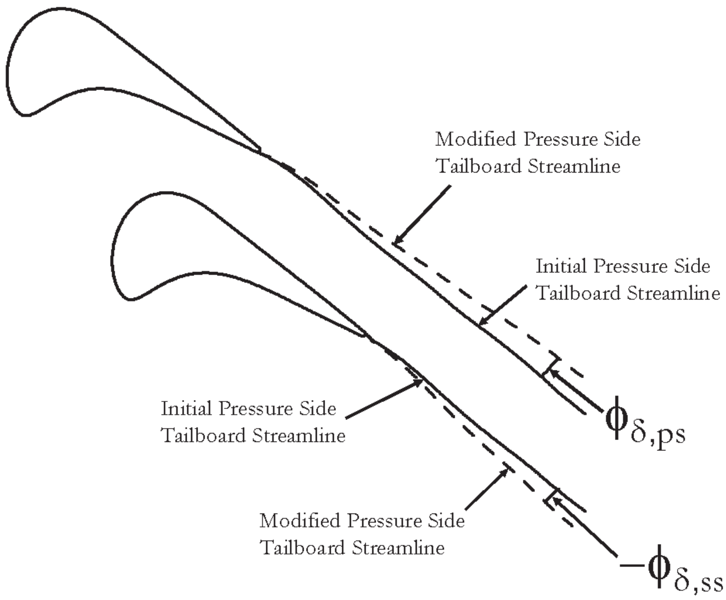

Figure 2.25: Definition of rotation angles for pressure and suction side blade surfaces. Complete blades are shown in this figure for ease of identification.

The blade shape has been distorted to ensure protection of proprietary information.

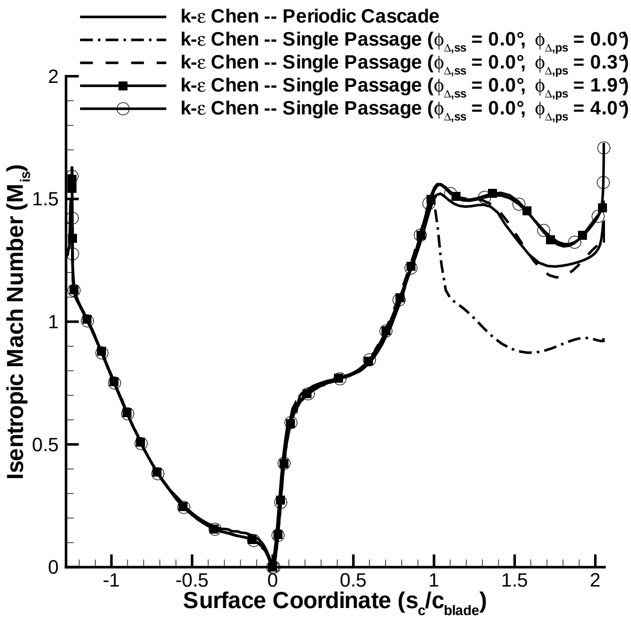

Figure 2.26: Comparison of M_{is} distributions for various pressure tailboard angles.

even faster flow over the suction side wall. These results also indicate that beyond an angle of approximately $\phi_{\delta,ps} \approx 1.90°$, there is limited change in the surface pressure distribution. In all cases, there was no noticeable effect on the location of the stagnation points due to the changing of the exit wall geometry.

The initial build for the single passage used a tailboard angle of $\phi_{\delta,ps} = 0.3°$. This was found experimentally to produce the previously described strong normal shock. After successive experimental iterations, the implemented tailboard angle was $\phi_{\delta,ps} = 1.90°$, this produced a pressure distribution that closely followed the infinite cascade simulation, which differs significantly from the prediction.

This could be heuristically described as a “safety margin” to account for the 3-D effects that resulted from thicker tailboard boundary layers than those predicted by the 2-D RANS design process. It should be added that the bleed exit geometry was adjusted during construction of the actual model due to practical concerns with frictional choking in the as-built geometry. Consequently, the shape of the exit portion of the bleeds is significantly different than those shown in previous subsections. Table 2.6 compares the total predicted mass flow for the two designs, showing that the new design has increased flow requirements compared to the initial design.

Table 2.6: Comparison of computed total mass flow rates for different designs.

Parameter	Buck and Prakash Design	New Design
Total Mass Flow Rate ($\dot{m}_{total}$, $\frac{\text{kg}}{\text{s}}$)	0.546	0.616

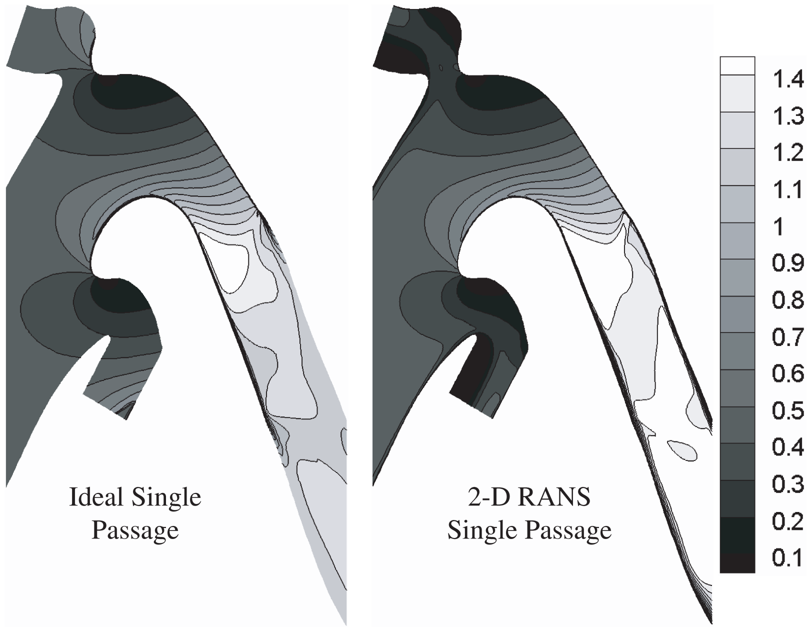

Figure 2.27: Contour plots of Mach number for infinite cascade and 2-D RANS-design single passage with $\phi_{\delta,ps} = 1.90°$.

The blade shape has been distorted to ensure protection of proprietary information.

Figures 2.27 and 2.28 show that the entry passage contouring improves the agreement between the experimental and infinite cascade flowfields in the subsonic region of the flow. Figure 2.28 shows the maximum error is under 4% in the subsonic region of the flow. Surprisingly, in the inviscid core of the supersonic region of the flow, the Buck and Prakash design appears to be generally more accurate, on a percentage basis. This is probably a direct consequence of the previously mentioned built-in "safety margin". The exception to this observation is the flow behavior in the immediate vicinity of the suction side wall. This is verified by the wall pressure distribution that consistently shows that this new design produces a more accurate representation of the infinite cascade result. For completeness, figure 2.29 shows the "error" in Mach number for a design where $\phi_{\delta,ps} = 0.3°$. Recall that this was shown to give the best M_{is} agreement with the infinite cascade in figure 2.26. This figure clearly shows that high quality agreement with the infinite cascade M_{is} distribution ensures a flowfield that closely matches that found in an infinite cascade. This is an important result as it suggests that precisely matching the desired M_{is} distribution guarantees a match to the flowfield conditions.

Further Analysis of Optimal Single Passage Design

Given the small differences in the flowfield between that in the single passage with $\phi_{\delta,ps} = 0.3°$ and the infinite cascade: How well would the turbulence fields agree? Ideally, these two fields would be comparable, inferring that any effect on heat transfer and film cooling effectiveness due to the turbulence field in a linear cascade would be mirrored in the single passage experiment. This particular computation was chosen as it provided the best agreement in the flowfield when compared to that for the infinite cascade. Figure 2.30 shows that there are substantial differences in the two computed turbulent kinetic energy fields. What is surprising is the uniformity of the difference, suggesting that the relative values of the turbulent kinetic energy are identical in the two cases, but their absolute values differ. Laskowski et al. (2005) observed similar behavior. A possible explanation for this discrepancy is the fact that the infinite cascade and single passage simulation have specified turbulence intensities, rather than the magnitude of the turbulent kinetic energy. Recall that the single passage simulation uses a bellmouth with a semi-circular inlet. Consequently, the inlet velocities are much lower than that for the linear cascade computation that had an inlet Mach number of approximately 0.4. This resulted in inlet turbulent kinetic energy values that are considerably higher in the linear cascade simulation than that for the single passage. Thus matching the inlet turbulence intensity, does not result in matching the turbulent kinetic energy.

Exhaust Manifold Design

One practical problem with setting up the flow facility for this particular blade geometry was the design of the exhaust system. The model was designed to sit on a plenum with flow passing upwards towards the blade surfaces. Due to the highly-cambered blade geometry, the flow turns approximately 120° from inlet to exit. For practical reasons it was necessary to have the flow exhaust oriented in a horizontal direction. This compelled the design of a diffuser geometry that turned the high speed flow approximately 40° without

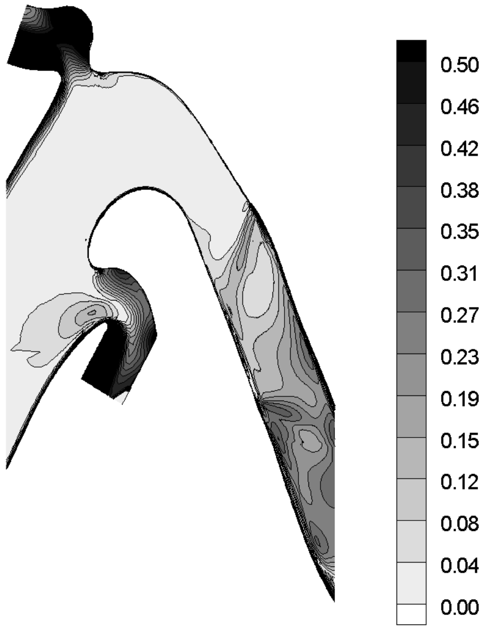

Figure 2.28: Contour plot of error in Mach number between infinite cascade and 2-D RANS-design single passage with $\phi_{\delta,ps} = 1.90°$ ($\epsilon_{M_{IC}} = \frac{M_{IC}}{M_{2DRANS}} - 1$).
The blade shape has been distorted to ensure protection of proprietary information.

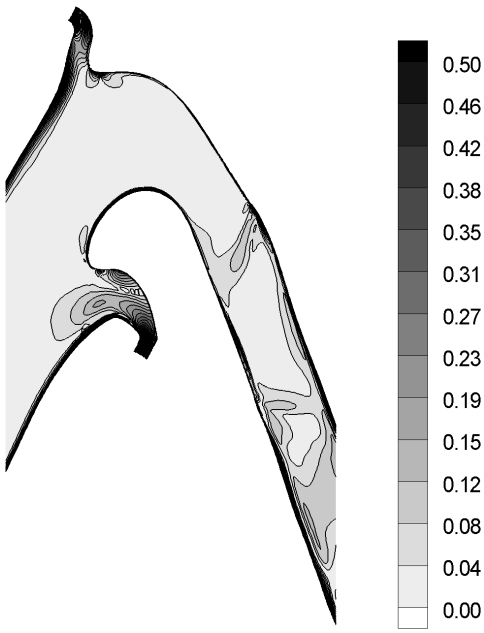

Figure 2.29: Contour plot of error in Mach number between infinite cascade and 2-D RANS-design single passage with $\phi_{\delta,ps} = 0.3°$ ($\epsilon_{M_{IC}} = \frac{M_{IC}}{M_{2DRANS}} - 1$).
The blade shape has been distorted to ensure protection of proprietary information.

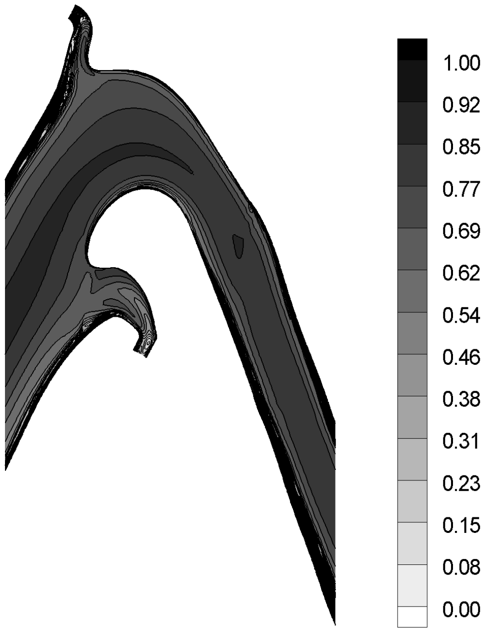

Figure 2.30: Contour plot of error in TKE between infinite cascade and 2-D RANS-design single passage with $\phi_{\delta,ps} = 0.3°$ ($\epsilon_{TKE_{IC}} = \frac{TKE_{IC}}{TKE_{2DRANS}} - 1$).
The blade shape has been distorted to ensure protection of proprietary information.

back-pressuring the flow facility. Back-pressuring is where downstream flow restrictions raise the exit pressure of the model: if this value is large enough, supersonic flow cannot be achieved (Hodge and Koenig (1995)).

Figure 2.31 shows the generic form of the supersonic diffuser section with its key dimensions. This design assumes that the incoming flow is already supersonic, the nozzle then has a gradual turn with increasing area. The combination of these two features gives the best chance of efficiently turning the flow without back-pressuring the upstream test section. The parameters that can be adjusted in this design are the ratio of duct heights, $\phi_H = \frac{H_2}{H_1}$, the start and finish flow angles (θ_1 and θ_2) and the initial and final points of the lower wall (($x^R_{1,1}$, $x^R_{2,1}$) and ($x^R_{1,2}$, $x^R_{2,2}$)). Two fifth-order polynomial functions, $f^R_1(\theta)$ and $f^R_2(\theta)$, presented in indicial notation in equation 2.5 are used to smoothly shape the duct, gradually changing the radii of curvature of the two walls from inlet to exit.

$$f^R_i(\theta) = \sum_{k=0}^{5} \kappa^R_{k,i}\theta^k \tag{2.5}$$

$$i = 1, 2$$

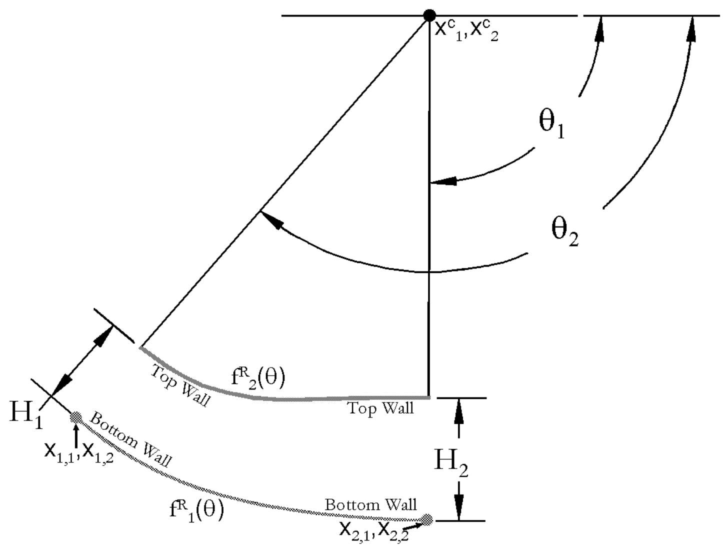

Figure 2.31: Generic form of supersonic diffuser for model exit.

Equation 2.6 is used to generate the coefficients of the above polynomials ($\kappa^R_{k,i}$) and the center of curvature for the radius of curvature functions (x^C_i). This represents a set of 18 linear equations which can be solved by standard linear algebra procedures.

$$\begin{aligned} f^R_i(\theta_j) - R_{i,j} = 0 \\ f'^R_i(\theta_j) = 0 \\ f''^R_i(\theta_j) = 0 \\ \sum_{i=1}^{2}(-1)^{i+1}R_{i,j} - H_j = 0 \\ x^C_i - x^R_{i,j} - R_{i,j}cos(\theta_j) = 0 \end{aligned} \tag{2.6}$$

One inherent deficiency with this design is the formation of oblique shocks on the convex (upper) surface. If these shocks are strong enough, a separation zone will develop, restricting the flow. This feature of the flow is controlled by the local radius of curvature along the wall; the smaller the radius of curvature, the stronger the shock.

Table 2.7 presents the values for the key parameters for the exhaust manifold used in this configuration. The start and end points for the lower wall, ($x^R_{1,1}$, $x^R_{2,1}$) and ($x^R_{1,2}$, $x^R_{2,2}$), were determined by finding the intersection of the chosen tailboard shapes with lines drawn at the axial locations identified in table 2.7. The starting points were chosen to be at least

Table 2.7: Exhaust manifold design parameters.

Parameter	Value
ϕ_H	1.3
H_1	$0.467c$
Lower Wall (axial start and end points, relative to trailing edge of blade)	$0.290c$, $1.532c$
Upper Wall (axial start and end points, relative to trailing edge of blade)	$0.679c$, $1.826c$
θ_1, θ_2	-130.5°, -90.0°

0.25-chord lengths downstream of the trailing edges of the airfoil to limit any effects of the manifold on the flow conditions in the passage. The end points were chosen to provide as gradual turn as possible within the constraints of the overall flow facility. 2-D RANS calculations confirmed that this arrangement achieved these objectives.

2.1.4 2-D Simulation Sensitivity and Comparative Studies

A series of computational studies were conducted to evaluate some characteristics of the numerical solution. These were done as precursors to a three-dimensional computation, to determine if the domain could be simplified and if the two-dimensional grid had adequate resolution. The importance of these tests was linked to minimizing the amount of numerical resources required for the 3-D RANS computation.

Grid Refinement Study

A grid refinement study was performed on the optimal CFD-design for the single passage ($\phi_{\Delta,ps} = 0.3°$). This was done simply because these calculations were performed before the experimental model was constructed, however, it is strongly believed that these results shown here can be easily extended. The number of grid points was doubled in the streamwise and the wall normal directions, resulting in a 230,000-cell grid. Figure 2.32 displays the M_{is} distributions for the coarse and fine calculations. Figure 2.33 is a contour plot of the parameter $\epsilon_{M_{GR}} = \frac{M_{2DRANS,fine}}{M_{2DRANS,coarse}} - 1$, where the fine grid result was interpolated onto the coarse grid. This figure establishes that the observed differences in the M_{is} distribution are

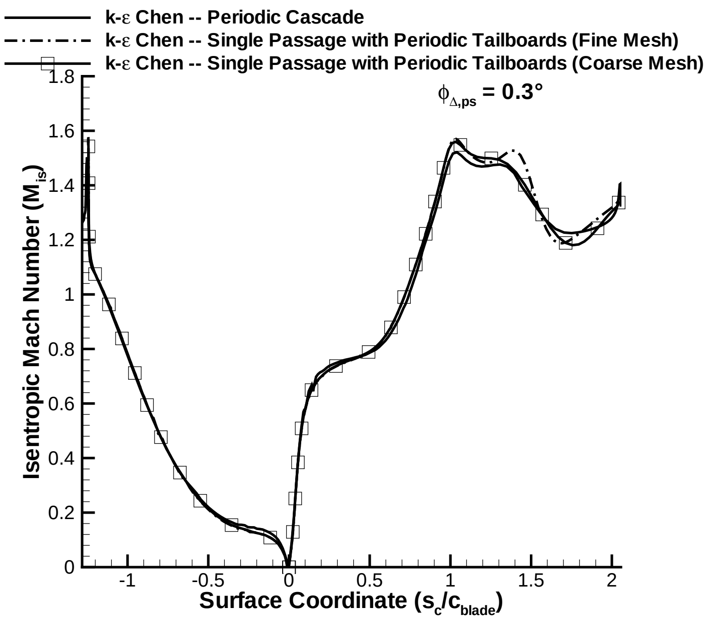

Figure 2.32: Examination of effect of grid resolution on M_{is} distribution.

due to changes in the near-wall region, and that the overall differences were less than 4%. This certified that the coarse grid solution was adequately resolved.

Inlet Truncation Effect

Figure 2.34 presents the full domain consisting of bellmouth, inlet duct, single passage model and exhaust duct. Also indicated is the location of the inlet plane for a truncated domain. This is approximately 1.32-chord-axial-lengths upstream of the blade surfaces, consistent with the inlet mean flow and turbulence measurements to be presented in Section 2.4.6. The wall normal grid resolution is nearly identical for these two cases. Figure 2.35 shows the calculated isentropic Mach number distributions for these two cases, demonstrating that the inlet location has no significant effect on the calculated flow in the single passage.

2.1.5 3-D Simulation Results

The actual model had limited optical access, so there was no option to perform 3-D flowfield measurements in the passage. Thus a 3-D RANS calculation was necessary to

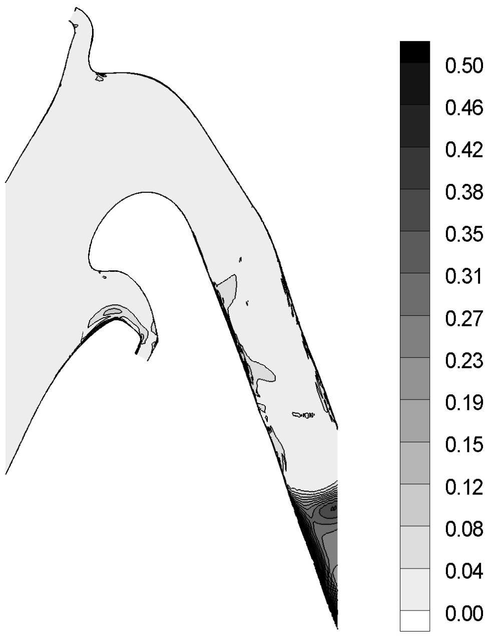

Figure 2.33: Contour plot of error in Mach number between coarse (57600 cells) and fine (230400 cells) 2-D RANS simulations of full geometry single passage ($\epsilon_{M_{GR}} = \frac{M_{2DRANS,fine}}{M_{2DRANS,coarse}} - 1$).

evaluate the three-dimensionality of the flow. The additional purpose of this calculation was to ascertain if the GEAE "best practice" choice for the model height of $AS = 1.27$ was sufficient in relegating the 3-D effects in the passage to a manageable portion of the channel height.

The calculation domain included one-half of the channel width with a symmetry boundary condition at the channel centerline. A hyperbolic tangent grid stretching was used to resolve the endwall boundary layers. Figure 2.36 presents an overall view of the domain and grid used in these calculations. The grid contained approximately 2.6 million cells, with y^+ values ranging from $1.3(10)^{-4} \leq y^+ \leq 3.0$.

Figure 2.37 presents M_{is} distributions at mid-span of the model, where the symmetry plane is applied ($Z' = \frac{Z}{H_{MODEL}} = 0.0$), the 2-D simulation and the infinite cascade result. These distributions demonstrate that the 2-D simulation is a good representation of the mid-span flow conditions. Figures 2.38, 2.39 and 2.40 compare the M_{is} distribution at the endwall ($Z' = -0.5$), at the centerline ($Z' = 0.0$) and several intermediate locations ($Z' = -0.4375$, $Z' = -0.375$ and $Z' = -0.25$). These figures demonstrate that the 3-D nature of the flow is limited to region $-0.5 \leq Z' \leq -0.25$. The effect of three-dimensionality is

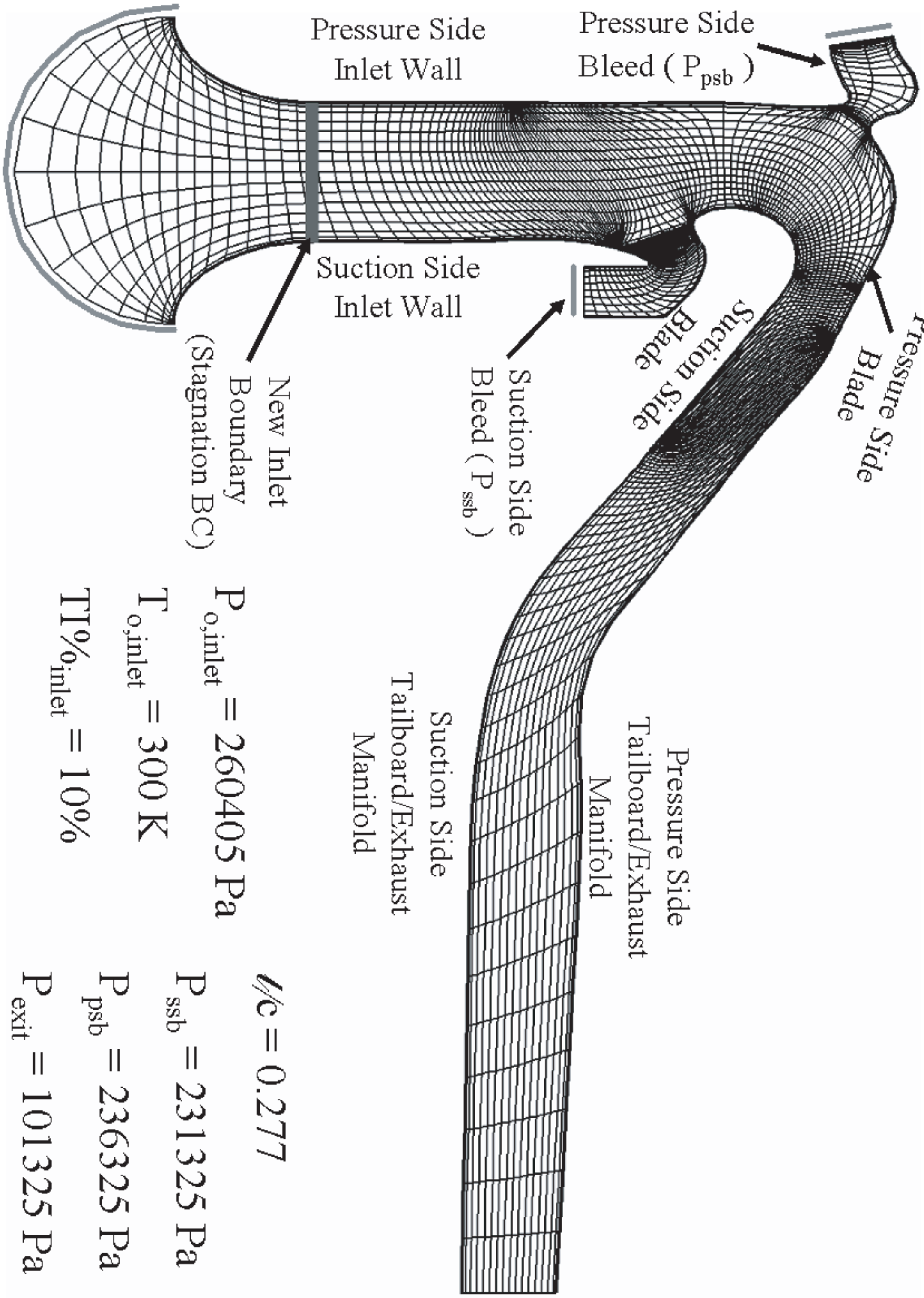

Figure 2.34: Full and truncated computational domains with applied boundary conditions. *The blade shape has been distorted to ensure protection of proprietary information.*

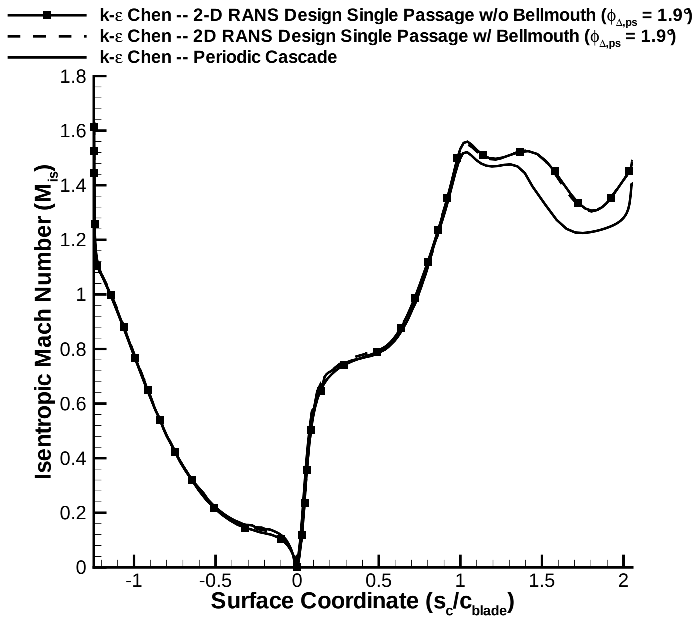

Figure 2.35: Examination of effect of bellmouth truncation on M_{is} distribution.

primarily observed on the suction side wall. This was subsequently attributed to the effect of the passage vortex.

Two parameters was used to identify 3-D flow structures and further determine the areas of two-dimensional flow in the single passage model. One proposed by Chong et al. (1990) visualizes the vortical structures using isosurfaces of the second invariant of the velocity gradient tensor, $\mathcal{Q}$, defined in equation 2.7, below.

$$\mathcal{Q} = -\frac{1}{2} A_{ij} A_{ji} \tag{2.7}$$

Where A_{ij} is defined as the local velocity tensor which can be written as:

$$A_{ij} = \partial_i u_j \tag{2.8}$$

Positive values of $\mathcal{Q}$ indicate locations where rotation is dominant and negative values depict regions where strain is dominant. Figures 2.41 and 2.42 presents different views of the isosurface $\mathcal{Q} = 1(10)^8$ showing the vortical structures that form at the stagnation points of both airfoil surfaces. The vortex that forms at the pressure side stagnation wall is called the passage vortex by researchers such as Langston (1980) and Chung et al. (1991). This vortex moves across the endwall from the pressure side wall to the opposite suction side

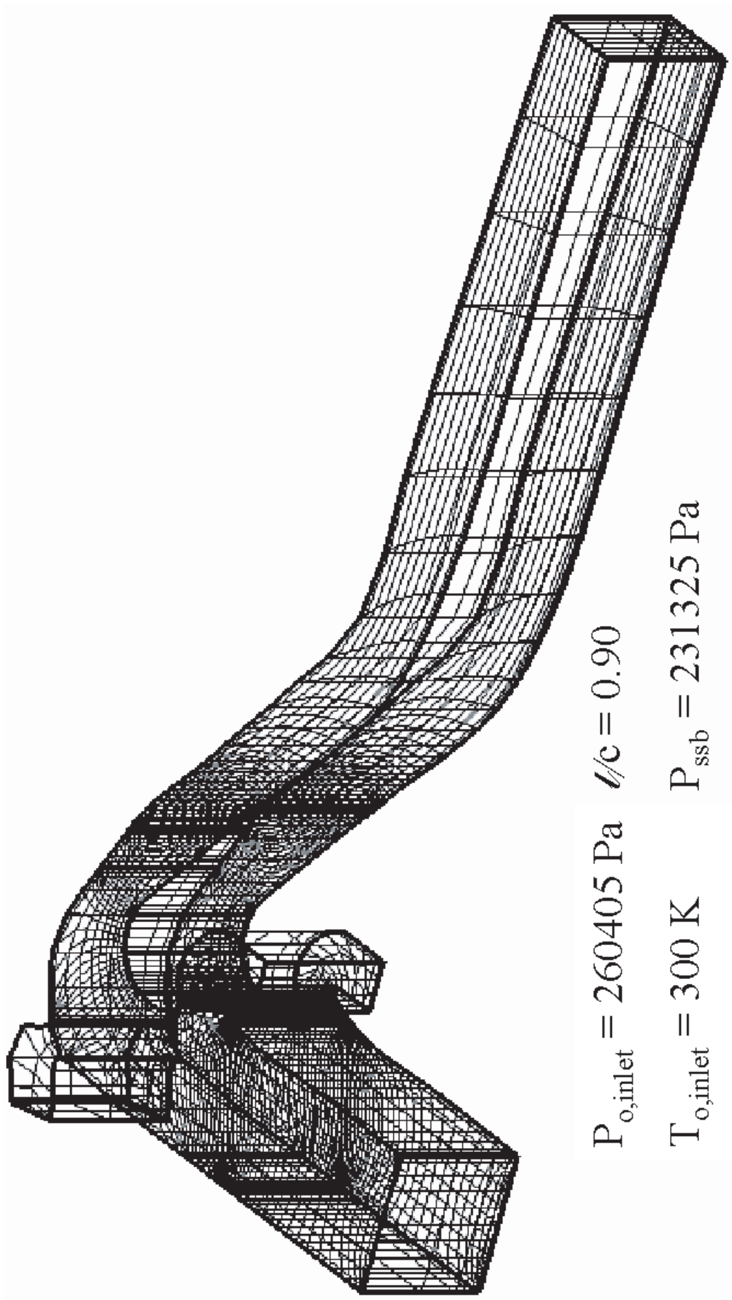

Figure 2.36: Simplified 3D computational grid with applied boundary conditions.

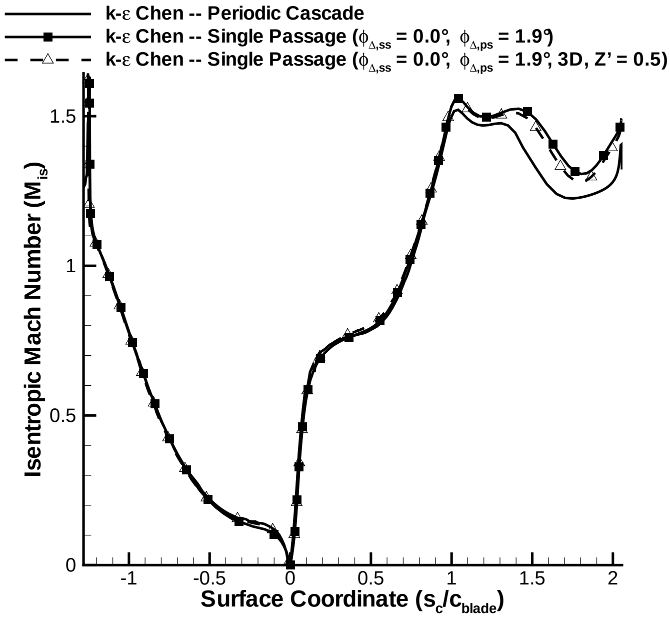

Figure 2.37: Comparison of M_{is} distribution at $Z' = 0.0$ (centerline) to 2-D simulation and infinite cascade results.

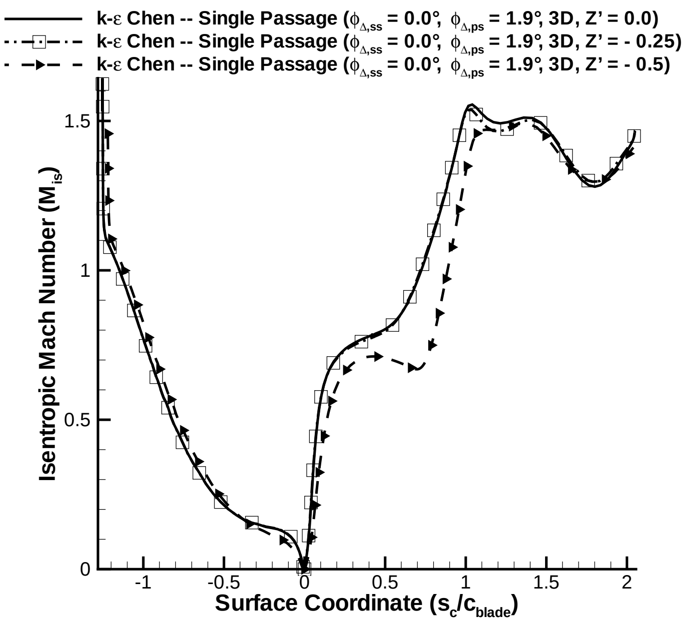

Figure 2.38: Comparison of M_{is} distributions at $Z' = 0.0$ (centerline), $Z' = -0.25$ and $Z' = -0.5$ (endwall).

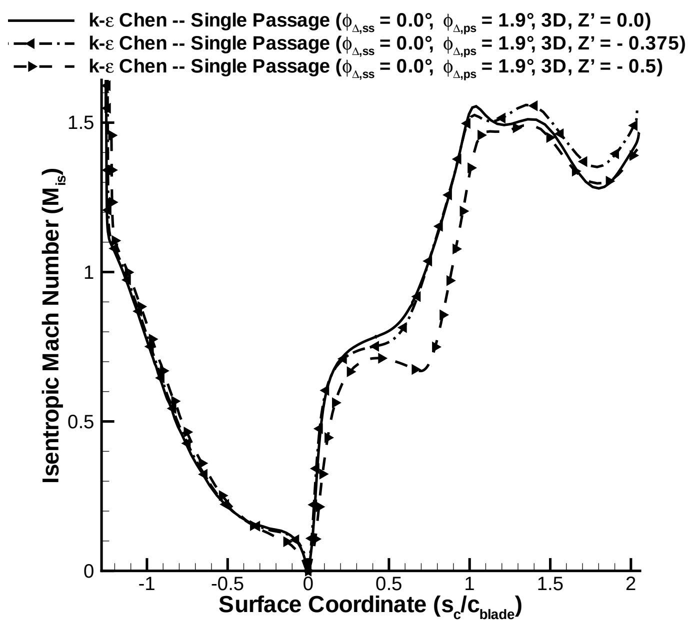

Figure 2.39: Comparison of M_{is} distributions at $Z' = 0.0$ (centerline), $Z' = -0.375$ and $Z' = -0.5$ (endwall).

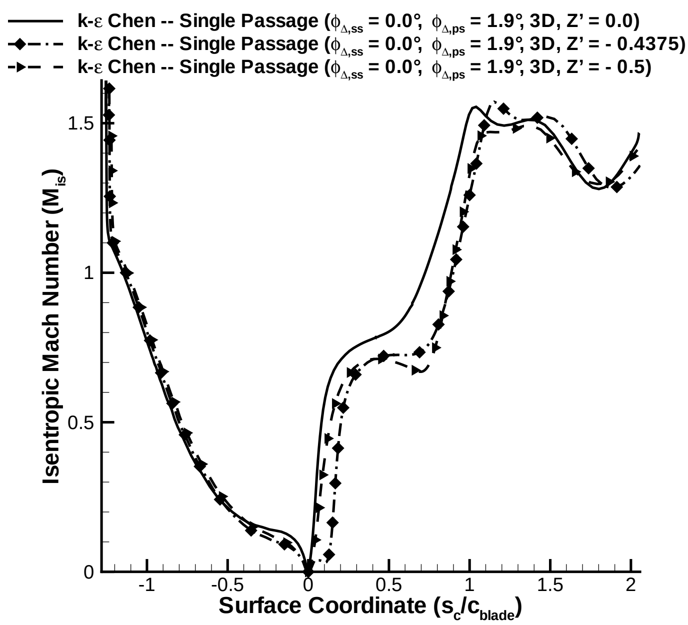

Figure 2.40: Comparison of M_{is} distributions at $Z' = 0.0$, $Z' = -0.4375$ and $Z' = -0.5$.

wall by the transverse pressure gradient. It then appears to merge with the counter-rotating vortex from the suction side, forming a single structure which convects downstream. These observations are consistent with figure 2.43 showing the characteristic three-dimensional flow features that results from blade-endwall boundary layer interactions. An examination of these figures suggests that this vortex does not appear to move from one endwall to the other. Additionally, figures 2.41 and 2.42 suggest the development of smaller vortical structures that seem to coincide with the shock locations in the passage.

Another technique directly contrasted the Farve-averaged velocity in the z-direction, $\tilde{w}$, to the total velocity magnitude at specific locations, as shown in equation 2.9. In locations dominated by secondary flow, this value was expected to be close to one. In comparison, in areas which are largely two-dimensional, this value is expected to be close to zero. There are some exceptions to this rule: for example, near the stagnation point.

$$\mathcal{S} = \frac{\tilde{w}}{\sqrt{\tilde{u}^2 + \tilde{v}^2 + \tilde{w}^2}} \tag{2.9}$$

The condition for two-dimensionality is defined as:

$$\mathcal{S} \leq 0.10 \tag{2.10}$$

Figure 2.44 presents the isosurface $\mathcal{S} = 0.10$. This figure suggests that two-dimensional flow is achieved on both blade surfaces in the region $-0.25 \leq Z' \leq 0.25$, agreeing with the behavior observed in the M_{is} distributions.

2.2 Physical Single Passage Model Design and Fabrication

As the purpose of this flow facility is to perform steady state heat transfer measurements, it was imperative that a low thermal conductivity material was used in model construction. Consistent with this philosophy, all major components of the model were fabricated out of Ren Shape 450 (a high-density polyurethane material) with a thermal conductivity of approximately $k = 0.2\frac{W}{m\ K}$ (Vantico Corporation (2001), Mukerji and Eaton (2002)). Figure 2.45 presents a layout of the model. The suction and pressure airfoil surfaces were integral parts containing both the appropriate blade surface and part of the bleed geometry. All components shown in this figure were machined within a tolerance of ± 0.076-mm using a three-axis CNC (computer numerical control) milling machine, using a fabrication control program, MASTERCAM (CNC Software (2000)) to generate the necessary machine instructions from AutoCAD drawings. Highly accurate and repeatable machining was critical due

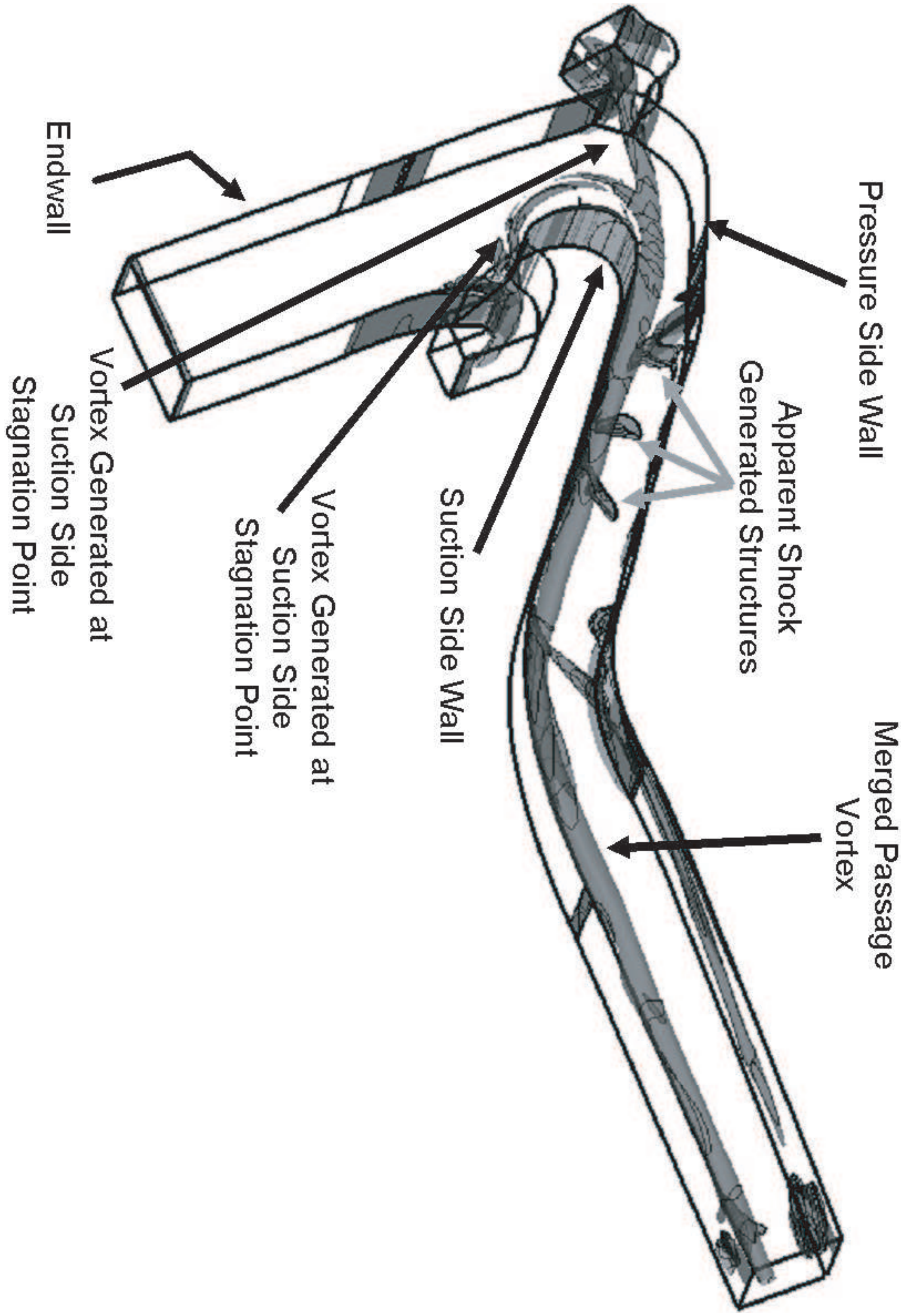

Figure 2.41: $\mathcal{Q} = 1(10)^8$ isosurface showing formation of vortical structures due to endwall boundary layer-stagnation point interaction.

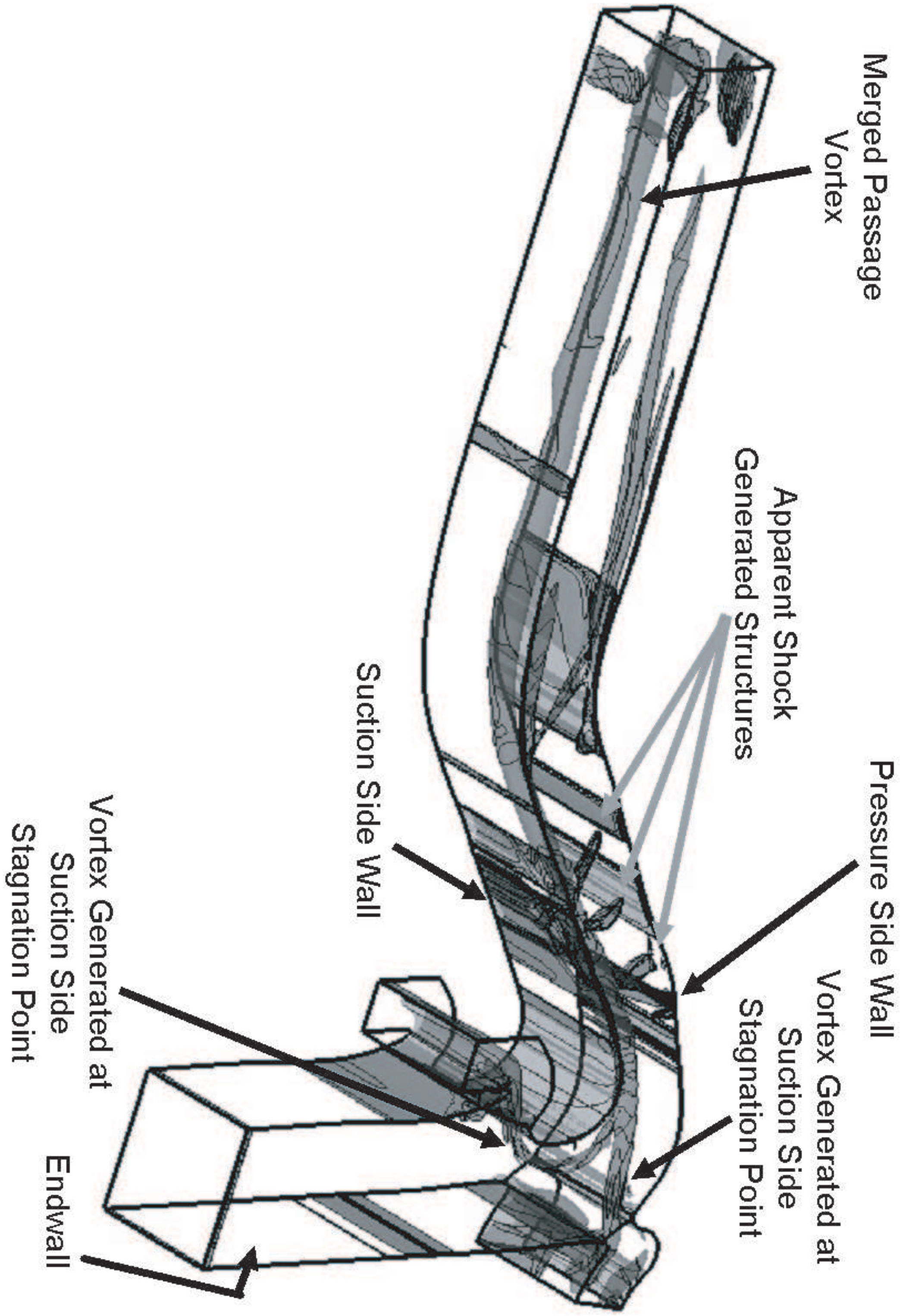

Figure 2.42: Reverse angle view of $\mathcal{Q} = 1(10)^8$ isosurface showing formation of vortical structures due to endwall boundary layer-stagnation point interaction.

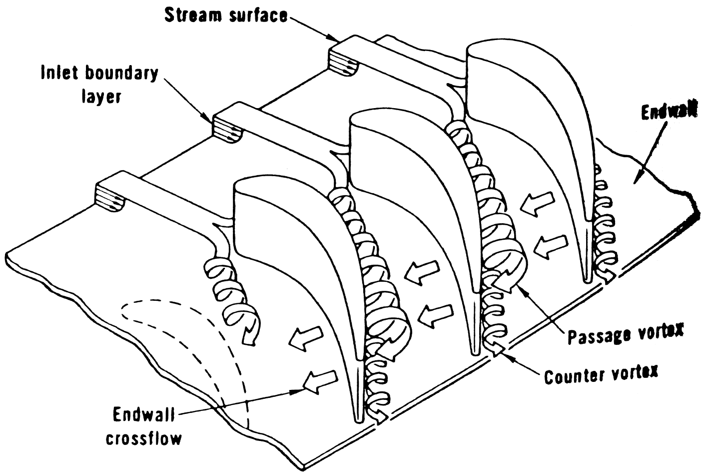

Figure 2.43: Three-dimensional separation of a boundary layer entering a turbine cascade (from Langston (1980)).

to the previously demonstrated sensitivity of the shock structures in the passage to subtle geometry changes.

Each piece shown in figure 2.45 was designed to be modular, easily replaced and accurately positioned. The thickness of each piece was 50.8-mm, as determined by the chosen aspect ratio. 1.59-mm thick Viton gaskets, precision cut using a CO_2 laser were used to seal these pieces against the endwalls. Other edges were sealed with GE RTV 106 sealant. Once fully compressed between the model pieces and the endwalls, the effective passage height became 52.5-mm. A series of 3.15 +0/-0.025-mm diameter dowel pins (Best Carbide Cutting Tools, Inc.) were used to position each piece. To accommodate the repeated assembly of the model, drill bushings with an outside diameter of 6.35-mm, inside diameter of 3.175mm+.10-mm and length 12.7-mm (McMaster-Carr Company #8491A077) were used to prevent any wear damage on the Ren Shape, affecting the alignment of the components. The dowel pins and their matching drill pin bushings were strategically positioned throughout the model. At least two dowel pins on both sides of each component were used, this was deemed to be the minimum number of pins necessary to repeatably position each model piece within $\pm$0.13-mm.

The two inlet walls form a two-dimensional bellmouth which smoothly directs the flow from the plenum into the model. Corresponding contoured inlets that matched the shape of the bellmouth with 12.7-mm radii were machined into the endwalls. This resulted in a 3-to-2 height reduction entering the model. Consequently, the combination of the bellmouth

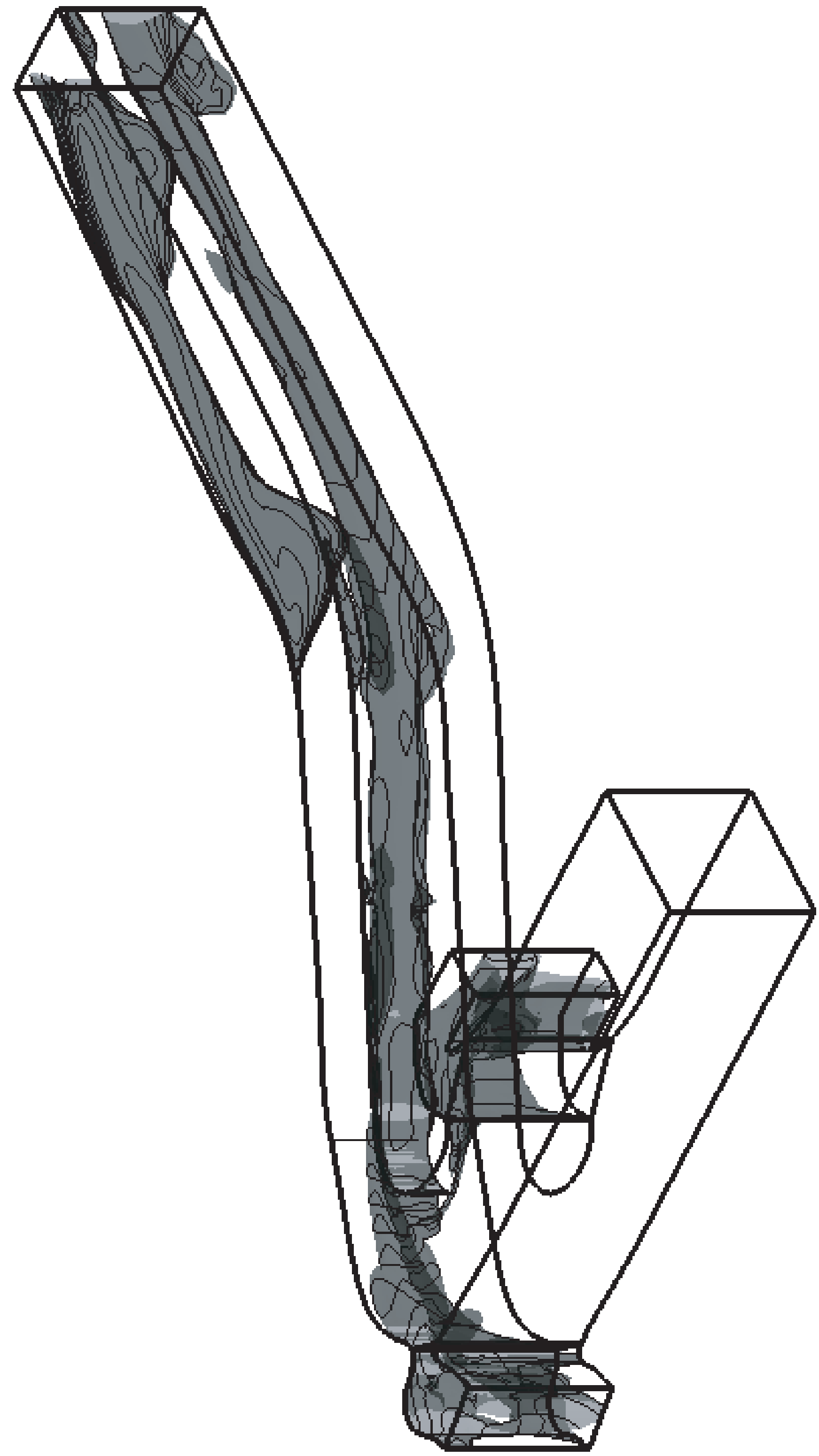

Figure 2.44: 3-D plot of isosurface $\mathcal{S} = 0.10$.

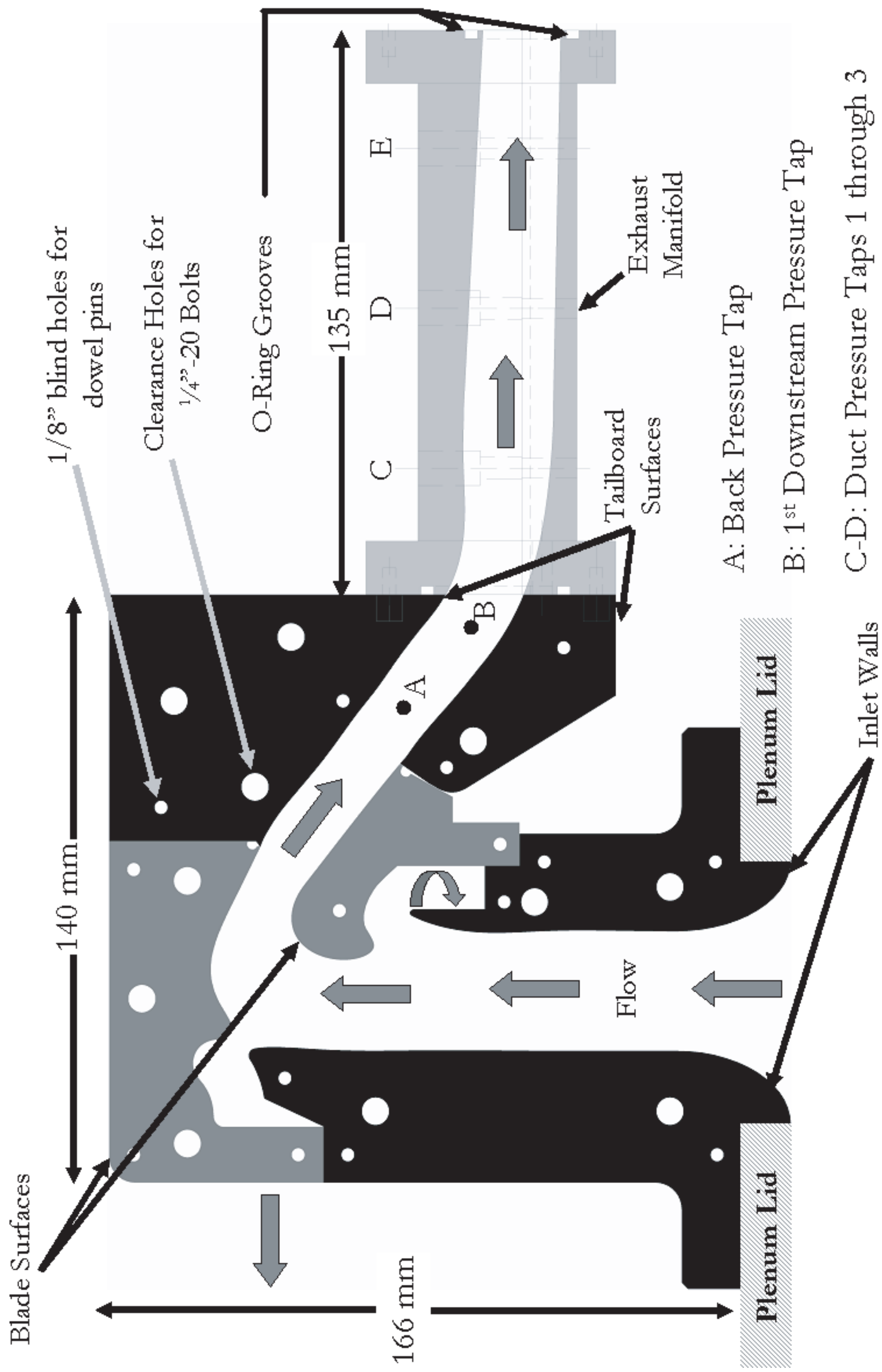

Figure 2.45: Schematic of single passage experiment.
The suction side bleed exits through the endwalls, as indicated by the curved arrow.
The blade shape has been distorted to ensure protection of proprietary information.

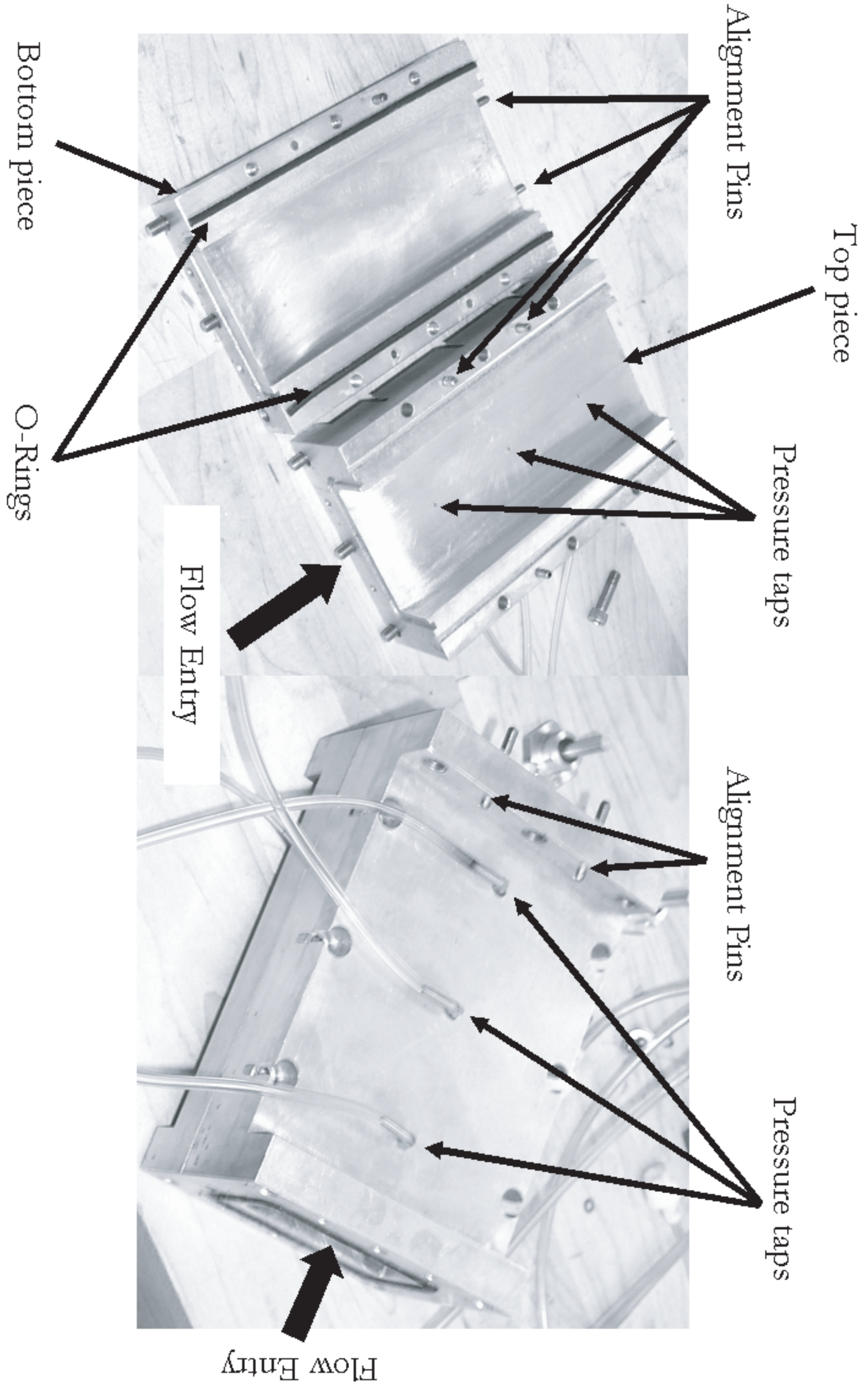

Figure 2.46: Figure of various views of exhaust manifold.

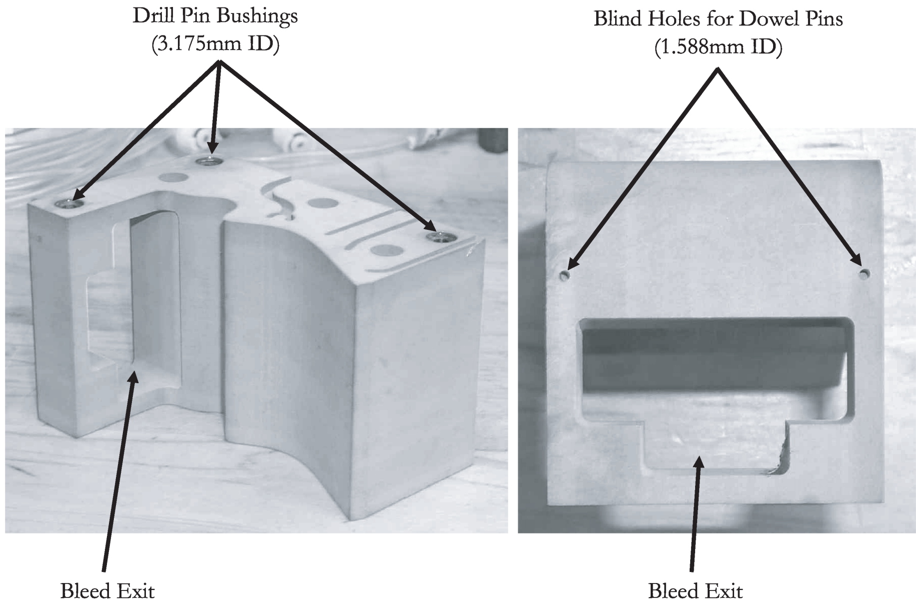

Figure 2.47: Figure of pressure side bleed fitting installed on pressure side measurement surface.

and the contoured endwall inlets gave a three-dimensional contraction with a 3.3-to-1 area reduction.

The exit diffuser geometry described in section 2.1.3 initiated in the tailboard pieces and then continued into the exhaust manifold. Figure 2.46 presents various views of the exhaust manifold, which was machined out of aluminum. Three 0.61-mm diameter pressure taps were installed in the top surface of this assembly. The exit diffuser was sealed against the tailboards using an O-ring.

The pressure side bleed flow is removed through a slot in the outer model wall piece as indicated by an arrow on figure 2.45. The exit slot is shown in figure 2.47. The cross-sectional area of the slot was defined to be equal or greater than the entry cross-sectional area of the bleed. This was found to be extremely important in ensuring that the appropriate mass flow is removed from the single passage. Figure 2.48 shows the pressure side bleed fitting that attaches to the bleed slot. This fitting has lofted surfaces which gradually transition from a rectangular to a circular cross-section. The shape of the lofted surfaces

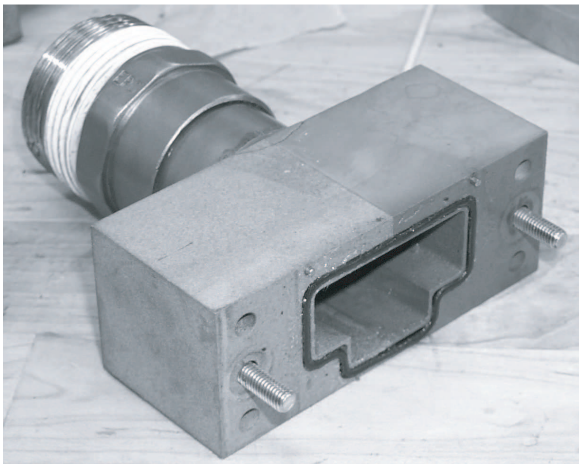

Figure 2.48: Picture of pressure side bleed fitting.

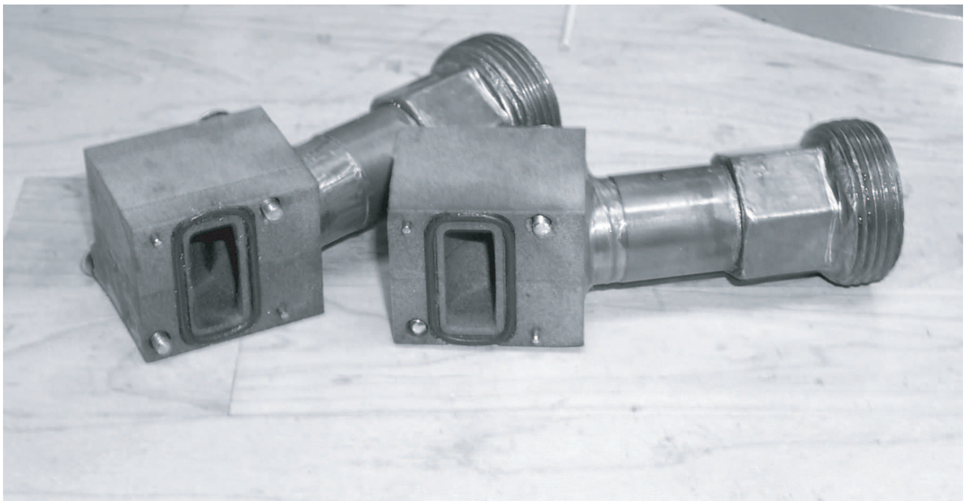

Figure 2.49: Picture of suction side bleed fittings.

was computed using intrinsic routines in MASTERCAM which can produce smoothed transition surfaces between two distinct contours. This piece is machined out of Ren Shape as two halves which are subsequently glued together with a translucent epoxy (Scotch Weld 2216 B/A). A copper tube is glued into the circular exit of the fitting. The suction side bleed flow is removed from slots placed symmetrically in the end walls and aligning with the rectangular cavity in the suction side bleed. The bleed fittings that were manufactured in the same manner as the pressure side fitting are shown in figure 2.49.

2.3 Experimental Test Facility

The single passage model is attached to a flow supply and various external measurements devices that provide monitoring information during experimental runs. The following subsections detail these accessories and their importance.

2.3.1 Supply System

The airflow supply is provided by a large rotary screw compressor (Ingersoll-Rand Model SSR XF 400) which can provide mass flow rates up to 1 $\frac{\mathrm{kg}}{\mathrm{s}}$ (2.2 $\frac{\mathrm{lbs}}{\mathrm{s}}$) with an approximate supply pressure of 7.5 atm. The compressed air passes from this machine through an air filter (Ingersoll-Rand Model TM1900), a thermal mass-type air dryer (Ingersoll-Rand Model IR2000) and into a tank. A 3-inch-size copper pipe runs from the tank into the test cell via the route shown in figure 2.50 which was installed by DeGraaff (2000). The flow passes through a general purpose cyclone filter (NORGREN F18-C00-A3DA) with a 5μm filter and a pilot operated regulator (NORGREN R18-C00-RNXA). During operation, this regulator was set to provide an exit pressure of approximately 4.76 atm (70 psig), limiting any pressure variation effects upstream of the regulator due to fluctuations in the supply tank or the compressor. The mass flow rate at this pressure is then controlled by a butterfly valve (Milwaukee Valve Company #8115-24-L).

The air supply has two subsystems to adjust the mainstream temperature of the compressed air supply. One is a shell-and-tube heat exchanger (CMS Heat Transfer Division S/N 1383) installed immediately upstream of the butterfly valve. The heat exchanger is supplied with chilled water at an approximate mean temperature of 278K. The other is a series of pipe heaters firmly attached to the copper pipe and covered in fiberglass insulation (McMaster-Carr #6140K18). Two types of heaters were used over a 3m length of pipe: heating tape (BH Thermal Corp. #BWH101120L) and pipe band heaters (Watlow Corp. #STB3A1J6). These systems were powered by nine 110V variable AC transformers, each of which could output a maximum current of 20 A. During operation, the heat exchanger chilled water flowrate and the power level to each of the heaters were adjusted concurrently to set and maintain the plenum within ± 0.1°C of the desired total temperature.

Figure 2.50 also shows several ball shut-off valves that allow access to different orifice plate metering runs to measure the mass flow rate through the system. Type 304 Stainless Steel, paddle-type, thin-plate (3.175 mm), square-edged orifice meters with bore-and-bevel

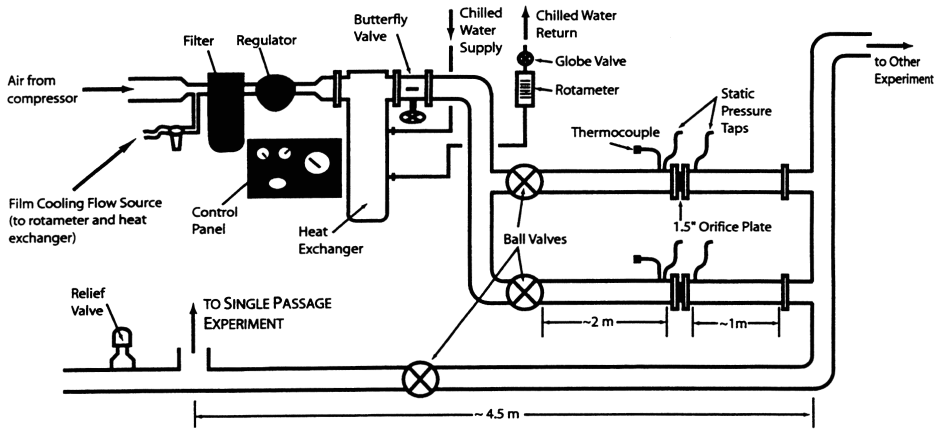

Figure 2.50: Flow system preceding single passage model (from Mukerji and Eaton (2002)).

type bores of diameters of D_{bore} =1.5" (Crane Manufacturing, Inc. S/N #R991367) and D_{bore} =2.0" (Crane Manufacturing, Inc. S/N #J991367), were installed in the two runs. This allowed dual ranges for accurate mass flow measurement. Pressure ports with taps of diameter of 0.61-mm were drilled at locations D_{pipe} upstream and $\frac{D_{pipe}}{2}$ downstream of each plate to measure the pressure drop. A Setra 239 differential pressure transducer with a range of 0-10 psid was used to measure the pressure drop across a specified orifice plate, while a Setra 280E absolute pressure transducer with a range of 0-100 psia was used to measure the upstream absolute pressure. To determine the fluid viscosity upstream of the plate, $\frac{1}{8}$"-diameter sheathed type-K thermocouples were installed D_{pipe} upstream of each orifice meter and a Fluke 80TK thermocouple module was used to amplify and offset the thermocouple junction voltage, producing a signal voltage that could be read on a handheld multimeter. The maximum measurable mass flow rates and estimated uncertainties for the first run was 0.484±0.014 (P = 0.95) $\frac{\mathrm{kg}}{\mathrm{s}}$ and 0.933±0.014 (P = 0.95) $\frac{\mathrm{kg}}{s}$ for the second.

The flow then passed into an aluminum diffuser section designed by Mukerji and Eaton (2002). Figure 2.51 presents an overview of the diffuser and the attached plenum with key dimensions identified. The diffuser consisted of a 0.80-m-long diffuser with a half-angle of ten degrees. Two flanges with perforated plates were installed along the length of the diffuser to prevent the development of separated flow. The diffuser then turned 90 degrees, vertically, through another flange with a perforated plate into the plenum. The plenum is cubical with a side dimension of 0.4-m. The diffuser was constructed of $\frac{3}{8}$" thick aluminum walls. All the flanges were sealed with $\frac{1}{16}$" thick vegetable fiber gaskets (McMaster-Carr #9453K504) and Dow Corning 732 RTV sealant. The lid on the plenum had a rectangular hole of dimensions 78 mm by 63 mm and a surrounding O-ring groove to accommodate the three-dimensional entry of the single passage model.

The underside of the plenum lid was designed to accept an "egg crate" type grid (DeGraaff (2000)) to provide well-contrasted turbulence inlet conditions. The grid had triangular tabs spaced 19-mm apart in both directions. Figure 2.52 shows top and side view photographs of the grid used in this experiment, the overall dimensions of the grid were 114-mm x 86-mm x 22-mm. Given these dimensions and the spacing of the tabs, the grid had 42% flow blockage. DeGraaff (2000) demonstrated that this grid design could produce turbulence intensity levels as high as $TI\% = 25\%$ which is consistent with the high turbulence levels characteristic of gas turbine engine combustors. Measurements at experimental test conditions revealed that there was approximately a 5.3% drop in total pressure across the grid.

The total pressure, temperature and humidity ratio in the plenum are monitored using a wall static pressure tap, and two $\frac{1}{8}$"-diameter sheathed type-K thermocouples, one of which is immersed in a water-soaked wicking. It was assumed and subsequently verified that the conditions in the plenum closely approximate stagnation conditions. The humidity ratio was computed using equations presented in Appendix B.

2.3.2 Exhaust System

The single passage has three exhausts: one is the mainstream exhaust, the other two were for the boundary layer bleeds. Figure 2.53 shows a schematic of the mainstream exhaust which attaches to the end of the exhaust manifold described previously. This system consists of two $\frac{1}{2}$-inch thick aluminum flanges with 6"-pipe-size PVC fittings with one side turned down to fit inside of a PVC-reinforced plastic hose (McMaster-Carr #5796K19). One flange was attached to the exhaust manifold, the other to a high volumetric flow muffler (Universal Silencer, Inc. Model Number #SU5-6, #14106AA). This approach was taken to provide increased flexibility to account for any mis-alignment between the single passage model exit and the muffler inlet.

Figure 2.54 presents a schematic of the orifice plate metering runs for the boundary layer bleeds. It was critical that the cross-sectional area of these runs is large enough to admit the necessary mass flow to correctly position the airfoil stagnation points. Hence, these

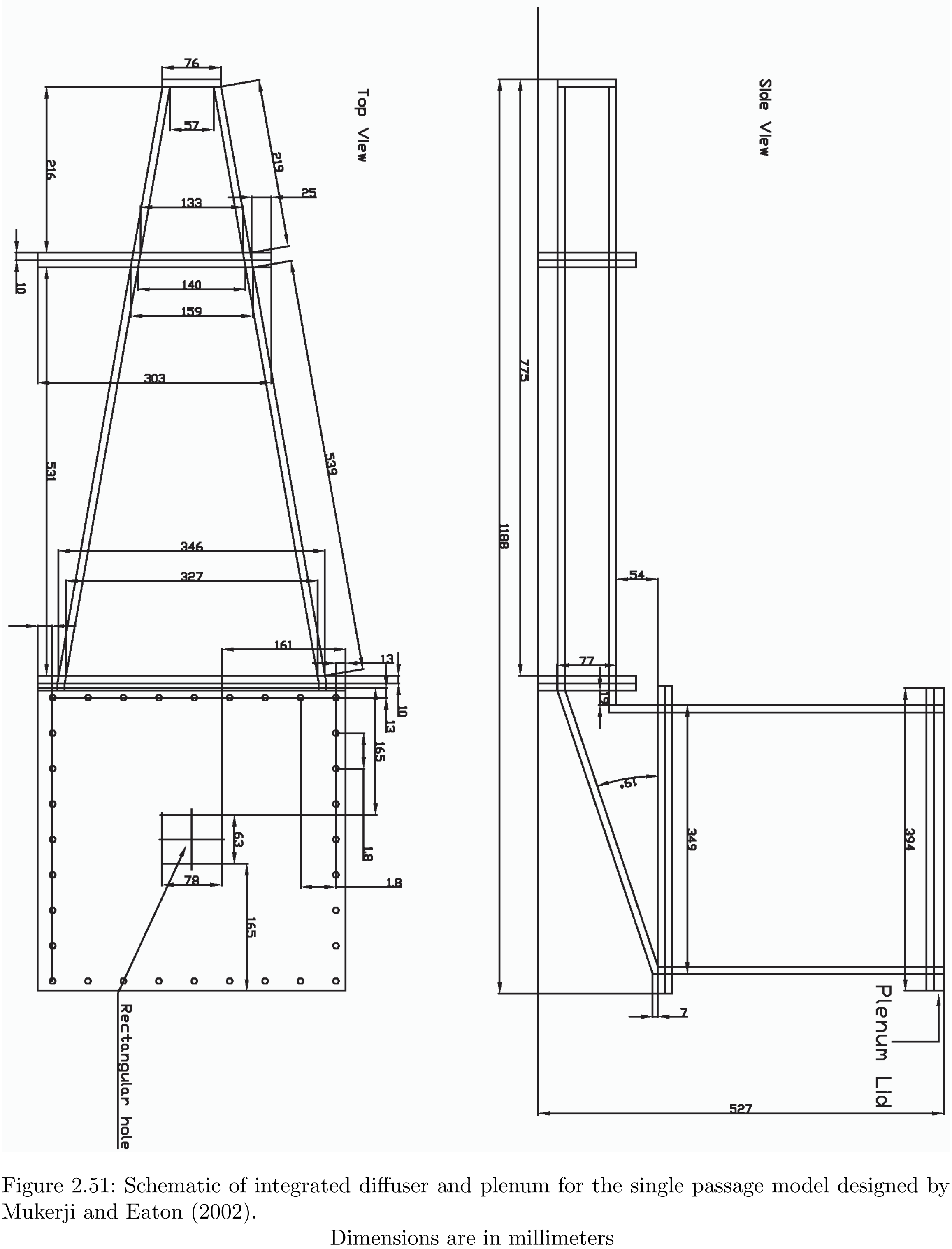

Figure 2.51: Schematic of integrated diffuser and plenum for the single passage model designed by Mukerji and Eaton (2002).

Dimensions are in millimeters

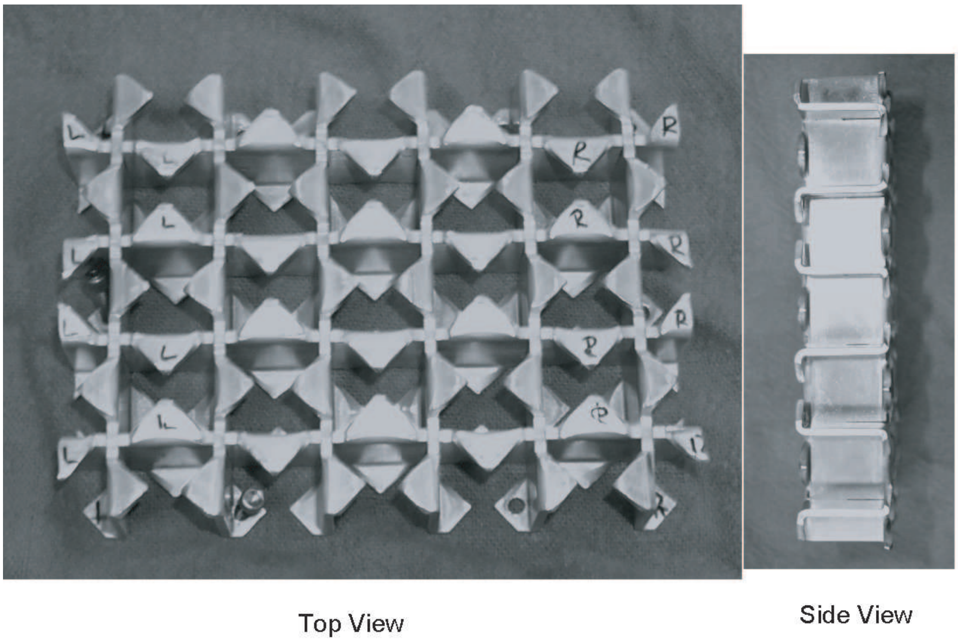

Figure 2.52: Pictures of turbulence grid designed by DeGraaff (2000).

metering runs were constructed out of 2-inch-size (52.50-mm ID), type 304/304L stainless steel pipe (McMaster-Carr #44635K442) and flanges (McMaster-Carr #44685K56). To allow the positioning of various orifice plates with different bores, orifice fittings (Crane Manufacturing #OFCMWW2-NS) were installed along the line. Figure 2.55 presents the salient features of this device and figure 2.56 shows the fully assembled orifice plate runs installed in the experimental test cell. Two pairs of pressure taps were pre-installed one-inch upstream and downstream of the orifice plate. This allowed not only the measurement of pressure, but temperature at these locations as well. A 1.59-mm sheathed thermocouple was installed one-inch upstream of both orifice plates using one of these ports. Initial tests revealed that the bore diameter was found to regulate the mass flow, consequently 2" orifice plates with 1.34" bore size (Crane Manufacturing Number #UOP-230418) were used to both regulate and measure the bleed mass flow rates. The pipes were welded into the flanges, and then precision machined to ensure that each flange was perpendicular to the pipe. Two 1.59-mm blind reamed holes with dowel pins were used to accurately align each pipe. According to Bean (1983), the necessary lengths of pipe to use standard orifice plate calibration data are $\frac{L'_{pipe}}{D_{pipe}} = 10$ and $\frac{L'_{pipe}}{D_{pipe}} = 6$ upstream and downstream of the orifice plate, respectively. The flow straighteners – which were of flange type (Crane Manufacturing #

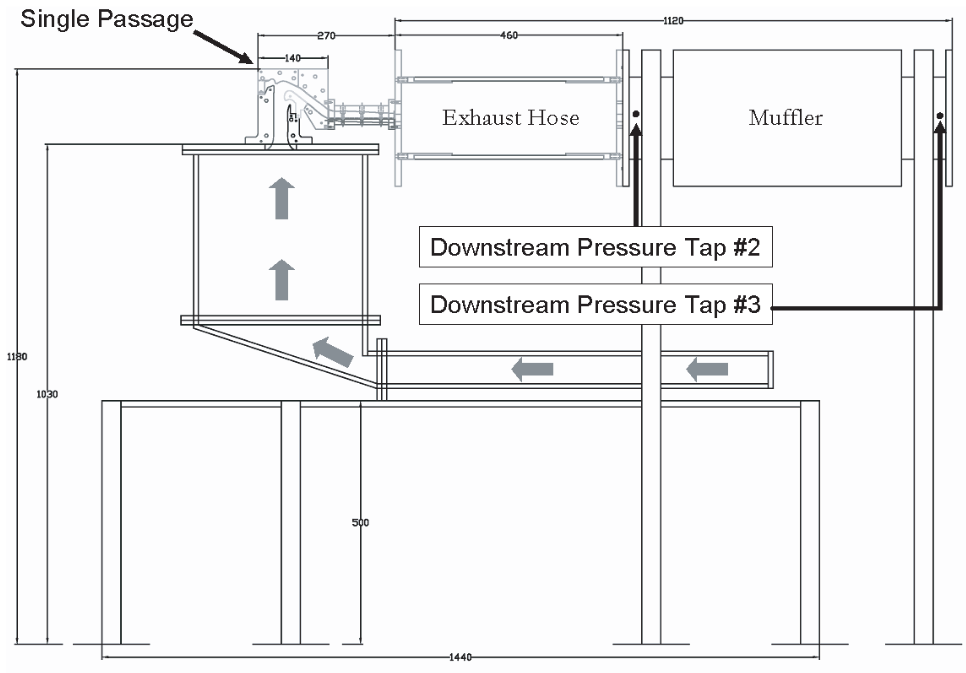

Figure 2.53: Figure of the overall flow system, showing the exhaust system for the experiment. Dimensions are in millimeters

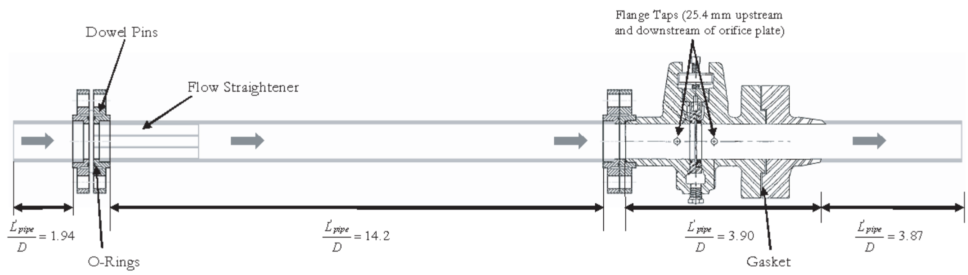

Figure 2.54: Orifice plate runs for measuring boundary layer bleed mass flow rates.

FT-2S40) – were used to reduce the necessary amount of pipe length upstream of the orifice plate to properly condition the flow from $\frac{L_{pipe}}{D_{pipe}} = 15$ to $\frac{L_{pipe}}{D_{pipe}} = 10$. Two ports of a 48-port Scanivalve (Scanivalve Corporation #SSS-38C Mk III) were connected to two 4-way valves allowing the measurement of the upstream and downstream pressure on either bleed orifice plate run during the experiment. A Setra 239 differential pressure transducer with a 0-50 psid range, measured the pressure drop across the orifice plate. The low-pressure port of the Setra 239 was connected to the output of the Scanivalve and the high-pressure port was connected to the plenum wall static tap. A Scanivalve Digital Interface Unit (Scanivalve

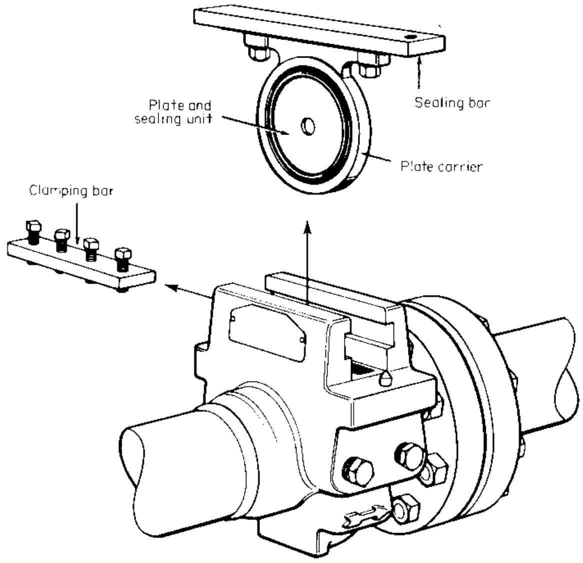

Figure 2.55: Orifice fitting from Miller (1983).

Figure 2.56: Picture showing installed boundary layer bleed orifice plate runs.

Figure 2.57: Picture of liquid CO_2 dewar system.

Corporation #SDIU Mk 5) controlled via GPIB (General Purpose Interface Bus) was used to actuate the Scanivalve to the upstream and downstream ports.

2.3.3 Film Cooling Supply System

The experimental test cell included two low mass flow rate orifice plate runs: a $\frac{3}{4}$"-inch pipe size with an orifice plate with a 0.500" bore and a $\frac{1}{2}$"-inch pipe size with an orifice plate with a 0.300" bore. Both orifice plates were constructed of type 304 Stainless Steel and bore-and-bevel type orifices. These runs were supplied either by compressed air from the main air supply system or CO_2 supplied by a vaporizer (Praxair # A4ALBTM5) connected to a liquid dewar (Praxair # LC-CD170) via an armor-wrapped hose (Praxair # JNI308FF-72.OAR) as pictured in figure 2.57. The output of this system is connected to a regulator (Praxair # CON 18066531) set to 120-psig. Both the carbon dioxide and compressed air systems had upstream regulators that were set to approximately 80 psig. The orifice plate runs were nearly identical to that presented in figure 2.54. The two differences were: the presence of an upstream needle valve that controlled mass flow rate through the orifice plate run and that orifice fittings were not used to ensure concentricity between the centerline

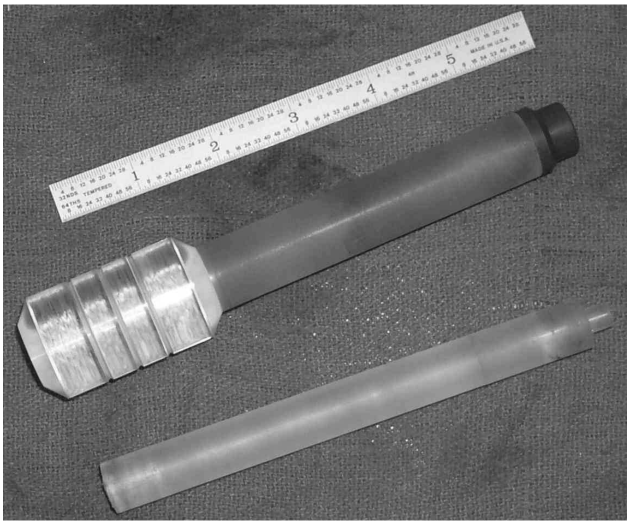

Figure 2.58: Picture of Plexiglas tools for ensuring concentricity between orifice plate bore and pipe.

of the orifice bore and the pipe internal diameter. Raised-face, stainless steel flanges were soldered to brass pipe instead. A Plexiglas tool, pictured in figure 2.58, was manufactured that formed a slip fit with the pipe internal diameter was used to ensure concentricity of the two flanges with orifice plate bore. Pressure taps were installed D_{pipe} upstream and $\frac{D_{pipe}}{2}$ downstream of the orifice plates. A Setra 239 differential pressure transducer with a range of 0-0.5" WC (inches of water) was used to measure the pressure drop across each orifice. A separate Setra 280E absolute pressure transducer with a 0-100 psia range was used to measure the upstream absolute pressure. A series of valves were used to connect these transducers to the desired orifice plate run, in a similar fashion to that for the boundary layer bleed orifice plates. A sheathed 1.59-mm thermocouple (Omega #KMQXL-062U-6) was installed upstream of each orifice plate.

The two runs both connected to individual single-pass heat exchangers – an approach also used by Mukerji and Eaton (2002) – each of which consisted of a coil of approximately 11-m of 9.53-mm diameter copper tubing immersed in a water-glycol solution heated by a PID-controlled immersion heater (Cole-Parmer Model # 12112-10). The water-glycol mixture allowed the achievement of higher bath temperatures, due to the increased boiling point of the solution. The heat exchanger chassis consisted of an insulated container with a five gallon capacity. Figure 2.59 presents a picture of the heat exchanger bath assembly. The film cooling flow then passed through a $\frac{1}{4}$" OD Dayco Poly-Flo polyethylene tubing encased with $\frac{3}{8}$" ID, $\frac{3}{4}$" thick tube extruded polyethylene foam insulation (McMaster-Carr

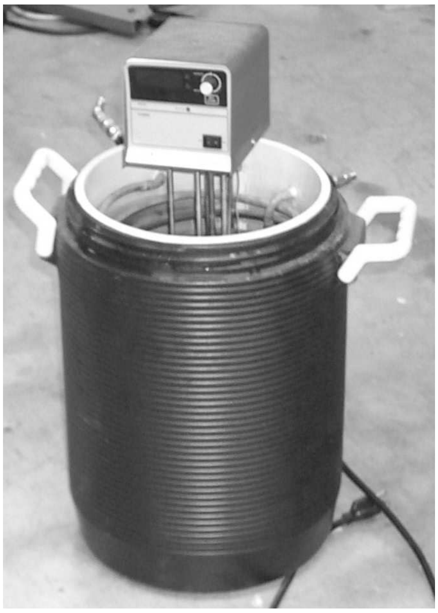

Figure 2.59: Picture heat exchanger bath, consisting of five gallon container, immersion heater and copper tube coil.

#4734K151). Such a system allowed the film cooling flow to achieve total temperatures 15°C above ambient when the cooling flow reached the model, allowing for thermal losses between the heat exchanger and the model.

2.3.4 Orifice Plate Implementation

As orifice plates are used extensively to measure mass flow in this experiment, it is useful to present some of the key equations and procedures that form the basis of this technique. Miller (1983) and Bean (1983) provide detailed procedures for installing the flowmeters, including required tolerancing for standardized applications.

There are three equations which are solved simultaneously to determine the mass flow through a device that causes a differential pressure drop, such as an orifice plate.

$$\begin{aligned} \dot{m} &= C_2 C_D \\ Re_D &= C_1 \dot{m} \\ C_D &= f(Re_D) \end{aligned} \tag{2.11}$$

Where C_1 is a constant, defined as:

$$C_1 = \frac{4}{\mu D \pi} \tag{2.12}$$

The first line of equation 2.11 is a restatement of the definition of the discharge coefficient, C_D which is simply the ratio of the ideal mass flow rate (C_2), calculated using the pressure difference between two points as shown in equation 2.13 and the actual mass flow rate, $\dot{m}$. Equation 2.14 accounts for gas compressibility effects in the ideal mass flow rate equation and $\beta_{op} = \frac{D_{bore}}{D_{pipe}}$, the ratio of the orifice plate bore and the pipe internal diameter.

$$C_2 = \dot{m}_{ideal} = \frac{\sqrt{2}\pi}{4} \frac{Y d^2}{\sqrt{1 - \beta_{op}^4}} \sqrt{\Delta P \rho_1} \tag{2.13}$$

$$Y = 1 - (0.41 + 0.35\beta_{op}^4) \frac{\Delta P}{P_1} \frac{1}{\gamma} \tag{2.14}$$

Miller (1983) quotes standard correlations for the discharge coefficient of the form shown in equation 2.15. The Reynolds number is based on the internal pipe diameter. Equations 2.16 and 2.17 correspond to suggested correlations for C_∞ for the main supply and bleed systems, respectively. As these correlations depend on Re_D it was necessary to use an iterative solving technique such as Newton-Raphson to determine the measured mass flow rate.

$$\begin{gathered} C_D = C_\infty + \frac{b}{Re_D^n} \\ b = 91.71\beta^{2.5} \quad n = 0.75 \end{gathered} \tag{2.15}$$

$$C_\infty = 0.5959 + 0.0312\beta_{op}^{2.1} - 0.184\beta_{op}^8 + 0.039\frac{\beta_{op}^4}{1 - \beta_{op}^4} - 0.0158\beta_{op}^3 \tag{2.16}$$

$$C_\infty = 0.5959 + 0.0312\beta_{op}^{2.1} - 0.184\beta_{op}^8 + 0.039\frac{\beta_{op}^4}{1 - \beta_{op}^4} - 0.0337\frac{\beta_{op}^3}{D_{pipe}} \tag{2.17}$$

However, this approach could not be used for the film cooling orifice plate runs as the pipe sizes and expected pipe Reynolds numbers made the correlation approach inaccurate. Consequently, two 1% NIST calibrated rotameters with ranges of 10-120 scfh of air ($9.3(10)^{-5}$ - $1.12(10)^{-3}$ $\frac{\text{kg}}{\text{s}}$, King Instruments # 74-232G042-422510, S/N 45467-990715-001) and 120-600 scfh of air ($1.12(10)^{-3}$ - $5.59(10)^{-3}$ $\frac{kg}{s}$, King Instruments # 7456P21341, S/N 62826-020617-0001) were used to develop discharge coefficient curves for each run. These were connected to the orifice runs, the flow passing immediately from the rotameter into quiescent air. The rotameters could not be used to accurately measure the film cooling mass flow

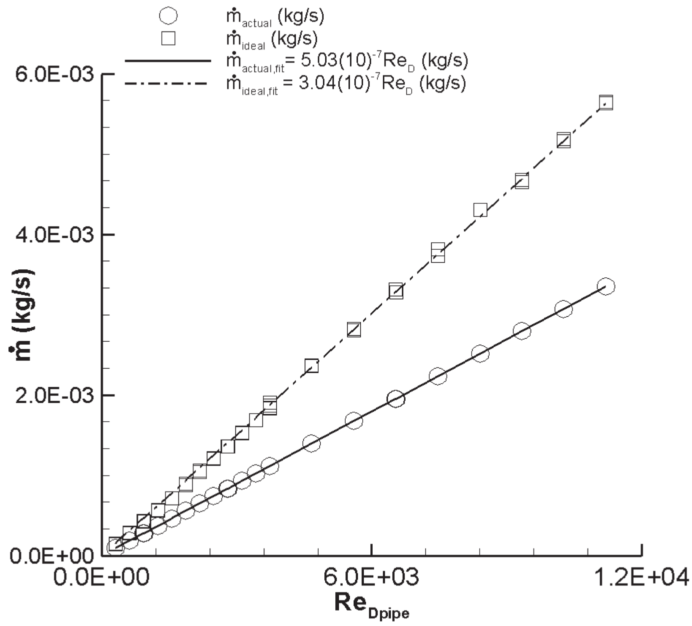

Figure 2.60: Plot of ideal and measured mass flow rates as a function of pipe ID Reynolds number ($Re_{D_{pipe}}$) for orifice plate run #1.

rates during testing as they require the exhaust to be at atmospheric or some well defined exit pressure during operation. Mukerji and Eaton (2002) proposed a validated correction for rotameters with a back pressure of less than 5-psig. However, the flow conditions and film cooling rates in the current work strongly suggested that the back pressures as high as 70-psig would be encountered during testing. Furthermore, this would be expected to vary widely from different film cooling tests.

With each run initially at atmospheric pressure with no mass flow, the upstream needle valve was gradually opened to achieve designated mass flow rates through the rotameter. This raised both the pressure drop across the orifice plate and the upstream absolute pressure. The discharge coefficients for the low mass flow orifice plates were found to be nearly constant over a relatively wide range of Reynolds numbers. This was believed to be due to a choked condition at the end of each run where a reducer was placed that directed the flow to a $\frac{1}{4}$" OD polyethylene tube. Figures 2.60 and 2.61 compare the measured and ideal mass flow rates of air for the two orifice runs over the calibrated Reynolds number range. Figures 2.62 and 2.63 shows the computed discharge coefficient, $C_D = \frac{\dot{m}_{actual}}{\dot{m}_{ideal}}$ computed from measured data and from linear fits to data shown in figures 2.60 and 2.61. Using these

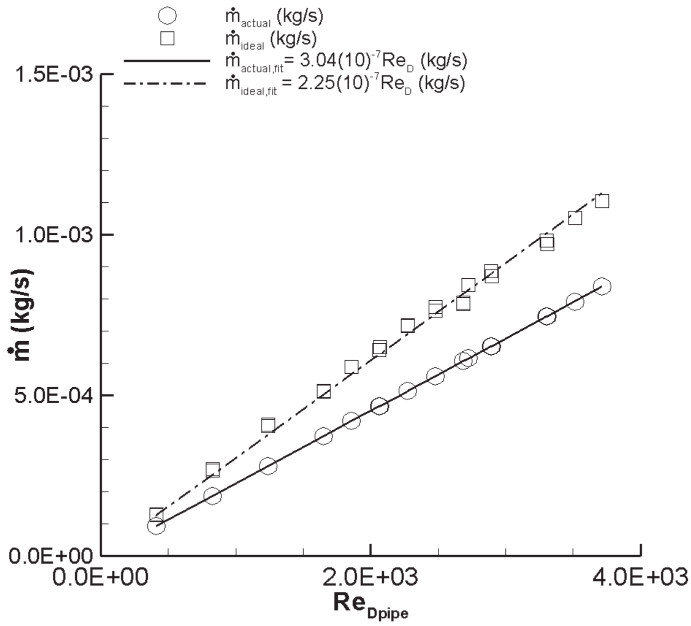

Figure 2.61: Plot of ideal and measured mass flow rates as a function of pipe ID Reynolds number ($Re_{D_{pipe}}$) for orifice plate run #2.

Table 2.8: Discharge coefficients for film cooling runs.

Run	Discharge Coefficient (C_D)	Uncertainty (%)
Orifice Plate Run #1	0.595	±5.14 (P = 0.95)
Orifice Plate Run #2	0.742	±3.75 (P = 0.95)

data, the discharge coefficient for each run was computed and tabulated as shown in table 2.8.

Orifice Plate Uncertainties

Table 2.9 summarizes the calculated uncertainties at nominal conditions for each orifice plate run. Appendix A details the contribution of the various experimental sub-systems to these values.

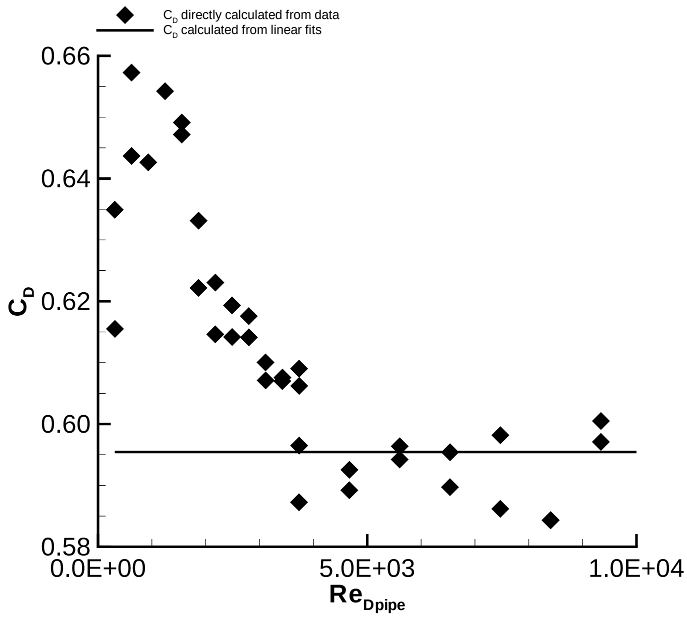

Figure 2.62: Plot of directly computed and fitted discharge coefficients as a function of pipe ID Reynolds number ($Re_{D_{pipe}}$) for orifice plate run #1.

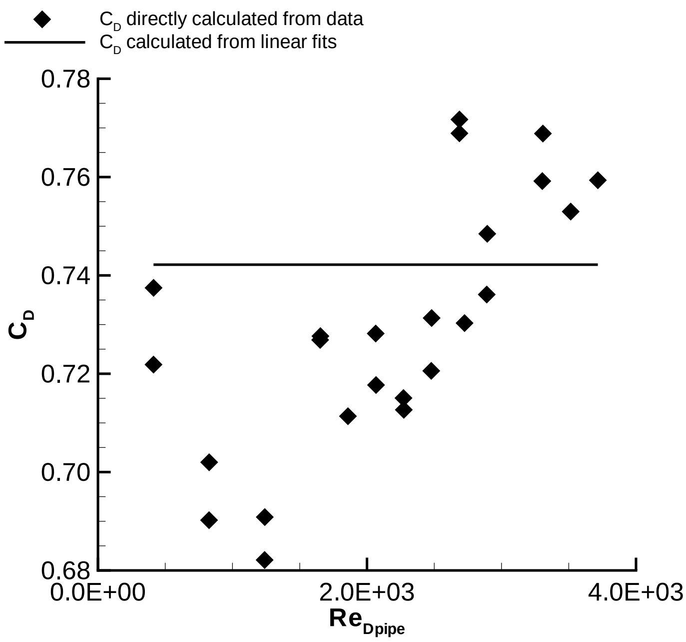

Figure 2.63: Plot of directly computed and fitted discharge coefficients as a function of pipe ID Reynolds number ($Re_{D_{pipe}}$) for orifice plate run #2.

Table 2.9: Nominal uncertainties for orifice plate runs.

Run	Mass Flow Rate, $\dot{m}$ ($\frac{\mathrm{kg}}{\mathrm{s}}$)	Uncertainty (%)
Pressure Side Bleed Orifice Run	0.1	±5.75 (P = 0.95)
Suction Side Bleed Orifice Run	0.1	±5.75 (P = 0.95)
Orifice Plate Run #1	$9.95(10)^{-4}$	±5.41 (P = 0.95)
Orifice Plate Run #2	$5.26(10)^{-4}$	±3.96 (P = 0.95)

2.4 Flow Validation and Conditions

This section documents the collection of tests used to validate the conditions in the single passage model. This included the M_{is} distribution on the two airfoil surfaces, inlet velocity, Mach number, stagnation pressure, static temperature and pressure distributions and inlet turbulence profiles. The following subsections describe the instrumentation, measurement procedures and the measurement results.

2.4.1 Atmospheric Pressure Measurement

A Setra 280E absolute pressure transducer with uncertainty of $\delta P_{atm} = \pm$ 1020 Pa was used to measure the atmospheric pressure. This was necessary as a reference for ascertaining the plenum total pressure. As mentioned in Section 2.3.2, most of the model pressure taps were read by a Setra 239 differential pressure transducer with the plenum total pressure as the high-pressure reference, as shown in equation 2.18.

$$\Delta P_i = P_o - P_i \tag{2.18}$$

However, to quantitatively establish the plenum total pressure, the Scanivalve was set to output the atmospheric pressure. The differential pressure transducer then measured the difference:

$$\Delta P_i = P_{o,plenum} - P_{atm} \tag{2.19}$$

2.4.2 Temperature Measurement

Type-K (chromel-alumel junction) thermocouples were used extensively in this experiment, for both aerodynamics and heat transfer experiments. As described in the recommendations from the ASTM Committee E-20 on Temperature Measurement (1974), it was necessary to construct a well-defined reference temperature. To achieve this, two AWG #36 reference thermocouples were inserted in a glass tube, which was subsequently immersed in a vacuum flask containing a transparent slush consisting of finely crushed ice and a small amount of water. The slush was replaced at the start of each experiment and was checked regularly during data acquisition. The second reference thermocouple was included as a redundant check. The bottom 20-mm of the glass tube was filled with silicon oil to ensure good thermal contact. The tip of the glass tube was positioned 120-mm below the surface of the slurry.

All thermocouples were connected to a single insulated zone box with 20 channels. This box was connected to a scanner (Hewlett Packard # HP3497A) which was actuated using GPIB control. The outputted voltage was measured by an autoranging digital multimeter (Fluke #8842A). This sampled the thermocouple voltage signal in "slow" mode for maximum noise rejection and was monitored via GPIB interface.

The uncertainty of the thermocouple measurement system was considered to be $\pm 0.1°C$. This was based on previous experience presented by Mukerji and Eaton (2002) and Elkins and Eaton (1997).

2.4.3 Pressure Measurement

Pressure measurements were made with a 48-port Scanivalve system (Scanivalve Corporation #SSS-48C Mk III). The port on the Scanivalve was set using a Scanivalve Digital Interface Unit (Scanivalve Corporation #SDIU Mk 5). The SDIU was controlled using GPIB interface. The output of the Scanivalve was connected to the low-end of a Setra 239 differential pressure transducer with a 0-50 psid range. The high-end was connected to the total pressure tap in the supply plenum. The transducer was calibrated with the low-end exposed to atmospheric pressure against a mercury Bourdon Tube as the supply system was gradually ramped up to full conditions in approximately 5" Hg increments.

This approach resulted in an uncertainty at nominal conditions of $\Delta P = 159080 \pm 2160$ Pa computed using standard analysis procedures. The full extent of this analysis is provided in Appendix A.

2.4.4 Pitot and Kiel Probes

To fully document the inlet flow conditions, a 1.59-mm stem diameter pitot probe (United Sensor #PCA-12-KL) was used to measure velocity, stagnation pressure and static pressure profiles approximately 1.2-chord-lengths along the axial blade direction upstream of the blade surfaces. Two Kiel probes were used to interrogate the variation of stagnation quantities from the plenum to the model inlet with and without a turbulence grid installed. One measured only the stagnation pressure (United Sensor #KAA-6, 1.59-mm stem diameter), the other measured both total stagnation pressure and temperature using a Type-K thermocouple (United Sensor part # KT-4-K-6-C, 3.2-mm stem diameter). It is important to note that both types of probe used in this work, Kiel and Pitot-type probes, were found to cause wakes that affected the pressure distribution along the airfoil. As a consequence, these were inserted during stand-alone tests and removed immediately afterwards.

A traverse (Velmex Corporation part #MA1506B-S1.5) equipped with a stepper motor (Vexta Corporation #PX245-01AA), powered by a digital-controlled motor driver (Dahnaher Motion/Slo-Syn Model #SS2000MD4) was used to traverse the pitot probe with an accuracy of ± 0.032-mm. The probe was moved along perpendicular center planes from pressure to suction side inlet walls and from endwall-to-endwall. Figure 2.65 presents a top view of the passage inlet defining the two profile directions, Y' and Z'. A sealing chamber with labyrinth seals, similar in design to that developed by DeGraaff (2000), constructed and placed at the end of the traverse, eliminating any leakage from the single passage around the probe. Figure 2.64 displays a picture of the traverse inserted through the pressure side inlet wall.

The probe position was calibrated by touching the surface of the probe against a 1-mm-thick gage block firmly adhered to one wall. The probe was then traversed to the opposite wall and this process repeated. The probe was then moved to the midpoint of this distance.

It was assumed that there was no pressure loss between the probe tip and the static pressure tap location. This allows the computation of the local Mach number at the tip of the probe using $\Delta P = P_\circ - P$ measurements. Equation 2.20 details that this calculation is identical to that for the isentropic Mach number, M_{is}. The local static density was then computed using equation 2.21.

$$M = M_{is} = \sqrt{\frac{2}{\gamma - 1}\left(\left(\frac{P_{\circ,inlet}}{P}\right)^{\frac{\gamma-1}{\gamma}} - 1\right)} \tag{2.20}$$

$$\frac{\rho}{\rho_\circ} = \left(1 + \frac{\gamma - 1}{2}M^2\right)^{-\frac{\gamma}{\gamma-1}} \tag{2.21}$$

The Kiel probes were used to verify the total pressure measurements of the Pitot probe at the passage center, and identify any losses in total temperature between the plenum and

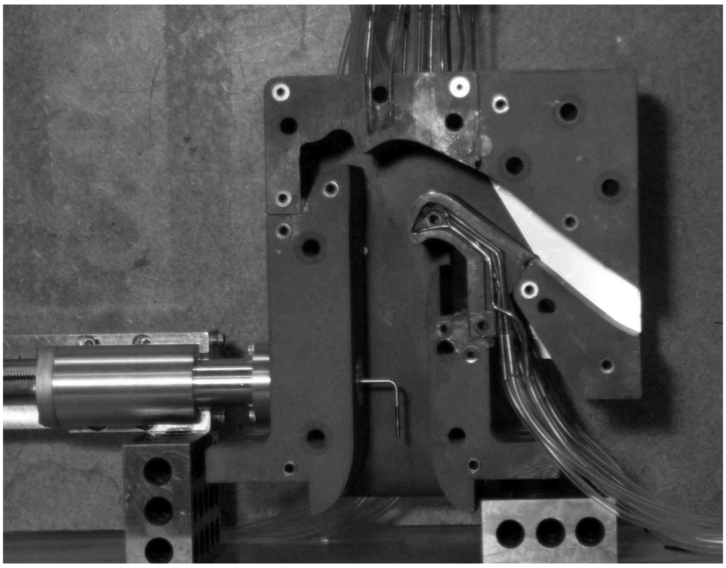

Figure 2.64: Picture of single passage traverse holding Pitot probe, inserted through pressure side inlet wall.

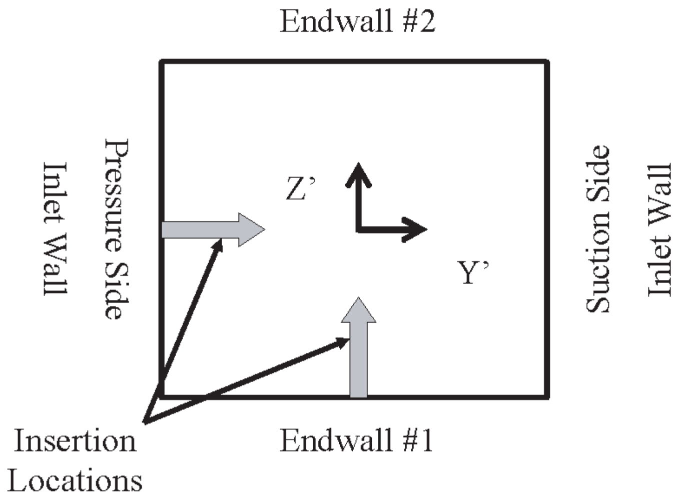

Figure 2.65: Schematic of profile directions for single passage inlet.

the model inlet. These measurements verified that the total temperature at the model inlet was accurately represented by the plenum total temperature (i.e. $T_{\circ,inlet} = T_{\circ,plenum}$). This was found to be the case both with and without the turbulence grid installed. This allows the computation of the local static temperature using equation 2.22.

$$\frac{T}{T_\circ} = \left(1 + \frac{\gamma - 1}{2} M^2\right)^{-1} \tag{2.22}$$

2.4.5 Hotwire Calibration and Measurement Procedures

Hotwire measurements were used to document turbulence properties at the inlet of the single passage. Measurements included the inlet turbulence intensity, the integral length scale, and one-dimensional turbulence spectra.

Overview of Process

A single 5-μm-diameter and 2-mm-long platinum-plated tungsten wire hotwire mounted on a probe (TSI #1212BR) was used to determine the turbulence characteristics at the inlet of the model. Typical resistances for the installed wire at ambient conditions ranged around 4.9Ω. The probe was inserted into a single sensor support (TSI #1150-6), moved by the same traversing system as that used for the Pitot probe. The position of the probe was determined using a method derived from DeGraaff and Eaton (1999), a 1-mm-thick gage block was firmly adhered to one of the bounding surfaces. A probe without a hotwire was inserted into the sensor support. When the probe touched the gage block, the two probe prongs made electrical contact, completing the probe circuit. This was verified by measuring the resistance across the probe prong tips using a multimeter. This was repeated for the opposite wall, and the probe was moved to midpoint of the these positions, thereafter.

The hotwire bridge circuit consisted of a commercially-available system (TSI #IFA-100), as annunciated by previous researchers such as Elkins and Eaton (1997), DeGraaff and Eaton (1999) and Hacker and Eaton (1995). This was used to operate the hotwire at constant temperature mode, with the wire resistance overheat ratio ($a_w = \frac{R_w}{R_w - R_e}$, where R_w is the resistance of the heated wire and R_e is the resistance of the cold wire) set to 1.8. The hotwire circuit was set to provide a maximum frequency response of approximately 250 kHz. Before applying low-pass and cutoff filters to the signal, the bridge circuit imposed a 2-volt offset and a factor of 8 amplification to the signal. The bridge circuit then applied a 500 kHz low pass filter to the hotwire signal. The low-pass filter value was considerably higher than previous works, since the velocities in the single passage inlet were as high as 160 $\frac{\mathrm{m}}{\mathrm{s}}$. An analog-to-digital converter (ADC) system (National Instruments part #PCI-MIO-16E-1) was programmed to sample the bridge circuit voltage at a rate of 1.2 Mhz. To ensure converged statistics for mean, fluctuating and spectral flow properties, 640 data sets of 8192 samples were recorded. The data sets were concatenated to estimate the turbulent kinetic energy and mean mass flux. The energy spectrum was computed by ensemble-averaging spectra for each data set. The number of sets and samples were chosen after a series of preliminary tests.

Calibration Approach

The hotwire measurement procedure in this experiment is somewhat complicated as the flow at the inlet of the model is in the subsonic compressible regime. Stainback and Nagabushana (1993) reported that there are significant complexities in calibrating and interpreting the hotwire response in this flow regime. Smits et al. (1983) demonstrated that the result of this analysis can be reduced to the form of equation 2.23, as shown below.

$$(\rho u)^n = M_2(T_\circ)V^2 + L_2(T_\circ) \tag{2.23}$$

Where V is the measured voltage across the hotwire and M_2 and L_2 are calibration constants that are functions of the local total temperature.

There are two possible approaches to developing a calibration using equation 2.23: one is to fix the local static density, ρ, and to vary the mean velocity (as performed with a de Laval nozzle by Drost and Bölcs (1999)), the other is to vary the mass flux. In the first approach, equation 2.23 reduces to the standard form of King's Law, allowing the direct measurement of the Reynolds averaged velocity and fluctuations, $\overline{u}$ and u'. The calibration procedure in this experiment used the single passage inlet where the only possibility was to vary the mass flux. Thus the hotwire was used to measure mass flux, rather than velocity.

A Pitot probe was positioned at the center of the single passage inlet to measure the mass flux, ρu, at this location as the mass flow through the passage was increased. Figures 2.66 and 2.67 present the facility calibration curves without and with the turbulence grid installed. These flow calibration curves can be expressed in linear fit form as:

$$\overline{(\rho u)} = A_{\rho u}\dot{m} \tag{2.24}$$

Table 2.10 presents the coefficient values and uncertainties for conditions with and without

Table 2.10: Flow facility coefficients for single passage.

Parameter	$A_{\rho u}$ ($\frac{1}{m^2}$)	Uncertainty ($\delta A_{\rho u}$)
Without Grid	662.9	$2.69(10)^{-2}$
With Grid	673.8	$2.69(10)^{-2}$

the turbulence grid installed.

The Pitot probe was then removed and the hotwire inserted. The mass flow through the system was gradually increased and measured using the upstream orifice plate system introduced in Section 2.3.1. At each setting, the mean hotwire voltage and mass flow through the single passage was measured. During this process, the total temperature in the plenum was controlled within $\pm 0.5°$ of a predetermined value using a combination of heat input via the pipe heaters and adjustment of the chilled water flowrate through the heat exchanger. The hotwire calibration curve was then constructed, choosing values for M_2, L_2 and n that minimized the mean-square-root error between the calculated fit and the calibration data. The mean mass flux varied in range of $110 \leq \rho u \leq 450 \frac{\mathrm{kg}}{\mathrm{m^2 s}}$ and the measured mean hotwire signal voltage was found to vary in the range $2 \leq V \leq 2.8$V. Typical values for the hotwire calibration constants were $M_2 = 22.0$, $L_2 = -65.0$ and $n = 0.8$. This gave an uncertainty of in the measurement of the instantaneous mass flux of $\delta \rho u = 22.3 \frac{\mathrm{kg}}{m^2 s}$ (P = 0.95).

Measurement Approach

Using the Strong Reynolds Analogy (Smits et al. (1983)), the relative magnitudes of density to velocity fluctuations can be estimated using equation 2.25. As the inlet Mach number was measured to be about $M = 0.5$, equation 2.25 gives that density fluctuations were of the order of 10% of the velocity fluctuations. This observation is also in agreement with Morkovin's hypothesis (Morkovin (1962)) that states that for boundary layers with $M < 5$ density fluctuations are small in comparison to velocity fluctuations.

$$\frac{\rho'_{rms}}{\overline{\rho}} = (\gamma - 1) M^2 \frac{u'_{rms}}{\overline{u}} \tag{2.25}$$

Consequently, the following procedure was used to interpret the instantaneous hotwire signal:

1. measure $\rho u_i = \overline{(\rho u_i)} + (\rho u_i)'$ using equation 2.23.

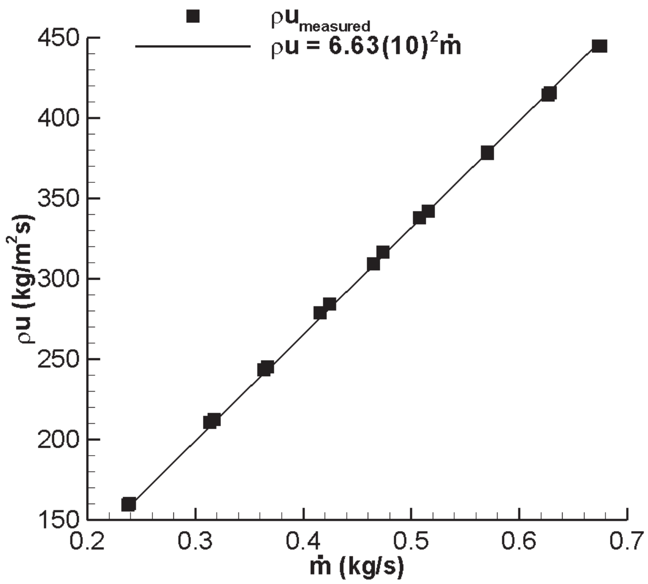

Figure 2.66: Plot calibration curve for ρu vs. $\dot{m}$ at the center of the single passage inlet without the turbulence grid installed.

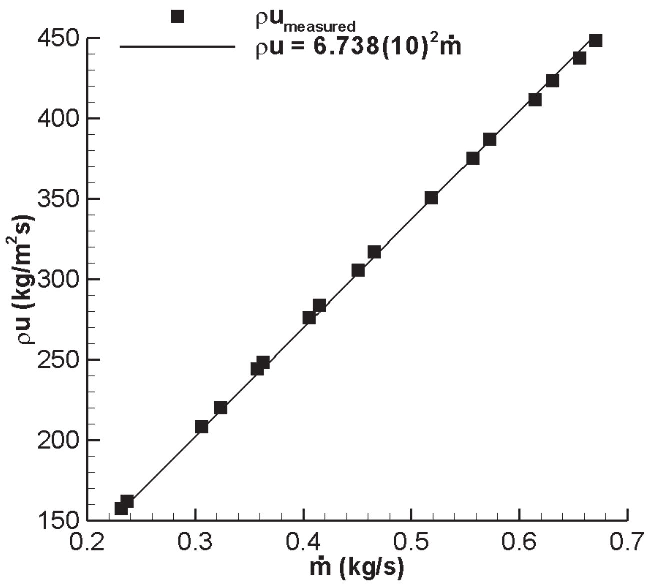

Figure 2.67: Plot calibration curve for ρu vs. $\dot{m}$ at the center of the single passage inlet with the turbulence grid installed.

2. measure $\overline{T_\circ} \approx T_\circ$, $\overline{P_\circ} \approx P_\circ$; assuming $\frac{T'_\circ}{T_\circ} \approx 0$, $\frac{P'_o}{P_o} \approx 0$

3. solve for the local Mach number, M using equation 2.26.

$$\rho u = M P_\circ \frac{\gamma}{RT_\circ}^{\frac{1}{2}} \left(1 + \frac{\gamma - 1}{2} M^2\right)^{-\frac{\gamma+1}{2(\gamma-1)}} \tag{2.26}$$

4. using equation 2.21, compute the instantaneous density, invoking Morkovin's hypothesis, i.e. $\frac{\rho'_\circ}{\rho_\circ} \approx 0$.

5. compute the instantaneous velocity using the local Mach number and static temperature.

To account for temperature drift during measurement, the method proposed by Bearman (1971) was used to pre-process the hotwire voltages. This correction was implemented as shown in equation 2.27.

$$\begin{aligned} V_{corr} &= V \left(1 + \frac{\alpha(T_{\circ,m} - T_{\circ,cal})}{2(OH - 1)}\right) \\ \alpha &= 3.4(10)^{-3} \\ OH &= 1.8 \end{aligned} \tag{2.27}$$

Where V_{corr} is the corrected voltage, V is the measured voltage, α is the thermal coefficient of resistance for the hotwire, OH is the overheat ratio, $T_{o,m}$ is the measured total temperature, and $T_{o,cal}$ is the calibration total temperature. However, the validity of this equation is uncertain for compressible flow. Consequently, the total temperature was tightly controlled within ±0.5°C of the calibration total temperature during measurement to limit the necessity of applying this correction.

Computation of Turbulence Intensity

The instantaneous mass flux measured by the hotwire is Reynolds-averaged in conservative form, resulting in a decomposition of:

$$\rho u_i = \overline{(\rho u_i)} + (\rho u_i)' \tag{2.28}$$

The turbulence intensity was then defined as:

$$TI\% = \frac{\sqrt{\overline{(\rho u_i)'^2}}}{\overline{(\rho u_i)}} \tag{2.29}$$

The numerator in this equation was computed by first assembling all acquired mass flux data sets in a single record. The mean mass flux is subtracted from these values to obtain the fluctuating component. Then $\overline{(\rho u_i)'^2}$ is calculated by:

$$\overline{(\rho u_i)'^2} = \frac{1}{N-1}\sum_{j=1}^{N}(\rho u_i(t_j))'^2 \tag{2.30}$$

Computation of Integral Length Scale

The integral length scale was assumed to be the longest distance over which the hotwire signal remained correlated with itself. This general definition allowed the extension of previously-developed incompressible turbulence experimental analysis techniques to compressible flow. We define the two-point covariance, R_{ij} as:

$$R_{ij}(\mathbf{r},t) = \overline{(\rho u_i)'(\mathbf{x}+\mathbf{r})(\rho u_j)'(\mathbf{x},t)} \tag{2.31}$$

Thus, the spatial autocovariance of the hotwire signal can be defined, using terminology from Pope (2000), as:

$$R_{11}(r,t) = \overline{(\rho u_1)'(\mathbf{x}+e_1 r)(\rho u_1)(\mathbf{x},t)} \tag{2.32}$$

Where $\mathbf{r} = e_1 r$, the unit vector in the longitudinal direction. The longitudinal autocorrelation, f_{xx}, is consequently defined as:

$$f_{xx}(r,t) = \frac{R_{11}(r,t)}{\overline{(\rho u)'^2}} \tag{2.33}$$

and the longitudinal length scale is defined as:

$$L_{11} \equiv \int_0^\infty f_{xx}(r,t)dr \tag{2.34}$$

The *frozen turbulence approximation* (Taylor (1938)), which states that a single stationary probe may be used with statistically stationary flows in which (at the measurement location) the turbulent fluctuations are small compared to the mean velocity (i.e. $u' \ll \overline{u}$) allows the spatial coordinate, r to be defined as:

$$r = \overline{u}\tau \tag{2.35}$$

Defining the integral time scale, T_E as:

$$T_E = \int_0^\infty f_{xx}(\tau)d\tau \tag{2.36}$$

Thus T_E can be computed from the hotwire time-dependent signal at a single location. Using this approximation, the integral length scale ℓ can be determined from T_E as shown in equation 2.37.

$$\ell \equiv \int_0^\infty f_{xx}(r,t)dr = \int_0^\infty f_{xx}(r)dr \tag{2.37}$$

inserting 2.35 into 2.37:

$$\ell = \overline{u}\int_0^\infty f_{xx}(\tau\overline{u})d\tau = \overline{u}T_E. \tag{2.38}$$

The computation of the integral time scale relies on the *correlation theorem* or equivalently termed the *Wiener-Khinchine Theorem*. This theorem states that the squared magnitude of the Fourier transform of the signal is equal to the Fourier transform of the autocorrelation (Gray and Goodman (1995)). As the hotwire signal is sampled at discrete intervals with sampling frequency f_s, this theorem is applied on the discrete fourier transform (DFT). Representing this signal as $g_n(t)$, the DFT of this signal is calculated as:

$$G(f^c) = \sum_{n=0}^{N-1} g_n e^{-i2\pi\frac{f^c}{f_s}n} \tag{2.39}$$

where f^c is defined as:

$$f^c \; \epsilon \; \left\{0, \frac{f_s}{N}, \ldots, \frac{(N-1)f_s}{N}\right\} \tag{2.40}$$

Recalling the correlation theorem in discrete form the longitudinal autocovariance $R_{11,n}$ can be expressed as:

$$|G(f^c)|^2 = \sum_{n=0}^{N-1} R_{11,n} e^{-i2\pi\frac{f^c}{f_s}n} \tag{2.41}$$

Which using the inverse DFT can be subsequently expressed as:

$$R_{11}(\tau_n) = \frac{1}{N}\sum_{k=0}^{N-1} |G(f_k^c)|^2 e^{i2\pi\frac{f_k^c}{f_s}n} \tag{2.42}$$

Where τ is defined as:

$$\tau_n = n\Delta t \tag{2.43}$$

All the DFT calculations above utilized the Fast-Fourier Transform to reduce computational time.

Bendat and Piersol (1993) argue that direct implementation of the algorithm above introduces a bias error due to the inherent nature of the Fourier series. Defining the directly computed autocovariance using convolution integrals as $\hat{R}$ and the autocovariance computed using the method above as $\hat{R}^c(\tau)$:

$$\hat{R}^c(\tau) = \mathcal{F}^{-1}(|G(f_c)|^2) \tag{2.44}$$

has a bias error of:

$$\hat{R}^c(\tau) = \frac{T-\tau}{T}\hat{R}(\tau) + \frac{\tau}{T}\hat{R}(T-\tau) \tag{2.45}$$

Where $T = N\Delta t$ and $\Delta f = \frac{1}{N\Delta t}$.

Bendat and Piersol (1993) explain that the usual way to eliminate this problem is to extend the original time record, $g_n(t)$, $0 \leq t \leq T$, with an additional record segment of length T with $g_n(t) = 0$ and perform the previously described transformations. Defining the autocovariance computed using a this approach as $\hat{R}^s(\tau)$:

$$\hat{R}^s(\tau) = \frac{T-\tau}{T}\hat{R}(\tau) \qquad 0 \leq \tau \leq T$$

$$\hat{R}^s(\tau) = \frac{\tau-T}{T}\hat{R}(2T-\tau) \qquad T \leq \tau \leq 2T \tag{2.46}$$

The autocorrelation is computed using the fact that by the definition of the autocovariance:

$$R_{11}(0) = \overline{(\rho u)'^2} \tag{2.47}$$

thence, by definition:

$$f_{xx}(\tau) = \frac{R_{11}(\tau)}{R_{11}(0)}. \tag{2.48}$$

Typical methods to compute the integral time scale involve integrating the autocorrelation function up to the point of the first zero crossing, as presented by Camp and Shin (1995) and Huyer and Snarski (2003). Hinze (1975) pointed out that such an approach can be highly inaccurate, especially if the f_{xx} curve frequently crosses the zero axis. The more significant power at high amplitudes is observed, the more oscillatory the autocorrelation curve becomes, requiring longer than practical integration interval times and, by extension, sampling times. To account for this issue, a method by Townsend (1947) was suggested. This involves multiplying the autocorrelation function with another function $\phi_E(\tau)$ which meets the following conditions:

1. $\int_0^\infty f_{xx}(\tau)\phi_E(\tau)d\tau = \int_0^\infty f_{xx}(\tau)d\tau = \ell$

2. $\int_0^\infty \phi_E(\tau)e^{i2\pi\frac{f_k^c}{f_s}\frac{\tau}{\Delta t}}d\tau$ converges

The explanation for the second condition can be determined by expanding the integrand $f_{xx}(\tau)\phi_E(\tau)$ as shown in equations 2.49 and 2.50 below:

$$f_{xx}(\tau) = f_{xx}(\tau_n) = f_{xx}(n\Delta t) = \frac{1}{\overline{(\rho u)'^2}} \frac{1}{N} \sum_{k=0}^{N-1} |G(f_k^c)|^2 e^{i2\pi \frac{f_k^c}{f_s} n} \tag{2.49}$$

Thence:

$$\ell = \int_0^\infty f_{xx}(\tau)\phi_E(\tau)d\tau = \frac{1}{\overline{(\rho u)'^2}} \frac{1}{N} \sum_{k=0}^{N-1} |G(f_k^c)|^2 \int_0^\infty \phi_E(\tau) e^{i2\pi \frac{f_k^c}{f_s} \frac{\tau}{\Delta t}} d\tau \tag{2.50}$$

Hinze (1975) argued that candidate functions for $\phi_E(t)$ should be near unity when $f_{xx}(t)$ has a noticeable value to meet the first condition. Furthermore, this function should decrease to zero for large values of t so that the integral shown in equation 2.50 converges. Hinze (1975) demonstrated that a function which satisfies these requirements is:

$$\phi_E(t) = \left(1 + \frac{t}{t_\circ}\right) e^{-\frac{t}{t_\circ}} \tag{2.51}$$

when $t_\circ \gg T_E$. The value for $t_\circ$ was chosen as to provide the largest estimate of T_E, as by definition this was the longest average time over which the hotwire signal remained correlated with itself.

2.4.6 Validation Experiment Results

Operating Conditions

Table 2.11 summarizes the typical operating conditions for the single passage. The approximate pressure ratio across the blade row $\frac{P_{exit}}{P_{\circ,plenum}} \approx 2.57$. The back pressure and downstream pressure taps served as diagnostic tools to ensure the presence of supersonic flow in between the blade surfaces. These were primarily used during debugging tests to ensure the supersonic dump design and tailboard geometry were operating as predicted. The nominal plenum total pressure was slightly higher for experimental runs with the turbulence grid installed (275000 Pa) due to losses across the grid.

Inlet Mean Flow Measurements

Figures 2.68 and 2.69 present Mach number profiles across the inlet of the model from suction-to-pressure inlet wall and endwall-to-endwall with (hereafter termed the high turbulence condition) and without (low turbulence case) the turbulence grid installed. These

Table 2.11: Operating conditions.

Parameter	Test Condition
Total Mass Flow ($\frac{\text{kg}}{\text{s}}$)	0.670
Plenum Total Pressure (Pa)	260400
Plenum Total Temperature (K)	300
Pressure Side Bleed Mass Flow ($\frac{\text{kg}}{\text{s}}$)	0.072
Suction Side Bleed Mass Flow ($\frac{\text{kg}}{\text{s}}$)	0.082
Inlet Pressure (Pa)	221000
Estimated Back Pressure (Pa)	64740
1^{st} Downstream Pressure (Pa)	89000
Duct Pressure Tap #1	45000
Duct Pressure Tap #2	50000
Duct Pressure Tap #3	52000
2^{nd} Downstream Pressure (Pa)	103900
3^{rd} Downstream Pressure (Pa)	107100
Humidity Ratio ($\frac{\dot{m}_{water}}{\dot{m}_{air}}$)	$7(10)^{-3}$
Relative Humidity ($\frac{P_{v,w}}{P_{water,sat}}$)	0.95

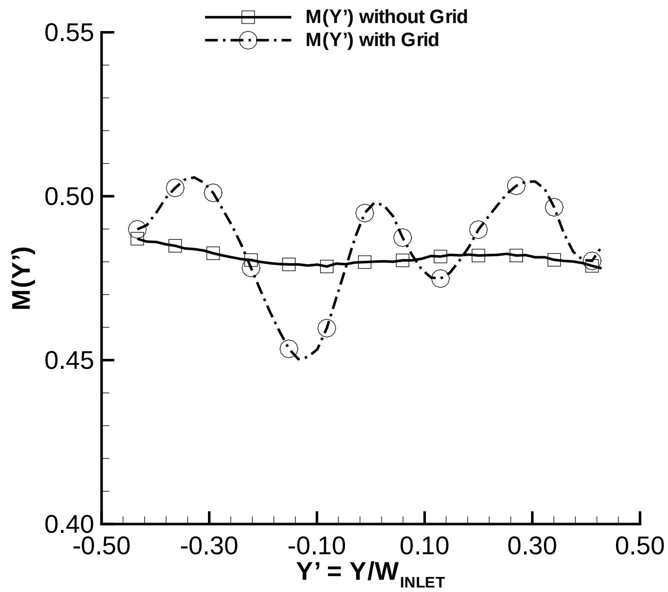

Figure 2.68: Plot of Mach number from pressure side to suction side inlet wall along centerline of channel.

revealed variations of 2% and 11% across the majority of passage inlet at low and high turbulence conditions, respectively. Figures 2.70 and 2.71 display profiles of the static temperature across the model inlet showing very small variations across the inlet plane.

Using the static temperature profiles, the local velocity may be computed along the centerlines of the passage. Figures 2.70 and 2.71 demonstrate that these follow the variations observed in the Mach number profiles, exactly. These were normalized by the estimated centerline velocity at the nominal conditions listed in table 2.11. At the these conditions, this velocity was computed to be $u_{nom} = 164.6\frac{\mathrm{m}}{\mathrm{s}}$. Figures 2.74 and 2.75 present the directly-measured variation of total pressure across the inlet, following the variation in the Mach number distribution across the inlet. These values were normalized relative to the measured total pressure in the plenum $P_{o,plenum}$, in order to include the total pressure loss effects from the plenum to the model inlet. These figures show that in both Y' and Z' directions, that there is negligible loss in total pressure from plenum to inlet at the low turbulence condition. At the high turbulence condition, figure 2.75 shows that the loss in total pressure was nearly uniform across the majority of the passage in the Z' direction, except in narrow regions at the endwalls. However, figure 2.74 shows significant variation

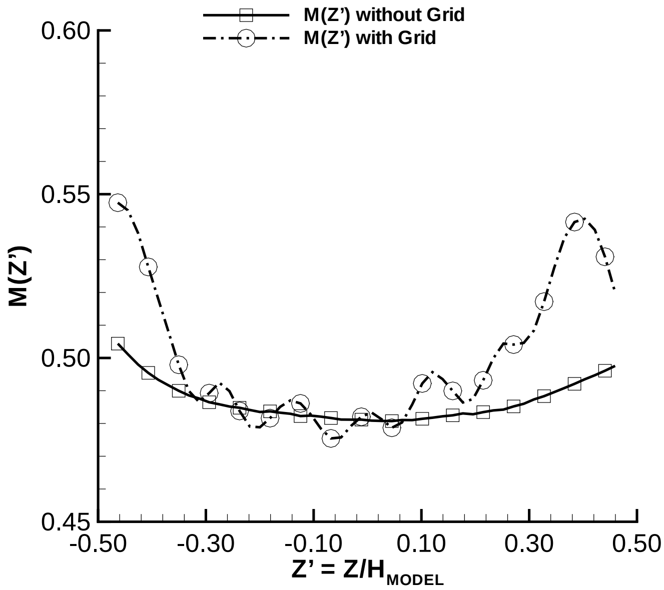

Figure 2.69: Plot of Mach number from endwall to endwall wall along centerline of channel.

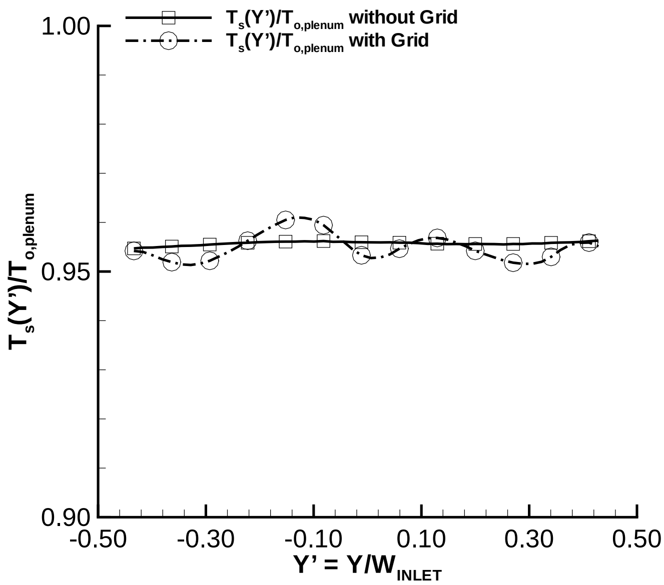

Figure 2.70: Plot of static temperature profile expressed as $\frac{T(Y')}{T_{o,plenum}}$ from pressure side to suction side inlet wall along centerline of channel.

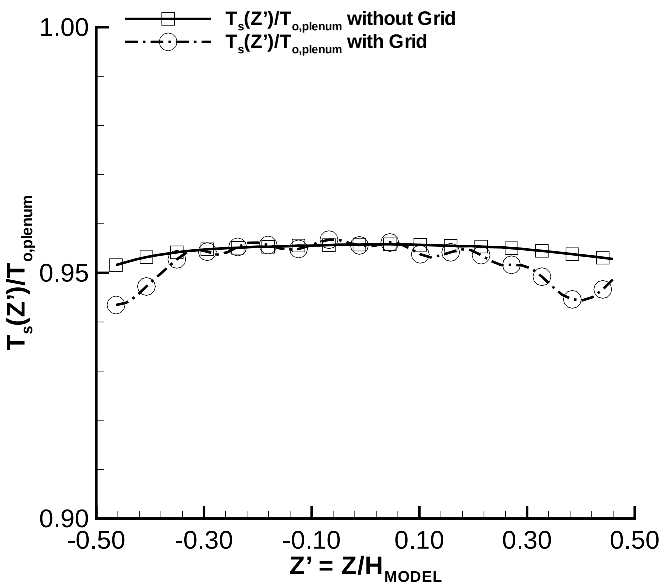

Figure 2.71: Plot of static temperature profile expressed as $\frac{T(Y')}{T_{o,plenum}}$ from endwall to endwall wall along centerline of channel.

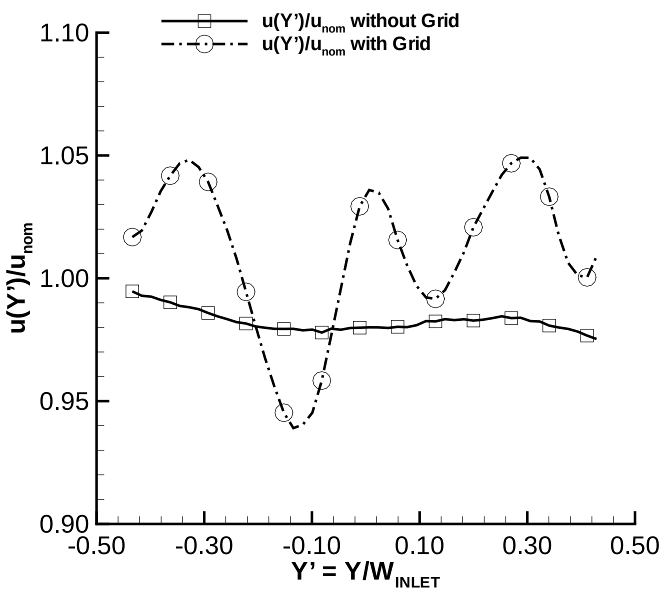

Figure 2.72: Plot of velocity profile expressed as $\frac{\overline{u}}{u_{nom}}$ from pressure side to suction side inlet wall along centerline of channel.

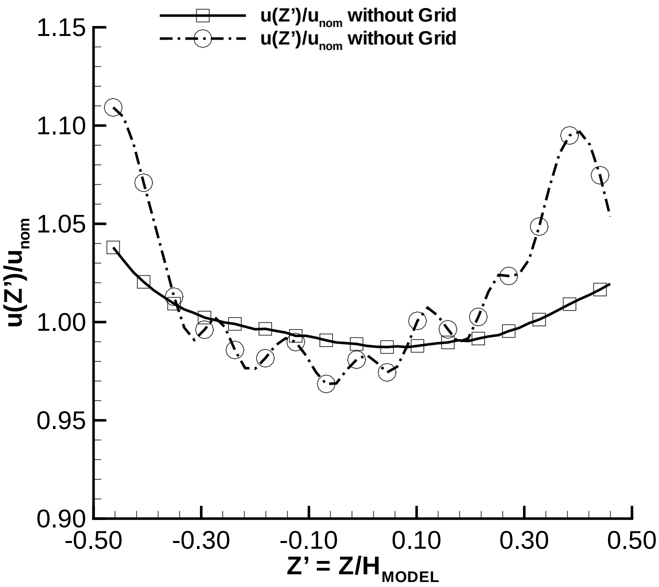

Figure 2.73: Plot of velocity profile expressed as $\frac{\overline{u}}{u_{nom}}$ from endwall to endwall wall along centerline of channel.

at the high turbulence condition in the Y' direction.

Measurements of the local static pressure, shown in figures 2.76 and 2.77, revealed that this variable did not exactly reflect the variations characteristic of the turbulence grid effects, especially in the inlet wall-to-inlet wall direction. In these figures, the static pressure (P) is normalized by the plenum total pressure ($P_{\circ,plenum}$), again to reflect any losses between the plenum and the model inlet.

The local static density can be computed given the local static pressure and static temperature. Profiles of this flow property ρ, normalized by the plenum total density ($\rho_\circ$) are shown in figures 2.78 and 2.79. These profiles again reflect the variations in static pressure in the inlet wall-to-inlet wall and endwall-to-endwall directions.

The velocity and density profiles can be multiplied and integrated to estimate the mass flow into the passage. Despite the fact that these data were only taken along perpendicular centerlines, estimates of the mass flow agreed with the upstream orifice plates within $\pm 1\%$. Additionally, data from the low turbulence case showed that a 1-D velocity-profile approximation was appropriate.

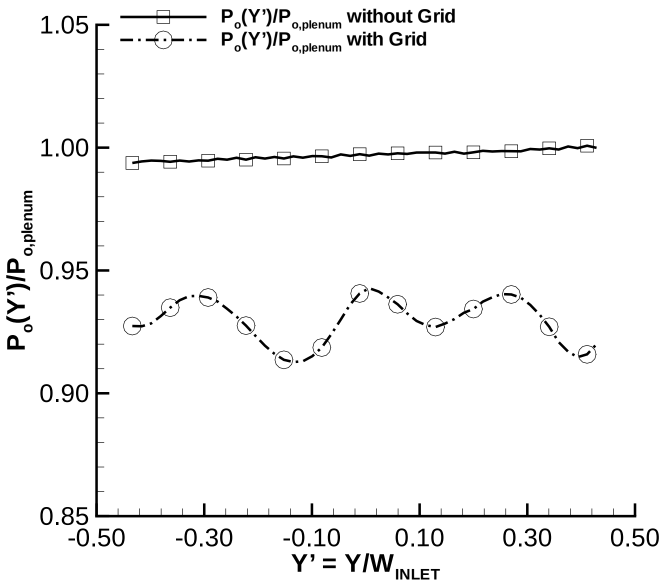

Figure 2.74: Plot of total pressure profile expressed as $\frac{P_\circ(Y')}{P_{\circ,plenum}}$ from pressure side to suction side inlet wall along centerline of channel.

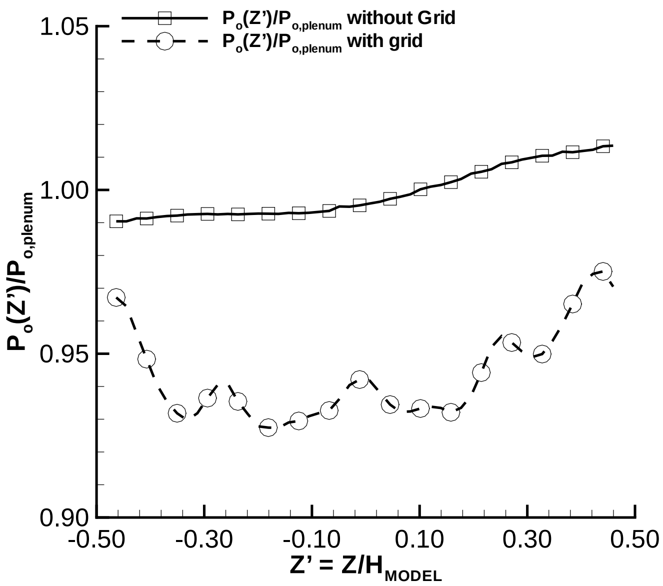

Figure 2.75: Plot of total pressure profile expressed as $\frac{P_\circ(Y')}{P_{\circ,plenum}}$ from endwall to endwall wall along centerline of channel.

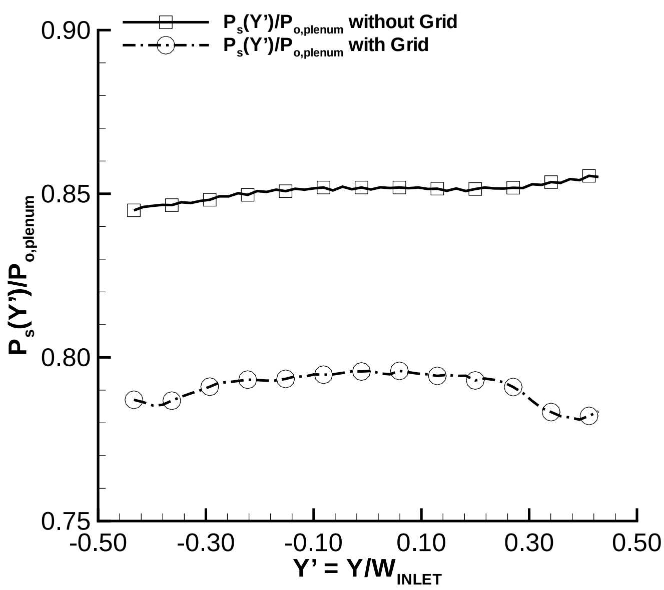

Figure 2.76: Plot of $\frac{P(Y')}{P_{o,plenum}}$ from pressure side to suction side inlet wall along centerline of channel.

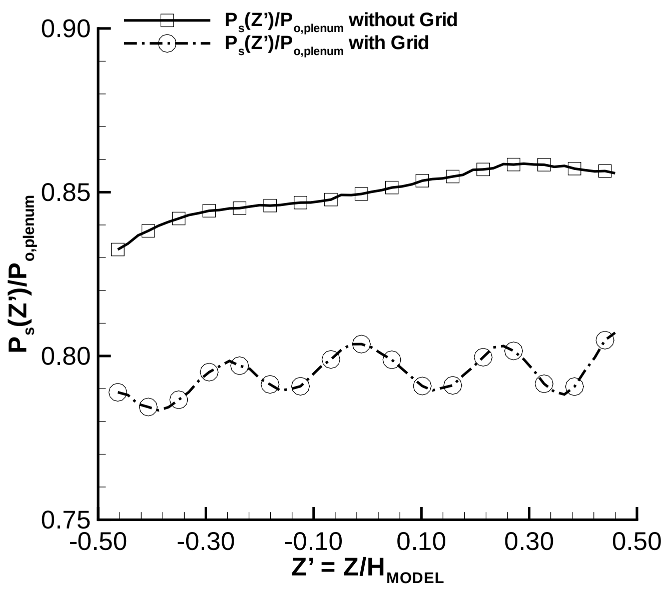

Figure 2.77: Plot of $\frac{P(Y')}{P_{o,plenum}}$ from endwall to endwall wall along centerline of channel.

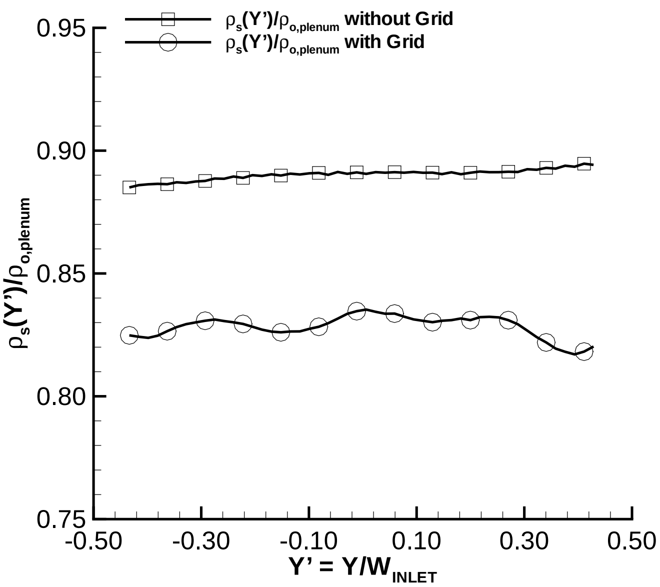

Figure 2.78: Plot of static density profile expressed as $\frac{\rho(Y')}{\rho_{o,plenum}}$ from pressure side to suction side inlet wall along centerline of channel.

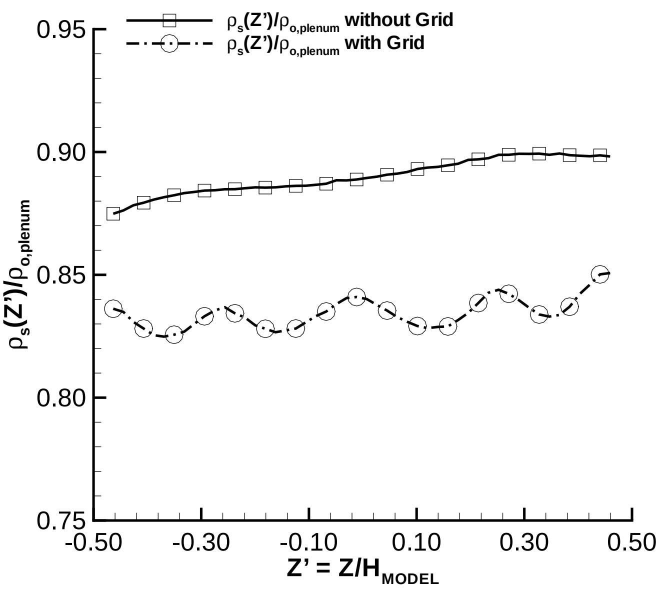

Figure 2.79: Plot of static density profile expressed as $\frac{\rho(Y')}{\rho_{o,plenum}}$ from endwall to endwall wall along centerline of channel.

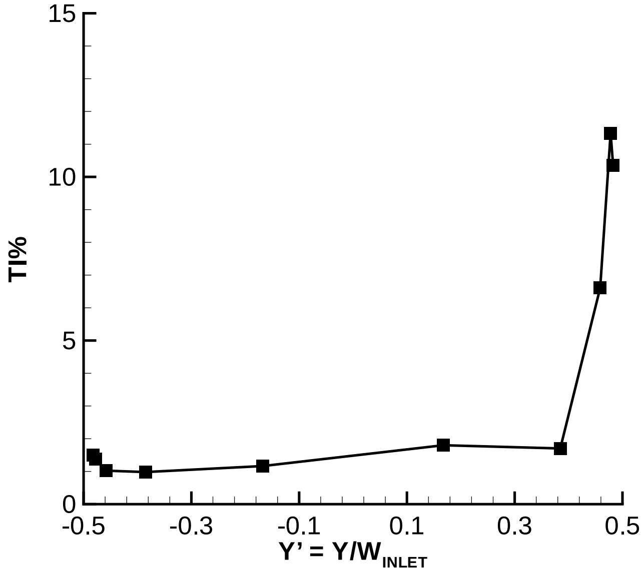

Figure 2.80: Measurements of turbulence intensity $TI\%$ from pressure inlet wall to suction side inlet wall.

Inlet Turbulence Quantities

Figures 2.80 and 2.81 display turbulence intensity profiles for the low turbulence flow condition. The turbulence intensity is relatively constant across the majority of the passage with a value of approximately $TI\% \approx 1\%$ to $TI\% \approx 2\%$. These figures appear to capture the effect of the boundary layer along the suction side inlet wall (at $Y' = 0.5$) and the far-side endwall (at $Z' = 0.5$). This observed asymmetric behavior could be due the fact that the streamwise pressure gradient is larger along the suction side inlet wall than the pressure side wall. A more adverse pressure gradient would cause a faster thickening of the boundary layer, which is apparent from these results.

Similar profiles could not be achieved with the high turbulence case, as the high levels of turbulence in the passage caused the hotwire to break too frequently to take profiles of turbulent quantities. Additionally, these elevated turbulence levels for the high turbulence case prevented turbulence measurements at actual flow conditions. Thus data taken at the center of the passage inlet at lower velocities were used to develop an extrapolated estimate at full flow conditions. This approach gave an estimated turbulence intensity of $TI\% \approx 30\%$.

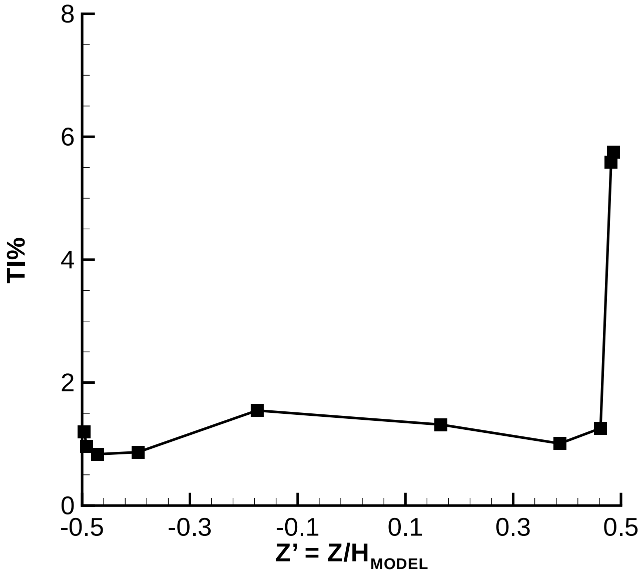

Figure 2.81: Measurements of turbulence intensity $TI\%$ from pressure inlet wall to suction side inlet wall.

Figures 2.82 and 2.83 present power spectra measured at the center of the single passage inlet with increasing mean flow velocities at low and high turbulence conditions. The frequency value shown on the ordinate axis of these plots was normalized by a frequency defined by the nominal center velocity and the inlet width ($f_{nom} = \frac{u_{nom}}{W_{INLET}}$). The $(\rho u)_{rms}$ value was normalized by the nominal value of the mass flux at the conditions labeled in table 2.11. One observation that is apparent from the spectrum at $\frac{u}{u_{nom}} = 0.984$ in figure 2.82 at a low turbulence condition is the presence of distinct peaks at approximate frequencies of $\frac{f}{f_{nom}} \approx 1.57$, $\frac{f}{f_{nom}} \approx 3.27$ and $\frac{f}{f_{nom}} \approx 4.91$. These were believed to be due to vortex shedding off the hotwire probe stem, which at the measurement flow conditions, caused the probe to vibrate. White (1991) documents that the Strouhal number, defined as:

$$St = \frac{f\tilde{u}}{D} \tag{2.52}$$

has an estimated value of $St \approx 0.2$ for a cylinder of diameter D exposed to a normal cross flow for a Reynolds number in the range, $100 \leq Re_D \leq 10^5$. Using this basis, a fundamental shedding frequency of $\frac{f}{f_{nom}} = 1.745$ was predicted – agreeing with the measurements presented in figure 2.82. At higher frequencies, instead of the spectrum continuing to roll-off, a secondary broad-based peak is observed. The spectra in figure 2.82 clearly shows that this

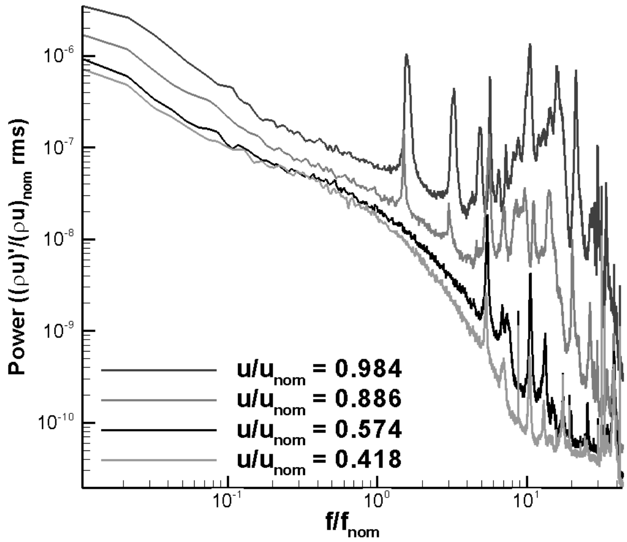

Figure 2.82: Power spectrum at various inlet velocities and low turbulence condition.

characteristic becomes more pronounced as the passage inlet velocity is increased.

In comparison, figure 2.83 demonstrates the high turbulence case not only produced a increased turbulence intensity, but much broader power spectrum. The secondary broad-based peak at the high-end of the spectrum is not as apparent as in the low turbulence case. Despite these differences, distinct peaks in the spectrum are observed at frequencies of $\frac{f}{f_{nom}} \approx 2.26$, $\frac{f}{f_{nom}} \approx 6.73$ and $\frac{f}{f_{nom}} \approx 12.50$. It was unclear why these do not occur at the same fundamental and harmonic frequencies as in the low turbulence case. One possible explanation is the substantially greater variations in the velocity across the inlet of the model, due to the inherent nature of the turbulence grid.

Figures 2.84 and 2.85 present the computed autocorrelation curves for a range of inlet velocities for the low and high turbulence cases. As the inlet velocity increases, broadening the range of turbulent eddies in the flow, the autocorrelation curve becomes increasingly oscillatory. A series of preliminary sensitivity tests determined that the technique advocated by Hinze (1975) is relatively robust when faced with wide-ranging spectra with localized peaks due to some characteristic unsteadiness in the flow. The full spectrum was used to compute an initial estimate of the integral time scale. A series of filters were then applied to the initial hotwire data sets to explore the sensitivity of the estimated integral

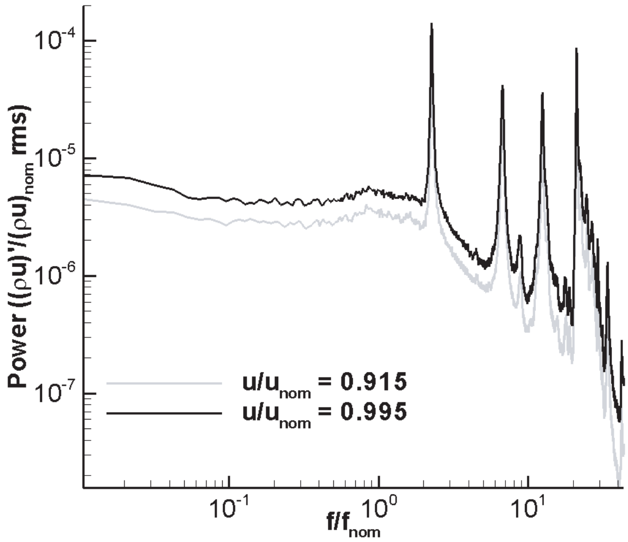

Figure 2.83: Power spectrum at various inlet velocities and high turbulence condition.

time scale to perturbations to the energy spectrum. Table 2.12 presents the filters applied individually to the hotwire signal and the resulting estimates for the integral time and length scales. Table 2.13 displays the corresponding data for the high turbulence case. These tables make it apparent that the smaller the low-pass filter cutoff for a given spectrum, the larger the integral time scale becomes. Additionally, these cases demonstrate that the approach for computing the integral length scale is relatively insensitive to the previously described distinctive peaks apparently due to shedding off the hotwire probe. As there was no compelling physical reason to arbitrarily apply a low-pass filter at some limit, it was decided to use the spectrum with a series of bandstop filters in measurements of the length scale. Thus, these tests indicated that the integral length scale and its associated uncertainty at the center of the passage is $\frac{\ell}{c_{blade}} = 0.53^{+0.5}_{-0.4}$ for the low turbulence case and $\frac{\ell}{c_{blade}} = 0.026^{+0.07}_{-0.02}$ for the high turbulence case.

Figures 2.86 and 2.87 present profiles in inlet wall-to-inlet wall and endwall-to-endwall directions of the estimated integral length scale, ℓ, normalized by the blade chord length, c for the low turbulence flow condition. Similar profiles could not be achieved with the high turbulence case, as the excessive levels of turbulence in the passage caused the hotwire to break too frequently. These profiles suggest that the integral length scale increases in

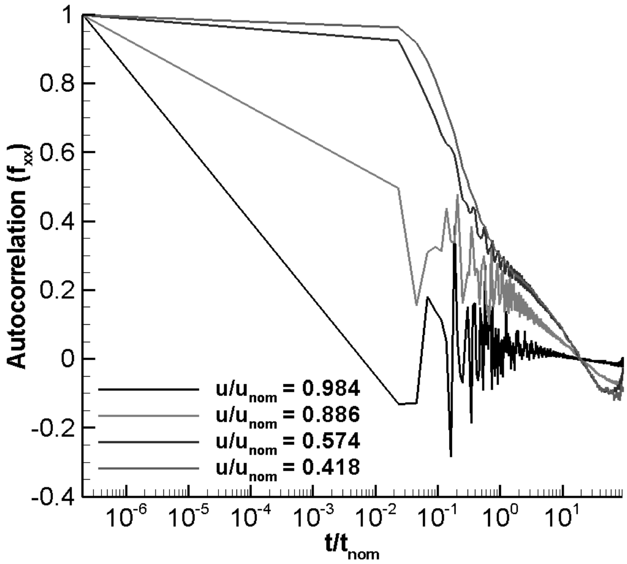

Figure 2.84: Autocorrelation function f_{xx} at various inlet velocities and low turbulence condition.

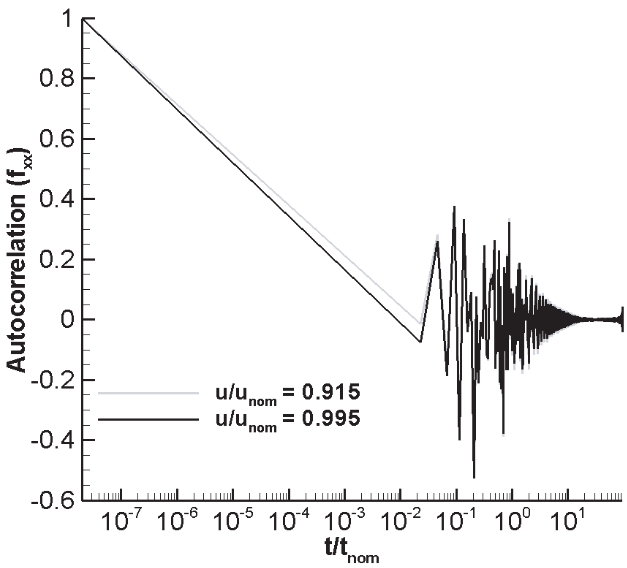

Figure 2.85: Autocorrelation function f_{xx} at various inlet velocities and high turbulence condition.

Table 2.12: Sensitivity test for integral length scale – low turbulence condition

Applied Filter(s)	Filter Ranges ($\frac{f}{f_{nom}}$)	$\frac{T_E}{t_{nom}}$	$\frac{\tilde{u}}{u_{nom}}$	$\frac{\ell}{c_{blade}}$
None	N/A	0.66	1.0	0.52
Low-Pass	5.2	1.9	1.0	1.6
Low-Pass	10.4	1.1	1.0	1.1
Low-Pass	18.7	1.9	1.0	0.93
Bandstop (2)	1.2-1.7, 2.6-3.6	0.64	1.0	0.53

Table 2.13: Sensitivity test for integral length scale – high turbulence condition

Applied Filter(s)	Filter Ranges ($\frac{f}{f_{nom}}$)	$\frac{T_E}{t_{nom}}$	$\frac{\tilde{u}}{u_{nom}}$	$\frac{\ell}{c_{blade}}$
None	N/A	$1.0(10)^{-2}$	0.91	$7.3(10)^{-3}$
Bandstop	2.1-2.4	$2.5(10)^{-2}$	0.91	$1.8(10)^{-2}$
Bandstop (2)	2.1-2.4, 6.3-7.3	$2.8(10)^{-2}$	0.91	$2.1(10)^{-2}$
Bandstop (3)	2.1-2.4, 6.3-7.3, 10.4-14.0	$3.5(10)^{-2}$	0.91	$2.6(10)^{-2}$
Bandstop (3), Low-Pass	2.1-2.4, 6.3-7.3, 10.4-14.0, 20.0	$1.1(10)^{-2}$	0.91	$8.0(10)^{-2}$

the vicinity of the walls. However, it is unclear if this is due to the actual nature of the flow, or to some a deficiency in the measurement. Figures 2.88 and 2.89 exhibit profiles of the ratio $\frac{T_E}{t_\circ}$, to verify the assumptions used in calculating the integral length scale, ℓ. With the exception of the near-wall regions, these plots evince that the method proposed by Townsend (1947) can be applied to the spectral data collected at these locations as indeed $t_\circ \gg T_E$ in the core of the inlet flow. For the high turbulence case, measurements at the center of the passage suggested that this ratio had the approximate value of $\frac{T_E}{t_\circ} \approx 0.2$.

Pressure Distribution

To evaluate the flow conditions in the blade passage, two airfoil surfaces with closely spaced pressure taps were installed in the model. The taps consisted of cross-drilled holes; the tap on the surface was a 0.62-mm diameter hole, drilled perpendicular to the local surface tangent and the cross-drilled port was 1.6-mm diameter hole. A 1.59-mm diameter copper tube with an internal diameter of 0.88-mm was glued into the port. 1.59-mm diameter Tygon tubes were push-fit over the ends of the copper tubes and connected to the Scanivalve. The tap and port sizes were chosen, consistent with recommendations listed by Mattingly (1996).

Figure 2.90 presents the measured M_{is} distribution without a turbulence grid installed.

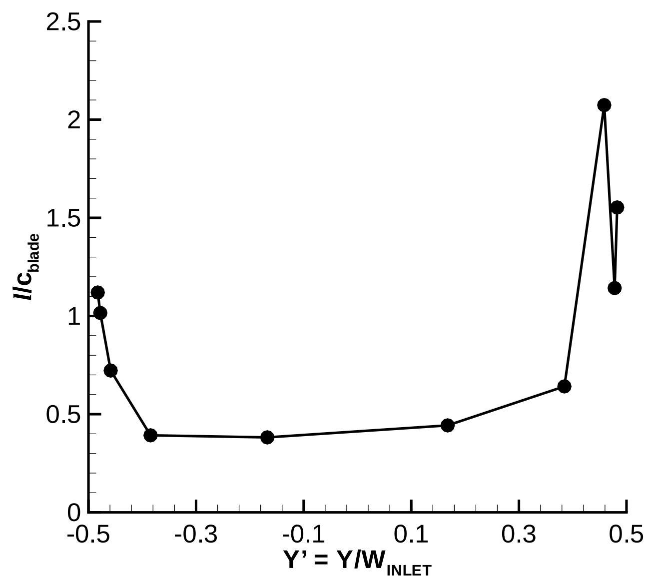

Figure 2.86: Measurements of integral length scale ℓ from pressure inlet wall to suction side inlet wall for low turbulence condition.

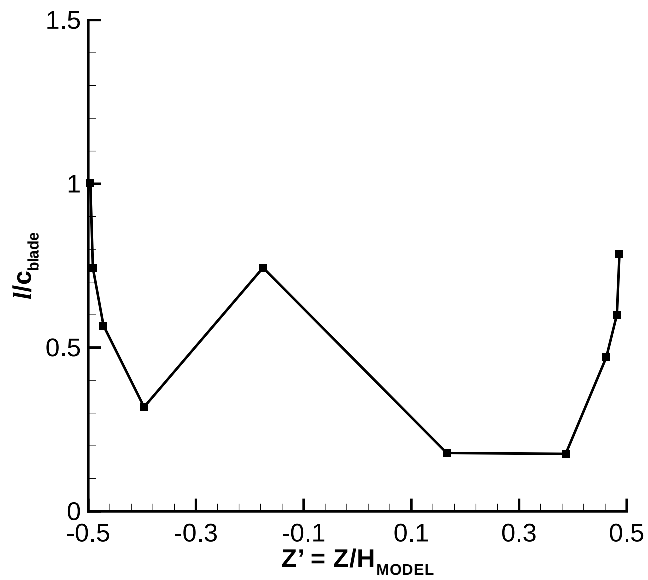

Figure 2.87: Measurements of integral length scale ℓ from endwall to endwall for low turbulence condition.

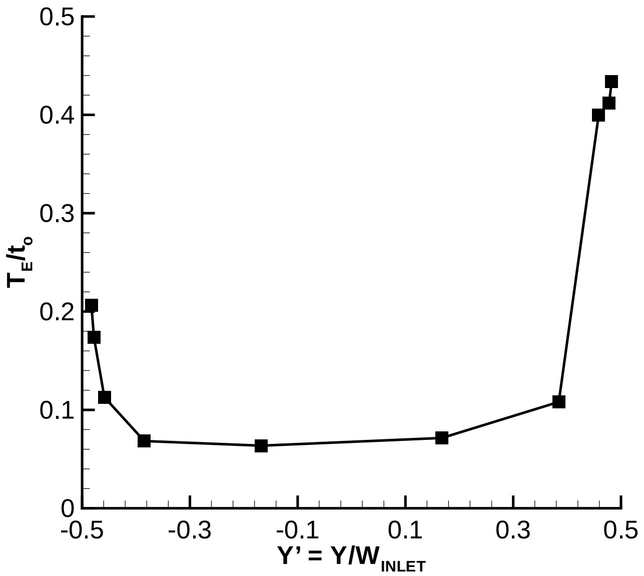

Figure 2.88: Measurements of $\frac{T_E}{t_\circ}$ from pressure inlet wall to suction side inlet wall for low turbulence condition.

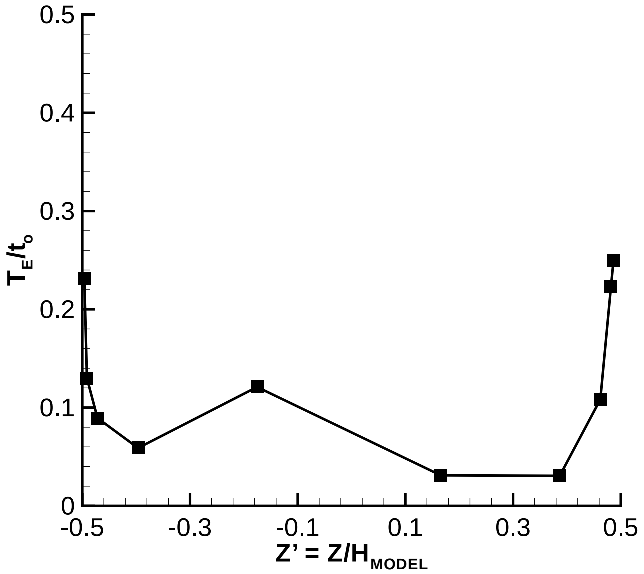

Figure 2.89: Measurements of turbulence intensity $TI\%$ from pressure inlet wall to suction side inlet wall for low turbulence condition.

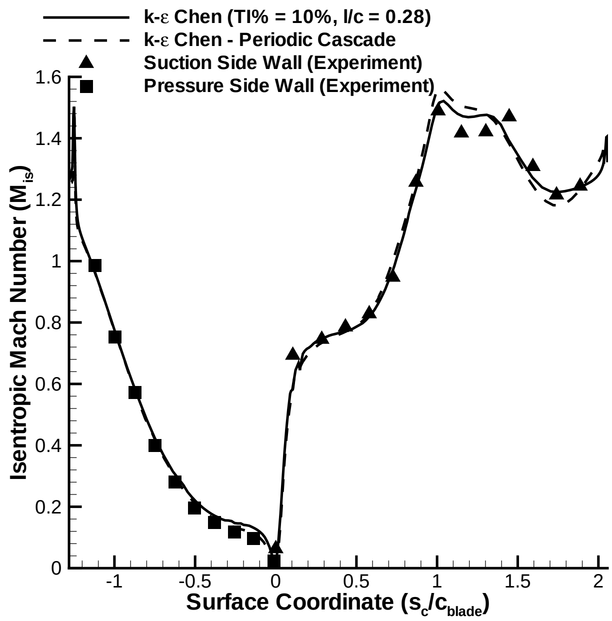

Figure 2.90: Measurements of M_{is} for low turbulence condition.

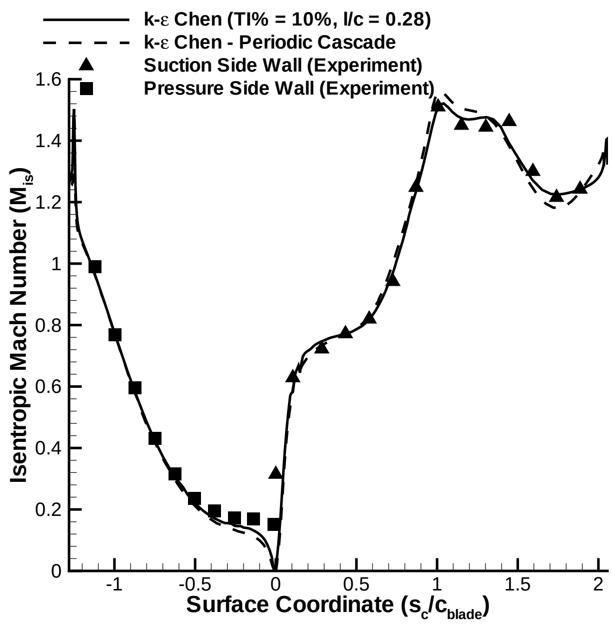

Figure 2.91: Measurements of M_{is} for high turbulence condition

For comparison, the desired pressure distribution for the given airfoil geometry and the computed M_{is} distribution for the periodic single passage is included. The uncertainty of M_{is} was computed to be ± 0.046 (P = 0.95). These results show close agreement with the desired pressure distribution for the given airfoil geometry.

With respect to the high turbulence case (shown in figure 2.91), the total pressure used to compute the M_{is} distribution was computed using the plenum total pressure and the measured total pressure loss across the grid. What is very apparent in this figure is the fact that the pressure taps located at the expected stagnation point locations measure pressures which are significantly lower than the estimated total pressure. This effect appears to decay rapidly along the blade. It was believed that this was caused by significant variations in the upstream total pressure with the grid installed, as demonstrated in Section 2.4.6.

The uncertainty in these measurements was found to vary between from $1.8\% \leq \frac{\delta M_{is}}{M_{is}} \geq 7.1\%$. The highest uncertainty was found to occur at the peak values of M_{is}. Appendix A details how these values were determined.

Chapter 3

Heat Transfer Experiment Methodology

This chapter describes the modification of the single passage model for heat transfer measurements which involved spatially-resolved, steady state surface temperature measurements utilizing Thermochromic Liquid Crystals (TLCs). However, due to the relatively complex nature of the single passage, two fundamental complexities were encountered: achieving optical access and accurately calibrating the thermochromic liquid crystal response. Consequently, this chapter discusses the rationale for these approaches and the design and construction of salient components.

3.1 Optical Access Apparatus and Implementation

Linear cascade experiments such as that performed by Drost and Bölcs (1999) and Giel et al. (2004) have demonstrated the feasibility of applying optical measurement techniques, such as TLCs to linear cascades of modern blade geometries. In these facilities, optical access was achieved with large, flat optically clear windows. A composite spatial map of the surfaces of interest was constructed from several strategically positioned cameras.

In comparison, Mukerji and Eaton (2002) imaged the suction side of a 1970-era first stage rotor blade airfoil in single passage model first used by Buck and Prakash (1995) for mass transfer experiments. Given the size of the model, flat viewing windows could not be installed. Instead, optical access was achieved through a precision machined Plexiglas window that also functioned as the pressure side wall of the passage. A single camera was used to image the entirety of the suction side wall. Given the much higher flow rates and larger turning angle in the transonic single passage, such an approach was deemed impractical. Instead, small scopes were used to view the measurement surfaces. These optical tools are specifically designed for remote viewing and are used extensively for qualitative inspection of operating machinery, medical examinations such as endoscopy and general surveillance. However, as far as is known in the open literature, these tools have not been used for quantitative fluid mechanics or heat transfer measurements. There are two general classifications of remote viewing scopes, fiberscopes and borescopes. Figure 3.1 displays the

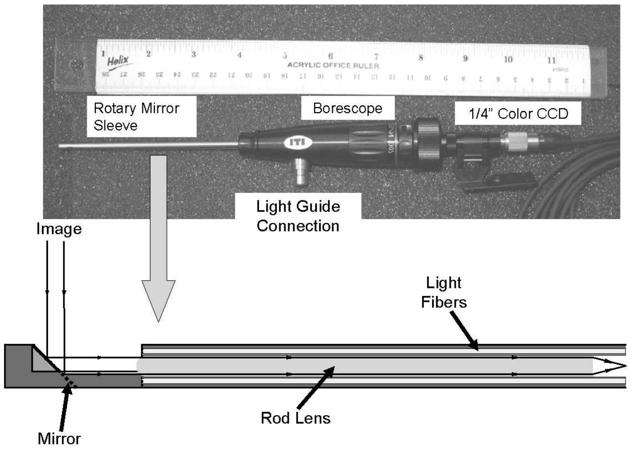

Figure 3.1: Picture of ITI Borescope with single-chip $\frac{1}{4}$" CCD camera attached and detailed view of the rotary mirror sleeve assembly.

Figure 3.2: Picture of a fiberscope (Imaging Products Group (2004)).

primary features of a standard borescope with a rotary mirror sleeve (RMS) installed for periscopic viewing. These devices use rod lenses enclosed in a rigid stainless steel sheath for imaging. Illumination is provided co-axially through light fibers that envelope the sheath. In comparison, fiberscopes use fiber bundles for both lighting and viewing allowing a pliable configuration that generally has more versatility than standard borescopes. Essentially, fiberscopes trade increased versatility and flexibility for reduced optical clarity and brightness. Figure 3.2 presents the general characteristics of a fiberscope, the eyepiece can be replaced with a camera, converting the assembly into a so-called videoscope.

Dods (1999) determined, given the constraints presented by the single passage model, that the most appropriate choice for optical access was a miniature periscope, consisting of a rigid borescope with a rotary mirror sleeve as pictured in figure 3.1. As lenses, rather than fibers were used to transmit the image through the system, this setup would provide the highest level of optical resolution. The standard, unobtrusive application for such an optical tool was to install a *viewing well* in the surface opposite the one of interest. Such a well consisted of two cross-drilled holes: one with a flat, spot-faced, optically-clear, sapphire window glued in place, and the other providing entry for the borescope. The window would typically have the dimensions of an aspirin tablet. There were several challenges that this approach presented: Borescopes, due to their small size have a very low light throughput and generate relatively dim observed images, thus requiring a powerful light source. Often this problem requires an iterative solution, experimenting with different light levels. This experimentation is necessary especially if the light source is co-axial with the imaging optics. This is because from previous experience with full-scale optical systems for heat transfer measurements as reported by Smith et al. (2001) and Hacker and Eaton (1995) it was found that such arrangements have large amounts of glare that become more pronounced with greater illumination. Furthermore, Dods (1999) detailed that the high-precision, high-quality rod lenses in borescopes tend to produce images with color resolution that is skewed "greyish-greenish" and highly non-linear optical distortions that are particularly apparent on the edges of the image. These issues will be revisited in subsequent sections.

3.1.1 Implementation of Borescopes to the Single Passage Model

The choice of borescope and method of achieving optical access was driven by the following rationale: use the fewest number of viewing wells to observe as much as possible of the measurement surfaces. This effectively meant that the borescopes had to have relatively large fields of view (FOV) and optical windows larger than that used in standard applications. This constraint made it vital that the installed viewing wells presented negligible flow disturbances. The 3-D calculations presented in section 2.1.5 demonstrated that the two-dimensional portion of the flow approximately ranged from $-0.25 \leq Z' \leq 0.25$. As this was a fairly large area, it was decided to use conformal "strip" windows. These were installed in separate Ren Shape components with machined grooves to accept the window and the borescope. This meant that both the window and the installation piece had to be machined to a high level of precision (± 0.013mm) to ensure that the assembled piece was two-dimensional and had a smooth, high tolerance interface between the window and surrounding material. It was decided to use a borescope with a 100-mm long, 4.8-mm

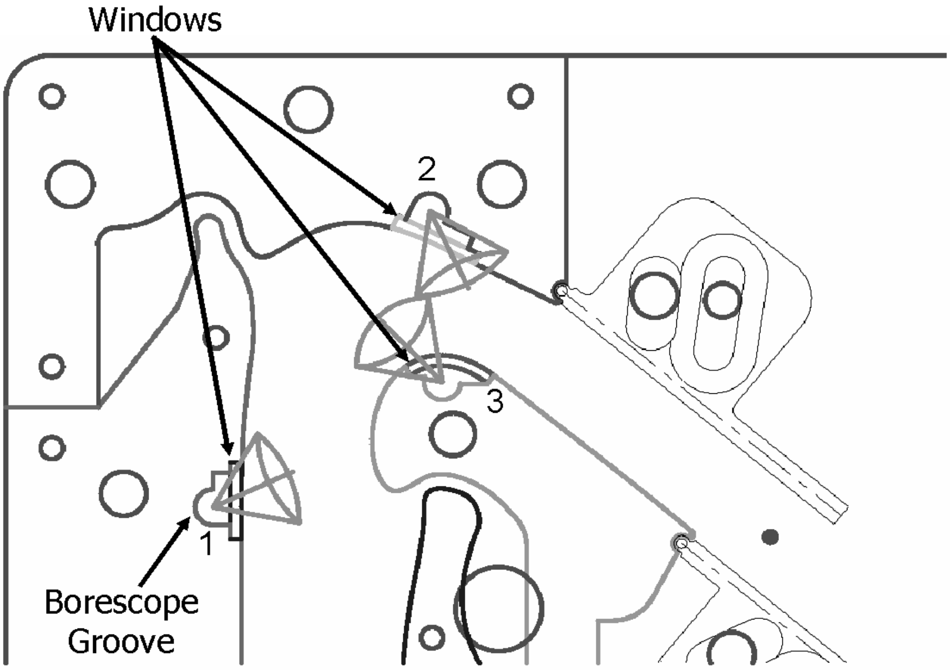

Figure 3.3: Single passage model viewing wells.

diameter rotary mirror sleeve (RMS) and a 70° field of view (Instrument Technology Inc. #123004/4.8/10/70/F-RMS). The diameter of the borescope was important in maximizing the light throughput to the attached camera, and combined with the sizes of the field of view and the mirror in the RMS, determined the viewable region on the surface of interest. The mirror in the RMS had a 45° angle of inclination, as indicated in figure 3.1.

Figure 3.3 displays the chosen locations of three borescope viewing wells; 1 and 2 were designed to view the suction side wall, 3 was designed to view the pressure side wall. The single passage model shown is an older generation version of the experimental flow facility: hence, the presence of straight tailboards and constricted bleed geometries. Nevertheless, the design procedure used for these viewing wells can be extended to any geometry, and the windows shown in this figure were found to be acceptable for the redesigned model as well. The conical shapes emanating behind each window correspond to the fields of view for each borescope.

To limit the effects of glare and increase the illumination levels across the observed surface, lighting was provided through an improvised borescope designed by Dods (2001). This consisted of a light guide that was slid into a rotary mirror sleeve, replacing the borescope rod lenses with fiberoptics. The mirror at the end of the RMS was replaced with a stainless steel plug with a finely polished angled surface. The polished surface had an angle of inclination of 30°.

Image Processing System

The image acquisition system consisted of a NTSC Sony XC-003 3 CCD camera connected to a 3 × 8-bit Matrox Meteor II frame grabber (digitizer) board installed in a Gateway Pentium III 450 Mhz computer with 64 MB of RAM. This camera had three 1/3" CCD arrays for each color component (red, green and blue) with full spatial resolution (752(H)x582(V) pixel resolution). Light entering the camera struck a prism, directing various spectral bands to the appropriate CCD. The importance of this characteristic is discussed in greater detail in section 3.2.2. Furthermore, this camera represented a significant improvement over cameras previously used by researchers such as Hacker and Eaton (1995) as it had a lower signal-to-noise ratio (59dB for the XC-003 to 48dB for the DXC-151), a wide range of gain settings (0-18dB, with 1dB steps), a selectable gamma correction and a long exposure time feature. Hacker and Eaton (1995) reported that although the response of a CCD array is very nearly linear with changing levels of illumination, the NTSC standard provides for a nonlinear "correction". Thiele (1994) quotes that the standard NTSC gamma correction alters the CCD response from linear to logarithmic, mimicking the response of the human eye. For reasons that are discussed in section 3.2.2, thermochromic liquid crystal temperature measurements require a linearized CCD response. Hence, this feature was turned off for measurements.

Another critical feature of this camera is it long exposure time feature. This allows the CCD arrays to be exposed to longer integration times, allowing for the low light throughput for the borescope. The camera automatically calculated the integration time based on an interactively set number of frames through an on-screen menu. At the end of each integration interval, the camera would output a video frame (odd then even frames). Consequently, it was necessary to synchronize the acquisition cycle of the frame grabber board to the camera output. It was found experimentally that before the camera outputs an image, it outputs a TTL *write enable* (WEN) signal, which can be used to trigger image acquisition. Several Visual C++ drivers, embedded in LabView virtual instruments, were developed to control this interaction. Such drivers can be purchased for other frame grabber boards from Graftek Imaging (3601 South Congress Avenue, Building C, Suite 104, Austin Texas, 78704), but these were unavailable for this particular application and frame grabber board.

Construction of Viewing Well Windows

The Ren Shape window holding pieces were manufactured using similar techniques described in section 2.2, except with smaller tolerances and grooves for the window and borescope. Each of the conformal windows shown in figure 3.3 were designed to have a thickness of 1.52-mm, a 1-D stress analysis indicated that the maximum deflection would be less than 0.025-mm under actual flow conditions. The geometries shown in figure 3.3 could not be machined out of glass due to their complex curvature and the requirement that both sides had to be optically clear. Consequently, an in-house manufacturing procedure suggested by Hasler et al. (2000) was developed to machine these thin two-dimensional windows out of Plexiglas. This process for constructing each window involved first machining two high-precision Plexiglas blocks, one for the window and the other as a sacrificial support. The blocks would have at least two dowel pin blind holes for accurate alignment. MASTERCAM was used to generate the necessary machine instructions from AutoCAD drawings to cut the window and support pieces. The blocks were then machined within a tolerance of ± 0.003-mm using a three-axis CNC (computer numerical control) milling machine. The inside of the window was machined first using a small, carbide ball-end mill climb cutting at a high speed (4000 RPM, 0.1 $\frac{\mathrm{mm}}{\mathrm{s}}$ feed rate) along the length of the window. The negative of this surface would then be machined into the sacrificial block. This surface would then be "painted" with vacuum grease (Dow Corning # 976V) to ensure the window is fully supported. The outside of the window was then machined. Figure 3.4 is a picture showing a block with the negative of the suction side window interior, another with the interior of this window and a piece with the fully-machined window which has also been polished. Before polishing, the window was very nearly opaque.

The polishing process was vital in producing a Plexiglas piece with high optical clarity. The following process was developed from a series of trial-and-error tests, and involves both sandpaper of various grits and polishing compounds. The following list provides the general order these materials were used to polish the windows.

1. 200-grit sandpaper
2. 320-grit sandpaper
3. fine emery cloth

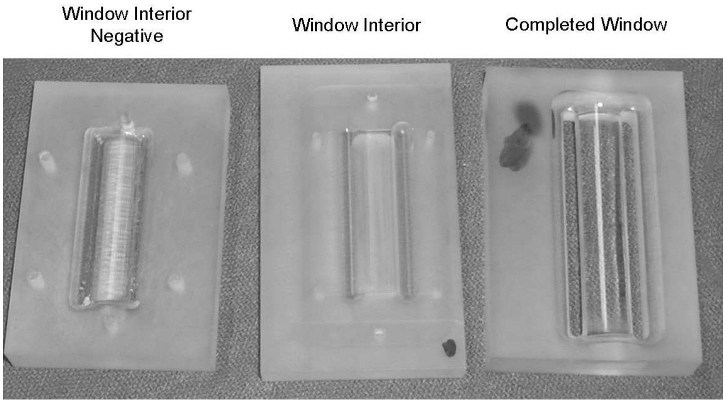

Figure 3.4: Borescope window pieces.

4. 600-grit sandpaper
5. super-fine emery cloth
6. 800-grit sandpaper
7. 1500-grit sandpaper
8. 2000-grit sandpaper
9. Novus #3 heavy scratch remover
10. cerium oxide paste
11. Novus #2 fine scratch remover
12. Novus #1 plastic polish remover

However, this order was adjusted based on the size and depth of various scratches that would emerge in the window surface during the process. The cerium oxide paste was a thoroughly blended mixture consisting of a 2:1 powder-to-water ratio by volume. The sandpaper is designed to remove ridges from the machining process, and the polishing compounds remove the scratches from the sandpaper. Each item was applied in a circular or crossing pattern to the surfaces of the windows. The polishing compounds were applied with a synthetic chamois cloth (McMaster-Carr # 7286T1).

The machined and polished window was then epoxied into place using a translucent epoxy (Scotch Weld 2216 B/A). The ends of the window were then trimmed to ensure its

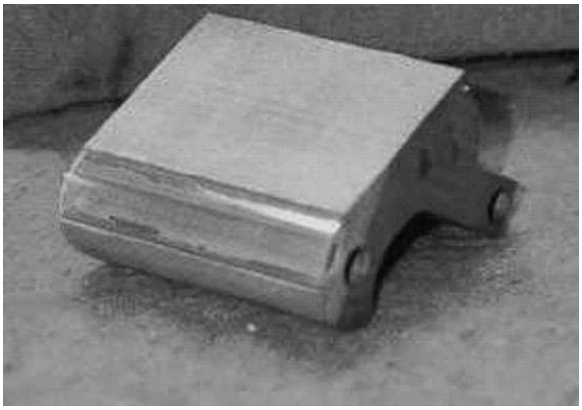

Figure 3.5: Suction side window piece.

lengths matched the thickness of the Ren Shape piece. Figure 3.5 shows the suction side window piece used for viewing the pressure side wall.

Design of Borescope Positioning System

Hammer (2001) developed and constructed a high-accuracy ($\pm$0.127-mm) positioning system for the borescopes, allowing near repeatable positioning of the rotary mirror sleeves at various angular settings. This system featured aluminum cradle supports for the borescopes, which attached to the body of the borescope. An indexed, press-fit, circular piece was slid over the rotary mirror sleeve dial. This allowed the RMS to be repeatably positioned within $\pm 2.5°$. A tight-fitting aluminum sealing plug was inserted into the cradle support over the rotary mirror sleeve. This was used to accurately position the assembly when attached to the single passage model. The lengths of the plugs were determined by the desired insertion length for the borescope. For the viewing borescope, this was chosen to ensure that its receiving optics were at the centerline of the model channel. Figure 3.6 is a schematic of the imaging and illumination system for the pressure side view through the suction side conformal window. Aluminum sub-plates were attached to the exterior walls of the flow facility, these were designed to accept the borescope cradles. Figure 3.7 presents pictures of the borescope cradles. Johal (2002) developed and constructed a brass fixture to accurately and repeatably position the camera opening relative to the rear of the borescope. This was found to be vital in ensuring consistency between calibration and experimental runs. As borescopes had not been used for quantitative measurements, this problem had not been noted previously (Dods (2002)). This piece was constructed out of brass to ensure

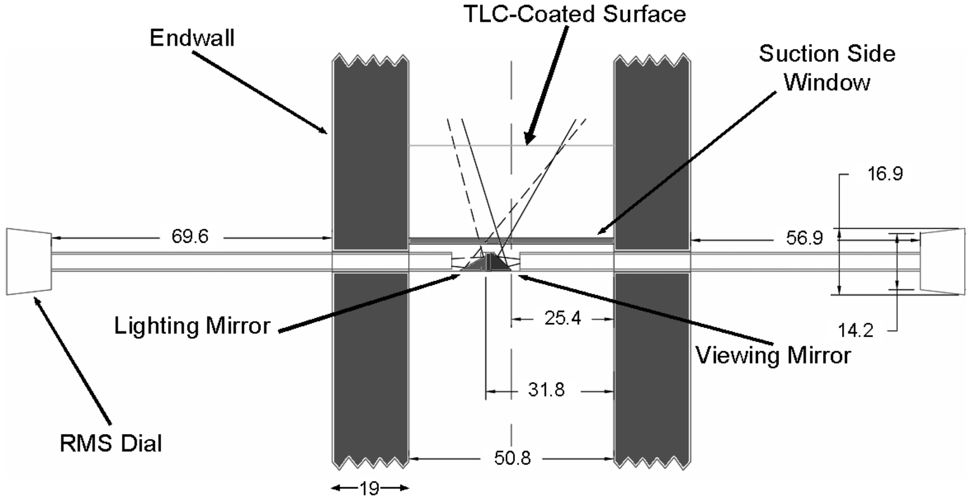

Figure 3.6: Schematic of borescope illumination and viewing optical system.

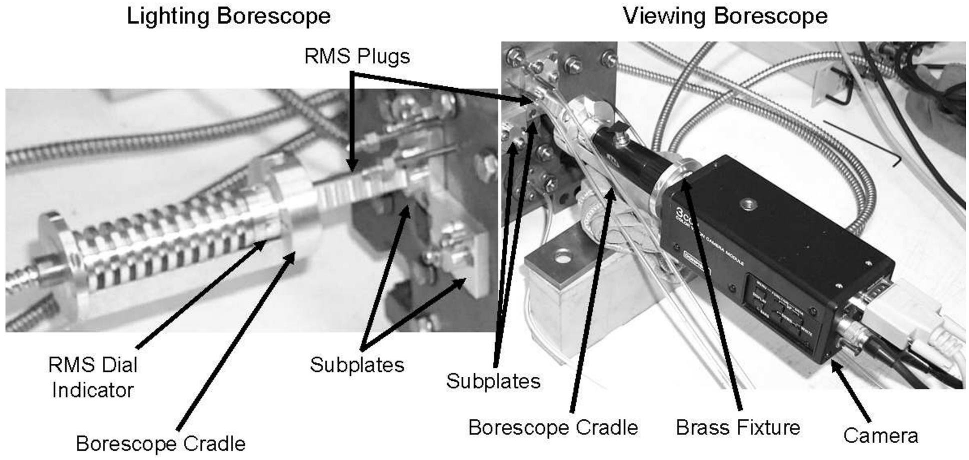

Figure 3.7: Picture of lighting and viewing borescope positioning systems.

the tightest tolerances, and featured a threaded end that screwed into the camera and a press-fit that slid over the back of the borescope. This replaced a manufacturer-supplied piece that allowed the camera opening to shift relative to the back of the borescope when these two pieces were re-assembled.

Flow Validation

To verify the effect of the suction side window piece on the flow conditions in the passage, M_{is} measurements were performed on the pressure side wall. Figures 3.8 and 3.9 present

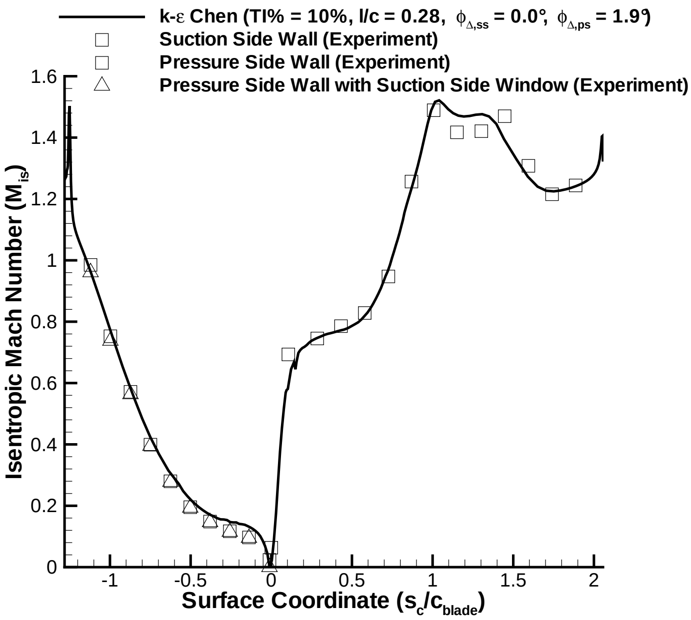

Figure 3.8: Measured M_{is} distribution along pressure side wall with suction side window installed – low turbulence case.

this distribution for low and high turbulence conditions. From these data it was concluded that any flow disruption effects due to the window piece were negligible.

3.1.2 Geometry Correction Algorithms

A significant concern with the application of borescopes as optical access tools are the observed strong optical distortions that occur due to:

1. the rod lenses contained in the borescope which have inherent nonlinearities that produce a fisheye effect;
2. the thin, conformal, curved window which covers the viewing well, causing an astigmatic-type effect; and
3. the highly curved measurement surface.

Due to the complexities listed above, corrections based on linear interpolation or geometric relations, as performed by Mukerji and Eaton (2002), could not be implemented. Instead, an in-situ geometry calibration process was developed based on the work of Goshtasby

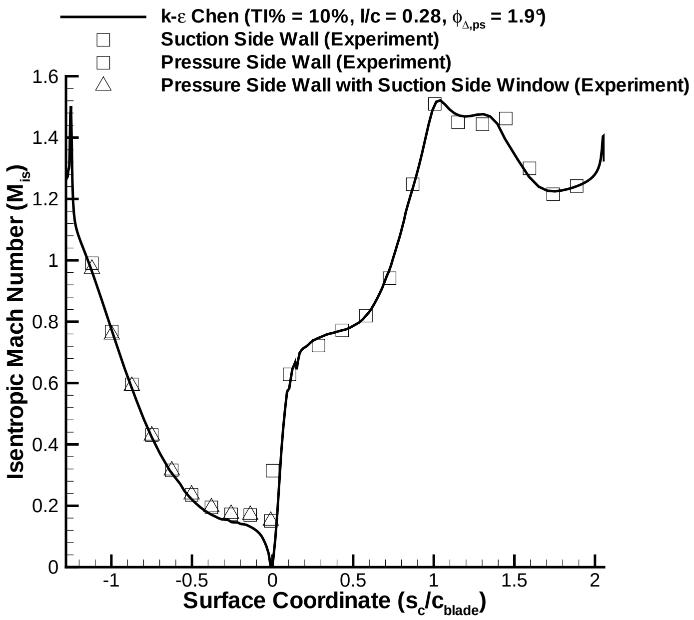

Figure 3.9: Measured M_{is} distribution along pressure side wall with suction side window installed – high turbulence case.

(1993) and Jackowski et al. (1997). The following subsections outline the development and application of this approach which relies on the use of Rational Gaussian functions (RaGs) to develop the correction functions for observed images.

Introduction to Rational Gaussian Functions

The correction technique uses a series of Gaussian functions to describe curves and surfaces in parametric form. It has the advantage over comparable interpolation algorithms such as nonuniform rational B-spline (NURBS) curves in that RaGs can fit to irregularly spaced points and are elastic. The elasticity of RaG can be varied to determine the tightness of the fit. In 1-D, given a sequence of points $\{\mathcal{D}_i : i = 1, \ldots, n\}$ the RaG curve approximating the points is defined by:

$$P(\breve{u}) = \sum_{i=1}^{n} \mathcal{D}_i g_i(\breve{u}) \qquad 0 \leq \breve{u} \leq 1 \tag{3.1}$$

Where $g_i(\breve{u})$ is the i^{th} RaG basis function of the curve, which is defined as:

$$g_i(\breve{u}) = \frac{W_i G_i(\breve{u})}{\sum_{j=1}^{n} W_j G_j(\breve{u})} \tag{3.2}$$

and $G_i(\check{u})$ is:

$$G_i(\check{u}) = e^{-(\check{u}-\check{u}_i)^2/2\sigma_{G,i}^2} \tag{3.3}$$

$\mathcal{D}_i$ is the ith control point, with a parameter value $\check{u}_i$ at which the ith basis function is centered (also termed as the ith node of the curve). $\sigma_{G,i}$ is the standard deviation of the ith Gaussian basis function, this is a chosen value that affects the "smoothness" of the basis function. W_i represents the weight associated with the ith basis function and control point. The parameter values are specified by the data, and the control point values are computed by solving a series of linear equations.

The application of this technique can be demonstrated as follows: Given a data set $\{(x_i, y_i) : i = 1, \ldots, N\}$, a fitting function h_x^t is sought that satisfies the constraint:

$$y_i \approx h_x^t(x_i) \qquad i = 1, \ldots, N \tag{3.4}$$

RaGs are used as basis functions to construct a representation of the fitting function. However, the values of the control points are unknown and need to be solved for once, before the interpolation can be used. First, the independent variable values are normalized using equation 3.5.

$$\check{u}_i = \frac{x_i - x_{min}}{x_{max} - x_{min}} \qquad i = 1, \ldots, N \tag{3.5}$$

Then a set of linear equations to solve for $\mathcal{D}_i$ can be constructed:

$$P(\check{u_k}) = y_k = \sum_{i=1}^{n} \mathcal{D}_i g_i(\check{u_k}) \qquad \check{u_k} \in [0, 1] \tag{3.6}$$

This means that the number of rational Gaussian functions that can be applied to a set of data is determined by the number of data points. The standard deviation of each Gaussian may be varied, controlling the sensitivity or elasticity of the interpolation function. For ease of implementation, they are often assumed to be identical for each basis function. Goshtasby (1995) pointed out that as $\sigma_{G,i}$ becomes smaller, a rational Gaussian function approaches a piecewise linear function. This is the most elastic case, as it exactly follows the changes in the interpolated data, including its aberrations. As $\sigma_{G,i}$ increases, the interpolation function becomes smoother.

Application of RaG Technique to Single Passage Experiment

Following the approach of Jackowski et al. (1997): Suppose $\{(x_i, y_i) : i = 1, \ldots, N\}$ represents the true x and y locations on the measurement surface. Furthermore, let $\{(X_i, Y_i) :$

$i = 1, \ldots, N\}$ be outputted pixel locations from the camera. To perform the geometry correction, two transformation functions must be constructed that satisfy the constraints shown in equation 3.7, below.

$$\begin{aligned} x_i &\approx f_x^t(X_i, Y_i) \\ y_i &\approx f_y^t(X_i, Y_i) \\ i &= 1, \ldots, N \end{aligned} \tag{3.7}$$

Jackowski et al. (1997) pointed out the transformation functions f_x^t and f_y^t are three-dimensional surfaces that can be represented with Rational Gaussian (RaG) surfaces. To perform this transformation, first defining two parameters: $\check{u}_i$ and $\check{v}_i$:

$$\check{u}_i = \frac{X_i - X_{min}}{X_{max} - X_{min}} \quad \check{v}_i = \frac{Y_i - Y_{min}}{Y_{max} - Y_{min}} \qquad u \in [0, 1] \tag{3.8}$$

Defining V_i^x and V_i^y as control point sets for f_x^t and f_y^t, respectively; sets of linear equations can be generated for the array of control points for each transformation function as shown in equations 3.9 and 3.10:

$$P(\check{u_k}, \check{v_k}) = x_k = \sum_{i=1}^{n} V_i^x g_i(\check{u_k}, \check{v_k}) \qquad \check{u_k}, \check{v_k} \in [0, 1] \tag{3.9}$$

$$P(\check{u_k}, \check{v_k}) = y_k = \sum_{i=1}^{n} V_i^y g_i(\check{u_k}, \check{v_k}) \qquad \check{u_k}, \check{v_k} \in [0, 1] \tag{3.10}$$

Where the basis functions $g_i(\check{u_k}, \check{v_k})$ are defined as:

$$g_i(\check{u}, \check{v}) = \frac{W_i G_i(\check{u}, \check{v})}{\sum_{j=1}^{n} W_j G_j(\check{u}, \check{v})} \tag{3.11}$$

Where:

$$G_i(\check{u}) = e^{-[(\check{u} - \check{u}_i)^2 + (\check{v} - \check{v}_i)^2]/2\sigma_{G,i}^2} \tag{3.12}$$

A LabView-based program was developed to implement this algorithm. An in-situ geometry calibration was then performed using an exact geometry pressure side wall with a regularly spaced grid glued to the surface, as shown in figure 3.10. This piece would then be removed at the completion of this process. At each borescope setting, the observed grid intersections were stored and the interpolation surfaces generated. The standard deviation was adjusted iteratively to achieve optimum performance. This was set to be a constant for each borescope setting. Typical values for each adjustment ranged from $\sigma_{G,i} = 0.05$ to $\sigma_{G,i} = 0.1$. The weights for each point were always chosen to be a constant value, $W_j = 1$. The uncertainty of the positioning system was estimated to be $\delta s_c = \delta z = \pm 0.5mm$.

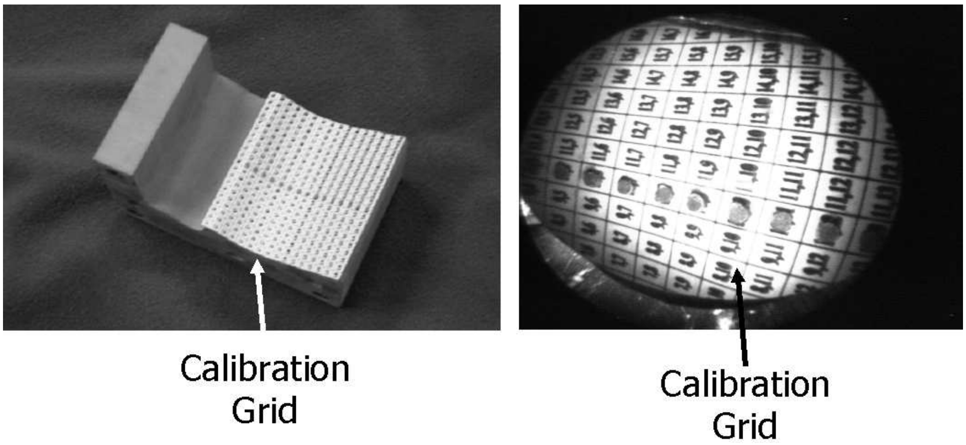

Figure 3.10: Pressure side geometry calibration piece.
The picture on the right hand side is the surface viewed through the borescope and suction side window.

3.2 General Aspects of Thermochromic Liquid Crystal Application

Thermochromic Liquid Crystals are widely used to provide high-spatial resolution temperature maps for an array of flow situations. With changing temperature, their spectral reflectivity changes, resulting in a change in their perceived color when illuminated with white light. Their primary advantage over competing techniques such as infrared thermography and temperature sensitive phosphor paints is their drastically reduced cost and ease of implementation, as documented by Wiberg and Lior (2004). However, their practical application to experimental hardware generates numerous complexities. In view of this, the following sections provide a brief introduction to TLCs and the many issues that had to be confronted to achieve low uncertainty measurements. Additionally, this section provides results that qualified the accuracy of the TLC measurement system as applied to the single passage model.

3.2.1 Introduction to Thermochromic Liquid Crystals and Their Properties

The term *liquid crystal* generally refers to a stable, intermediate, or *meso* thermodynamic phase between a pure solid and a pure liquid phase that some substances (usually organic in nature) can exhibit under specific conditions. These conditions are:

1. mechanical shear, pressure
2. electric and magnetic fields
3. chemical reactions
4. thermally induced processes (thermotropic)

The liquid crystal phase combines some of the mechanical properties of an isotropic liquid (e.g. surface tension, viscosity and weak intermolecular bonds) with the properties of a crystalline solid (e.g. anisotropy to light, circular dichroism and birefringence). Collings and Hird (1997) fully document the characteristics and properties of liquid crystals in general. *Cholesteric liquid crystals*, the generally accepted grouping to which TLCs belong, have three temperature dependent phases. Below the defined activation temperature of the crystals, defined as the smectic phase, the molecules of the material form layers with their long axes (directors) aligned in a certain direction. At this condition, the liquid crystal has a transparent appearance (i.e. optically inactive). As the temperature is increased, the alignment of these layers changes continuously through the material thickness, forming a chiral (twisted) structure as shown in figure 3.11. This molecular structure has birefringent nature that has a high spectral reflectance over a narrow band of wavelengths, much like the constructive interference of X-rays. Roberts and East (1996) argued that the center of this band can be simply modeled using Bragg diffraction analysis. Following Collings and Hird (1997), and defining $\phi_{TLC,i}$ and $\phi_{TLC,s}$ as light incidence and viewing angles, respectively:

$$n\lambda = \frac{P}{2cos\theta_{TLC}}\left[1 + cos(\phi_{TLC,i} + \phi_{TLC,s})\right] \tag{3.13}$$

where P is the distance over which the director moves through 360°, thence the structure repeats itself over a distance equal to $\frac{P}{2}$. n is an integer greater than zero. This is the cholesteric phase of the crystal, and is the primary identifying characteristic of TLCs. With increasing temperature or application of a shear stress, the orientation of this helical structure can change, modifying the spectral reflectance of the liquid crystal sample. With additional heating, the liquid crystal typically undergoes a further phase transition to an isotropic liquid, which is also optically inactive.

Figure 3.12 presents the typical liquid crystal response as a function of temperature, demonstrating that the crystal reflected color passes from red at its activation temperature to yellow, green and violent before transforming to an isotropic liquid and becoming transparent. For this reason, TLC's are applied under or over a thin layer of optically black

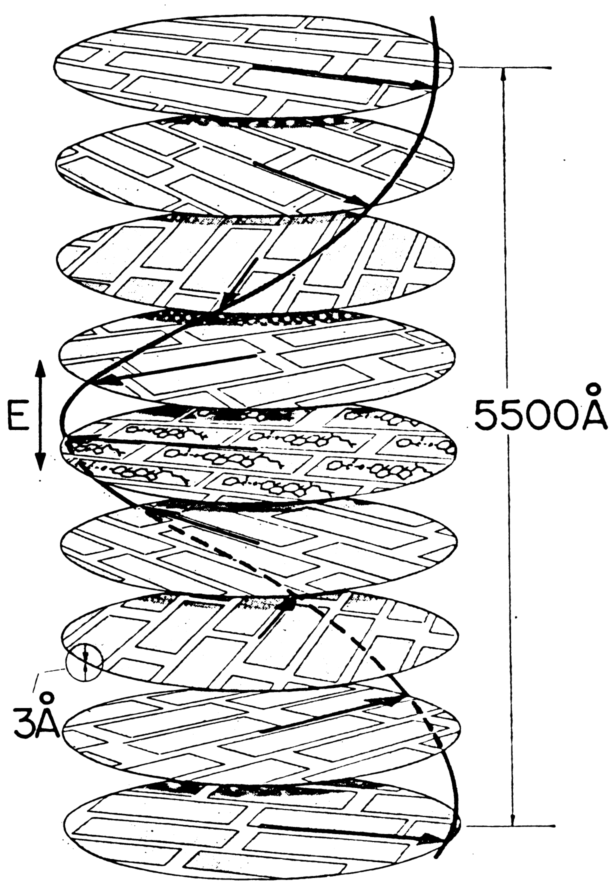

Figure 3.11: Probable organization of the cholesteric phase (from Fergason (1966a)). In actuality, the molecules are not precisely arranged in layers. Fergason (1966a), using X-ray measurements, determined the average molecular thickness was 3Å.

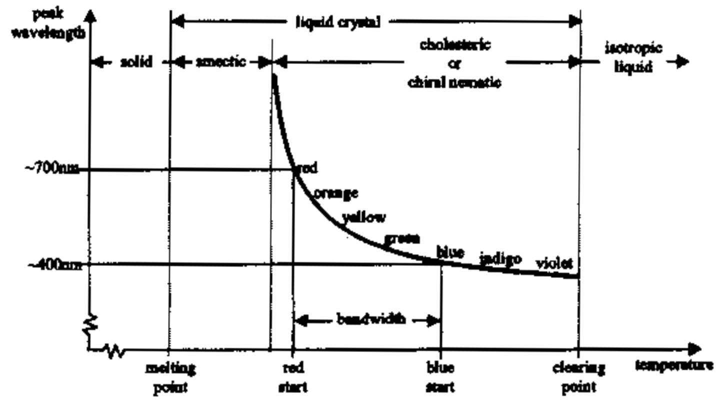

Figure 3.12: Variation of wavelength of maximum reflectance and molecular state as a function of temperature for a typical TLC mixture (from Anderson and Baughn (2004) and Parsley (1991a)).

paint, depending on the direction of viewing (Baughn (1995)).

Roberts and East (1996) stated, however, that the color response of the crystal can be tailored by the manufacturer so that the reflected wavelength can range from infrared to ultraviolet wavelengths. Furthermore, the sensitivity of TLCs to shear stress may be negated by a process called microencapsulation. This, in effect, involves encapsulating microscale droplets of TLCs in transparent polymeric spheres with a diameter of $\mathcal{O}(10)$-μm (Parsley (1991a)). This process has added benefits as it also reduces the sensitivity of the TLCs to degradation due to ultraviolet light, solvents and impurities. These factors give encapsulated TLCs increased stability and adaptability to a range of applications. In their unsealed form, TLCs have consistencies that range from thin oils to viscous pastes which make application difficult. Encapsulated TLCs take the form of an aqueous slurry that can be easily and consistently applied using an airbrush or printed onto a surface. Additionally, microencapsulation allows the combination of different liquid crystal formulations to produce a mixture with a different color responses with changing temperature.

For most practical uses TLCs are designed to have activation start temperatures that range from -30°C to 150°C and have bandwidths (red start temperature to blue start temperature) that range from 1°C (defined as narrow-band TLCs) to 50°C (defined as wide-band TLCs). This information is typically provided in the manufacturer part number for the TLC paint. For example, the part number for the liquid crystal paint used in this research, Hallcrest Type BM/R25C5W/C17-10, describes that this TLC has a red start temperature of 25°C and a bandwidth of 5°C (from R25C5W). The "BM" and "C17-10"

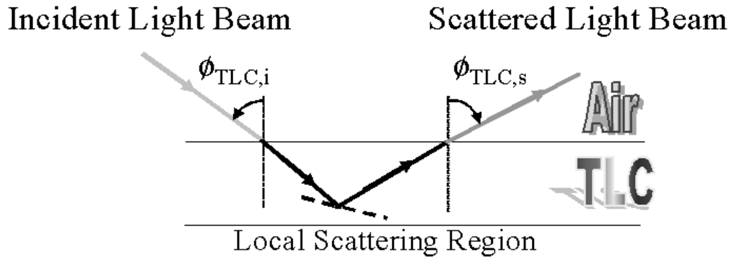

Figure 3.13: Definition of angles $\phi_{TLC,i}$ and $\phi_{TLC,s}$ with respect to a TLC-coated surface.

indicates that the TLC is micro-encapsulated and characterizes the encapsulation material.

An important practical distinction between narrow-band and wide-band TLC formulations is the perceived observed color shift due to variation in lighting and viewing angle. Fergason (1966a) derived from first principles the change in the wavelength of peak spectral reflectance as a function of lighting and viewing angles. This is expressed in equation 3.14:

$$\lambda = \lambda_n \left[cos \frac{1}{2} \left\{ sin^{-1} \left(\frac{n_{air}}{\overline{n}_{TLC}} sin(\phi_{TLC,i}) \right) - sin^{-1} \left(\frac{n_{air}}{\overline{n}_{TLC}} sin(\phi_{TLC,s}) \right) \right\} \right] \tag{3.14}$$

Where n_{air} is the index of refraction for air and $\overline{n}_{TLC}$ is the average index of refraction for TLCs ($\overline{n}_{TLC} \approx 1.5$), λ is the wavelength of maximum scattering at $\phi_{TLC,i}$ angle of incidence and a viewing angle of $\phi_{TLC,s}$ and λ_n is the wavelength of maximum scattering for normal incidence and observation. Figure 3.13 shows how these angles are defined. Figure 3.13 is a polar plot illustrating the variation of the maximum spectral reflectance wavelength fixing the indices of refraction for air and TLC at their approximate values. Two cases are examined in this figure, an on-axis arrangement were a white light source and angle of observation are moved together over a TLC-coated isothermal surface ($\phi_{TLC,i} = -\phi_{TLC,s}$) and the situation where the white light source is maintained normal to the surface ($\phi_{TLC,i} = 0°$) and $\phi_{TLC,s}$ is varied. This behavior is at variance with results from Herold and Wiegel (1980) and implemented by Farina et al. (1994) who argued that an on-axis arrangement provides a negligible shift in the perceived color. This is believed to be due to a misinterpretation of the angle definitions when Herold and Wiegel (1980) built on the work presented by Fergason (1968). Equation 3.14 instead suggests that the lighting angle and viewing angle should be positioned opposite to each other. These effects have been found to be less important with narrow-band crystals (Baughn (1995), Camci et al. (1993) and Drost and Bölcs (1999)) because the data processing techniques are based on the observation of color change, rather than a measurement of the perceived TLC color.

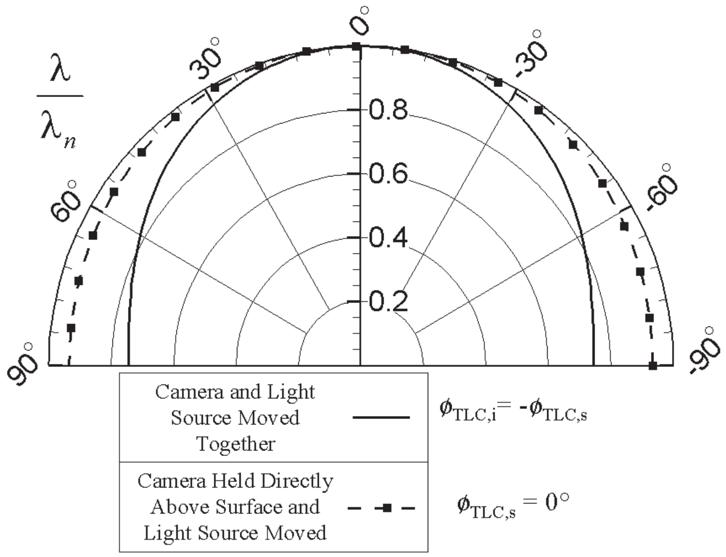

Figure 3.14: Lighting and viewing angle effects on wavelength of maximum reflectance (derived from Fergason (1968)).

Fergason (1968) and Herold and Wiegel (1980) both observed that TLCs circularly polarize incident white light. Hacker and Eaton (1995) and Farina et al. (1994) used this fact to improve the signal to noise ratio of their system by placing crossed linear polarizers on the light source and receiving optics. This only allows the colored component of light to pass into the observation system.

If TLCs are heated beyond their activation range, even for short periods of time, their color response when cooling differs substantially (Baughn et al. (1999)). Anderson and Baughn (2004) suggested that this hysteresis effect was linked to slight changes in the organization of the cholesteric phase. These were found to be reversible if the TLCs are cooled below their activation start temperature. The higher the temperature was raised above the activation temperature range, the more pronounced and permanent this shift can become.

Evans et al. (1998) found no significant shifts in the color response of TLCs in the presence of electric fields up to 150 kV/m. Ireland and Jones (2000) investigated the effects of pressures up to 133 bars, and observed no effect on encapsulated TLCs. Syson et al. (1996) found no discernable effect on the encapsulated TLC response under rotational acceleration up to $1.6(10)^4$g. Wiberg and Lior (2004) performed a range of tests that revealed that thicker TLC coatings are less susceptible to aging and thickness non-uniformities. Furthermore, these tests revealed that the spectral reflectance of a TLC-coated surface is sensitive to the paint thickness. These authors also reported that thicker layers are generally less sensitive.

Fergason (1968) found that the thermal response time of unencapsulated cholesteric liquid crystals was about 100 ms. Interestingly, Ireland and Jones (1987 and 2000) found that the response time of encapsulated TLCs was a few milliseconds with a TLC layer thickness of 10-μm applied to a heater foil. Wiberg and Lior (2004) reported that the response time is not only due to the physics of TLCs, but the thickness of the applied layer – thinner films have faster response times.

Fergason (1966a, 1966b and 1968) and Parsley (1991a and 1991b) provide additional details on the fundamental structure and characteristics of cholesteric liquid crystals. Furthermore, these references provide some direction on modeling some of the key behaviors of TLCs.

3.2.2 Introduction to TLC Thermography

There are two classes of TLC temperature measurement approaches, the single isotherm (narrow-band) technique and the true-color (wide-band) technique. Clearly, these names suggest the appropriate choice for bandwidth of the applied TLC. The single isotherm technique has been used for and developed over a longer time. It has the advantage of requiring very little in the way of imaging equipment and uses TLCs with an activation bandwidth of typically 1°C or less. Due to this technique's near binary nature, it can be very accurate. This measurement technique is typically used with transient experiments to indicate when a certain temperature is achieved. It can also be used in steady state experiments, but due to its intrinsic nature it cannot give full-field surface measurements with a constant surface thermal boundary condition. Consequently, a large number of images are required to completely map out a surface. Martinez-Botas et al. (1995), Ireland and Jones (1985, 1986 and 1987), Hippensteele and Russell (1988), Giel et al. (1996) and Camci et al. (1993) have developed and demonstrated the successful application of this technique to wide ranging flow conditions and situations.

The wide-band TLC measurement technique has become more widely used with the introduction of lower cost cameras and data acquisition hardware. The primary challenge with this approach is calibrating the TLC response over the active temperature range (10-15°C), while maintaining a high level of accuracy. The issue of representing the perceived color of a TLC-painted surface and calibrating the crystal response has been the subject of research for more than 20 years. Papers by Akino et al. (1983, 1986, 1987, 1989 and 1989) formed the basis for the implementation of digital image processing to the interpretation and calibration of the TLC color response. In typical video processing, the reflected spectral distribution from the liquid crystal surface is decomposed into three components, red (R), green (G) and blue (B) as shown below:

$$\begin{aligned} R &= \int_{-\infty}^{\infty} g_R(\lambda) O(\mathbf{x}, \lambda) d\lambda \\ G &= \int_{-\infty}^{\infty} g_G(\lambda) O(\mathbf{x}, \lambda) d\lambda \\ B &= \int_{-\infty}^{\infty} g_B(\lambda) O(\mathbf{x}, \lambda) d\lambda \end{aligned} \tag{3.15}$$

Where $g_R(\lambda)$, $g_G(\lambda)$ and $g_B(\lambda)$ are the filter transmissivities for their respective channels and $O(\mathbf{x}, \lambda)$ represents the spatial spectral distribution incident on the receiving optics of the overall system. The camera outputs these components as analog voltages. Depending on the digital resolution of the frame grabber (digitizer) board, these components are converted from analog voltages to unsigned 8-bit integers, ranging from $0 \leq R \leq 255$. Hacker and Eaton (1995) pointed out that the set of equations shown above is a rather simplistic model of the spectral distribution incident on the camera. These authors developed a more thorough analysis on the incident spectral distribution; incorporating, the effects of the view factor of the illumination, camera and surface location of interest, camera aperture, and the pure reflection at the binder surface as shown in figure 3.13. The conclusion of this analysis revealed that $O(\mathbf{x}, \lambda)$ can be expressed as a linear combination of the TLC reflected component (defined as $C(\mathbf{x}, \lambda)$) and a component that consists of any pure reflection in the optical path (defined as $W(\mathbf{x}, \lambda)$):

$$O(\lambda) = W(\mathbf{x}, \lambda) + C(\mathbf{x}, \lambda) \tag{3.16}$$

Inserting this form into equation 3.15 produces the following functions for the behavior of each color component as a function of temperature:

$$\begin{aligned} R(T(\mathbf{x})) &= \overline{C}_R(\mathbf{x}, T) + \varphi_R \\ G(T(\mathbf{x})) &= \overline{C}_G(\mathbf{x}, T) + \varphi_G \\ B(T(\mathbf{x})) &= \overline{C}_B(\mathbf{x}, T) + \varphi_B \end{aligned} \tag{3.17}$$

Where φ_R, φ_G and φ_B are constants, given a constant illumination level. The terms $\overline{C}_R(\mathbf{x},T)$, $\overline{C}_G(\mathbf{x},T)$ and $\overline{C}_B(\mathbf{x},T)$ are defined as:

$$\begin{aligned}
\overline{C}_R(\mathbf{x},T) &= \int_{-\infty}^{\infty} g_R(\lambda)C(\mathbf{x},\lambda)d\lambda \\
\overline{C}_G(\mathbf{x},T) &= \int_{-\infty}^{\infty} g_G(\lambda)C(\mathbf{x},\lambda)d\lambda \\
\overline{C}_B(\mathbf{x},T) &= \int_{-\infty}^{\infty} g_B(\lambda)C(\mathbf{x},\lambda)d\lambda
\end{aligned} \tag{3.18}$$

The R, G, B components can be directly calibrated to the temperature response using a 4-D hypersurface of the form:

$$T \approx f_c^t(R(T), G(T), B(T)). \tag{3.19}$$

There are three reasons why this approach is not followed: unavoidable variations in illumination strength applied to the liquid crystal coated surface and historical and practical reasons. Instead these components are combined to form a color index, expressed as a hue angle (which shall be termed as Q). This allows direct examination of the calibration resolution and gives greater control of its resulting accuracy. In other words, the definition of hue angle can be adjusted, using variation combinations of R, G and B to conform to given constraints. Hacker and Eaton (1995) argue from a physical perspective that a robust definition of Q should conform to the following requirements:

1. It produces a monotonic calibration function of temperature for all TLCs.

2. It is invariant to linear changes in lighting intensity, i.e. $Q(R,G,B) = Q(\varrho R, \varrho G, \varrho B)$.

3. It is reflection invariant for white light, $Q(R,G,B) = Q(R+\varphi_R, G+\varphi_G, B+\varphi_B)$.

Hacker and Eaton (1995) and Farina et al. (1994) stressed the importance of these properties with respect to developing a TLC calibration that was portable and even allowed the use of different lighting sources under the following conditions: the light source is white, i.e. $\varphi_R = \varphi_G = \varphi_B$ and the reflected spectral response to illumination intensity changes is linear. Hacker and Eaton (1995) detail, after much experimentation, that the definition of hue that best meets this requirement is:

$$Q = \frac{255}{2\pi} tan^{-1} \left\{ \frac{\frac{1}{2}R - \frac{1}{2}G}{-\frac{1}{4}R - \frac{1}{4}G + \frac{1}{2}B} \right\}. \tag{3.20}$$

This parameter was defined to vary between $0 \leq Q \leq 255$. If direct application of equation 3.20 gives values outside this range, $\frac{2\pi}{255}$ is added or subtracted, to ensure the value falls in the desired range.

Wang et al. (1996), Hay and Hollingsworth (1996 and 1998) have investigated other definitions of hue angle. It is crucial to note that these definitions refer to the interpretation of the observed TLC color. Most recent studies that examine the behavior of TLC use a measurement of the perceived color via hue angle, rather than direct measurement of the wavelength of maximum spectral reflectance. This means that depending on the definition of the hue angle, the perceived changes in color depend not only changes in structure of the applied TLCs, but its corresponding color interpretation.

3.3 In-situ TLC Calibration System

A survey of narrow and wide-band TLC measurement techniques reveals that *in-situ* calibrations are generally more robust and accurate than their portable counterparts (Moffat (1990), Babinsky and Edwards (1996) and Sabatino et al. (2000)). The primary reason is the optical path for both illumination and viewing are identical from calibration to measurement. This loosens many of the requirements for the TLC thermography as described by Farina et al. (1994) and Hacker and Eaton (1995). For example, the borescope imaging system did not use crossed linear polarizers. This was done for two reasons: due to the size of the rotary mirror sleeves, inserting and verifying the orientation of polarizing film discs was found near impossible and the lack of cooling caused the polarizing film to gradually degrade when exposed to light. Hacker and Eaton (1995) reported that polarization greatly reduces the light throughput for the system: practically and paradoxically increasing, rather than reducing, the signal-to-noise ratio of the resulting measurement. An obvious response to this problem is to increase the intensity of the light source – increasing the rate of degradation of the polarizer. These authors suggested that their proposed definition of Q could account for the impact of pure reflection, eliminating the need for polarizers.

Hollingsworth et al. (1989) found variations in the perceived color along a relatively large (0.385-m x 0.215-m), flat isothermal surface. This was traced to slight changes in lighting and viewing angle along the surface. This was accounted for by arbitrarily dividing the image into ten, equally-sized, rectangular blocks and establishing a calibration curve for each. Günther and von Rohr (2002) reported that the variation in viewing angle along a flat surface can be removed by the use of a telecentric lens, reducing the dependence of perceived color to only illumination angle. Mukerji and Eaton (2002) extended this approach to a highly curved surface in a 1970-era first stage rotor blade single passage model with 42 rectangular zones, with their sizes chosen in accordance with local changes in lighting and viewing angle. This calibration approach also involved multiple camera aperture settings for the acquisition of a single TLC temperature map. Again, this is due to the large changes in illumination across the surface, causing corresponding signal variations. Sabatino et al. (2000) presented a point-wise calibration technique for TLC measurement, consisting of almost $2(10)^5$ calibration curves for a single image. This approach essentially trades computational efficiency for increased accuracy when compared to a zonal calibration system.

All the previously mentioned in-situ calibration techniques rely on an isothermal surface that has the same geometry as the measurement surface. The surface temperature would be slowly raised through the activation range of the applied liquid crystal. At each set temperature, the surface would be imaged, and the calibration curves would be constructed. Elkins et al. (2001) developed a mini calibrator that can be placed on multiple sites on curved surfaces. This has the advantage of applying wide-band liquid crystal thermography to large, curved surfaces where an isothermal, in-situ calibration process is impractical.

Due to the more complex nature of the imaging system applied in the single passage model under study, it was necessary to develop a calibration system that ensured high accuracy ($\pm 0.1^{\circ}$C) thermography, accounting for the strong distortion effects of the borescope, conformal window and highly-curved measurement surfaces.

3.3.1 In-situ Calibration Apparatus

Following the approach presented by Mukerji and Eaton (2002), two oxygen-free, high conductivity (OFHC) calibration pieces were machined corresponding to suction and pressure side measurement surfaces. As with other components, the calibration components were machined with extremely tight tolerances, to ensure geometric fidelity with the geometry calibration and measurement surfaces. These pieces consisted of the calibration surface and a thermal mass that sandwiched arrays of thermoelectric coolers (TECs). Both components were machined within a tolerance of ± 0.025-mm using a three-axis CNC milling machine, using a fabrication control program, MASTERCAM (CNC Software (2000)) to generate the necessary machine instructions from AutoCAD drawings. The thickness of all pieces was 50.8-mm, consistent with the measurement surfaces. Figure 3.15 presents

Table 3.1: Pressure side calibrator TEC configuration.

Zone	Melcor TEC Part Number	Dimensions (mm)	Number of TECs
TEC PS #1	CP 1.0-17-05L	12 x 12 x 3.16	3
TEC PS #2	CP 1.0-17-05L	13 x 12 x 3.16	3
TEC PS #3	CP 1.0-63-05L	15 x 15 x 3.16	3

Table 3.2: Suction side calibrator TEC configuration.

Zone	Melcor TEC Part Number	Dimensions (mm)	Number of TECs
TEC SS #1	CP 1.0-7-05L	8 x 8 x 3.16	5
TEC SS #2	CP 1.0-7-05L	8 x 8 x 3.16	5
TEC SS #3	CP 1.4-127-045L	40 x 40 x 3.3	1

labeled cross-sectional views of the calibrator assemblies. The calibrators were accurately positioned in the single passage model using dowel pins installed in the Ren Shape endwalls.

The TECs were used to heat or cool the calibration surface to set and maintain an arbitrary uniform surface temperature (within $\pm 0.1°C$) above or below the ambient temperature. As most standard TECs come in square dimensions it was necessary to construct rectangular arrays of coolers for each zone labeled in figure 3.15. These TECs were soldered together side-by-side with a low temperature bismuth-tin solder (Melcor # SLD-BiSn-2W). Tables 3.1 and 3.2 list part numbers for the thermoelectric coolers for each zone shown in figure 3.15. To ensure that the assembled part met the necessary tolerances, each TEC was lapped to ensure the thicknesses shown had a tolerance of ± 0.0127-mm. Before installation, the TECs were coated in a thin layer of heat sink compound (Dow Corning # 340).

The temperature of the calibration surface was measured by an array of eleven strategically positioned thermistors with an interchangeable error of $\pm 0.1°C$ (Cornerstone Sensors #T320D103-CA, $R_{25} = 10\text{k}\Omega$). These thermistors had been experimentally found by Elkins et al. (2001) to provide temperature measurements as accurate as type-K thermocouples with minimal noise problems. Furthermore, the control and monitoring system for thermistors was less cumbersome than that required for thermocouples. For strain relief purposes the original thermistor leads (nickel bifilar) were severed and 36-gage wires were soldered, using an acrylic adhesive (Permabond # 810) rather than solder flux for bonding purposes. Each thermistor assembly was then inserted into wells drilled into the calibration surface and secured with thermally conductive epoxy (Omegabond 101 #OB-101-1/2). The locations of these wells were chosen to ensure that each zone shown in figure 3.15 was instrumented with at least 5 thermistors (some of which overlapped). Figure 3.16 presents the completed pressure side calibrator installed in the single passage model. Also, this figure shows the suction side window piece that is used to view the calibrator and measurement surface.

It was necessary to construct circuitry to power the TECs and extract temperature data from the thermistors installed in the calibrators. The power circuit for the TECs was derived from Elkins et al. (2001) by Glassman (2000). It consisted of three National Semiconductor LM12 80W operational amplifiers powered by a dual output DC power source (Power-One #HCC15-3-A, ±12V, ±3.4A). Figure 3.17 presents a simplified circuit diagram of the power supply for the calibrator thermoelectric cooler system. Not shown in this figure is a cooling fan (Digi Key # CR148-ND) and heat sinks (Digi-Key # HS149-ND) that were used to cool the amplifiers. Two data acquisition cards with digital-to-analog converter (DAC) outputs were used to operate each amplifier. The size of the resistors R_3 shown in figure 3.17 were chosen to maximize the current output of the power supply at the maximum output of the DAC (±10V). This was computed using equation 3.21, shown below:

$$I_L = \frac{2V_{DAC}}{R_3}. \tag{3.21}$$

This was derived from standard operational amplifier analysis techniques (Malik (1995)). This analysis generated an optimal resistance of $R_3 = 18.0\Omega$ (Digi-Key 18W-10-ND, 18Ω, 10W, 5%) with maximum current output of $I_L = \pm 1.1$A with an input voltage $V_{in} = \pm 10$V.

The thermistor sensing circuit was again based on work developed by Elkins et al. (2001). Figure 3.18 presents the a simplified current divider circuit used to measure the resistance of the thermistor. V_1 is the supply voltage, V_2 is the measured voltage drop across the thermistor leads and R_1 is a control resistance used to limit the current through the circuit ($< 50\mu A$, $R_1 = 30$ kΩ) and a reference for computing the resistance response of the thermistor, as shown in equation 3.22.

$$R_{therm} = R_1 \frac{V_2}{V_1 - V_2} \tag{3.22}$$

The ratio $\frac{R_{therm}}{R_{25}}$, where R_{25} is the known resistance at 25°C and R_{therm} is the measured resistance, is then used to determine the measured temperature, via standardized calibration curves provided by the manufacturer (Cornerstone Curve D). With this basis, Elkins et al. (2001) developed a circuit using a regulated voltage supply (Maxim # ICL7663) –

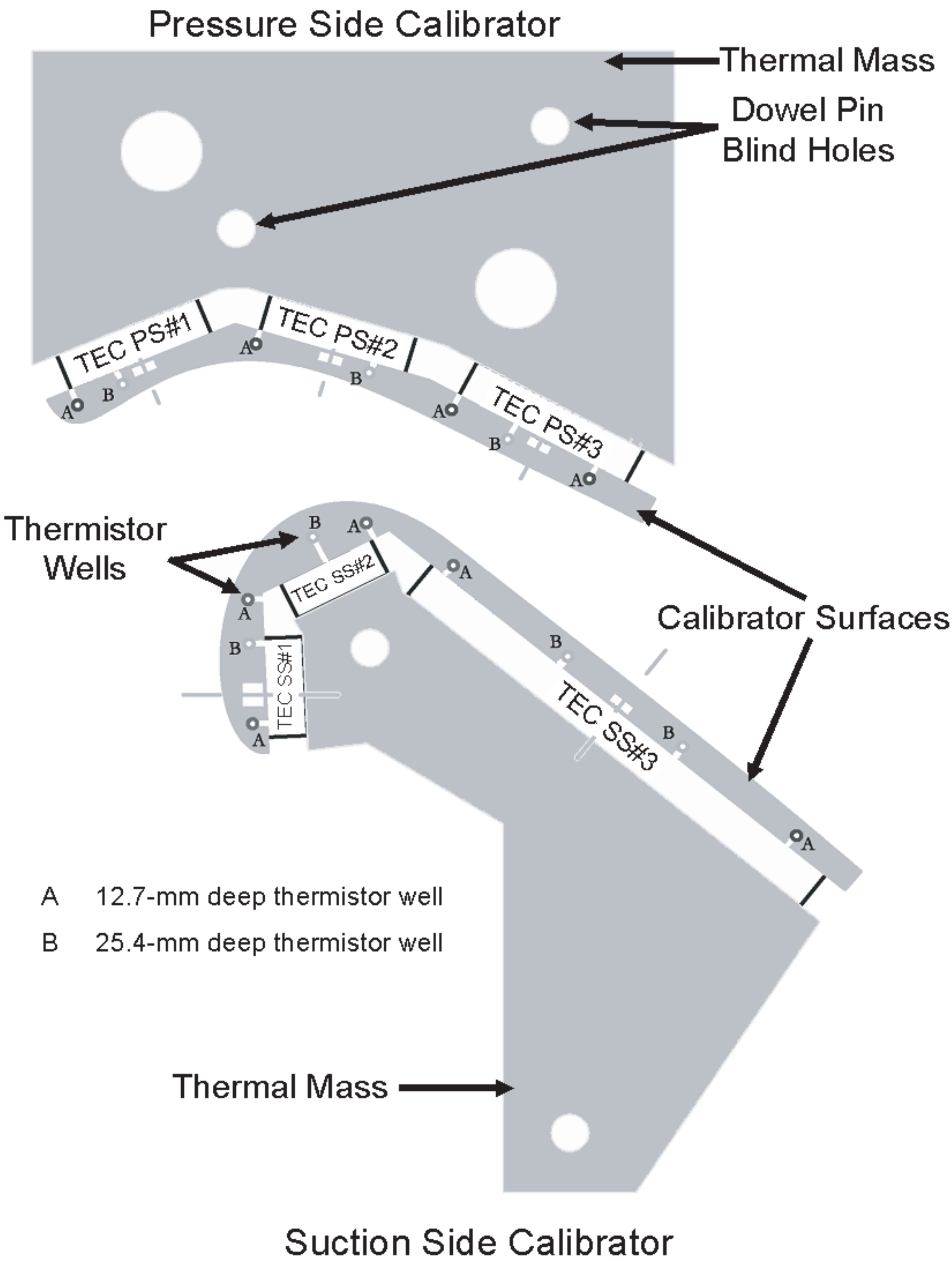

Figure 3.15: Schematic of pressure and suction side copper calibrator pieces.

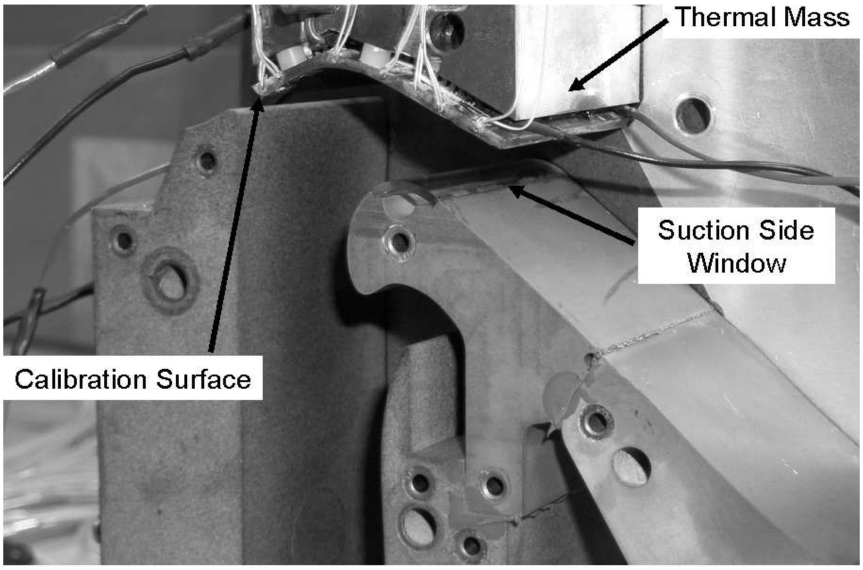

Figure 3.16: Pressure side copper calibrator installed in single passage model.

as shown in figure 3.19. The regulator was implemented with settings listed in this figure. A single thermistor was used to monitor the temperature of the mini calibrator. However, in the current application, several thermistors were used requiring the implementation of a multiplexer (Maxim # DG406), a schematic of which is shown in figure 3.20. Figure 3.21 presents the complete thermistor measurement circuit. The digital input/output (DIO) of a National Instruments DAQ card (MIO-16-E) installed in the liquid crystal measurement PC was used to set the multiplexer channel.

The temperature of the calibrator surface was set with a LabView-based proportional-differential-integral control with constants set iteratively based on a systematic trial-and-error process. This involved sequentially adjusting each constant until the transient response of the system was optimized. Typical control values for the pressure side calibrator were $K_p = 0.1$, $K_d = 0.5$ and $K_i = 0.0$.

3.3.2 Sample Preparation

As indicated in section 3.2.1, a micro-encapsulated thermochromic liquid crystal with a "red start to blue start" range 25°C to 30°C was used for temperature measurements (Hallcrest # BM/R25C5W/C17-10). Both the measurement and calibration surfaces were

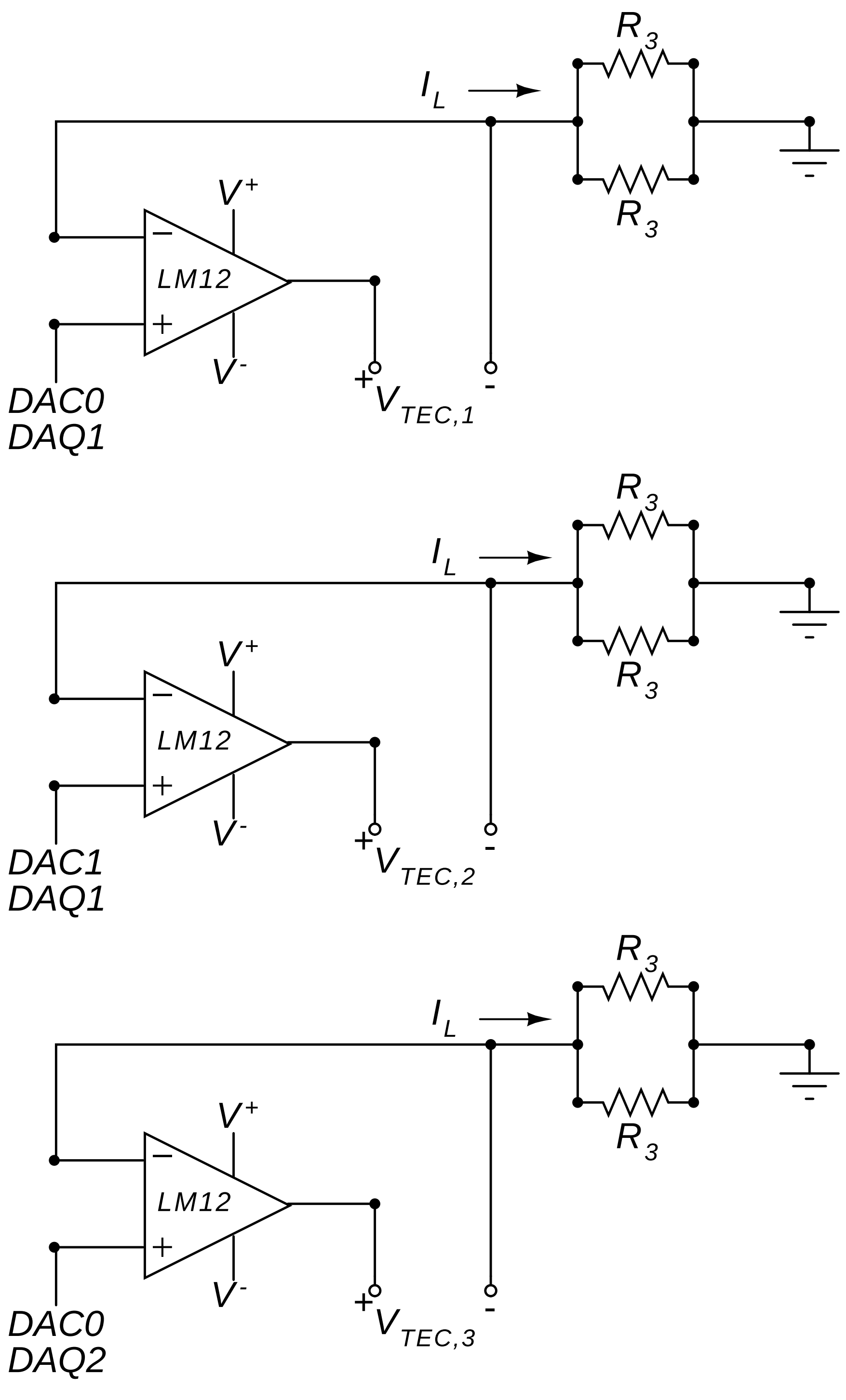

Figure 3.17: Calibrator thermoelectric cooler power circuit (modeled after Elkins et al. (2001)).

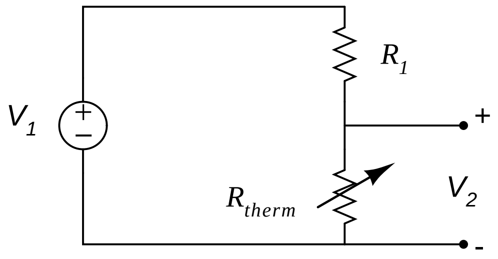

Figure 3.18: Simplified thermistor circuit.

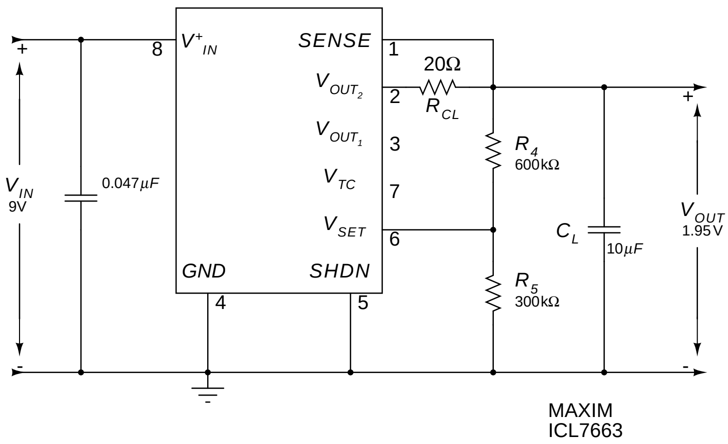

Figure 3.19: Maxim ICL7663 Voltage regulator for thermistor measurement circuit. *The numbers shown correspond to pin numbers*

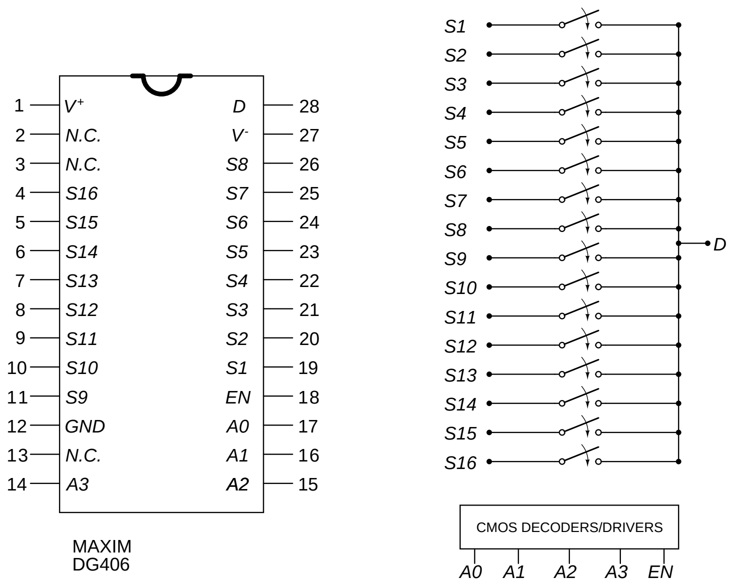

Figure 3.20: Maxim DG406 16-channel CMOS analog multiplexer for thermistor circuit. *The numbers shown correspond to pin numbers*

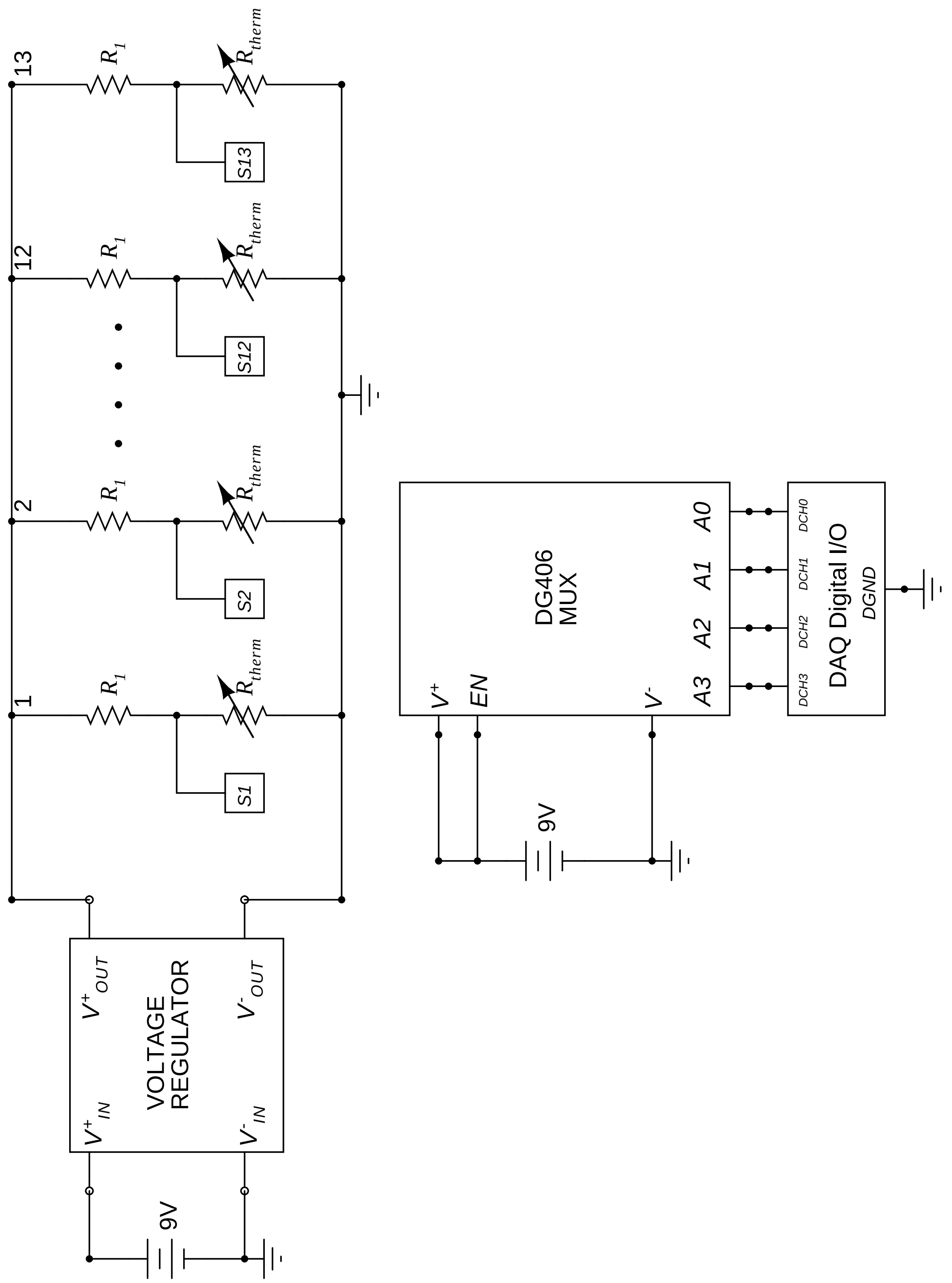

Figure 3.21: Overall multi-thermistor circuit.
The numbers shown correspond to thermistors

painted at the same time to ensure consistent application. It was vital that the calibration surface have nearly identical paint thickness and consistency. The copper calibration surface was cleaned with metal polish (Brasso) and ethyl alcohol. The measurement surface was carefully cleaned with ethyl alcohol and a kimwipe, using techniques similar to cleaning optical components. This process was conducted ensuring that the measurement surface was not scratched. Two cardboard platforms were used to hold the two surfaces side-by-side. A separate 254-mm $\times$ 50.8-mm card calibration strip (Kodak Polycontrast RC III photographic paper) was simultaneously prepared along with the copper calibration and measurement surface during this process. This was to quantify the degradation of the light source during measurements (this is described in greater detail in section 3.3.3)

Farina et al. (1994) presented a systematic procedure for applying such a coating. This process consists of two steps: application of a black backing paint and the application of the TLC coating. A Paasche single-action type H airbrush with a steady compressed air supply at 50 psi was used to apply both coats. The airbrush was equipped with a fine-tip mixing nozzle (#1). To prevent contamination, separate nozzles were used to apply the black and TLC paint. A 1:1 volume ratio of Hallcrest BB-G1 black backing paint and distilled water was thoroughly mixed with a magnetic stirrer for at least ten minutes. The diluted mixture was injected through a 25-mm syringe filter holder (VWR # 28163-045) containing a 43-μm (VWR # 28498-236) into an airbrush reservoir. The paint was applied in thin coats to both surfaces in smooth, sweeping strokes: the surfaces were rotated regularly between passes to ensure that final coat was even. For the surfaces in question, approximately 9-cc of the black paint mixture was used.

The TLC slurry was mixed with distilled water in the ratio 2:1 by volume. This mixture was applied in the same fashion as the backing paint. Wiberg and Lior (2004) reported that TLC layer should be as thick as possible, making the coat less susceptible to the effects of aging during calibration and measurement and thickness non-uniformities. Additionally, exploratory tests revealed that thicker films have increased overall spectral reflectivity, providing a “brighter” color response. This was especially important in maximizing the measurement signal-to-noise ratio considering the low-light throughput of the borescope imaging system. Thus, the TLC-water mixture was applied to the calibration and measurement surfaces until they appeared grey in their optically inactive state (approximately 12-cc of the mixture was used). The estimated total thickness of the BB-G1-TLC-coat was computed to be 50-μm.

3.3.3 TLC System Light Source

In spite of previous work by Hacker and Eaton (1995) and Mukerji and Eaton (2002), finding the appropriate light source for this imaging system required extensive experimentation. Trial-and-error tests determined that there were two crucial requirements for the light source: minimal illumination degradation and infrared (IR) and ultra-violet (UV) filtration, only allowing wavelengths in the visible range to pass. The first requirement recommended the use of tungsten halogen lamps instead of incandescent light sources. In contrast to incandescent lamps, tungsten halogen lamps rely on a complex chemical interaction between tungsten, oxygen and a halide to extend the service life of the lamp. In an ordinary incandescent lamp, tungsten from the hot filament vaporizes and deposits on the inner wall of the bulb. Over a period of time, the bulb wall blackens, light output decreases, and the filament narrows and weakens. In contrast, a halogen-cycle lamp contains a halogen gas (such as iodine) in addition to the normal gas fill. The halogen combines with the vaporized tungsten particles, and the compound migrates towards the filament. This molecule breaks down near the cooler areas of the filament redepositing the tungsten. This cycle increases lamp life while maintaining the output light spectrum and intensity. The IR and UV filtration limited radiative heating of the measurement surface and degradation of polarizers. This was very important as tungsten halogen lamps were exclusively used in this experiment. Halogens produce high-intensity light with about 90% of the energy being infrared. It was found more convenient and experimentally feasible to remove all polarization from the optical system. The issue of limiting degradation of the illumination spectrum and intensity was found to be essential to the entire TLC thermography system. This was because, as will be discussed in section 3.4, the calibration and measurement processes took lengthy (i.e. six week) periods to complete. To ensure the validity of the in-situ calibration, the quality of the light source had to be quantified and accurately maintained.

Two tungsten halogen light sources and three types of lamps were examined to identify which combination best met the constraints previously mentioned. Table 3.3 lists the combinations tested in decreasing order of peak brightness. Each of these lamps have slightly differing illumination spectral distributions. It was found that all of these lamps require approximately 4 - 5 hours of warm-up time after installation. Figure 3.22 present pictures of the HLX tungsten halogen lamp. This type of lamp was initially used to perform TLC temperature measurements in the single passage. However, it was discovered that the illumination spectral distribution degraded with time, with the overall light intensity of the

Table 3.3: Candidate light source and halogen bulb combinations.

Light Source	Halogen Bulb	Voltage	Power	Light Level (lm)	Bulb lifetime (h)
Schott # KL 2500 LCD	Osram, type HLX 64653	24V	250W	1300	50
Schott/Fostec Ace I # A20520	Ushio, type EKE	21V	150W	1080	200
Schott/Fostec Ace I # A20520	Eiko, type EKE	21V	150W	1080	200

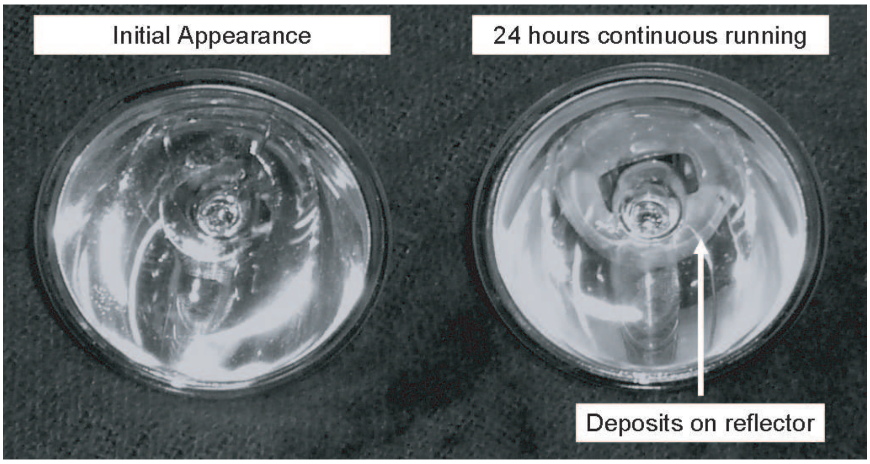

Figure 3.22: Initial and aged HLX tungsten halogen lamps.

lamp decreasing. Figure 3.23 presents average $\overline{R}$, $\overline{G}$ and $\overline{B}$ curves collected during sample runs with the mini calibrator to examine the effect of degradation on the TLC response. The second set of calibration data was taken after one-week of continuous operation, with no modification to the camera settings. Figure 3.24 presents the corresponding hue angle curves computed from the color component measurements. As this parameter is ultimately used to calibrate the TLC response and measure temperature, this figure makes it apparent that substantial measurement errors accrue as this particular lamp degrades. This was traced to deposits which formed on the lamp reflector, as indicated in figure 3.22. Figure 3.25 compares the appearance of Eiko and Ushio type EKE lamps. The sole difference between these two types is the configuration of their reflectors, the Eiko reflector produced

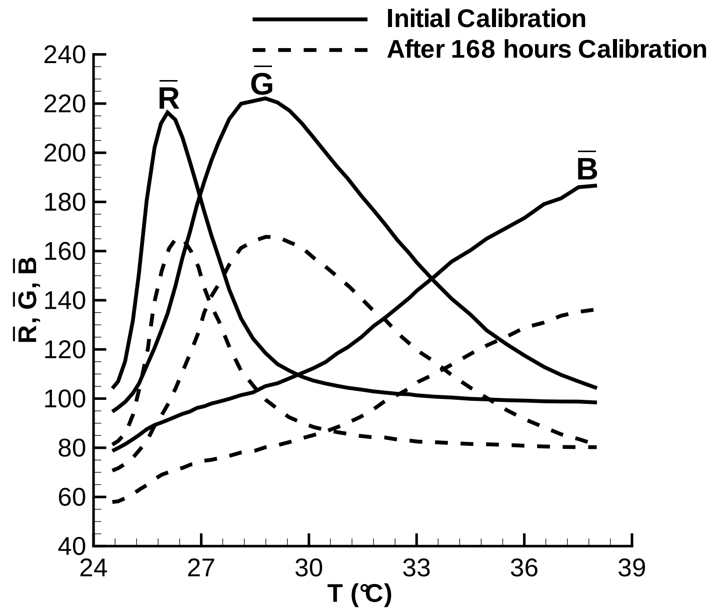

Figure 3.23: $\overline{R}$, $\overline{G}$, $\overline{B}$ curves showing degradation effects of HLX lamp illumination.

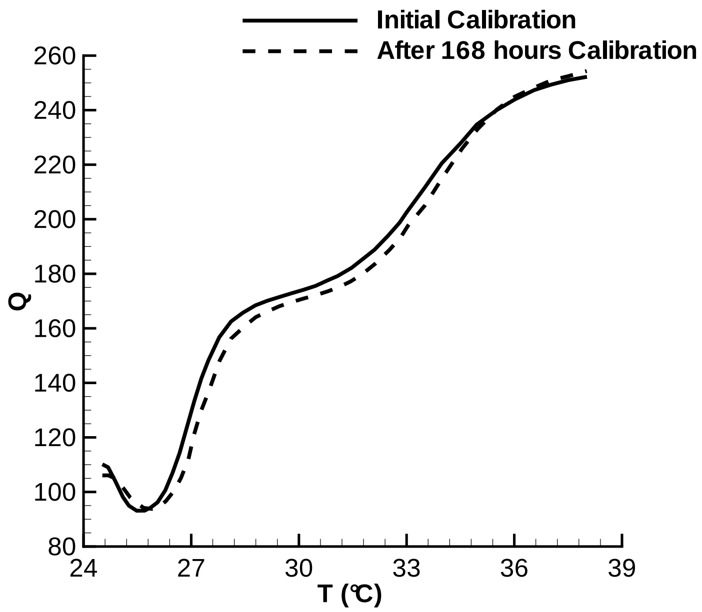

Figure 3.24: Q curves showing degradation effects of HLX lamp illumination.

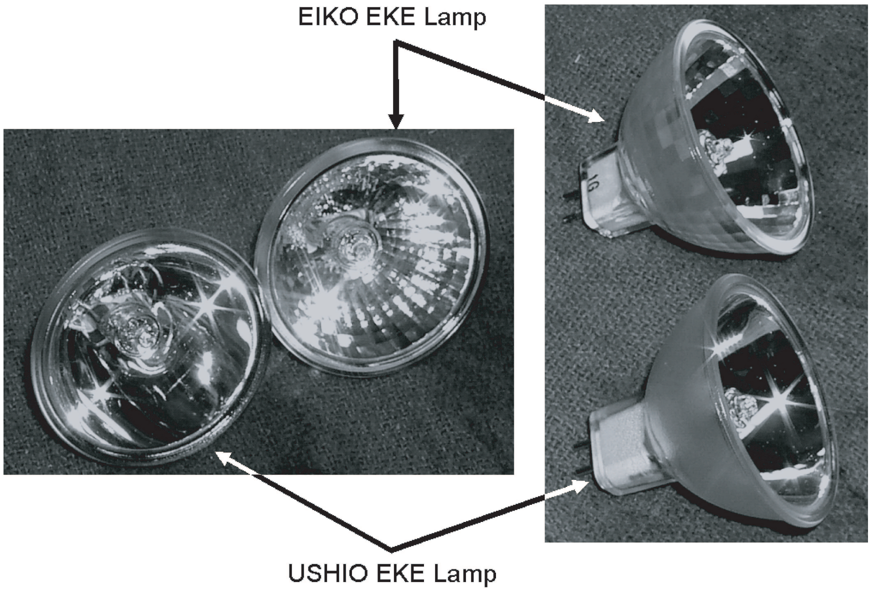

Figure 3.25: Eiko and Ushio EKE lamps.

more diffuse illumination. The lighting elements of the two lamps were found to be identical. Given that the light source requires the lamp to focus its illumination on the entry point of a light guide, the more diffuse the lamp reflector is, the less light is output at the end of the light guide. Figure 3.26 displays $\overline{R}$, $\overline{G}$ and $\overline{B}$ calibration curves over a 72 hour period. These curves show very little degradation of the illumination spectrum over this period. Figure 3.27 presents the resulting Q curve, showing that the effect of slight differences observed in figure 3.26 have a negligible impact ($< 0.1°$C shift at a given Q value) on the hue angle calibration curves. This behavior was duplicated in similar tests with the Ushio EKE lamp, and thus this configuration was used for all measurements. Additional qualification tests involved turning the light source off the on and repeating the calibration and replacing the lamp. These all showed that the changes in the illumination spectrum were $< 0.1°$C. Hence, it was possible to change lamps during data collection without invalidating the in-situ calibration, provided the camera settings remained identical. To ensure this was the case during measurement, the mini calibrator was used to test the light source during data acquisition. If any problems were detected, the lamp was replaced.

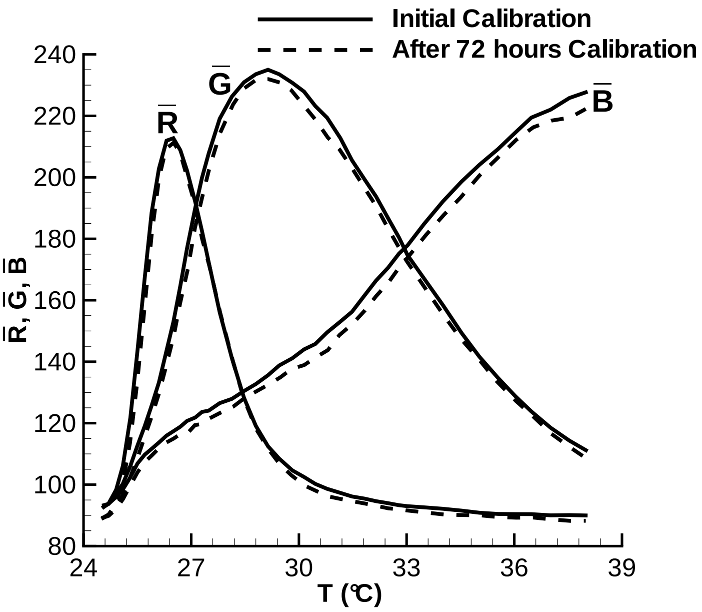

Figure 3.26: $\overline{\overline{R}}$, $\overline{\overline{G}}$, $\overline{\overline{B}}$ curves for EKE EIKO lamps, showing negligible illumination degradation.

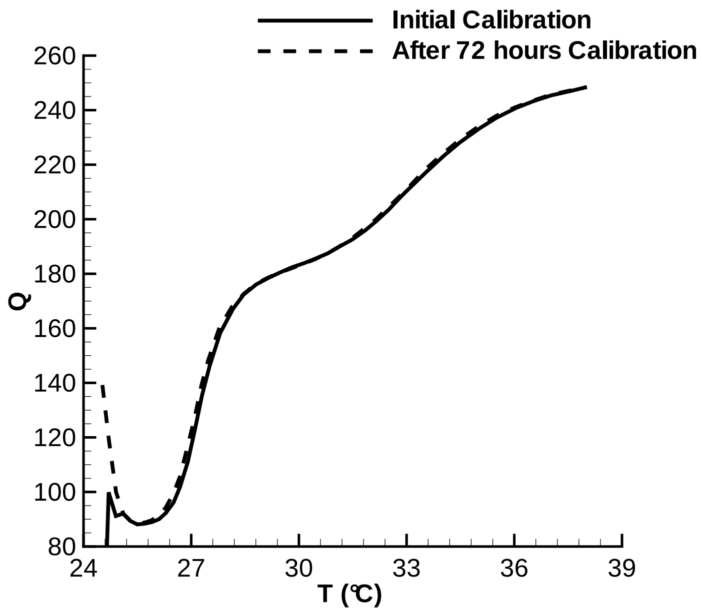

Figure 3.27: Q curves for EKE EIKO lamps, showing negligible illumination degradation.

3.4 TLC Calibration and Measurement Algorithms

The overall calibration process consisted of initially determining the RMS positions and camera settings necessary to image the pressure side wall. The geometry calibration surface was used to identify the necessary RMS settings on each borescope, as well as developing the geometry correction data as described in section 3.1.2. The pressure side in-situ copper calibration was then installed in the model. At each borescope setting, maps of color components R, G and B were stored at various temperatures. Additionally, during this process the camera settings (as described in greater detail in section 3.4.2) were determined. The color component maps were used to determine the gradients of perceived color across the observed regions of interest and thus determine the size and shape of the calibration zones to account for this effect. Due to the distortion effects along the optical path, the illumination of the surface at each borescope setting was highly uneven. Consequently, it was necessary to adjust the iris on the light source to prevent saturation of the image acquisition system. This was recommended by the light source manufacturer, as it kept the light intensity from the lamp constant, limiting any degradation effects. This process took approximately one-and-a-half weeks to complete and was concluded by a validation test where the calibration surface was set to a known temperature and temperature maps stored. The following subsections provide additional details on these steps and their rationale.

3.4.1 Borescope Adjustment Settings and Image Manipulation

Given the field of view of the borescopes and the locations of the suction side viewing wells, it was necessary to rotate the borescope RMS to several different angles to view the pressure side wall of the single passage airfoil geometry. It was also necessary to correct the viewed images for visual distortions due to the viewing optical path. Table 3.4 lists the typical borescope adjustments for measurements on this surface. The light (θ_{la}) and borescope angles (θ_{ba}) refer to the setting of the rotary mirror sleeves on the viewing and illumination borescopes. These were set to be identical for ease of implementation and empirical evidence that suggested that these should be identical to have the highest possible lighting intensity. Two linear image transformations were performed within the measurement software to correct for the orientation and mirroring of the borescope output image before conducting geometry correction and TLC measurement algorithms. Figure

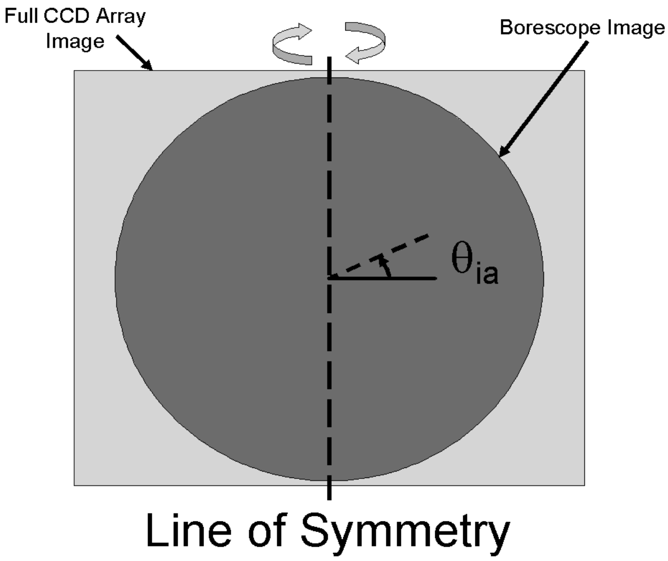

Figure 3.28: Linear transformation operations accounting for borescope mirroring and rotation effects.

Table 3.4: Borescope settings to observe pressure side wall.

Zone	θ_{la}	θ_{ba}	θ_{ia}	$\sigma_{G,i}$
1	-60°	-60°	-34.0°	0.050
2	-40°	-40°	-52.0°	0.100
3	0°	0°	-98.0°	0.150
4	20°	20°	-120.0°	0.150

3.28 demonstrates the "flipping" and rotation operations on the camera image by a user-defined angle θ_{ia} to account for the mirror and RMS effects on the output borescope image. The smoothness parameter, $\sigma_{G,i}$ is set during the geometry calibration process on the linear transformed camera image, as described in section 3.1.2.

3.4.2 Imaging System Settings

After exploratory tests, it was found, as shown in figure 3.26 that for the applied TLC the peaks for $\overline{R}$, $\overline{G}$ and $\overline{B}$ approximately occur at 26.7°C, 29.1°C and 38.0°C, respectively. These were used as set-points to determine the various camera settings and establish cells for the in-situ calibration. This was because it was believed that these temperatures corresponded to conditions where the greatest variations in perceived color would be observed.

Table 3.5: Sony XC-003 Camera settings for measurements.

Parameter	Value
Gain	04dB
C.Temp	3200K
Wht. Balance	Manual
R. Gain	-015
B. Gain	+010
Shutter	Normal
Speed	006-FRM
Frm/Fld	FRM

Table 3.5 summarizes the typical Sony XC-003 camera settings. In normal acquisition mode, the display rate for the imaging system (camera and digitizer) is thirty frames per second. The shutter speed can be decreased to raise the integration time of the camera's CCD arrays. The "speed" setting shown in table 3.5 corresponds to the number of frames over which the CCDs are exposed (thus 006-FRM corresponds to a 6-frame integration interval with a display rate of approximately 5 frames per second). The longer the integration interval for each image, the longer the data acquisition time. 10 images were used to compute a single average image, this represented a compromise between necessary sampling time and statistically converged data. Another parameter which affects the output camera signal is the gain setting. Experimental tests found that the higher this value was set the greater the noise of the resulting measurements. Thus this value was selected as the smallest value that produces near saturated images for the brightest measurement locations.

The red and blue gain settings (R. Gain and B. Gain) were adjusted to correct for the borescope color skewing effect mentioned in section 3.1. These were set empirically using a similar procedure as discussed in section 3.4.4. These values can be considered as coarse gain control for the appropriate color components.

Table 3.6 presents typical settings for the imaging system, including the light source iris setting derived from the preliminary tests described in this section. Each group of settings is termed as a measurement *zone*. The higher letter designation correspond to brighter light source settings. Each letter increment corresponds to an approximate 20% change in lighting intensity, with F corresponding to the maximum iris diameter. These are arbitrary positions of the light source iris that were user-defined.

Table 3.6: Imaging system settings for measurement.

Zone	θ_{la}	θ_{ba}	θ_{ia}	Camera Gain	Light Aperture
1	-65.0°	-65.0°	-29.5°	07dB	F
2	-40.0°	-40.0°	-52.0°	07dB	F
3	0.0°	0.0°	-98.0°	03dB	F
4	0.0°	0.0°	-98.0°	03dB	B
5	0.0°	0.0°	-98.0°	03dB	A
6	20.0°	20.0°	-120.0°	03dB	F
7	20.0°	20.0°	-120.0°	03dB	B
8	20.0°	20.0°	-120.0°	03dB	A

3.4.3 Calibration Grid Algorithm

At each setting listed in table 3.6 one or more of the collected color component maps was used to determine the calibration grid, once the overall ROI coordinates ([X_{min},Y_{min}], [X_{max},Y_{max}]) had been determined. These maps represented ensemble-averaged images $\overline{R}(X,Y)$, $\overline{G}(X,Y)$ and $\overline{B}(X,Y)$. The grid was determined by an adaptive, iterative algorithm that can be described as: Given an ROI of pixel dimensions [$X_{min,0}$,$Y_{min,0}$], [$X_{max,0}$,$Y_{max,0}$], spatial averages for each component are computed using the equation set shown below:

$$\begin{aligned}
\overline{\overline{R}}_0 &= \frac{1}{\vartheta}\int_{X_{min,0}}^{X_{max,0}}\int_{Y_{min,0}}^{Y_{max,0}} \overline{R}(X,Y)dXdY \\
\overline{\overline{G}}_0 &= \frac{1}{\vartheta}\int_{X_{min,0}}^{X_{max,0}}\int_{Y_{min,0}}^{Y_{max,0}} \overline{G}(X,Y)dXdY \\
\overline{\overline{B}}_0 &= \frac{1}{\vartheta}\int_{X_{min,0}}^{X_{max,0}}\int_{Y_{min,0}}^{Y_{max,0}} \overline{B}(X,Y)dXdY
\end{aligned} \tag{3.23}$$

Where ϑ is defined as:

$$\vartheta = (X_{max,0} - X_{min,0})(Y_{max,0} - Y_{min,0}) \tag{3.24}$$

As indicated in figure 3.29, the ROI is divided into four equal-sized sub-ROIs, which are defined as *cells* for the purposes of the grid algorithm. The spatial averages $\{\overline{\overline{R}}_i : i = 1, \ldots, 4\}$, $\{\overline{\overline{G}}_i : i = 1, \ldots, 4\}$ and $\{\overline{\overline{B}}_i : i = 1, \ldots, 4\}$ are then computed for each cell using the appropriate forms of equation 3.23. Defining ε_R, ε_G and ε_B as the difference between

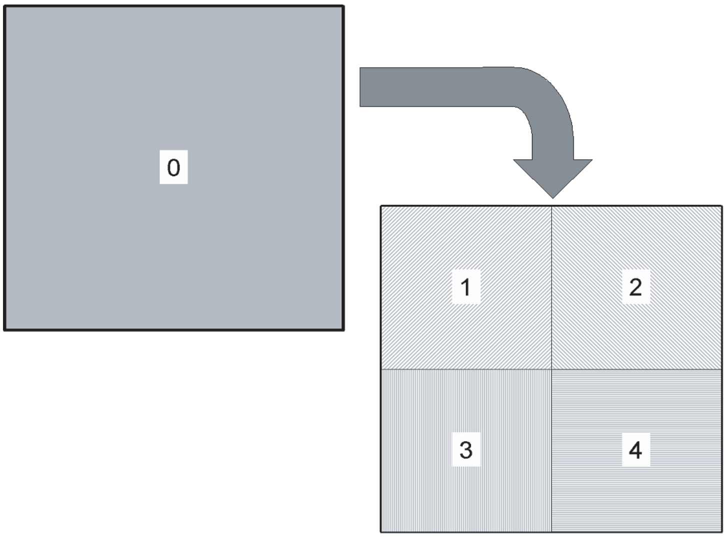

Figure 3.29: Linear transformation operations accounting for borescope mirroring and rotation effects.

the mean component values for the sub-ROI versus the main ROI, as shown below:

$$\varepsilon_R = \sum_{i=1}^{3} (\overline{\overline{R}}_0 - \overline{\overline{R}}_i)^2$$
$$\varepsilon_G = \sum_{i=1}^{3} (\overline{\overline{G}}_0 - \overline{\overline{G}}_i)^2 \tag{3.25}$$
$$\varepsilon_B = \sum_{i=1}^{3} (\overline{\overline{B}}_0 - \overline{\overline{B}}_i)^2$$

The overall mean difference is defined as:

$$\varepsilon_{RGB} = \sqrt{\varepsilon_R^2 + \varepsilon_G^2 + \varepsilon_B^2} \tag{3.26}$$

The algorithm proceeds by continuing this division for each subregion, unless the following condition is satisfied:

$$\varepsilon_{RGB} \leq \chi_{RGB} \tag{3.27}$$

where χ_{RGB} is an user-defined value which was set to $\chi_{RGB} = 1.67$ for the results presented here. The algorithm was also stopped when a minimum subregion size was achieved, this was set to $min(\Delta X, \Delta Y) = 10$. Once complete, $\overline{\overline{R}}$, $\overline{\overline{G}}$ and $\overline{\overline{B}}$ were computed for each cell. The cells were then filtered given maximum and minimum color component values $\mathcal{Z}_{max}$

and $\mathcal{Z}_{min}$. This removed cells dominated with saturated or extremely dim pixels.

Figures 3.30 and 3.31 present sample calibration grids for two imaging system settings (zones # 1 and # 4), exemplifying the application of the calibration grid algorithm. These figures consist of a borescope-captured image of the calibration surface at $T = 26.7°$C, an R component contour map and a numbered calibration grid. The "lip" at the top of the image in figure 3.30 corresponded to the interface between the conformal window and the surrounding Ren Shape. To account for situations where θ_{ba} and θ_{la} were fixed and the light intensity adjusted through different iris settings, overlapping calibration grids were generated for each setting. This is demonstrated in figure 3.31, displaying the calibration grid for zone # 4 with the silhouette of zone #3.

3.4.4 Black and White Reference Setting

Before the digitizer converts the analog R, G and B voltages from the camera to unsigned 8-bit integers, an arbitrary offset and gain may be applied. This essentially improves the resolution of the digitizer. Hacker and Eaton (1995) reported that this process is crucial in ensuring that the response of the imaging system satisfies the white light assumption as discussed in section 3.2.2. Let MV be the measured analog voltage for a given channel from the camera. The reference operation can be expressed, assuming linearity, as:

$$\mathcal{Z} = 0, \qquad MV \leq V_{REF,BL} \tag{3.28}$$

$$\mathcal{Z} = (MV - V_{REF,BL}) \left[\frac{\mathcal{Z}_{max} - \mathcal{Z}_{min}}{V_{REF,WH} - V_{REF,BL}} \right], \qquad V_{REF,BL} \leq MV \leq V_{REF,WH} \tag{3.29}$$

$$\mathcal{Z} = 255, \qquad MV \geq V_{REF,WH} \tag{3.30}$$

Where $\mathcal{Z}$ is the channel value and $\mathcal{Z}_{min}$ and $\mathcal{Z}_{max}$ are the desired minimum and maximum desired integer values for the specified channel. For an unsigned 8-bit integer range, $\zeta_{min} = 0$ and $\zeta_{max} = 255$. $V_{REF,BL}$ and $V_{REF,WH}$ are the black and white reference voltages. For the Matrox Meteor II these are set in the ranges: $0.6\text{V} \leq V_{REF,BL} \leq 1.6\text{V}$ and $1.6\text{V} \leq V_{REF,WH} \leq 2.6\text{V}$. Practically, these reference values are user-defined as unsigned 8-bit integers (termed as reference values $\mathcal{Z}_{REF,BL}$ and $\mathcal{Z}_{REF,WH}$) through LabView control VIs.

Hacker and Eaton (1995), Elkins et al. (2001) and Mukerji and Eaton (2002) used a procedure involving two conditions: totally dark, where the camera lens is capped and "gray", where a card of uniform 18% spectral reflectance (Eastman Kodak Company # 847-8174)

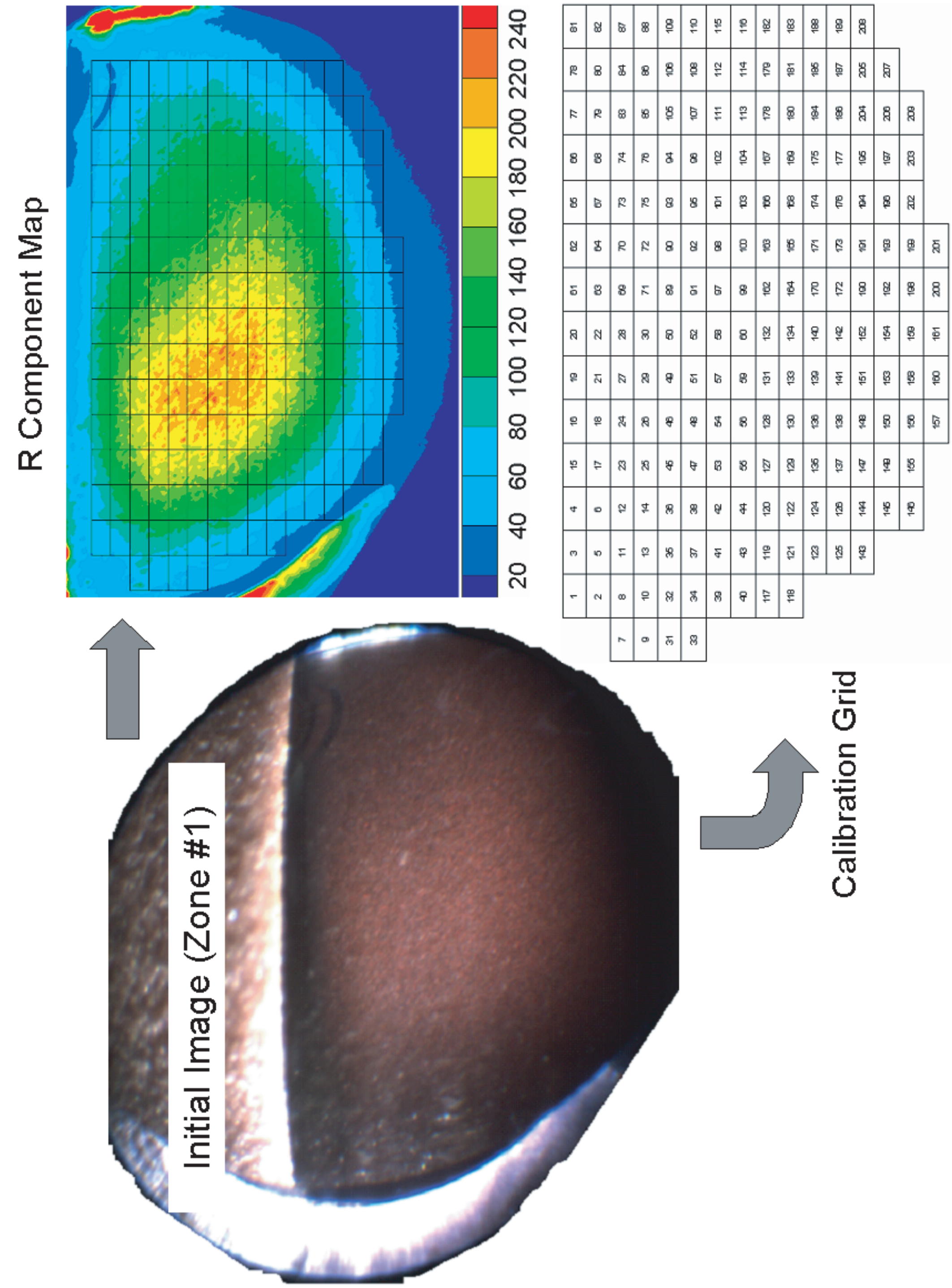

Figure 3.30: Calibration grid for zone #1.

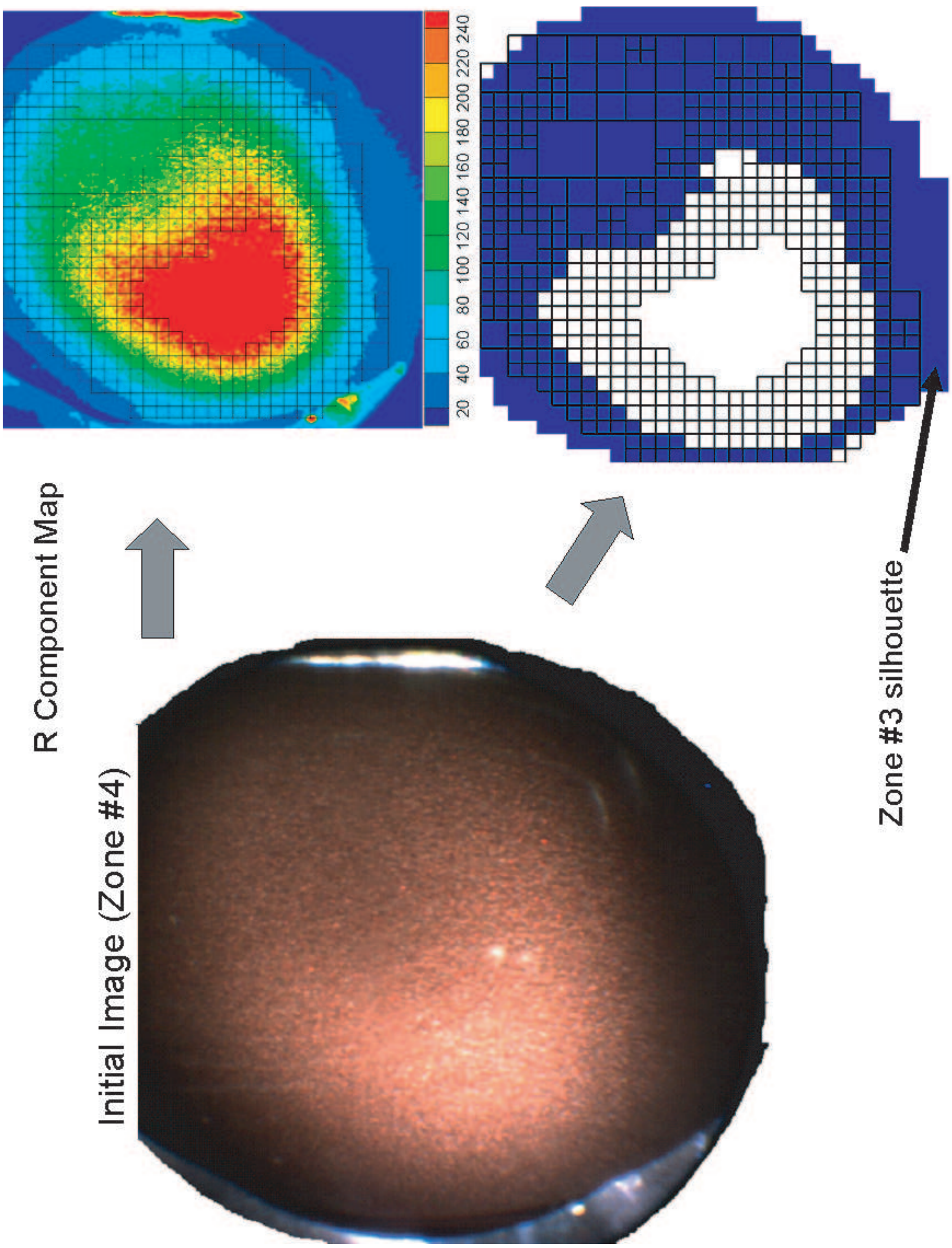

Figure 3.31: Calibration grid for zone #4.

is observed under normal illumination and optical path conditions. Under totally dark conditions, the average color component values $\overline{R}$, $\overline{G}$ and $\overline{B}$ were successively computed over a small region of interest (ROI) as the black reference values were gradually increased from 0. As each channel's average dropped below some cutoff value ($\overline{R} \leq 4.0$, for example), the reference value was saved. The white reference values were determined by first adjusting either the aperture on the camera or light source until the maximum average color component value for a small ROI imaging the gray card was ≈ 240 with $R_{REF,W} = G_{REF,W} = B_{REF,W} = 255$. The white reference values for each channel are slowly reduced until the average color component for each channel reaches the limit $R \geq 250$.

To attempt this procedure in the single passage, small gray card discs were glued onto the geometry calibration surface, as shown in figure 3.10. However, due to the large illumination gradients across the surface it was found to be impractical to use this protocol. Instead, it was realized that hue angle is simply a chosen representation of the measured averaged $\overline{R}$, $\overline{G}$ and $\overline{B}$ components for each calibration cell. Therefore, it was proposed that the reference values would be adjusted to gain the individual channels to increase the resolution of the $Q = f(\overline{R}(T), \overline{G}(T), \overline{B}(T))$ curve. To implement this approach at each imaging system setting, with the reference values for each channel set to $\mathcal{Z}_{REF,BL} = 0$ and $\mathcal{Z}_{REF,WH} = 255$, color component maps were stored at the various set-point temperatures and calibration grids were generated. A 14-point calibration curve was conducted, raising the calibrator's temperature from 24.5°C to 38.0°C, an iterative algorithm was implemented to estimate the reference values for each channel. Figures 3.32 and 3.33 demonstrate the effects of adjusting the white and black reference values on the calibration curves. This shows that depending on the initial calibration curve, the black reference values should be adjusted such that the channels are equalized when the liquid crystal response is "black". Achieving this results in a $Q = f(\overline{R}(T), \overline{G}(T), \overline{B}(T))$ curve which is entirely monotonic with higher hue angle versus temperature resolution, and thus more accurate measurements over a larger interval.

3.4.5 TLC Calibration Procedure

Having set the white and black reference values, a 43-point calibration is conducted at each imaging system setting. A LabView-based program was used to control the calibrator temperature and image the surface. At each set-point, 30 acquired images were averaged producing 2D color component arrays for $\overline{\mathcal{Z}}(X, Y)$ expressed as real numbers in the range

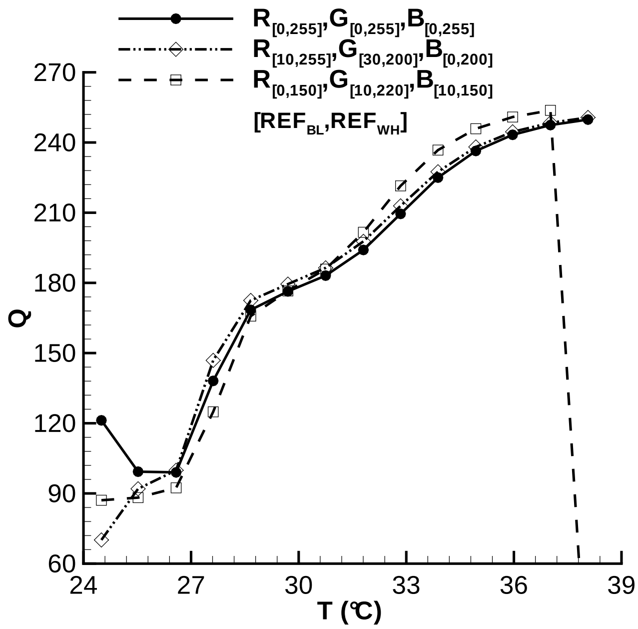

Figure 3.32: Effect of reference value on $Q = f(\overline{R}, \overline{G}, \text{ and } \overline{B})$ curve.

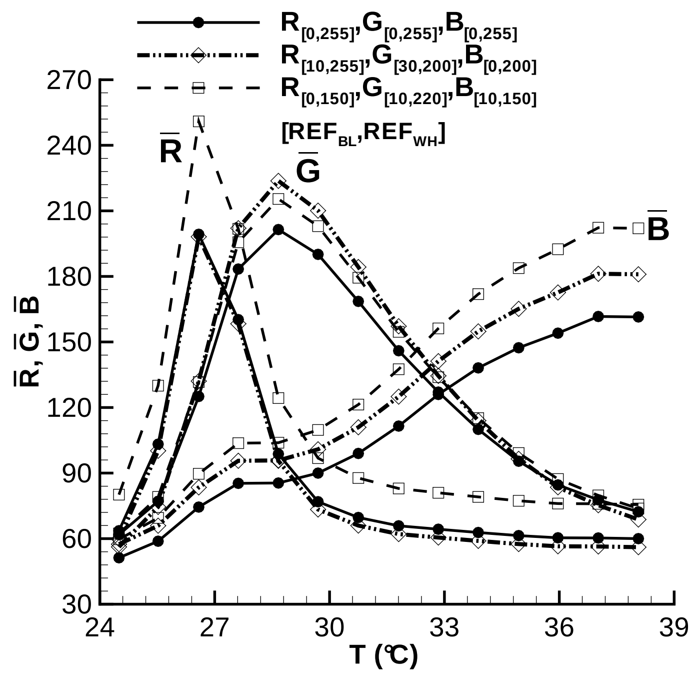

Figure 3.33: Effect of reference value on $\overline{R}$, $\overline{G}$, and $\overline{B}$ curves.

$0 \leq \overline{\mathcal{Z}}(X,Y) \leq 255$. The number of images for averaging was determined as a compromise between signal-to-noise issues and minimizing the time necessary to complete the calibration process. These are then spatially averaged for each calibration cell, producing $\overline{\overline{\mathcal{Z}}}_i$. These values are then used to compute the following parameters:

$$V'_{1,i} = -\frac{1}{4}\overline{\overline{R}}_i - \frac{1}{4}\overline{\overline{G}}_i + \frac{1}{2}\overline{\overline{B}}_i \qquad V'_{1,i} \epsilon \ [-128, 127] \tag{3.31}$$

$$V'_{2,i} = \frac{1}{2}\overline{\overline{R}}_i - \frac{1}{2}\overline{\overline{G}}_i \qquad V'_{2,i} \epsilon \ [-128, 127] \tag{3.32}$$

Both these parameters are expressed as real numbers. To expedite the computation of the hue angle, a 2-D look-up table array of the form shown in equation 3.33 was generated. By pre-computing this array, it was unnecessary to calculate the arc tangent and ensure that Q was correctly normalized for each pixel. Exploratory tests verified that this approach had tremendous time savings for both calibration and measurement stages.

$$Q_{m,n} = \frac{255}{2\pi} tan^{-1}\frac{m}{n} \qquad m, n \ \epsilon \ [-128, 127], \ Q \ \epsilon \ [0, 255] \tag{3.33}$$

2-D linear interpolation, using the computed values of $V'_{1,i}$ and $V'_{2,i}$ as indices, was performed on this array to produce the hue angle. Figures 3.34 and 3.35 compare the calibration curves for two calibration cells from zone # 1. The $\overline{\overline{\mathcal{Z}}}$(T) curves show that the maxima locations remain identical regardless of the calibration cell, but the magnitudes of the components vary dramatically. On average, the pixel intensities in cell # 111 were one-half of those in cell # 24. An unexpected result was the good agreement between the hue angle curves for the two cells under study. Nevertheless, recalling that the hue angle effectively depends on the relative magnitudes of the color components, this result emphasizes that the discretization of viewable image should be based on $\overline{\mathcal{Z}}$, rather than on $\overline{Q}$ to achieve low uncertainty measurements. Additional calibration curves for this zone closely followed those shown in figure 3.35. This raises the possibility that a smaller number of calibration cells can be used, maintaining the same accuracy.

For completeness, figures 3.36 and 3.37 compare calibration curves between zone #1, cell #111, zone #2, cell # 84 and zone #2, cell # 360. The first two cells nominally correspond to the same spatial location on the pressure side calibration surface. Figure 3.38 presents a layout of zone #2 for reference purposes. These curves confirm that the maxima of the $\overline{\overline{\mathcal{Z}}}$(T) curves are identical for different imaging system settings, although their magnitudes differ. The $Q = f(\overline{\overline{R}}, \overline{\overline{G}}, \overline{\overline{B}})$ curves for cells # 111 and # 84 agree well, despite the fact that

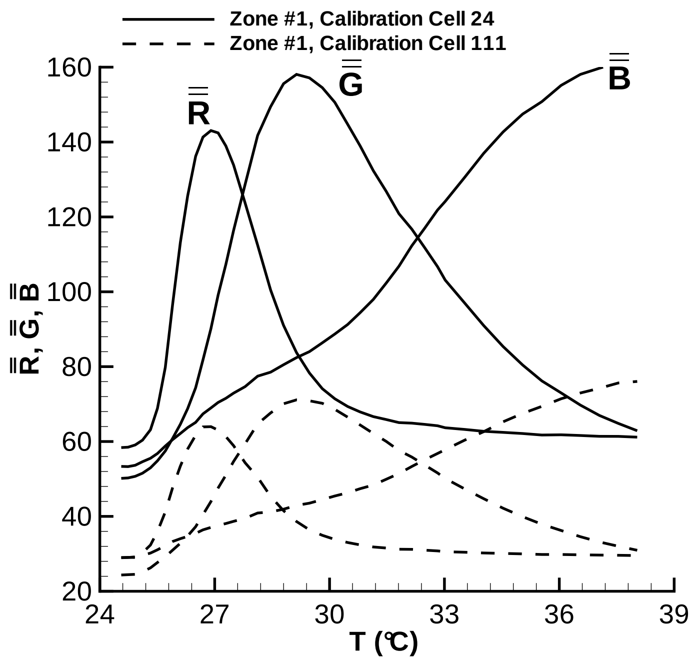

Figure 3.34: $\overline{\overline{R}}$, $\overline{\overline{G}}$ and $\overline{\overline{B}}$ curves for two calibration cells in zone #1.

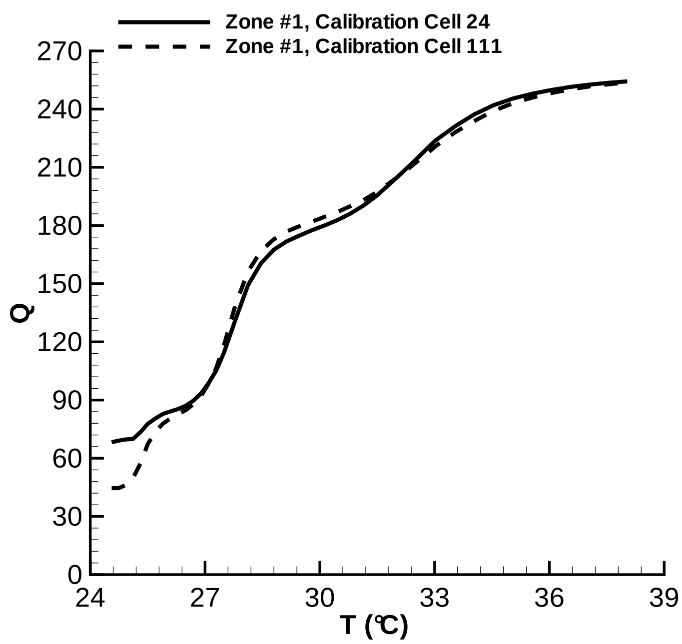

Figure 3.35: Q, S and I curves for two calibration cells in zone #1.

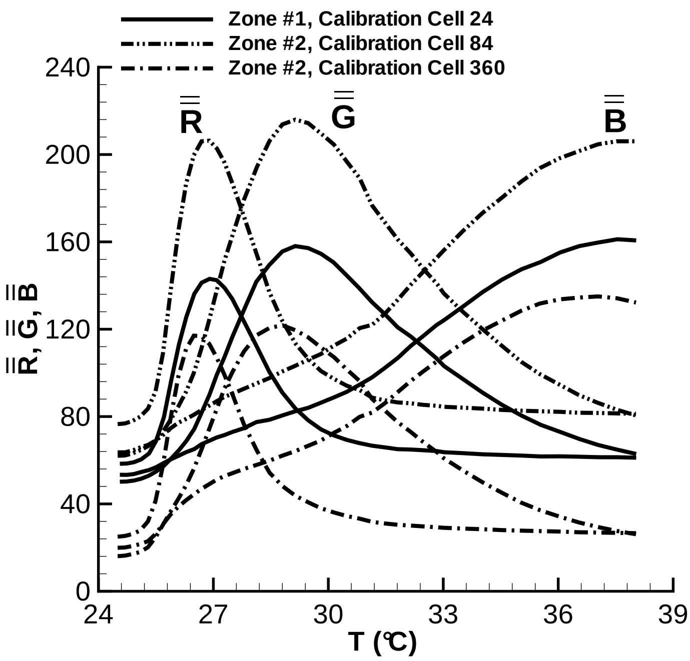

Figure 3.36: $\overline{\overline{R}}$, $\overline{\overline{G}}$ and $\overline{\overline{B}}$ curves for three calibration cells in zones #1 and #2.

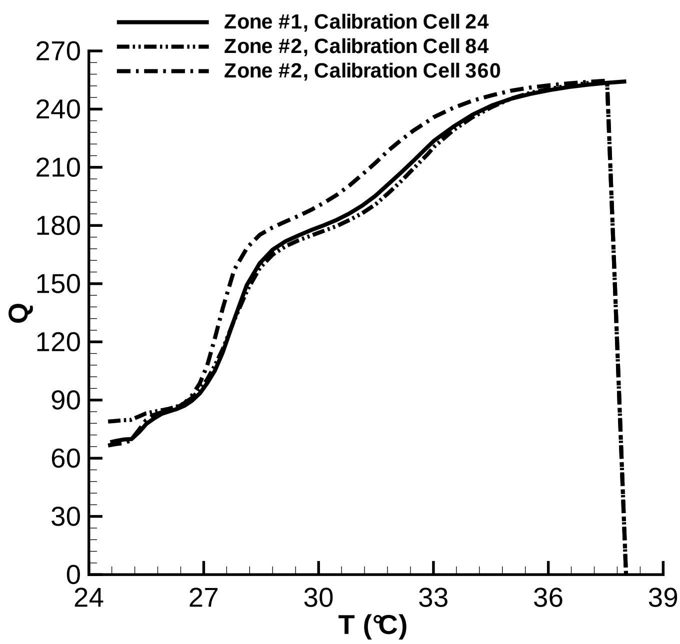

Figure 3.37: Q curves for three calibration cells in zones #1 and #2.

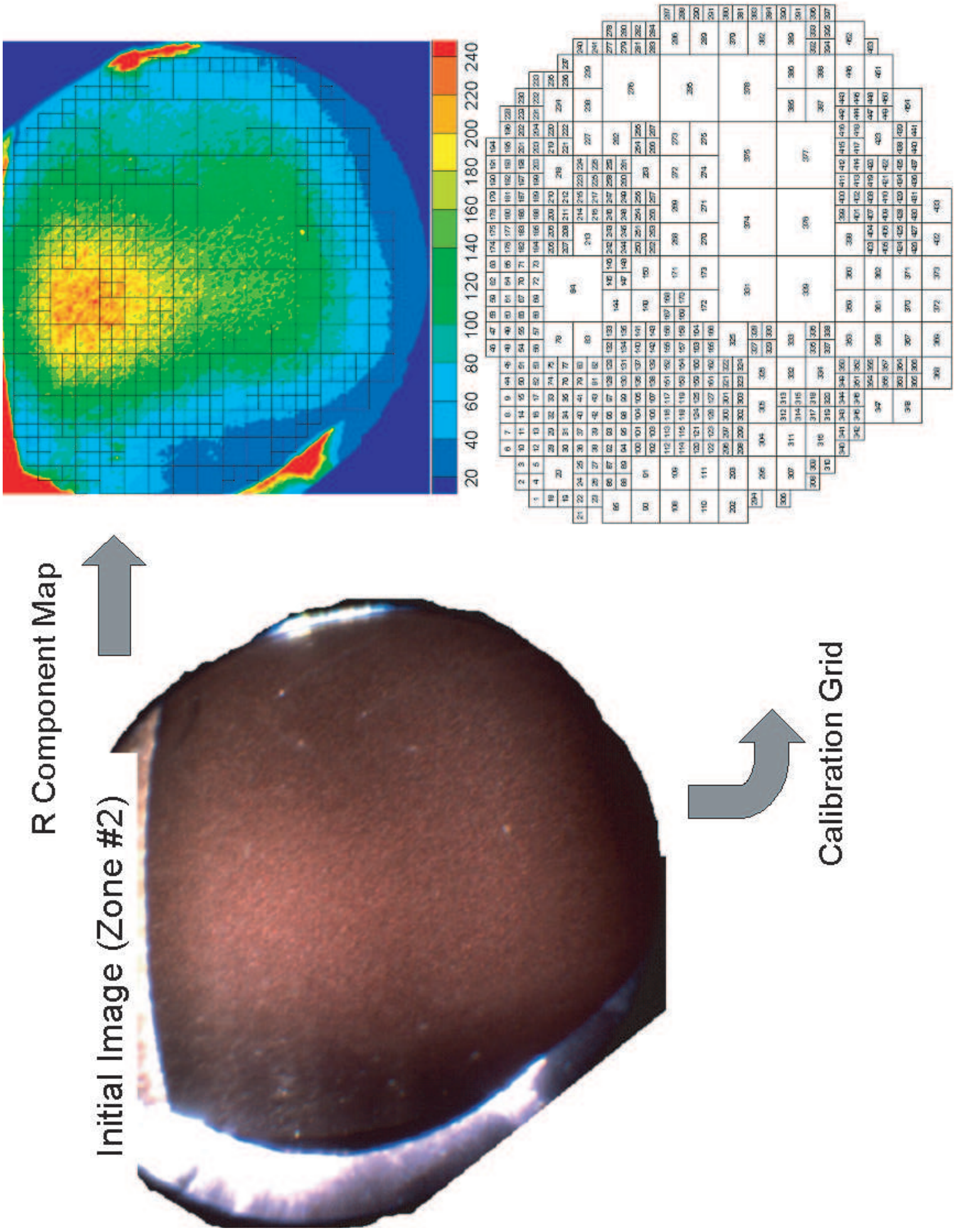

Figure 3.38: Calibration grid for zone #2.

the imaging system setting are different for the two zones. The $\overline{\overline{\mathcal{Z}}}$(T) calibration curves for cell # 360 reveal not only reduced pixel intensities, but a slight "shifting" of the color component maxima from approximately 26.9°C, 29.1°C and 37.8°C to 26.5°C, 28.8°C and 37.0°C for $\overline{\overline{R}}$(T), $\overline{\overline{G}}$(T) and $\overline{\overline{B}}$(T), respectively. Figure 3.37 presents the significant effect of these changes on the $Q = f(\overline{\overline{R}}, \overline{\overline{G}}, \overline{\overline{B}})$. It was unclear if this phenomenon is due to lighting and viewing angle changes or the local thickness of the TLC-coat. Nevertheless, the calibration process accounts for this variation.

The calibration process took approximately 3 hours to complete for each setting, this calibration time increased with more zones. Upon the completion of this process, a 1-D look-up table for the function $Q = f(T)$ was generated using cubic splines fit to the monotonic portion of the calibration data. For values of Q outside this region, the corresponding temperature was set to output "-999", indicating that the pixel was out of range.

To verify the accuracy of the calibrations, the copper calibrator surface temperature was set to specific set points, and 2-D temperature maps $(T(X,Y) = f(\overline{R}(X,Y), \overline{G}(X,Y), \overline{B}(X,Y)))$ were generated to verify the accuracy of the calibration. The average temperature for each calibration cell was computed using:

$$\overline{T}_i = \frac{1}{\vartheta} \int_{X_{min,i}}^{X_{max,i}} \int_{Y_{min,i}}^{Y_{max,i}} T(X,Y) dX dY \tag{3.34}$$

Section 3.4.7 describes the temperature measurement algorithm in more detail. Figure 3.39 presents histograms plots of $\overline{T}_i$ for zone # 1 at four set temperatures. To compare temperature data at these temperatures, T_{set} is subtracted from $\overline{T}_i$, revealing the fraction of calibration cells falling into the desired accuracy range, $T_{set} \pm 0.1$°C. Due to the changing TLC color response and the fact that some zones are near the edges of the image, certain cell calibrations either are or become invalid at different temperatures. Thus the percentage of invalid cells increases from 4% at $T_{set} = 26.2$°C to 22% at $T_{set} = 34.0$°C. Virtually all cells which are in-range, according to this figure, fall in the range $\overline{T_i} \pm 0.1$°C. This behavior was ensured by adjusting the reference values to increase the local resolution of the $Q = f(\overline{R}, \overline{\overline{G}}, \overline{\overline{B}})$ curve as much as possible. In spite of the high precision, it is apparent that the difference $|\overline{T_i} - T_{set}|$ increases to an approximate maximum of ≈ 0.1°C at $T_{set} = 34.0$°C. This was due to the decreased local resolution of the $Q = f(T)$ calibration curve at these elevated temperatures.

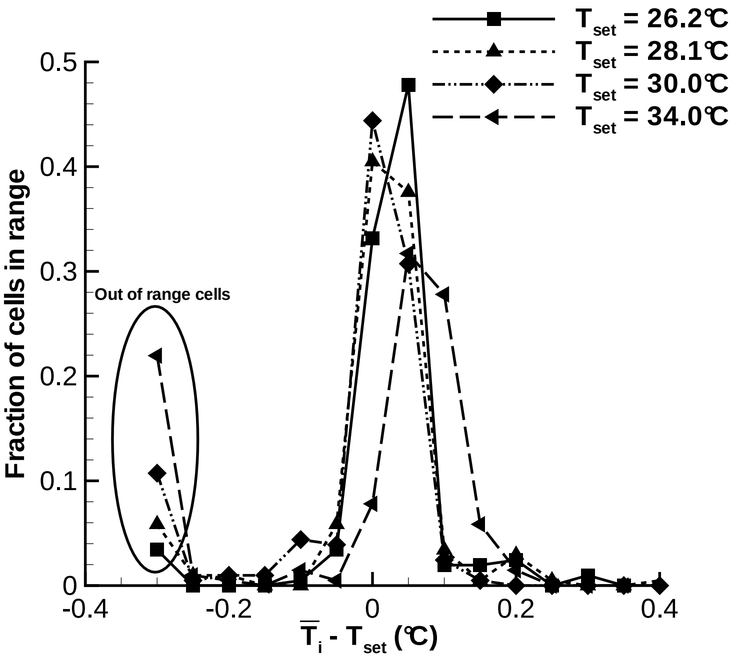

Figure 3.39: Histograms of calibration cell temperatures for zone # 1 imaging system setting.

3.4.6 Borescope Re-positioning Error

For both calibration and measurement steps, the rotary mirror sleeves on both lighting and viewing borescopes are repeatedly adjusted. Additionally, as the calibration and measurement phases took several days to complete, there was a concern that the light source degraded with time. Thus at the end of the calibration process, the borescopes are repositioned to the initial configuration. Another calibration is conducted and compared to one collected earlier. Figures 3.40 and 3.41 present hue angle and color component curves combining the effects of borescope repositioning and changing the light source lamp. Figure 3.40 shows that the maxima of the $\overline{\overline{R}}(T)$, $\overline{\overline{G}}(T)$ and $\overline{\overline{B}}(T)$ curves remain at nearly identical temperatures, although their magnitudes change slightly. Figure 3.41 demonstrates that the borescope repositioning provides a negligible shift in the calibration curves. This figure also shows a calibration curve taken within 2 hours after the insertion of a new lamp. This curve shows a definitive shift in the calibration curve when a new lamp is inserted, especially in areas where $\frac{dQ}{dT}$ is large. This variation was found to decay as the lamp warmed, and become larger near the end of the lifetime of the lamp. Nevertheless, these differences were within the desired uncertainty of the system, $\pm 0.1°$C.

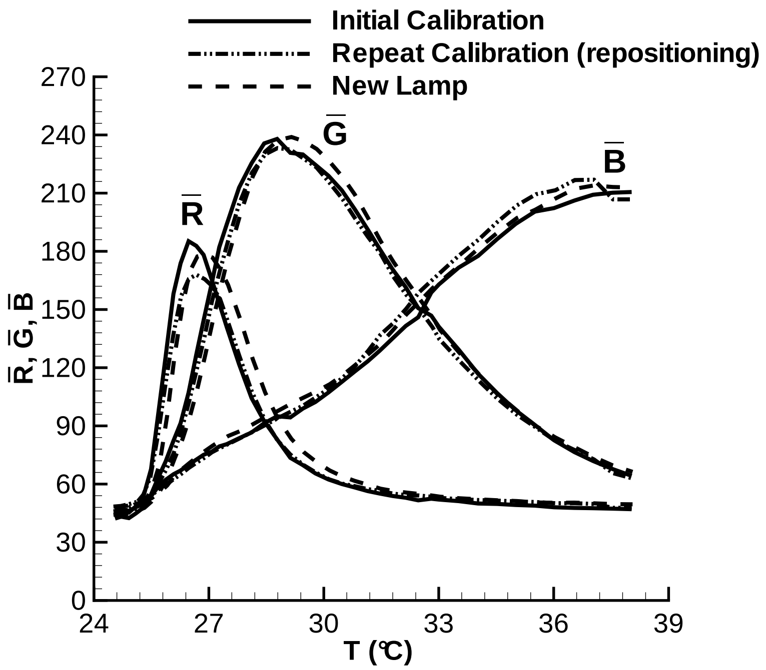

Figure 3.40: Effect of borescope repositioning on $\overline{\overline{R}}$, $\overline{\overline{G}}$ and $\overline{\overline{B}}$ curves.

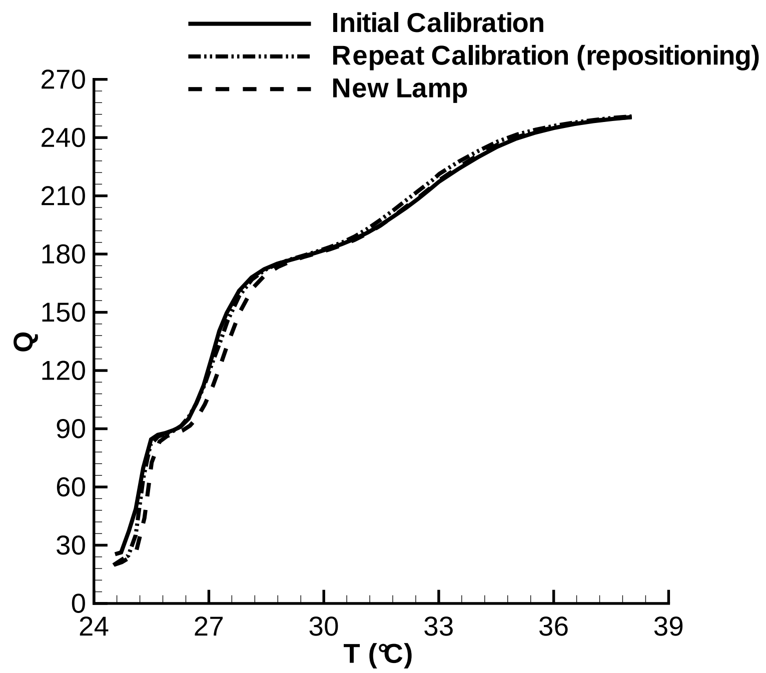

Figure 3.41: Effect of borescope repositioning on $Q = f(\overline{\overline{R}}, \overline{\overline{G}}, \overline{\overline{B}})$.

3.4.7 Temperature Measurement

Once the calibration grids and curves had been established for each imaging system setting, the light source lamp was replaced, the calibration surface was removed and the measurement surface (described in section 3.5.1) was inserted. A light calibration, using the mini calibrator, was performed to monitor the evolution of the illumination spectrum and intensity as a function of time.

Following the approach presented by Mukerji and Eaton (2002), $Q = f(T)$ look-up tables were generated, or retrieved from a previously saved file, and stored in memory for each calibration cell. To reduce the RGB image-to-temperature map conversion times, this 1-D look-up table was converted to a 2-D look-up table of the form $T = f(m, n)$ where m and n are integers which are in the range $m \epsilon [-128 \ldots 127]$. At each pixel location, V_1' and V_2' are computed from the local R, G and B data, forming the indices to determine the corresponding temperature. Hue values that fell outside the calibration range were assigned to output "-999", indicating that the pixel in question was out of range.

Hacker and Eaton (1995) pointed out that to avoid bias errors, the temperature measurement process should mirror the calibration process. That is, the conversion of perceived color to temperature should be performed on the averaged color image, rather than averaging individual temperature maps. This fact can be represented in the form of an inequality:

$$\overline{T(Q(R, G, B))} \neq T(Q(\overline{R}, \overline{G}, \overline{B})) \tag{3.35}$$

To circumvent this problem in the current system, all temperature maps were converted from averaged RGB images. Thirty acquired images were used to generate all data sets, consistent with the calibration process. The 2-D look-up tables for each cell were then applied, and a single temperature map was constructed.

Before outputting the temperature map $T(X, Y)$ to the file, the RaG algorithm was engaged to convert each pixel location to spatial coordinates. As this process was inherently nonlinear, the resulting spatial resolution for each zone changed continuously across the temperature maps. Figure 3.42 presents a subset of the spatial grid for zone # 1, showing the local distortions resulting from the optics of the borescope and highly-curved window and measurement surfaces. Similar $T(x, y)$ maps were generated for each imaging system setting, blanketing the observed measurement surface.

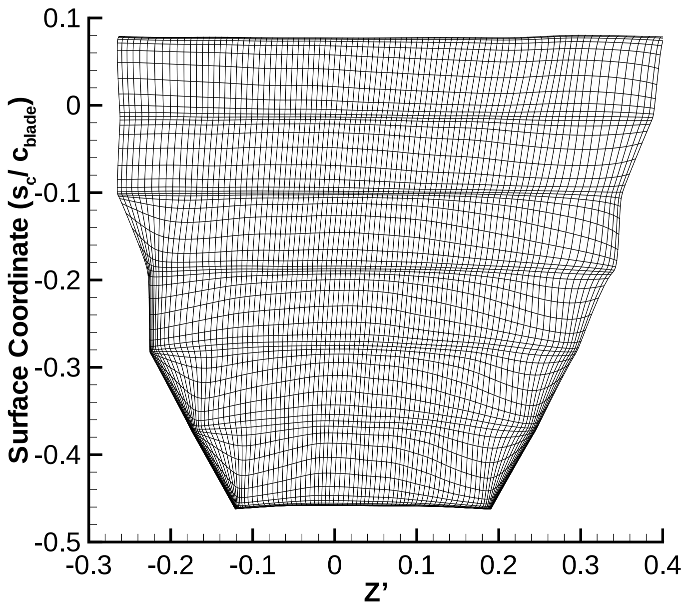

Figure 3.42: Zone #1 spatial grid, mapping image pixels to spatial coordinates.

Data Reduction

As several overlapping temperature maps with varying spatial resolutions are used to map out the measurement surface, it was necessary to develop software to construct a single temperature map with a consistent spatial resolution for the entire surface. Representing the collected temperature maps from n zones as $\{T_j(x_i, y_i) : i = 1, \ldots, N,\ j = 1, \ldots, n\}$: a constant-spaced background grid of dimensions $x\epsilon[x_{min}, x_{max}]$, $y\epsilon[y_{min}, y_{max}]$ and approximate spatial resolution of $9\mu m^2$/pixel is generated. The resolution was determined by taking the smallest δx and δy spacings from all the measurement zones. A FORTRAN program was written to interpolate each T_j map onto this background grid. In range co-located data from each zone were averaged. Figure 3.43 presents a visual depiction of this process. This figure also shows the typical resolutions for each zone and silhouettes of the acquired temperature map for each zone.

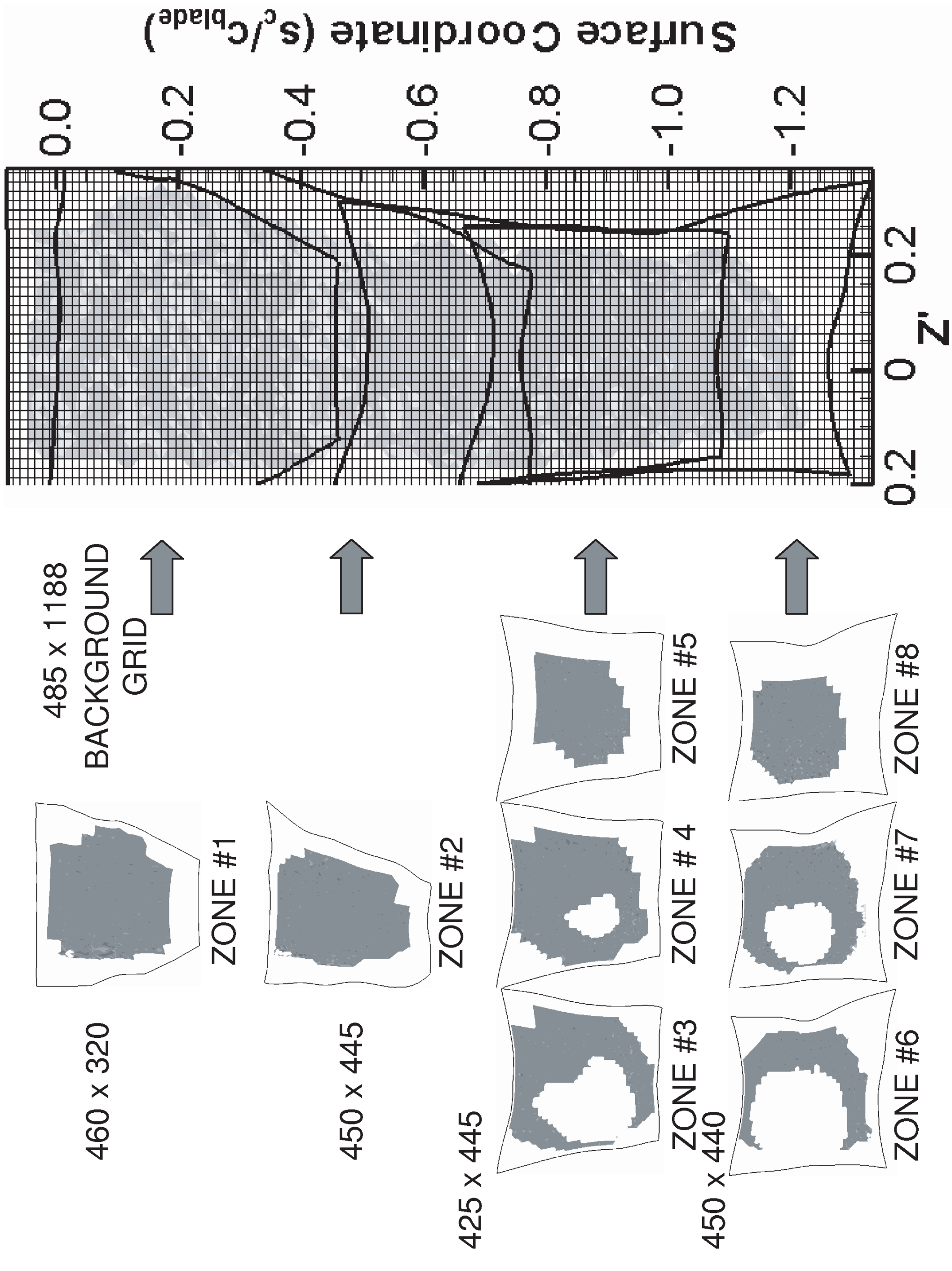

Figure 3.43: Overview of background grid interpolation process.

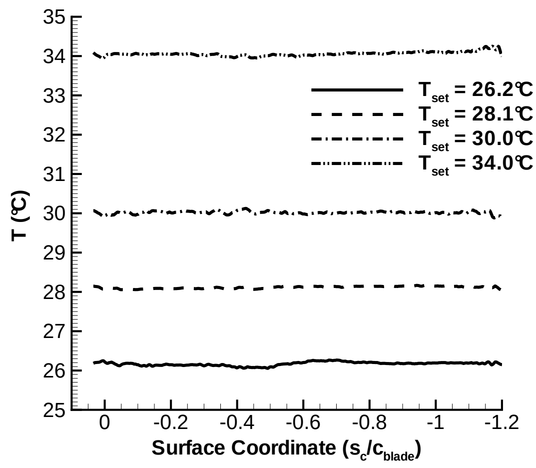

Figure 3.44: Spanwise-averaged calibrator surface temperatures ($\overline{T}(s_c)$) at various set temperatures.

3.4.8 Measurement System Validation

Two sets of tests were formulated to quantify the overall uncertainty of the liquid crystal thermography system: in-situ tests performed on the calibrator and validation tests performed on the measurement surface at actual flow conditions. In the first case, temperature maps were stored at each borescope setting at various set point temperatures during the calibration process. These were then converted to spatial locations and interpolated onto a background grid, as described in section 3.4.7. Figure 3.44 presents four spanwise-averaged, median-filtered (on an 8-point symmetric stencil) temperature profiles along the pressure side calibrator surface. Such curves were collected at the end of each calibration session to verify the quality of the calibration. The majority of each of these curves were found to be within the desired uncertainty of the system, $\pm 0.1°$C, irrespective of the set temperature. This observation can be confirmed by an examination of figures 3.45, 3.46, 3.47 and 3.48. Figure 3.49 displays a spatially-resolved temperature map derived from images of the pressure side copper calibrator at a set temperature of $T_{set} = 26.2°$C. Also shown in this figure is a picture of the painted pressure side calibrator, for reference. This contour plot along with the spanwise-averaged data confirms that the calibration process corrects for the TLC lighting/viewing angle dependency and borescope optics distortion effects.

The validation tests performed at actual flow conditions involved measuring the recovery temperature (T_{rec}) distribution along the pressure side wall of the single passage

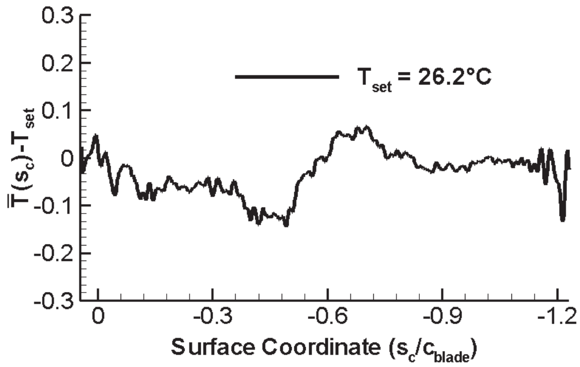

Figure 3.45: Plot of difference between spanwise-averaged and set temperatures ($\overline{T}(s_c) - T_{set}$) at $T_{set} = 26.2°$C.

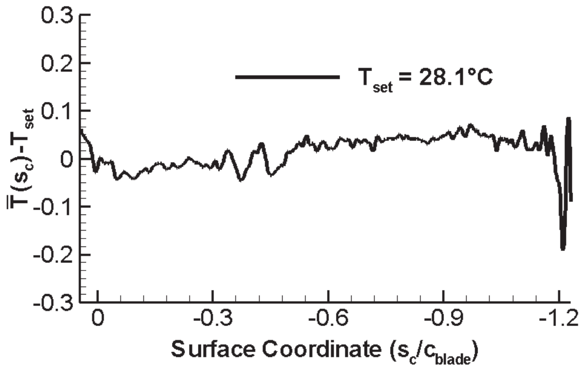

Figure 3.46: Plot of difference between spanwise-averaged and set temperatures ($\overline{T}(s_c) - T_{set}$) at $T_{set} = 28.1°$C.

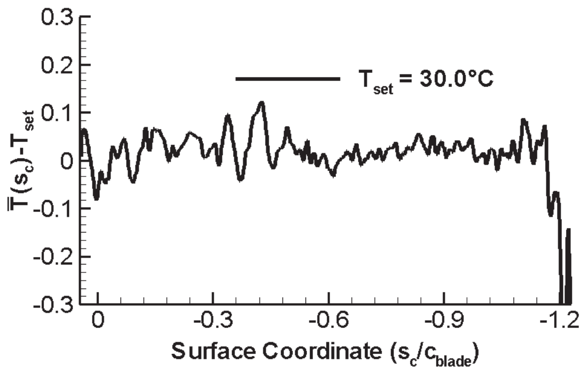

Figure 3.47: Plot of difference between spanwise-averaged and set temperatures ($\overline{T}(s_c) - T_{set}$) at $T_{set} = 30.0°$C.

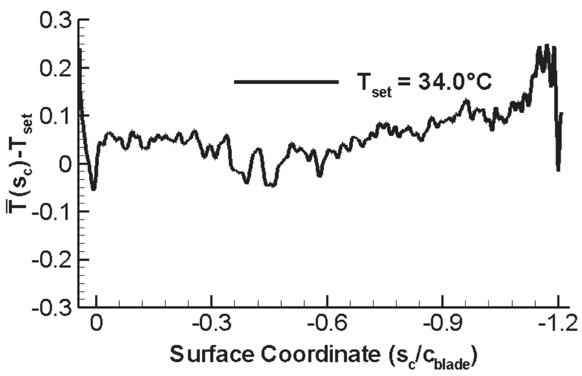

Figure 3.48: Plot of difference between spanwise-averaged and set temperatures ($\overline{T}(s_c) - T_{set}$) at $T_{set} = 34.0°$C.

model without presence of film cooling (uncooled). The construction details of this surface are discussed in section 3.5.1. The collected data from this test were compared to a prediction using the M_{is} distribution for the single passage. It was assumed, and subsequently verified in chapter 4, that the uncooled recovery temperature distribution can be accurately predicted using:

$$\frac{T_{rec}}{T_\infty} = 1 + \frac{1}{2} r_\infty (\gamma - 1) M_{is}^2 \tag{3.36}$$

$$\frac{T_\circ}{T_\infty} = 1 + \frac{\gamma - 1}{2} M_{is}^2.$$

Using the results of Deissler and Loeffler (1958) and numerical analysis by Kays and Crawford (1993), the recovery factor was assumed to be:

$$r_\infty \approx Pr^{1/3}, \ Pr \approx 0.73 \tag{3.37}$$

Figure 3.50 compares the predicted and TLC-measured spanwise-averaged $T_{rec}(s_c)$ profiles at three total temperature conditions, $T_\circ = 27.6°$C, $T_\circ = 31.5°$C and $T_o = 33.6°$C. This figure demonstrates that the liquid crystal measurement system closely follows the expected trends in the surface temperature. Figures 3.51, 3.52 and 3.53 present the difference between the predicted and measured curves at the three flow conditions. These show that the best agreement between predicted and measured profiles occurred at the lowest total temperature ($T_o = 27.6°$C), with the difference within the desired uncertainty of the measurement system. The other cases have differences as large as 0.6°C. It was believed that these differences were more attributable to backlosses, i.e. the surface was not perfectly adiabatic rather than additional measurement system error.

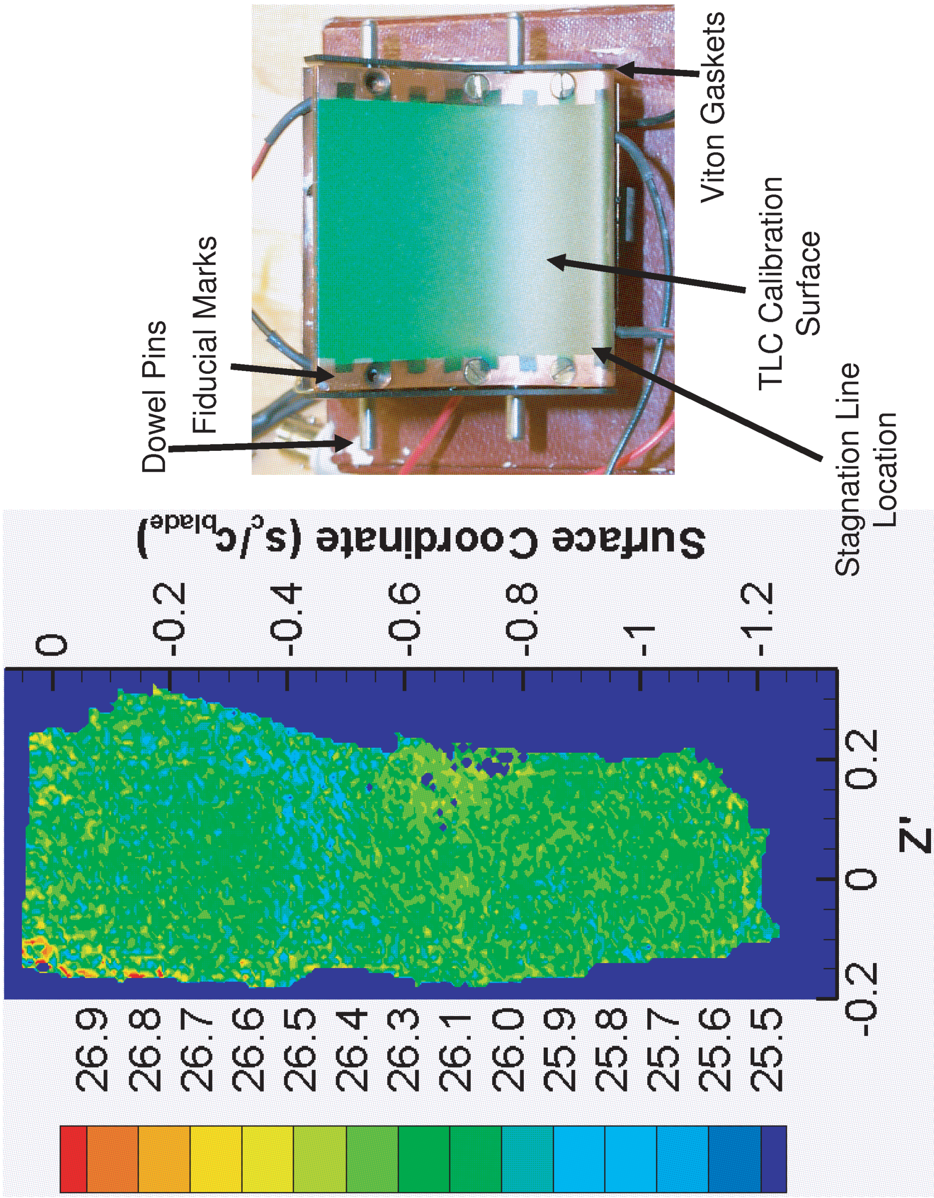

Figure 3.49: Sample spatially-resolved temperature map and TLC-painted copper calibrator surface for comparison.

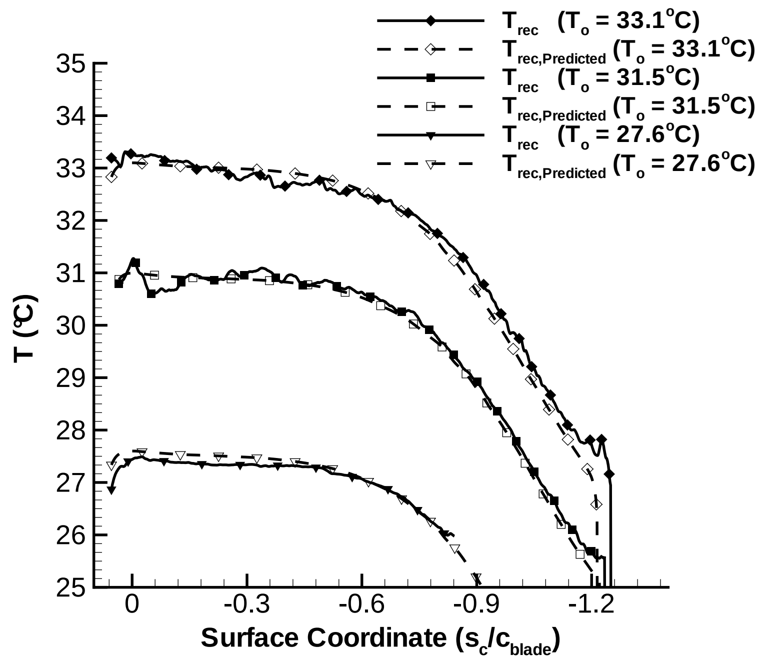

Figure 3.50: Plot comparing spanwise-averaged recovery temperature measurements versus prediction suggested from Deissler and Loeffler (1958).

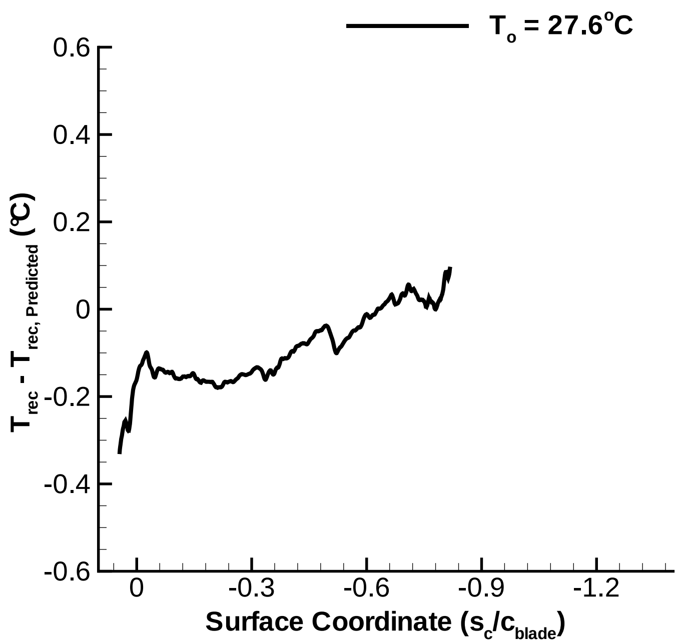

Figure 3.51: Plot showing the difference $T_{rec,TLC} - T_{rec,Predicted}$ with $T_o = 27.6°\text{C}$.

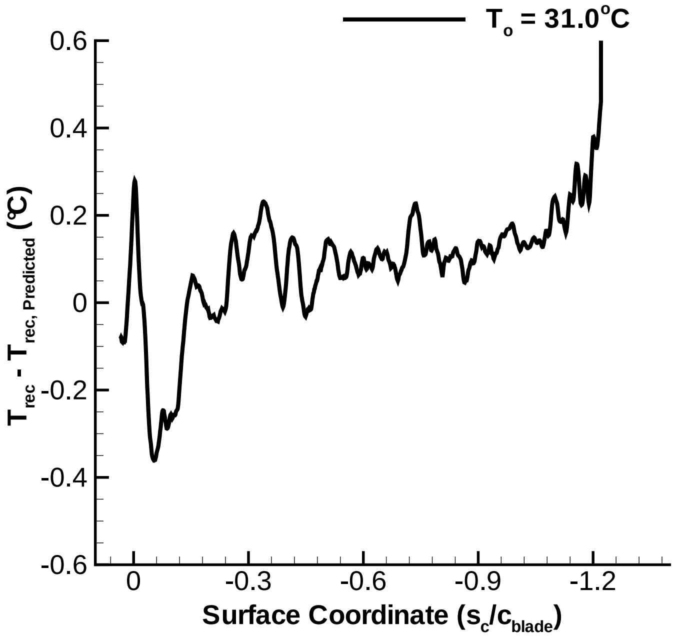

Figure 3.52: Plot showing the difference $T_{rec,TLC} - T_{rec,Predicted}$ with $T_o = 31.5°\text{C}$.

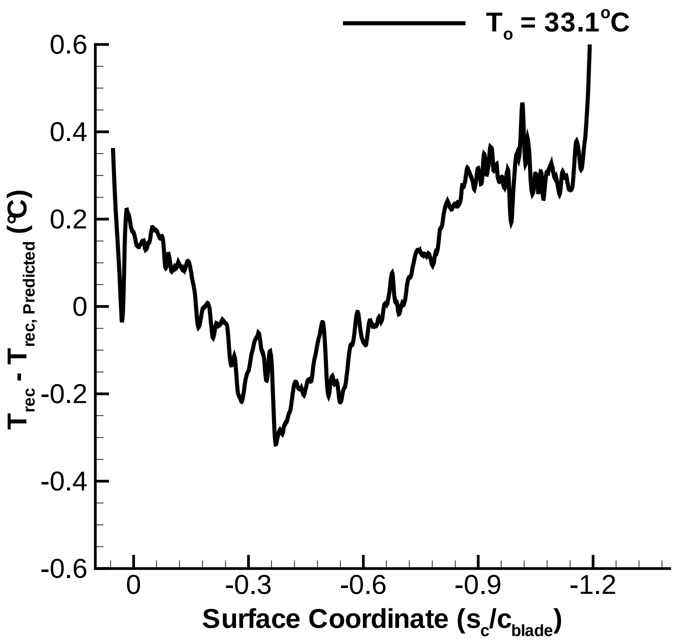

Figure 3.53: Plot showing the difference $T_{rec,TLC} - T_{rec,Predicted}$ with $T_o = 33.6°\text{C}$.

3.5 Heat Transfer Measurement Techniques and Implementation

The objective of these experiments was to obtain spatially-resolved surface temperature maps on the pressure side surface of highly-cambered, transonic turbine blade geometry, under steady state conditions. These maps would be measured under different thermal and flow boundary conditions and then combined to provide spatially-resolved surface maps of the adiabatic film effectiveness (η) and heat transfer coefficient (h). For convenience, equations 3.38 and 3.39 restate the definition of these parameters, first presented in section 1.2. These definitions have been modified slightly to reflect their spatial dependence.

$$\eta(x,y) = \frac{T_{aw}(x,y) - T_{rec}(x,y)}{T_{w2} - T_{rec}(x,y)} \tag{3.38}$$

$$q''(x,y) = h(x,y)(T_{iso}(x,y) - T_w(x,y)) \tag{3.39}$$

To measure $\eta(x,y)$, two temperature maps were acquired: both of which were measured at identical total temperatures. $T_{rec}(x,y)$ is the two-dimensional temperature profile on the uncooled adiabatic measurement surface. $T_{iso}(x,y)$ corresponded to the temperature profile on an adiabatic surface at an isoenergetic condition where $T_{\circ,c} = T_{\circ,\infty}$. $T_{aw}(x,y)$ is the two-dimensional temperature profile on the adiabatic measurement surface with coolant injection with an exit temperature of T_{w2}. Other researchers, such as Drost and Bölcs (1999), have used the coolant total temperature. However, Buck (2002) pointed out that the coolant temperature at the hole exit can be substantially different than the total plenum temperature. This makes comparisons with similar experiments and simulations difficult when the plenum temperature is used. Additionally, the heat flux boundary condition used in codes that predict the three-dimensional temperature profile inside a cooled component assume the definition of η shown in equation 3.38.

The convective heat transfer coefficient ($h(x,y)$) was measured by subtracting two 2-D surface temperature distributions with film cooling applied: $T_{aw}(x,y)$ is defined as the two-dimensional wall temperature on an adiabatic surface and $T_w(x,y)$ is the temperature profile on the measurement surface with a known heat flux distribution applied ($q''(x,y)$). Buck (1999) argued that the total temperature of the coolant should be identical to the mainstream total temperature for both temperature profiles ($T_{\circ,c} = T_{\circ,\infty}$), ensuring that $h(x,y)$ is only a function of the heat flux thermal boundary condition and the flowfield resulting from the interaction of the film cooling jets and the mainstream flow. As it was crucial to quantify the augmentation effects of film cooling on $h(x, y)$, heat transfer data with no film cooling also were collected.

As the single passage flow facility operated at near ambient conditions, Mukerji and Eaton (2002) found that it was more convenient to perform measurements with the film cooling flow at a slightly higher total temperature than the mainstream flow ($T_{\circ,c} > T_{\circ,\infty}$). Nevertheless, Goldstein (1971) and Sinha et al. (1991a) found that this inverse heat transfer problem is functionally identical to the case where $T_{\circ,c} < T_{\circ,\infty}$ for both incompressible and compressible flows. In the interests of simplicity, the term "film cooling" will be used throughout, although the functional heat transfer problem under study is "film heating". On an absolute temperature scale, all film cooling tests had temperature ratios of approximately unity ($\frac{T_{\circ,c}}{T_{\circ,\infty}} \approx 1.0$). This raised an obvious concern with respect to modeling the substantial temperature (and by extension density) gradients present in the real film cooling problem, especially if air is used for the coolant. Sinha et al. (1991a) suggested with measurements that the injection of a foreign gas, such as CO_2 along a flat plate, produces thermal and flow conditions which are entirely analogous to those taken at engine representative conditions where air is used as the coolant.

As indicated in chapter 1 the flow physics of the film cooling jet and crossflow interaction and the subsequent effects on the downstream thermal field depends on a wide range of parameters. The single passage flow facility, in essence, establishes a well-defined flow condition that includes enough of the characteristic complexities of a modern gas turbine rotor stage. With this baseline, the parameters that were varied are:

1. Hole geometry and location.
2. Density ratio, $DR = \frac{\rho_j}{\rho_\infty}$.
3. Inlet turbulence intensity and length scale, $TI\%$ and ℓ.
4. Mass flux of film cooling flow, versus mass flux of mainstream flow (i.e. the blowing ratio, $BL = \frac{\rho_j u_j}{\rho_\infty u_\infty}$).
5. Momentum flux of film cooling flow, versus momentum flux of mainstream flow (i.e. the momentum ratio, $I = \frac{\rho_j u_j^2}{\rho_\infty u_\infty^2}$).

Table 3.7 summarizes the compound angle round hole geometry installed in the pressure side wall of the single passage model. These parameters were chosen based on interactions

Table 3.7: Film cooling hole geometry.

Row #	1	2
Number of Holes	17	25
$\frac{s_c}{c_{blade}}$	-0.110	-0.427
M_{is}	0.067	0.156
α	38.39°	47.81°
β	52.00°	65.00°
$\alpha_{sw,radial}$	26.00°	25.00°
Pitch $\frac{p}{d}$	5.29	3.53
$\frac{L}{d}$	6.03	3.05
Pinned Diameter, d (mm)	0.4293	0.4293
$\dot{m}_{hole} = (\rho u)_j A_{hole}$ at $BL = 1$	$1.01(10)^{-5}$	$2.36(10)^{-5}$

with GEAE. The rationale for the number of holes is provided in section 3.5.1. The mass flow through each film cooling hole (m_{hole}) is computed using the equation:

$$\dot{m}_{hole} = (\rho u)_{\infty} A_{hole} = P_{\infty} M_{is} \sqrt{\frac{\gamma_{\infty}}{R_{\infty} T_{\infty}}} A_{hole} \tag{3.40}$$

where the ∞ subscript refers to the properties of the mainstream flow. P_{∞} and T_{∞} refer to the static pressure and temperature at the location of the film cooling hole with no film cooling applied. It was assumed that mass flow rate through each film cooling hole was identical. Tables 3.8 and 3.9 presents the matrix of cases that were examined. The parameter values were chosen to generally examine the effects of inlet turbulence on the various jet-in-crossflow regimes, the interaction of two film cooling rows and the effects of density ratio. For each case, three temperature maps were measured: $T_{iso}(x, y)$, $T_{aw}(x, y)$ and $T_w(x, y)$. The T_{iso} profile generally closely followed the $T_{rec}(x, y)$ profile, as will be shown in Chapter 5, and thus served an additional purpose of providing continual validation of the TLC measurement system. Furthermore, this profile had two uses: providing a baseline for the $h(x, y)$ measurements and examining an additional measurement of the film effectiveness. Goldstein (1971) suggested another definition for the film effectiveness that uses $T_{iso}(x, y)$, rather than $T_{rec}(x, y)$ as the reference temperature, as shown below:

$$\eta_{iso}(x, y) = \frac{T_{aw}(x, y) - T_{iso}(x, y)}{T_{w2} - T_{iso}(x, y)} \tag{3.41}$$

Table 3.8: Parameter matrix for uncooled surface.

Parameter	Value
Turbulence Intensity, $TI\%$	1.5%, 30%
Turbulence Length Scale, $\frac{\ell}{c_{blade}}$	0.53, 0.02
Nominal Heat Flux, $(\frac{W}{m^2})$	6.0,8.0,9.0,12.0

Goldstein et al. (1974) postulated that the film cooled case, $T_{aw}(x, y)$ would have approximately the same amount of viscous dissipation, provided the local Mach (M) and Prandtl (Pr) numbers were about the same. On this basis, it was argued that the definition shown in equation 3.41 minimizes the impact of viscous dissipation in the high-velocity boundary layer, thus giving parity for low and high speed film effectiveness data. $T_{iso}(x, y)$ was typically measured with total temperatures in the range 31°C $< T_{\circ,\infty} <$ 33°C, to ensure that the entirety of the measurement surface was within the activation range of the applied TLC paint. The T_{aw}(x,y) surface temperature profile was measured with typical total temperatures of $T_{\circ,\infty} \approx 27.0$°C and $T_{\circ,c} \approx 38$°C. These values were chosen to minimize the uncertainty in the measurement of the parameters of interest. T_w(x,y) was measured with $T_{\circ,\infty} \approx 25.0$°C, to ensure that upon application of a heat flux, the majority of the measurement surface was within the active range of the liquid crystals. To minimize any hysteresis errors in each case, steady state conditions were approached by gradually warming the mainstream and coolant flows. Additionally, the mainstream was cooled to $T_\circ \approx 22.0$°C with no coolant in between data sets to reset the crystal response. All temperatures were controlled to within ±0.1°C of their nominal value and constantly monitored during testing. Due to the tight restrictions on the allowable drift of the various temperatures in the single passage, individual data sets took several hours to collect. Unfortunately, the compressor supply air had a significant amount of particulates including fine metal filings and oil droplets. These substances coated the measurement surface, but it was unclear if this significantly affected the measurements. The measurements presented in the following chapters suggest that this effect is negligible. As the thickest possible layer of liquid crystal was applied to the surface, it was believed that this would limit any degradation issues. However, the presence of these contaminants is clearly non-ideal.

Table 3.9: Parameter matrix for film-cooled surface.

Parameter	Value
Blowing Ratio, $BL = \frac{\rho_j u_j}{\rho_\infty u_\infty}$	0.85, 1.5, 2, 4, 5, 6
Density Ratio, $DR = \frac{\rho_j}{\rho_\infty}$	1, 2.26
Turbulence Intensity, $TI\%$	1.5%, 30%
Turbulence Length Scale, $\frac{\ell}{c_{blade}}$	0.53, 0.02
Nominal Heat Flux, $(\frac{W}{m^2})$	7.0

3.5.1 Heat Transfer Surface Design and Construction

There were two pressure side heat transfer surfaces constructed for this experiment: with and without film cooling holes. This was done to examine the augmentation effect of film cooling on the uncooled heat transfer coefficient with varying blowing rates, density ratios and turbulence conditions. A review of the open literature revealed that the augmentation effects on heat transfer coefficient can be extremely localized to the immediate vicinity of the film cooling holes. Therefore, it was necessary that the heating film provide a well-defined boundary condition directly around film cooling holes as well. Additionally, the film-cooled surface could also be used for measuring the adiabatic film effectiveness under the same wide range of conditions. Both pieces were machined from Ren Shape 450, which was selected for its relatively low-thermal conductivity. An advantage with the single passage model is the fact that substantial amounts of insulating material can be placed behind the measurement surfaces, minimizing backlosses.

Figure 3.54 presents a picture of the cross-sectional view of the Ren Shape substrate for the heat flux surfaces. This piece is practically identical to that used for aerodynamics measurements, except that pressure side airfoil surface was inset 0.0635-mm to compensate for the heat flux film thickness and the BB-G1/TLC coating. This was instrumented with five Type-K, 36-gauge thermocouples installed at the centerline of the measurement piece. The thermocouples were inserted into 25.4-mm deep, 1.27-mm diameter holes with thermally conductive epoxy (Omegabond 101 #OB-101-1/2). 1.78-mm deep channels were machined into the side of the Ren Shape piece, to direct the thermocouple wires out of the model. Table 3.10 lists the perpendicular distances where the thermocouples were installed relative to the measurement surface, and the corresponding surface coordinate along the measurement surface.

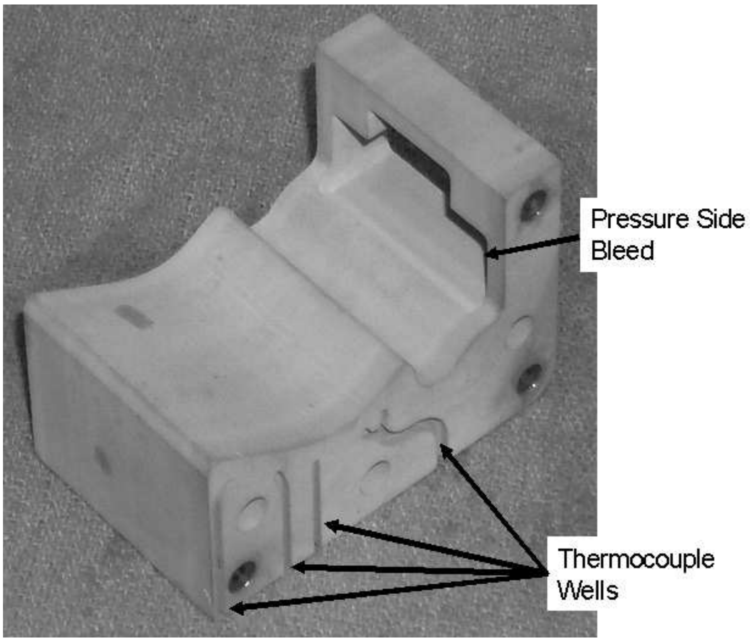

Figure 3.54: Picture of Ren Shape 450 pressure side wall substrate for heat flux film.

Table 3.10: Backloss thermocouple locations.

Thermocouple	Perpendicular Distance ($\frac{\mathcal{P}}{c_{blade}}$)	Surface Coordinate ($\frac{s_c}{c_{blade}}$)
1	0.138	-0.179
2	0.140	-0.271
3	0.139	-0.515
4	0.139	-0.745
5	0.139	-1.077

To avoid unheated starting length issues with the constant heat flux measurements, as encountered and documented by Mukerji and Eaton (2002), it was necessary to have the heat flux surface extend past the stagnation point, into the boundary layer bleed chamber. This meant that the applied heating film had to bend around an extremely small radius of curvature (1.27-mm) near the leading edge of the airfoil. Given this radius of curvature, the 125-μm thick polyester film sputter-deposited with an indium/tin oxide (ITO) layer used by Mukerji and Eaton (2002) (CP Films Inc. # OC100 ST504) could not be used. Exploratory tests revealed that the ITO layer would delaminate from the polyester substrate when bent around the leading edge. With this experience, it was concluded that the heating film should

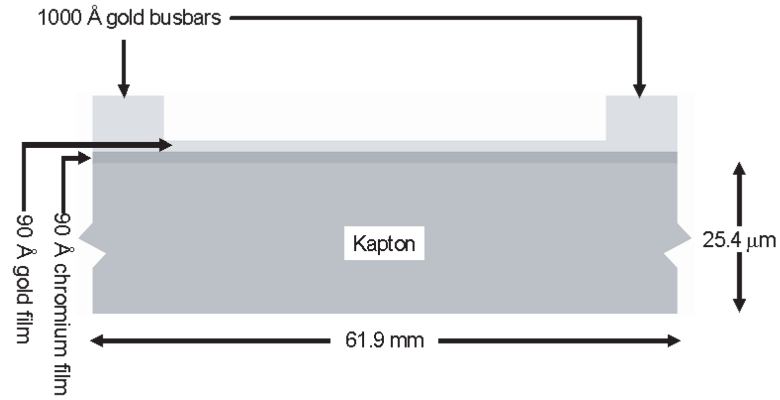

Figure 3.55: Cross-sectional view of heating film.

have a total thickness of approximately 25-μm and a very flexible conductive surface. The first iteration of this design involved using a 25-μm thick conductive vinyl film (Intelicoat 1-mil Carbon/Release Support), but it was found that the vinyl reacted to the applied TLC paint, changing the resistance of the film. The implemented heat flux surface consisted of a 25.4-μm thick Kapton (Shercon # QDD16562) with 90 Å vacuum-deposited layers of chromium and gold. The gold layer served as the heat flux surface and the chromium acted as an adhesion layer to the Kapton substrate. The design of this surface was based on previous work from Carver (2003) and Elkins et al. (2001). Figure 3.55 presents a cross-sectional view of the heating film, which was made slightly larger than the desired size. Figure 3.56 presents the three masks that were constructed from 0.76-mm thick aluminum to allow the deposition of the base heating film and busbars. The masks were aligned using four crosses placed in the corners of the masks and the Kapton film. One aluminum piece was used as a support for the Kapton substrate. A cut sheet of high-quality inkjet photo paper (Kodak # 1712736) was pressed onto the metal-deposited surface of the heating film with removable glue (Avery # 0151). The glue was applied as a thin layer to the paper, ensuring no "clumps" or particles were embedded in the layer. The importance of this paper support was to act as a protective cover for the application process to the Ren Shape piece and act as sacrificial support during the installation of the film cooling holes. The paper-covered film was then cut to the dimensions 50.8-mm × 59.7-mm using a CO_2 laser to conform with the measurement surface dimensions. The final piece had busbar widths of 3.18-mm. All the preceding steps were performed using clean-room standard laboratory techniques, to ensure that the resulting heating film had very few scratches, which would

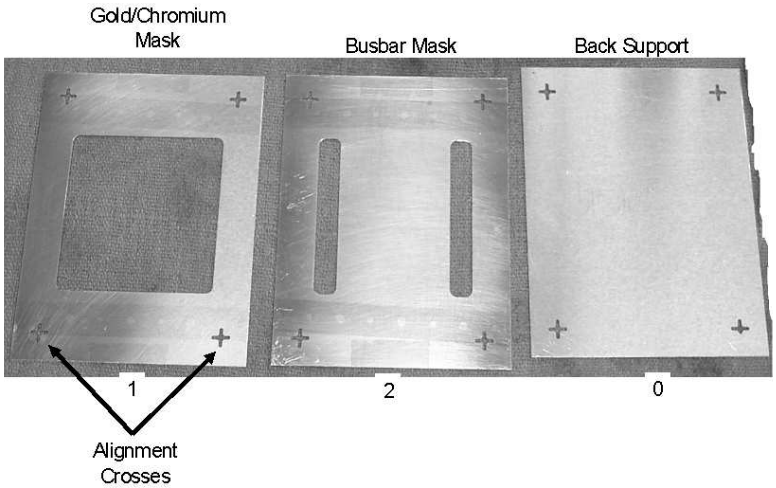

Figure 3.56: Masks for the heat flux surface.

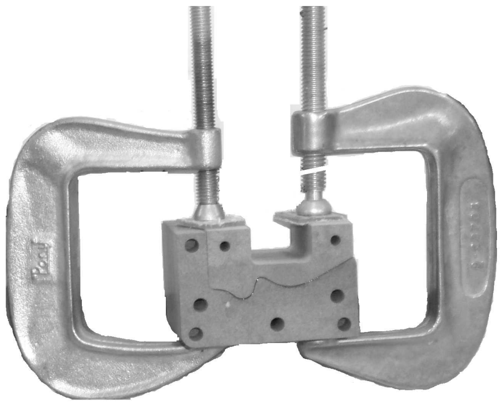

Figure 3.57: Clamping arrangement for heat flux surface.

cause local “hot spots”.

The Ren Shape surface was first coated with a thin layer of 2-ton clear epoxy (Devcon #14310). The film was then placed over the surface and compressed into placed using another Ren Shape piece machined with the negative of the measurement surface. Figure 3.57 presents a picture of this assembly. This compression squeezed out the excess epoxy. A critical issue was setting the appropriate clamping force: too much, and the texture of the underlying Ren Shape would wrinkle the heating film, too little and air gaps would form under the heating film. Once painted with BB-G1 and the TLC, any slight non-uniformities in the film were filled in, leaving a near flat matte finish.

For the uncooled surface, the fabrication was complete at this point and the paper cover was removed. Preliminary tests revealed that the 1000Å gold busbars did not provide enough conductivity to ensure a two-dimensional potential field across the heated surface. Consequently, two 3.175-mm wide strips of cleaned copper tape (3M #1181-1/4) were bonded in the streamwise direction of the heating film with conductive two-part silver epoxy (SPI Supplies #05067-AB). This silver epoxy was also used to connect the busbars to two lead wires which lead out of the model. Figure 3.58 presents a picture of the TLC-painted uncooled heat transfer surface, installed in the single passage model. The construction of the film-cooled heat flux surface differed somewhat from the uncooled surface. Before installing the busbars and electrical leads, the film cooling holes and supply plena were installed. The paper cover over the heat flux surface was important to prevent any burrs developing during the drilling of the film cooling holes, as well as protecting the surface during the machining of the film cooling plena. Buck (2000) suggested the film cooling holes for each row should span the range $-\frac{1}{3} \leq Z' \leq \frac{1}{3}$ to ensure the downstream flowfield was two-dimensional. Based on this constraint, and the requirement that the number of holes should be odd numbered, with the mid-span hole at the centerline of the passage, the following equation was derived for the required number of holes:

$$N_{fc,holes} = \frac{2}{3}\frac{H_{MODEL}}{p} + 1 \tag{3.42}$$

Before drilling the film cooling holes, two additional angles were defined for ease of machining purposes. These angles are a subset of six angles, any of two of which define the shape of a compound angle round hole. Figure 3.59 schematically presents these angles while table 3.11 explicitly defines them. The swept angles, $\alpha_{sw,radial}$ and $\beta_{sw,axial}$ are typically used for machining purposes, as it is generally far easier and more accurate to orient a highly curved turbine airfoil surface using these angles, rather than the more obvious choice of α and β. Figure 3.60 presents the fixtures used for drilling the compound angle round holes. They consisted of a precision-machined Plexiglas block with one face machined to a specific angle, corresponding to one of the hole-defining angles. The assembly was then rotated to the other desired angle.

To ensure that the mass flow through each film cooling hole was identical, the cross sectional areas of the film cooling plena were chosen to be at least four times the total exit area of the film cooling holes. This resulted in plenum diameter to hole diameter ratios of $\frac{d}{D_{plenum}}_1 = 0.094$ and $\frac{d}{D_{plenum}}_2 = 0.070$. Based on the works examined in section 1.5.6, these

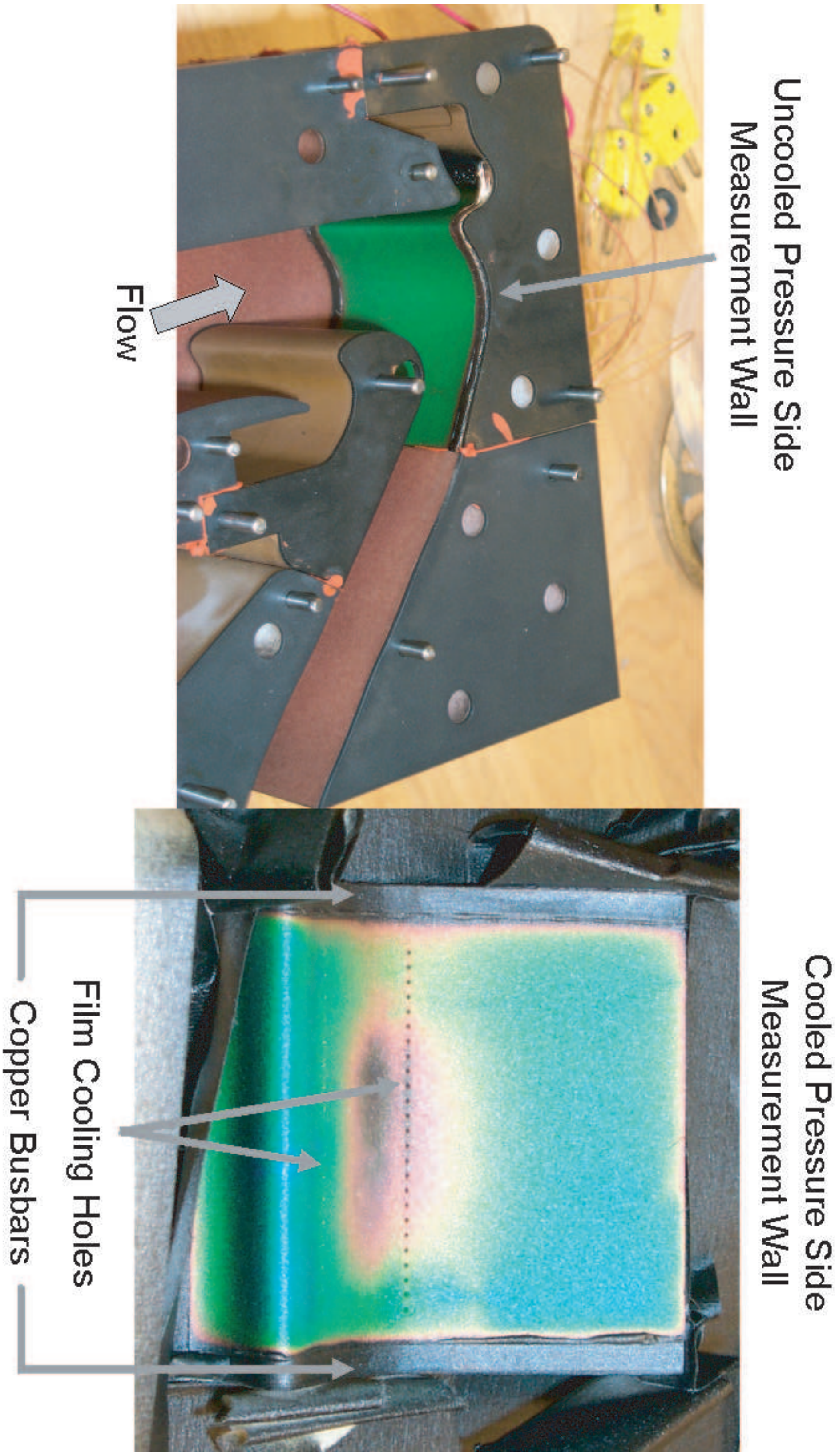

Figure 3.58: Pictures of uncooled and cooled heat flux surfaces.

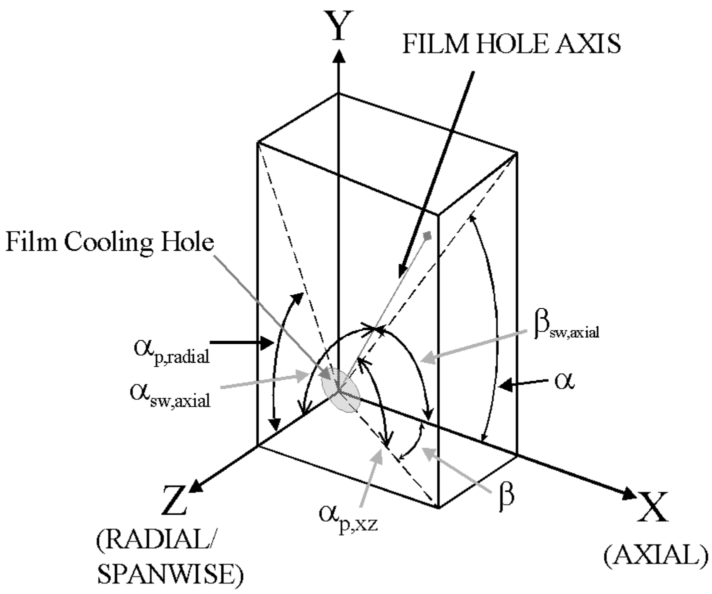

Figure 3.59: Schematic of compound angle round hole film cooling definition angles.

Table 3.11: Definitions of compound angle round hole definition angles (derived from Buck (2000)).

Angle	Definition
α	angle between projection of film hole axis (FHA) on airfoil cross section (XY plane) and axial tangent (X)
β	angle between projection of FHA on airfoil surface (XZ plane) and axial tangent (X)
$\alpha_{sw,radial}$	swept angle between FHA and radial tangent (Z)
$\beta_{sw,axial}$	swept angle between FHA and axial tangent (X)
$\alpha_{p,radial}$	angle between projection of FHA on radial cross section (YZ plane) and radial tangent (Z)
$\alpha_{p,xz}$	angle between FHA and projection of FHA on airfoil surface (XZ plane)

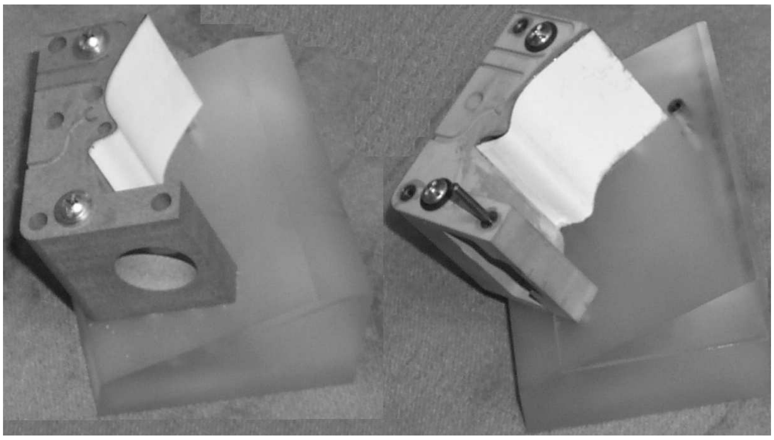

Figure 3.60: Picture of Plexiglas fixtures for heat flux surface film cooling holes.

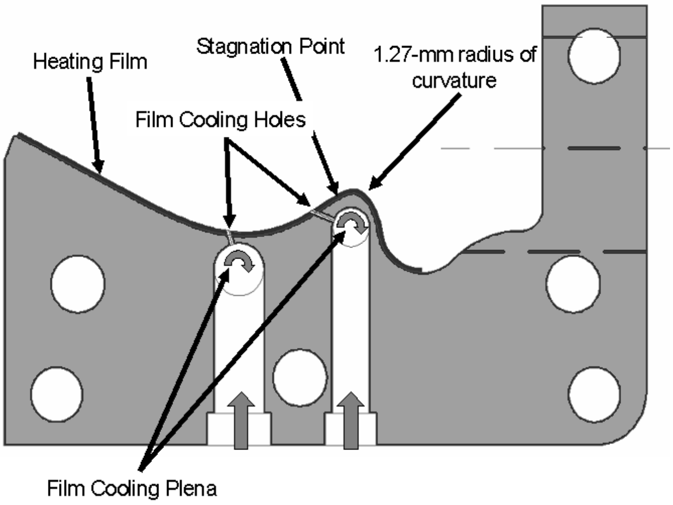

Figure 3.61: Schematic of assembled heat flux surface.

dimensions suggest that plena have negligible effects on the film cooling flow conditions. The plena consisted of two equal diameter cross-drilled holes, with the supply at the centerline of the measurement piece. Figure 3.61 displays a side view of the completed pressure side cooled heat flux surface. Two holes were installed to the corresponding locations for each plenum in the endwalls designed to monitor the coolant total pressure ($P_{\circ,c}$) and temperature ($T_{\circ,c}$). One was a sheathed 1.59-mm thermocouple (Omega #KMQXL-062U-6) whose tip was placed at the center of the plenum. The other was a 0.61-mm diameter pressure tap. A separate Setra 239 pressure transducer with a 0-100 psia range, connected

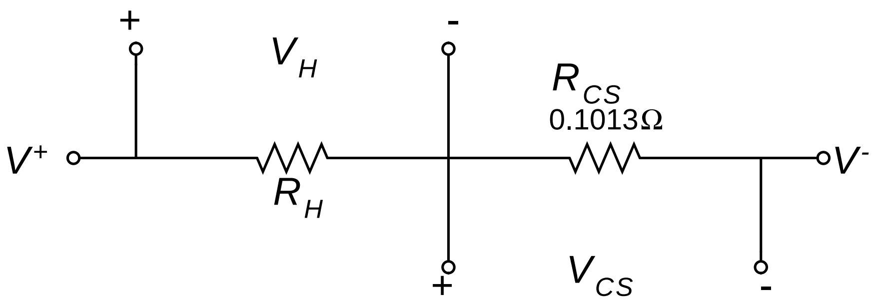

Figure 3.62: Schematic of current sense resistor circuit.

to a three-way valve, was used to monitor the total pressure for each row.

A DC power supply (Hewlett-Packard #6034A, 200W) was used to power the heat transfer surfaces. The voltage applied to the heating film (V_H) and a 1% precision current sense resistor (Caddock Electronics #SR10-0.10-1%) with a measured resistance of $R_{CS} = 0.1013\Omega$ connected in series was measured via the thermocouple zone box system described in section 2.4.2. Figure 3.62 presents the circuit diagram for this subsystem.

Chapter 4

Uncooled Heat Transfer Experiments: Results and Analysis

This chapter presents and discusses the results taken on the pressure side surface of an advanced transonic blade geometry. These experiments were conducted to form a baseline for the film cooling results presented in the next chapter and to investigate some fundamental issues with compressible flow heat transfer. This was to gain additional insight to improve numerical predictions of the convective heat transfer coefficient on airfoil geometries. As discussed in chapter 1, a key impediment to the augmentation of numerical prediction tools is the availability of well-resolved, low uncertainty experimental data at realistic conditions with well-defined boundary conditions. Consequently, when comparing numerical and experimental results it is difficult to discern if observed differences are due to the numerical models or issues with the experimental techniques. This observation is discussed in greater detail in section 1.2. One example of this predicament is the fact that most experiments for real turbine blade geometries at realistic conditions use transient heat transfer techniques to measure the heat transfer coefficient. This approach implicitly assumes that the energy equation (presented in section 1.6.1) is linear, even if the flow conditions are compressible. With this basis, it is inferred that the heat transfer coefficient is not a function of the time-resolved heat flux applied to the measurement surface. Generally, the comparative numerical simulations are steady state. This raises the question of compatibility between these two approaches.

4.1 Experimental Results

The following sections present measured data at low and high turbulence conditions at various heat flux settings. The objective of this parametric study was to examine the augmentation effects of turbulence on the uncooled surface heat transfer coefficient. Additionally, these measurements were conducted to form a baseline for the film cooled results presented in Chapter 5. These data have been spanwise-averaged over the intersection of the predicted the two-dimensional portion of the flow, as shown in section 2.1.5 ($-0.25 \leq Z' \leq 0.25$), and the valid viewing area of the borescope system ($-0.12 \leq Z' \leq 0.24$).

4.1.1 Recovery Temperature Measurements

The recovery temperature was measured with no heating applied. The flow facility was set to provide elevated total temperatures to ensure that the liquid crystals painted on the surface were within their active range. These distributions were used to determine the recovery temperature distribution ($\frac{T_{rec}(s_c/c_{blade})}{T_\circ} = f(M_{is})$) and recovery factor ($r_\infty$).

Figure 4.1 presents the measured temperature maps for both the low and high turbulence cases. A careful examination of these maps revealed that the $T_{rec}(Z', s_c/c_{blade})$ distributions were nearly identical. Figure 4.2 presents the spanwise-averaged and median-filtered (on a symmetric 8-point stencil) temperature data, compared to a prediction using equations 3.36 and 3.37 with a recovery factor of $r_\infty = 0.9$. These experimental results suggest that $T_{rec}(Z', s_c/c_{blade})$ has a negligible dependence on the inlet turbulence intensity ($TI\%$) and integral length scale (ℓ).

With this baseline, the total temperature for the test is lowered such that the measurement surface is within the active range of the liquid crystals when current is applied to the heat flux surface. For all the tests presented in this chapter, $T_\circ = 25°C$. The $\frac{T_{rec}(s_c/c_{blade})}{T_\circ}$ distribution was used to estimate the $T_{rec}(s_c/c_{blade})$ distribution and generate $T_{rec}(Z', s_c/c_{blade})$ spatially-resolved maps for this new total temperature case.

To demonstrate the evaluation of the adiabatic nature of the measurement surface, table 4.1 presents typical recorded thermocouple data from an operating test with $T_\circ = 33.1°$. Additionally, this table presents the estimated conduction heat flux (q''_{cond}) using the equation:

$$q''_{cond,i} = \frac{k_s}{\mathcal{P}}(T_{w,i} - T_{bl,i}) \tag{4.1}$$

where k_s is the thermal conductivity of the Ren Shape substrate, $k_s = 0.2\,\frac{W}{m \cdot K}$ and $\mathcal{P}$ is the perpendicular distance between the backloss thermocouple and the surface. When used to estimate the heat flux at the surface, these data indicate that the measurement surface can indeed be considered as adiabatic. Assuming a heat transfer coefficient of $h = 500\,\frac{W}{m^2 \cdot K}$, these data indicate an approximate temperature difference of $|T_w - T_{rec}| \approx 0.2°$. For the T_{rec} measurements, this observation was consistent for all test cases conducted.

Several simulations were performed to ensure that the $\overline{T_{rec}}(s_c/c_{blade})$ could be reproduced using RANS simulations. Figure 4.3 compares T_{rec} computed using a recovery factor

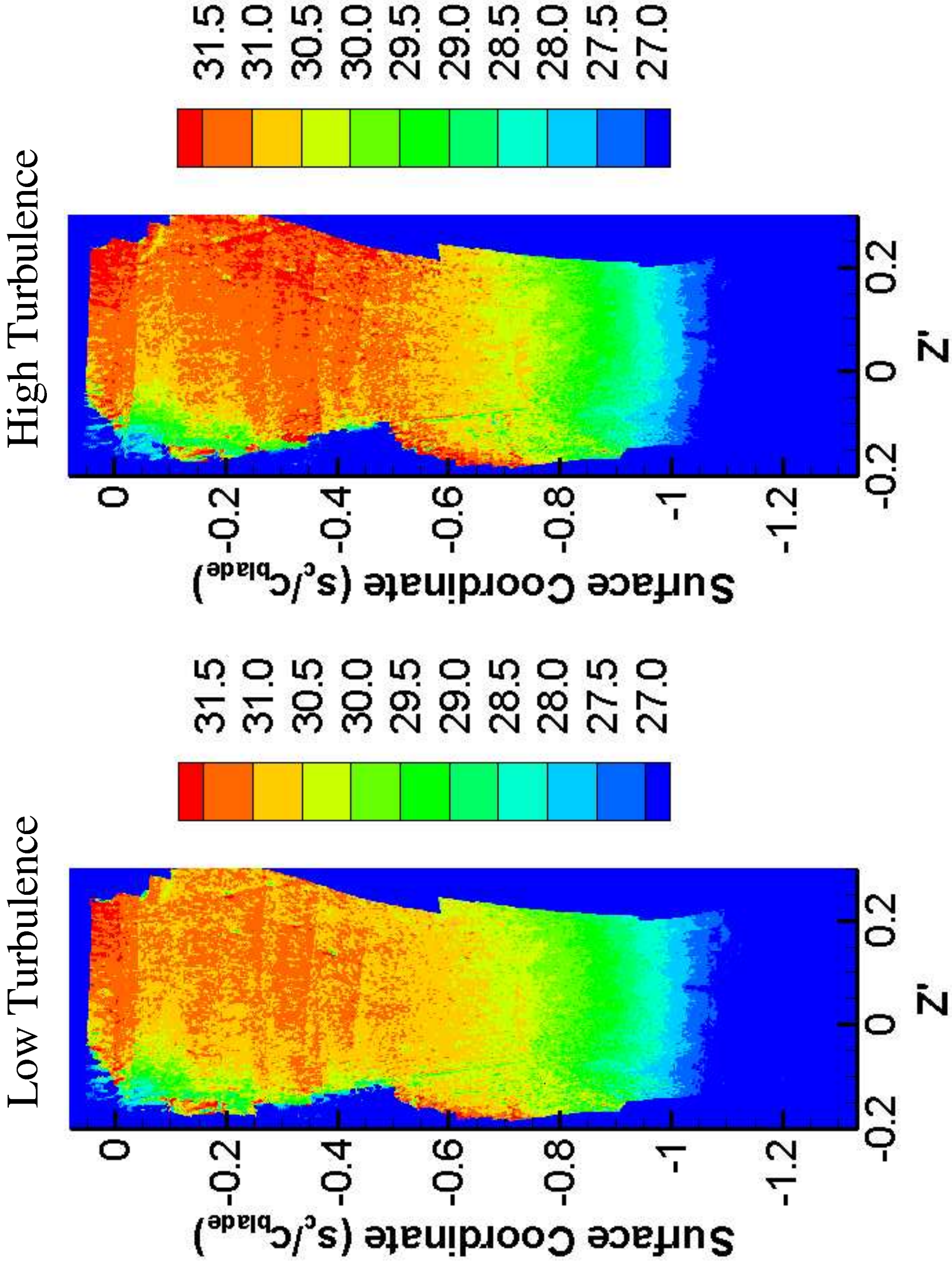

Figure 4.1: Measured spatially-resolved maps of $T_{rec}(Z', s_c/c_{blade})$ with $T_\circ = 31.0°$ for low and high turbulence cases (in $°C$).

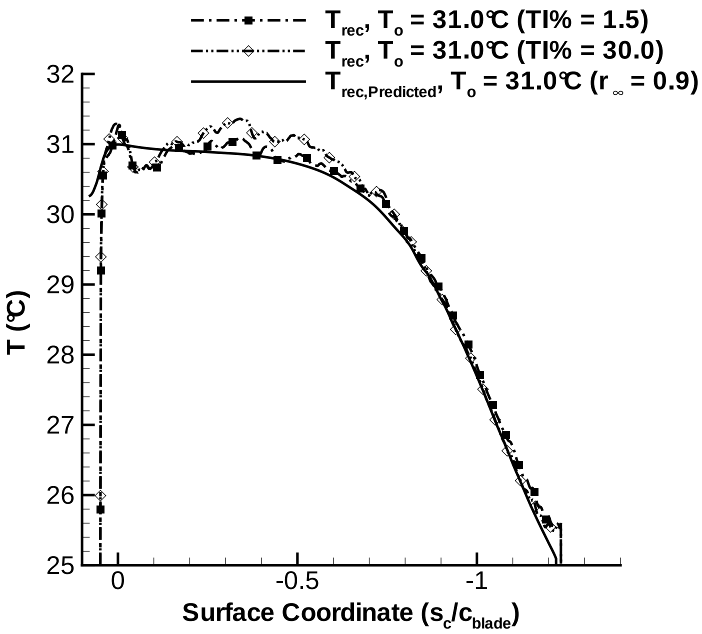

Figure 4.2: Measured spanwise-averaged $\overline{T_{rec}}$ distributions for low and high turbulence cases with $T_\circ = 31.0°$C.

Table 4.1: Sample backloss evaluation for uncooled heat transfer experiment ($T_\circ = 33.1°$).

Thermocouple	Perpendicular Distance ($\frac{\mathcal{P}}{c_{blade}}$)	$T_{w,i}$ (°C)	$T_{bl,i}$ (°C)	$q''_{bl,i}$ ($\frac{W}{m^2}$)
1	0.138	33.13	31.79	53.8
2	0.140	32.88	31.21	66.5
3	0.139	32.70	30.94	70.2
4	0.139	32.17	30.43	69.6
5	0.139	28.91	29.50	-23.1

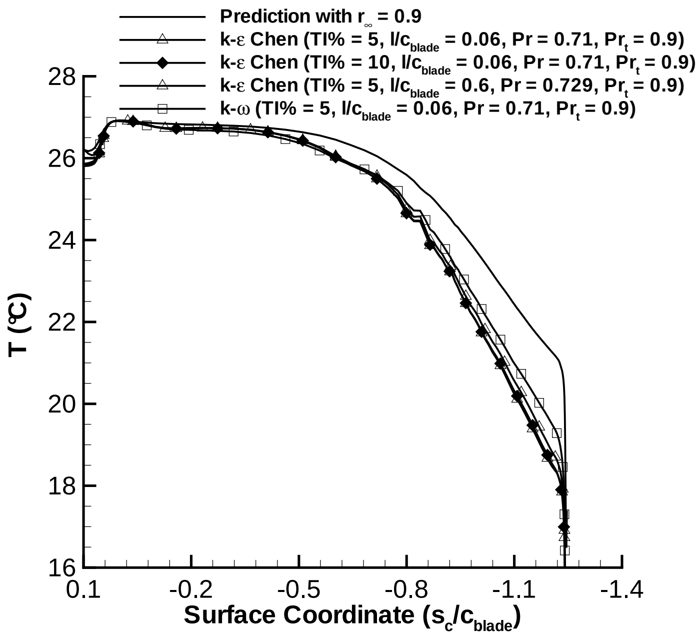

Figure 4.3: Computed $T_{rec}(s_c/c_{blade})$ distributions for airfoil pressure side surface using a range of turbulence models with varying inlet $TI\%$, $\frac{\ell}{c_{blade}}$ and Prandtl numbers.

of $r_\infty = 0.90$ and several calculations with different inlet turbulence intensity levels, integral length scales, Prandtl numbers and turbulence models. The results in this figure show that irrespective of the combination of parameters, the RANS simulations significantly under-predict $T_{rec}(s_c/c_{blade})$. The difference between the RANS results and "correct" distribution increases as the flow accelerates. As T_{rec} serves as reference temperature upon which h is calculated, unless T_w reflects the same behavior, significant errors would be built into the resulting h predictions. In all cases shown in figure 4.3, the turbulent Prandtl number was fixed at Pr_t. Figures 4.4 and 4.5 show the results of several simulations where this parameter was gradually adjusted. The optimal constant value that gives the "best" agreement was found to be $Pr_t = 1.02$ for the Chen and Kim 1987 variant of k-ε and $Pr_t = 1.0$ for the k-ω model, as implemented by Medic and Durbin (2002a). Additionally, it was found that adjusting Pr_t had no effect on predictions of the M_{is} for both airfoil surfaces. Therefore the effect of adjusting Pr_t was localized to the developing thermal boundary layers on the measurement surfaces. This suggests that for this geometry and flow condition, assuming a constant value of Pr_t builds an inherent error into the prediction. What has not been tested here are more complicated models that allow Pr_t to vary throughout the domain, as

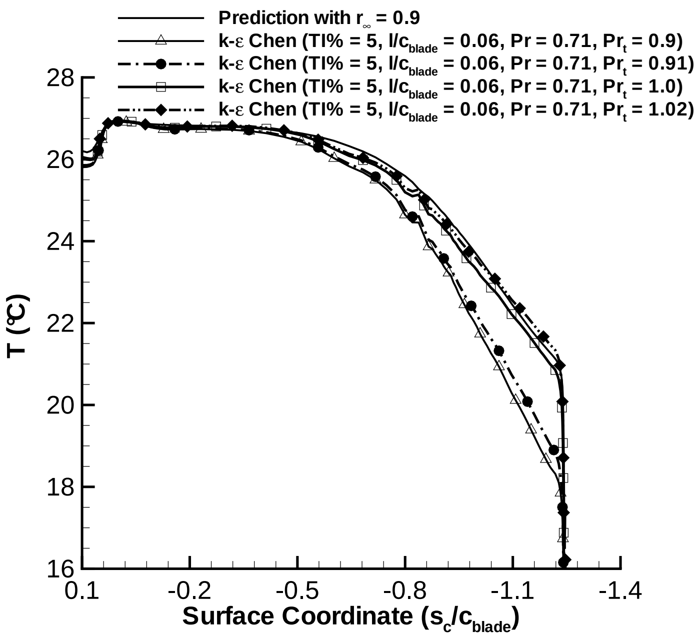

Figure 4.4: Computed $T_{rec}(s_c/c_{blade})$ distributions for airfoil pressure side surface using Chen and Kim 1987 variant of k-ε with varying values of Pr_t.

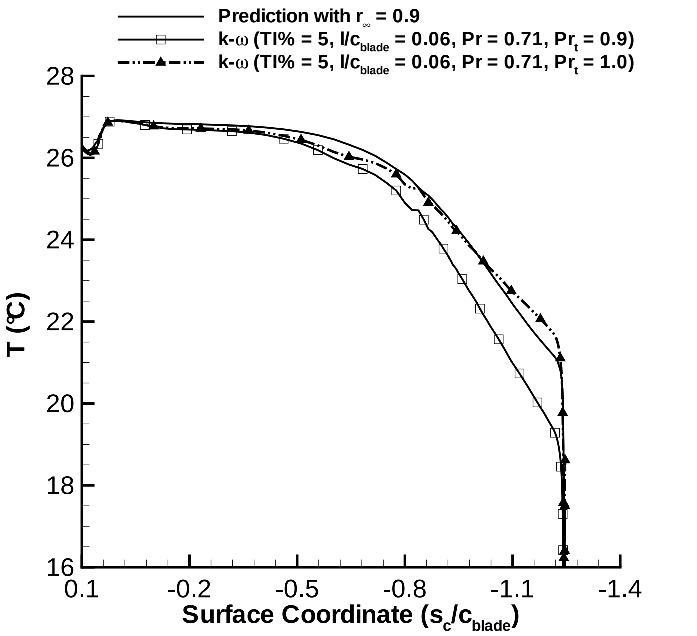

Figure 4.5: Computed $T_{rec}(s_c/c_{blade})$ distributions for airfoil pressure side surface using Medic and Durbin 2002a implementation of k-ω with varying values of Pr_t.

discussed by Kays and Crawford (1993).

4.1.2 Heat Transfer Coefficient Data Acquisition Process and Uncertainty Analysis

The total temperature for the flow system was set to $T_{\circ,\infty} = 25.0°$ and a heat flux was applied to the pressure side measurement surface. The resistance of the heat flux surface for the uncooled heat transfer tests was measured to be $R_H \approx 3.43\Omega$ with an estimated uncertainty of less than 1%. The following equation was used to compute the spatially-resolved, local heat transfer coefficient:

$$h(Z', s_c/c_{blade}) = \frac{\frac{\overline{P_H}}{A_H} - q''_{cond} - q''_{rad}}{T_w(Z', \frac{s_c}{c_{blade}}) - T_{rec}(Z', \frac{s_c}{c_{blade}})} \tag{4.2}$$

where $\overline{P_H}$ is the "time-averaged" power applied to the heat flux surface, A_H is the area of the heated surface, q''_{cond} is the conduction loss through the Ren Shape substrate and q''_{rad} is the loss due to radiation from the heated surface. $\overline{P_H}$ was determined by averaging several measurements from the current sense resistor circuit before and after heat transfer measurements were taken. This was then divided by the exposed area of the film (A_H = 44.45-mm $\times$ 59.69-mm = $2.653(10)^{-3}$-m^2). P_H and A_H were both estimated to have uncertainties of 2%.

The conductive backloss heat flux was estimated to have a maximum value of $q''_{cond} \approx 200\,\frac{W}{m^2}$ based on the backloss thermocouple data for the range of tests conducted. This value was less than 2% of the applied heat flux. The radiative heat flux from the surface was estimated using the equation:

$$q''_{rad} = \epsilon\sigma_R(T_w^4 - T_{rec}^4) \tag{4.3}$$

where σ_R is the Stefan-Boltzmann constant ($\sigma_R = 5.673(10)^{-8}\,\frac{W}{m^2 \cdot K^4}$)and ϵ corresponds to the surface emissivity of the painted surface. Batchelder and Moffat (1997) presented measurements for a TLC-coated surface that indicated that $\epsilon = 0.9$ for such a surface. This analysis also assumed that all surfaces that engage in a radiative exchange with the measurement surface were at the recovery temperature achieved with an isentropic Mach number of $M_{is} \approx 1.5$ and total temperature of $T_{\circ,\infty} = 26.7°$C. With these assumptions, the recovery temperature was computed to be $T_{rec} = 17.6°$C. Thence, estimated radiative heat flux was computed to be $q''_{rad} \approx 125\,\frac{W}{m^2}$. Appendix A details the uncertainty analysis

Table 4.2: Heating film conditions for low turbulence flow condition.

Case	$\overline{V_{CS}}$ (V)	$\overline{V_H}$ (V)	$\overline{P_{DISS}}$ (W)	$\overline{R_H}$ (Ω)	$\overline{I_{CS}}$ (A)	$\overline{P_H}$ (W)	$\overline{q''}$ $(\frac{kW}{m^2})$
1	0.22	7.45	0.480	3.42	2.176	16.21	6.12
2	0.26	9.05	0.700	3.45	2.628	23.80	8.97
3	0.25	8.34	0.593	3.44	2.420	20.17	7.60
4	0.26	9.04	0.692	3.46	2.615	23.65	8.91
5	0.32	10.83	0.980	3.48	3.110	33.69	12.70

procedure for the heat transfer coefficient. This analysis concluded with an estimated maximum uncertainty for the heat transfer coefficient of $\frac{\delta h}{h} \approx 8.6\%$ (P = 0.95).

4.1.3 Heat Transfer Coefficient Measurements

Low Turbulence Results

Table 4.2 presents the typical measured values from the current sense resistor for the five heat flux settings explored at the low turbulence flow condition. Some of the cases shown in table 4.2 are repeated experiments to ensure the consistency of the collected measurements.

Figure 4.6 presents the spanwise-averaged, median-filtered temperature distributions for the heated surface ($\overline{T_w}(s_c/c_{blade})$). These data were used primarily to estimate the back-losses from the measurement surface. They also demonstrate the substantial variations in temperature along the surface due to the complex nature of the flow. Compared to a flat plate flow, as shown in section C.1, where the temperature profile monotonically increases with streamwise distance, these data show that the spanwise-averaged temperature profile peaks at a surface coordinate of $\frac{s_c}{c_{blade}} \approx -0.27$ where the isentropic Mach number has an approximate value of $M_{is} \approx 0.2$. As the flow continues to accelerate and approaches supersonic conditions, $\overline{T_w}$ drops significantly. As the surface heat flux is increased, these profiles "shift up", consistent with expectations. Where nearly identical heat fluxes are applied, the resulting temperature profiles closely follow each other, as expected. At higher heat fluxes, portions of the liquid crystal-coated surface are out of their calibrated temperature range. This manifests itself as "gaps" in the $\overline{T_w}$ profile, as observed in the profile for $q'' = 12.72\frac{kW}{m^2}$. Figure 4.7 presents spatially-resolved maps of T_w, showing the two-dimensionality of the surface temperature profile. Additionally, these maps show how the region $-0.2 \leq \frac{s_c}{c_{blade}} \leq -0.6$ falls out of range with increasing surface flux. Also of interest in

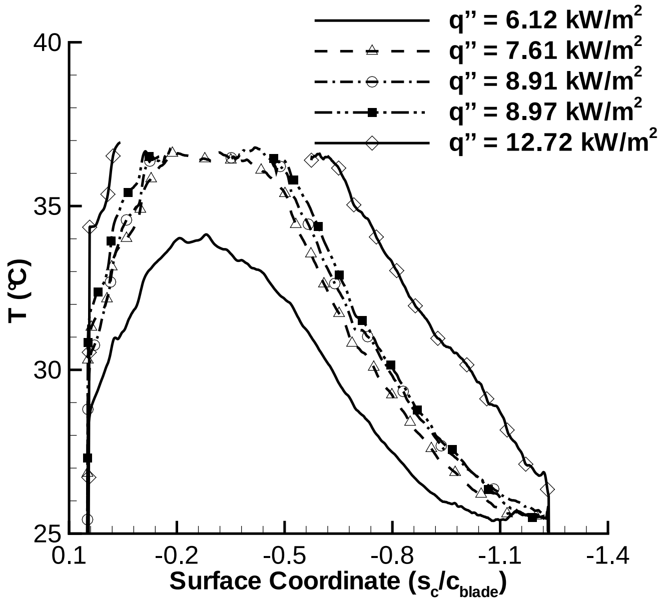

Figure 4.6: Measured spanwise-averaged $\overline{T_w}(s_c/c_{blade})$ distributions for low turbulence cases with various heat fluxes applied.

these maps are the barely discernable lengthwise “streaks” that cross nearly perpendicularly to surface isotherms. These were believed to be due to streamwise vortices, as described in section 1.5.10. It should be noted that an examination of the two-dimensional recovery temperature profiles T_{rec} shown in figure 4.1 do not reflect these “streaks”.

Figure 4.8 presents spatially-resolved maps of the convective heat transfer coefficient. These maps show that the heat transfer coefficient peaks near the airfoil stagnation line with an approximate value of $h(Z', 0) \approx 1100\frac{W}{m^2}$. As the flow progresses downstream, h decreases over the range $0 \leq s_c/c_{blade} \leq -0.4$. Over this region, the temperature rises sharply, and if the applied heat flux is large enough, the liquid crystals will move outside their active range. This manifests itself as “blind spots” in the $h(Z', s_c/c_{blade})$ distribution as shown for heat fluxes $q'' = 8.91\frac{W}{m^2}$, $q'' = 8.97\frac{W}{m^2}$ and $q'' = 12.7\frac{W}{m^2}$. As the flow accelerates, h increases and reaches a peak value in the range $-0.8 \leq s_c/c_{blade} \leq -1.2$ after which it decreases again. Interestingly, the location of the isocontour of maximum h appears to move further downstream with increasing heat flux. Comparison of the maps of T_w and h in figures 4.7 and 4.8 suggests that the line of maximum h coincides with locations closer to the airfoil trailing edge where the measured surface temperature falls near the “start temperature” of

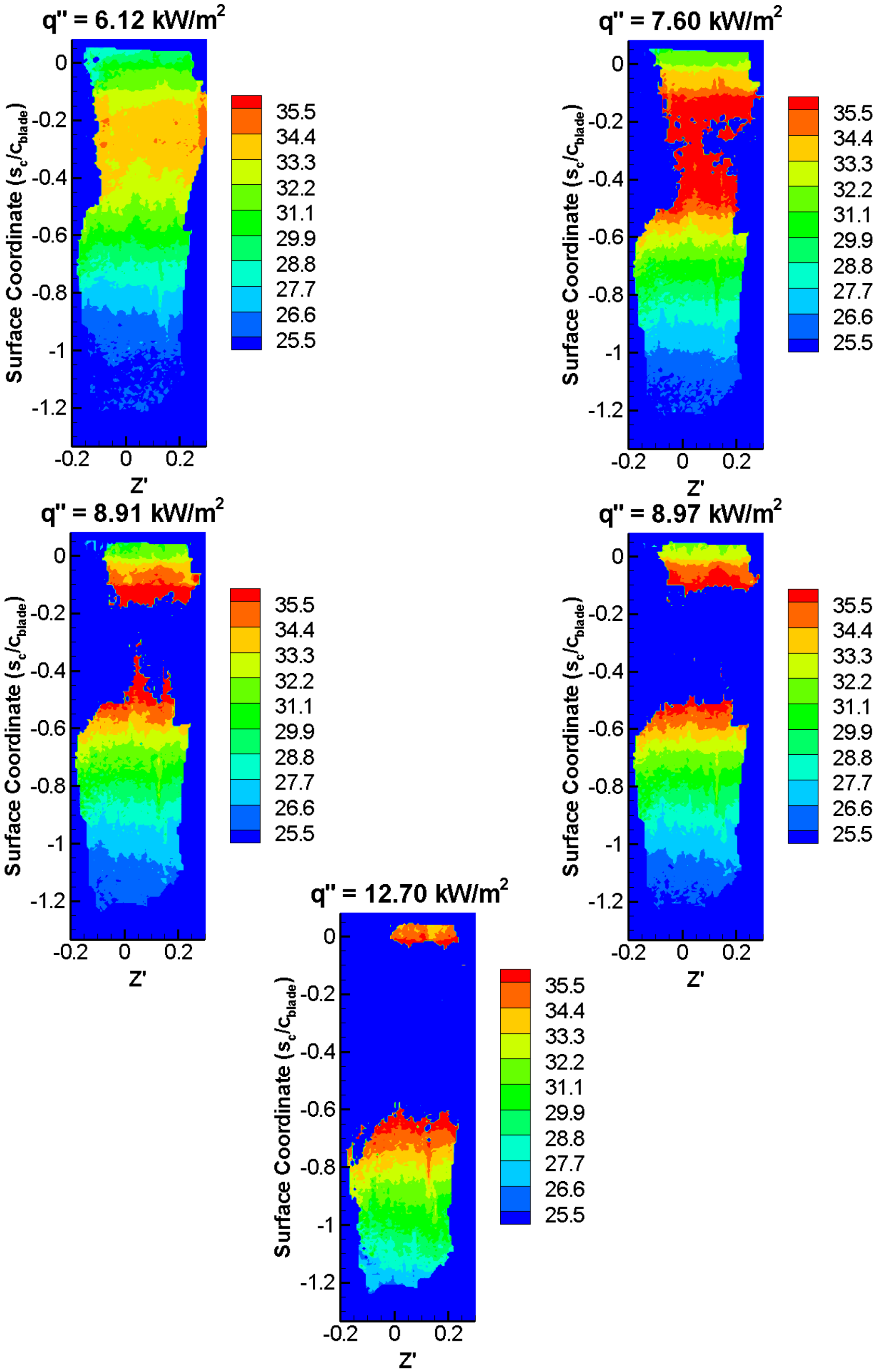

Figure 4.7: Measured spatially-resolved maps of $T_w(Z', s_c/c_{blade})$ at various heat flux settings (in $^{\circ}C$).

Table 4.3: Estimated locations and values of $\overline{h}(s_c/c_{blade})$ maxima for low turbulence flow condition.

$q''(\frac{W}{m^2})$	$(s_c/c_{blade})_{max}$	$\overline{h}(s_c/c_{blade})(\frac{W}{m^2 \cdot K})$
6.12	-0.89	1800
7.60	-0.94	1640
8.91	-0.94	1720
8.97	-0.94	1700
12.70	-1.20	1750

the liquid crystals. However, this trend appears to be consistent even when the measured values of T_w are well-within the liquid crystal active range. The streamwise "streaks" discussed in the spatially-resolved maps of $T_w(Z', s_c/c_{blade})$ are somewhat apparent in these figures.

Figures 4.9, 4.10, 4.11 and 4.12 present the spanwise-averaged heat transfer coefficient ($\overline{h}(s_c/c_{blade})$) for the various cases. In all cases, the spanwise-averaged stagnation line heat transfer coefficient was calculated to be $\overline{h}(0) \approx 1100\frac{W}{m^2 \cdot K}$. From this point, these plots show that $\overline{h}$ decreases as the flow accelerates, reaching an approximate minimum value of $\overline{h}(-0.26) \approx 700$. All curves for the low turbulence case collapse to this minimum value. Beyond this point, as the flow becomes increasingly compressible, differences begin to emerge between test cases with varying surface heat flux. In the baseline case, with an applied heat flux of $q'' = 6.12\frac{kW}{m^2}$, the heat transfer coefficient reaches as peak value of $\overline{h}(-0.90) \approx 1800$. Physically, it can be hypothesized that this peak represents a balance between two competing effects on the thermal boundary layer: the flow acceleration causes heat transfer augmentation through the thinning of thermal boundary layer, but at the same time, the increase in viscous dissipation depresses the heat transfer rate into the freestream. As the surface heat flux is changed, the location of this balance point moves further downstream and the peak value of $\overline{h}$ generally decreases. Table 4.3 summarizes the location and value of the maximum spanwise-averaged heat transfer coefficient for the various heat flux settings.

High Turbulence Results

Table 4.4 presents the typical measured values from the current sense resistor for the four heat flux settings examined at the high turbulence flow condition. As with the low

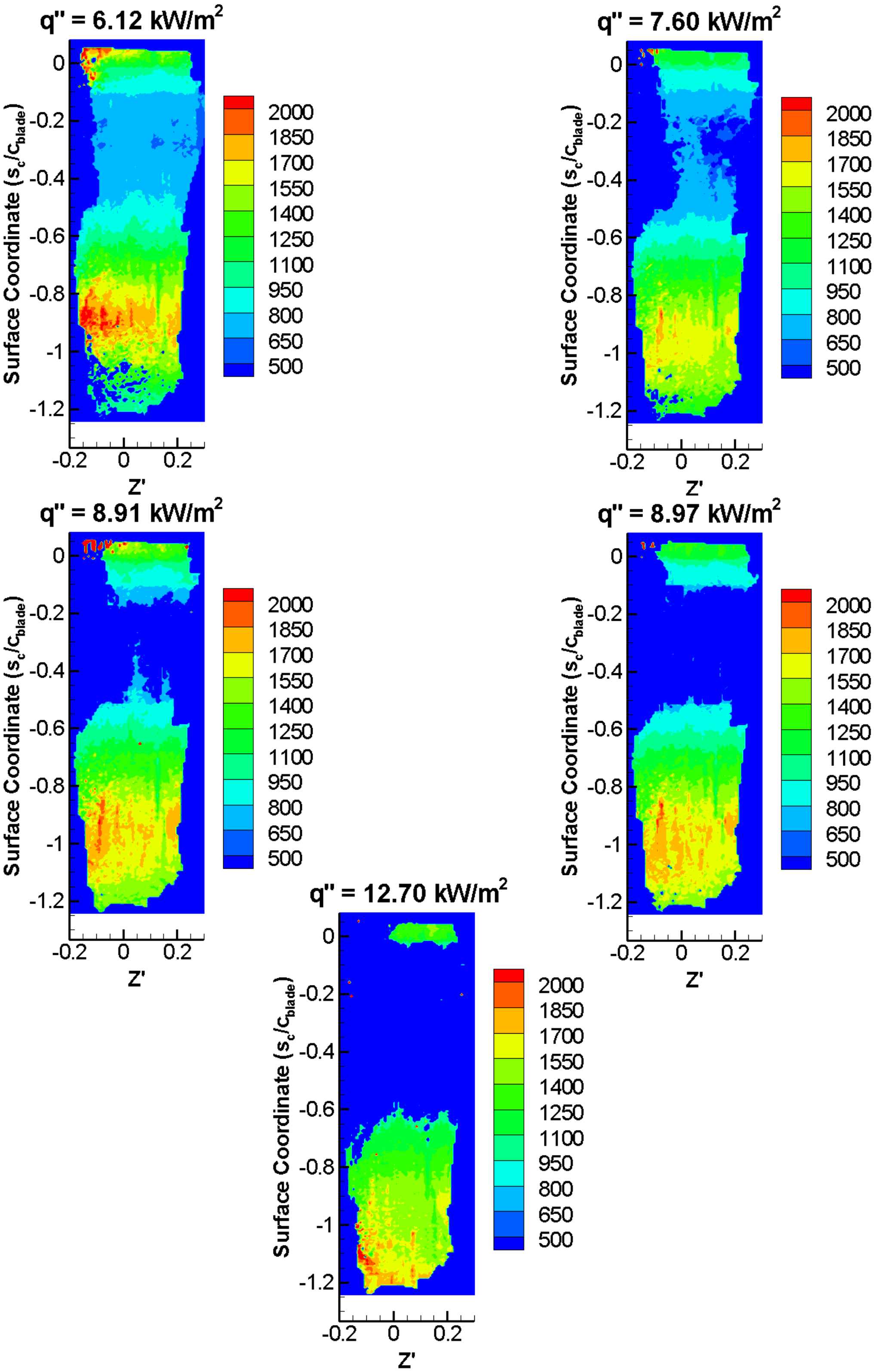

Figure 4.8: Measured spatially-resolved maps of $h(Z', s_c/c_{blade})$ at various heat flux settings (in $\frac{W}{m^2 \cdot K}$).

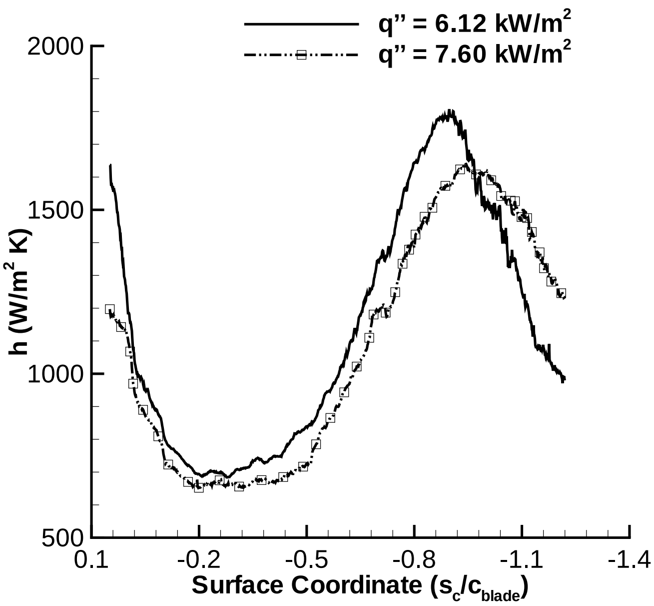

Figure 4.9: Measured spanwise-averaged $\overline{h}(s_c/c_{blade})$ distributions for low turbulence case with heat fluxes $q'' = 6.12\frac{kW}{m^2}$ and $q'' = 7.60\frac{kW}{m^2}$ applied.

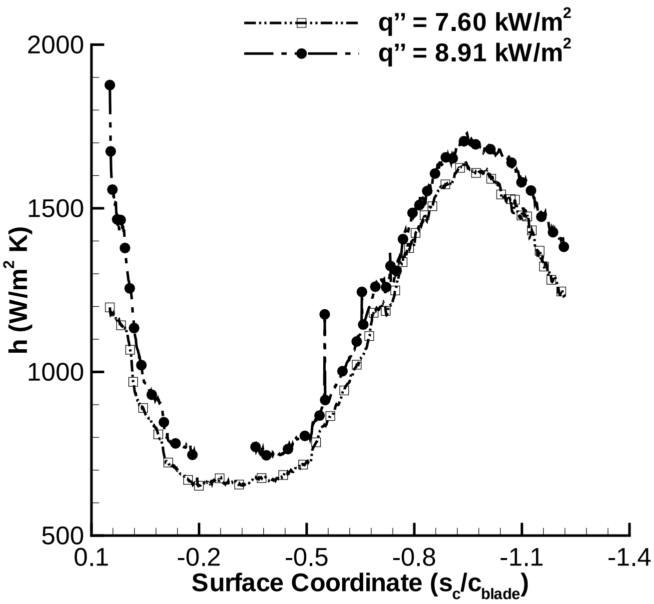

Figure 4.10: Measured spanwise-averaged $\overline{h}(s_c/c_{blade})$ distributions for low turbulence case with heat fluxes $q'' = 7.60\frac{kW}{m^2}$ and $q'' = 8.91\frac{kW}{m^2}$ applied.

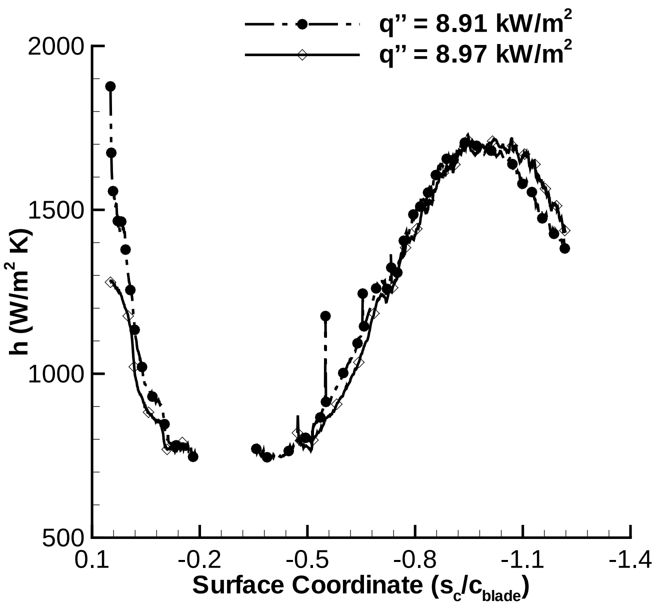

Figure 4.11: Measured spanwise-averaged $\overline{h}(s_c/c_{blade})$ distributions for low turbulence case with heat fluxes $q'' = 8.91\frac{kW}{m^2}$ and $q'' = 8.97\frac{kW}{m^2}$ applied.

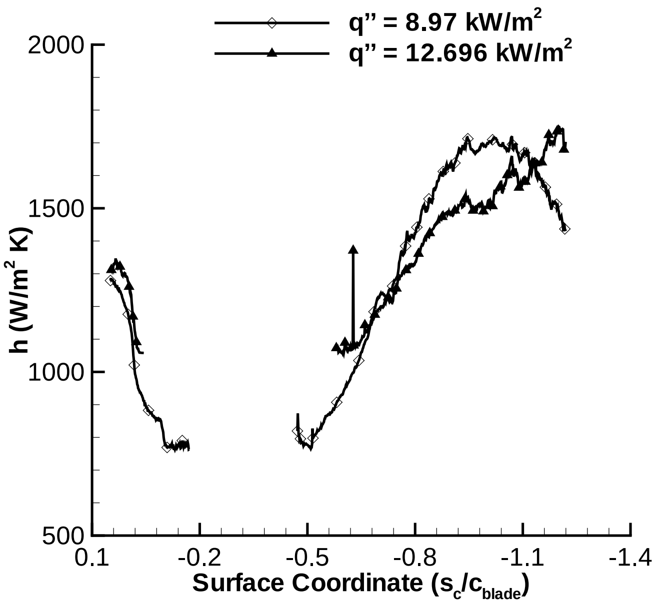

Figure 4.12: Measured spanwise-averaged $\overline{h}(s_c/c_{blade})$ distributions for low turbulence case with heat fluxes $q'' = 8.97\frac{kW}{m^2}$ and $q'' = 12.70\frac{kW}{m^2}$ applied.

Table 4.4: Heating film conditions for high turbulence flow condition.

Case	$\overline{V_{CS}}$ (V)	$\overline{V_H}$ (V)	$\overline{P_{DISS}}$ (W)	$\overline{R_H}$ (Ω)	$\overline{I_{CS}}$ (A)	$\overline{P_H}$ (W)	$\overline{q''}$ $(\frac{kW}{m^2})$
1	0.22	7.43	0.475	3.43	2.165	16.08	6.06
2	0.27	9.22	0.729	3.44	2.682	24.74	9.32
3	0.27	9.22	0.722	3.45	2.669	24.62	9.28
4	0.32	10.79	0.983	3.46	3.116	33.63	12.68

Table 4.5: Estimated locations and values of $\overline{T}(s_c/c_{blade})$ maxima.

$q''(\frac{W}{m^2})$	$(s_c/c_{blade})_{max}$	$\overline{T}(s_c/c_{blade})$(°C)
6.12 ($TI\% = 1.5$)	-0.27	34.1
6.06 ($TI\% = 30.0$)	-0.31	31.5
9.28 ($TI\% = 30.0$)	-0.38	35.0
9.32 ($TI\% = 30.0$)	-0.34	35.8

turbulence data, some of the cases shown in table 4.4 are duplicated experiments to determine the repeatability of the measurements.

Figures 4.13 and 4.14 compare the spanwise-averaged temperature profile ($\overline{T_w}(s_c/c_{blade})$) for comparable surface heat flux rates for low and high turbulence cases, to show the effect of the increased turbulence levels on the developing thermal boundary layer. Firstly, these figures show that the measured temperature rise is noticeably lower over the range $0 \leq \frac{s_c}{c_{blade}} \leq 0.8$. After this point, it generally appears that the temperature profiles for comparable heat fluxes collapse upon each other, regardless of the inlet turbulence level. Unlike the low turbulence data, the location of peak spanwise-averaged temperature appears to shift with increasing heat flux. To quantify this observation, table 4.5 lists the locations and values for the $\overline{T_w}$ maxima for the cases shown in figure 4.13. The case $q'' = 12.70\frac{kW}{m^2}$ is not shown in this table, as the location of $\overline{T_w}(s_c/c_{blade})_{max}$ is outside the range of the applied liquid crystal paint.

Figure 4.15 presents spatially-resolved temperature maps of the heated measurement surface with a high turbulence inlet condition. The longitudinal "streaks" observed previously are also seen here. The more energetic high turbulence flow has the greatest effect (relative to the low turbulence case) over the region $-0.1 \leq \frac{s_c}{c_{blade}} \leq -0.6$. This behavior manifests itself as a significant reduction in the temperature rise. This observation agrees

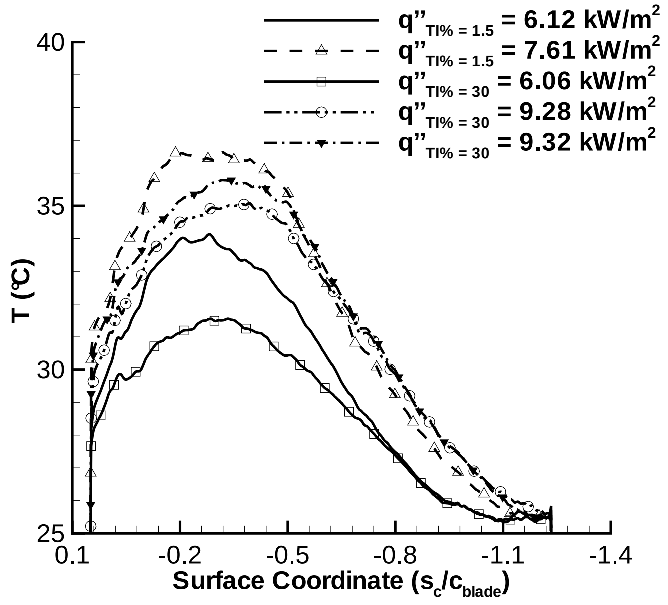

Figure 4.13: Measured spanwise-averaged $\overline{T_w}(s_c/c_{blade})$ distributions for low and high turbulence cases with heat fluxes $q'' = 31.0°$.

with the spanwise-averaged data shown in figures 4.6. These spatially-resolved maps indicate that this effect is fairly uniform across the width of the measurement surface.

Figure 4.16 presents spatially resolved maps of the convective heat transfer coefficient with the high turbulence flow condition specified. These results show comparable features to those enumerated with h data for the low turbulence condition. However, the effect of increased turbulence levels is also apparent in these figures. The heat transfer coefficient reached an approximate value of $h(Z', 0) \approx 1400\frac{W}{m^2}$ along the airfoil stagnation line. This is 27% higher than for the low turbulence case. As the flow begins to accelerate, the augmentation effect of increased turbulence becomes even more noticeable. The isocontour of minimum h appeared to occur at $\frac{s_c}{c_{blade}} \approx -0.4$ with a an estimated value of $h \approx 800\frac{W}{m^2}$ which is 14% higher than the minimum value for the low turbulence data. As the flow continues to accelerate, the h data suggest that the trends identified with the low turbulence case are nearly exactly duplicated in the high turbulence case. These observations are given further support by the spanwise-averaged heat transfer coefficients that are presented in figures 4.19, 4.17 and 4.18. These show that if the same surface heat flux rate is specified, the location and value of the maximum heat transfer coefficient does not change with the

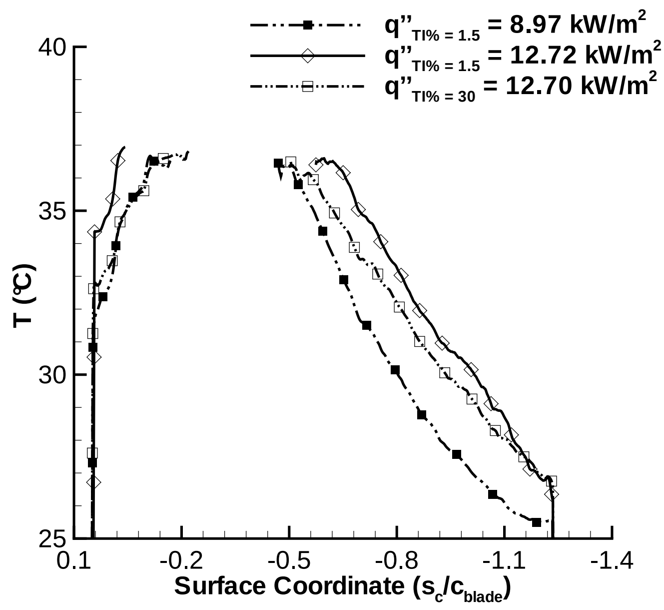

Figure 4.14: Measured spanwise-averaged $\overline{T_w}(s_c/c_{blade})$ distributions for low and high turbulence cases with various heat fluxes applied.

Table 4.6: Estimated locations and values of $\overline{h}(s_c/c_{blade})$ maxima for high turbulence flow condition.

$q''(\frac{W}{m^2})$	$(s_c/c_{blade})_{max}$	$\overline{h}(s_c/c_{blade})(\frac{kW}{m^2})$
6.06	-0.90	1750
9.28	-0.98	1670
9.32	-1.02	1710
12.70	-1.08	1500

inlet turbulence condition. This could be due to the fact that the flow had accelerated so substantially that the turbulence intensity for the two cases had become too small to affect the boundary layer. The only exception to this observation can be found examining the high and low turbulence cases where $q'' = 12.7\frac{kW}{m^2}$. These data indicate that $\overline{h}$ is slightly lower for the high turbulence case, which can also be observed from maps of $h(Z', s_c/c_{blade})$ shown in figures 4.8 and 4.16. Table 4.6 summarizes the location and value of the maximum spanwise-averaged heat transfer coefficient for the various heat flux settings.

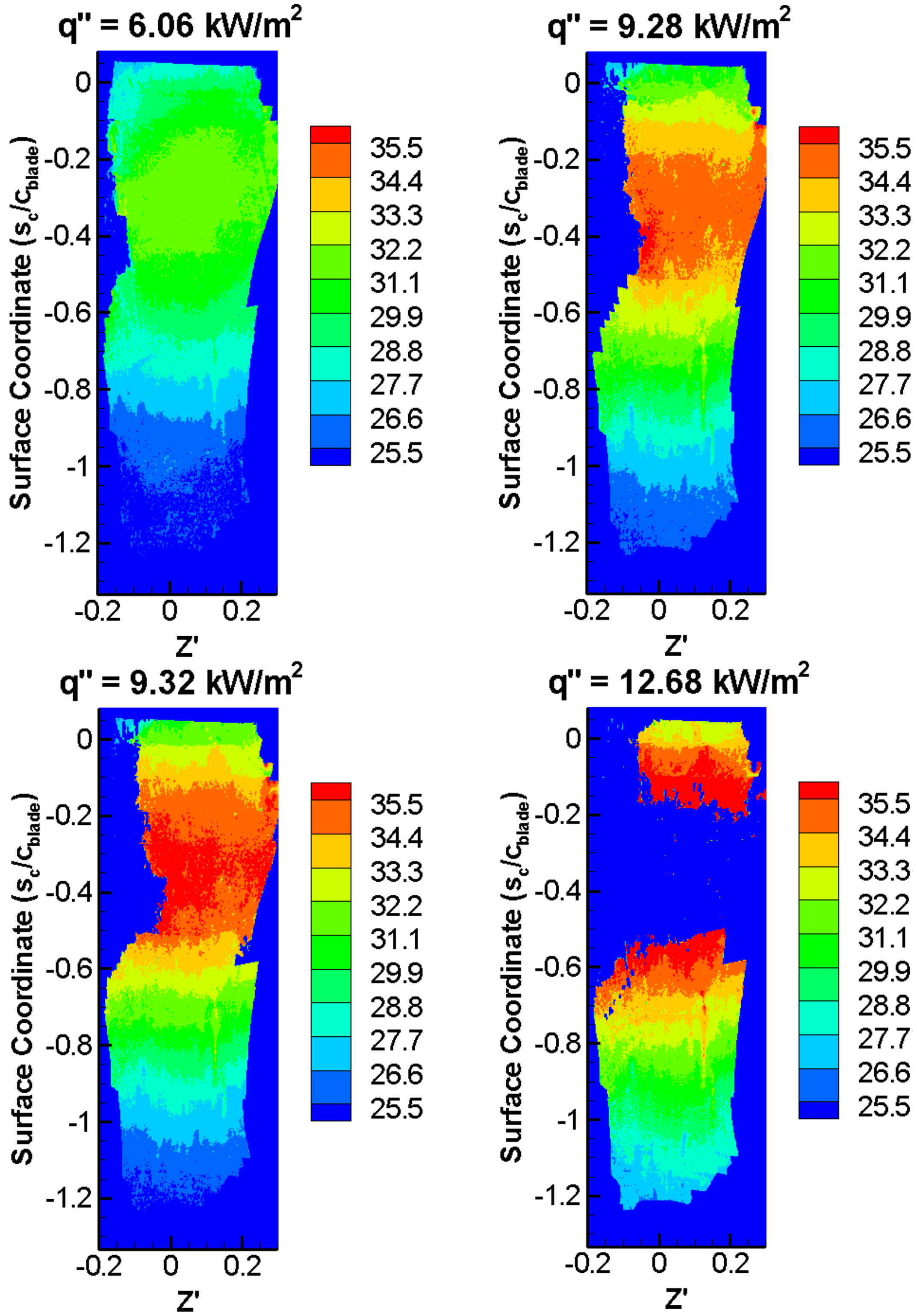

Figure 4.15: Measured spatially-resolved maps of $T_w(Z', s_c/c_{blade})$ at various heat flux settings with high turbulence flow conditions (in $°C$).

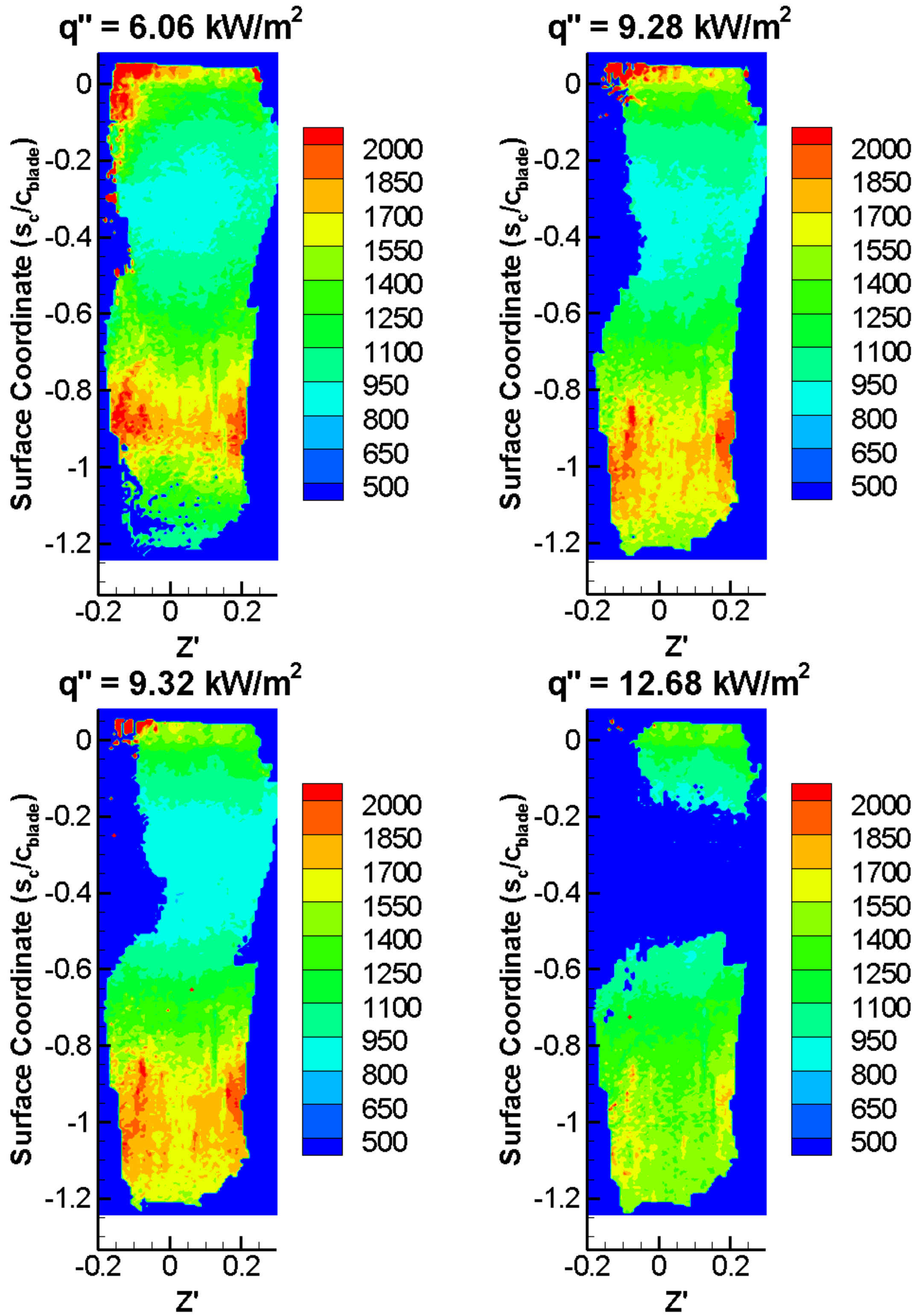

Figure 4.16: Measured spatially-resolved maps of $h(Z', s_c/c_{blade})$ at various heat flux settings (in $\frac{W}{m^2 \cdot K}$).

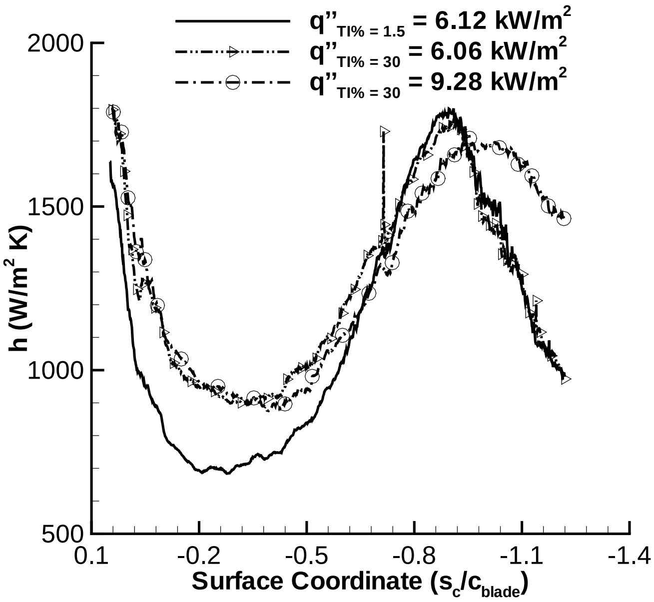

Figure 4.17: Measured spanwise-averaged $\overline{h}(s_c/c_{blade})$ distributions for low and high turbulence cases at various heat flux settings.

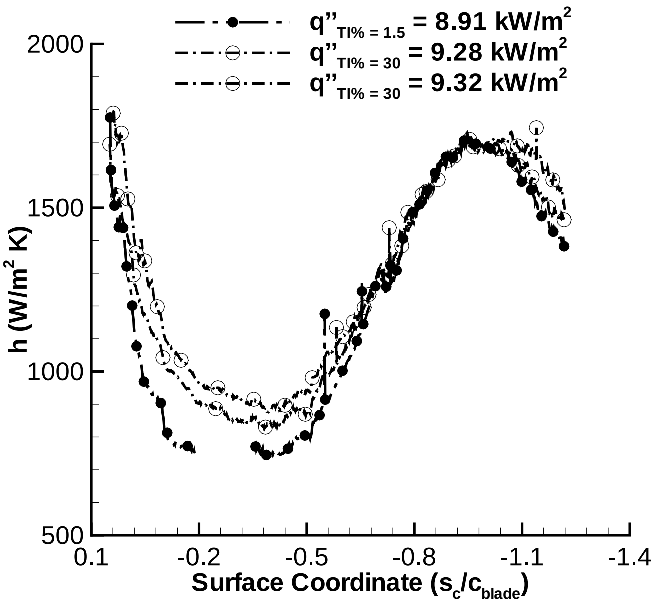

Figure 4.18: Measured spanwise-averaged $\overline{h}(s_c/c_{blade})$ distributions for low and high turbulence cases at various heat flux settings.

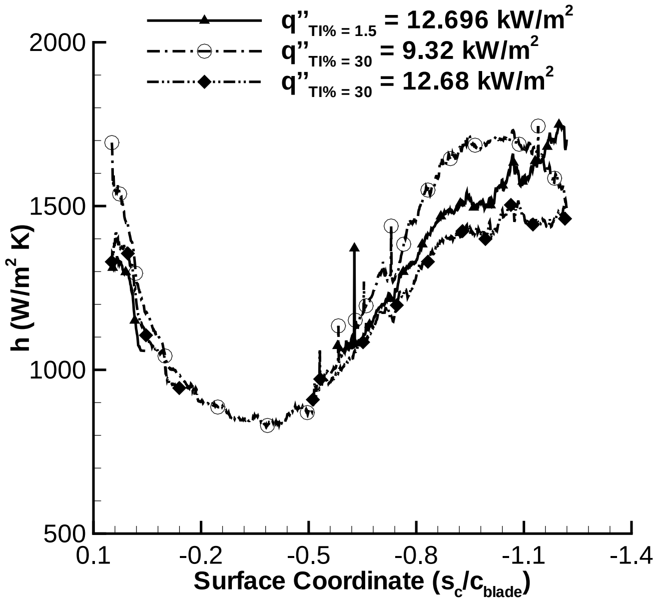

Figure 4.19: Measured spanwise-averaged $\overline{h}(s_c/c_{blade})$ distributions for low and high turbulence cases at various heat flux settings.

Comparison to RANS Predictions

As further verification of the $\overline{h}$ distributions presented in this section and their apparent dependence on the applied heat flux, full-geometry, two-dimensional RANS calculations were performed using STAR-CD and the numerical procedures outlined in Chapter 2. The inlet turbulence intensity and integral length scale were specified as $TI\% = 5$ and $\frac{\ell}{c_{blade}} = 0.06$. Having set the value of the turbulent Prandtl number to ensure close agreement with the measured recovery temperature profile $(\overline{T_{rec}}(s_c/c_{blade}))$, heat fluxes of $q'' = 6\frac{kW}{m^2}$ and $q'' = 12\frac{kW}{m^2}$ were applied to the pressure side airfoil surface in the single passage. Figure 4.20 compares the data to predictions using two turbulence models and shows that both models appear to be unable to capture the effects of compressibility and substantial acceleration on the developing thermal boundary later. Both models produce a temperature field that responds linearly to the applied heat flux, that is they both produce the same $\overline{h}$ distribution, irrespective of the surface heat flux rate. The k-ε model appears to totally fail for this particular test case. It overpredicted the stagnation point heat transfer coefficient by approximately 13%, whereas the k-ω model predicted values of h that were bounded by the measurements. Furthermore, the trends predicted by the k-ε model for

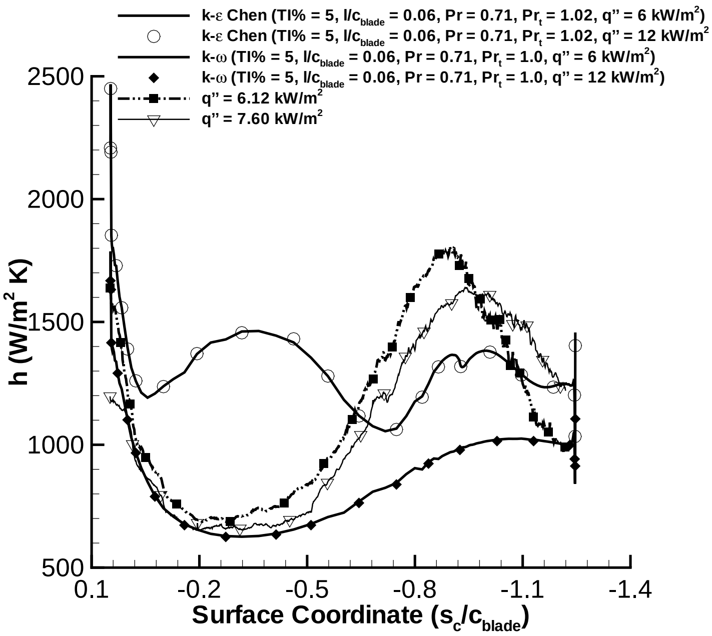

Figure 4.20: Computed and measured spanwise-averaged $\overline{h}(s_c/c_{blade})$ distributions at various heat flux settings.

h differed substantially from measurements and the distribution predicted using the k-ω model. Instead of the heat transfer coefficient gradually decreasing from the stagnation point to an minimum at $\frac{s_c}{c_{blade}} \approx -0.27$, the k-$\varepsilon$-predicted distribution oscillates around the $h = 1250\frac{W}{m^2 \cdot K}$. The k-$\omega$ model produces a distribution that closely follows the low turbulence data up to $\frac{s_c}{c_{blade}} \approx -0.25$, but beyond this point, the model predicts a slow increase in h, well-below the measurements shown in this figure.

There are several candidate explanations for the behavior of the two turbulence models shown here. One issue is simply the implementation of the surface boundary conditions in the applied mean flow solver and subsequent possible numerical errors. Wilcox (2000) discusses several adjustments for both k-ε and k-ω models to better account for compressible effects. However, it is unclear from these works if these corrections improve the subsequent heat transfer predictions.

4.2 Discussion

The experimental results presented in section 4.1.3 suggest the dependence of the heat transfer coefficient on the surface heat flux. Additionally, these data indicate that once the flow in the passage becomes near-supersonic, the effect of the inlet turbulence condition is practically negligible. The observation suggesting the dependance of $h = h(q'')$ was peripherally supported by laminar flow flat plate calculations. However, full-geometry, two-dimensional RANS calculations did not capture such a relationship.

Clearly, if this observation is proven accurate, it suggests that the fundamental assumption used for transient tests in compressible flow conditions is invalid. The degree of concern this may cause would appear to be geometry and flow condition specific. The results shown in this chapter demonstrate this effect can be as much as 10%. This issue would also extend to experimental tests that use a variable surface heat flux to determine a single heat transfer coefficient distribution, such as the isotherm technique described in section 3.2.2.

Another interesting observation from these results is the fact that all the turbulence models used could not accurately replicate the T_{rec} profile, unless the turbulence Prandtl number (Pr_t) was adjusted. This reinforces the discussion presented in section 1.6.3 that the assumption of $Pr_t = 0.9$ can "build-in" errors with the prediction of the heat transfer coefficient, and therefore better understanding of the limitations of this approach and possible corrections are vital to improved heat transfer predictions. With respect to the apparent effect of the surface heat flux on the heat transfer coefficient, the results presented in Appendix C provide circumstantial evidence to demonstrate that the energy equation cannot be considered linear once the flow becomes compressible. The results presented in this appendix confirmed that under certain circumstances, the surface heat transfer coefficient can depend significantly on the surface heat flux rate. Furthermore, these results showed that the mean flow conditions can remain nominally unchanged, despite substantial changes in the heat transfer coefficient. Given that the temperature rise along the heated surface was relatively small, on an absolute scale, it was argued that there was no physical mechanism for significant changes in the characteristics of the flow through the single passage. To validate this hypothesis, the airfoil suction side wall pressure measurement piece was installed in the model. The pressure distribution was measured along the suction side wall with a surface heat flux of $q'' = 12.9\frac{kW}{m^2}$ applied to the pressure side wall, a low turbulence inlet flow state and an inlet total temperature of $T_{\circ,\infty} = 25.3°\text{C}$. Figure 4.21

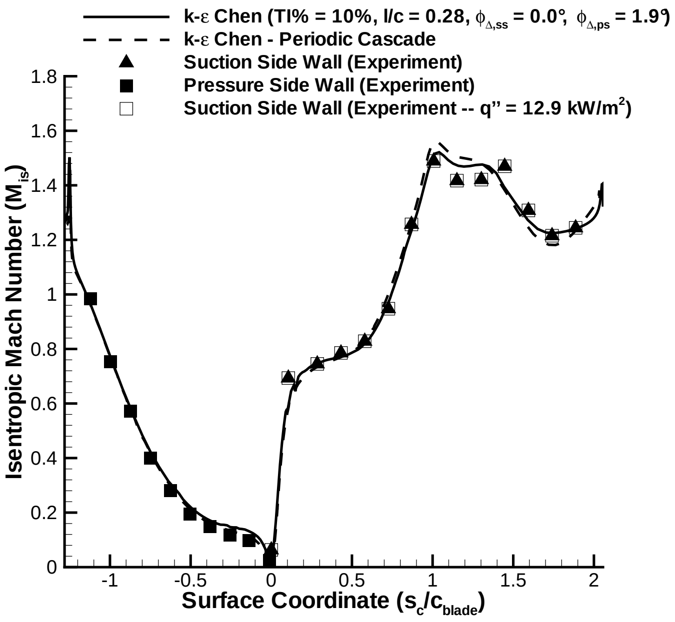

Figure 4.21: Comparison of baseline M_{is} distribution with measured suction side M_{is} with $q'' = 12.9\frac{kW}{m^2}$.

displays the suction side surface M_{is} distribution for this situation, providing additional evidence that suggests a negligible effect of the surface heat flux on the flow characteristics in the passage. Despite the relatively poor agreement in h for the two-dimensional RANS calculations, these results from these simulations also showed no effect on the pressure distribution due to heating on the pressure side airfoil surface.

An unresolved issue with these data is the evaluation of the condition of the boundary layer around the measurement surface. As a turbulent correlation for r_∞ generated a $T_{rec}(s_c/c_{blade})$ profile that closely followed measurements, it was assumed that the boundary layer around the blade was fully turbulent. Further evidence to support this assumption can be derived from the aerodynamics simulations presented in Chapter 2. These implicitly assume that the boundary later is fully turbulent around the blade and achieve good predictions. Finally, the k-ω model, as implemented by Medic and Durbin (2002a), gave close agreement with measurements of the spanwise-averaged heat transfer coefficient close to the stagnation point on the airfoil surface.

Chapter 5

Cooled Heat Transfer Experiments: Results and Discussion

This chapter presents and discusses film cooling performance measurements along the pressure side wall of a modern, transonic turbine blade geometry. As indicated in section 3.5, two rows of compound angle round holes were drilled into a Ren Shape measurement piece, coated with a thin heating film. Two-dimensional surface temperature distributions were measured with various surface thermal and flow boundary conditions applied. The first set of measurements at each flow condition corresponded to the *isoenergetic* condition, where the total temperature of the film cooling and mainstream flows were nominally identical ($T_{\circ,\infty} = T_{\circ,c}$). It is typically assumed that the presence of film cooling at this condition has no effect on the thermal boundary layer. This means that the adiabatic surface temperature distribution measured on the uncooled surface, the recovery temperature ($T_{rec}(x, y)$), is identical to that measured at the isoenergetic condition. Using these assumptions, if the heat transfer coefficient is defined as:

$$h(x, y) = \frac{q''}{T_{iso}(x, y) - T_w(x, y)} \tag{5.1}$$

this can take the form:

$$h(x, y) = \frac{q''}{T_{rec}(x, y) - T_w(x, y)}. \tag{5.2}$$

However, there is scant evidence to evaluate the range of validity of this assumption. Goldstein (1971), in fact suggested quite the opposite, presenting an alternative definition of the film effectiveness. The measurements presented in section 5.4 were used to examine the effect of various parameters on the surface temperature distribution. With these data, the heat transfer coefficient (h) and the adiabatic film cooling effectiveness (η) were computed using both T_{rec} and T_{iso}. These measurements also required the acquisition of temperature distributions with a constant surface heat flux applied and isoenergetic conditions (T_w) and film cooling conditions where the film coolant total temperature was significantly raised above the total temperature of the mainstream flow ($T_{\circ,c} > T_{\circ,\infty}$).

5.1 Data Reduction and Measurement Uncertainty

Before presenting the measurements, this section discusses the parameters of interest and how these were calculated from quantities measured during experimental testing. Additionally, this section presents the uncertainty estimates for each derived measurement quantity.

Blowing Ratio (BL)

By definition, the blowing ratio has the form:

$$BL = \frac{\rho_j u_j}{\rho_\infty u_\infty} \tag{5.3}$$

where the j subscript refers to the coolant jet and ∞ refers to the mainstream flow. The mainstream mass flux is determined from the pressure and temperature conditions at the location of the exit of the film cooling hole. Thence,

$$\rho_\infty u_\infty = P_\infty M_{is} \sqrt{\frac{\gamma_\infty}{R_\infty T_\infty}} \tag{5.4}$$

where P_∞ and T_∞ refer to the static pressure and temperature of the mainstream flow, M_{is} is the isentropic Mach number and γ_∞ and R_∞ correspond to the ratio of specific heats and ideal gas constant, respectively. The mass flux through each film cooling hole was defined to be:

$$\rho_j u_j = \frac{\dot{m}_{fc,\circ}}{N_{fc,holes} A_{fc,hole}} \tag{5.5}$$

where $\dot{m}_{fc,\circ}$ is the total mass flow rate supplied to the film cooling plenum, $N_{fc,holes}$ is the number of film cooling holes attached to the plenum, and $A_{fc,hole}$ is the circular cross sectional area of an individual film cooling hole. This equation implicitly assumes that the mass flow through each hole is nearly identical.

Based on the analysis summarized in section 2.3.4, the uncertainties in the blowing ratio for rows # 1 and # 2 were $\frac{\delta BL_1}{BL_1} = 4.0\%$ (P = 0.95) and $\frac{\delta BL_2}{BL_2} = 5.4\%$ (P = 0.95).

Density Ratio (DR)

This is typically defined as:

$$DR = \frac{\rho_j}{\rho_\infty} \tag{5.6}$$

where ρ_∞ is the static density of the mainstream flow at the location of the exit of the film cooling hole, and ρ_j is the static density of the cooling jet at the injection location. ρ_∞ was computed using M_{is} via the equation:

$$\rho_\infty = \rho_{\circ,\infty}\left(1+\frac{\gamma-1}{2}M_{is}^2\right)^{-\frac{1}{\gamma-1}} \tag{5.7}$$

As the flow in this experiment is inherently compressible, the density of the film cooling jet was expected to change as it passes from the supply plenum to the hole exit. This required the knowledge of both the static pressure and temperature of the jet at the hole exit. As mentioned in section 1.5.5, the presence of film cooling can dramatically alter the pressure distribution on the cooled surface, thus without pressure measurements at the exit of the film cooling hole, it was deemed impossible to evaluate ρ_j. On this basis, it was decided to re-define this parameter using the total pressure and temperature in the film cooling plenum. Thence, equation 5.6 becomes:

$$DR = \frac{\rho_{fc,\circ}}{\rho_\infty} \tag{5.8}$$

The uncertainty in this parameter was less than 1%.

Momentum Ratio (I)

Recall the definition of the momentum ratio:

$$I = \frac{\rho_j u_j^2}{\rho_\infty u_\infty^2} \tag{5.9}$$

The mainstream momentum flux was again computed using the static pressure and temperature at the location of the exit. Thence,

$$\rho_\infty u_\infty^2 = \gamma_\infty P_\infty M_{is}^2 \tag{5.10}$$

The jet momentum flux was computed using isentropic flow functions, as:

$$\rho_j u_j^2 = P_{fc,\circ}\gamma M_{is,j}^2\left(1+\frac{\gamma-1}{2}\right)^{-\frac{\gamma}{\gamma-1}}. \tag{5.11}$$

The isentropic Mach number for the coolant jet ($M_{is,j}$) is solved iteratively using the measured total flow properties in the film cooling plenum ($P_{fc,\circ}$, $T_{fc,\circ}$) via the equation:

$$\rho_j u_j = P_{fc,\circ}M_{is,j}\left(\frac{\gamma_c}{R_c T_{fc,\circ}}\right)^{\frac{1}{2}}\left(1+\frac{\gamma-1}{2}M_{is,j}^2\right)^{-\frac{\gamma+1}{2(\gamma-1)}}. \tag{5.12}$$

The uncertainty in this parameter was estimated to be nearly identical to that for the blowing ratio: $\frac{\delta I_1}{I_1}$ = 4.0% (P = 0.95) and $\frac{\delta I_2}{I_2}$ = 5.4% (P = 0.95).

Hole Exit Temperature (T_{w2})

The definition of η advocated by researchers such as Buck (2000) requires the knowledge of the temperature of the coolant at the exit of the film cooling hole (T_{w2}). However, this could not be directly measured due to complexity and flow conditions of the single passage. Instead, a control volume analysis was developed to estimate the loss in temperature from the film cooling plenum to the hole exit. In this derivation, the hole wall was assumed to be at a constant surface temperature equal to the mainstream flow recovery temperature at the location where the film cooling hole would be drilled (T_{rec}). Given a hole perimeter P_h, film cooling hole mass flow rate $\dot{m}_j$ and film cooling hole inlet mean temperature $T_{m,i}$, the hole exit temperature was estimated using equation 5.13 below.

$$\frac{T_{rec} - T_{w2}}{T_{rec} - T_{fc,rec}} = exp\left[-\frac{P_h L}{\dot{m}_j c_p}\overline{h}_L\right] \tag{5.13}$$

By definition, the length-averaged heat transfer coefficient ($\overline{h}_L$) is:

$$\overline{h}_L = \frac{1}{L}\int_0^L h(x)dx. \tag{5.14}$$

The cooling hole inlet mean temperature was estimated to be identical to the recovery temperature for the film cooling flow, $T_{fc,rec}$, computed as:

$$\frac{T_{fc,\circ}}{T_{fc,\infty}} = 1 + \frac{\gamma+1}{2}M_{is,j}^2 \tag{5.15}$$

$$\frac{T_{fc,\infty}}{T_{fc,rec}} = 1 + r_c\frac{\gamma+1}{2}M_{is,j}^2 \tag{5.16}$$

where $M_{is,j}$ is the isentropic Mach number for the film cooling jet, given a specified mass flow rate through the cooling hole ($\dot{m}_j$) and film cooling plenum total pressure ($P_{fc,\circ}$), as shown in section 5.1. $T_{fc,\circ}$ is the measured film cooling plenum total temperature. To determine $\overline{h}_L$, the length-averaged Nusselt number ($\overline{Nu}_{D,L}$) is computed using a set of correlations for laminar and turbulent flows, based on the film cooling hole Reynolds number. Given the length of the holes used in the cooled experiments, it was assumed that both the hydrodynamic and thermal boundary layers were undeveloped over the length of the hole. For laminar flow conditions ($Re_D \leq Re_D^l = 3000$), the correlation proposed by Whitaker (1972) is used:

$$\overline{Nu_{D,L}^l} = 1.86\left(\frac{Re_D Pr}{L/D}\right)^{\frac{1}{3}}\left(\frac{\mu_f}{\mu_s}\right)^{0.14} \tag{5.17}$$

where μ_f refers to the viscosity of the injected fluid at the *film temperature*, T_f. This is defined as:

$$T_f = \frac{T_{fc,\circ} + T_{fc,s}}{2} \tag{5.18}$$

When the flow through the film cooling hole was considered fully turbulent ($Re_D \geq Re_D^t = 10000$), a correlation proposed by Molki and Sparrow (1986), as shown in equation 5.19 is used.

$$\frac{\overline{Nu_{D,L}^t}}{Nu_{D,fd}^t} = 1 + \frac{a}{(L/D)^b} \tag{5.19}$$

where the constants a and b are computed as:

$$a = 23.99 Re_D^{-0.230}, \quad b = -2.08(10)^{-6} Re_D + 0.815. \tag{5.20}$$

and the fully-developed, turbulent Nusselt number is computed using the correlation proposed by Gnielinski (1976):

$$Nu_{D,fd}^t = \frac{(f/8)(Re_D - 1000)Pr}{1 + 12.7\left(\frac{f}{8}\right)^{\frac{1}{2}}(Pr^{\frac{2}{3}} - 1)}. \tag{5.21}$$

where f is the *friction factor* computed for a fully turbulent flow using the correlation proposed by Pethukov (1970):

$$f = (0.790 \ln Re_D - 1.64)^{-2}. \tag{5.22}$$

In the transitional Re_D range ($Re_D^l < Re_D < Re_D^t$), a linear function was used to blend values for $\overline{Nu^l}$ and $\overline{Nu^t}$.

This analysis was found to give values of T_{w2} that were 1-2 °C lower than the film cooling plenum temperature ($T_{fc,\circ}$). This analytical procedure suggested that T_{w2} differed from one row to the next. This difference became more substantial as the blowing ratio was increased. This was estimated to have an uncertainty of $\delta T_{w2} \approx 0.5°C$.

Applied Definitions of Film Cooling Effectiveness (η)

Four definitions were used to compute the film effectiveness: two using the isoenergetic temperature profile as an attempt to isolate the effects of compressibility on the film cooling effectiveness and two of which use the estimate of the film cooling hole exit mean temperature. As all the film cooling tests were run with nominally identical total temperature in the film cooling plena, the easiest definitions to apply were those that depended on the film cooling plenum total temperature, as shown in equations 5.23 and 5.24. It was assumed that the film cooling flow field for each row of holes were independent of each other, in a thermal sense. In other words, the definition for η, as shown in equations 5.25 and 5.26, used the hole exit temperature for the film cooling row immediately upstream of the measurement location. This was found to give slightly higher values than those shown in maps of η_T.

$$\eta_T(Z', s_c/c_{blade}) = \frac{T_{aw,c}(Z', s_c/c_{blade}) - T_{rec}(Z', s_c/c_{blade})}{T_{fc,\circ}(Z', s_c/c_{blade}) - T_{rec}(x, y)} \tag{5.23}$$

$$\eta_{T,iso}(Z', s_c/c_{blade}) = \frac{T_{aw,c}(Z', s_c/c_{blade}) - T_{iso}(Z', s_c/c_{blade})}{T_{fc,\circ}(Z', s_c/c_{blade}) - T_{iso}(Z', s_c/c_{blade})} \tag{5.24}$$

$$\eta(Z', s_c/c_{blade}) = \frac{T_{aw,c}(Z', s_c/c_{blade}) - T_{rec}(Z', s_c/c_{blade})}{T_{w2} - T_{rec}(Z', s_c/c_{blade})} \tag{5.25}$$

$$\eta_{iso}(Z', s_c/c_{blade}) = \frac{T_{aw,c}(Z', s_c/c_{blade}) - T_{iso}(Z', s_c/c_{blade})}{T_{w2} - T_{iso}(Z', s_c/c_{blade})} \tag{5.26}$$

The film cooling plena were installed relatively close to the measurement surface (with minimum distances relative to the measurement surfaces of $\frac{\mathcal{P}_{row\#1}}{c_{blade}} \approx 0.042$ and $\frac{\mathcal{P}_{row\#2}}{c_{blade}} \approx 0.026$). Thus, conductive heat transfer between the plena and the measurement surface was believed to be more significant than in the uncooled measurements. The effect on conduction on the surface temperature distribution was estimated to be less than 0.2°C based on backloss calculations for each set of measurement conditions. Given estimated uncertainties of $\delta T_{aw,c} \approx 0.2$°C, $\delta T_{w2} \approx 0.2$°C, $\delta T_{rec} \approx 0.2$°C and $\delta T_{iso} \approx 0.2$°C, the uncertainty at the highest values of η were computed to be $\frac{\delta\eta}{\eta} \approx 10\%$ near the injection locations and increase to $\frac{\delta\eta}{\eta} \approx 48\%$ as η approached zero. Appendix A contains more details on the uncertainty analysis for the film cooling data.

Applied Definitions of Heat Transfer Coefficient (h)

The resistance of the heat flux surface for the cooled heat transfer tests was measured to be $R_H \approx 3.06\Omega$ with an estimated uncertainty of less than 1%. The following equations were used to compute the spatially-resolved, local heat transfer coefficients:

$$h(Z', s_c/c_{blade}) = \frac{\overline{\frac{P_H}{A_H}} - q''_{cond} - q''_{rad}}{T_w(Z', \frac{s_c}{c_{blade}}) - T_{rec}(Z', \frac{s_c}{c_{blade}})} \tag{5.27}$$

Table 5.1: Nominal heating film conditions for film cooling experiments.

$\overline{V_{CS}}$ (V)	$\overline{V_H}$ (V)	$\overline{P_{DISS}}$ (W)	$\overline{R_H}$ (Ω)	$\overline{I_{CS}}$ (A)	$\overline{P_H}$ (W)	$\overline{q''}$ $(\frac{kW}{m^2})$
0.24	7.36	0.591	2.42	3.044	17.78	6.70

where $\overline{P_H}$ is the "time-averaged" power applied to the heat flux surface, A_H is the area of the heated surface, q''_{cond} is the conduction loss through the Ren Shape substrate and q''_{rad} is the loss due to radiation from the heated surface. $\overline{P_H}$ was determined by averaging several measurements from the current sense resistor circuit before and after heat transfer measurements were taken. This was then divided by the exposed area of the film (A_H = 44.45-mm $\times$ 59.69-mm = 2.653(10)$^{-3}$-m^2). P_H and A_H were both estimated to have uncertainties of 2%.

The conductive backloss heat flux was estimated to have a maximum value of $q''_{cond} \approx 200\,\frac{W}{m^2}$ based on the backloss thermocouple data for the range of tests conducted. This value was less than 2% of the applied heat flux. The radiative heat flux from the surface was estimated using the equation:

$$q''_{rad} = \epsilon\sigma_R(T_w^4 - T_{rec}^4) \tag{5.28}$$

where σ_R is the Stefan-Boltzmann constant ($\sigma_R = 5.673(10)^{-8}\,\frac{W}{m^2 \cdot K^4}$)and ϵ corresponds to the surface emissivity of the painted surface. Batchelder and Moffat (1997) presented measurements for a TLC-coated surface that indicated that $\epsilon = 0.9$ for such a surface. This analysis also assumed that all surfaces that engage in a radiative exchange with the measurement surface were at the recovery temperature achieved with an isentropic Mach number of $M_{is} \approx 1.5$ and total temperature of $T_{\circ,\infty}$ = 26.7°C. With these assumptions, the recovery temperature was computed to be T_{rec} = 17.6°C. Thence, estimated radiative heat flux was computed to be $q''_{rad} \approx 125\,\frac{W}{m^2}$. Appendix A details the uncertainty analysis procedure for the heat transfer coefficient. This analysis concluded with an estimated maximum uncertainty for the heat transfer coefficient of $\frac{\delta h}{h} \approx 8.6\%$ (P = 0.95). Table 5.1 presents the nominal conditions for the heating film for each flow condition.

5.2 Flow Conditions for Experimental Cases

Table 5.2 below lists the nominal non-dimensionalized flow conditions for each condition studied in this work. The blowing ratios of the two rows of film cooling holes were varied

Table 5.2: Nominal Dimensionless Parameters Values for T_{iso} measurements.

Case	BL_1	BL_2	I_1	I_2	DR_1	DR_2	$TI\%$	$\frac{\ell}{c_{blade}}$
1	N/A	N/A	N/A	N/A	N/A	N/A	1.5	0.53
2	N/A	N/A	N/A	N/A	N/A	N/A	1.5	0.53
3	0.770	0.930	0.588	0.839	1.007	1.018	1.5	0.53
4	1.080	0.910	1.152	0.810	1.010	1.022	30.0	0.03
5	1.600	0.950	2.469	0.884	1.031	1.041	1.5	0.53
6	1.993	1.175	3.766	1.321	1.046	1.057	30.0	0.03
7	2.012	1.077	3.800	1.116	1.057	1.067	1.5	0.53
8	2.641	1.543	4.140	1.504	1.098	1.109	1.5	0.53
9	2.681	1.477	4.301	1.392	1.654	1.671	1.5	0.53
10	2.915	2.014	7.388	3.410	1.133	1.144	1.5	0.53
11	5.180	3.401	17.495	7.629	1.493	1.508	30.0	0.03
12	5.186	5.761	17.870	14.535	1.463	1.478	1.5	0.53
13	5.268	5.682	18.225	14.495	1.480	1.494	30.0	0.03
14	6.477	4.330	18.243	7.940	2.224	2.246	1.5	0.53
15	6.513	6.879	17.980	14.006	2.285	2.308	30.0	0.03
16	6.441	7.047	17.527	14.588	2.294	2.317	1.5	0.53
17	6.580	6.984	18.512	13.860	2.262	2.284	30.0	0.03
18	3.569	2.481	6.687	3.380	1.878	1.896	1.5	0.53

extensively to examine the two major regimes of jet-in-crossflow interaction: where the film cooling jet is attached to the surface and past the point where the jet blows off from the surface. It was then decided to explore the effects of density ratio and turbulence level on these regimes. The literature cited in chapter 1 indicated that denser jets generally perform better, improving the film effectiveness. Additionally, this research indicated that increased turbulence quickly dissipates the film layer, leading to reduced effectiveness.

5.3 Flow Conditions for CFD and Literature Comparisons

This section discusses how the measured data in this chapter may be implemented for a CFD version of this experiment to improve modeling efforts for film cooling. As discussed in chapter 2 the flow conditions in the single passage were designed to closely approximate

Table 5.3: Nominal Dimensionless Parameters Values for $T_{aw,c}$ Measurements.

Case	BL_1	BL_2	I_1	I_2	DR_1	DR_2	$TI\%$	$\frac{\ell}{c_{blade}}$
1	N/A	N/A	N/A	N/A	N/A	N/A	1.5	0.53
2	N/A	N/A	N/A	N/A	N/A	N/A	1.5	0.53
3	0.761	0.908	0.599	0.821	1.002	1.012	1.5	0.53
4	1.080	0.907	1.172	0.808	0.998	1.008	30.0	0.03
5	1.600	0.956	2.528	0.873	1.005	1.015	1.5	0.53
6	2.333	1.122	3.869	1.122	1.022	1.032	30.0	0.03
7	2.018	1.081	3.988	1.782	1.036	1.047	1.5	0.53
8	2.589	1.521	3.435	1.463	1.633	1.649	1.5	0.53
9	2.497	1.265	3.961	1.131	1.619	1.635	1.5	0.53
10	2.911	2.016	7.500	3.440	1.114	1.125	1.5	0.53
11	5.193	3.420	17.919	7.878	1.464	1.478	30.0	0.03
12	5.256	5.715	18.439	15.132	1.440	1.454	1.5	0.53
13	5.257	5.426	18.125	14.516	1.434	1.448	30.0	0.03
14	6.491	4.248	17.688	7.841	2.185	2.206	1.5	0.53
15	6.411	6.831	17.411	14.247	2.235	2.256	30.0	0.03
16	6.411	6.831	17.438	14.292	2.231	2.253	1.5	0.53
17	6.422	6.959	18.960	14.265	2.213	2.235	30.0	0.03
18	3.908	2.569	7.907	3.559	1.825	1.843	1.5	0.53

Table 5.4: Nominal Dimensionless Parameters Values for T_w Measurements.

Case	BL_1	BL_2	I_1	I_2	DR_1	DR_2	$TI\%$	$\frac{\ell}{c_{blade}}$
1	N/A	N/A	N/A	N/A	N/A	N/A	1.5	0.53
2	N/A	N/A	N/A	N/A	N/A	N/A	1.5	0.53
3	0.775	0.917	0.590	0.809	1.110	1.121	1.5	0.53
4	1.083	0.903	1.138	0.785	1.014	1.020	30.0	0.03
5	1.598	0.932	2.423	0.837	1.048	1.058	1.5	0.53
6	2.041	1.354	3.853	1.702	1.072	1.083	30.0	0.03
7	1.997	1.069	3.665	1.076	1.080	1.090	1.5	0.53
8	2.378	1.505	3.281	1.398	1.710	1.727	1.5	0.53
9	2.544	1.315	3.768	1.077	1.702	1.719	1.5	0.53
10	2.912	2.006	7.196	3.304	1.161	1.173	1.5	0.53
11	5.193	3.427	17.189	7.571	1.528	1.543	30.0	0.03
12	5.228	5.844	17.693	14.562	1.502	1.517	1.5	0.53
13	5.171	5.597	17.296	13.897	1.504	1.519	30.0	0.03
14	6.318	4.262	16.975	7.540	2.279	2.302	1.5	0.53
15	6.335	6.868	16.648	13.669	2.341	2.364	30.0	0.03
16	6.335	6.868	16.675	13.713	2.337	2.360	1.5	0.53
17	6.589	7.020	18.122	13.680	2.319	2.342	30.0	0.03
18	3.831	2.513	7.553	3.405	1.912	1.931	1.5	0.53

that of an infinite cascade. Section 2.4.6 contains all the necessary boundary condition information, i.e. total and static pressure and temperature distributions, mean flow profiles and turbulence intensity and integral length scale information. However, it may be necessary to geometrically rotate the single passage domain and boundary condition data to apply to the infinite cascade domain, as indicated in section 2.1. This approach is suggested over numerically simulating the single passage facility, considering the necessary cell counts required for the most accurate RANS calculations, as described in section 1.6.3.

With respect to the surface boundary conditions, it is recommended that both adiabatic surface and conjugate calculations are performed to examine the effects of conduction through the substrate wall. For the film cooling flow, the tables 5.5, 5.6, 5.7 can be used to set the boundary conditions for the film cooling plena, i.e. film cooling plena total pressure ($P_{\circ,fc}$) and total temperature ($T_{\circ,fc}$). Tables 5.2, 5.3 and 5.4 would be used to "fine tune" the boundary condition values to achieve specific blowing/momentum ratios. There was no means to obtain turbulence intensity and length scale measurements for the film cooling supply system in this facility, and therefore they would have to be estimated in the numerical calculation.

Table 5.8 presents the typical values from fundamental experiments examining the physics of film cooling jet-in-crossflow interaction and compares this to the characteristic values for this experiment.

5.4 Isoenergetic Temperature Distributions

Table 5.5 presents some of flow conditions used for the isoenergetic flow condition measurements. One problem with these tests is the apparent loss in total temperature from the plenum ($T_{\circ,PLENUM}$) to the pressure side stagnation point ($T_{\circ,\infty}$). This difference was derived from thermocouple measurements from the supply plenum and spanwise-averaged measured temperature at the airfoil stagnation point. As this problem could not be identified during data acquisition, the film cooling plena total temperatures ($T_{\circ,fc,1}$ and $T_{\circ,fc,2}$) were typically higher than mainstream total temperature. The $BL_1 = BL_2 = 0.0$ cases were used as a baseline for the measurement system. The film cooling plena inlets were sealed off during these tests; however, for practical reasons, inserts were not placed in the film cooling plena themselves. Consequently, it could not be verified *a priori* if there was any flow unsteadiness from the interaction of plena cavities with the mainstream flow, which

Table 5.5: $T_{\circ,fc}$ and $P_{\circ,fc}$ for T_{iso} measurements.

Case	$T_{\circ,PLENUM}$ (°C)	$T_{\circ,\infty}$ (°C)	$T_{\circ,fc,1}$ (°C)	$T_{\circ,fc,2}$ (°C)	$P_{\circ,fc,1}$ (Pa)	$P_{\circ,fc,2}$ (Pa)
1	28.05	27.25	27.99	27.56	N/A	N/A
2	30.48	29.78	30.36	29.86	N/A	N/A
3	29.99	29.45	29.98	30.03	262567.4	263227.3
4	32.47	31.94	32.50	32.51	265478.0	263065.7
5	31.46	30.52	31.48	31.53	270718.7	262588.7
6	32.50	32.00	32.51	32.49	276969.3	269693.0
7	33.70	32.80	33.70	33.67	278752.8	268071.3
8	32.48	31.79	32.48	32.51	290680.8	267376.3
9	31.99	31.02	32.00	31.99	289358.0	266261.6
10	32.98	32.11	33.02	33.02	299935.8	300277.3
11	29.98	29.99	29.98	29.98	394480.3	369544.0
12	32.46	31.94	32.48	32.44	387979.0	545585.2
13	32.24	31.84	32.29	32.28	388435.7	524864.8
14	30.49	29.61	30.54	30.50	387501.8	374098.4
15	32.53	32.04	32.49	32.52	397855.2	521488.0
16	30.49	29.34	30.48	30.47	397184.8	519354.8
17	32.50	31.85	32.55	32.50	394156.0	547533.3
18	32.69	31.80	32.70	32.71	325019.9	298852.0

Table 5.6: $T_{\circ,fc}$ and $P_{\circ,fc}$ for $T_{aw,c}$ measurements.

Case	$T_{\circ,PLENUM}$ (°C)	$T_{\circ,\infty}$ (°C)	$T_{\circ,fc,1}$ (°C)	$T_{\circ,fc,2}$ (°C)	$T_{w2,1}$ (°C)	$T_{w2,2}$ (°C)	$P_{\circ,fc,1}$ (Pa)	$P_{\circ,fc,2}$ (Pa)
1	N/A	N/A	N/A	N/A	N/A	N/A	N/A	N/A
2	N/A	N/A	N/A	N/A	N/A	N/A	N/A	N/A
3	27.51	27.00	29.49	29.51	29.08	29.16	262567.4	263227.3
4	27.42	26.79	33.87	33.90	32.46	33.14	265478.0	263065.7
5	27.50	27.24	38.00	37.99	36.26	36.91	270718.7	262588.7
6	27.51	27.54	39.68	39.67	37.97	38.45	276969.3	269693.0
7	27.47	27.05	37.49	37.45	35.98	36.39	278752.8	268071.3
8	27.51	27.40	39.13	39.12	37.65	37.96	290680.8	267376.3
9	27.48	27.28	40.42	40.41	38.78	39.23	289358.0	266261.6
10	27.48	27.04	37.82	37.77	36.28	36.26	299935.8	300277.3
11	27.47	27.02	38.03	38.01	36.09	35.86	394480.3	369544.0
12	27.46	26.87	37.99	37.95	36.01	35.55	387979.0	545585.2
13	27.51	27.46	39.70	39.75	37.55	37.26	388435.7	524864.8
14	27.54	27.07	37.96	37.99	36.16	36.38	387501.8	374098.4
15	27.49	27.31	39.15	39.20	37.23	37.32	397855.2	521488.0
16	27.49	27.31	39.15	39.20	37.23	37.31	397184.8	519354.8
17	27.52	27.07	39.30	39.31	37.32	37.48	394156.0	547533.3
18	27.51	27.35	39.27	39.23	37.56	37.70	325019.9	298852.0

Table 5.7: $T_{\circ,fc}$ and $P_{\circ,fc}$ for T_w measurements.

Case	$T_{\circ,PLENUM}$ (°C)	$T_{\circ,fc,1}$ (°C)	$T_{\circ,fc,2}$ (°C)	$P_{\circ,fc,1}$ (Pa)	$P_{\circ,fc,2}$ (Pa)
1	N/A	N/A	N/A	N/A	N/A
2	24.98	29.12	30.47	N/A	N/A
3	25.12	25.14	25.16	262567.4	263227.3
4	24.98	25.03	25.05	265478.0	263065.7
5	25.01	25.05	25.00	270718.7	262588.7
6	24.99	24.99	25.03	276969.3	269693.0
7	24.98	25.01	25.00	278752.8	268071.3
8	25.01	25.02	24.97	290680.8	267376.3
9	24.99	24.99	24.97	289358.0	266261.6
10	24.98	25.02	25.01	299935.8	300277.3
11	24.99	25.00	24.95	394480.3	369544.0
12	24.98	25.05	25.00	387979.0	545585.2
13	25.00	25.00	25.02	388435.7	524864.8
14	24.97	25.02	24.99	387501.8	374098.4
15	25.01	25.05	24.98	397855.2	521488.0
16	25.01	25.05	24.98	397184.8	519354.8
17	25.00	25.02	25.01	394156.0	547533.3
18	24.98	25.03	25.06	325019.9	298852.0

Table 5.8: Comparison of studied film cooling parameters for various experiments.

Author(s)	Andreo-poulos and Rodi (1984)	Baldauf et al. (2002b)	Bergeles et al. (1976)	Etheridge et al. (2001)	Fric and Roshko (1994)	Kelso et al. (1996)	Current Work
Hole Arrange-ment	Single	Row	Single	Several Rows	Single	Single	Dual Rows
Flow Geometry	Flat Plate	Flat Plate	Flat Plate	Double Passage	Flat Plate	Flat Plate	Single Passage
Hole Spacing ($\frac{P}{D}$)	∞	2, 3, 5	∞	5.6	∞	∞	5.29, 3.53
Row Spacing ($\frac{S}{D}$)	∞	∞	∞	30, 53, 84	∞	∞	-9.18, -35.6
Hole Length ($\frac{L}{D}$)	12	6	22.5	3.09	$\ll 1$	3.5	6.03, 3.05
Injection Angle (α)	90°	30°, 60°, 90°	50°	90°	90°	90°	38.39°, 47.81°
Lateral Angle (β)	0°	0°	0°	0°	0°	0°	47.81°, 65.00°
Density Ratio ($DR = \frac{\rho_j}{\rho_\infty}$)	1.0	1.2, 1.5, 1.8	1.0	1.1, 1.6	1.0	1.0	1.0 – 2.25
Blowing Ratio ($BL = \frac{\rho_j u_j}{\rho_\infty u_\infty}$)	0.5, 1.0, 2.0	0.2–2.5	0.046–0.50	0.2–1.5	2.0–10.0	2.0–6.0	0.8–7.0
Momentum Ratio ($I = \frac{\rho_j u_j^2}{\rho_\infty u_\infty^2}$)	0.25, 1.0, 4.0	$3.33(10)^{-2}$–3.47	$2.11(10)^{-3}$–$2.50(10)^{-3}$	$5.00(10)^{-2}$–1.2	4.0–100	4.0–36.0	0.6–18.4
Boundary-Layer Displacement Thickness ($\frac{\delta^*}{D}$)	0.035	0.1	0.05	< 0.17	$2.90(10)^{-2}$–$8.70(10)^{-2}$	$5.88(10)^{-2}$–$1.63(10)^{-1}$	≈ 1.0
Mainstream Turbulence	very low ($TI\% = 0.05$)	low ($TI\% = 1.5$)	low ($TI\% = 1.5$)	very low and very high ($TI\% = 0.5, 20$)	very low ($TI\% \approx 0.2$)	laminar	very low and very high ($TI\% = 1.5, 30$)
Hole Diameter (mm)	50.0	5.00	22.2	7.80	38.0	95.5	0.43, 0.43
$Re_{\infty,\delta^*} = \frac{U_\infty \delta^*}{\nu_\infty}$	$1.53(10)^3$	$6.80(10)^2$–$14.0(10)^3$	$1.74(10)^3$	$2.25(10)^2$	$3.80(10)^3$–$1.10(10)^4$	$2.13(10)^2$–$4.18(10)^2$	$7.71(10)^2$, $1.75(10)^3$

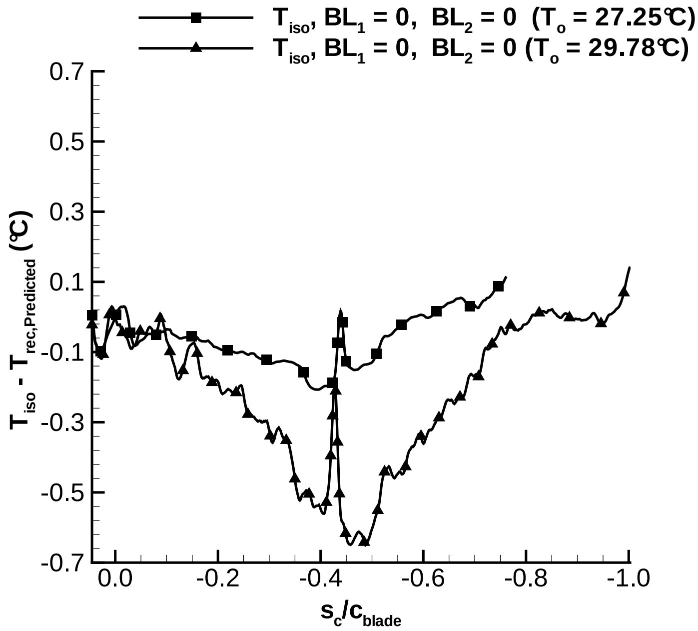

Figure 5.1: Difference between measured and predicted spanwise-averaged isoenergetic condition temperature distribution ($\overline{T_{iso}} - T_{rec}(M_{is})$).

could affect the resulting measurement significantly.

Figure 5.1 presents the difference $\overline{T_{iso}} - T_{rec}(M_{is})$ with two inlet total temperatures ($T_{\circ,\infty}$) conditions applied. $\overline{T_{iso}}$ is the measured spanwise-averaged temperature distribution (median-filtered on a centered 8-point stencil), and $T_{rec}(M_{is})$ is the predicted surface temperature distribution using the M_{is} distribution and a recovery factor of $r_\infty = 0.9$. The "peak" in these profiles corresponds to the location of the second row of film cooling holes. The film cooling plena were installed relatively close to the measurement surface. However, these data show an apparent decrease in the surface temperature in the vicinity of the second film cooling plenum, which contradicts expectations. It was hypothesized that this effect was possibly due to unsteady heat transfer occurring from the measurement surface to the film cooling plenum. This could not be definitely verified. For completeness, figure 5.2 compares $\overline{T_{iso}}$ to $T_{rec}(M_{is})$ for these two cases. In spite of this, it should be observed that the difference between measurements and predictions is ultimately no worse than that for the uncooled surface, as shown in section 3.4.8. The importance of these results will be demonstrated in subsequent sections.

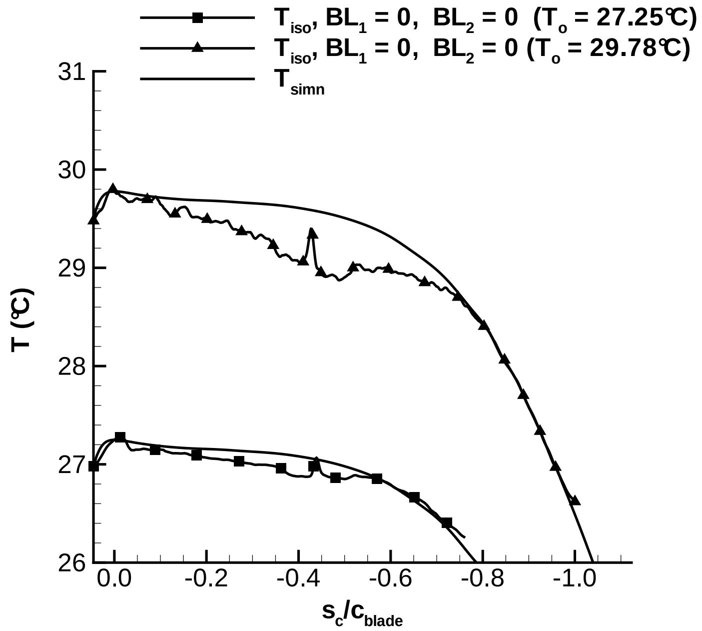

Figure 5.2: Plots of measured ($\overline{T_{iso}}$) and predicted spanwise-averaged isoenergetic condition temperature distributions ($T_{rec}(M_{is})$).

5.4.1 Effects of Blowing Ratio

Figure 5.3 presents $\overline{T_{iso}}$ profiles for cases 3, 4, 5 and 7. Figure 5.4 shows the difference between the profiles for the same cases. The maximum blowing ratio for these cases was $BL_1 = 2.012$. These results show no consistent trend between cases, the maximum deviation between T_{iso} and T_{rec} along each temperature profile was barely outside the nominal uncertainty of the temperature measurement system ($\delta T \approx \pm 0.2°\text{C}$). Nevertheless, when the blowing ratio of the second row was increased beyond $BL_2 = 3.4$ the spanwise-averaged $\overline{T_{iso}}$ and $\overline{T_{iso}} - T_{rec}(M_{is})$ profiles shown in figures 5.5 and 5.6 suggest that injected coolant had small, albeit discernable cooling effect over the range $-0.8 < s_c/c_{blade} < -0.45$. It is unclear if this was due to fundamental changes in the thermal and momentum boundary layers or a film-cooling effect. The analytical model for the film cooling exit temperature, presented in section 5.1, shows that the film cooling hole exit temperature can be slightly cooler than the film cooling plenum temperature. This effect would be more noticeable at higher blowing ratios, as the injected coolant is more expanded.

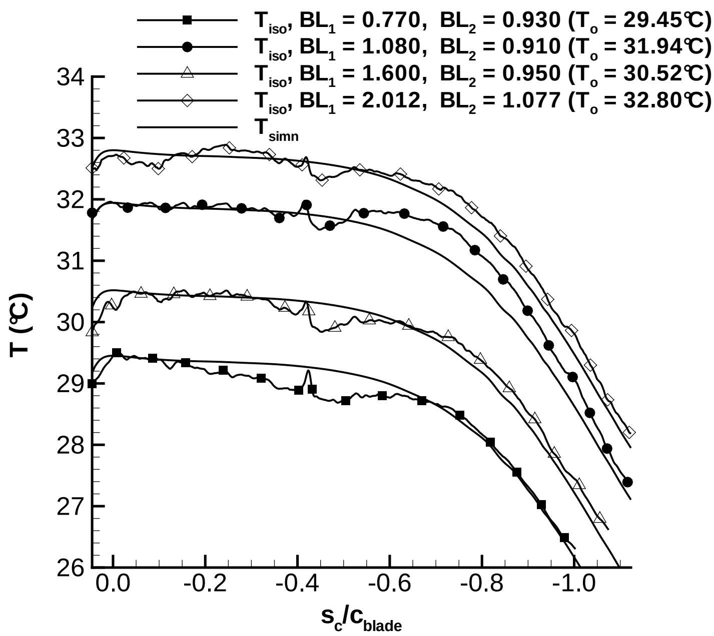

Figure 5.3: Plots of measured ($\overline{T_{iso}}$) and predicted spanwise-averaged isoenergetic condition temperature distributions ($T_{rec}(M_{is})$) for experimental cases 3, 4, 5, and 7.

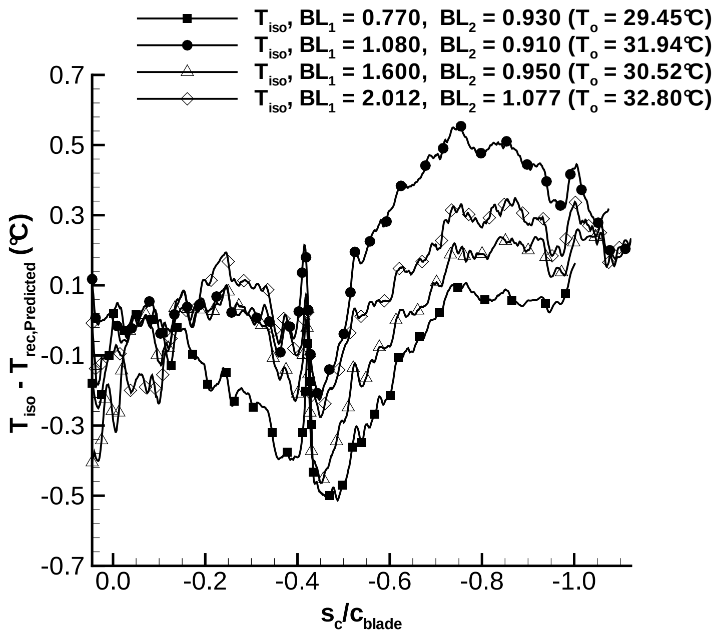

Figure 5.4: Difference between measured and predicted spanwise-averaged isoenergetic condition temperature distribution ($\overline{T_{iso}} - T_{rec}(M_{is})$) for experimental cases 3, 4, 5, and 7.

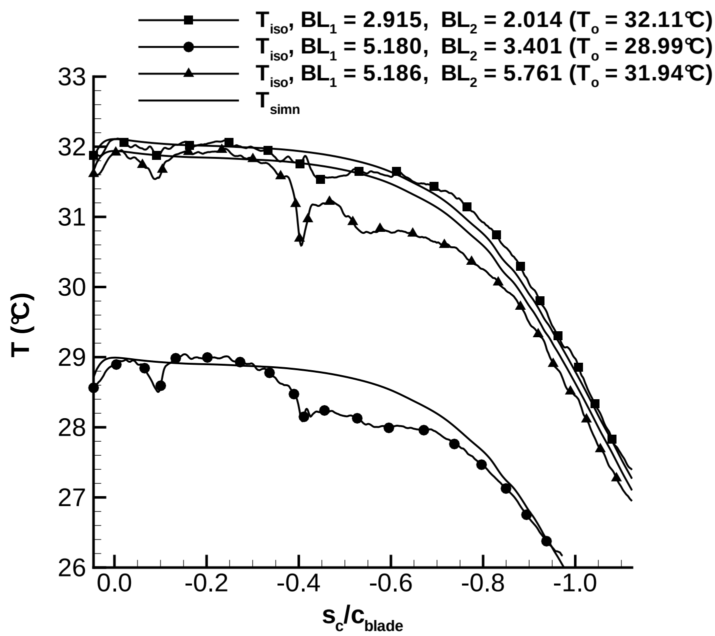

Figure 5.5: Plots of measured ($\overline{T_{iso}}$) and predicted spanwise-averaged isoenergetic condition temperature distributions ($T_{rec}(M_{is})$) for experimental cases 10, 11, and 12.

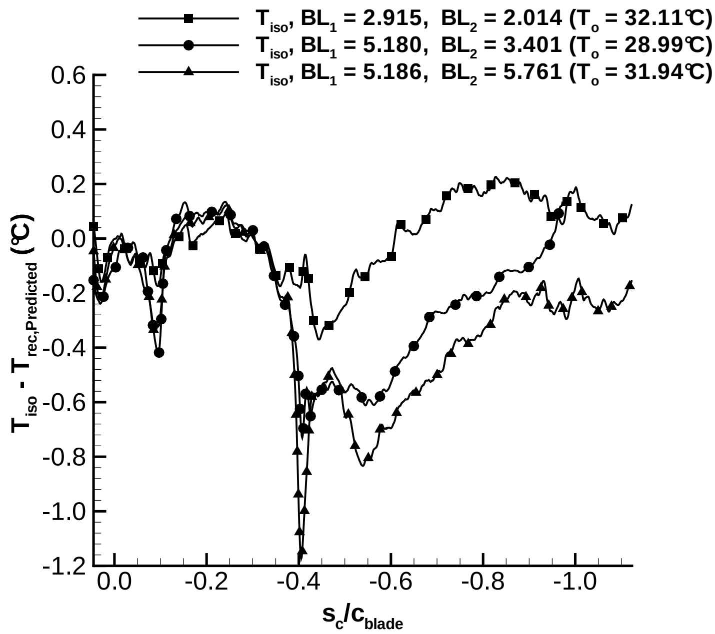

Figure 5.6: Difference between measured and predicted spanwise-averaged isoenergetic condition temperature distribution ($\overline{T_{iso}} - T_{rec}(M_{is})$) for experimental cases 10, 11, and 12.

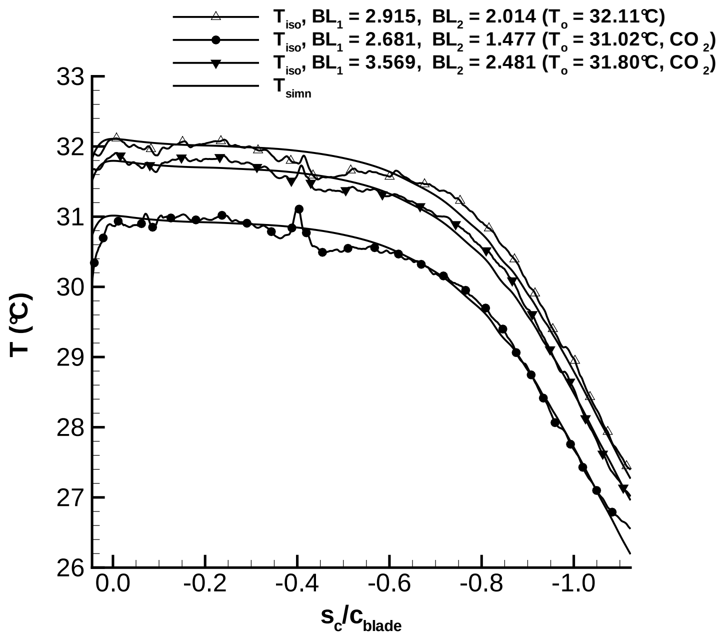

Figure 5.7: Plots of measured ($\overline{T_{iso}}$ and predicted spanwise-averaged isoenergetic condition temperature distributions ($T_{rec}(M_{is})$) for experimental cases 10, 9, and 18.

5.4.2 Density Ratio effects

Figures 5.7, 5.8, 5.9 and 5.10 present profile for cases where carbon dioxide was used as the coolant. No functional differences were observed using different gases, the behavioral changes in the isoenergetic temperature appear to be consistently dependent on blowing ratio.

5.4.3 Turbulence effects on isoenergetic temperature distribution

Figures 5.11, 5.12, 5.13 and 5.14 present spanwise-averaged, median-filtered temperature profiles for flow conditions where a high turbulence inlet condition was specified and both air and CO_2 were used for film cooling. These profiles are compared to their low turbulence counterparts. These results suggest that turbulence has no effect. Consistent with previous results, the predominant effect on the temperature profiles is due to increasing the blowing ratios of the two rows. As BL is increased, the referenced profiles show an increasing cooling effect downstream of the second row of film cooling holes.

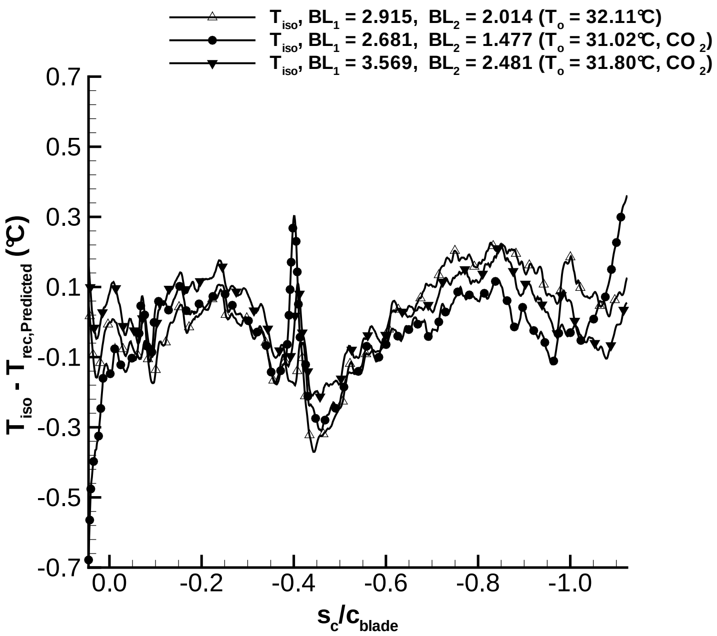

Figure 5.8: Difference between measured and predicted spanwise-averaged isoenergetic condition temperature distribution ($\overline{T_{iso}} - T_{rec}(M_{is})$) for experimental cases 10, 9, and 18.

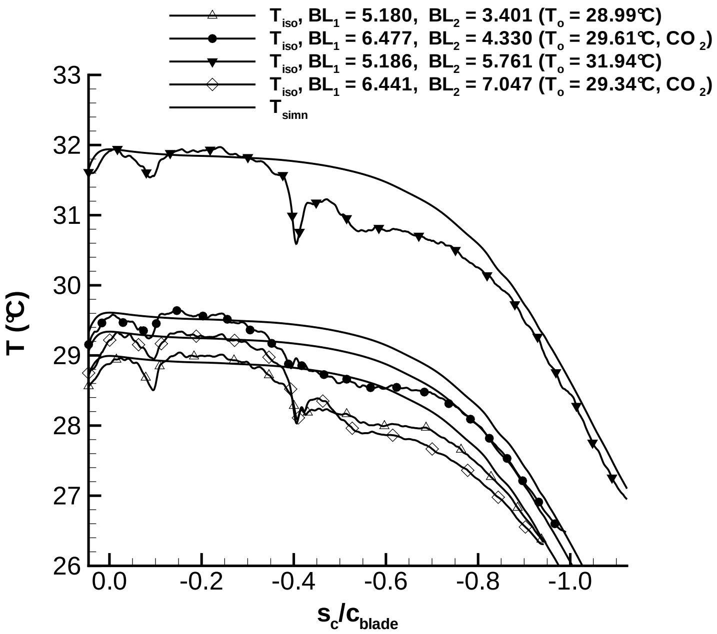

Figure 5.9: Plots of measured ($\overline{T_{iso}}$) and predicted spanwise-averaged isoenergetic condition temperature distributions ($T_{rec}(M_{is})$) for experimental cases 11, 14, 12 and 15.

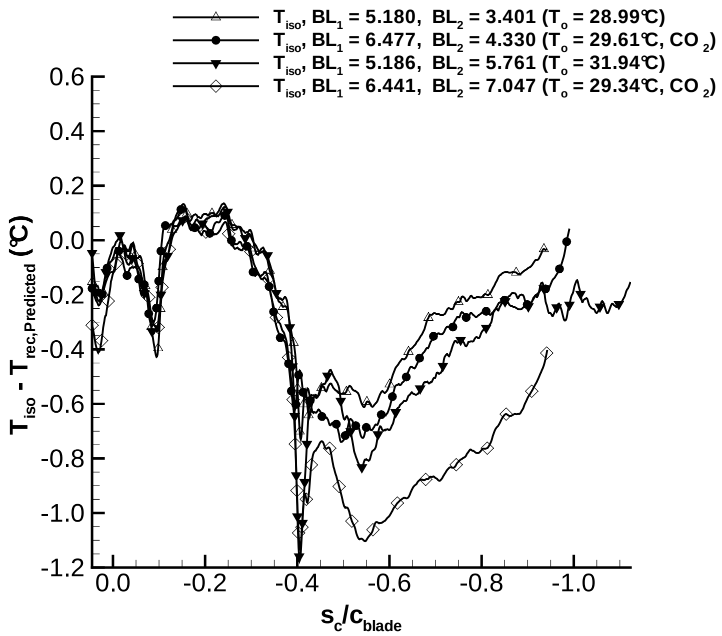

Figure 5.10: Difference between measured and predicted spanwise-averaged isoenergetic condition temperature distribution ($\overline{T_{iso}} - T_{rec}(M_{is})$) for experimental cases 11, 14, 12 and 15.

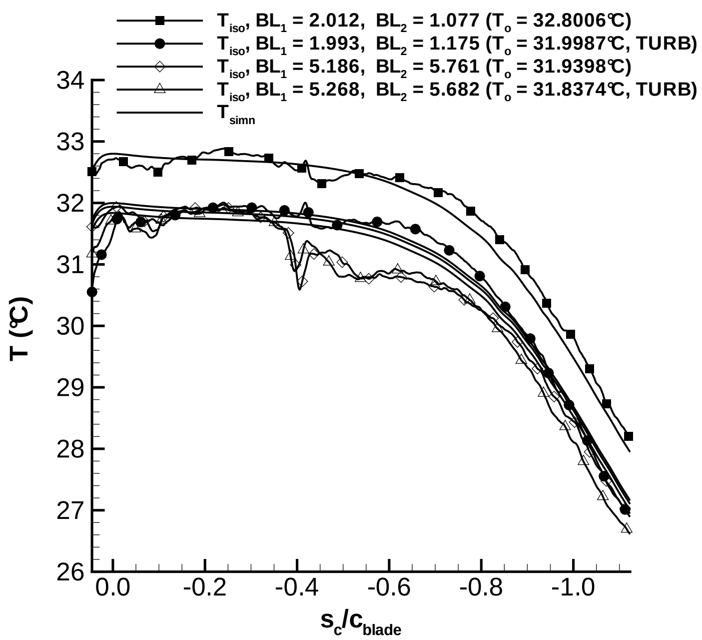

Figure 5.11: Plots of measured ($\overline{T_{iso}}$) and predicted spanwise-averaged isoenergetic condition temperature distributions ($T_{rec}(M_{is})$) for experimental cases 7, 6, 12 and 13.

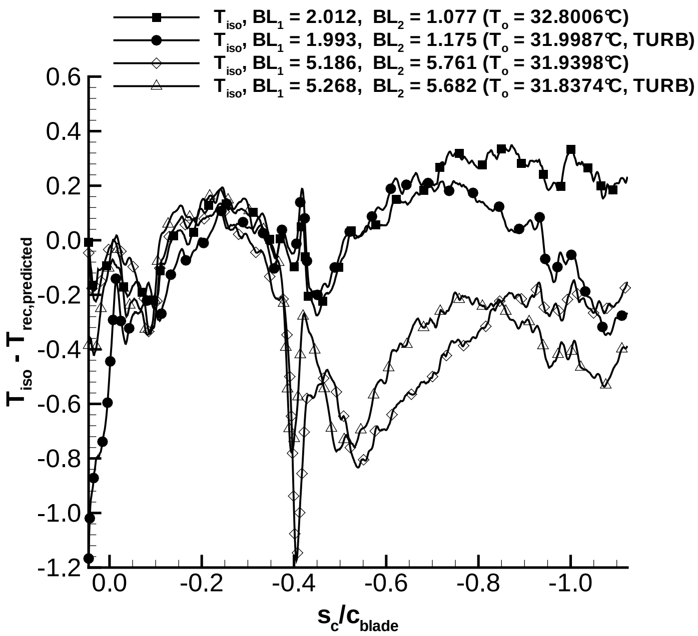

Figure 5.12: Difference between measured and predicted spanwise-averaged isoenergetic condition temperature distribution ($\overline{T_{iso}} - T_{rec}(M_{is})$) for experimental cases 7, 6, 12 and 13.

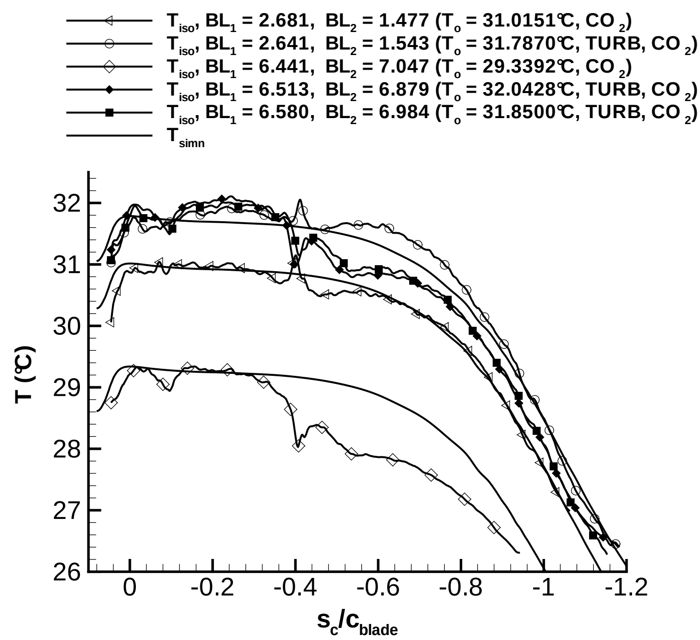

Figure 5.13: Plots of measured ($\overline{T_{iso}}(s_c/c_{blade})$) and predicted spanwise-averaged isoenergetic condition temperature distributions ($T_{rec}(M_{is})$) for experimental cases 9, 8, 16 and 18.

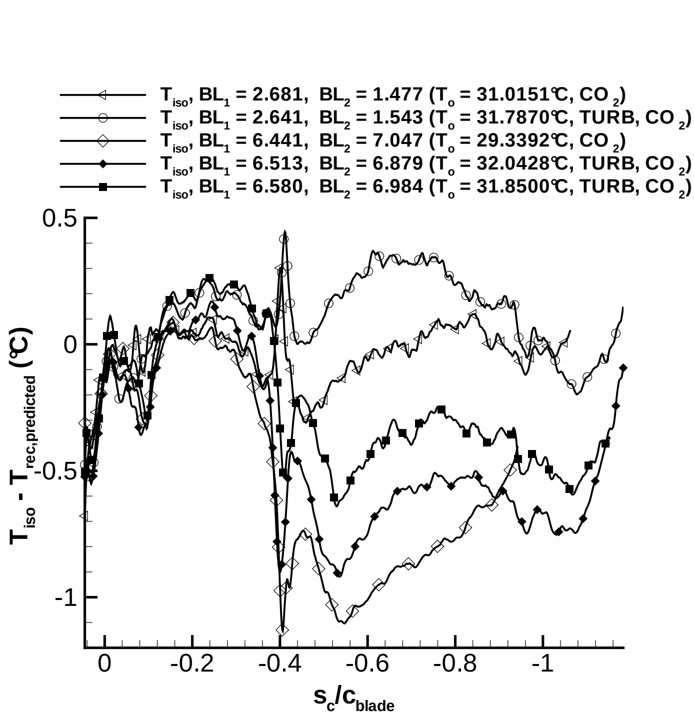

Figure 5.14: Difference between measured and predicted spanwise-averaged isoenergetic condition temperature distribution ($\overline{T_{iso}} - T_{rec}(M_{is})$) for experimental cases 9, 8, 16 and 18.

5.4.4 Discussion

The data presented in this section indicate that the isoenergetic film-cooled temperature distribution appears to significantly differ from the recovery temperature distribution, especially at high blowing ratios. This is an important result as it could suggest that the presence of film cooling can significantly change the structure of the thermal boundary layer, affecting the surface temperature profile. However, as this difference is generally just outside the uncertainty of the thermochromic liquid crystal measurement system, the exact trend from one flow condition to the next is difficult to discern. Furthermore, it is not completely evident that the observed cooling effect is not due to the fact that the injected coolant expanding as it passes from the plenum to the surface. Hence, to determine if the barely discernable trends observed in these data are physical, the measurements of η_{iso} and h_{iso} would provide additional evidence to assist this exploratory process.

5.5 Film-Cooling Effectiveness Results

This section presents film-cooling effectiveness measurements with various flow conditions specified. The mainstream total temperature at the inlet of the blade row was estimated by measuring the spanwise-averaged temperature along the measurement surface at its stagnation point ($\overline{T_{aw,c}}(0)$). Table 5.6 presents the supply and film cooling plena temperature for each test case explored. As with the isoenergetic temperature profile results shown in section 5.4, the data in this table shows a slight drop in total temperature from the plenum to the measurement surface.

5.5.1 Effects of blowing ratio on film-effectiveness

Figures 5.15 and 5.16 presents maps of η_T for the flow conditions where air was used for injectant and the blowing ratio was varied. Flow passes from top to bottom in these figures. The hole shape has been superimposed. As can be observed from these plots, there is some uncertainty in the position of the film cooling holes. This was tied to the repeatability of the borescope positioning, as described in section 3.1.2. This can be further observed via comparison of additional maps and spanwise-averaged data throughout this report. There is a minimal amount of spanwise mixing between film cooling holes in both rows. This is based on the observation that there are distinct areas of high film cooling effectiveness ("streaks") in-line with the film cooling holes adjacent to areas of low film cooling effectiveness.

These figures show the expected general behavior for film cooling jets in cross flow: film cooling footprints form immediately downstream of each film cooling hole. These initially lengthen with increasing blowing ratio. As the injected jets blow-off from the surface, the effectiveness begins to drop immediately downstream of the holes. Depending on whether the film cooling jets reattach, there appears to be an improvement in film cooling performance further downstream.

One interesting observation is the improvement in film effectiveness as the blowing ratio of the first row is increased from $BL_1 = 0.761$ to $BL_1 = 1.080$, while the blowing ratio of the second row is maintained at $BL_2 \approx 0.9$. As BL_1 is increased further, the performance of the second row degrades. A possible hypothesis for this behavior can be proposed given the belief that film cooling causes increased levels of turbulence in the boundary layer and also provides a slight momentum deficit in the momentum boundary layer. This explanation is supported experimentally by measurements presented by Bons et al. (1996) and Afejuku et al. (1983). It can be suggested from the data shown that the momentum deficit effect dominates over this range, allowing the improvement downstream of the second row of holes.

The film cooling jets emanating from the first row appeared to totally blow-off from the measurement surface in the range $2.911 < BL_1 < 5.193$, identified as a sudden drop in effectiveness in the spanwise-averaged film effectiveness ($\overline{\eta_T}$) shown in figures 5.17 and 5.18.

Another unexpected observation is the apparent enhancement in film effectiveness immediately upstream of the second row of film cooling holes as the blowing ratio is increased. This effect could be in part due to conduction from the second film cooling plenum, but an examination of the spanwise-averaged film effectiveness data show that the overall surface film effectiveness is higher at lower blowing ratios. This effect was hypothesized to be due to the film cooling jets from the first row encountering the flow blockage of the second and consequently reattaching to the measurement surface. The results presented by Bergeles et al. (1976) provides additional evidence that film cooling jet can effectively serve as an obstruction to the flow upstream of the injection location.

Figures 5.19 and 5.20 present maps of $\eta_{T,iso}$, these are significantly different to those shown for η_T. This was attributed in some cases to the fact that T_{iso} was measured at relatively low total temperatures, leading to slightly higher uncertainties on a percentage basis. This was especially true for the $\eta_{T,iso}$ map for case 3, which was characterized by a high level of “noise”. For the high blowing ratio cases such as case 10 shown in figure 5.20, the values of $\eta_{T,iso}$ were slightly higher than those shown in figure 5.16. It is unclear why this is the case, whether this is due to compressibility effects that have been “subtracted” out, or some characteristic measurement error.

A disadvantage with the measurement of temperature to determine the film-effectiveness, rather than sampling the concentration of a tracer gas such as carbon dioxide, is the presence of conduction around the injection hole geometry. This is identified as the “smearing” around the hole. It should be stated that measurements by Haven and Kurosaka (1997) demonstrated that the boundary layers within the coolant hole can spill out around the hole as a consequence of the vortical structures that form at the injected jet interacting with the mainstream flow. Hence, no thermal corrections were applied to these data, as it

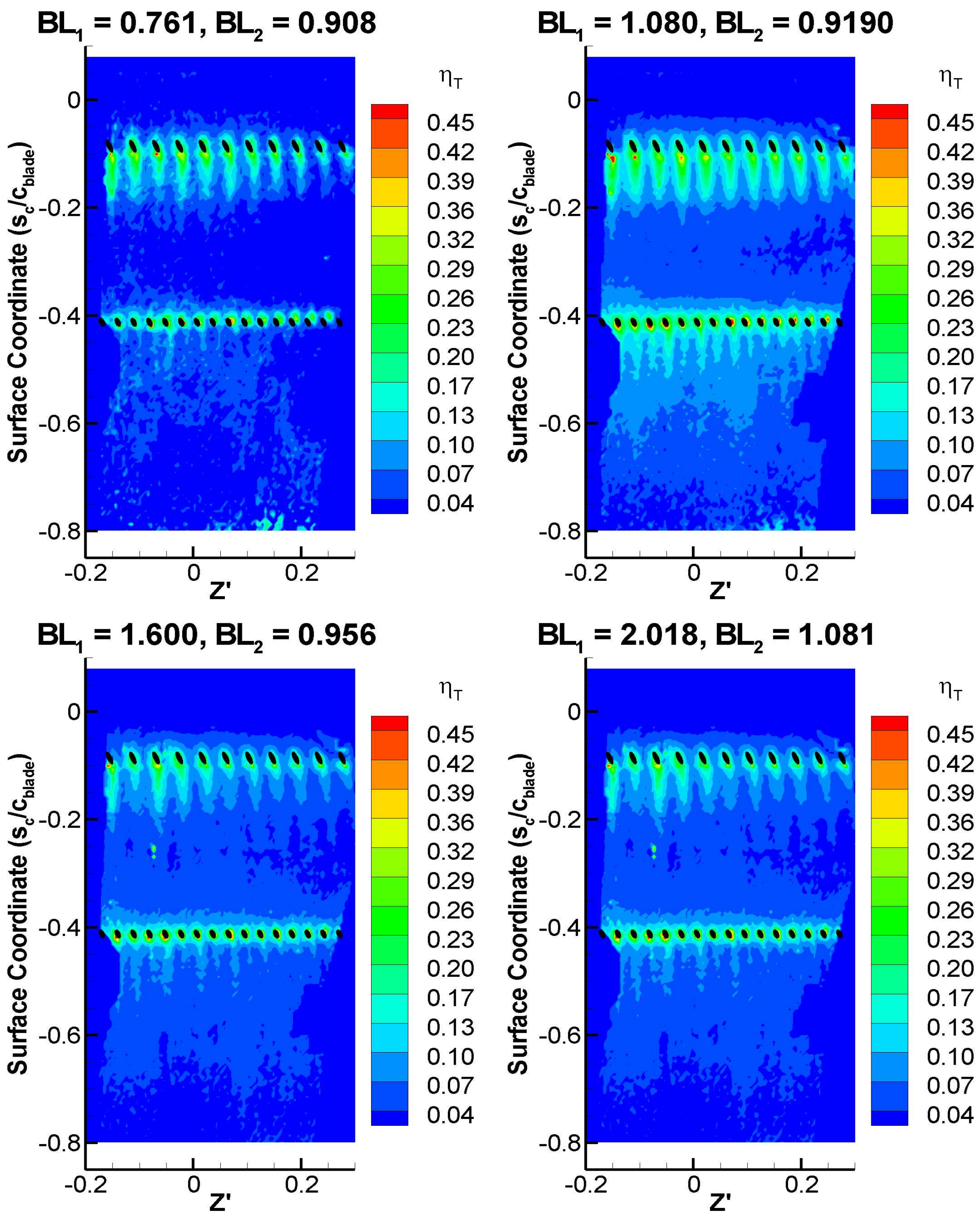

Figure 5.15: Spatially-resolved maps of η_T showing effects of blowing ratio for cases 3, 4, 5 and 7.

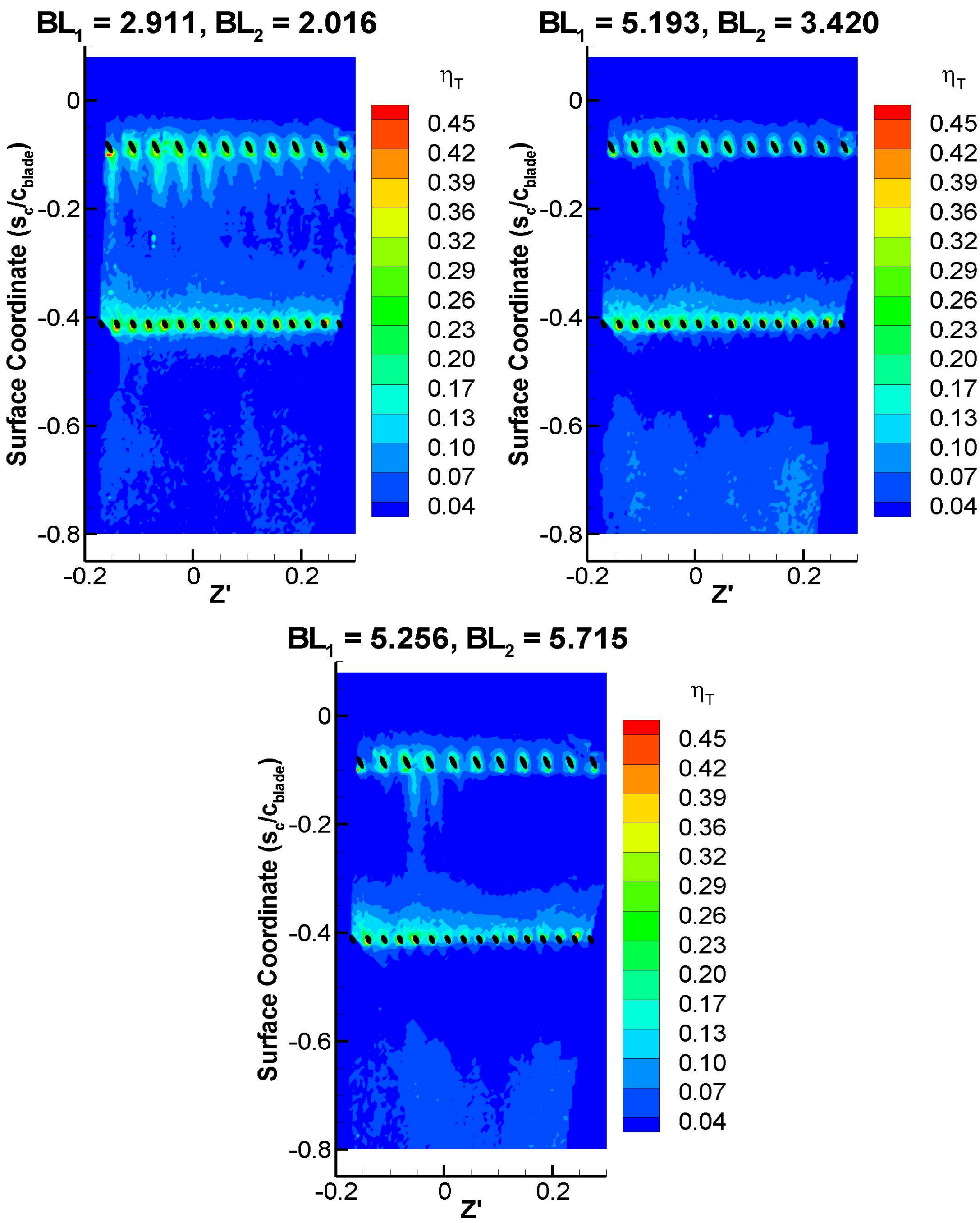

Figure 5.16: Spatially-resolved maps of η_T showing effects of blowing ratio for cases 10, 11 and 12.

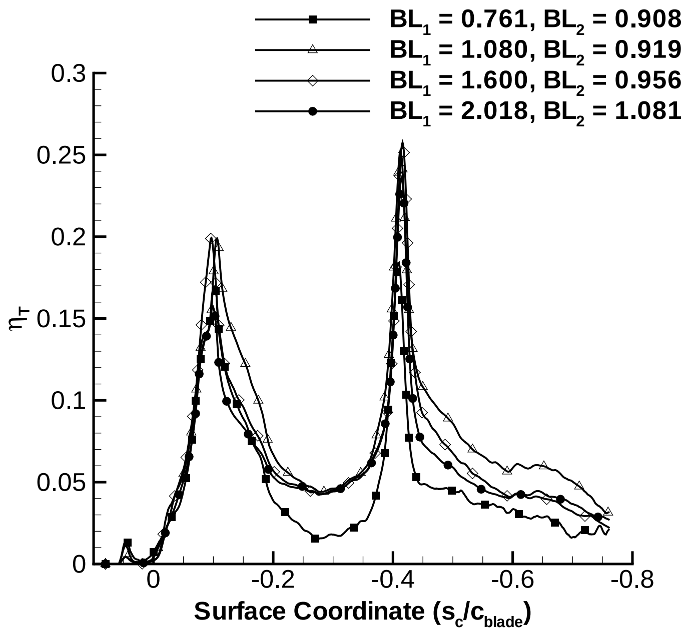

Figure 5.17: Plots of $\overline{\eta_T}(s_c/c_{blade})$ showing the effect of blowing ratio for cases 3, 4, 5 and 7.

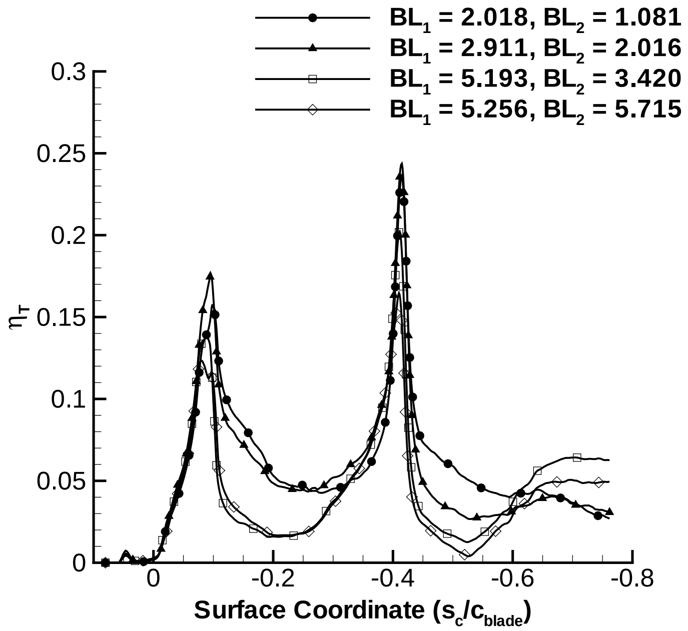

Figure 5.18: Plots of $\overline{\eta_T}(s_c/c_{blade})$ showing the effect of blowing ratio for cases 7, 10, 11 and 12.

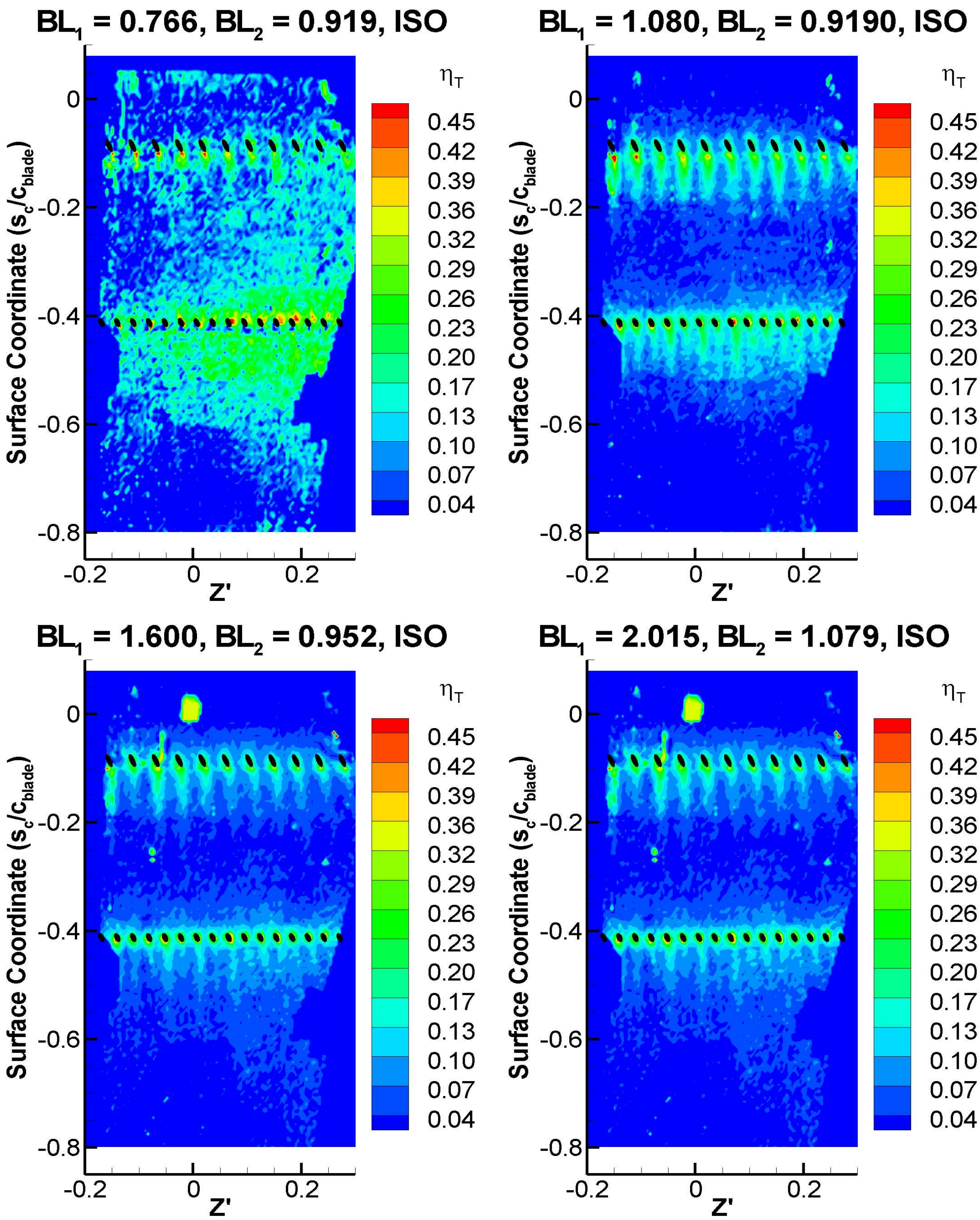

Figure 5.19: Spatially-resolved maps of $\eta_{T,iso}$ showing effects of blowing ratio for cases 3, 4, 5 and 7.

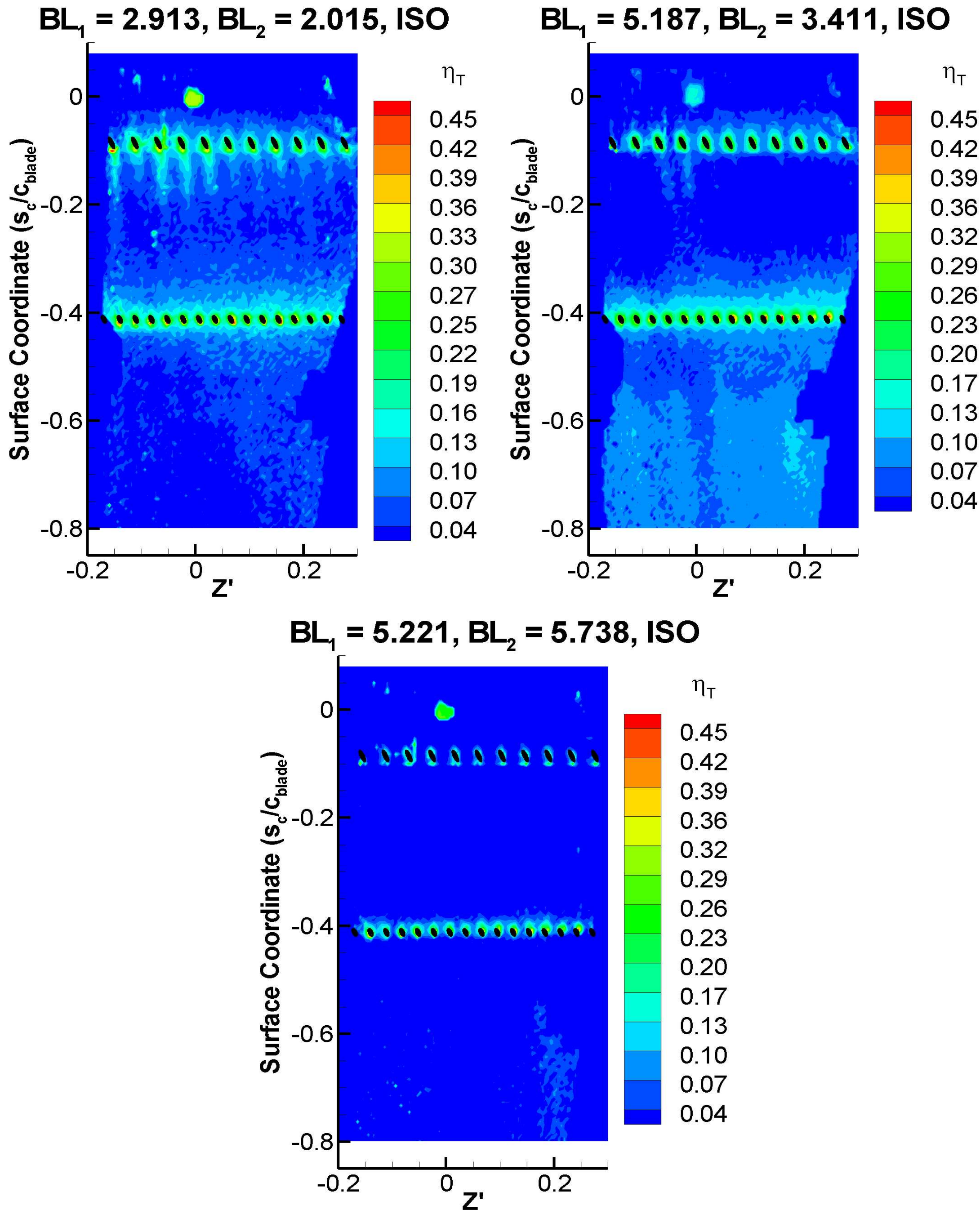

Figure 5.20: Spatially-resolved maps of $\eta_{T,iso}$ showing effects of blowing ratio for cases 10, 11 and 12.

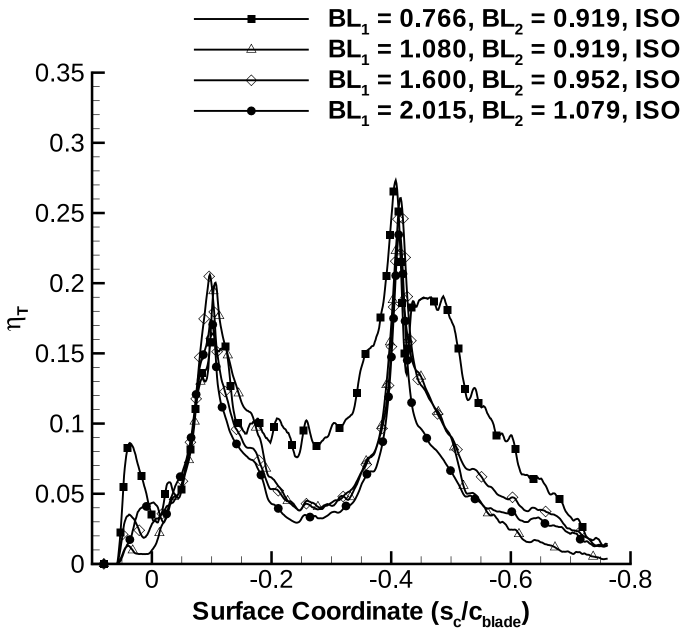

Figure 5.21: Plots of $\overline{\eta_{T,iso}}$ showing the effect of blowing ratio for cases 3, 4, 5 and 7.

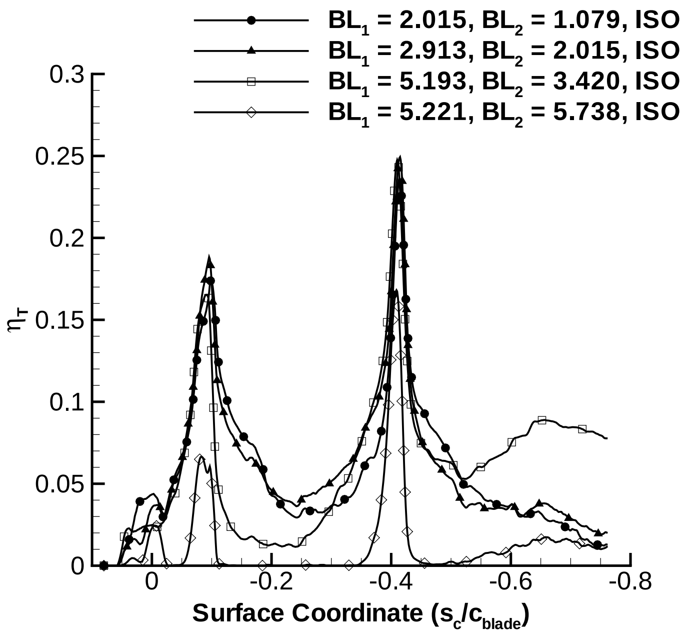

Figure 5.22: Plots of $\overline{\eta_{T,iso}}$ showing the effect of blowing ratio for cases 7, 10, 11 and 12.

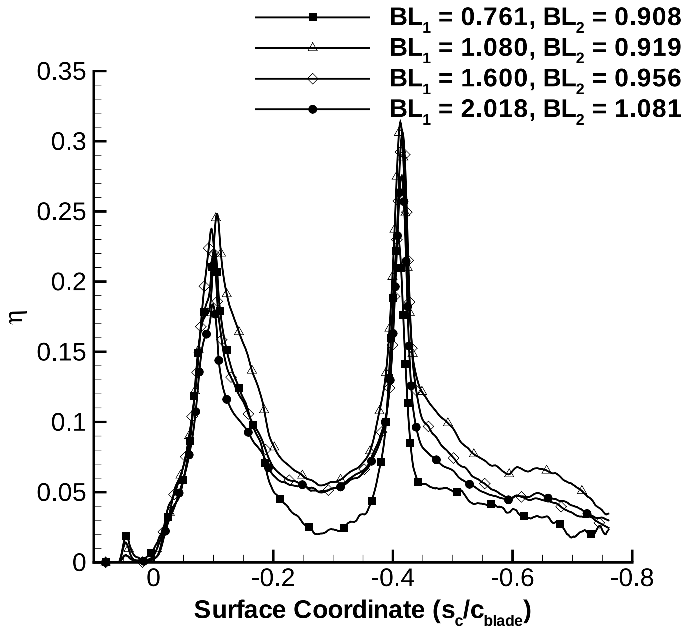

Figure 5.23: Plots of $\overline{\eta}$ showing the effect of blowing ratio for cases 3, 4, 5 and 7.

was uncertain what was a fluid dynamical effect or conduction through the measurement substrate material.

In the interests of completeness, figures 5.23, 5.24 present spanwise-averaged values of the film-effectiveness (η) computed using equation 5.25. As the hole exit temperature was slightly lower than the film -cooling plenum temperature, the values of η were slightly higher than those for η_T. However, the overall trends and dependencies on blowing ratio are the same.

5.5.2 Density Ratio Effects

Figure 5.27 presents spatially-resolved maps of η_T for cases where carbon dioxide is used as the injectant. Figures 5.28 and 5.29 present spanwise-averaged curves for these quantities. Maps of η, η_{iso} and $\eta_{T,iso}$ are not shown for brevity. However, figures 5.30, 5.31, 5.32, 5.33, 5.34 and 5.35 show their spanwise-averaged counterparts. These results show that the denser injectant appears to have improved film cooling performance when the film cooling jets are attached, holding the blowing ratio constant. The film cooling footprints behind the film cooling holes, suggest that the denser coolant persists far longer distances downstream. This observation was especially true for the second row of holes.

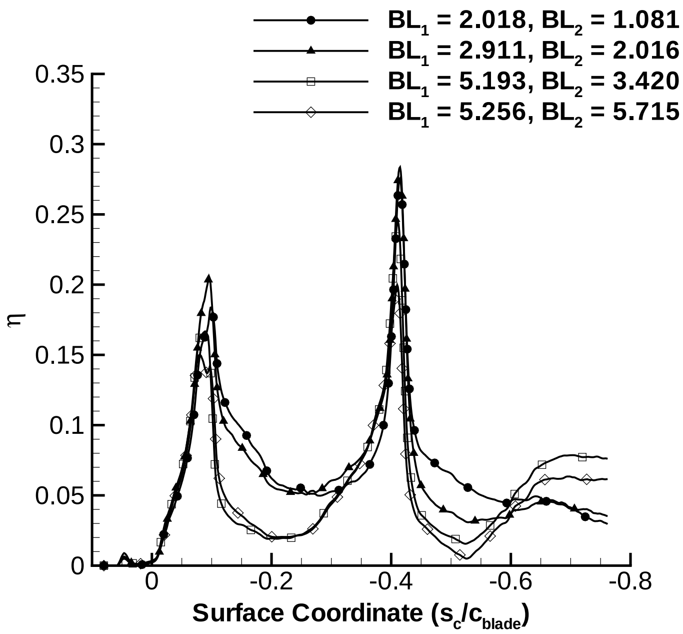

Figure 5.24: Plots of $\overline{\eta}$ showing the effect of blowing ratio for cases 7, 10, 11 and 12.

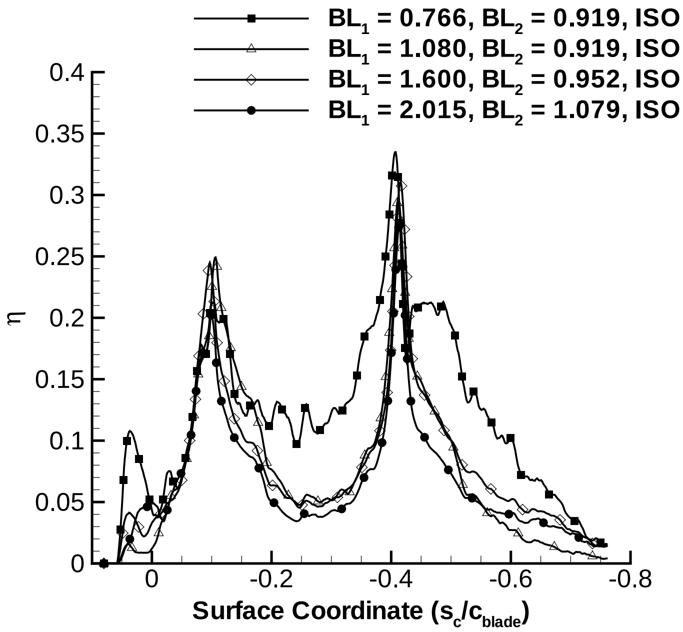

Figure 5.25: Plots of $\overline{\eta_{iso}}$ showing the effect of blowing ratio for cases 3, 4, 5 and 7.

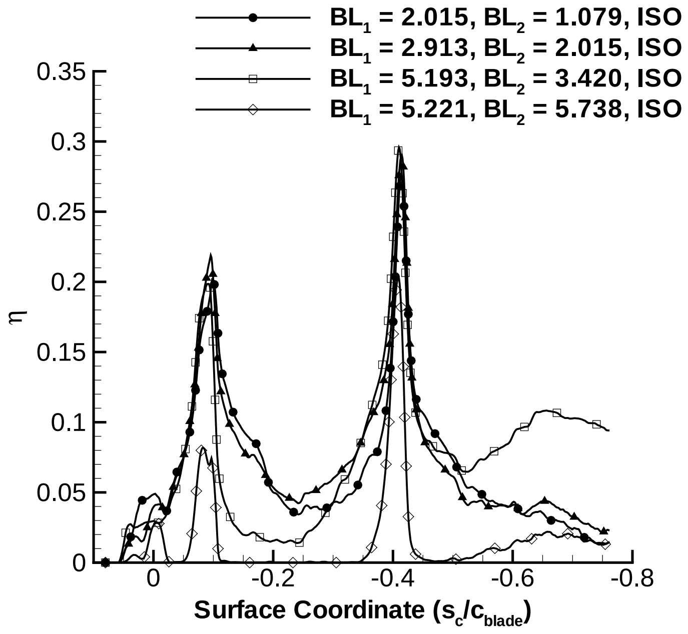

Figure 5.26: Plots of $\overline{\eta_{iso}}$ showing the effect of blowing ratio for cases 7, 10, 11 and 12.

Once the film cooling jets detach, the spatially-resolved maps and spanwise-averaged film effectiveness indicate no functional difference between injecting air or CO_2 through the film cooling holes.

5.5.3 Turbulence effects on film effectiveness

The predicted behavior of increased turbulence levels is the rapid degradation of the film cooling layer if the injected jets are attached. Furthermore, it was expected that there would be increased spanwise mixing. In the case where the film cooling jets are detached, the increased levels of turbulence were expected to allow the jets to reattach to the surface over a shorter distance. The results shown in this subsection agree with these previously noted results. Figure 5.36 presents maps of η_T taken at the high turbulence condition using both air and carbon dioxide injection. These results were then spanwise-averaged as shown in figures 5.37 and 5.38. The trends using other definitions of film-effectiveness were consistent with these observations and thus are not presented here.

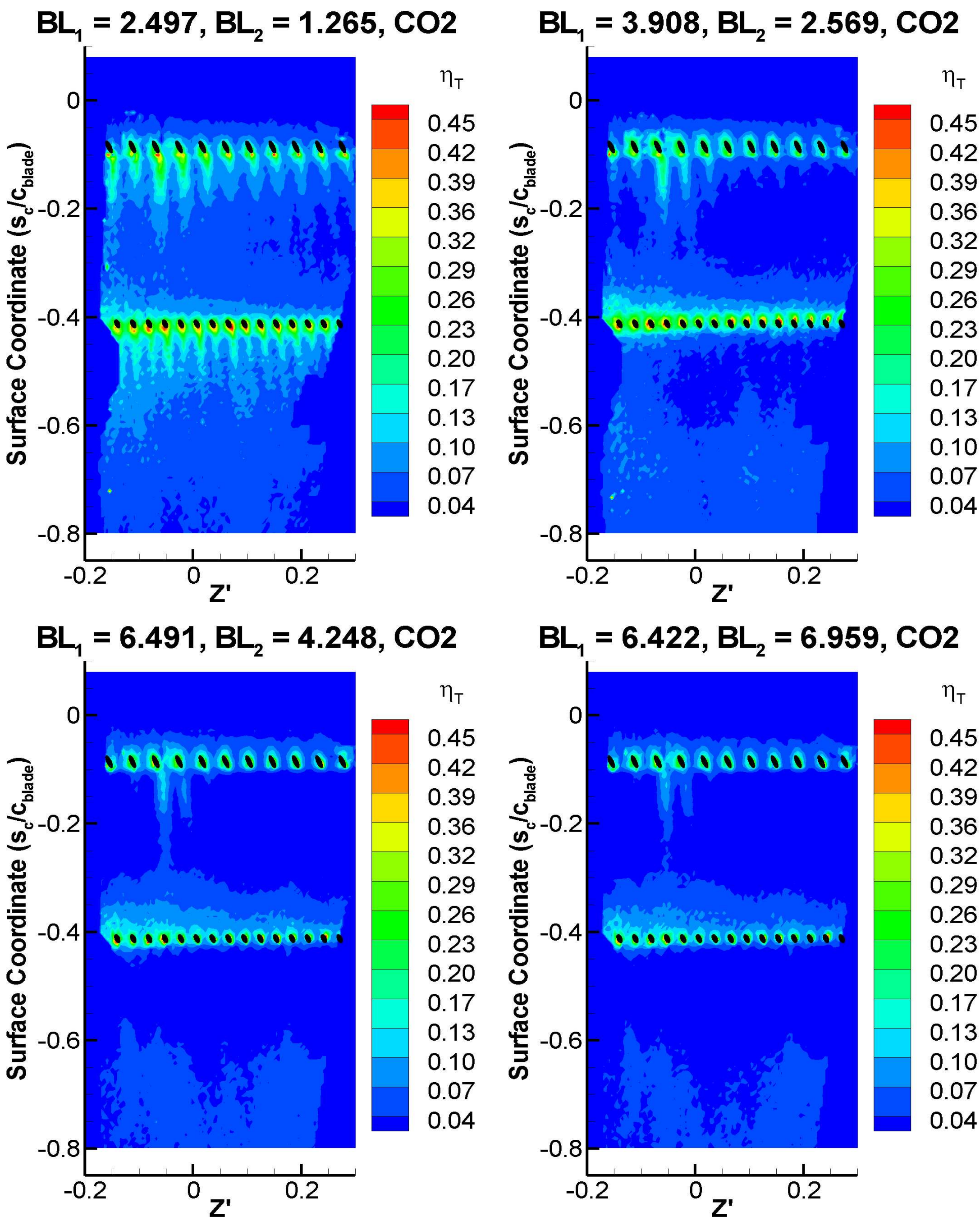

Figure 5.27: Spatially-resolved maps of η_T showing effects of density ratio for cases 9, 18, 14 and 17.

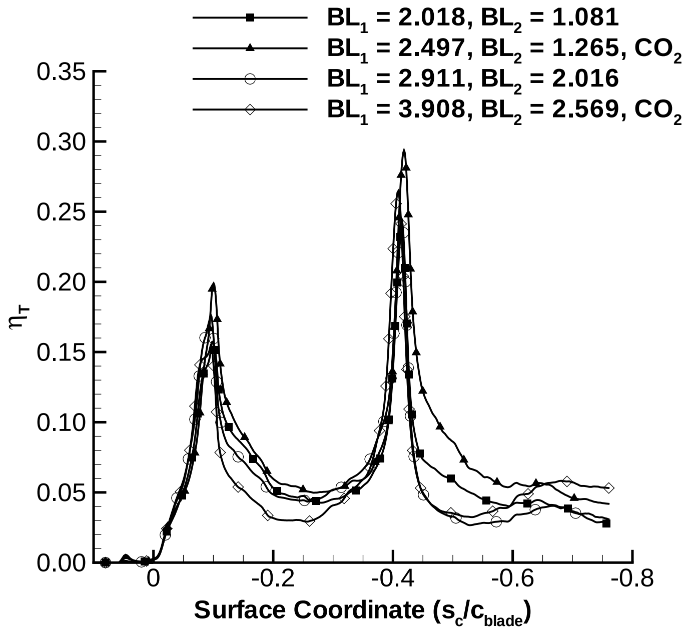

Figure 5.28: Plots of $\overline{\eta_T}$ showing the effect of injectant for cases 7, 9, 10 and 18.

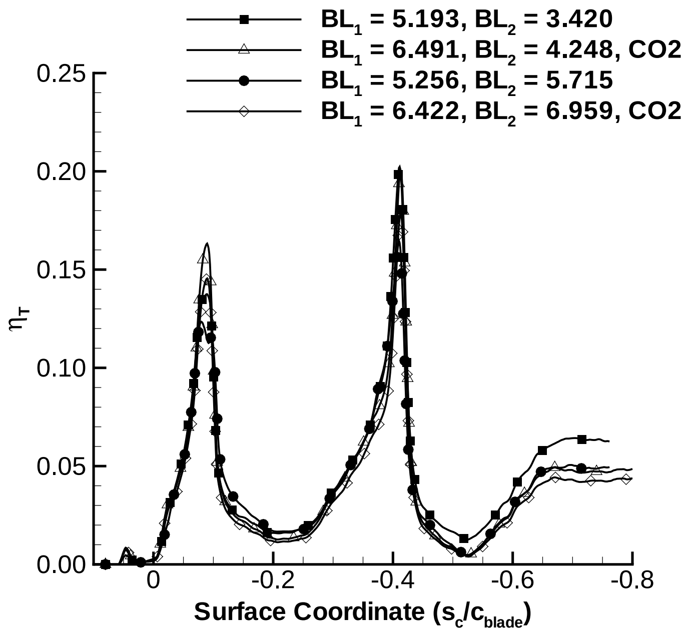

Figure 5.29: Plots of $\overline{\eta_{iso}}$ showing the effect of injectant for cases 11, 14, 12 and 17.

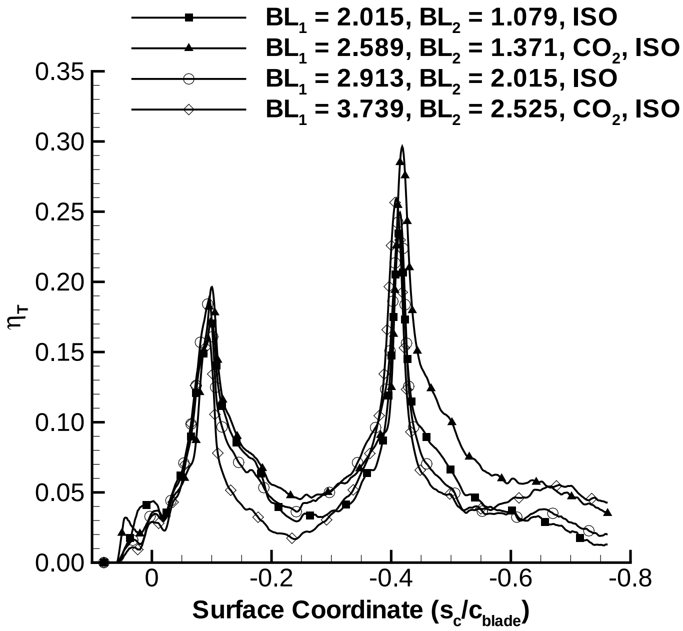

Figure 5.30: Plots of $\overline{\eta_{T,iso}}$ showing the effect of injectant for cases 7, 9, 10 and 18.

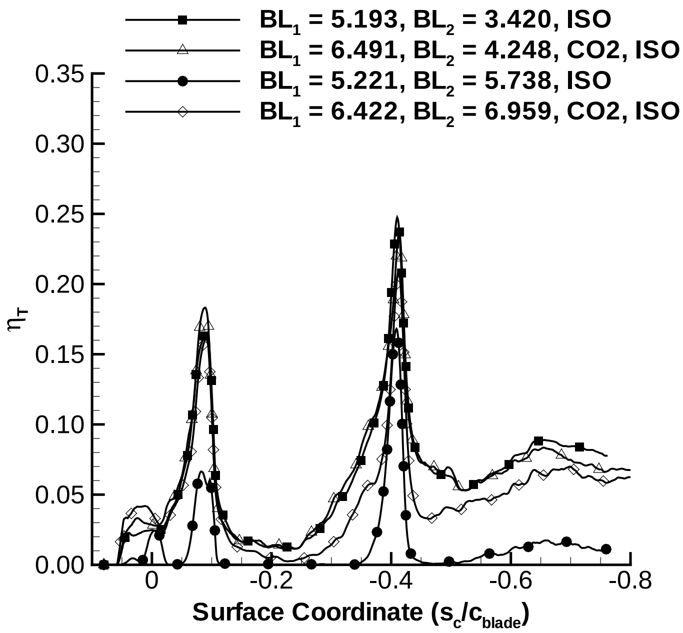

Figure 5.31: Plots of $\overline{\eta_{T,iso}}$ showing the effect of injectant for cases 11, 14, 12 and 17.

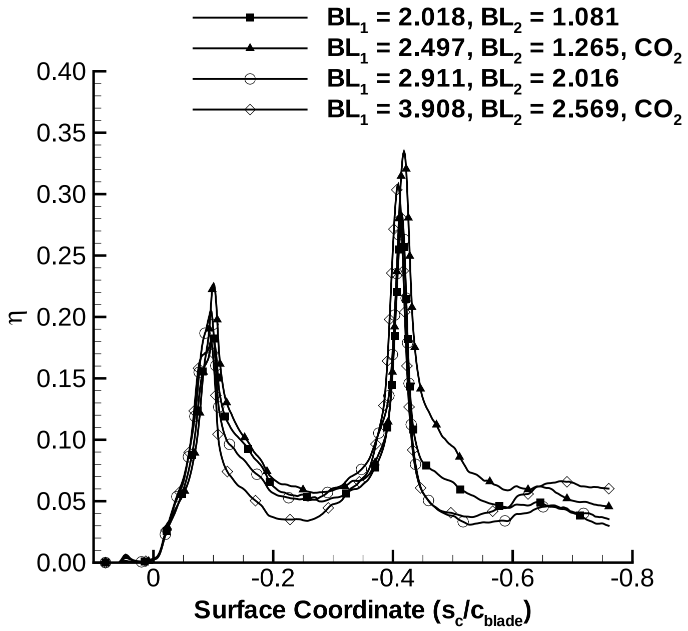

Figure 5.32: Plots of $\overline{\eta}$ showing the effect of injectant for cases 7, 9, 10 and 18.

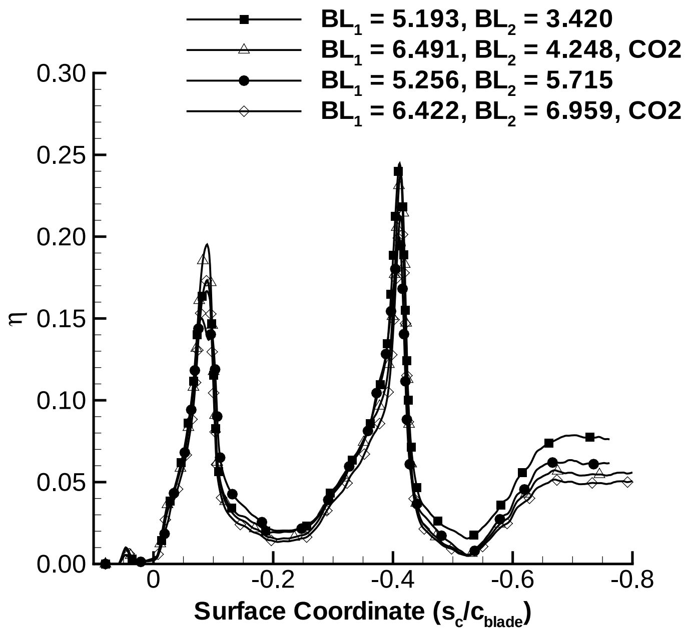

Figure 5.33: Plots of $\overline{\eta}$ showing the effect of injectant for cases 11, 14, 12 and 17.

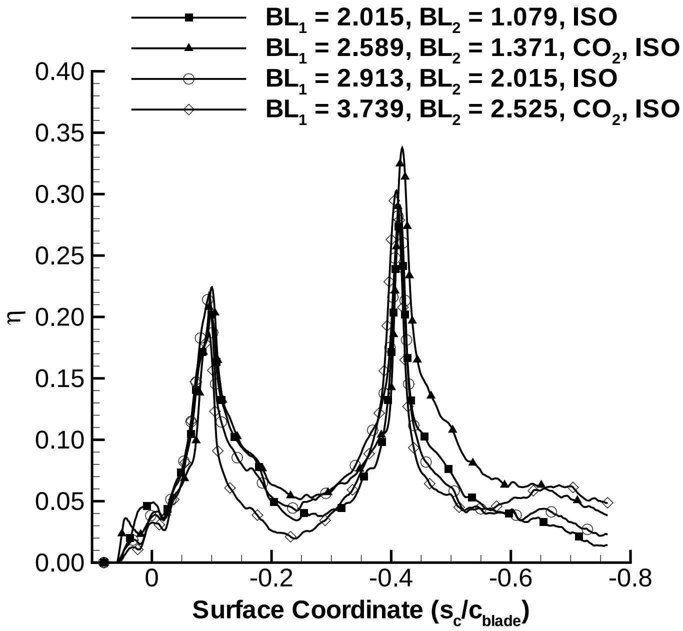

Figure 5.34: Plots of $\overline{\eta}$ showing the effect of injectant for cases 7, 9, 10 and 18.

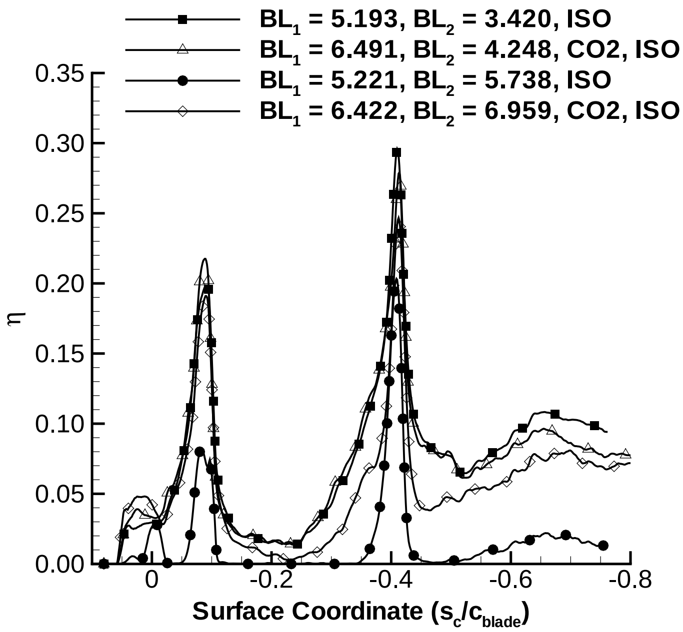

Figure 5.35: Plots of $\overline{\eta_{iso}}$ showing the effect of injectant for cases 11, 14, 12 and 17.

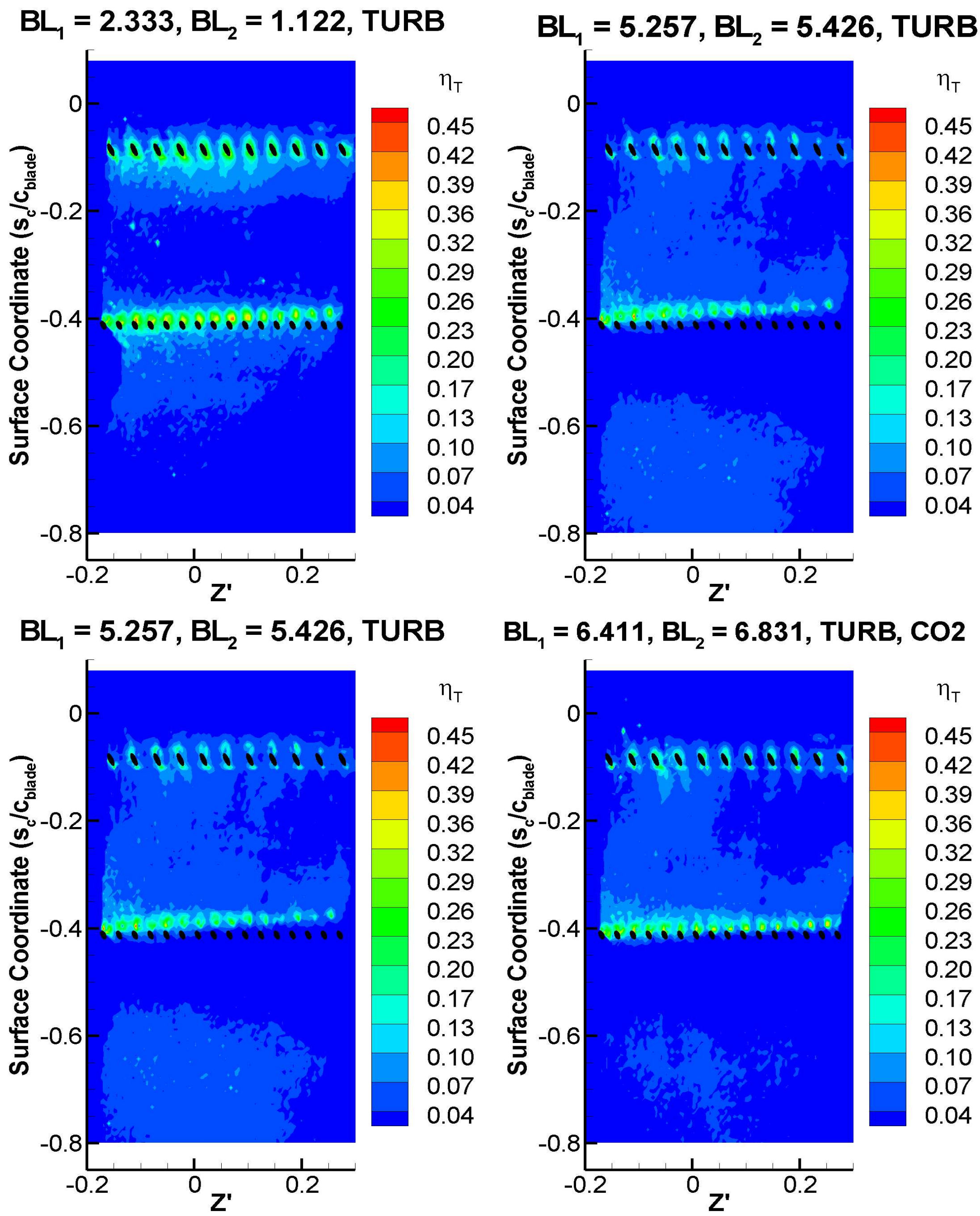

Figure 5.36: Spatially-resolved maps of η_T showing effects of turbulence level for cases 3, 4, 5 and 7.

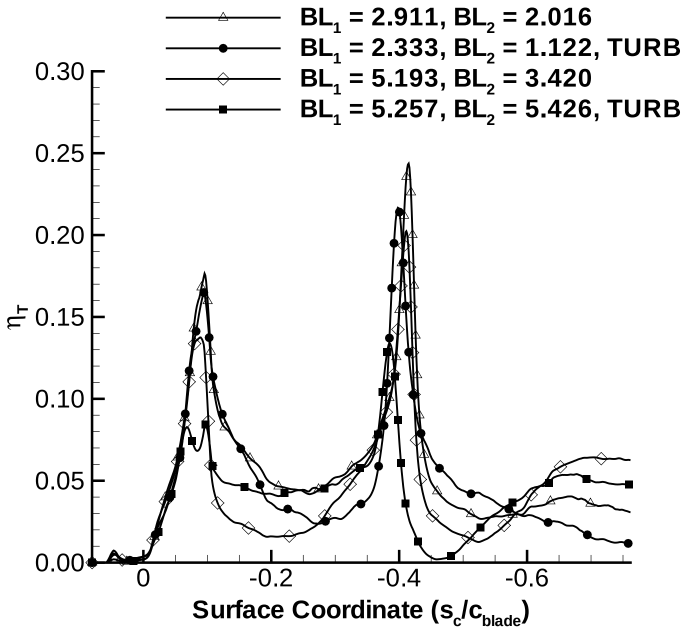

Figure 5.37: Plots of $\overline{\eta_T}$ showing the effect of turbulence for cases 10, 6, 11 and 13.

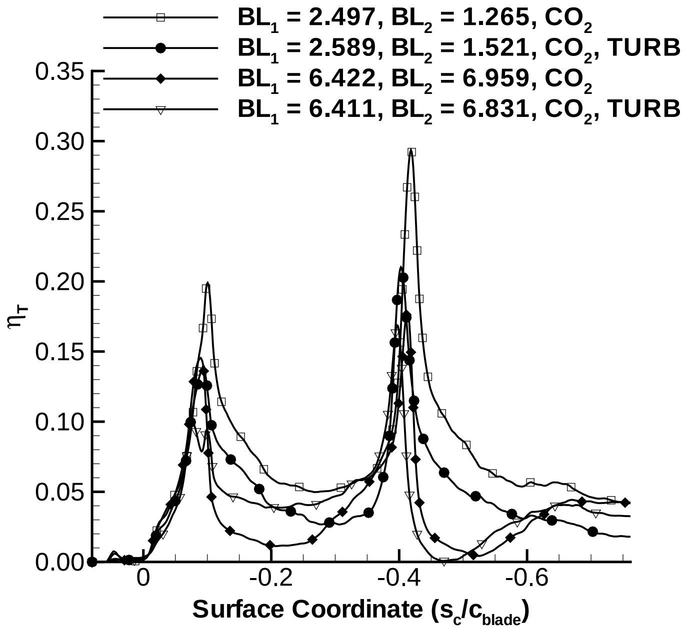

Figure 5.38: Plots of $\overline{\eta_T}$ showing the effect of turbulence for cases 8, 6, 17 and 16.

5.5.4 Discussion of Film Cooling Results

The trends suggested by the parametric studies presented in Chapter 1 are confirmed in these results. The film cooling jets were clearly observed to move from jet attachment to lift-off with increasing blowing ratio. The use of denser gases was found to improve the size of the cooled area and increase the overall film effectiveness. Increasing turbulence level was found to reduce the film effectiveness when the cooling jets were attached, but encouraged jet attachment once blow-off occurred. Additionally, the increased turbulence levels increased the amount of spanwise mixing, eradicating the normally observed streaks observed with the low-turbulence case.

The definition for film effectiveness using the isoenergetic temperature (η_{iso}) was found to produce results that were substantially different that those using the recovery-temperature-based film effectiveness (η). It is unclear if this was due to compressibility effects that were subtracted out using the isoenergetic temperature profile or some unknown reason. To fully answer this question, additional incompressible data with the same curvature conditions would be needed. The η_{iso} definition produced results that appeared to collapse on each other when the film cooling jets are attached at the low turbulence condition and air as the injectant.

5.6 Heat Transfer Coefficient Results

This section presents some of the heat transfer coefficient data collected in the single passage. The objective of these measurements was to develop an understanding of the effect of film cooling injection on the heat transfer coefficient and its sensitivity to changes in the density of the injection fluid and upstream turbulence levels. Furthermore, the secondary objective of these measurements was to provide a comparison database for numerical simulation efforts for film cooling.

5.6.1 Baseline Comparison

Before conducting experiments with active film cooling, heat transfer data were collected with no blowing. This was to ascertain how well the surface approximated a constant heat flux surface, and consequently agreed with the data presented in Chapter 5. Figure 5.39 presents the heat transfer coefficient map defined using equations 5.1 (h_{iso}) and 5.2 (h). These figures generally agree with those shown in Chapter 5, except near the leading edge and around the film cooling holes. Figure 5.40 presents this spanwise-averaged quantity compared to the uncooled data presented in section 4.1.3 and the alternative definition for h shown in equation 5.27. These data suggest that the heating film had significant defects that caused local "hot spots" that affected the measurement. Figure 5.39 presents the ratio $h_{ratio} = \frac{h}{h_{no\ fc}}$ to more clearly demonstrate the localized distortion effects within the constant heat flux surface. These effects were primarily near the stagnation point and the areas around the film cooling holes. It could not be determined if the observed distortion effect around the holes was due solely to problems with the heating film, or an unsteady effect from flow passing into and out of the film cooling holes. This made further understanding of the augmentation effect of film cooling more difficult. The difference between the baseline profile and the measurements performed on the drilled heated surface was estimated to be as high as 30% near the leading edge due to local disruptions of the heat flux boundary condition near the stagnation point and decrease to approximately 5% over the majority of the measurement surface.

Additionally, these data show that certainly for the baseline case, the two proposed definitions of h do produce comparable profiles, within the uncertainty of the measurement.

5.6.2 Effects of Blowing Ratio on Heat Transfer Coefficient

Figures 5.41, 5.42 presents maps of the heat transfer coefficient computed using the recovery temperature (equation 5.2) and normalized by the heat transfer coefficient measured on the film-cooled surface with no blowing ($h_{ratio,2} = \frac{h}{h_{BL=0}}$). Figures 5.43, 5.44, 5.45 and 5.46 present the ratio of the spanwise-averaged film-cooled heat transfer coefficient versus that measured with no blowing ($\overline{h}_{ratio,2} = \frac{\overline{h}}{\overline{h}_{BL=0}}$). These results show that the effect of blowing ratio is generally monotonic with the greatest augmentation occurring downstream of the second row of film cooling holes with an increase of as much as 100% over the uncooled heat transfer coefficient value. This can be interpreted as the presence of film cooling increasing the level of turbulence in the boundary layer, due to enhanced mixing with the freestream flow. The location of maximum heat transfer appears to coincide with this location of jet attachment, when these results are contrasted with the film-effectiveness results shown in section 5.5.1.

With respect to the second row of cooling holes, there appears to be an augmentation

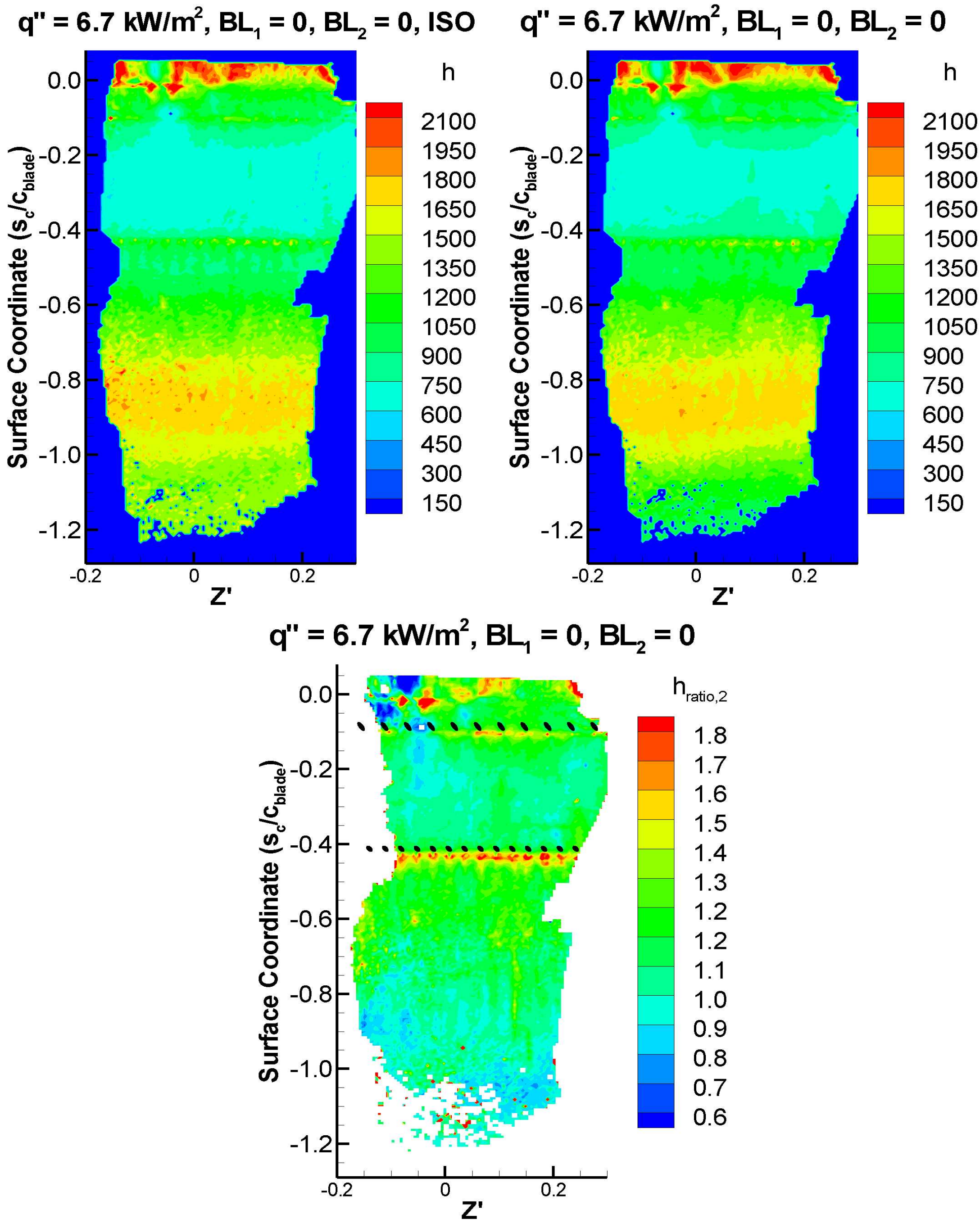

Figure 5.39: Spatially-resolved maps of h_{iso}, h and $h_{ratio} = \frac{h}{h_{no\ fc}}$.

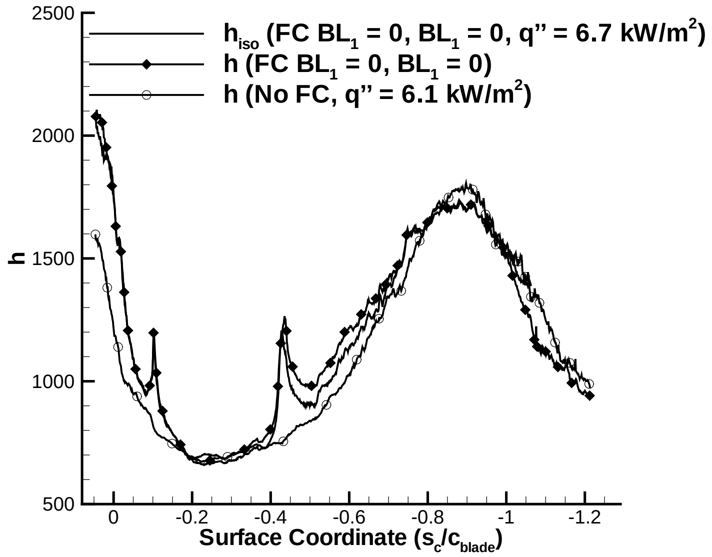

Figure 5.40: Plots of $\overline{h}$, $\overline{h_{iso}}$ and $\overline{h_{no\ fc}}$and compared to the uncooled results from section 4.1.3 showing the effect of distortion of heat flux boundary condition.

effect in between the film cooling holes. This map shows that the heat transfer augmentation behind each film cooling hole in the second row is fairly asymmetric, as demonstrated by measurements presented in section 1.5.4. This was not the case for the first row, even once blow-off had been achieved. A possible explanation for this observation is the fact that the hole spacing for the second row of holes is much smaller than that for the first row.

A surprising result is the reduction in the heat transfer coefficient downstream of the second row of film cooling holes for the $BL_1 = 1.083$, $BL_2 = 0.903$ case. The effect of augmentation was found to be relatively far-reaching downstream. What adds to the confusion of this result is the fact that the case below this with blowing ratios of $BL_1 = 0.775$, $BL_2 = 0.917$ shows a slight increase in the spanwise-averaged heat transfer coefficient.

Figures 5.41, 5.42 presents maps of the heat transfer coefficient computed using the isoenergetic temperature (equation 5.1) and normalized by the heat transfer coefficient measured on the film-cooled surface with no blowing ($h_{iso,ratio,2} = \frac{h_{iso}}{h_{iso,BL=0}}$). Figures 5.43, 5.44, 5.51 and 5.52 present the ratio of the spanwise-averaged film-cooled heat transfer coefficient versus that measured with no blowing ($\overline{h}_{iso,ratio,2} = \frac{\overline{h}_{iso}}{\overline{h}_{iso,BL=0}}$). These results show smaller augmentation effect downstream of the second row of film cooling holes once

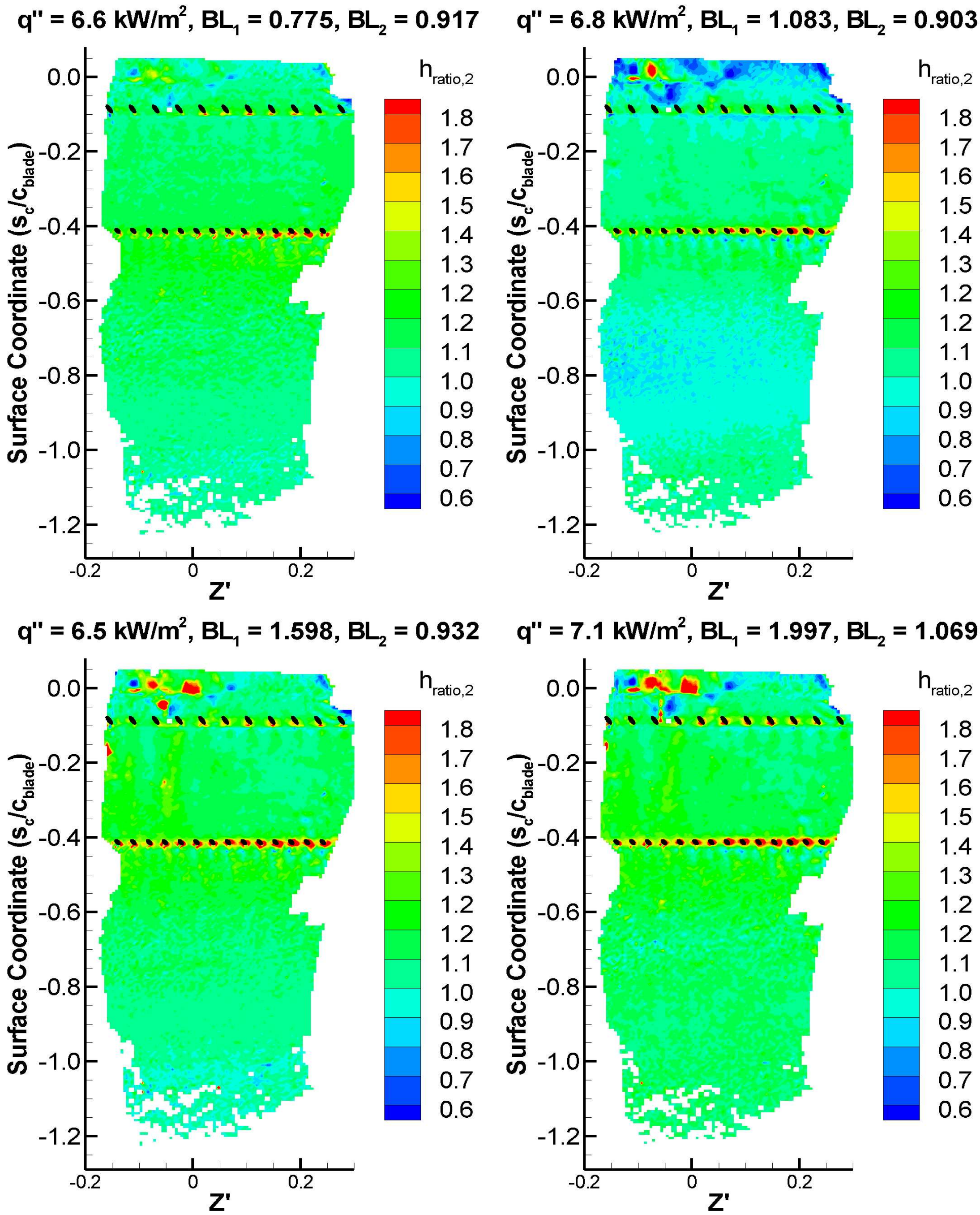

Figure 5.41: Spatially-resolved maps of $h_{ratio,2} = \frac{h}{h_{BL=0}}$ showing the effects of blowing ratio for cases 3, 4, 5, and 7.

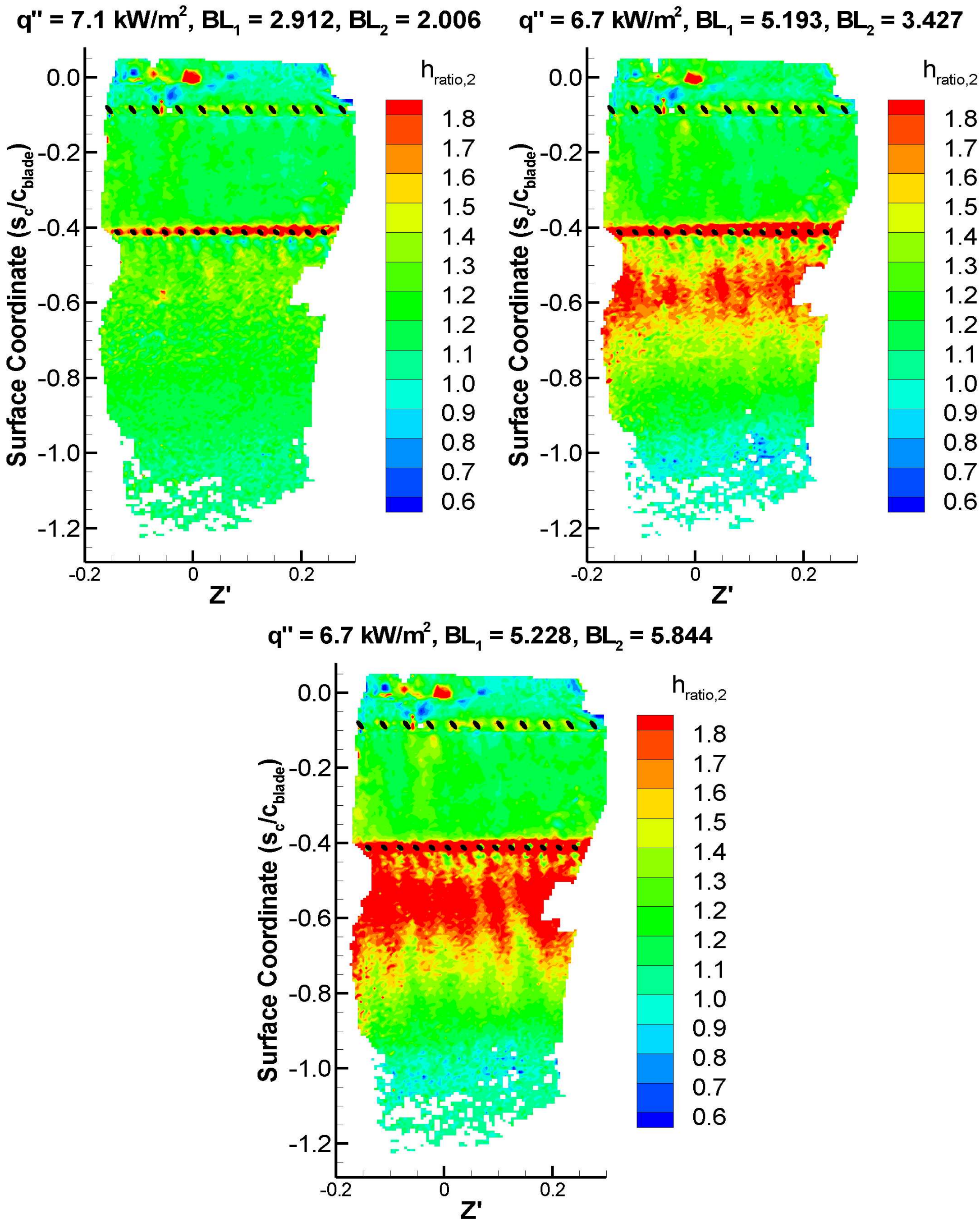

Figure 5.42: Spatially-resolved maps of $h_{ratio,2} = \frac{h}{h_{BL=0}}$ showing the effects of blowing ratio for cases 10, 11 and 12.

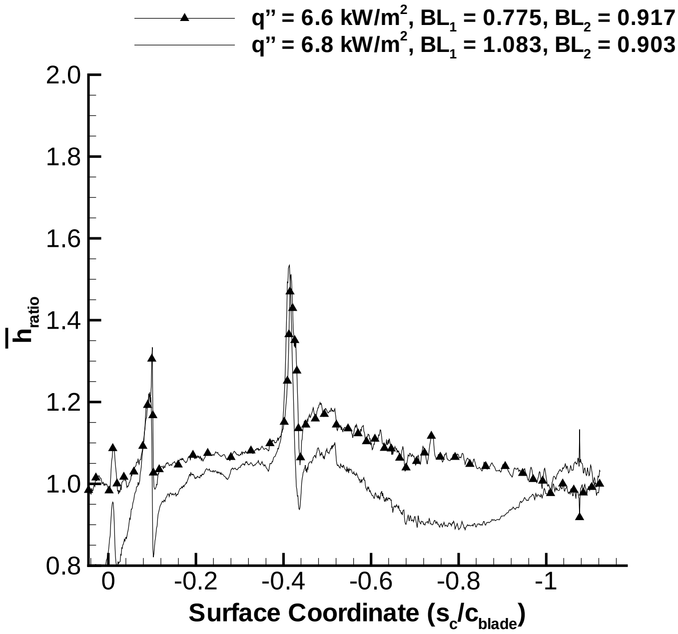

Figure 5.43: Plots of $\overline{h}_{ratio,2} = \frac{\overline{h}}{h_{BL=0}}$ showing the effect of blowing ratio for cases 3 and 4.

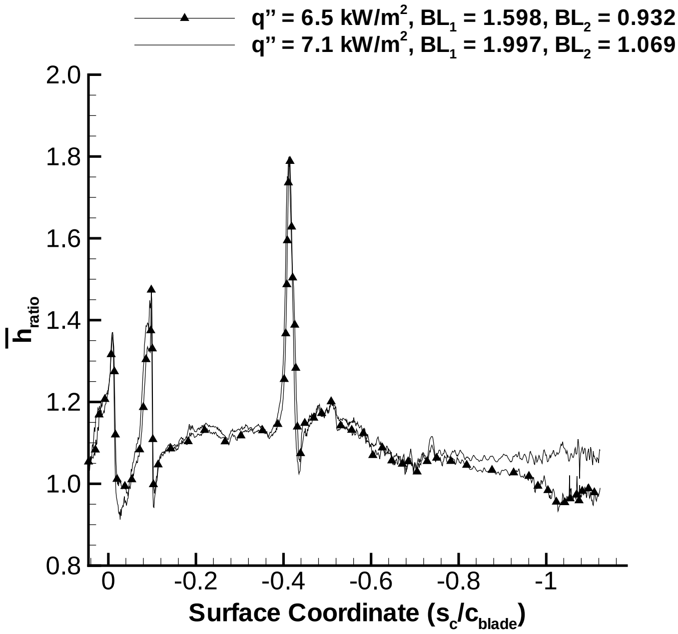

Figure 5.44: Plots of $\overline{h}_{ratio,2} = \frac{\overline{h}}{h_{BL=0}}$ showing the effect of blowing ratio for cases 5 and 7.

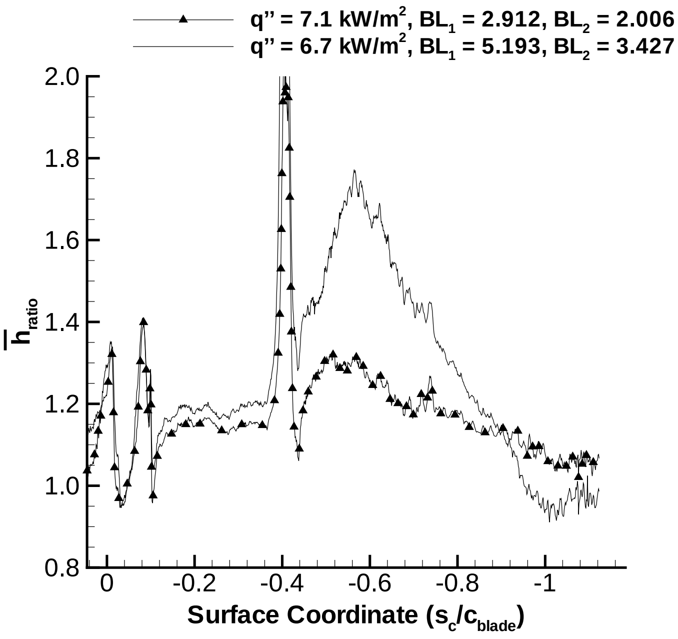

Figure 5.45: Plots of $\overline{h}_{ratio,2} = \frac{\overline{h}}{h_{BL=0}}$ showing the effect of blowing ratio for cases 10 and 11.

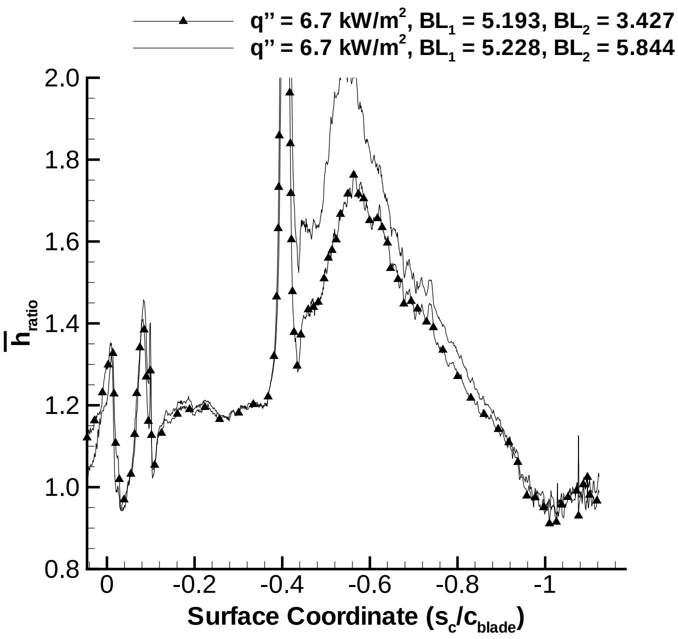

Figure 5.46: Plots of $\overline{h}_{ratio,2} = \frac{\overline{h}}{h_{BL=0}}$ showing the effect of blowing ratio for cases 11 and 12.

jet blow-off occurs, where viscous dissipation was expected to become significant. If the jets were found to remain attached, the h_{iso} definition shows very little augmentation.

These data clearly suggest that there is a difference between the two definitions of the heat transfer coefficient, and this difference can be quite substantial for the high blowing cases. Thus these results demonstrate that it is critical that experimentalists and numerical analysts have consistency in computed and measurement quantities, otherwise these in-built differences would be interpreted as modeling errors rather than simply a definition misinterpretation.

5.6.3 Effects of Density Ratio in Heat Transfer Coefficient

Referring to section 1.5.8, the generally expected trend with the injection of a denser gas is the increased augmentation of the heat transfer coefficient. An examination of the h maps for various blowing ratios and $\overline{h}_{ratio,2} = \frac{\overline{h}}{h_{BL=0}}$ curves shown in figures 5.53, 5.54 and 5.55 clearly contradict this hypothesis. Instead a suppression effect is observed. This is particularly apparent for conditions where jet blow-off was detected. The location of maximum heat transfer appears to coincide with this location, as also observed with the low-density jets. When the film cooling jets are attached to the surface, the effect of increased density ratio on the heat transfer coefficient appears to be minimal. This suggests that there are two regimes for the augmentation effect, one where the turbulence level within the boundary layer is increased due to jet injection, the second where inviscid jet dynamics of the detached film cooling jets sweep the mainstream flow near the surface. An unexpected result is the apparent reduction of heat transfer coefficient downstream of the first row of film cooling holes as the blowing ratios of the carbon dioxide jets was increased from $BL_1 = 6.318, BL_2 = 4.262$ to $BL_1 = 6.589, BL_2 = 7.020$. It is uncertain why this is the case.

It is difficult to develop a physical understanding of this behavior. It could be hypothesized that the denser gas has a lower thermal conductivity, better insulating the surface. But that would suggest that the film cooling jets would have to be attached to the surface, something which clearly is not the case when blow-off occurs. Additionally, if the momentum ratio for the high density jet cases are compared to cases where air is used as the injectant, it can be observed that the heat transfer coefficient behavior does not scale on the momentum ratio.

Figure 5.56 displays maps of the heat transfer coefficient computed using the isoenergetic

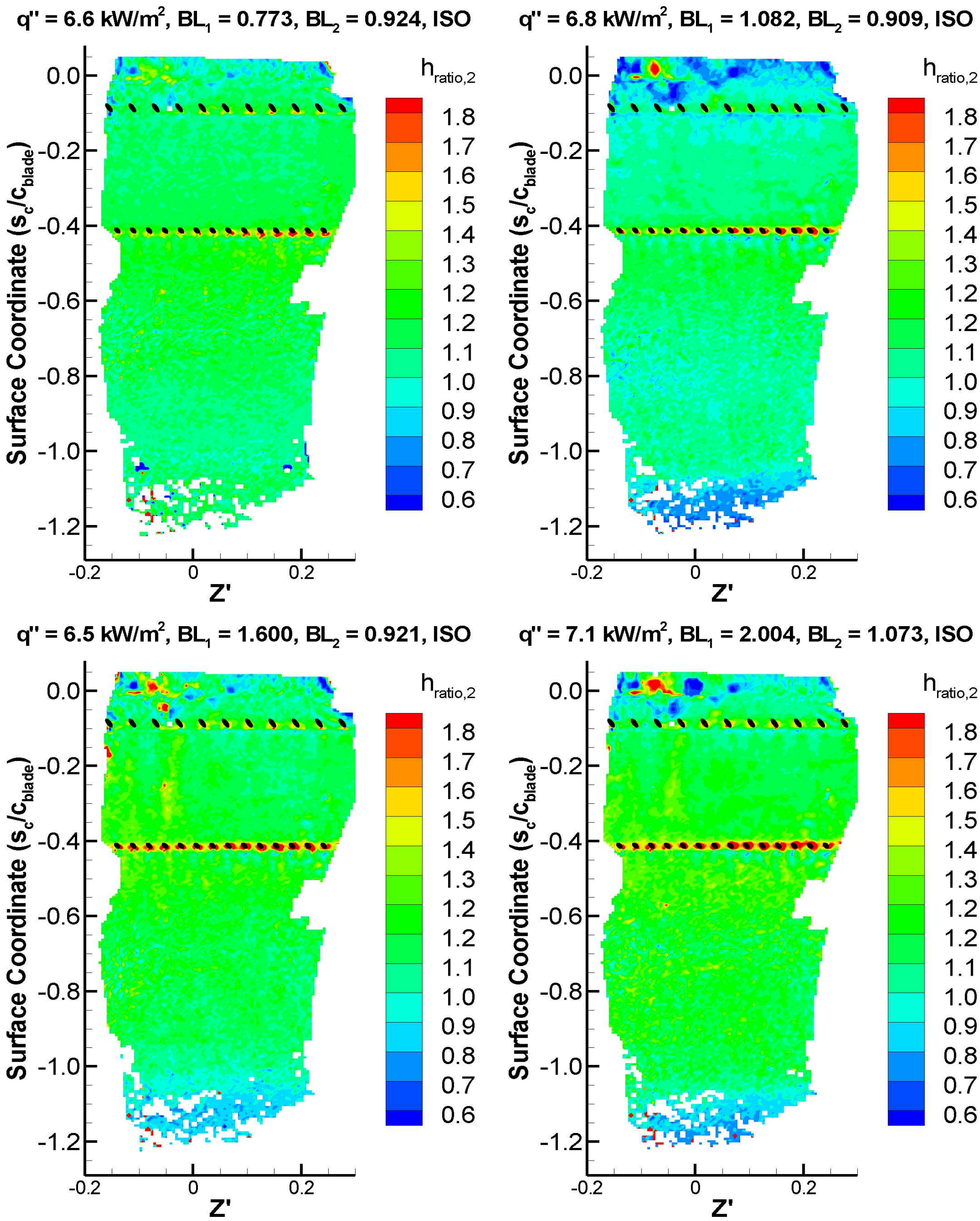

Figure 5.47: Spatially-resolved maps of $h_{iso,ratio,2} = \frac{h_{iso}}{h_{iso,BL=0}}$ showing the effects of blowing ratio for cases 3, 4, 5, and 7.

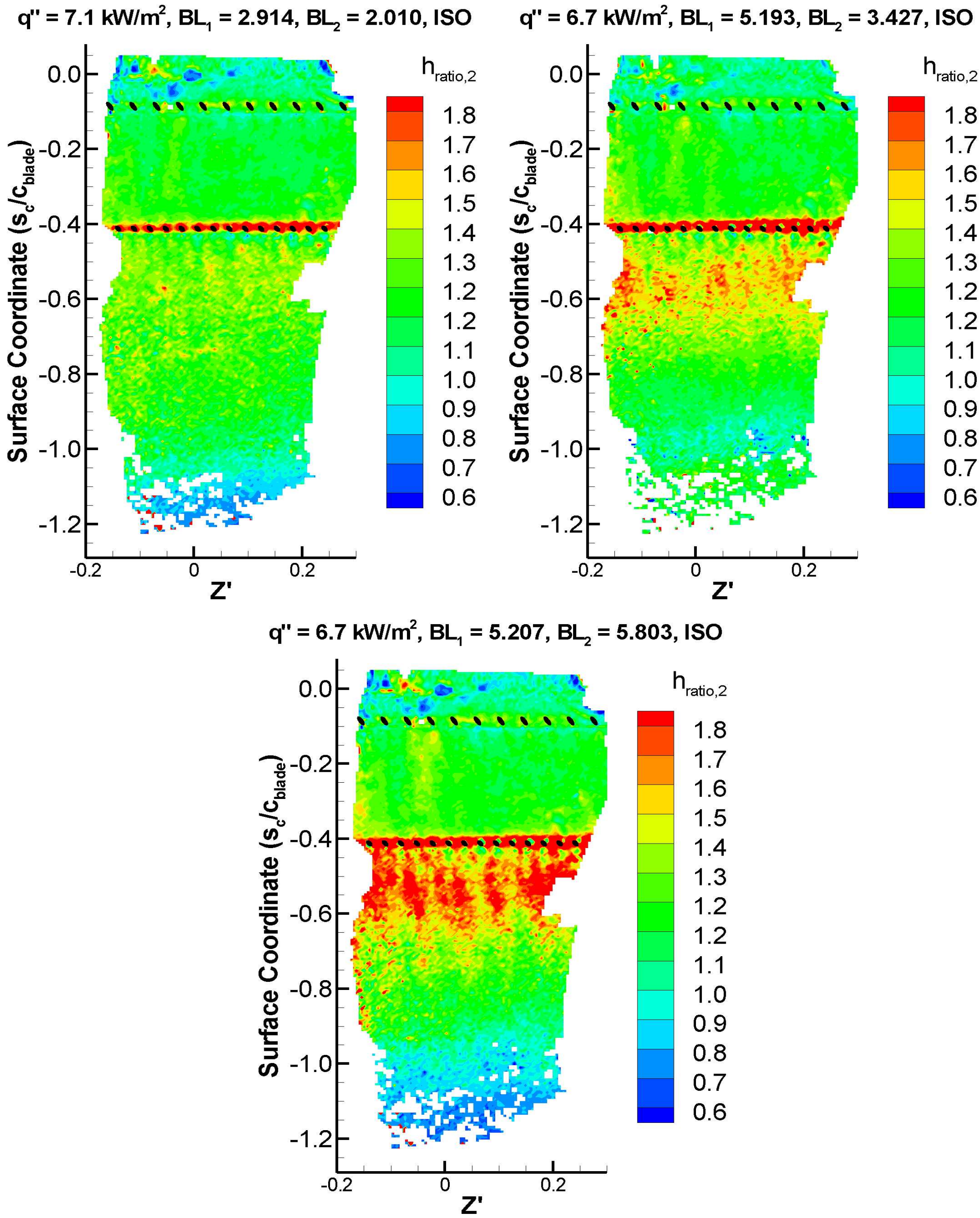

Figure 5.48: Spatially-resolved maps of $h_{iso,ratio,2} = \frac{h_{iso}}{h_{iso,BL=0}}$ showing the effects of blowing ratio for cases 10, 11 and 12.

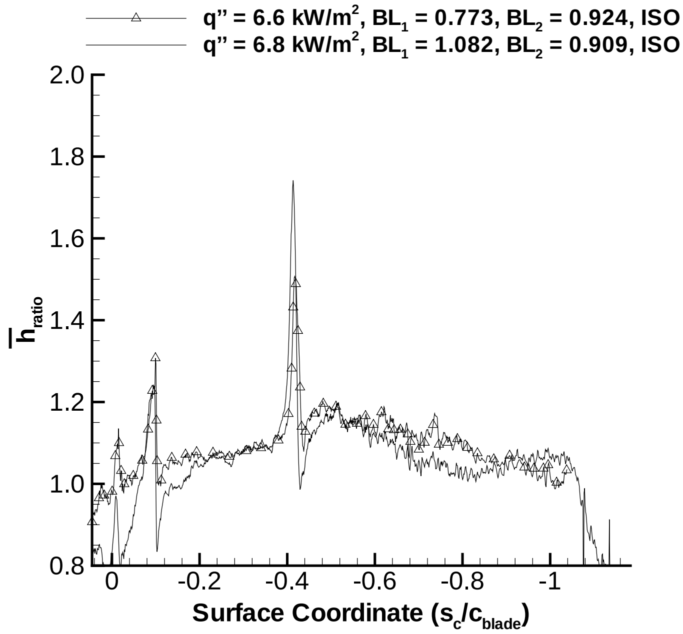

Figure 5.49: Plots of $\overline{h}_{iso,ratio,2} = \frac{\overline{h}_{iso}}{h_{iso,BL=0}}$ showing the effect of blowing ratio for cases 3 and 4.

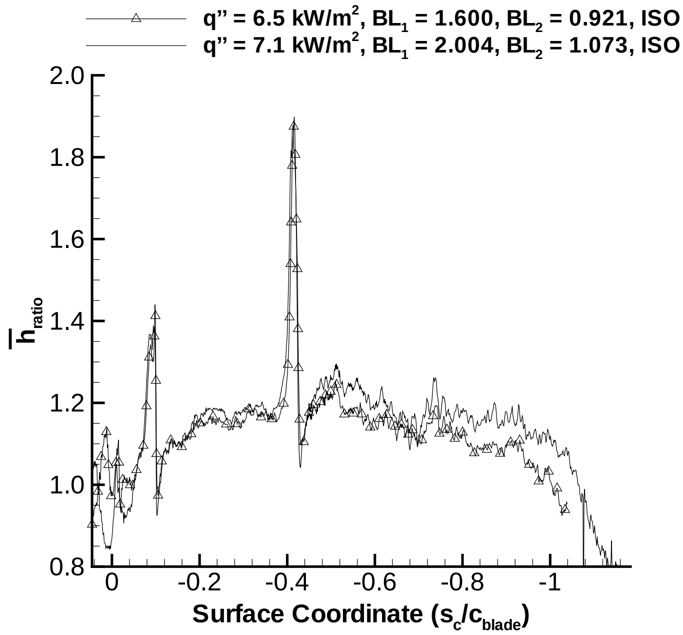

Figure 5.50: Plots of $\overline{h}_{iso,ratio,2} = \frac{\overline{h}_{iso}}{h_{iso,BL=0}}$ showing the effect of blowing ratio for cases 5 and 7.

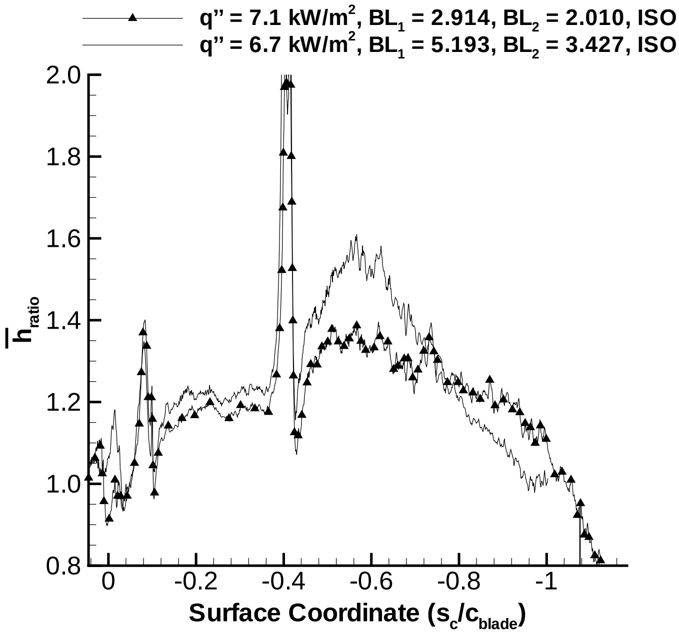

Figure 5.51: Plots of $\overline{h}_{iso,ratio,2} = \frac{\overline{h}_{iso}}{h_{iso,BL=0}}$ showing the effect of blowing ratio for cases 10 and 11.

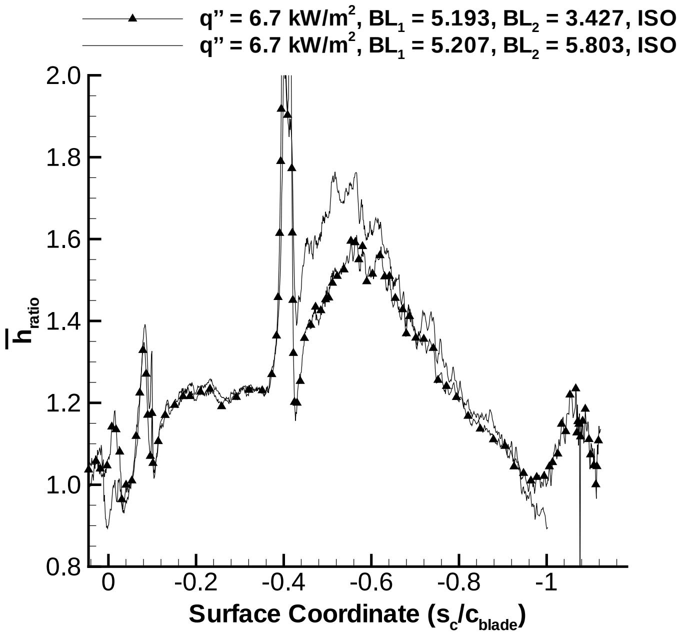

Figure 5.52: Plots of $\overline{h}_{iso,ratio,2} = \frac{\overline{h}_{iso}}{h_{iso,BL=0}}$ showing the effect of blowing ratio for cases 11 and 12.

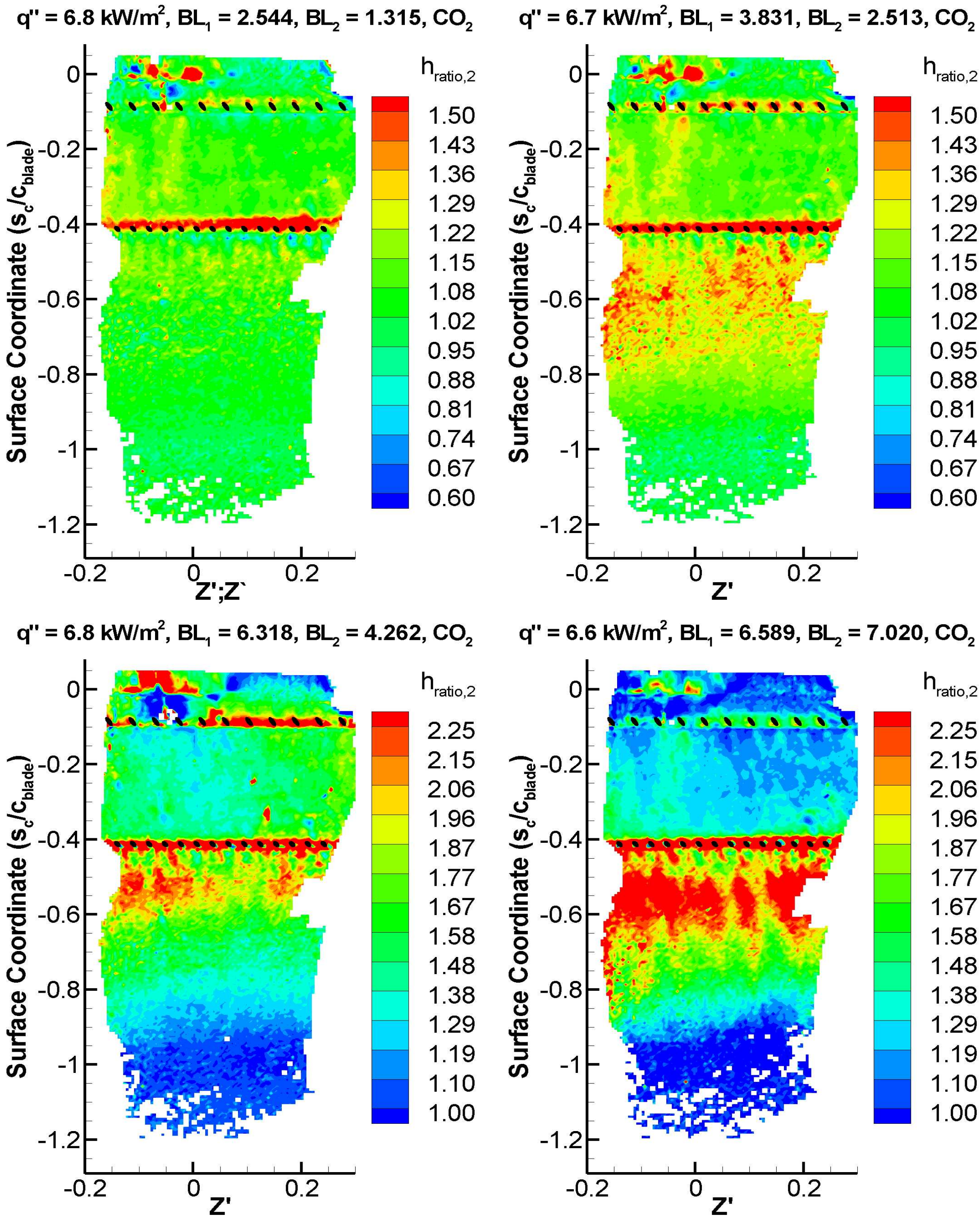

Figure 5.53: Spatially-resolved maps of $h_{ratio,2} = \frac{h}{h_{BL=0}}$ showing the effects of density ratio for cases 9, 18, 14, and 17.

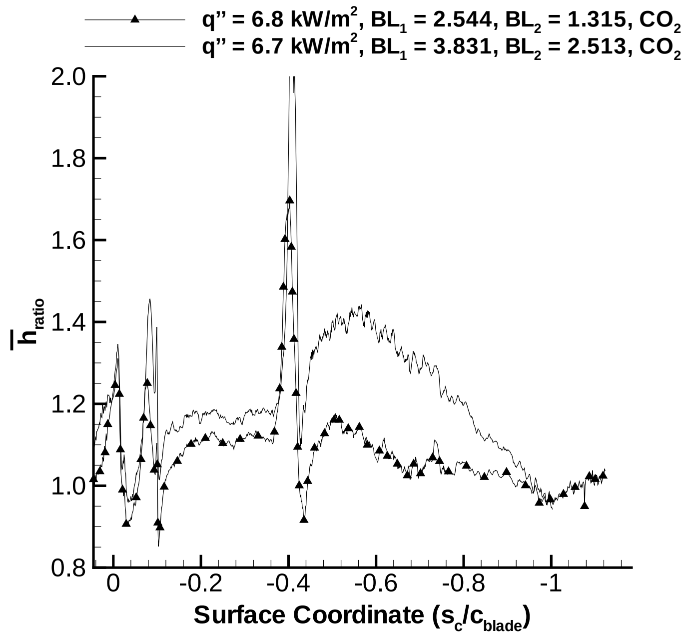

Figure 5.54: Plots of $\overline{h}_{ratio,2} = \frac{\overline{h}}{h_{BL=0}}$ showing the effect of density ratio for cases 9 and 18.

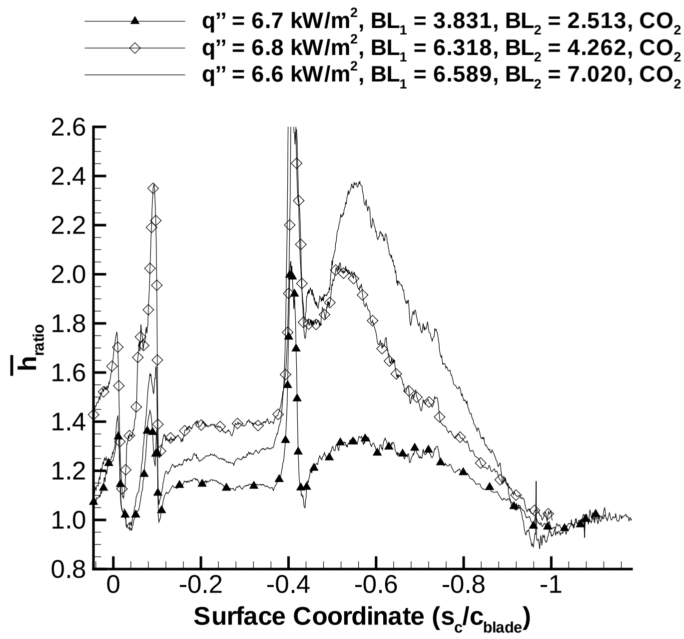

Figure 5.55: Plots of $\overline{h}_{ratio,2} = \frac{\overline{h}}{h_{BL=0}}$ showing the effect of density ratio for cases 18, 14 and 17.

temperature (equation 5.1) and normalized by the heat transfer coefficient measured on the film-cooled surface with no blowing ($h_{iso,ratio,2} = \frac{h_{iso}}{h_{iso,BL=0}}$). Figures 5.57 and 5.58 present the ratio of the spanwise-averaged film-cooled heat transfer coefficient versus that measured with no blowing ($\overline{h}_{iso,ratio,2} = \frac{\overline{h}_{iso}}{\overline{h}_{iso,BL=0}}$). These results again show that the isoenergetic definition of heat transfer coefficient gives similar trends with respect to the application of a denser jet, i.e. the results show the suppression of heat transfer coefficient augmentation. However, the absolute values are considerably lower than that measured using the heat transfer coefficient based on the recovery temperature.

5.6.4 Effects of Turbulence on Heat Transfer Coefficient

Figure 5.59 present maps of the recovery-temperature-based heat transfer coefficient, and figures 5.60 and 5.61 presents their corresponding $\overline{h}_{ratio,2} = \frac{\overline{h}}{h_{BL=0}}$ curves with a high turbulence inlet condition. These results show that the increased levels of turbulence seem to overwhelm any effect on the thermal and momentum boundary layer caused by the injection of film cooling from the first row of film cooling holes. This is evidenced by a comparison of these results from those shown in figure 5.44, and examining the $BL_1 = 2.041, BL_2 = 1.354$ case. As the blowing ratio of the first row is increased, or density ratio changes, the augmentation effect due to first row film cooling is minimal. As the flow accelerates, the augmentation effect dies out, just as shown in the uncooled results presented in section 4.1.3.

With increasing blowing ratio for the second row of film cooling holes, additional augmentation of the heat transfer coefficient is observed. However, the peak value for the heat transfer coefficient at the highest blowing condition is lower than that for the low turbulence condition. This suggest that the increased levels of turbulent mixing counteracts the sweeping motion of mainstream flow near the wall due to the film cooling jets.

The suppression effect observed with high density jets appeared to be either reversed or totally negated in the presence of elevated turbulence levels. An examination of the open literature provides no explanation for this observation. A possible explanation for this observation is the increased mixing due the presence of turbulence that overwhelms the effect of the film cooling jets.

Figure 5.62 present maps of the recovery-temperature-based heat transfer coefficient, and figures 5.63 and 5.64 presents their corresponding $\overline{h}_{iso,ratio,2} = \frac{\overline{h_{iso}}}{h_{iso,BL=0}}$ curves with a high turbulence inlet condition. The isoenergetic heat transfer coefficient definition suggests

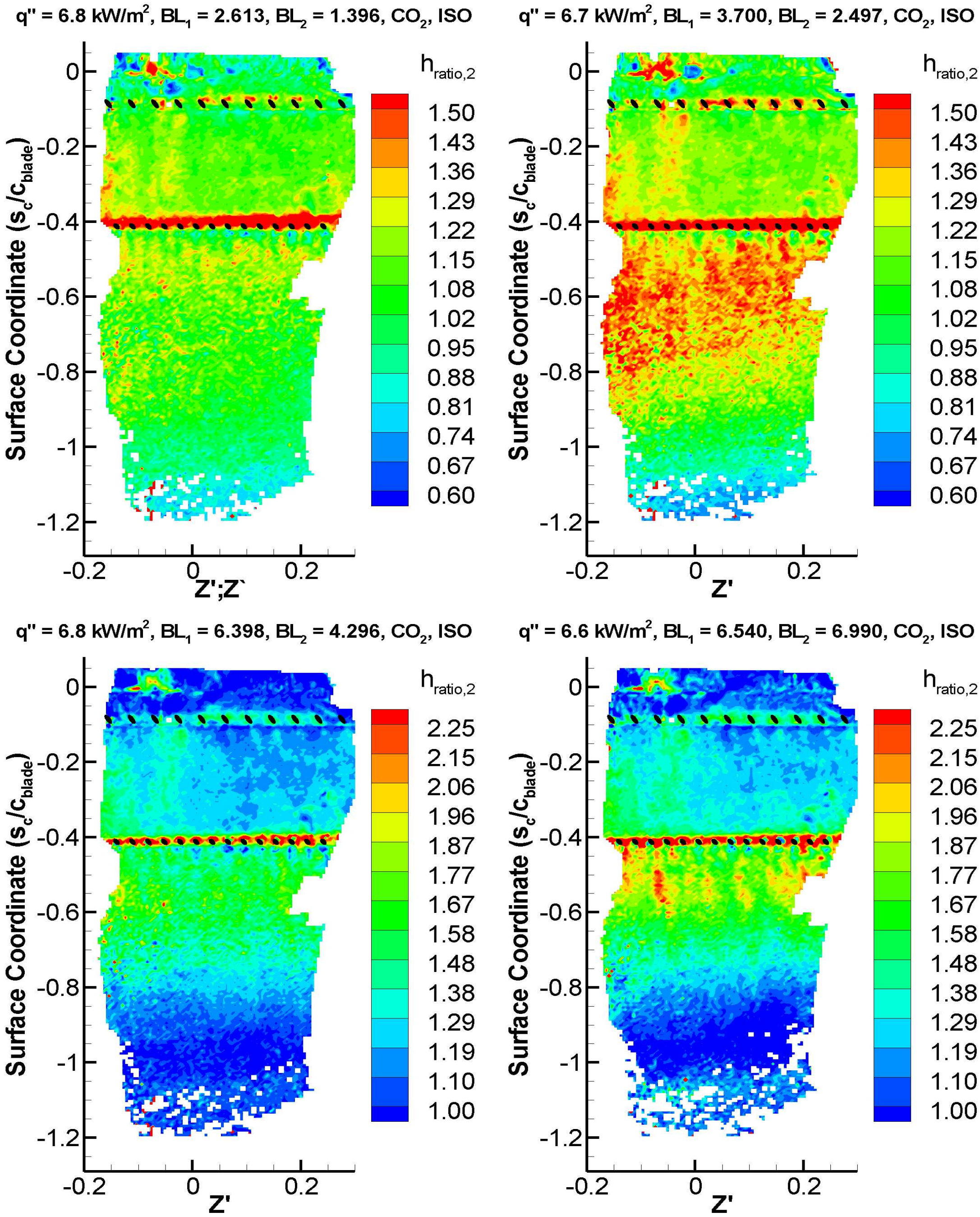

Figure 5.56: Spatially-resolved maps of $h_{iso,ratio,2} = \frac{h_{iso}}{h_{iso,BL=0}}$ showing the effects of density ratio for cases 9, 18, 14, and 17.

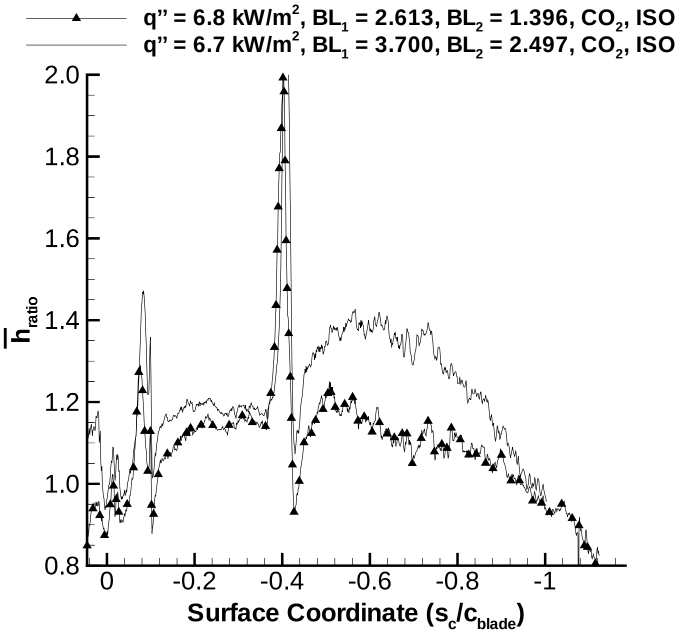

Figure 5.57: Plots of $\overline{h}_{iso,ratio,2} = \frac{\overline{h}_{iso}}{h_{iso,BL=0}}$ showing the effect of density ratio for cases 9 and 18.

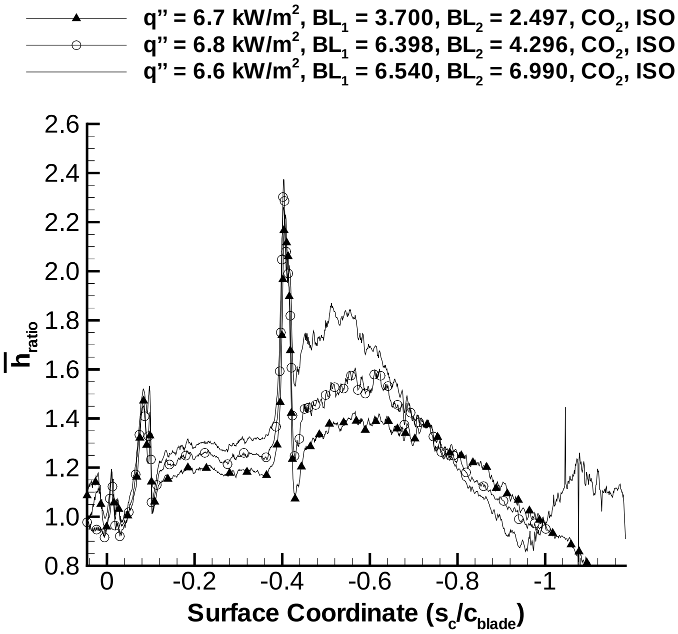

Figure 5.58: Plots of $\overline{h}_{iso,ratio,2} = \frac{\overline{h}}{h_{iso,BL=0}}$ showing the effect of density ratio for cases 18, 14 and 17.

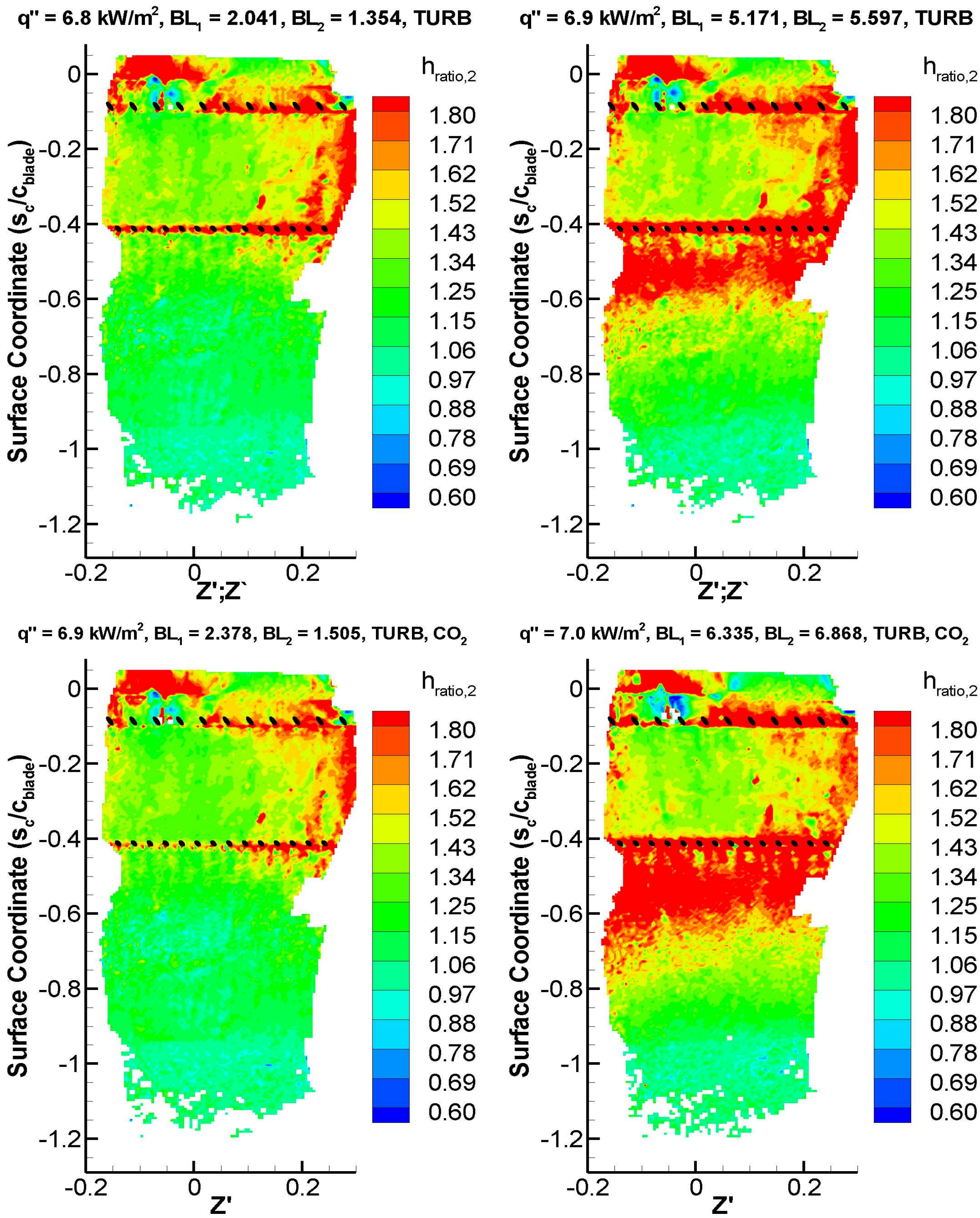

Figure 5.59: Spatially-resolved maps of $h_{ratio,2} = \frac{h}{h_{BL=0}}$ showing the effects of turbulence for cases 6, 13, 8, and 16.

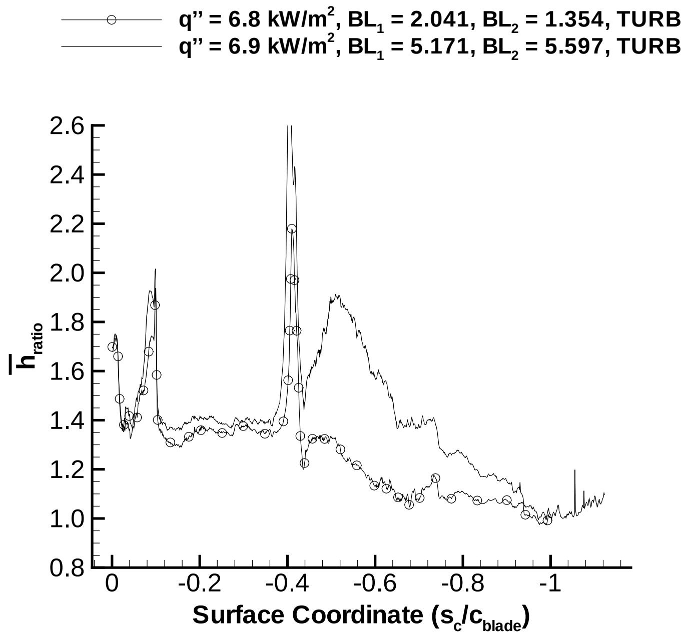

Figure 5.60: Plots of $\overline{h}_{ratio,2} = \frac{\overline{h}}{h_{BL=0}}$ showing the effect of turbulence for cases 6 and 13.

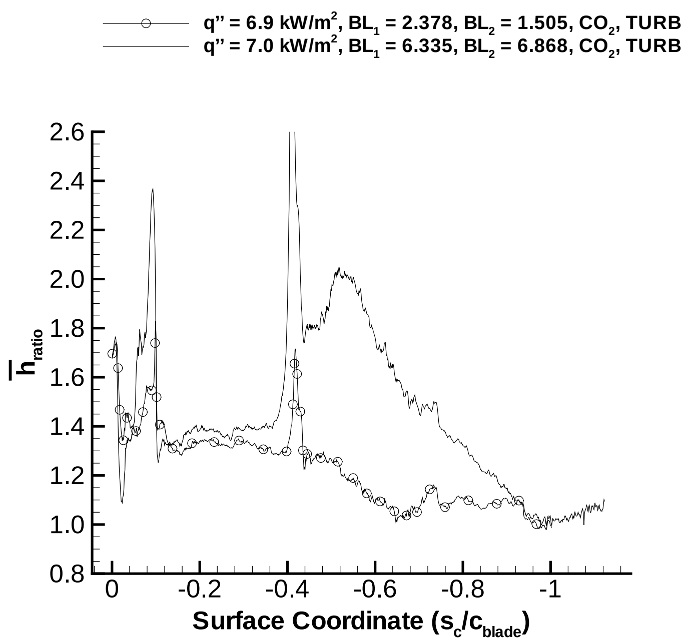

Figure 5.61: Plots of $\overline{h}_{ratio,2} = \frac{\overline{h}}{h_{BL=0}}$ showing the effect of density ratio for cases 8 and 16.

a suppression in the heat transfer coefficient downstream of the first row of film cooling holes when dense jets are injected at a high blowing ratio. This was an unexpected result which appears contrary to physical intuition, and the trends observed using the recovery-temperature-based heat transfer coefficient. The h_{iso} definition shows a suppression in the augmentation effect downstream of the second row of film cooling holes with carbon dioxide injection.

5.6.5 Discussion of Heat Transfer Coefficient Measurements

The heat transfer coefficient results shown in this section have shown that the two definitions of the heat transfer coefficient proposed in the open literature can give significantly different trends. Generally, both definitions for h show an augmentation effect due to increasing blowing ratio which is suppressed using denser injectant. Additionally, these results show that the augmentation trends due to film cooling and the interaction of density ratio and turbulence level are not necessarily monotonic. Measurements taken at the high turbulence conditions shows that the increased levels of turbulence counteracts the augmentation effects from the film cooling jets. This is particularly interesting as Andreopoulos (1985) pointed out that a critical parameter in jet-in-crossflow is the thickness of the local boundary layer relative to the hole diameter ($\frac{\delta^*}{D}$). If the hole diameter is much larger than the local boundary layer, the mixing processes due to the interaction of the injected jet and the meanflow dominates the characteristics the subsequent flow field. In this experiment, $\frac{\delta^*}{D} \approx 1.0$, and these results clearly show that the mainstream flow conditions has a significant effect on the jet-crossflow interaction.

5.7 Overall Discussion of Results

In essence, these results reveal the complexities involved in the practical application of film cooling to real turbine blade geometries. From a physical perspective, it is conceivable that the data shown here can be explained in a consistent manner. For both film cooling effectiveness and heat transfer coefficient, two distinct regimes have been identified in these results. One is where the film cooling jet is rapidly entrained into the local boundary layer, the other where the jet blows straight through. The parameter which controls the mixing regime is the blowing ratio. As this is increased, the film effectiveness generally improves and then decreases as jet liftoff is approached. The heat transfer coefficient was found to

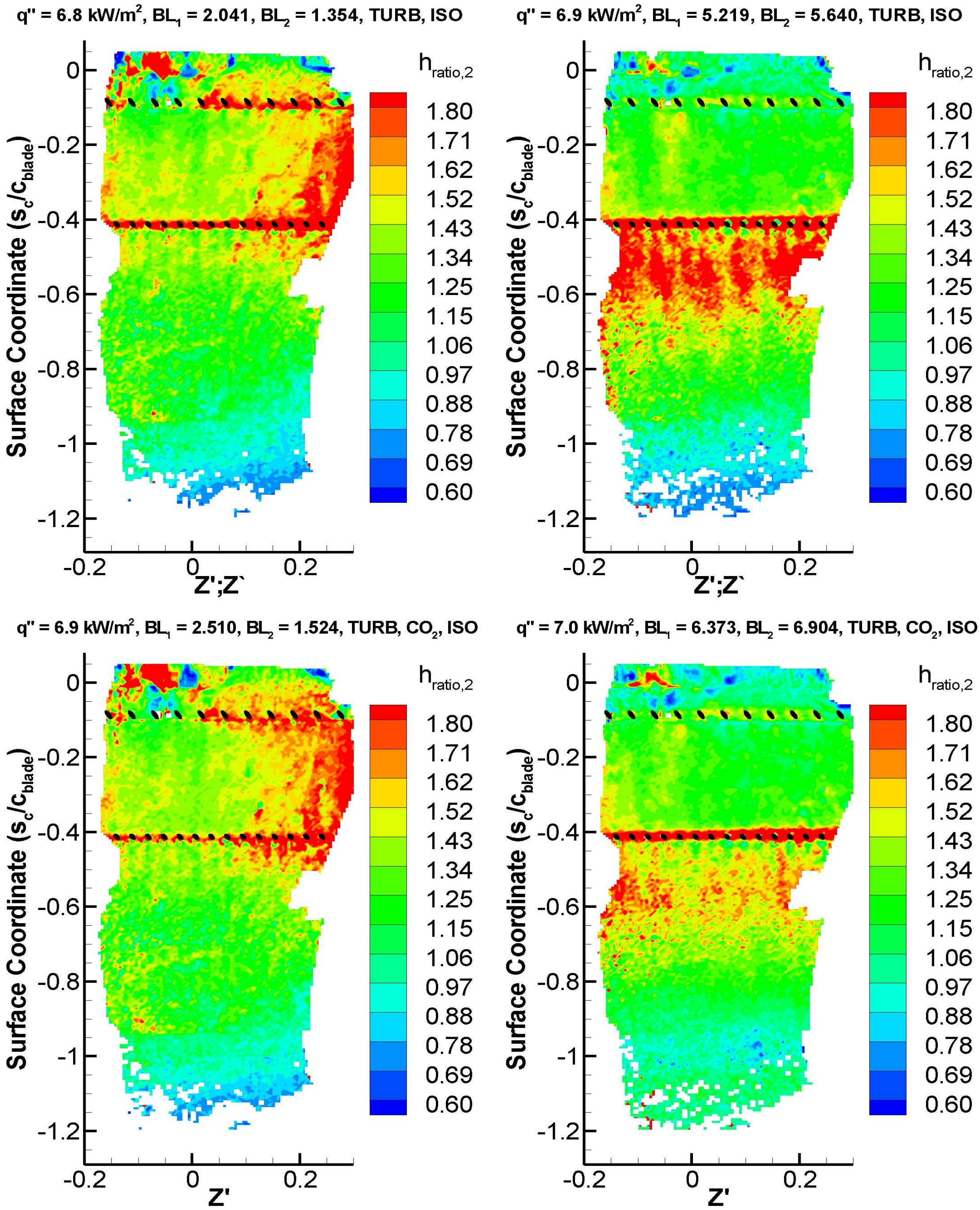

Figure 5.62: Spatially-resolved maps of $h_{iso,ratio,2} = \frac{h}{h_{BL=0}}$ showing the effects of turbulence for cases 6, 13, 8, and 16.

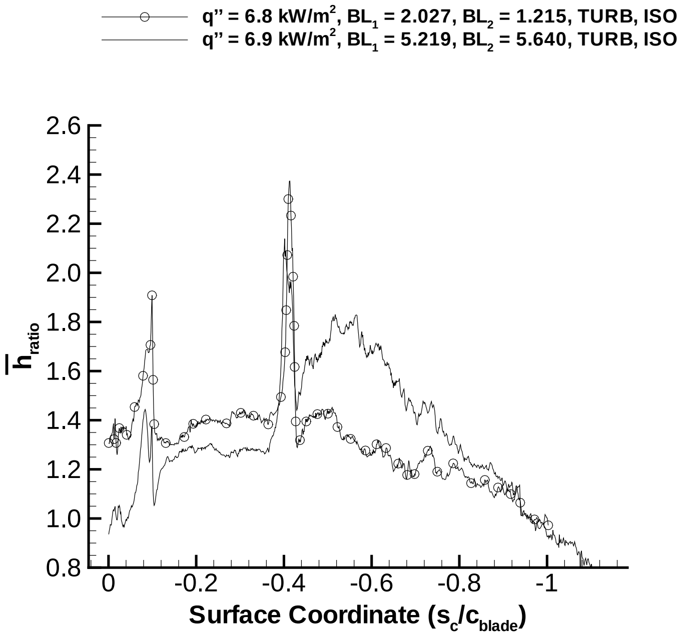

Figure 5.63: Plots of $\overline{h}_{iso,ratio,2} = \frac{\overline{h}_{iso}}{h_{iso,BL=0}}$ showing the effect of turbulence for cases 6 and 13.

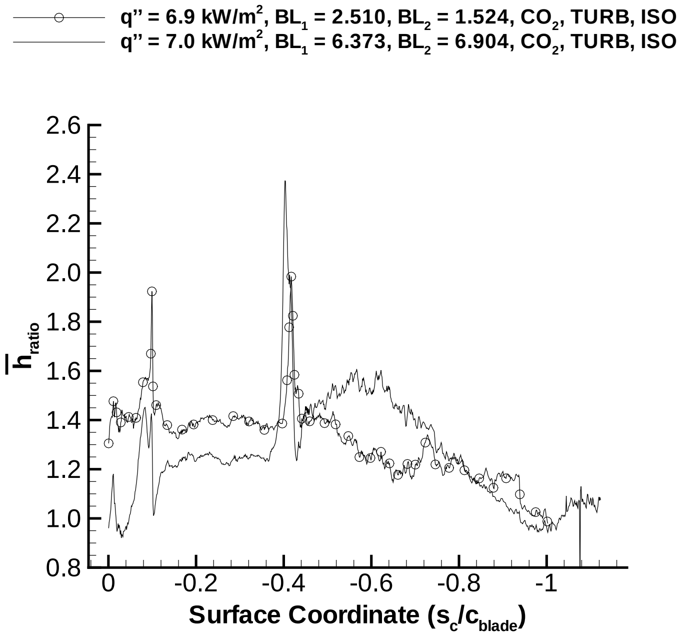

Figure 5.64: Plots of $\overline{h}_{iso,ratio,2} = \frac{\overline{h}_{iso}}{h_{iso,BL=0}}$ showing the effect of density ratio for cases 8 and 16.

monotonically increase with increasing blowing ratio. Denser cooling jets improve the film effectiveness in this regime and suppress the augmentation effect on the heat transfer coefficient.

Once jet blow-off occurs, the effects of increased density ratio appear to be negligible. What was particularly interesting about these results is the observation that the location of jet reattachment does not appear to be sensitive to density ratio. Increasing the level of turbulence appears to improve film effectiveness values once jet blow-off occurs by causing the detached jets to more quickly reattach to the cooled surface.

Many of the results discussed here conform with trends observed from the exhaustive fundamental research discussed in chapter 1. The important dimension that this new work adds is the combination of steady state surface boundary conditions and well-defined inlet boundary and flow conditions. This is crucial because to augment the capability to accurately predict these values using numerical methods it is crucial to have low-uncertainty measurements for η and h for comparative purposes. The fact that these data sets follow reasonable trends, lends credibility to their value, but it is not a sufficient condition for their applicability for modeling purposes. The detailed data sets presented in this chapter for a realistic geometry and flow conditions offer an opportunity for careful testing of models for film cooling. With respect to the types of models, these data would be used to examine predicted surface temperature profiles using, most likely, macro-models for film cooling, such as that described in section 1.6.4. The usefulness of RANS in replicating these results is debatable, as discussed in section 1.6.3. Ideally, these measurements would be paired with measurements of turbulent kinetic energy and dissipation to determine if problems with the predictions are due to fundamental modeling issues with respect to the mixing processes contained in the momentum or thermal boundary layers. This would provide leverage to specifically test the outcomes of various assumptions used in RANS simulations or parametric models for film cooling.

Chapter 6

Conclusions and Future Work

This thesis presents the development of a transonic single passage model for heat transfer and film cooling performance tests. The basis for this approach results from an examination of current modeling and experimental measurement techniques for film cooling performance, and their associated deficiencies. The rationale for this experiment centers on the premise of "bridging the gap" between fundamental and realistic experiments for turbomachinery heat transfer predictions.

Comparisons of numerical simulations to their experimental counterparts presented in the open-literature often show consistent, substantial discrepancies. It is difficult to discern if these are due to modeling shortcomings or boundary conditions. This suggests a strong need for turbomachinery experiments that combine low uncertainty, high resolution heat transfer data with well-resolved boundary conditions and realistic flow conditions. These requirements were found to be paradoxical, given an examination of the open literature. These experiments could be generally classified into two subsections: Fundamental experiments typically fall into the general category of flat plate experiments at relatively low speeds, where the flow is incompressible. Prior experiments are characterized by well-resolved boundary conditions and carefully controlled parametric studies that can be used to identify the individual effects of differing parameters. The primary deficiency with these data for the purposes of both design and improving numerical models for film cooling is the fact that these experiments do not have the necessary compressibility effects and streamwise curvature to be immediately applicable. Realistic experiments are defined as experiments that combine much of the necessary flow characteristics typical of a modern gas turbine engine, including upstream wakes, rotation, compressibility effects and streamwise curvature. The more realism that is included in these experiments, the higher the uncertainty of the subsequent measurements.

It is on this basis that it became clear that any approach to improving numerical prediction capabilities required a range of experiments with gradually increasing flow complexity, carefully tied to numerical model development. Additionally, there is increased difficulty in resolving the applied thermal and flow boundary conditions for a particular experiment.

This would be necessary to ensure consistency between experiment and simulation. This effort would require a high level of collaboration between experimentalists and numerical modelers to fully understand the drawbacks of various approaches and systematically account for each.

A model designed to simulate the two-dimensional flow around a modern, highly-cambered, transonic turbine airfoil with relative Mach number as high as 1.5 is developed to demonstrate this philosophy. The objective for constructing this model was to provide uncooled and film-cooled heat transfer data at low and high turbulence conditions. This experiment can be constructed to achieve a high-level of consistency with respect to the comparative numerical approach.

A CFD-driven, heuristic design procedure was developed to ensure that the constructed model accurately represented the desired flow conditions. The single passage experiment was used to produce spatially-resolved, steady state heat transfer coefficient (h) and adiabatic film cooling effectiveness measurements (η). A low thermal conductivity material was used to minimize thermal losses as much as possible, and to isolate the effects of film cooling injection on the thermal and momentum boundary layers as much as possible.

The steady state uncooled heat transfer coefficient measurements indicated a dependence of the heat transfer coefficient on the applied heat flux. This observation, if true, would suggest that in compressible flow situations, measurement techniques that depend on a varying heat flux have an inherent error. To determine the rationality of the experimental observations, several flat plate, laminar compressible flow simulations were conducted as an attempt to verify if, even at near ambient conditions, the assumption of linearity is valid. These computations, along with an analysis presented by Kays and Crawford (1993), revealed that the structure of the compressible thermal boundary layer can indeed depend on the applied heat flux. This indicates that the heat transfer coefficient would also vary, supporting the experimentally observed results in this work.

Furthermore, data collected at high and low turbulence levels indicated that as the flow in the passage accelerates to supersonic conditions, the heat transfer coefficient becomes independent of the inlet turbulence level. This effect could be obscured in similar measurements, because the heat transfer measurement techniques are transient and therefore have this in-built error.

Two-equation turbulence models installed in a commercial flow solver (STAR-CD) were used to generate predictions for this geometry. The results indicate that these models cannot capture the effects of compressibility on the thermal boundary layer. The two-layer, k-ε model achieved extremely poor overall agreement.

The cooled results reinforce the well-documented behavior of film cooling jets in crossflow. Jet blow-off and reattachment are observed, and are found to be sensitive to whether the injectant was air or carbon dioxide and the level of inlet turbulence. Denser jets were found to have a more coherent film structure that took longer to be mixed out by the mainstream flow. High levels of turbulence are found to rapidly obliterate the film cooling layer when the jets are totally attached to the cooled surface. Additionally, the increased turbulence increases the level of lateral mixing, causing the film cooling footprints from adjacent holes to rapidly merge. Despite the use of a low thermal conductivity material, it was clear that there are still significant conduction losses near the measurement surface around the film cooling holes, suggesting that numerical modeling of the film-cooling data should include a conjugate analysis for a more accurate comparison.

The heat transfer coefficient data are difficult to interpret for several reasons. The first is the significant distortion of the heat flux boundary condition due to local hot spots in the heating film. Despite this deficiency, clear augmentation trends were observed due to the presence of blowing. This effect generally appeared to be monotonic. The use of a denser injectant appeared to suppress this augmentation effect. Experimental data collected at a high turbulence condition ($TI\% = 30$) suggests that in the case where the film cooling hole diameter is of the same order as the boundary layer thickness, increases in the inlet turbulence intensity also suppresses the augmentation effect. This was an unexpected result, the explanation of which could be linked to the breaking down of the large scale vortical structures due to the film cooling jets by the increased turbulent mixing of the mainstream flow.

With respect to future work with the single passage model experiment, there are several additional tests that can be performed. Firstly, a full range of hole geometries and their subsequent performance can be evaluated in this experiment. Additionally, this facility provides the ability to examine the resulting aerodynamic effects of film cooling on both suction and pressure side airfoil surfaces. Considerable improvements can be made to the measurement of the inlet turbulence intensity and length scale measurements, which may be critical in improving the usefulness of the measurements shown in this thesis for comparison with numerical simulation approaches. Another issue which may be important with the film cooling performance data is possible unsteadiness in the film cooling supply system. An improved understanding of this possible deficiency would be useful for ensuring consistency with comparable computations. An issue which should definitely be revisited is the quality of the constant heat flux boundary condition for the film cooling tests. There were significant hot spots observed in this surface which increased the levels of uncertainty in the measurements. This was attributed not only the drilling of film cooling holes through the surface, but issues with the application of the film itself. Future measurements should include revised construction and data processing techniques to counter these challenges.

In terms of the single passage model approach, the time and energy required to design, construct and implement the model makes it a difficult choice for integration into the aggressive time frame for the design of a new turbine engine. However, it does represent a significant savings over competing measurement facilities such as linear cascades. Additionally, when viewed from the perspective of improving prediction tools for heat transfer, such models do have a place in the range of options necessary to tackle this important task.

Appendix A

Detailed Uncertainty Analyses

This appendix details the various uncertainty analyses for various results detailed in this thesis. The essence of these analyses is based on root-sum-square technique (RSS) method as advocated by Moffat (1988) and Kline and McClintock (1975) which estimates the propagation of elemental uncertainties in actual measured variables to the desired result. Given an arbitrary result, $\mathcal{R}$, which depends on a set of independent variables $\mathcal{V}_i$ through some functional form, defined as:

$$\delta\mathcal{R} = f(\mathcal{V}_1, \mathcal{V}_2, \ldots, \mathcal{V}_{N_\mathcal{V}}). \tag{A.1}$$

The RSS approach estimates the *zero-order* uncertainty in $\mathcal{R}$ as:

$$\delta\mathcal{R} = \left[\sum_{i=1}^{N_\mathcal{V}} \left(\left.\frac{\partial\mathcal{R}}{\partial\mathcal{V}_i}\right|_{\mathcal{V}_i} \delta\mathcal{V}_i \right)^2 \right]^{\frac{1}{2}}. \tag{A.2}$$

The partial derivative term can be computed directly by taking the derivative of the function shown in equation A.1, or a perturbation analysis. In the latter case, a central-difference approximation is used to compute each partial derivative, as shown below:

$$\left.\frac{\partial\mathcal{R}}{\partial\mathcal{V}_i}\right|_{\mathcal{V}_i} = \frac{\mathcal{R}_i^+ - \mathcal{R}_i^-}{2\delta\mathcal{V}_i} \tag{A.3}$$

where the $\mathcal{R}_i^+$ and $\mathcal{R}_i^-$ are defined as:

$$\begin{aligned} \mathcal{R}_i^+ &= f(\mathcal{V}_1, \mathcal{V}_2, \ldots, \mathcal{V}_i + \delta\mathcal{V}_i, \ldots, \mathcal{V}_{N_\mathcal{V}}) \\ \mathcal{R}_i^+ &= f(\mathcal{V}_1, \mathcal{V}_2, \ldots, \mathcal{V}_i - \delta\mathcal{V}_i, \ldots, \mathcal{V}_{N_\mathcal{V}}) \end{aligned} \tag{A.4}$$

A.1 Pressure Measurement Uncertainty

Pressure transducers are used extensively in this experiment, examples include measurements of the atmospheric pressure, airfoil pressure distribution, film cooling plenum stagnation pressures and orifice plate pressure drops. The following is a general derivation to estimate the uncertainty in these measurements. Equation A.5 below describes the linear response of both absolute and differential pressure transducers.

$$\mathcal{P} \equiv P, \Delta P = \mathcal{A}_p(V - V_\circ) \tag{A.5}$$

In this equation V is the measured voltage, $V_\circ$ is the calibration-determined offset voltage where a zero absolute or differential pressure is measured. Using equation A.2 the zero-order uncertainty in $\mathcal{P}$ can be computed as:

$$\delta_\circ \mathcal{P}^2 = \left| \frac{\partial \mathcal{P}}{\partial \mathcal{A}_p} \delta A_p \right|^2 + \left| \frac{\partial \mathcal{P}}{\partial V_\circ} \delta V_\circ \right|^2 + \left| \frac{\partial \mathcal{P}}{\partial V} \delta V \right|^2 \tag{A.6}$$

To complete the calculation of the uncertainty, the instrument uncertainty (δ_c) is combined with the zero-order uncertainty, as shown below:

$$\delta_d \mathcal{P} = \sqrt{\delta \mathcal{P}_\circ^2 + \delta \mathcal{P}_c^2} \quad (95\%) \tag{A.7}$$

where δ_d is defined as the *design-stage* uncertainty. The instrument uncertainty is a specified quantity, provided by the manufacturer.

Table A.1 describes the uncertainties for each of the transducers used in this experiment. The nominal values at which these uncertainties are computed are included for completeness. The uncertainty in the calibration slope and offset voltage were assumed to be approximately 1 % ($\frac{\delta \mathcal{A}_p}{\mathcal{A}_p} \approx \frac{\delta V_\circ}{V_\circ} \approx 0.01$). The uncertainty in the measured voltage was considered to be one-half of the resolution of the data acquisition board. This had a 12-bit resolution with auto-ranging measurement ranges of $\Delta V_{range} = 0$ to 5, 0 to 10, -5 to 5 and -10 to 10 volts. The *least significant bit* (LSB) was computed as:

$$LSB = \frac{V_{max} - V_{min}}{2^{12}\ bits} \tag{A.8}$$

and the uncertainty in the measured voltage is:

$$\frac{\delta V}{V} = \frac{1}{2} LSB. \tag{A.9}$$

Table A.2 presents the RSS contributions of these elemental uncertainties on the final result along with the manufacturer provided instrument error. Additionally shown in this table is the total estimated uncertainty in each result.

Table A.1: Pressure transducer elemental uncertainties.

Transducer	$\mathcal{P}$ (Pa)	$\mathcal{A}_p$ (Pa/V)	V (V)	$V_\circ$ (V)	$\frac{\delta \mathcal{A}_p}{\mathcal{A}_p}$	$\frac{\delta V}{V}$	$\frac{\delta V_\circ}{V_\circ}$
Electronic Barometer							
Setra 280E, 0-25 psia (P)	$1.01(10)^5$	$3.446(10)^4$	2.970	$2.92(10)^{-2}$	$1.0(10)^{-2}$	$2.055(10)^{-4}$	$1.0(10)^{-2}$
Main Orifice Plate Transducers $\dot{m} = 0.481\frac{\text{kg}}{\text{s}}$							
Setra 239, 0-10 psid (ΔP)	$6.74(10)^4$	$1.379(10)^4$	4.859	$-2.84(10)^{-2}$	$1.0(10)^{-2}$	$2.513(10)^{-4}$	$1.0(10)^{-2}$
Setra 280E, 0-100 psia (P)	$3.17(10)^5$	$1.379(10)^5$	2.375	$7.40(10)^{-3}$	$1.0(10)^{-2}$	$2.570(10)^{-4}$	$1.0(10)^{-2}$
Film Cooling Orifice Plate Transducers $\dot{m}_{fc\#1} = 9.95(10)^{-4}\frac{\text{kg}}{\text{s}}$							
Setra 239, 0-0.5" WC (ΔP)	3.14(10)	2.488(10)	1.172	$-9.00(10)^{-2}$	$1.0(10)^{-2}$	$2.513(10)^{-4}$	$1.0(10)^{-2}$
Setra 280E, 0-100 psia (P)	$2.07(10)^5$	$1.379(10)^5$	1.508	$7.40(10)^{-3}$	$1.0(10)^{-2}$	$2.570(10)^{-4}$	$1.0(10)^{-2}$
Pressure Measurement/Boundary Layer Bleed Transducer $\Delta P = 1.59(10)^5$ Pa							
Setra 239, 0-50 psid (ΔP)	$1.59(10)^5$	$6.90(10)^4$	2.306	$-1.22(10)^{-3}$	$1.0(10)^{-2}$	$2.647(10)^{-4}$	$1.0(10)^{-2}$

Table A.2: Pressure transducer error propagation.

Transducer	$\mathcal{P}$ (Pa)	$\frac{\partial \mathcal{P}}{\partial \mathcal{A}_p}\delta \mathcal{A}_p$	$\frac{\partial \mathcal{P}}{\partial V_\circ}\delta V_\circ$	$\frac{\partial \mathcal{P}}{\partial V}\delta V$	$\delta \mathcal{P}_\circ$	$\delta \mathcal{P}_c$	$\delta \mathcal{P}_{RSS}$ (95 %)
Electronic Barometer							
Setra 280E, 0-25 psia (P)	$1.01(10)^5$	$1.01(10)^3$	$-1.01(10)$	$2.10(10)$	$1.01(10)^3$	$1.32(10)^2$	$1.02(10)^3$
Main Orifice Plate Transducers $\dot{m} = 0.481\frac{\text{kg}}{\text{s}}$							
Setra 239, 0-10 psid (ΔP)	$6.74(10)^4$	$6.740(10)^2$	-3.92	$1.68(10)$	$6.74(10)^2$	$9.65(10)$	$6.81(10)^2$
Setra 280E, 0-100 psia (P)	$3.17(10)^5$	$3.170(10)^3$	$-1.02(10)$	$8.42(10)$	$3.17(10)^3$	$7.58(10)^2$	$3.26(10)^3$
Film Cooling Orifice Plate Transducers $\dot{m}_{fc\#1} = 9.95(10)^{-4}\frac{\text{kg}}{\text{s}}$							
Setra 239, 0-0.5" WC (ΔP)	$3.14(10)$	$3.140(10)^{-1}$	$-2.24(10)^{-2}$	$7.33(10)^{-3}$	$3.15(10)^{-1}$	$1.74(10)^{-1}$	$3.60(10)^{-1}$
Setra 280E, 0-100 psia (P)	$2.07(10)^5$	$2.070(10)^3$	$1.02(10)$	$5.34(10)$	$2.07(10)^3$	$7.58(10)^2$	$2.21(10)^2$
Pressure Measurement/Boundary Layer Bleed Transducer $\Delta P = 1.59(10)^5$ Pa							
Setra 239, 0-50 psid (ΔP)	$1.59(10)^5$	$1.590(10)^3$	$-8.42(10)^{-1}$	$9.71(10)$	$1.59(10)^3$	$3.79(10)^2$	$1.64(10)^3$

A.2 Isentropic Mach Number (M_{is}) Measurement Uncertainty

Following the procedure outlined at the beginning of this appendix, given the relation used to compute M_{is}, repeated here for simplicity:

$$M_{is} = \sqrt{\frac{2}{\gamma - 1}\left(\left(\frac{P_{\circ,\infty}}{P}\right) - 1\right)} \tag{A.10}$$

However, as indicated in section 2.4.3 the static and total pressures used in equation A.10 are measured relative to atmospheric pressure using a differential pressure transducer, via the equations:

$$\Delta P_{\circ,\infty} = P_{\circ,\infty} - P_{atm} \tag{A.11}$$

and

$$\Delta P = P_{\circ,\infty} - P. \tag{A.12}$$

Inserting these definitions into equation A.10 gives:

$$M_{is} = \sqrt{\frac{2}{\gamma - 1}\left(\left(\frac{\Delta P_{\circ,\infty} + P_{atm}}{\Delta P_{\circ,\infty} + P_{atm} - \Delta P}\right) - 1\right)} \tag{A.13}$$

The uncertainty in M_{is} can be computed as:

$$\delta_{\circ} M_{is}^2 = \left|\frac{\partial M_{is}}{\partial \Delta P_{\circ,\infty}}\delta \Delta P_{\circ,\infty}\right|^2 + \left|\frac{\partial M_{is}}{\partial \Delta P}\delta \Delta P\right|^2 \tag{A.14}$$

where the partial derivative terms are expressed as:

$$\frac{\partial M_{is}}{\partial \Delta P_{\circ,\infty}} = -\frac{\Delta P}{C_4(\Delta P_{\circ,\infty}, \Delta_P)} C_3(\Delta P_{\circ,\infty}, \Delta P)^{\frac{1}{2}} \tag{A.15}$$

and

$$\frac{\partial M_{is}}{\partial \Delta P} = \frac{P_{\circ,\infty} + P_{atm}}{C_4(\Delta P_{\circ,\infty}, \Delta_P)} C_3(\Delta P_{\circ,\infty}, \Delta P)^{\frac{1}{2}}. \tag{A.16}$$

The functions $C_3(\Delta P_{\circ,\infty}, \Delta_P)$ and $C_4(\Delta P_{\circ,\infty}, \Delta_P)$ are defined as:

$$C_3(\Delta P_{\circ,\infty}, \Delta P) = \frac{2}{\gamma - 1}\left(\left(\frac{\Delta P_{\circ,\infty} + P_{atm}}{\Delta P_{\circ,\infty} + P_{atm} - \Delta P}\right) - 1\right) \tag{A.17}$$

and

$$C_4(\Delta P_{\circ,\infty}, \Delta P) = (\gamma - 1)(\Delta P_{\circ,\infty} + P_{atm} - \Delta P)^2. \tag{A.18}$$

The uncertainties in the measured pressure differentials ($\delta \Delta P_{\circ,\infty}$, $\delta \Delta P$) are computed including the estimated transducer uncertainties described in section and n^{th}-*order* ad hoc uncertainties to account any error from tap mis-alignment or leakage ($\delta \frac{\Delta P}{\Delta P}\big|_{t.e.}$) or leaks in the Scanivalve system ($\delta \frac{\Delta P}{\Delta P}\big|_{s.v.}$). These were assumed to have the values:

$$\left.\frac{\delta \Delta P}{\Delta P}\right|_{t.e.} \approx 0.005 \tag{A.19}$$

and

$$\left.\frac{\delta \Delta P}{\Delta P}\right|_{s.v.} \approx 0.005. \tag{A.20}$$

Thus total estimated uncertainty in the pressure differential was computed as:

$$\delta \Delta P = \sqrt{\delta \Delta P_{xducer}^2 + \delta \Delta P_{t.e.}^2 + \delta \Delta P_{s.v.}^2} \tag{A.21}$$

Table A.3 presents the estimated uncertainty for measurements of M_{is} at various values. This shows a that the uncertainty ranges from $1.8\% \leq \frac{\delta M_{is}}{M_{is}} \geq 7.1\%$.

A.3 Mass Flow Rate Measurement Uncertainty

This section presents the results from the uncertainty analysis performed on the air supply, film cooling and boundary layer bleed orifice plate systems described in sections 2.3.1 and 2.3.3. The equations used to compute the mass flow rate from the measured pressure drop and absolute static and total temperature upstream of the air supply and boundary layer bleed orifice plates are described in section 2.3.4. Miller (1983) provides details on the uncertainty of each correlation used in calculating the mass flow rate. Using this information, tables A.4 and A.5 were constructed using the perturbation approach described at the beginning of this Appendix.

The uncertainty analysis for the film cooling supply orifice plates was slightly more convoluted as the discharge coefficient was a calibrated quantity, rather than approximated using a correlation. Table 2.8 presents the uncertainty in C_D for both orifice plate runs, determined using a perturbation analysis on each calibration point, using the resolution of the rotameter and the estimated uncertainty of the measurement pressure transducers. These values are inserted into the analysis shown in tables A.6 and A.7 which use the same procedure as previously described for the air supply and boundary layer orifice plate systems.

Table A.3: Estimated Uncertainty for Various Values of M_{is}.

M_{is}	$\frac{\partial M_{is}}{\partial \Delta P_{\circ,\infty}}$	$\frac{\partial M_{is}}{\partial \Delta P}$	$\delta \Delta P_{t.e.} = \delta \Delta P_{s.v.}$	$\delta \Delta P$	$\frac{\partial M_{is}}{\partial \Delta P_{\circ,\infty}} \delta P_{\circ,\infty,RSS}$	$\frac{\partial M_{is}}{\partial \Delta P} \delta P_{RSS}$	$\delta M_{is}(95\%)$
0.1	$-3.02(10)^{-8}$	$4.34(10)^{-6}$	9.07	$1.64(10)^{3}$	$-4.96(10)^{-5}$	$7.12(10)^{-3}$	$7.12(10)^{-3}$
0.2	$-1.23(10)^{-7}$	$4.48(10)^{-6}$	3.58(10)	$1.64(10)^{3}$	$-2.02(10)^{-4}$	$7.35(10)^{-3}$	$7.35(10)^{-3}$
0.3	$-2.85(10)^{-7}$	$4.71(10)^{-6}$	7.88(10)	$1.64(10)^{3}$	$-4.69(10)^{-4}$	$7.75(10)^{-3}$	$7.76(10)^{-3}$
0.4	$-5.29(10)^{-7}$	$5.07(10)^{-6}$	$1.36(10)^{2}$	$1.65(10)^{3}$	$-8.73(10)^{-4}$	$8.36(10)^{-3}$	$8.41(10)^{-3}$
0.5	$-8.71(10)^{-7}$	$5.55(10)^{-6}$	$2.04(10)^{2}$	$1.67(10)^{3}$	$-1.45(10)^{-3}$	$9.24(10)^{-3}$	$9.35(10)^{-3}$
0.6	$-1.34(10)^{-6}$	$6.18(10)^{-6}$	$2.81(10)^{2}$	$1.69(10)^{3}$	$-2.25(10)^{-3}$	$1.04(10)^{-2}$	$1.07(10)^{-2}$
0.7	$-1.96(10)^{-6}$	$7.01(10)^{-6}$	$3.63(10)^{2}$	$1.72(10)^{3}$	$-3.36(10)^{-3}$	$1.21(10)^{-2}$	$1.25(10)^{-2}$
0.8	$-2.78(10)^{-6}$	$8.08(10)^{-6}$	$4.48(10)^{2}$	$1.76(10)^{3}$	$-4.89(10)^{-3}$	$1.42(10)^{-2}$	$1.50(10)^{-2}$
0.9	$-3.86(10)^{-6}$	$9.44(10)^{-6}$	$5.32(10)^{2}$	$1.80(10)^{3}$	$-6.97(10)^{-3}$	$1.70(10)^{-2}$	$1.84(10)^{-2}$
1.0	$-5.27(10)^{-6}$	$1.12(10)^{-5}$	$6.14(10)^{2}$	$1.86(10)^{3}$	$-9.79(10)^{-3}$	$2.08(10)^{-2}$	$2.29(10)^{-2}$
1.1	$-7.12(10)^{-6}$	$1.34(10)^{-5}$	$6.92(10)^{2}$	$1.91(10)^{3}$	$-1.36(10)^{-2}$	$2.56(10)^{-2}$	$2.90(10)^{-2}$
1.2	$-9.53(10)^{-6}$	$1.62(10)^{-5}$	$7.65(10)^{2}$	$1.96(10)^{3}$	$-1.87(10)^{-2}$	$3.19(10)^{-2}$	$3.69(10)^{-2}$
1.3	$-1.27(10)^{-5}$	$1.98(10)^{-5}$	$8.32(10)^{2}$	$2.02(10)^{3}$	$-2.55(10)^{-2}$	$4.00(10)^{-2}$	$4.74(10)^{-2}$
1.4	$-1.67(10)^{-5}$	$2.44(10)^{-5}$	$8.93(10)^{2}$	$2.07(10)^{3}$	$-3.46(10)^{-2}$	$5.04(10)^{-2}$	$6.12(10)^{-2}$
1.5	$-2.20(10)^{-5}$	$3.02(10)^{-5}$	$9.47(10)^{2}$	$2.12(10)^{3}$	$-4.65(10)^{-2}$	$6.40(10)^{-2}$	$7.91(10)^{-2}$
1.6	$-2.88(10)^{-5}$	$3.76(10)^{-5}$	$9.96(10)^{2}$	$2.16(10)^{3}$	$-6.22(10)^{-2}$	$8.13(10)^{-2}$	$1.02(10)^{-1}$

Table A.4: Estimated Uncertainty for Main Air Supply Mass Flow Rate $\dot{m}$ (kg/s).

Parameter	Baseline Value	Estimated Uncertainty $(\frac{\delta\mathcal{V}_\rangle}{\mathcal{V}_\rangle})$	$\frac{\partial\mathcal{R}}{\partial\mathcal{V}_i}\Big\|_{\mathcal{V}_i}\delta\mathcal{V}_i$	$\delta\dot{m}_{RSS}(95\%)$
ΔP (Pa)	$3.30(10)^{4}$	$1.01(10)^{-2}$	$3.20(10)^{-3}$	
P_1 (Pa)	$3.29(10)^{5}$	$3.15(10)^{-3}$	$4.30(10)^{-3}$	
T_1 (K)	$3.00(10)^{2}$	$1.00(10)^{-2}$	$-2.00(10)^{-4}$	
C_D	$6.09(10)^{-1}$	$6.76(10)^{-3}$	$1.31(10)^{-4}$	
Y	$9.66(10)^{-1}$	$4.01(10)^{-3}$	$5.90(10)^{-3}$	
D (m)	$7.58(10)^{-2}$	$5.00(10)^{-3}$	$-1.90(10)^{-3}$	
d (m)	$5.08(10)^{-2}$	$5.00(10)^{-3}$	$8.30(10)^{-3}$	
$\dot{m}(\frac{\text{kg}}{\text{s}})$	0.672			$1.40(10)^{-2}$

Table A.5: Estimated Uncertainty for Boundary Layer Bleed Mass Flow Rate $\dot{m}(\frac{\text{kg}}{\text{s}})$.

Parameter	Baseline Value	Estimated Uncertainty $(\frac{\delta\mathcal{V}_\rangle}{\mathcal{V}_\rangle})$	$\frac{\partial\mathcal{R}}{\partial\mathcal{V}_i}\Big\|_{\mathcal{V}_i}\delta\mathcal{V}_i$	$\delta\dot{m}_{RSS}(95\%)$
ΔP (Pa)	$2.04(10)^{4}$	$1.76(10)^{-2}$	$8.10(10)^{-5}$	
P_1 (Pa)	$1.22(10)^{5}$	$1.76(10)^{-3}$	$3.02(10)^{-3}$	
T_1 (K)	$3.00(10)^{2}$	$1.00(10)^{-2}$	$1.76(10)^{-5}$	
C_D	$4.41(10)^{-1}$	$6.48(10)^{-3}$	$4.90(10)^{-5}$	
Y	$9.44(10)^{-1}$	$6.69(10)^{-3}$	$4.90(10)^{-5}$	
D (m)	$5.25(10)^{-2}$	$5.00(10)^{-3}$	$3.60(10)^{-3}$	
d (m)	$3.40(10)^{-2}$	$5.00(10)^{-3}$	$4.90(10)^{-3}$	
$\dot{m}(\frac{\text{kg}}{\text{s}})$	0.1			$5.75(10)^{-3}$

Table A.6: Estimated Uncertainty for Film Cooling Orifice Plate Run #1 $\dot{m}(\frac{\text{kg}}{\text{s}})$.

Parameter	Baseline Value	Estimated Uncertainty $(\frac{\delta\mathcal{V}_\rangle}{\mathcal{V}_\rangle})$	$\frac{\partial\dot{m}}{\partial\mathcal{V}_i}\Big\|_{\mathcal{V}_i}\delta\mathcal{V}_i$	$\delta\dot{m}_{RSS}(95\%)$
ΔP (Pa)	$3.14(10)^{1}$	$1.00(10)^{-2}$	$5.00(10)^{-6}$	
P_1 (Pa)	$2.07(10)^{5}$	$4.00(10)^{-3}$	$2.50(10)^{-6}$	
T_1 (K)	$3.00(10)^{2}$	$1.00(10)^{-2}$	$-4.40(10)^{-5}$	
C_D	$5.95(10)^{-1}$	$5.14(10)^{-3}$	$5.20(10)^{-5}$	
Y	1.00	$6.08(10)^{-6}$	$5.00(10)^{-7}$	
D (m)	$2.09(10)^{-2}$	$5.00(10)^{-3}$	$-1.00(10)^{-6}$	
d (m)	$1.27(10)^{-2}$	$5.00(10)^{-3}$	$1.20(10)^{-5}$	
$\dot{m}(\frac{\text{kg}}{\text{s}})$	$9.96(10^{-4})$			$5.39(10)^{-5}$

Table A.7: Estimated Uncertainty for Film Cooling Orifice Plate Run #2 $\dot{m}(\frac{\text{kg}}{\text{s}})$.

Parameter	Baseline Value	Estimated Uncertainty ($\frac{\delta \mathcal{V}_\rangle}{\mathcal{V}_\rangle}$)	$\frac{\partial \dot{m}}{\partial \mathcal{V}_i}\Big\vert_{\mathcal{V}_i} \delta \mathcal{V}_i$	$\delta \dot{m}_{RSS}(95\%)$
ΔP (Pa)	$6.97(10)^1$	$1.00(10)^{-2}$	$2.60(10)^{-6}$	
P_1 (Pa)	$2.07(10)^5$	$4.00(10)^{-3}$	$1.00(10)^{-6}$	
T_1 (K)	$3.00(10)^2$	$1.00(10)^{-2}$	$-2.60(10)^{-6}$	
C_D	$7.42(10)^{-1}$	$5.14(10)^{-3}$	$1.97(10)^{-5}$	
Y	1.00	$6.08(10)^{-6}$	≈ 0	
D (m)	$1.58(10)^{-2}$	$5.00(10)^{-3}$	$-3.00(10)^{-7}$	
d (m)	$7.62(10)^{-3}$	$5.00(10)^{-3}$	$5.60(10)^{-6}$	
$\dot{m}(\frac{\text{kg}}{\text{s}})$	$5.26(10^{-4})$			$2.08(10)^{-5}$

A.4 Hotwire Measurement Uncertainty

Section 2.4.5 details the equations used to measure mass flux through the experiment and for calibration process. Equation A.22 below repeats how the mass flux is computed, given a known hotwire voltage.

$$(\rho u)^n = M_2(T_\circ)V^2 + L_2(T_\circ) \tag{A.22}$$

As the coefficients M_2, L_2 and n are found by minimizing the mean-square-root error between the calculated fit and the calibration data, it was necessary to determine the error in the calibration data (ρu and V) and its effect on the coefficients. Recalling equation 2.24, which is restated below for ease of reference, the mass flux (ρu) at the center of the passage inlet is calibrated against the measured upstream mass flow rate.

$$\overline{(\rho u)} = A_{\rho u}\dot{m} \tag{A.23}$$

The uncertainty in this measurement is computed in the approach outlined in equation A.2. The uncertainty in the mass flow rate was estimated to be $\frac{\delta \dot{m}}{\dot{m}}\Big\vert_{\dot{m}=0.676\frac{\text{kg}}{\text{s}}} = 0.0174$ based on previous analyses. Using a perturbation analysis on the calibration data presented in section 2.4.5, the uncertainty in the slope of the facility calibration curve was estimated to be:

$$\frac{\delta A_{\dot{m}}}{A_{\dot{m}}}\Bigg\vert_{A_{\dot{m}}=662.93m^{-2}} = 0.0270. \tag{A.24}$$

On this basis, the corresponding uncertainty in the mean mass flux is:

$$\frac{\delta \overline{\rho u}}{\overline{\rho u}}\Bigg\vert_{\overline{\rho u}=448.14\frac{\text{kg}}{\text{m}^2\text{s}}} = 0.0174. \tag{A.25}$$

To find the uncertainty in each coefficient shown in equation A.22, this equation was rearranged to solve for each coefficient as shown below in equations A.26, A.27 and A.28.

$$M_2 = \frac{(\overline{\rho u})^n}{V^2} - L_2 \tag{A.26}$$

$$L_2 = (\overline{\rho u})^n - M_2 V^2 \tag{A.27}$$

$$n = \frac{\ln(M_2 E^2 + L_2)}{\ln(\overline{\rho u})} \tag{A.28}$$

Each of these equations was differentiated with respect to $\overline{\rho u}$ and V, following the approach delineated in equation A.2. These derivatives were found to be:

$$\begin{aligned}\frac{\partial M_2}{\partial \overline{\rho u}} &= \frac{1}{V^2}\left(n(\overline{\rho u})^{n-1}\right)\\ \frac{\partial M_2}{\partial V} &= -\frac{2}{V^3}(\overline{\rho u})^n\end{aligned} \tag{A.29}$$

$$\begin{aligned}\frac{\partial L_2}{\partial \overline{\rho u}} &= n(\overline{\rho u})^{n-1}\\ \frac{\partial L_2}{\partial V} &= -2M_2 V\end{aligned} \tag{A.30}$$

$$\begin{aligned}\frac{\partial n}{\partial \overline{\rho u}} &= \frac{\ln(M_2 V^2 + L_2)}{\overline{\rho u}(\ln \overline{\rho u})^2}\\ \frac{\partial n}{\partial V} &= \frac{2M_2 V}{\ln \overline{\rho u}} \frac{1}{M_2 V^2 + L_2}\end{aligned} \tag{A.31}$$

Table A.8 below presents the propagation of elemental error into the coefficients for the hotwire mass flux equation. The uncertainty of the voltage measurement was assumed conservatively to be the maximum measured standard deviation during the calibration process ($\delta V \approx \sigma_{V,max} \approx 1.22(10)^{-2}$V). Having obtained the uncertainty in each coefficient, partial derivatives of the equation used to measure mass flux based on the hotwire voltage. These derivatives were found to be:

$$\frac{\partial \rho u}{\partial M_2} = \frac{V^2}{n}(M_2 V^2 + L_2)^{\frac{1}{n}-1} \tag{A.32}$$

$$\frac{\partial \rho u}{\partial E_2} = \frac{2VM_2}{n}(M_2 V^2 + L_2)^{\frac{1}{n}-1} \tag{A.33}$$

$$\frac{\partial \rho u}{\partial L_2} = \frac{1}{n}(M_2 V^2 + L_2)^{\frac{1}{n}-1} \tag{A.34}$$

$$\frac{\partial \rho u}{\partial n} = -\frac{1}{n^2}\ln(M_2 V^2 + L_2) e^{\frac{1}{n}\ln(M_2 V^2 + L_2)} \tag{A.35}$$

The uncertainty in each measurement of ρu is computed as shown in table A.9.

Table A.8: Estimated Uncertainty for Hotwire Calibration Coefficients.

Parameter	Baseline Value	$\frac{\partial \mathcal{R}}{\partial \overline{\rho u}} \delta \overline{\rho u}$	$\frac{\partial \mathcal{R}}{\partial V} \delta V$	$\delta \mathcal{R}_{RSS}$ (P = 95%)
V (V)	2.8	N/A	N/A	N/A
δV (V)	$1.22(10)^{-2}$	N/A	N/A	N/A
$\overline{\rho u}$	$4.48(10)^{2}$	N/A	N/A	N/A
$\delta \overline{\rho u}$	7.80	N/A	N/A	N/A
M_2	$2.23(10)^{1}$	$2.03(10)^{-1}$	$-3.64(10)^{-1}$	$4.17(10)^{-1}$
L_2	$-5.78(10)^{1}$	1.59	-1.52	2.20
n	$7.80(10)^{-1}$	$2.22(10)^{-3}$	$7.62(10)^{-4}$	$2.35(10)^{-3}$

Table A.9: Estimated Uncertainty for Hotwire Measurements of ρu.

Parameter	Baseline Value	Estimated Uncertainty ($\frac{\delta \mathcal{V}_{\rangle}}{\mathcal{V}_{\rangle}}$)	$\frac{\partial \mathcal{R}}{\partial \mathcal{V}_i}\Big\|_{\mathcal{V}_i} \delta \mathcal{V}_i$	$\delta \rho u_{RSS}(95\%)$
M_2	$2.23(10)^{1}$	$1.87(10)^{-2}$	1.60(10)	
L_2	$-5.78(10)^{1}$	$-3.81(10)^{-2}$	1.08(10)	
E_2	2.8	$4.36(10)^{-3}$	7.48	
n	$7.80(10)^{-1}$	$3.01(10)^{-3}$	-8.24	
$\rho u(\frac{\mathrm{kg}}{\mathrm{m^2 s}})$	$4.48(10)^{2}$			2.232(10)

A.5 Adiabatic Film Effectiveness Measurement Uncertainty

As discussed in 5.1, four definitions of the adiabatic film effectiveness are presented in this thesis, as presented in equations 5.23, 5.24, 5.25 and 5.26. These are repeated here for convenience.

$$\eta_T(Z', s_c/c_{blade}) = \frac{T_{aw,c}(Z', s_c/c_{blade}) - T_{rec}(Z', s_c/c_{blade})}{T_{fc,\circ}(Z', s_c/c_{blade}) - T_{rec}(x, y)} \tag{A.36}$$

$$\eta_{T,iso}(Z', s_c/c_{blade}) = \frac{T_{aw,c}(Z', s_c/c_{blade}) - T_{iso}(Z', s_c/c_{blade})}{T_{fc,\circ}(Z', s_c/c_{blade}) - T_{iso}(Z', s_c/c_{blade})} \tag{A.37}$$

$$\eta(Z', s_c/c_{blade}) = \frac{T_{aw,c}(Z', s_c/c_{blade}) - T_{rec}(Z', s_c/c_{blade})}{T_{w2} - T_{rec}(Z', s_c/c_{blade})} \tag{A.38}$$

$$\eta_{iso}(Z', s_c/c_{blade}) = \frac{T_{aw,c}(Z', s_c/c_{blade}) - T_{iso}(Z', s_c/c_{blade})}{T_{w2} - T_{iso}(Z', s_c/c_{blade})} \tag{A.39}$$

These definitions can be expressed in the general form:

$$\eta = \frac{T_{aw,c} - T_\kappa}{T_\chi - T_\kappa}. \tag{A.40}$$

Where the terms T_κ represents either T_{iso} or T_{rec} and T_χ corresponds to either T_{w2} or $T_{fc,\circ}$. Using the approach described in equation A.2, the uncertainty in the film effectiveness can be expressed as:

$$\delta\eta^2 = \left|\frac{\partial\eta}{\partial T_{aw,c}}\delta T_{aw,c}\right|^2 + \left|\frac{\partial\eta}{\partial T_\kappa}\delta T_\kappa\right|^2 + \left|\frac{\partial\eta}{\partial T_\chi}\delta T_\chi\right|^2. \tag{A.41}$$

The partial derivatives in equation A.41 are computed as:

$$\frac{\partial\eta}{\partial T_{aw,c}} = \frac{1}{T_\chi - T_\kappa} \tag{A.42}$$

$$\frac{\partial\eta}{\partial T_\kappa} = \frac{T_{aw,c} - T_\chi}{(T_\chi - T_\kappa)^2} \tag{A.43}$$

$$\frac{\partial\eta}{\partial T_\chi} = -\frac{T_{aw,c} - T_\kappa}{(T_\chi - T_\kappa)^2} \tag{A.44}$$

As discussed in section 5.1, the uncertainty in each measured temperature was estimated to be: $\delta T_{aw,c} \approx \delta T_\kappa \approx \delta T_\chi \approx 0.2°\mathrm{C}$. Table below presents the estimated uncertainty for various measured values for η. It is assumed in this table that $T_\kappa = 27.2°\mathrm{C}$ and $T_\chi = 39.0°\mathrm{C}$. Given a specific value of η, an estimated value for $T_{aw,c}$ is computed. Using this approach, the uncertainty monotonically varies from $2.40(10)^{-2} \leq \delta\eta \leq 4.10(10)^{-2}$ with increasing η.

A.6 Heat Transfer Coefficient Measurement Uncertainty

The heat transfer coefficient is measured in this experiment on uncooled and cooled surfaces, as shown in sections 4.1.2 and 5.1. The form of the equation used to measure the heat transfer coefficient as reproduced from equations 4.2 and 5.27, repeated here for clarity, is:

$$h(Z', s_c/c_{blade}) = \frac{\frac{\overline{P_H}}{A_H} - q''_{cond} - q''_{rad}}{T_w(Z', \frac{s_c}{c_{blade}}) - T_{rec}(Z', \frac{s_c}{c_{blade}})}. \tag{A.45}$$

This can be simplified to read:

$$h = \frac{\frac{\overline{P_H}}{A_H} - q''_{cond} - q''_{rad}}{T_w - T_{rec}}. \tag{A.46}$$

It is assumed that the conduction and radiation loss terms have constant values of $q''_{cond} \approx 200\frac{\mathrm{W}}{\mathrm{m}^2}$ and $q''_{rad} \approx 125\frac{\mathrm{W}}{\mathrm{m}^2}$. Therefore, the uncertainty in the heat transfer coefficient is computed as:

$$\delta h^2 = \left|\frac{\partial(h)}{\partial\overline{P_H}}\delta\overline{P_H}\right|^2 + \left|\frac{\partial h}{\partial A_H}\delta A_H\right|^2 + \left|\frac{\partial h}{\partial T_w}\delta T_w\right|^2 + \left|\frac{\partial h}{\partial T_{rec}}\delta T_{rec}\right|^2. \tag{A.47}$$

Table A.10: Estimated Uncertainty for Film Cooling Effectiveness Measurements.

η	$T_{aw,c}$	$\frac{\partial\eta}{\partial T_{aw,c}}\delta T_{aw,c}$	$\frac{\partial\eta}{\partial T_{\kappa}}\delta T_{\kappa}$	$\frac{\partial\eta}{\partial T_{\chi}}\delta T_{\chi}$	$\delta\eta$
0.0	27.20	$1.69(10)^{-2}$	$-1.69(10)^{-2}$	0.0	$2.40(10)^{-2}$
$2.50(10)^{-2}$	27.50	$1.69(10)^{-2}$	$-1.65(10)^{-2}$	$-2.12(10)^{-3}$	$2.38(10)^{-2}$
$5.00(10)^{-2}$	27.79	$1.69(10)^{-2}$	$-1.61(10)^{-2}$	$-4.24(10)^{-3}$	$2.38(10)^{-2}$
$7.50(10)^{-2}$	28.09	$1.69(10)^{-2}$	$-1.57(10)^{-2}$	$-6.36(10)^{-3}$	$2.39(10)^{-2}$
$1.00(10)^{-1}$	28.38	$1.69(10)^{-2}$	$-1.53(10)^{-2}$	$-8.47(10)^{-3}$	$2.43(10)^{-2}$
$1.25(10)^{-1}$	28.68	$1.69(10)^{-2}$	$-1.48(10)^{-2}$	$-1.06(10)^{-2}$	$2.49(10)^{-2}$
$1.50(10)^{-1}$	28.97	$1.69(10)^{-2}$	$-1.44(10)^{-2}$	$-1.27(10)^{-2}$	$2.56(10)^{-2}$
$1.75(10)^{-1}$	29.27	$1.69(10)^{-2}$	$-1.40(10)^{-2}$	$-1.48(10)^{-2}$	$2.65(10)^{-2}$
$2.00(10)^{-1}$	29.56	$1.69(10)^{-2}$	$-1.36(10)^{-2}$	$-1.69(10)^{-2}$	$2.75(10)^{-2}$
$2.25(10)^{-1}$	29.86	$1.69(10)^{-2}$	$-1.31(10)^{-2}$	$-1.91(10)^{-2}$	$2.87(10)^{-2}$
$2.50(10)^{-1}$	30.15	$1.69(10)^{-2}$	$-1.27(10)^{-2}$	$-2.12(10)^{-2}$	$3.00(10)^{-2}$
$2.75(10)^{-1}$	30.45	$1.69(10)^{-2}$	$-1.23(10)^{-2}$	$-2.33(10)^{-2}$	$3.13(10)^{-2}$
$3.00(10)^{-1}$	30.74	$1.69(10)^{-2}$	$-1.19(10)^{-2}$	$-2.54(10)^{-2}$	$3.28(10)^{-2}$
$3.25(10)^{-1}$	31.04	$1.69(10)^{-2}$	$-1.14(10)^{-2}$	$-2.75(10)^{-2}$	$3.43(10)^{-2}$
$3.50(10)^{-1}$	31.33	$1.69(10)^{-2}$	$-1.10(10)^{-2}$	$-2.97(10)^{-2}$	$3.59(10)^{-2}$
$3.75(10)^{-1}$	31.63	$1.69(10)^{-2}$	$-1.06(10)^{-2}$	$-3.18(10)^{-2}$	$3.75(10)^{-2}$
$4.00(10)^{-1}$	31.92	$1.69(10)^{-2}$	$-1.02(10)^{-2}$	$-3.39(10)^{-2}$	$3.92(10)^{-2}$
$4.25(10)^{-1}$	32.22	$1.69(10)^{-2}$	$-9.75(10)^{-3}$	$-3.60(10)^{-2}$	$4.10(10)^{-2}$

Table A.11: Estimated Uncertainty for Heat Transfer Coefficient Measurements.

$h(\frac{\mathrm{W}}{\mathrm{m}^2})$	$T_w - T_{rec}$ (°C)	$\frac{\partial(h)}{\partial P_H}\delta P_H$	$\frac{\partial(h)}{\partial A_H}\delta A_H$	$\frac{\partial(h)}{\partial T_w}\delta T_w$	$\frac{\partial(h)}{\partial T_{rec}}\delta T_{rec}$	δh
$5.00(10)^2$	1.16(10)	1.06(10)	−1.06	−8.65	8.65	1.62(10)
$6.00(10)^2$	9.63	1.27(10)	−1.27	−1.25(10)	1.25(10)	2.17(10)
$7.00(10)^2$	8.26	1.48(10)	−1.48	−1.70(10)	1.70(10)	2.82(10)
$8.00(10)^2$	7.23	1.69(10)	−1.69	−2.21(10)	2.21(10)	3.56(10)
$9.00(10)^2$	6.42	1.90(10)	−1.90	−2.80(10)	2.80(10)	4.40(10)
$1.00(10)^3$	5.78	2.11(10)	−2.11	−3.46(10)	3.46(10)	5.33(10)
$1.10(10)^3$	5.26	2.32(10)	−2.33	−4.19(10)	4.19(10)	6.36(10)
$1.20(10)^3$	4.82	2.54(10)	−2.54	−4.98(10)	4.98(10)	7.49(10)
$1.30(10)^3$	4.45	2.75(10)	−2.75	−5.85(10)	5.85(10)	8.72(10)
$1.40(10)^3$	4.13	2.96(10)	−2.96	−6.78(10)	6.78(10)	$1.00(10)^2$
$1.50(10)^3$	3.85	3.17(10)	−3.17	−7.78(10)	7.78(10)	$1.15(10)^2$
$1.60(10)^3$	3.61	3.38(10)	−3.38	−8.86(10)	8.86(10)	$1.30(10)^2$
$1.70(10)^3$	3.40	3.59(10)	−3.59	$-1.00(10)^2$	$1.00(10)^2$	$1.46(10)^2$
$1.80(10)^3$	3.21	3.80(10)	−3.81	$-1.12(10)^2$	$1.12(10)^2$	$1.63(10)^2$
$1.90(10)^3$	3.04	4.01(10)	−4.02	$-1.25(10)^2$	$1.25(10)^2$	$1.81(10)^2$
$2.00(10)^3$	2.89	4.23(10)	−4.23	$-1.38(10)^2$	$1.38(10)^2$	$2.00(10)^2$

The partial derivatives in equation A.47 are computed using equations A.48, A.49, A.50 and A.51 shown below.

$$\frac{\partial h}{\partial \overline{P_H}} = \frac{1}{A_H} \frac{1}{T_w - T_{rec}} \tag{A.48}$$

$$\frac{\partial h}{\partial A_H} = -\frac{1}{A_H^2} \frac{\overline{P_H}}{T_w - T_{rec}} \tag{A.49}$$

$$\frac{\partial h}{\partial T_w} = -\frac{\frac{\overline{P_H}}{A_H} - q''_{cond} - q''_{rad}}{(T_w - T_{rec})^2} \tag{A.50}$$

$$\frac{\partial h}{\partial T_{rec}} = \frac{\frac{\overline{P_H}}{A_H} - q''_{cond} - q''_{rad}}{(T_w - T_{rec})^2} \tag{A.51}$$

In the uncertainty analysis presented in table A.11, the following values are also assumed: $\overline{P_H} \approx 16.2 \pm 0.324$W and $\overline{A_H} \approx 2.653(10)^{-3} \pm 5.31(10)^{-6}\mathrm{m}^2$. The values in this table show a monotonic increase in the uncertainty as h increases, much like measurements of η. Over the range of h measured in this experiment, the uncertainty was found to vary $1.62(10) \leq \delta\eta \leq 2.00(10)^2$ with increasing values of h.

Appendix B

Humidity Measurement Methodology

This appendix details the methodology used to estimate the humidity ratio (ω_w) and relative humidity (ϕ_w) in the plenum supplying the single passage model. The development of these equations closely follows standard psychrometric analysis techniques found in standard thermodynamic texts such as: Reynolds and Perkins (1977) and Moran and Shapiro (2004). Figure B.1 presents a schematic of the wet-bulb thermometer used in this work. Essentially, this is tube with a water-soaked wicking inserted in one end. The air flow passes through one end, absorbs water contained in the wicking and the saturated air-water mixture passes around the thermocouple. In constructing the equations used for estimate the humidity of the air in the supply system, it was assumed that air freely passes through the assembly and this system can be modeled as steady state. Defining the mass flow rates of air at the inlet and outlet of the system as $\dot{m}_{a1}$ and $\dot{m}_{a3}$, and defining the mass flow rate of water at various stations in the system as $\dot{m}_{w1}$, $\dot{m}_{w2}$ and $\dot{m}_{w3}$; applying conservation of mass to the control volume presented in figure B.1 gives:

$$\dot{m}_{a,1} = \dot{m}_{a,2} = \dot{m}_{a,3}$$

$$\dot{m}_{w,1} + \dot{m}_{w,2} = \dot{m}_{w,3} \tag{B.1}$$

Defining the humidity ratio (ω_w) is as:

$$\omega_w = \frac{\dot{m}_w}{\dot{m}_a} \tag{B.2}$$

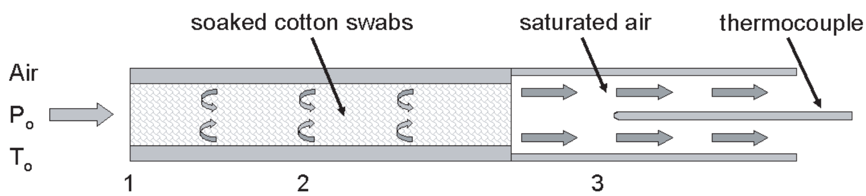

Figure B.1: Schematic of wet-bulb humidity sensor.

and inserting this definition into equation B.1 for $\dot{m}_{w,1}$ and $\dot{m}_{w,2}$ and dividing by the inlet air mass flow rate $\dot{m}_{a,1}$ gives:

$$\omega_{w,1} + \frac{\dot{m}_{w,2}}{\dot{m}_{a,2}} = \omega_{w,3} \tag{B.3}$$

which can be subsequently expressed as:

$$\frac{\dot{m}_{w,2}}{\dot{m}_{a,1}} = \omega_{w,3} - \omega_{w,1} \tag{B.4}$$

Applying a conservation of energy analysis to the control volume under study gives:

$$\dot{m}_{a,1}h^i_{a,1} + \dot{m}_{w,1}h^i_{w,1} + \dot{m}_{w,2}h^i_{w,2} = \dot{m}_{a,3}h^i_{a,3} + \dot{m}_{w,3}h^i_{w,3} \tag{B.5}$$

where h^i corresponds to enthalpy. Dividing this equation by $\dot{m}_{a1}$ and inserting equation B.4 and the definition of the humidity ratio given in B.2 evinces:

$$h^i_{a,1} + \omega_{w,1}h^i_{w,1} + (\omega_{w,3} - \omega_{w,1})h^i_{w2} = h^i_{a3} + \omega_{w,3}h^i_{w,3}. \tag{B.6}$$

Solving this equation for the humidity ratio of the incoming air, $\omega_{w,1}$ gives:

$$\omega_{w,1} = \frac{(h^i_{a,3} - h^i_{a,1}) + \omega_{w,3}(h^i_{w,3} - h^i_{w,2})}{h^i_{w,1} - h^i_{w,2}}. \tag{B.7}$$

Assuming that air may be modeled as a calorically perfect gas and evaluating the water enthalpy as that of saturated liquid for state 2 (the water in the soaked wicking) and that of the saturated vapor for state 1, equation B.7 may be recast as:

$$\omega_{w,1} = \frac{c_p(T_3 - T_1) + \omega_{w,3}(h^i_{fg,3})}{h^i_{g,1} - h^i_{f,2}} \tag{B.8}$$

where $h^i_{fg} = h^i_g - h^i_f$. If it is further assumed that the humidity measurement device acts as a perfect adiabatic saturation device, the air passing out of the water-soaked wicking can be assumed to be saturated. Using the ideal gas equation of state, the humidity ratio of the air-saturated water mixture can be computed as:

$$\omega_{w,3} = 0.662\frac{P_{w,3}}{P_{a,3}} = 0.662\frac{P_{w,3}}{P_3 - P_{w,3}} \tag{B.9}$$

where Dalton's rule has been used to replace the partial pressure of air as the difference between the measured static pressure (P_3) and the partial pressure of water ($P_{w,3}$). By definition, the relative humidity of the air-saturated water mixture is unity, therefore the partial pressure of water in the air-saturated water mixture is identical to the saturated vapor pressure of water at the measured temperature, i.e.

$$P_{w,3} = P_g(T_3) \tag{B.10}$$

It was assumed that the static pressure throughout the device is nominally identical to the measured total pressure in the flow supply plenum, i.e. $P_{\circ,\infty} \approx P_2 \approx P_3$.

Having computed $\omega_{w,1}$, the relative humidity can be computed using a variation of equation B.9 to compute the partial pressure of the water vapor in the plenum, as shown below:

$$P_{w,1} = \frac{\omega_{w,1} P_{\circ,\infty}}{0.622 + \omega_{w,1}}. \tag{B.11}$$

This is then divided by the saturated vapor pressure at the measured stagnation temperature in the flow supply plenum, $P_{sat}(T_{\circ,\infty}) \approx P_{sat}(T_1)$.

The properties of water used in this process were computed using polynomial fits to thermodynamic data provided by Reynolds (1979). Equations B.12, B.13, B.14 and B.15 below detail the functional form of these fits relating the property of interest to the static temperature. The order of the polynomial chosen was determined using an iterative process, seeking to have the lowest order polynomial which produced fits with correlation coefficient values of $R_{fit} = 0.9999$ or greater. Equation B.12 shows the function used to compute the saturation pressure P_{sat} of water vapor. Equation B.13 presents the function used to compute the vapor enthalpy. Equation B.14 presents the function used to compute the saturated liquid enthalpy. Equation B.15 shows the fit used to compute the saturated liquid specific volume at the wet bulb temperature.

$$P_{sat}(MPa) = 7.3783(10)^{-10}T^4 - 8.0652(10)^{-7}T^3 + 3.3269(10)^{-3}T^2 - 6.1333(10)^{-2}T + 4.2608 \tag{B.12}$$

$$h_g^i(\frac{kJ}{kg}) = -4.7405(10)^{-6}T^3 + 3.4595(10)^{-3}T^2 + 1.0189T + 2.0611(10)^3 \tag{B.13}$$

$$h_f^i(\frac{kJ}{kg}) = -2.4734(10)^{-5}T^3 + 2.3418(10)^{-2}T^2 - 3.1604T - 3.7995(10)^2 \tag{B.14}$$

$$v_f(\frac{m^3}{kg}) = -1.9805(10)^{-11}T^3 + 2.2434(10)^{-8}T^2 - 7.8380(10)^{-6}T + 1.8707(10)^{-3} \tag{B.15}$$

To calculate the enthalpy of the water contained in the wicking, an incompressible equation of state was used to include the effect of changing pressure from the saturation pressure (P_{sat}) to the stagnation pressure for the flow system ($P_{\circ,\infty}$), as shown in equation below.

$$h_{f,2}^i = h_f^i(T_2) + v_f(T_2)(P_{\circ,\infty} - P_{sat}(T_2)) \tag{B.16}$$

For the purposes of this device, it was assumed that the temperature of the water in the wicking could be reasonably approximated as being identical to the temperature of the air-saturated water mixture, i.e. $T_2 \approx T_3$.

Appendix C

Calibration and Sensitivity Study of RANS Heat Transfer Predictions

Several laminar and turbulent flat plate simulations at high subsonic and supersonic conditions were conducted to gain some fundamental understanding of compressible flow heat transfer. First, the flat plate recovery temperature distribution ($T_{rec}(x)$) was computed to determine the validity of typically-used models for the recovery factor, r_∞. Secondly, the assumption of the linearity of the energy equation with compressible flow was directly examined. This was done by applying different constant heat flux rates to a flat plate surface, computing the surface temperature distributions and determining the heat transfer coefficient using the equation:

$$h(x) = \frac{q''}{T_w(x) - T_{rec}(x)} \tag{C.1}$$

where $T_w(x)$ is the wall temperature distribution with the surface heat flux q'' applied. If differences were observed in the compressible flow thermal boundary layer for a simple flow that challenged the assumption of linearity, experiments for more complicated flow conditions should reflect similar behavior. Essentially, these simulations served as a "reality check" on the experimental results presented in section 4.1. Two sets of simulations were performed: laminar and turbulent. The laminar flow computations allowed the direct examination of the physical characteristics of the coupled Navier-Stokes equations, without the complication of a turbulence model. The turbulent flow calculations were conducted to explore the sensitivity of predictions of the $T_{rec}(x)$ distribution to adjustments of various parameters, specifically the turbulent Prandtl number (Pr_t).

C.1 Compressible Flow Over a Flat Plate

Before delving into the numerical analyses, it is useful to review the documented flow characteristics of a high velocity boundary layer over a flat surface with variable properties. In such situations, there is significant conversion of mechanical to thermal energy through viscous shear in the boundary layers along exposed surfaces. Kays and Crawford (1993) defined the *recovery temperature* (T_{rec}) as the temperature on an adiabatic wall when a steady state equilibrium is established between viscous energy dissipation and heat conduction. When the surface is non-adiabatic, the direction of heat transfer depends on whether the surface temperature is above or below T_{rec}.

Kays and Crawford (1993) present a detailed analysis for laminar flow over a flat plate with constant properties. This revealed that the recovery factor, to a good approximation may be represented as:

$$r_\infty \approx Pr^{\frac{1}{2}}. \tag{C.2}$$

Kays and Crawford reported that this approximation can be extended to flows with variable fluid properties using analytical results presented by Van Driest (1952). Defining the Nusselt number, Nu_x as:

$$Nu_x = \frac{h(x)\,x}{k} \tag{C.3}$$

Where x is a spatial coordinate and k is the fluid thermal conductivity. Assuming constant properties, Kays and Crawford found that the Nu_x distribution for a laminar flat plate, constant surface temperature flow is:

$$Nu_x = 0.332 Pr^{\frac{1}{3}} Re_x^{\frac{1}{2}} \tag{C.4}$$

To examine what happens with variable properties, recalling the definition of surface heat flux and the convective heat transfer coefficient:

$$q'' = k(T_w(x)) \left.\frac{\partial T}{\partial y}\right|_w = h(x)(T_w(x) - T_{rec}(x)) \tag{C.5}$$

If the assumption of linearity is valid, the heat transfer coefficient is independent of the surface heat flux rate, meaning if q'' is doubled, the temperature difference should double as well. In the case where k is constant, doubling q'', doubles $\left.\frac{\partial T}{\partial y}\right|_w$. When viscous dissipation becomes significant in the thermal boundary layer, it is unclear how far (if at all) the temperature field response differs from the linear case with various heat flux levels. In other words, if the viscous dissipation in the thermal boundary layer is receptive to modifications in the wall boundary conditions, it is uncertain if the linear response described above is accurate.

An important result of these laminar flow analyses is the special case where $Pr = 1.0$, the recovery factor has a value of $r_\infty = 1.0$. This means that the wall temperature recovers

Table C.1: Boundary condition values for flat plate simulations.

Parameter	Laminar	Turbulent
M_{INLET}	0.8, 1.7	0.8, 1.7
$P_{\circ}$ (Pa)	260405	260405
$\frac{P_{ref}}{P_{\circ}}$ (Pa)	0.66,0.20	0.66,0.20
$T_{\circ}$ (K)	300	300
$TI\%$	N/A	5
$\frac{\ell}{L_{PLATE}}$	N/A	0.02

to the total temperature of the flow. Kays and Crawford argue that this result can be extended to turbulent flow if $Pr_t = 1.0$. These two cases are explored as baselines for "calibrating" the computational heat transfer models used for comparisons with the single passage uncooled heat transfer results.

C.1.1 Numerical Preliminaries

Figure C.1 presents the domain and general boundary conditions used for these simulations. Table C.1 lists the boundary condition values for laminar and turbulent flow conditions. These were chosen from experience based on the single passage simulation. Air was used as the fluid in all simulations. The length of the plate was defined as $L_{plate} = 1.0$. The leading edge of the plate was simulated as a sharp edge, using a symmetry boundary condition of length $\frac{L_{plate}}{2}$. Constant pressure boundary conditions were implemented along the top of the domain, L_{PLATE} above the surface and at the exit of the domain, consistent with a zero pressure gradient. The specified pressure along these boundaries (P_{ref}) was determined using the isentropic flow functions and the desired mainstream Mach number, as shown in equation C.6 below.

$$\frac{P_{ref}}{P_{\circ}} = \left(1 + \frac{\gamma - 1}{2} M_{INLET}^2\right)^{-\frac{\gamma}{\gamma-1}} \tag{C.6}$$

A 33,500-cell cartesian, structured grid with hyperbolic grid stretching was used to resolve the leading edge of the plate, and the subsequent boundary layer. The cell heights along the flat plate wall fell into the range $0.04 < y^+ < 0.45$ for both laminar and turbulent simulations.

For the laminar flow cases, equations 1.4, 1.5 and 1.6 are solved directly using STAR-

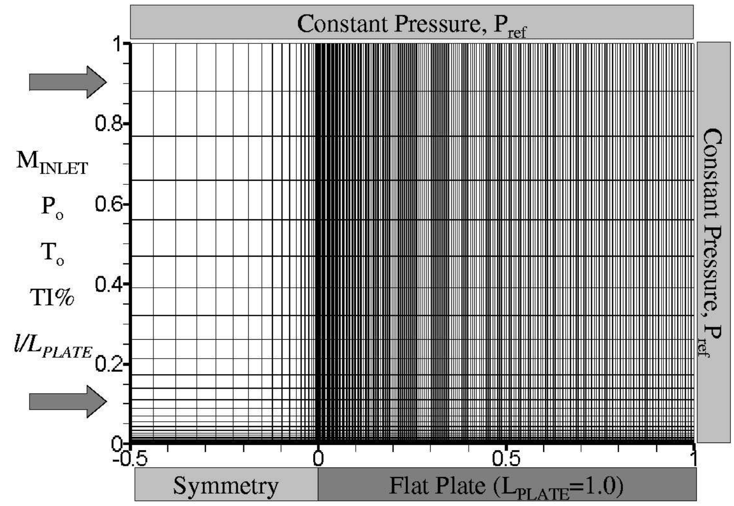

Figure C.1: Flat plate computational domain.

CD. The definition for thermal conductivity using the Prandtl number, presented in equation 1.10, was implemented using a user-defined subroutine. With respect to the turbulent flow simulations, the Chen and Kim (1987) k-ε variant and k-ω models were used to solve for the eddy viscosity (μ_t) used in the RANS equations (equations 1.16, 1.17 and 1.18).

C.1.2 Laminar Flow

Figure C.2 presents the computed flat plate recovery factor under the conditions listed in table C.1, with the Prandtl number fixed as $Pr = 1.0$ and constant specific heats. This value fell within 1% for both mainstream Mach numbers. Figures C.3 and C.4 present the computed freestream Mach number and pressure distributions along the top boundary ($\frac{P_{CNTRL}}{P_\circ}$) and flat plate surface ($\frac{P_w}{P_\circ}$) of the computational domain.

These figures confirm that the applied streamwise pressure gradient is small, as desired. As an additional check, the skin-friction along the plate was computed and compared to the approximation developed by Chapman and Rubesin (1949) as reported by White (1991). This can be expressed as:

$$C_{f,P} = \frac{2\tau_w}{\rho_\infty u_\infty} \approx \frac{0.664\, C_w^{\frac{1}{2}}}{Re_x^{\frac{1}{2}}}$$
$$C_w = \frac{\rho_w \mu_w}{\rho_\infty \mu_\infty} \tag{C.7}$$

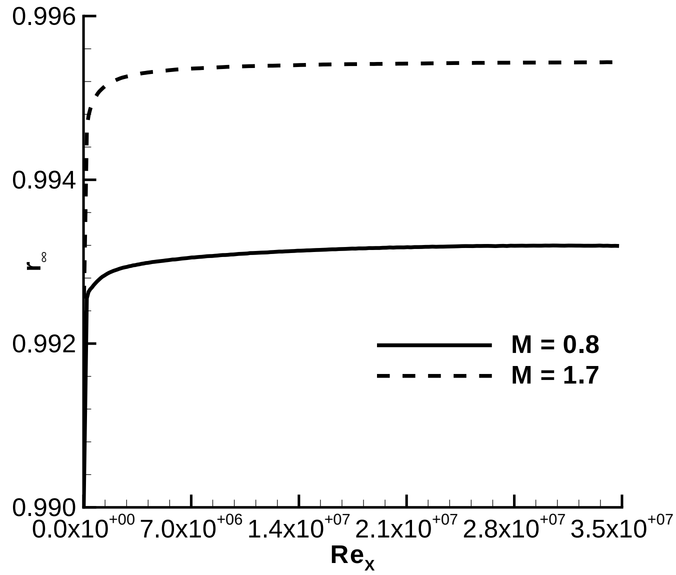

Figure C.2: Computed laminar flow, flat plate recovery factors (r_∞) with $Pr = 1.0$, $c_p = 1.0 \frac{kJ}{kg \cdot K}$.

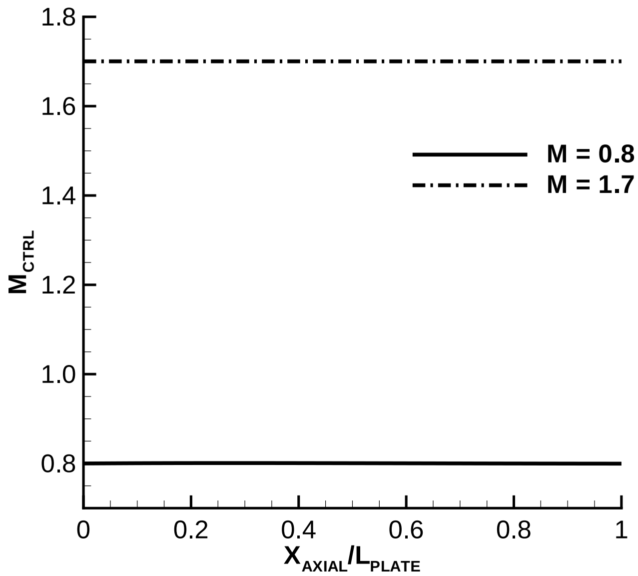

Figure C.3: Computed freestream Mach number distributions (M_{cntrl}) with $Pr = 1.0$, $c_p = 1.0 \frac{kJ}{kg \cdot K}$.

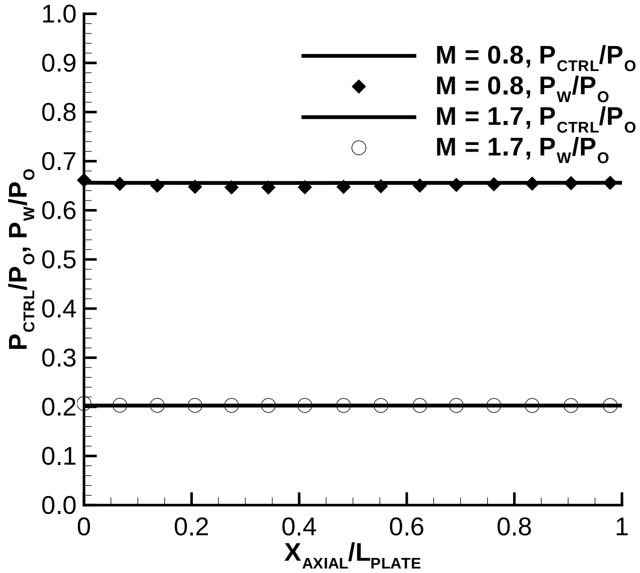

Figure C.4: Computed pressure distributions $(\frac{P}{P_\circ})$ with $Pr = 1.0$, $c_p = 1.0\frac{kJ}{kg \cdot K}$.

Figure C.5 compares the skin-friction coefficient C_f using numerical simulation and equation C.7. This figure shows a high level of agreement between the two approaches, further confirming the base accuracy of the numerical methods applied.

Having completed the previous series of tests, the Prandtl number was adjusted to $Pr = 0.71$, the characteristic value for air (still keeping c_p constant). Figure C.6, showing the skin friction coefficient distribution along the plate surface, confirms that this adjustment has a negligible effect on the mean flow. Nevertheless, figure C.7 showing the recovery factor distribution shows good agreement between the accepted correlation for laminar compressible flow.

To examine the linearity of the energy equation and the effect of mean flow parameters with changing thermal boundary conditions, two heat flux settings ($q_1'' = 2500\frac{W}{m^2}$ and $q_2'' = 5000\frac{W}{m^2}$) were applied to the flat plate surface at both mainstream conditions. Figure C.8 shows the non-dimensional wall temperature distribution $(\frac{T_w(x)}{T_\circ})$ for these cases. According to these calculations, the surface temperature rise was computed to be as much as $|T_w - T_\circ| = 15°\text{C}$ and $|T_w - T_\circ| = 90°\text{C}$ for heat fluxes q_1'' and q_2'', respectively. These distributions suggest that increasing mainstream Mach number leads to a reduction in the heat transfer coefficient. This is confirmed in figure C.9 showing the dimensional heat transfer coefficient

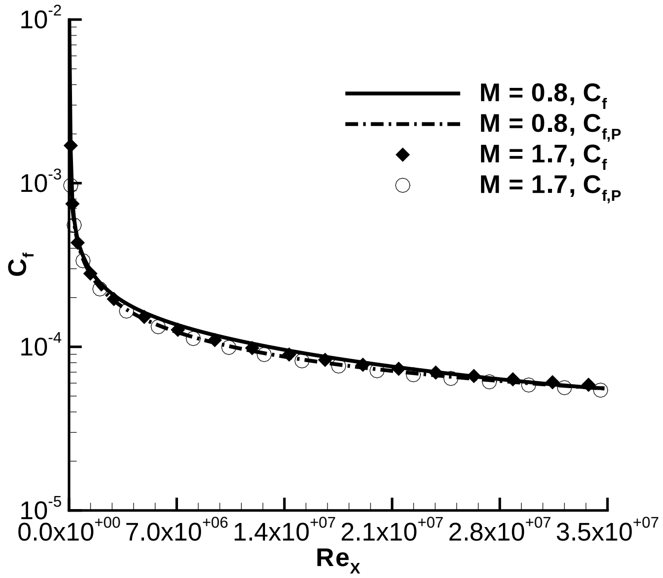

Figure C.5: Computed and predicted flat plate skin friction coefficients (C_f) with $Pr = 1.0$, $c_p = 1.0\frac{kJ}{kg \cdot K}$.

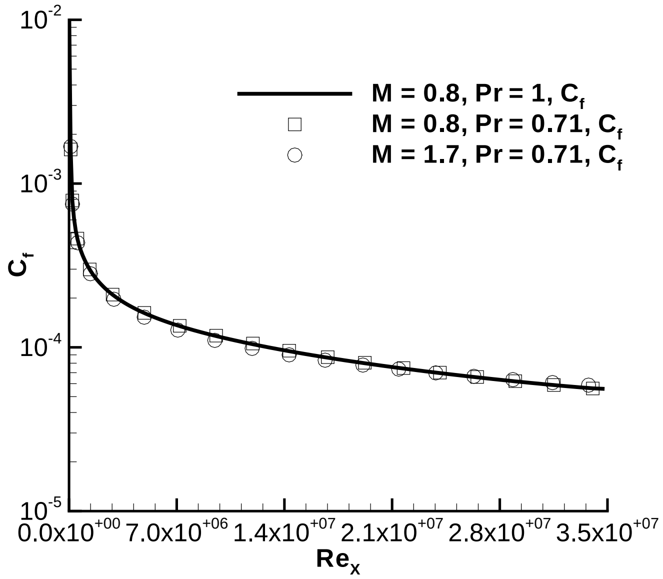

Figure C.6: Computed flat plate skin friction coefficients (C_f) with $Pr = 0.71$, $c_p = 1.0\frac{kJ}{kg \cdot K}$.

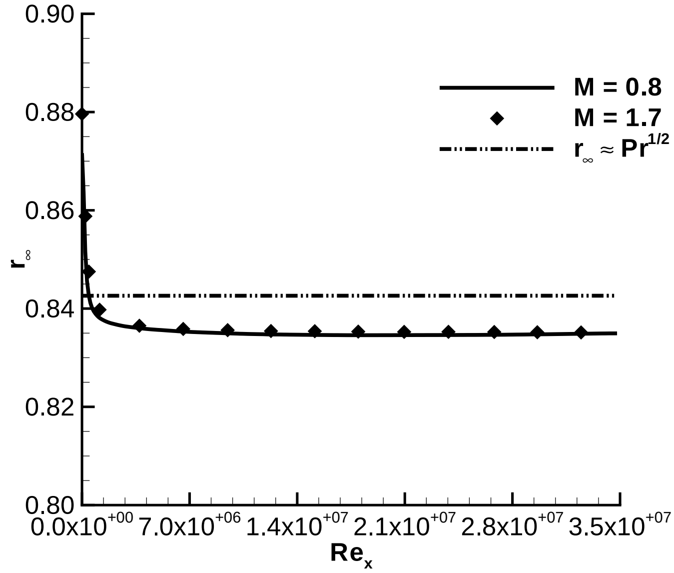

Figure C.7: Computed laminar flow, flat plate recovery factors (r_∞) with $Pr = 0.71$, $c_p = 1.0\frac{kJ}{kg \cdot K}$.

distributions for all computed cases. This is consistent with the observations reported by Kays and Crawford (1993) for variable property laminar and turbulent boundary layer flows. Nevertheless, considering experience with constant property flows, one would expect faster flows to engender higher heat transfer rates. This suggests that this modification is due to changes in the thermal boundary layer. Another fact which is apparent from figure C.9 is the linearity at of the results at specific flow conditions. In other words, the heat transfer coefficient distribution at each flow condition appears unchanged as the surface heat flux is doubled. This observation is consistent with experimental results from a heated spot in a two-dimensional turbulent boundary layer with a freestream Mach number of $M_{CNTRL} = 0.8$ presented by Elkins and Eaton (1999). Figures C.10 and C.11 present the skin friction coefficient distribution as a function of the applied surface heat flux settings. These results suggest that there is no change in the characteristics of the laminar momentum boundary layer. Figures C.12 and C.13 present the computed surface pressure ($\frac{P_w}{P_\circ}$) and M_{is} distributions, these figures show that although there is significant heating of the surface due to the applied constant heat flux, the effect on the flowfield is negligible. Finally, figure C.14 presents the ratio of dimensional heat transfer coefficients ($h_{ratio} = \frac{h_{q''_1}}{h_{q''_2}}$) for the two flow conditions and heat flux settings. These results suggest that the difference between

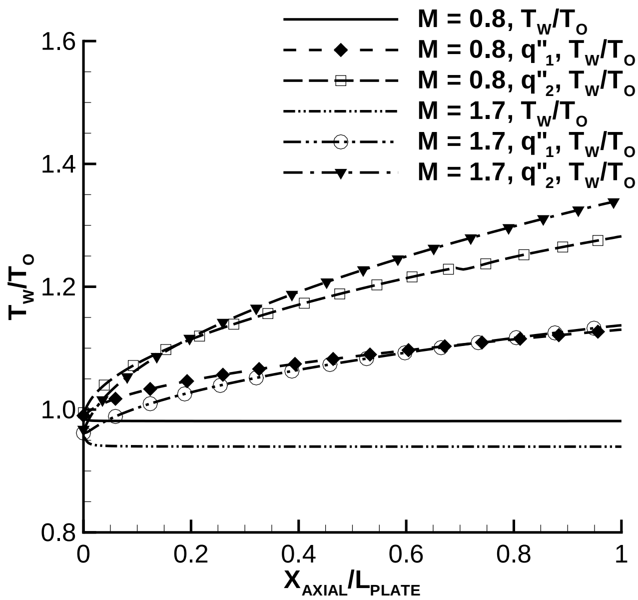

Figure C.8: Computed $\frac{T_w}{T_\circ}$ profiles for various flow conditions and applied heat fluxes with $Pr = 0.71$, $c_p = 1.0 \frac{kJ}{kg \cdot K}$.

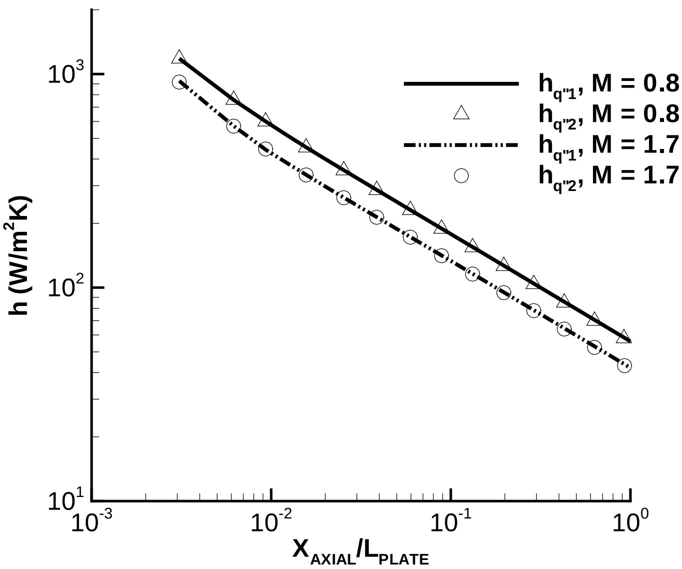

Figure C.9: Computed h distributions with $Pr = 0.71$, $c_p = 1.0 \frac{kJ}{kg \cdot K}$ with $M = 0.8$ and $M = 1.7$.

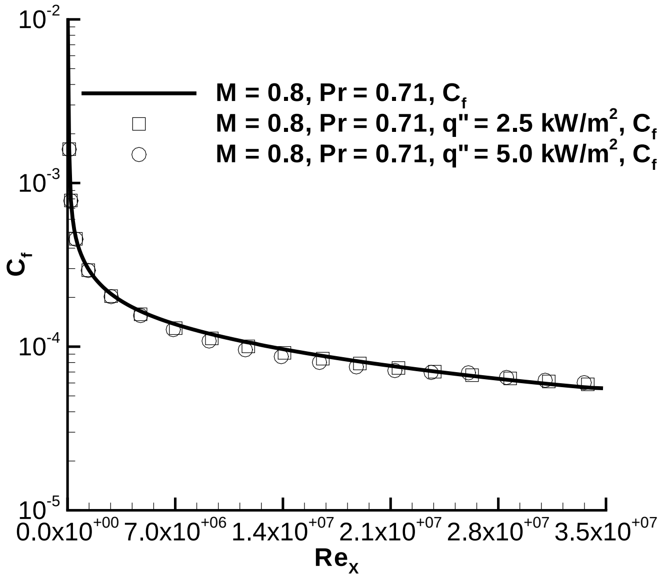

Figure C.10: Computed flat plate skin friction coefficients (C_f) with $Pr = 0.71$, $c_p = 1.0 \frac{kJ}{kg \cdot K}$ at two heat flux settings with $M = 0.8$.

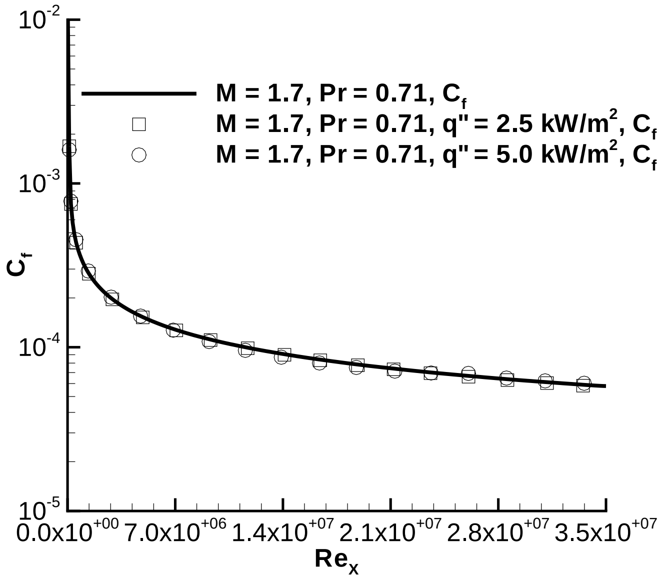

Figure C.11: Computed flat plate skin friction coefficients (C_f) with $Pr = 0.71$, $c_p = 1.0 \frac{kJ}{kg \cdot K}$ at two heat flux settings with $M = 1.7$.

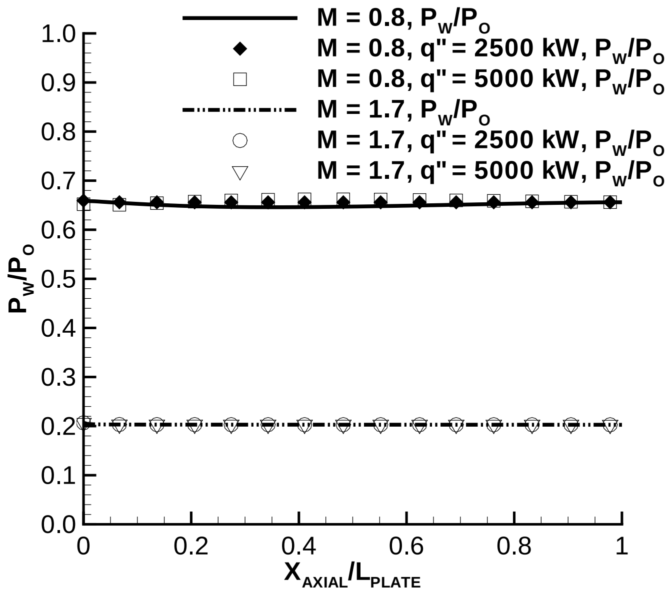

Figure C.12: Computed pressure distributions ($\frac{P}{P_\circ}$) with $Pr = 0.71$, $c_p = 1.0\frac{kJ}{kg \cdot K}$ at two heat flux settings with $M = 0.8$ and $M = 1.7$.

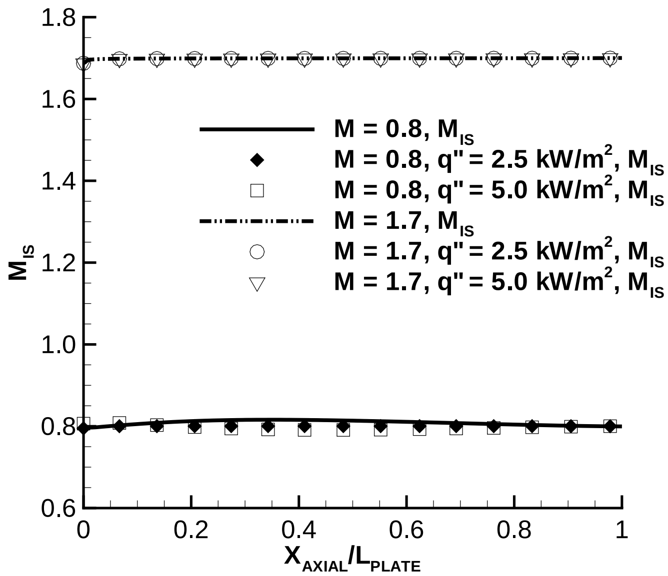

Figure C.13: Computed M_{is} distributions ($\frac{P}{P_\circ}$) with $Pr = 0.71$, $c_p = 1.0\frac{kJ}{kg \cdot K}$ at two heat flux settings with $M = 0.8$ and $M = 1.7$.

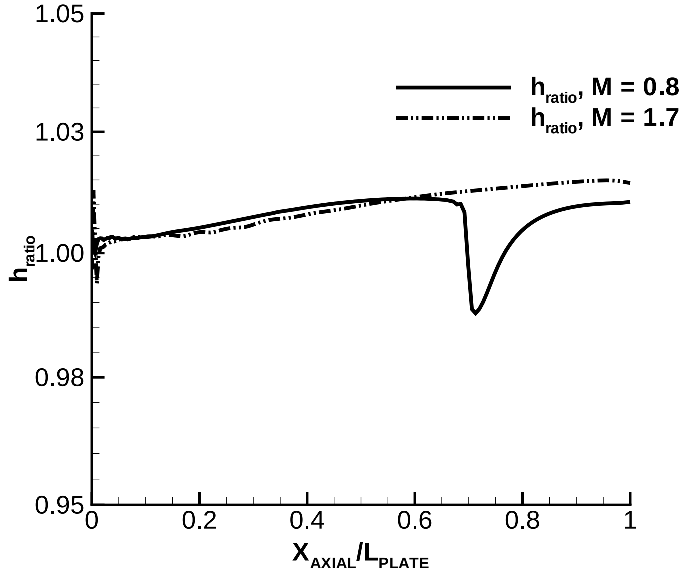

Figure C.14: Computed $h_{ratio} = \frac{h_{q_1''}}{h_{q_2''}}$ distributions with $Pr = 0.71$, $c_p = 1.0 \frac{kJ}{kg \cdot K}$ with $M = 0.8$ and $M = 1.7$.

the two heat flux cases is no more than a few percent. As a further step, the local Nusselt number (Nu_x) was computed using:

$$Nu_x = \frac{h\,x}{k_w} \tag{C.8}$$

where k_w is the conductivity of air along the heated surface. Figure C.15 presents the Nu_x distributions for all computed test cases, the constant Pr solution for Nu_x shown in equation C.4 is included for comparative purposes. Keeping k_w and flow conditions constant, increasing heat flux decreases Nu_x and by inference h. However, this is not reflected in the results shown in figure C.14. It is uncertain if this dependence is due to property variations transmitted through the definition of the Nu number or a physical phenomenon. In other words, if the observations shown in figure C.15 are due solely to the fact that a variable thermal conductivity, k_w, is inserted into the definition of Nu_x. Clearly with increasing heat flux, it is expected that the surface temperature will rise, and given that the thermal conductivity of gases increases with increasing temperature, the results shown in figure C.15 are not altogether unexpected. So an obvious question is, "given a flat plate compressible boundary layer flow with constant k, is h a function of q''?".

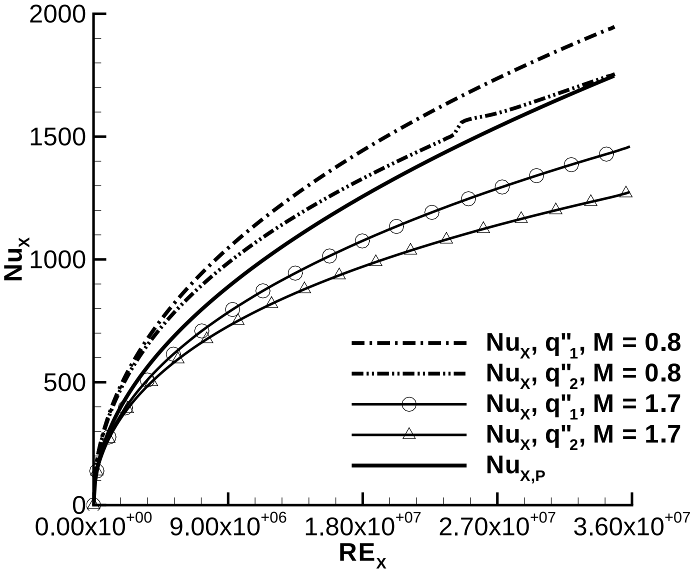

Figure C.15: Computed Nu_x distributions with $Pr = 0.71$, $c_p = 1.0\frac{kJ}{kg \cdot K}$ with q_1'' and q_2'' surface heat fluxes applied and $M = 0.8$ and $M = 1.7$.

Kays and Crawford (1993) developed a similarity solution for a flat plate laminar boundary layer for a gas with variable properties. The result of this approximate analysis, as shown below is:

$$\frac{Nu_{x,\infty}}{Re_{x,\infty}^{\frac{1}{2}}} = \frac{\mu_w \rho_w}{\mu_\infty \rho_\infty} \frac{\tau'(0)}{\tau_{aw}(0) - \tau(0)} \tag{C.9}$$

where:

$$\tau = \frac{T}{T_\infty}. \tag{C.10}$$

This analysis confirmed the dependence of Nu_x on the local heat flux, however the significance of this effect depends on the variations in local freestream Mach (M_{CNTRL}) and Prandtl (Pr) numbers. However, this analysis provides no guidance if the variation in Nu_x is due specifically to the variation in k or the imposed temperature gradient at the wall. Thus, additional cases were examined with a constant thermal conductivity of $k = 0.026\frac{W}{mK}$ and heat fluxes q_1'' and q_2'' applied. This effectively allowed the Prandtl number to vary. No significant difference was observed in the fluid flow parameters, such as pressure distribution and skin friction. Figure C.16 presents the computed and correlation-predicted recovery factor distributions for a constant thermal conductivity flow with a mainstream Mach number

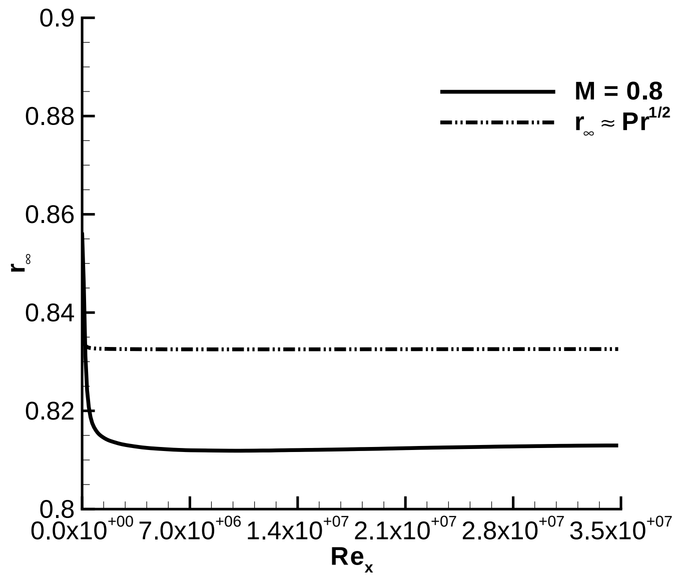

Figure C.16: Computed flat plate recovery factors (r_∞) with $Pr = 0.71$, $c_p = 1.0\frac{kJ}{kgK}$ and $k = 0.026\frac{W}{m\cdot K}$.

of $M = 0.8$. These results show a slightly larger difference than observed in figure C.7, probably due to the fact that the $r_\infty \approx Pr^{\frac{1}{2}}$ correlation assumes a constant value of Pr throughout the flowfield.

Figure C.17 shows the dimensional heat transfer coefficient with heat fluxes q_1'' and q_2'' applied and a constant thermal conductivity. These results are compared to the computed heat transfer coefficient with $k = k(T)$. These results show that changes in k allow the thermal boundary layer to respond in a linear fashion to the increased heat flux. This causes the heat transfer coefficient to remain constant. When the thermal conductivity is fixed, the heat transfer coefficient decreases with increasing heat flux. This suggests that the response of the thermal boundary layer is fundamentally different due to the restriction in the variation of k. This observation is emphasized in figure C.18, showing that doubling the heat flux roughly halves the heat transfer coefficient when k is held constant. Figure C.19 compares the wall temperature distributions for both heat flux settings for variable and fixed thermal conductivities. This figure shows that the temperature rise along the plate is very nearly identical, irrespective of the thermal conductivity model. Figure C.20 presents the Nu_x distributions for the two heat flux cases with constant k compared to

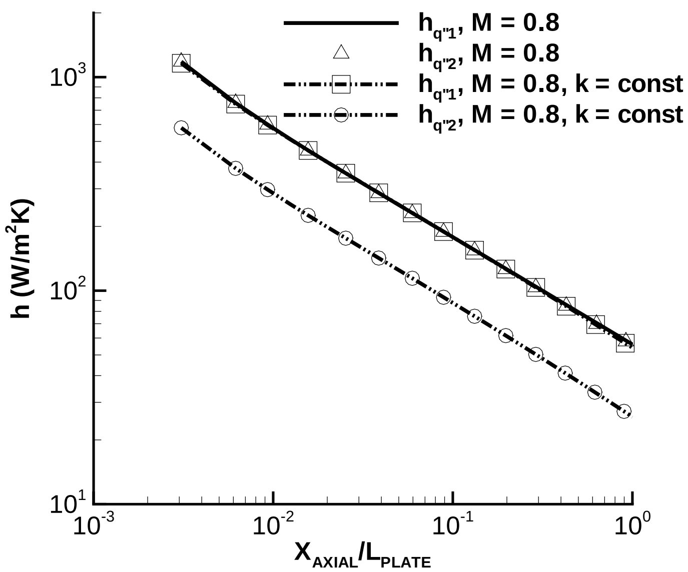

Figure C.17: Computed h distributions with $Pr = 0.71$, $c_p = 1.0\frac{kJ}{kg\cdot K}$ and $k = 0.026\frac{W}{m\cdot K}$ with $M = 0.8$.

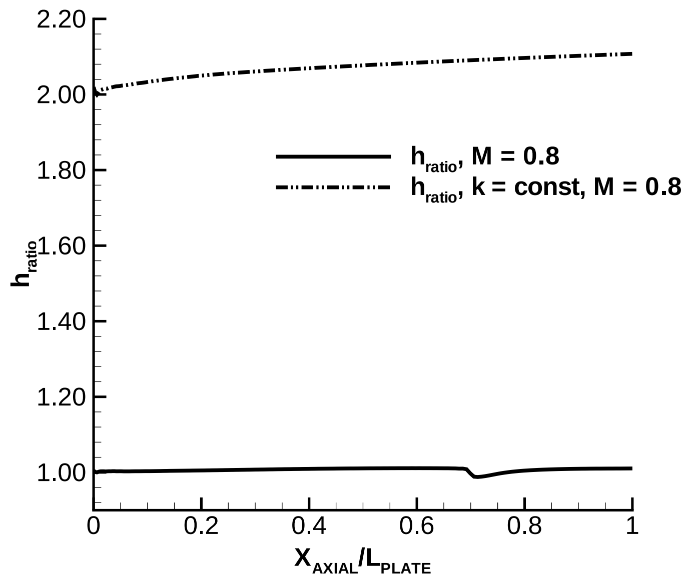

Figure C.18: Computed $h_{ratio} = \frac{h_{q_1''}}{h_{q_2''}}$ distributions with $Pr = 0.71$, $c_p = 1.0\frac{kJ}{kg\cdot K}$ and $k = 0.026\frac{W}{m\cdot K}$ with $M = 0.8$.

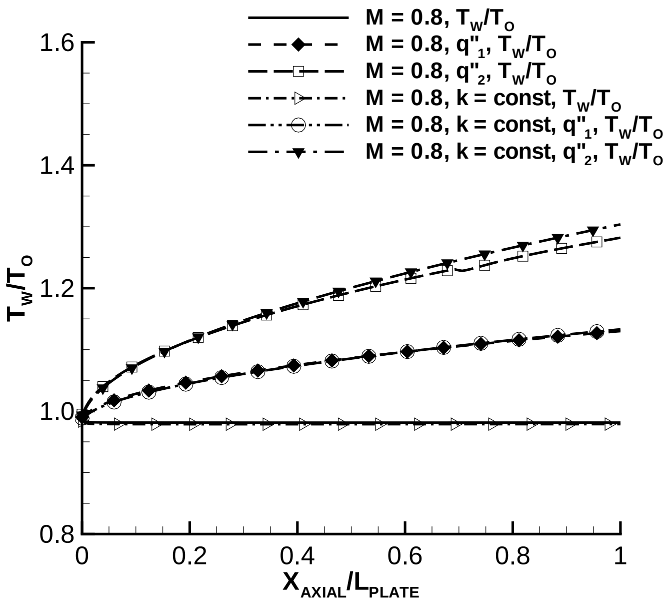

Figure C.19: Computed $\frac{T_w}{T_\circ}$ profiles for various flow conditions and applied heat fluxes with $Pr = 0.71$, $c_p = 1.0 \frac{kJ}{kg \cdot K}$ and $k = 0.026 \frac{W}{m \cdot K}$ with $M = 0.8$.

previous distributions with variable k. Nu_x directly reflects the behavior of the h distribution; since k is constant, as h approximately halves with a doubling of the heat flux, so does Nu_x. This behavior is not reflected in the Nu_x curves where k was allowed to vary.

These numerical experiments are nearly exact solutions of the Navier-Stokes equations, since no turbulence model is used. Hence, the observed differences in heat transfer coefficient are due to the nonlinearities inherent in these equations, a direct consequence of the compressibility of the flow. Furthermore, these results suggest that h can be a function of the applied temperature gradient at the wall, regardless of the temperature rise at the surface.

C.1.3 Turbulent Flow

Having developed a rudimentary understanding of the behavior of the flow equations, several turbulent boundary layer flat plate calculations were performed in preparation for uncooled heat transfer predictions for the single passage. The primary objective of these simulations was to quantify the effect of the turbulent Prandtl number (Pr_t) on predictions for the recovery temperature distribution (T_{rec}). This experience was used to "tune" Pr_t

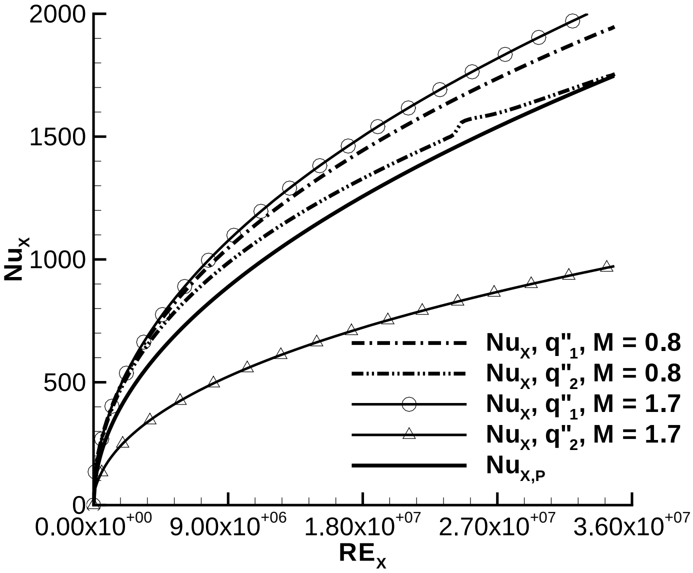

Figure C.20: Computed Nu_x distributions with $Pr = 0.71$, $c_p = 1.0\frac{kJ}{kg \cdot K}$ and $k = 0.026\frac{W}{m \cdot K}$ with q_1'' and q_2'' surface heat fluxes applied and $M = 0.8$.

to achieve as accurate as possible heat transfer predictions. Two turbulence models were applied: the two-layer k-ε Chen and Kim variant and k-ω, as implemented by Medic and Durbin (2002a). It was implicitly assumed that the boundary layer over the surface of the flat plate was fully turbulent. The same grid was used for these calculations as previously presented for the laminar calculations.

Figure C.21 shows the computed recovery factor distributions for the two main flow conditions and turbulence models with $Pr = 1.0$ and $Pr_t = 1.0$ using the two turbulence models. As suggested, the computed values for r_∞ agree within 1.5% to the empirically determined value of $r_\infty \approx 1.0$. Figure C.22 shows the computed skin friction coefficients (C_f) for these various cases, in the interests of completeness. As viscous flow parameters such as the skin friction coefficient (C_f) depend not only on the flow velocity, but the inlet turbulence intensity and integral length scale, these results were expected to match each other, rather than matching a particular target.

At this point, the Prandtl number was adjusted to $Pr = 0.71$. Successive calculations were performed with different values of Pr_t to examine the effect of this parameter on the recovery factor distribution. It was determined by these simulations that the effect

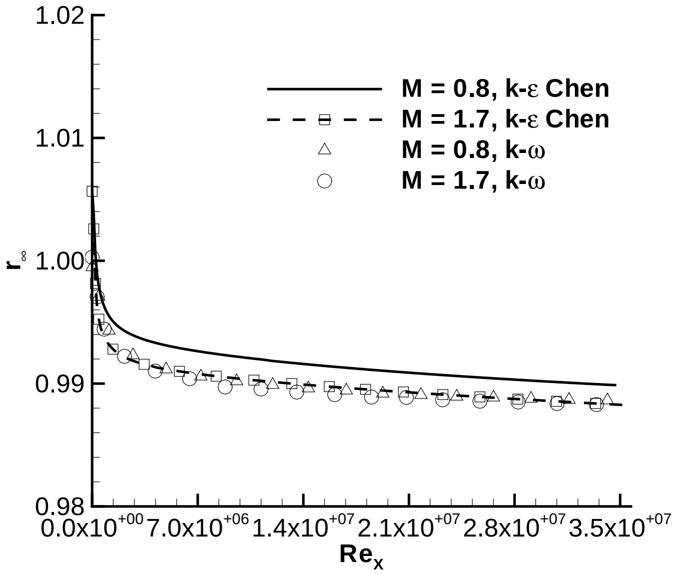

Figure C.21: Computed recovery factors r_∞ distributions using k-ε Chen and k-ω turbulence models with $Pr = 1.0$, $Pr_t = 1.0$ and $c_p = 1.0 \frac{kJ}{kg \cdot K}$ and $M = 0.8$ and $M = 1.7$.

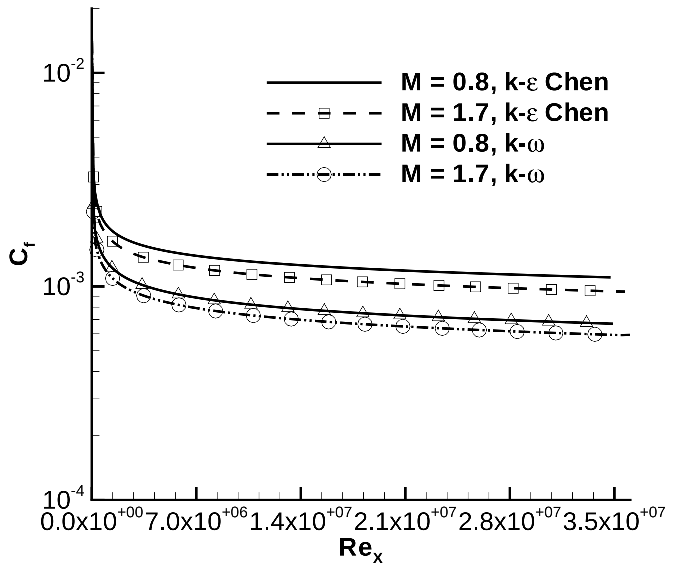

Figure C.22: Computed flat plate skin friction coefficients (C_f) using k-ε Chen and k-ω turbulence models $Pr = 1.0$, $Pr_t = 1.0$ and $c_p = 1.0 \frac{kJ}{kg \cdot K}$.

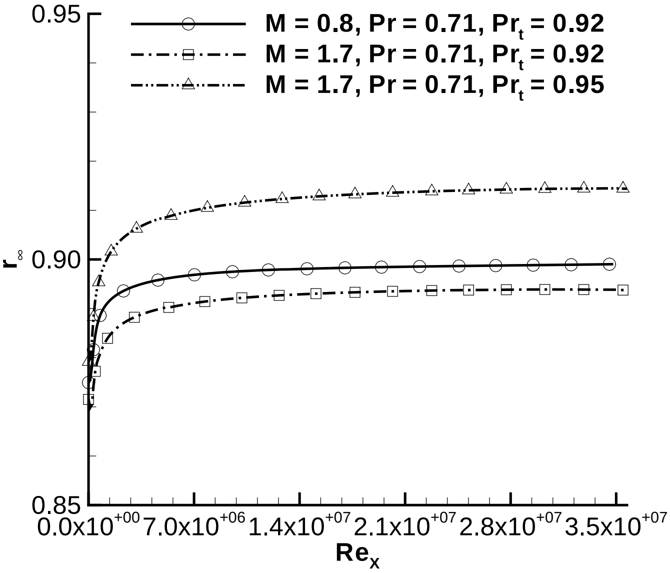

Figure C.23: Computed turbulent flat plate boundary layer recovery factors r_∞ using k-ε as proposed by Chen and Kim (1987) with $Pr = 0.71$ and various values of Pr_t specified.

of adjusting the Pr_t on the mean flow parameters was negligible. Figures C.23 and C.24 present computed r_∞ distributions for a turbulent flat plate boundary layer using k-ε Chen and Kim variant and k-ω turbulence models, respectively. These results show that the predicted r_∞ is not only a function of Pr_t, but the chosen turbulence model as well. For a given value of Pr_t, the applied k-ε model predicts slightly higher r_∞ values than the k-ω model. Higher values of Pr_t caused corresponding increases in r_∞. It should also be stated that these results have not been examined with other mean flow solvers. It is uncertain that adjusting Pr_t can be perceived as a "fix" for a deficient numerical algorithm, or a parameter that corrects the predicted physics of the thermal boundary layer.

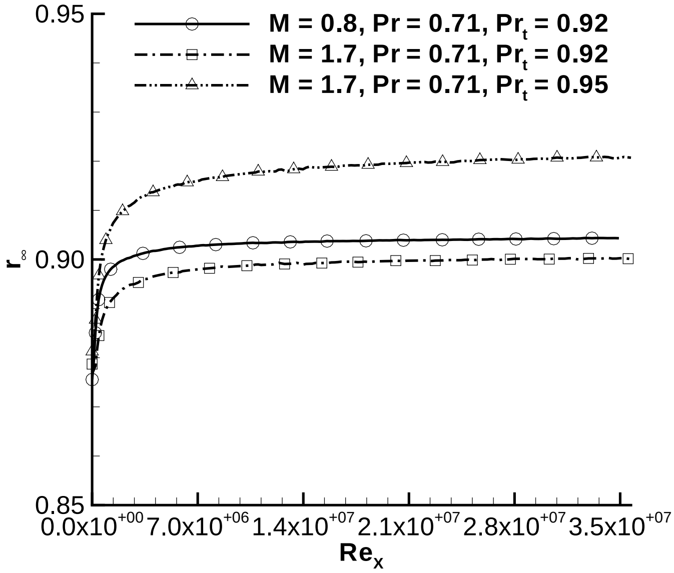

Figure C.24: Computed turbulent flat plate boundary layer recovery factors r_∞ using k-ω as implemented by Medic and Durbin (2002a) with $Pr = 0.71$ and various values of Pr_t specified.

References

Abhari, R. (1996). Impact of Rotor-Stator Interaction on Turbine Blade Film Cooling. *Journal of Turbomachinery 118*(1), 123–133.

Abhari, R. and A. Epstein (1994). An Experimental Study of Film Cooling in a Rotating Transonic Turbine. *Journal of Turbomachinery 116*(1), 63–70.

Abramovich, G. (1963). *The Theory of Turbulent Jets*. Massachusetts Institute of Technology, Cambridge, Massachusetts: M.I.T. Press.

Abuaf, N., D. Bunker, and C. Lee (1997). Heat Transfer and Film Cooling Effectiveness in a Linear Airfoil Cascade. *Journal of Turbomachinery 119*(2), 302–309.

Afejuku, W., N. Hay, and D. Lampard (1980). Film Cooling Effectiveness of Double Rows of Holes. *Journal of Engineering for Power 103*(3), 601–606.

Afejuku, W., N. Hay, and D. Lampard (1983). Measured Coolant Distributions Downstream of Single and Double Rows of Film Cooling Holes. *Journal of Engineering for Power 105*(1), 172–177.

Ajersch, P., J. Zhou, S. Ketler, M. Salcudean, and I. Gartshore (1997). Multiple Jets In a Crossflow: Detailed Measurements and Numerical Simulations. *Journal of Turbomachinery 119*(2), 330–342.

Akino, H., T. Kunugi, K. Ichimiya, K. Mitsushiro, and M. Ueda (1986). Improved Liquid Crystal Thermometry Excluding Human Color Sensation: Part II. Application to the Determination of Wall Temperature Distributions. *ASME HTD 58*, 63–68.

Akino, H., T. Kunugi, K. Ichimiya, K. Mitsushiro, and M. Ueda (1989). Improved Liquid-Crystal Thermometry Excluding Human Color Sensation. *Journal of Heat Transfer 111*, 558–565.

Akino, H., T. Kunugi, K. Ichimiya, M. Ueda, and A. Kurosawa (1987). Liquid Crystal Thermometry Based on Automatic Color Evaluation and Applications to Measure Turbulent Heat Transfer. *2nd International Symposium on Transport Phenomena in Turbulent Flows, Tokyo*.

Akino, H., T. Kunugi, M. Ueda, and A. Kurosawa (1989). A Study on Thermo-Cameras using a Liquid Crystal (Method of Multiple Regression Between Color and Temperature). *National Heat Transfer Conference, HTD v. 112*.

Akino, H., K. Suzuki, K. Sanokawa, and Y. Okamoto (1983). Visualization of Temperature and Heat Transfer Distributions Around a Promoter in a Parallel Plate Channel by Thermosensitive Liquid Crystal Film. *Flow Visualization 3-8*, 40–46.

Ammari, H., N. Hay, and D. Lampard (1990). The Effect of Density Ratio on the Heat Transfer Coefficient from a Film-Cooled Flat Plate. *Journal of Turbomachinery 112*(3), 444–450.

Ammari, H., N. Hay, and D. Lampard (1991). Effect of Acceleration on the Heat Transfer Coefficient on a Film-Cooled Surface. *Journal of Turbomachinery 113*(1), 464–471.

Anderson, M. and J. Baughn (2004). Hysteresis in Liquid Crystal Thermography. *Journal of Heat Transfer 126*(3), 339–346.

Andreopoulos, J. and W. Rodi (1984). Experimental Investigation of Jets in a Crossflow. *Journal of Fluid Mechanics 138*, 93–127.

Andreopoulos, J. (1985). On the Structure of Jets in a Crossflow. *Journal of Fluid Mechanics 157*, 163–197.

Armstrong, W. (1955). The Secondary Flow in a Cascade of Turbine Blades. *A.R.C. Report and Memorandum*.

Arts, T. and A. Bourguignon (1990). Behavior of a Coolant Film With Two Rows of Holes Along the Pressure Side of a High Pressure Nozzle Guide Vane. *Journal of Turbomachinery 112*(3), 512–550.

ASTM Committee E-20 on Temperature Measurement (1974). *Manual on the Use of Thermocouples in Temperature Measurement*, Volume ASTM Special Technical Publication 470A. ASTM.

Atassi, H., A. Ali, O. Atassi, and I. Vinogradov (2004). Scattering of incident disturbances by an annular cascade in a swirling flow. *Journal of Fluid Mechanics 499*, 111–138.

Athans, R. (2000). Private Communication.

Azzi, A. and D. Lakehal (2002). Perpectives in Modeling Film Cooling of Turbine Blades by Transcending Convential Two-Equation Turbulence Models. *Journal of Turbomachinery 124*(3), 472–484.

Babinsky, H. and J. Edwards (1996). Automatic Liquid Crystal Thermography for Transient Heat Transfer Measurements in Hypersonic Flow. *Experiments in Fluids 21*(4), 227–236.

Bailey, D. (1980). Study of mean- and turbulent-velocity fields in a large-scale turbine-vane passage. *Journal of Engineering for Power 102*(1), 88–97.

Baldauf, S., M. Scheurlen, A. Schultz, and S. Wittig (2002a). Correlation of Film-Cooling Effectiveness From Thermographic Measurements at Enginelike Conditions. *Journal of Turbomachinery 124*(4), 686–698.

Baldauf, S., M. Scheurlen, A. Schultz, and S. Wittig (2002b). Heat Flux Reduction from Film Cooling and Correlation of Heat Transfer Coefficients From Thermographic Measurements at Enginelike Conditions. *Journal of Turbomachinery 124*(4), 699–709.

Baldauf, S., A. Schultz, and S. Wittig (2001a). High-Resolution Measurements of Local Effectiveness from Discrete Hole Film Cooling. *Journal of Turbomachinery 123*(4), 758–764.

Baldauf, S., A. Schultz, and S. Wittig (2001b). High-Resolution Measurements of Local Heat Transfer Coefficients from Discrete Hole Film Cooling. *Journal of Turbomachinery 123*(4), 749–757.

Baldwin, B. and H. Lomax (1978). Thin-layer Approximation and Algebraic Model for Separated Turbulent Flows. *AIAA Paper 83-1693*.

Barlow, R. and J. Johnston (1985). Roll-Cell Structure in a Concave Turbulent Boundary Layer. *AIAA Paper 85-0297*.

Batchelder, K. and R. Moffat (1997, August). Towards a Method for Measuring Heat Transfer in Complex 3-D Flows. Technical Report TSD-108, Stanford, California 94305.

Baughn, J. (1995). Liquid Crystal Methods for Studying Turbulent Heat Transfer. *International Journal of Heat and Fluid Flow 16*(5), 365–375.

Baughn, J., M. Anderson, J. Mayhew, and J. Wolf (1999). Hysteresis of Thermochromic Liquid Crystal Temperature Measurement Based on Hue. *Journal of Heat Transfer 121*(4), 1067–1071.

Bean, H. (Ed.) (1983, April). *Fluid Meters: Their Theory and Application* (6th ed.). 345 East St., New York, NY, 10017: The American Society of Mechanical Engineers.

Second Printing with editorial changes.

Bearman, P. (1971). Corrections for the effect of ambient temperature drift on hot-wire measurement in incompressible flow. *Technical Report DISA Report 11*.

Bell, C., H. Hamakawa, and P. Ligrani (2000). Film Cooling from Shaped Holes. *Journal of Turbomachinery 122*(2), 224–232.

Bendat, J. and A. Piersol (1993). *Engineering Applications of Correlation and Spectral Analysis* (2nd ed.). 605 Third Avenue, New York, NY 10158-0012: John Wiley & Sons.

Bergeles, G., A. Gosman, and B. Launder (1976). Near-Field Character of a Jet Discharged Normal to a Mainstream. *Journal of Heat Transfer 119*(3), 373–378.

Bergeles, G., A. Gosman, and B. Launder (1977). Near-Field Character of a Jet Discharged through a Wall at 30° to a Mainstream. *AIAA Journal 15*(4), 499–504.

Bergeles, G., A. Gosman, and B. Launder (1978). The Turbulent Jet in a Cross Stream at Low Injection Rates: a Three-Dimensional Numerical Treatment. *Numerical Heat Transfer 1*, 217–242.

Bergeles, G., A. Gosman, and B. Launder (1980). Double-Row Discrete-Hole Cooling: An Experimental and Numerical Study. *Journal of Engineering for Power 102*(2), 498–503.

Blair, M. (1974). Experimental Study of Heat Transfer and Film Cooling on Large-Scale Turbine Endwalls. *Journal of Heat Transfer 96*(4), 524–529.

Blair, M. (1983). Influence of Free-Stream Turbulence on Turbulent Boundary Layer Heat Transfer and Mean Profile Development, Parts I and II. *Journal of Heat Transfer 105*(1), 33–47.

Blair, M. (1994). An Experimental Study of Heat Transfer in a Large-Scale Turbine Rotor Passage. *Journal of Turbomachinery 116*(1), 1–13.

Blair, M. and M. Werle (1980). The Influence of Free-Stream Turbulence on the Zero Pressure Gradient Fully Turbulent Boundary Layer. *(R80-914388-12), Contract No. F49620-78-C-0064. UTCRC, East Hartford, CT.*.

Bons, J., C. MacArthur, and R. Rivir (1996). The Effect of High Free-Stream Turbulence on Film Cooling Effectiveness. *Journal of Turbomachinery 118*(4), 814–825.

Bradshaw, P. (1973). Effects of Streamwise Curvature on Turbulent Flow. *AGARDOgraph No. 169*.

Brittingham, R. and J. Leylek (2000). A Detailed Analysis of Film Cooling Physics: Part IV - Compound-Angle Injection With Shaped Holes. *Journal of Turbomachinery 122*(1), 133–145.

Brown, A. and C. L. Saluja (1979). Film cooling from a single hole and a row of holes of variable pitch to diameter ratio. *International Journal of Heat and Mass Transfer 22*(4), 525–534.

Bryanston Cross, P., J. Camus, and P. Richards (1983). Dynamic Correlation on a Schlieren Image in a Transonic Airflow. *Springer Series in Optical Sciences 38*, 270–275.

Buck, F. (1999). Private Communication.

Buck, F. (2000). Private Communication.

Buck, F. (2002). Private Communication.

Buck, F. and C. Prakash (1995). Design and Evaluation of A Single Passage Test Model To Obtain Turbine Airfoil Film Cooling Effectivness Data. *American Society of Mechanical Engineers (Paper) 95-GT-19*.

Bunker, R. and J. Bailey (2001). Film Cooling Discharge Coefficient Measurements in a Turbulated Pasage With Internal Crossflow. *Journal of Turbomachinery 123*(4), 774–780.

Burd, S. and T. Simon (1997). The Influence of Coolant Supply Geometry on Film Coolant Exit Flow and Surface Adiabatic Effectiveness. *American Society of Mechanical Engineers (Paper) 97-GT-025*.

Burd, S. and T. Simon (1999). Measurements of Discharge Coefficients in Film Cooling. *Journal of Turbomachinery 121*(2), 243–248.

Camci, C. (1989). An Experimental and Numerical Investigation of Near Cooling Hole Heat Fluxes on a Film-Cooled Turbine Blade. *Journal of Turbomachinery 111*(1), 63–70.

Camci, C. and T. Arts (1985a). Experimental Heat Transfer Investigation Around the Film-Cooled Leading Edge of a High Pressure Gas Turbine Rotor Blade. *Journal of Engineering for Gas Turbines and Power 107*(4), 1016–1021.

Camci, C. and T. Arts (1985b). Short-Duration Measurements and Numerical Simulation of Heat Transfer Along the Suction Side of a Film-Cooled Gas Turbine Blade. *Journal of Turbomachinery 107*(4), 991–997.

Camci, C. and T. Arts (1990). An Experimental Convective Heat Transfer Investigation Around a Film-Cooled Gas Turbine Blade. *Journal of Turbomachinery 112*(3), 497–503.

Camci, C. and T. Arts (1991). Effect of Incidence on Wall Heating Rates and Aerodynamics on a Film-Cooled Transonic Turbine Blade. *Journal of Turbomachinery 113*(3), 493–501.

Camci, C., K. Kim, S. Hippensteele, and P. Poinsatte (1993). Evaluation of a Hue Capturing Based Transient Liquid Crystal Method for High-Resolution Mapping of Convective Heat Transfer on Curved Surfaces. *Journal of Heat Transfer 115*(2), 311–318.

Camp, T. and H.-W. Shin (1995). Turbulence Intensity and Length Scale Measurements in Multistage Compressors. *Journal of Turbomachinery 117*(1), 38–46.

Carver, T. (2003). Private Communication.

CD Adapco Group (2001). *STAR-CD Version 3.15 Methodology.* 60 Broadhollow Road, Melville, NY 11747: Computational Dynamics.

Chapman, D. and M. Rubesin (1949). Temperature and Velocity Profiles in the Compressible Laminar Boundary Layer with Arbitrary Distribution of Surface Temperature. *Journal of Aeronautical Science 20*, 547–565.

Chen, Y. and S. Kim (1987). Computation of turbulent flows using an extended $k - \epsilon$ turbulence closure model. *NASA CR-179204*.

Cho, H. and R. Goldstein (1995). Heat (Mass) Transfer and Film Cooling Effectiveness With Injection Through Discrete Holes: Part I – Within Holes and on the Back Surface. *Journal of Turbomachinery 117*(3), 440–450.

Cho, H., B. Kim, and D. Rhee (1998). Effects of Hole Geometry on Heat (Mass) Transfer and Film Cooling Effectiveness. *Proceedings of the 11th International Heat Transfer Conference 6*, 499–504.

Cho, H., G. Seung, and D. Rhee (2001). Heat/Mass Transfer Measurement Within a Film Cooling Hole of Square and Rectangular Cross Section. *Journal of Turbomachinery 123*(3), 806–814.

Choe, H., W. Kays, and R. Moffat (1976). Turbulent Boundary Layer on a Full-Coverage Film-Cooling Surface – An Experimental Heat Transfer Study. *NASA CR-2642*.

Chong, M., A. Perry, and B. Cantwell (1990). A general classification of three-dimensional flow fields. *Physics of Fluids 2*, 765–777.

Chung, J. and T. Simon (1991). Three-Dimensional Flow Near the Blade/Endwall Junction of a Gas Turbine: Application of a Boundary Layer Fence. *American Society of Mechanical Engineers (Paper) 90-WA/HT4-4*.

Chung, J., T. Simon, and J. Buddhavarapu (1991). Three-Dimensional Flow Near the Blade/Endwall Junction of a Gas Turbine: Visualization in a Large-Scale Cascade Simulator. *American Society of Mechanical Engineers (Paper) 91-GT-45*.

CNC Software (2000). *MASTERCAM Mill V7*. 671 Old Post Road, Tolland CT, 06084, USA: CNC Software.

Coakley, T. (1983). Turbulence Modeling Methods for the Compressible Navier-Stokes Equations. *AIAA paper 83-1693*.

Collings, P. and M. Hird (1997). *Introduction to Liquid Crystals*. 325 Chestnut St., 8th Floor, Philadelphia, PA 19106: Taylor & Francis Inc.

Compton, D. and J. Johnston (1992). Streamwise Vortex Production by Pitched and Skewed Jets in a Turbulent Boundary Layer. *AIAA Journal 30*(3), 640–647.

Crawford, M. and W. Kays (1976). STAN-5 Program for Calculation of Two-Dimensional Internal and External Boundary Layer Flows. *NASA CR-2742*.

Cutbirth, J. and D. Bogard (2002a). Evaluation of Pressure Side Film Cooling with Flow and Thermal Field Measurements – Part I: Showerhead Effects. *Journal of Turbomachinery 124*(3), 670–677.

Cutbirth, J. and D. Bogard (2002b). Evaluation of Pressure Side Film Cooling with Flow and Thermal Field Measurements – Part II: Turbulence Effects. *Journal of Turbomachinery 124*(3), 678–685.

Davis, R. (2000). Private Communication.

DeGraaff, D. (2000). Private Communication.

DeGraaff, D. and J. Eaton (1999, January). Reynolds Number Scaling of the Turbulent Boundary Layer on a Flat Plate and Swept and Unswept Bumps. Technical Report

TSD-118, Stanford, California 94305.

Deissler, R. and A. Loeffler (1958, April). Analysis of Turbulent Flow and Heat Transfer on a Flat Plate at High Mach Numbers with Variable Fluid Properties. Technical Note NACA TN 4262, Washington, D.C., 20001.

Demuren, A., W. Rodi, and Schönung (1986). Systematic study of film cooling with a three-dimensional calculation procedure. *Journal of Turbomachinery 108*(3), 124–130.

Diller, T. (1993). Advances in Heat Flux Measurements. *Advances in Heat Transfer 23*, 279–368.

Dittmar, J., A. Schulz, and S. Wittig (2003). Assessment of Various Film-Cooling Configurations Including Shaped and Compound Angle Holes Based on Large-Scale Experiments. *Journal of Turbomachinery 125*(1), 57–64.

Dods, D. (1999). Private Communication.

Dods, D. (2001). Private Communication.

Dods, D. (2002). Private Communication.

Dring, R., M. Blair, and H. Joslyn (1980). Experimental Investigation of Film Cooling on a Turbine Rotor. *Journal of Engineering for Power 102*(1), 81–87.

Drost, U. and A. Bölcs (1999). Investigation of Detailed Film Cooling Effectiveness and Heat Transfer Distribution on a Gas Turbine Airfoil. *Journal Of Turbomachinery 121*(2), 233–242.

Drost, U., A. Bölcs, and A. Hoffs (1997). Utilization of the Transient Liquid Crystal Technique for Film Cooling Effectiveness and Heat Transfer Investigations on a Flat Plate and Turbine Airfoil. *American Society of Mechanical Engineers (Paper) 97-GT-26*.

Du, H., S. Ekkad, and J. Han (1999). Effect of Unsteady Wake with Trailing Edge Coolant Ejection on Film Cooling Performance for a Gas Turbine Blade. *Journal of Turbomachinery 121*(3), 448–455.

Du, H., J. Han, and S. Ekkad (1997). Effect of Unsteady Wake on Detailed Heat Transfer Coefficient and Film Effectiveness Distributions for a Gas Turbine Blade. *Journal of Turbomachinery 120*(4), 808–813.

Du, H., J. Han, and S. V. Ekkad (1998). Effect of Unsteady Wake on Detailed Heat Transfer Coefficient and Film Effectiveness Distributions for a Gas Turbine Blade. *Journal of Turbomachinery 120*(4), 808–817.

Dunn, M. (1986). Heat-Flux Measurements for the Rotor of a Full-Stage Turbine: Part I – Time Averaged Results. *Journal of Turbomachinery 108*(3), 90–97.

Dunn, M. (2001). Convective Heat Transfer and Aerodynamics in Axial Flow Turbines. *Journal of Turbomachinery 123*(4), 637–686.

Dunn, M. and R. Chupp (1988). Time-Averaged Heat-Flux Distributions and Comparisons With Prediction for the Teledyne 702 HP Turbine Stage. *Journal of Turbomachinery 110*(1), 51–56.

Dunn, M., W. George, W. Rae, S. Woodward, J. Moller, and P. Seymour (1986). Heat-Flux Measurements for the Rotor of a Full-Stage Turbine: Part II – Description of Analysis Technique and Typical Time-Resolved Measurements. *Journal of Turbomachinery 108*(3), 98–107.

Dunn, M. and A. Hause (1982). Measurements of Heat Flux and Pressure in a Turbine Stage. *Journal of Engineering for Power 104*(1), 215–223.

Dunn, M., J. Kim, K. C. Civinskas, and R. J. Boyle (1994). Time-averaged Heat Transfer and Pressure Measurements and Comparison with Prediction for a Two-stage Turbine. *Journal of Turbomachinery 116*(1), 14–22.

Dunn, M., J. Kim, and W. Rae (1997). Investigation of the Heat Island Effect for Heat-Flux Measurements in Short Duration Facilities. *Journal of Turbomachinery 119*(4), 753–760.

Dunn, M. and F. Stoddard (1979). Measurement of Heat-Transfer Rate to a Gas Turbine Stator. *Journal of Engineering for Power 101*(2), 275–280.

Durbin, P. (1996). On the k-3 Stagnation Point Anomaly. *International Journal of Heat and Fluid Flow 17*, 89–90.

Durbin, P. (1998). Private Communication.

Eckert, E. (1976). *Analogies to Heat Transfer Processes*, pp. 397–423. New York, New York: Hemisphere Publishing Corporation.

Eckert, E. (1984). Analysis of Film Cooling and Full-Coverage Film Cooling of Gas Turbine Blades. *Journal of Engineering for Gas Turbines and Power 106*, 206–213.

Eckert, E. and R. Drake (1972). *Analysis of Heat and Mass Transfer* (1st ed.). San Francisco, California: McGraw-Hill, Inc.

Eibeck, P. and J. Eaton (1987). Heat Transfer Effects of a Longitudinal Vortex Embedded in a Turbulent Boundary Layer. *Journal of Heat Transfer 109*(1), 16–24.

Ekkad, S. and J. Han (2000). A transient liquid crystal thermography technique for gas turbine heat transfer measurements. *Measurment Science Technology 11*(7), 957–968.

Ekkad, S., A. B. Mehendale, J. C. Han, and C. Lee (1997). Combined Effect of Grid Turbulence and Unsteady Wake On Film Effectiveness and Heat Transfer Coefficient of a Gas Turbine Blade With Air and CO_2 Film Injection. *Journal of Turbomachinery 119*(3), 594–600.

Ekkad, S., D. Zapata, and J. Han (1997a). Film Effectiveness Over a Flat Surface With Air and CO_2 Injection Through Compound Angle Holes Using a Transient Liquid Crystal Image Method. *Journal of Turbomachinery 119*(3), 580–586.

Ekkad, S., D. Zapata, and J. Han (1997b). Heat Transfer Coefficients Over a Flat Surface With Air and CO_2 Injection Through Compound Angle Holes Using a Transient Liquid Crystal Method. *Journal of Turbomachinery 119*(3), 587–593.

Elkins, C. and J. Eaton (1997, April). Heat Transfer in the Rotating Disc Boundary Layer. Technical Report TSD-103, Stanford, California 94305.

Elkins, C. and J. Eaton (1999). A Thin Film Device for Convection Measurements in Complex Flows. *Bull. APS 52 GP.01*, 604–607.

Elkins, C., J. Fessler, and J. Eaton (2001). A Novel Mini Calibrator for Thermochromic Liquid Crystals. *Journal of Heat Transfer 123*(3), 604–607.

Epstein, A., G. Guenette, R. Norton, and C. Yuzhang (1986). High-frequency response heat flux gauge. *Review of Scientific Instruments 57*(4), 639–649.

Eriksen, V. and R. Goldstein (1974). Heat Transfer and Film Cooling Following Injection Through Inclined Circular Tubes. *Journal of Heat Transfer 104*(2), 239–245.

Eskinazi, S. and H. Yeh (1956). An Investigation on Fully Developed Turbulent Flows in a Curved Channel. *Journal of Aeronautical Science 23-34*.

Etheridge, M., J. Cutbirth, and D. Bogard (2001). Scaling of Performance for Varying Density Ratio Coolants on an Airfoil With Strong Curvature and Pressure Gradients Effects. *Journal of Turbomachinery 123*(2), 231–237.

Evans, M., C. Rapley, D. Wilcock, and T. Sheldrake (1998). Study of microencapsulated chiral nematics in the presence of electric fields. *International Journal of Heat and Mass Transfer 41*(22), 3685–3687.

Farina, D. J., J. M. Hacker, R. J. Moffat, and J. K. Eaton (1994). Illuminant Invariant Calibration of Thermochromic Liquid Crystals. *Experimental Thermal and Fluid Science 9*(1), 1–12.

Farve, A. (1965). Equations des gaz turbulents compressibles. *Journal de Mecanique 4*(3), 361–390.

Fay, J. (1994). *Introduction to Fluid Mechanics*. Massachusetts Institute of Technology, Cambridge, Massachusetts: M.I.T. Press.

Fergason, J. (1966a). Cholesteric Structure – I. *Molecular Crystals 1*, 293–307.

Fergason, J. (1966b). Cholesteric Structure – II. *Molecular Crystals 1*, 309–323.

Fergason, J. (1968). Liquid Crystals in Nondestructive Testing. *Applied Optics 7*(9), 1729–1737.

Findlay, M., M. Salcudean, and I. Gartshore (1999). Jets in a Crossflow: Effects of Geometry and Blowing Ratio. *Journal of Fluids Engineering 121*(3), 373–378.

Foster, N. and D. Lampard (1975). Effects of Density and Velocity Ratio on Discrete Hole Film Cooling. *AIAA Journal 13*, 1112–1114.

Foster, N. and D. Lampard (1980). The Flow and Film Cooling Effectiveness Following Injection through a Row of Holes. *Journal of Engineering for Power 102*(3), 584–588.

Fric, T. and A. Roshko (1994). Vortical Structure in the Wake of a Transverse Jet. *Journal of Fluid Mechanics 279*, 1–47.

Garg, V. (1999). Heat Transfer on a Film-Cooled Rotating Blade Using Different Turbulence Models. *International Journal of Heat and Mass Transfer 42*, 789–802.

Garg, V. and A. Ameri (2001). Two-equation turbulence model for prediction of heat transfer on a transonic turbine blade. *International Journal of Heat and Fluid Flow 22*(6), 593–602.

Garg, V. and R. Gaugler (1996). Leading Edge Film-Cooling Effects On Turbine Blade Heat Transfer. *Numerical Heat Transfer, Part A 30*, 165–187.

Garg, V. and R. Gaugler (1997a). Effect of Coolant Temperature and Mass Flow on Film Cooling of Turbine Blades. *International Journal of Heat and Mass Transfer 40*(2), 435–445.

Garg, V. and R. Gaugler (1997b). Effect of Velocity and Temperature Distribution at the Hole Exit on Film Cooling of Turbine Blades. *Journal of Turbomachinery 119*, 343–351.

Gartshore, I., M. Salcudean, and I. Hassan (2001). Film Cooling Injection Hole Geometry: Hole Shape Comparison for Compound Cooling Orientation. *AIAA Journal 39*(8), 1493–1499.

Gauntner, J. (1977). Effects of Film Injection Angle on Turbine Vane Cooling. *NASA TP-1095, NASA Technical Paper 1095*.

Giel, P., R. Boyle, and R. Bunker (2004). Measurements and Predictions of Heat Transfer on Rotor Blades in a Transonic Turbine Cascade. *Journal of Turbomachinery 126*(1), 110–121.

Giel, P., D. Thurman, G. Van Fossen, S. Hippensteele, and R. Boyle (1996). Endwall Heat Transfer Measurements in a Transonic Turbine Cascade . *American Society of Mechanical Engineers (Paper) 96-GT-180*.

Giel, P., G. Van Fossen, R. Boyle, D. Thurmann, and K. Civinskas (1999). Blade Heat Transfer Measurements and Predictions in a Transonic Turbine Cascade. *American Society of Mechanical Engineers (Paper) 99-GT-125*.

Glassman, J. (2000). Private Communication.

Gnielinski, V. (1976). New Equations for Heat and Mass Transfer in Turbulent Pipe and Channel Flow. *International Chemical Engineer 16*, 359–368.

Goebel, S., N. Abuaf, J. Lovett, and C. Lee (1993). Measurements of Combustor Velocity and Turbulence Profiles. *American Society of Mechanical Engineers (Paper) 93-GT-228*.

Goldstein, R. (1971). Film cooling. *Advances in Heat Transfer 7*, 321–379.

Goldstein, R. and H. Chen (1985). Film Cooling on a Gas Turbine Blade Near the End Wall. *Journal of Engineering for Gas Turbines and Power 107*(1), 117–122.

Goldstein, R. and H. Cho (1995). A Review of Mass Transfer Measurements Using Naphthalene Sublimation. *Experimental Thermal and Fluid Science 10*(4), 416–434.

Goldstein, R., H. Cho, and M. Jabbari (1997). Effect of Plenum Crossflow on Heat (Mass) Transfer Near and Within the Entrance of Film Cooling Holes. *Journal of Turbomachinery 119*, 761–769.

Goldstein, R., E. Eckert, and F. Burggraf (1974). Effects of Hole Geometry and Density on Three-Dimensional Film Cooling. *Journal of Turbomachinery 9*, 1–12.

Goldstein, R., E. Eckert, H. Chiang, and E. Elovic (1985). Effect of Surface Roughness on Film Cooling Performance. *Journal of Engineering for Gas Turbines and Power 107*(1), 111–116.

Goldstein, R., E. Eckert, V. Eriksen, and J. Ramsey (1970). Film Cooling Following Injection Through Inclined Circular Tubes. *Israel Journal of Technology 8*(1-2), 145–154.

Goldstein, R., E. Eckert, and J. Ramsey (1968). Film Cooling with Injection Through Holes: Adiabatic Wall Temperatures Down Stream of a Circular Hole. *Journal of Engineering for Power 90*(2), 384–395.

Goldstein, R. and P. Jin (2001). Film Cooling Downstream of a Row of Discrete Holes With Compound Angle. *Journal of Turbomachinery 123*(4), 222–230.

Goldstein, R. and R. Spores (1988). Turbulent Transport on the Endwall in the Region Between Adjacent Turbine Blades. *Journal of Heat Transfer 110*(4), 862–869.

Goldstein, R. and L. Stone (1997). Row-of-Holes Film Cooling of Curved Walls at Low Injection Angles. *Journal of Turbomachinery 119*(3), 574–579.

Goldstein, R. J., P. Jin, and R. L. Olson (1999). Film Cooling and Effectiveness and Mass/Heat Transfer Coefficient of One Row of Discrete Holes. *Journal of Turbomachinery 121*, 225–232.

Görtler, H. (1940). Über eine dreidimensionale Instabilität laminarer Grenzschichten an konkaven Wänden. *Nachr. Wiss. Ges. Göttingen, Math. Phys Klasse 2*(1).

Görtler, H. (1955). Dreidimensionale Instabilität der ebenen Staupunktströmung gegenüber wirbelartigen Strörungen. *In: H. Görtler: W. Tollmien (Hrsg): Fünfzig Jahre Grenzschichtforschung. Vieweg Verlag, Braunschweig*, 304–314.

Goshtasby, A. (1993). Design and Recovery of 2-D and 3-D Shapes Using Rational Gaussian Curves and Surfaces. *International Journal of Computer Vision 10*(3), 233–256.

Goshtasby, A. (1995). Geometric Modelling Using Rational Gaussian Curves and Surfaces. *Computer-Aided Design 27*(5), 363–375.

Gottlich, E., H. Lang, W. Sanz, and J. Woisetschlager (2002). Experimental Investigation of an Innovative Cooling System (ICS) for High Temperature Transonic Turbine Stages. *ASME 5*(A), 159–167.

Gray, R. and J. Goodman (1995). *Fourier Transforms: An Introduction for Engineers* (1st ed.). 233 Spring Street, New York, NY 10013: Kluwer Academic Publishers.

Gritsch, M., A. Schulz, and S. Wittig (1998a). Adiabatic Wall Effectiveness Measurements of Film-Cooling Holes with Expanded Exits. *Journal of Turbomachinery 120*(3), 549–556.

Gritsch, M., A. Schulz, and S. Wittig (1998b). Discharge Coefficient Measurements of Film-Cooling Holes with Expanded Exits. *Journal of Turbomachinery 120*(3), 557–563.

Gritsch, M., A. Schulz, and S. Wittig (2001). Effect of Crossflows on the Discharge Coefficient of Film Cooling Holes With Varying Angles of Inclination and Orientation. *Journal of Turbomachinery 123*(4), 781–787.

Guenette, G., A. Epstein, M. Giles, R. Haimes, and R. Norton (1989). Fully Scaled Transonic Turbine Rotor Heat Transfer Measurements. *Journal of Turbomachinery 102*, 1–7.

Günther, A. and P. von Rohr (2002). Influence of the Optical Configuration on Temperature Measurements with Fluid-Dispersed TLCs. *Experiments in Fluids 32*(5), 533–541.

Haas, W., W. Rodi, and B. Schönung (1992). The Influence of Density Difference Betweeen Hot and Coolant Gas on Film Cooling by a Row of Holes: Predictions and Experiments. *Journal of Turbomachinery 114*(4), 747–755.

Hacker, J. and J. Eaton (1995, June). Heat Transfer Measurements in a Backward Facing Step Flow with Arbitrary Wall Temperature Variations. Technical Report MD-71, Stanford, California 94305.

Hahn, S. and H. Choi (1997). Unsteady Simulation of Jets in a Cross Flow. *Journal of Computational Physics 134*(2), 342–356.

Haldeman, C. and M. Dunn (2004). Heat-Transfer Measurements and Predictions for the Vane and Blade of a Rotating High-Pressure Turbine Stage. *Journal of Turbomachinery 126*(1), 101–109.

Hale, C., M. Plesniak, and S. Ramadhyani (2000a). Film Cooling Effectiveness for Short Film Cooling Holes Fed by a Narrow Plenum. *Journal of Turbomachinery 122*(3), 553–557.

Hale, C., M. Plesniak, and S. Ramadhyani (2000b). Structural Features and Surface Heat Transfer Associated with a Row of Short-Hole Jets in Crossflow. *International Journal of Heat and Fluid Flow 21*(5), 542–553.

Haller, B. and J. Camus (1984). Aerodynamic Loss Penalty Produced By Film Cooling Transonic Turbine Blades. *Journal of Engineering for Gas Turbines and Power 106*(1), 198–205.

Hammer, J. (2001). Private communication.

Han, J. and A. Mehendale (1986). Flat Plate Film Cooling with Stream Injection One Row and Two Rows of Inclined Holes. *Journal of Turbomachinery 108*(1), 137–144.

Hancock, P. (1980). *Effect of High Free-Stream Turbulence in Turbulent Boundary Layers.* Imperial College, London University, UK: Ph.D. Thesis.

Häring, M., Bölcs, S. Harasgama, and J. Richter (1995). Heat Transfer Measurements on Turbine Airfoils Using the Napthalene Sublimation Technique. *Journal of Turbomachinery 117*(3), 432–439.

Harrington, M., M. McWaters, D. Bogard, C. Lemmon, and K. Thole (2001). Full-Coverage Film Cooling with Short Normal Injection Holes. *Journal of Turbomachinery 123*(4), 798–805.

Hasler, T., J. Hammer, and L. Johal (2000). Private Communication.

Haven, B. and M. Kurosaka (1997). Kidney and Anti-Kidney Vortices in Crossflow Jets. *Journal of Fluid Mechanics 352*(1), 27–64.

Hay, N., D. Lampard, and S. Benmansour (1983). Effect of Crossflows on the Discharge Coefficient of Film Cooling Holes. *Journal of Engineering for Power 105*(2), 243–248.

Hay, N., D. Lampard, and C. Saluja (1985). Effect of Cooling Films on the Heat Transfer Coefficient on a Flat Plate with Zero Mainstream Pressure Gradient. *Journal of Engineering for Gas Turbines and Power 107*(1), 105–110.

Hay, N., D. Lampard, and C. Saluja (1985). Effects of the Condition of the Approach Boundary Layer and of Mainstream Pressure Gradients on the Heat Transfer Coefficient on Film-Cooled Surfaces. *Journal of Engineering for Gas Turbines and Power 107*(1), 99–104.

Hay, N., S. Henshall, and A. Manning (1994). Discharge Coefficients of Holes Angled to the Flow Direction. *Journal of Turbomachinery 116*(1), 92–96.

Hay, N. and D. Lampard (1995). Effect of Crossflows on the Discharge Coefficient of Film Cooling Holes. *American Society of Mechanical Engineers (Paper) 95-GT-15*.

Hay, J. and D. Hollingsworth (1996). A Comparison of Trichromic Systems for Use in the Calibration of Polymer-Dispersed Thermochromic Liquid Crystals. *Experimental Thermal and Fluid Science 12*(1), 1–12.

Hay, J. and D. Hollingsworth (1998). Calibration of Micro-Encapsulated Liquid Crystals using Hue Angle and a Dimensionless Temperature. *Experimental Thermal and Fluid Science 18*(3), 251–257.

Herold, W. and D. Wiegel (1980). *Problems of the Photographic Documentation of Liquid Crystalline Thermographs*, pp. 1255–1259. Pergamon Press.

Hill, P. and C. Petersen (1992). *Mechanics and Thermodynamics of Propulsion* (2nd ed.). Reading, Massachusetts: Addison-Wesley.

Hinze, J. (1975). *Turbulence* (2nd ed.). San Francisco, California: McGraw-Hill.

Hippensteele, S. and L. Russell (1988). High resolution liquid-crystal heat-transfer measurements on the end wall of a turbine passage with variations in reynolds number. *NASA Technical Memo 100827*.

Hobson, G., T. M. Caruso, and J. R. Carlson (2003). Three-component LDV Measurements in the Wake of a Compressor Cascade with Flow Separation. *ASME 6*(A), 91–103.

Hoda, A. and S. Acharya (2000). Predictions of a Film Coolant Jet in Crossflow with Different Turbulence Models. *Journal of Turbomachinery 122*(3), 558–568.

Hodge, B. and K. Koenig (1995). *Compressible Fluid Dynamics with Personal Computer Applications*. Englewood Cliffs, N.J.: Prentice Hall.

Hollingsworth, D., A. Boehman, E. Smith, and R. Moffat (1989). Measurement of Temperature and Heat Transfer Coefficient Distributions in Complex Flow Using Liquid

Crystal Thermography and True-Color Image Processing. *Collected Papers in Heat Transfer, New York: The American Society of Mechanical Engineers*, 35–42.

Honami, S., T. Shizawa, and A. Uchiyama (1994). Behavior of the Laterally Injected Jet in Film Cooling: Measurements of Surface Temperature and Velocity/Temperature Field within the Jet. *Journal of Turbomachinery 116*(1), 106–112.

Hsu, K. and S. Lee (1991). A Numerical Technique for Two-Dimensional Grid Generation with Grid Control at All of the Boundaries. *Journal of Computational Physics 96*(2), 451–469.

Huyer, S. and S. Snarski (2003). Analysis of a Turbulent Propeller Inflow. *Journal of Turbomachinery 125*(2), 533–542.

Hyams, D. and J. Leylek (2000). A Detailed Analysis of Film Cooling Physics: Part III - Streamwise Injection With Shaped Holes. *Journal of Turbomachinery 122*(1), 122–132.

Imaging Products Group (2004).

Ireland, P. and T. Jones (1985). The Measurement of Local Heat Transfer Coefficients in Blade Cooling Geometries. *AGARD Conference on Heat Transfer and Cooling in Gas Turbines, CP390, Paper 28*.

Ireland, P. and T. Jones (1986). Detailed Measurements of Heat Transfer on and Around a Pedestal in Fully Developed Passage Flow. *Proceedings of 8th International Heat Transfer Conference*, 975.

Ireland, P. and T. Jones (1987). Response Time of a Surface Thermometer Employing Encapsulated Thermochromic Liquid Crystals. *Journal of Physics E, Science Instrumentation 20*, 1195–1199.

Ireland, P. and T. Jones (2000). Liquid Crystal Measurements of Heat Transfer and Surface Shear Stress. *Measurement Science and Technology 11*(7), 969–985.

Issa, R. (1986). Solution of the implicitly discretised fluid flow equations by operator-splitting. *Journal of Computational Physics 62*(1), 40–65.

Issa, R., A. Gosman, and A. Watkins (1986). The computation of implicit scheme. *Journal of Computational Physics 62*(1), 66–82.

Ito, S., R. Goldstein, and E. Eckert (1978). Film Cooling of a Gas Turbine Blade. *Journal of Engineering for Power 100*(3), 476–481.

Jabbari, M. and R. Goldstein (1978). Adiabatic Wall Temperature and Heat Transfer Downstream of Injection Through Two Rows of Holes. *Journal of Engineering for Power 100*(2), 303–307.

Jackowski, M., A. Goshtabsy, S. Bines, D. Roseman, and C. Yu (1997). Correcting the Geometry and Color of Digital Images. *IEEE Transactions Pattern Analysis and Machine Intelligence 19*(10), 1152–1158.

Johal, L. (2002). Private Communication.

Jones, T. and D. Schultz (1970). A Study of Film Cooling Related to Gas Turbines Using Transient Techniques. *University of Oxford Report No. 1121/70*.

Jones, W. and B. Launder (1972). Some Properties of Sink-Flow Turbulent Boundary Layers. *Journal of Fluid Mechanics 56*, 337–351.

Jubran, B. (1989). Correlation and Prediction of Film Cooling From Two Rows of Holes. *Journal of Turbomachinery 111*(4), 502–509.

Jubran, B. and A. Brown (1985). Film Cooling From Two Rows of Holes Inclined in the Streamwise and Spanwise Directions. *Journal of Turbomachinery 107*(1), 84–91.

Jumper, G., W. Elrod, and R. Rivir (1991). Film Cooling Effectiveness in High Turbulence Flow. *Journal of Turbomachinery 113*(3), 479–483.

Jung, I. and J. Lee (2000). Effects of Orientation Angles on Film Coling Over a Flat Plate: Boundary Layer Temperature Distributions and Adiabatic Film Cooling Effectiveness. *Journal of Turbomachinery 122*(1), 153–160.

Kadotani, K. and R. Goldstein (1979a). Effect of Mainstream Variables on Jets Issuing From a Row of Inclined Round Holes. *Journal of Engineering for Power 101*, 298–304.

Kadotani, K. and R. Goldstein (1979b). On the Nature of Jets Entering a Turbulent Flow: Part A - Jet Mainstream Interaction. *Journal of Engineering for Power 101*(3), 459–465.

Kadotani, K. and R. Goldstein (1979c). On the Nature of Jets Entering a Turbulent Flow: Part B - Film Cooling Performance. *Journal of Engineering for Power 101*(3), 466–470.

Kalitzin, G., X. Wu, and P. A. Durbin (2003). DNS of Fully Turbulent Flow in a LPT passage. *International Journal of Heat and Fluid Flow 24*(4), 636–644.

Kaszeta, R. and T. Simon (2000). Measurements of Eddy Diffusivity of Momentum in Film Cooling Flows With Streamwise Injection. *Journal of Turbomachinery 122*(1), 178–183.

Kaszeta, R., T. Simon, R. Oke, and S. Burd (1998). Flow Measurements in Film Cooling Flows With Lateral Injection. *American Society of Mechanical Engineers (Paper) 98-GT-054*.

Kays, W. and M. Crawford (1993). *Convective Heat and Mass Transfer* (3rd ed.). San Francisco, California: McGraw-Hill.

Kelso, R., T. Lim, and A. Perry (1996). An Experimental Study of Round Jets in Cross-Flow. *Journal of Fluid Mechanics 306*, 111–144.

Khalatov, A., A. Avramenko, L. Syskov, M. Litvinenko, and S. Khalatov (1993). Heat Transfer and Flow on the Convex and Concave Walls of Gas Turbine Nozzle Blades With Intensive Secondary and Vortex Flows. *Heat Transfer Research 25*(4), 468–481.

Khan, Z. and J. Johnston (2000). On Vortex Generating Jets. *International Journal of Heat and Fluid Flow 21*(5), 506–511.

Kim, J. (1985). An Analytical Mixing Model for Buoyancy Jet Injected Into Pipe Flow. *Journal of Heat Transfer 107*(3), 630–635.

Kline, S. and F. McClintock (1975). Describing Uncertainties in Single Sample Experiments. *Mechanical Engineering 75*, 3–8.

Ko, S.-Y., J.-Z. Xu, Y.-Q. Yao, and F.-K. Tsou (1983). Film Cooling Effectiveness and Turbulence Distribution of Discrete Holes on a Convex Surface. *International Journal of Heat and Mass Transfer 27*(9), 1551–1556.

Ko, S.-Y., Y.-Q. Yao, B. Xia, and F.-K. Tsou (1986). Discrete-Hole Film Cooling Characteristics over Concave and Convex Surfaces. *Proceedings of the Eighth International Heat Transfer Conference, San Francisco, CA*.

Kohli, A. and D. Bogard (1997). Adiabatic Effectiveness, Thermal Fields, and Velocity Fields for Film Cooling With Large Angle Injection. *Journal of Turbomachinery 119*, 352–358.

Kruse, H. (1984). Measurements of Film Cooling Effectiveness and Heat Transfer on a Flat Plate. *Heat and Mass Transfer in Rotating Machinery*, 451–461.

Kulisa, P., L. Lebeouf, and G. Perrin (1992). Computation of a Wall Boundary Layer With Discrete Jet Injections. *Journal of Turbomachinery 114*, 756–764.

Lakehal, D. (2002). Near-wall modeling of turbulent convective heat transport in film cooling of turbine blades with the aid of direct numerical simulation data. *Journal of Turbomachinery 124*(3), 485–498.

Lakshiminarayana, B. (1993). *Fluid Dynamics and Heat Transfer of Turbomachinery* (1st ed.). 605 Third Avenue, New York, NY 10158-0012: John Wiley & Sons.

Lander, R., R. Fish, and M. Suo (1972). External Heat-Transfer Distribution on Film Cooled Turbine Blades. *Journal of Aircraft 9*(10), 707–714.

Langston, L. (1980). Crossflows in a Turbine Cascade Passage. *Journal of Engineering for Power 102*(4), 866–874.

Langston, L., M. Nice, and R. Hooper (1977). Three-Dimensional Flow Within a Turbine Cascade Passage. *Journal of Engineering for Power 119*(1), 21–28.

Laskowski, G. (2000). Private Communication.

Laskowski, G., A. Vicharelli, G. Medic, C. Elkins, J. Eaton, and P. Durbin (2005). Inverse Design of and Experimental Measurements in a Double Passage Transonic Cascade Model. *To appear in Journal of Turbomachinery*.

Launder, B. and J. York (1974). Discrete-Hole Cooling in the Presence of Free Stream Turbulence and Strong Favorable Pressure Gradient. *International Journal of Heat and Mass Transfer 17*, 1403–1409.

Lavrich, P. and L. Chiappetta (1990). An Investigation of Jet in a Cross Flow for Turbine Film Cooling Applications. *UTRC Report No. 90-04*.

Le Brocq, P., B. Launder, and C. Priddin (1973). Discrete Hole Injection as a Means of Transpiration Cooling; An Experimental Study. *Proceedings of the Institution of Mechanical Engineering 187*, 149–157.

Le Grivès, E. (1978). Mixing Process Induced by the Vorticity Associated with Penetration of a Jet into a Cross Flow. *Journal of Engineering for Power 100*, 465–475.

LeBœuf, F., G.-P. Huang, P. Kulisa, and G. Perrin (1991). Model and Computation of Discrete Jets in Crossflow. *European Journal of Mechanics: B/Fluids 10*(6), 629–650.

Lee, S., Y. Kim, and J. Lee (1997). Flow Characteristics and Aerodynamic Losses of Film-Cooling Jets With Compound Angle Orientations. *Journal of Turbomachinery 119*(2), 310–319.

Lee, S., S. Lee, and S. Ro (1994). Experimental Study on the Flow Characteristics of Streamwise Inclined Jets in Crossflow on Flat Plate. *Journal of Turbomachinery 1*, 97–105.

Leylek, J. and R. Zerkle (1994). Discrete-Jet Film Cooling: A Comparison of Computational Results with Experiments. *Journal of Turbomachinery 116*, 358–586.

Licu, D., M. Findlay, I. Gartshore, and M. Salcudean (2000). Transient Heat Transfer Measurements Using a Single Wide-Band Liquid Crystal Test. *Journal of Turbomachinery 122*(3), 546–552.

Liess, C. (1975). Experimental Investigation of Film Cooling With Ejection From a Row of Holes for the Application of Gas Turbine Blades. *Journal of Engineering for Power 97*(1), 21–27.

Ligrani, P., A. Ortiz, S. Joseph, and D. Evans (1989). Effects of Embedded Vortices on Film-Cooled Turbulent Boundary Layers. *Journal of Turbomachinery 111*(1), 71–77.

Ligrani, P. and W. Williams (1990). Effects of an Embedded Vortex on Injectant From a Single Film-Cooling Hole in a Turbulent Boundary Layer. *Journal of Turbomachinery 112*(3), 428–436.

Ligrani, P., C. Subramanian, D. Craig, and P. Kaisuwan (1991). Effects of Vortices With Different Circulations on Heat Transfer and Injectant Downstream of a Single Film-Cooling Hole in a Turbulent Boundary Layer. *Journal of Turbomachinery 113*(3), 433–441.

Ligrani, P., S. Ciriello, and D. Bishop (1992). Heat Transfer, Adiabatic Effectiveness, and Injectant Distributions Downstream of a Single Row and Two Staggered Rows of Compound Angle Film-Cooling Holes. *Journal of Turbomachinery 114*(4), 687–700.

Ligrani, P. and S. Mitchell (1994a). Interactions between Embedded Vortices and Injectant from Film Cooling Holes with Compound Angle Orientations in a Turbulent Boundary Layer. *Journal of Turbomachinery 116*(1), 80–91.

Ligrani, P. and S. Mitchell (1994b). Effects of Embedded Vortices on Injectant from Film Cooling Holes with Large Spanwise Spacing and Compound Angle Orientations in a

Turbulent Boundary Layer. *Journal of Turbomachinery 116*(4), 709–720.

Ligrani, P., J. Wigle, S. Ciriello, and S. Jackson (1994). Film-Cooling from Holes with Compound Angle Orientations. Part 1. Results Downstream of two Staggered Rows of Holes with 3D Spanwise Spacing. *Journal of Turbomachinery 116*(2), 341–352.

Ligrani, P., J. Wigle, and S. Jackson (1994). Film-cooling from Holes with Compound Angle Orientations. Part 2. Results Downstream of a Single Row of Holes with 6D Spanwise Spacing. *Journal of Turbomachinery 116*(2), 353–362.

Ligrani, P. and A. Ramsey (1997a). Film Cooling From a Spanwise-Oriented Holes in Two Staggered Rows. *Journal of Turbomachinery 119*(3), 562–567.

Ligrani, P. and A. Ramsey (1997b). Film Cooling From a Single Row of Holes Oriented in Spanwise/Normal Planes. *Journal of Turbomachinery 119*(3), 770–776.

Ligrani, P., C. Saumweber, A. Schulz, and S. Wittig (2001). Shock Wave - Film Cooling Interactions in Transonic Flow. *Journal of Turbomachinery 123*(4), 788–797.

Luckey, D. and M. L'Ecuyer (1981). Stagnation Region Gas Film Cooling – Spanwise Angled Injection From Multiple Rows of Holes. *NASA CR 165333*.

Luckey, D., D. Winstanley, G. Hanus, and M. L'Ecuyer (1977). Stagnation Region Gas Film Cooling for Turbine Blade Leading-Edge Applications. *Journal of Aircraft 14*, 494–501.

Luo, J. and B. Lakshminarayana (1997). Numerical Simulation of Turbine Blade Boundary Layer and Heat Transfer Assessment of Turbulence Models. *Journal of Turbomachinery 119*(4), 794–801.

Lutum, E. and B. Johnson (1999). Influence of the Hole Length-to-Diameter Ratio on Film Cooling With Cylindrical Holes. *Journal of Turbomachinery 121*(2), 209–216.

MacCormack, R. (1995). *Numerical Computation of Compressible Viscous Flow.* Department of Aeronautical and Astronautics, Stanford, CA 94305-4035: Stanford University.

Maciejewski, P. and R. Moffat (1992). Heat transfer with very high free-stream turbulence. Part I. Experimental Data. *Journal of Heat Transfer 114*(4), 827–833.

MacMullin, R., W. Elrod, and R. Rivir (1989). Free-Stream Turbulence From a Circular Wall Jet on a Flat Plate Heat Transfer and Boundary Layer Flow. *Journal of Turbomachinery 111*(1), 78–86.

Makki, Y. and G. Jakubowski (1986). An Experimental Study of Film Cooling from Diffused Trapezoidal Shaped Holes. *AIAA Paper 86-1326*.

Malik, N. (1995). *Electronic Circuits: Analysis, Simulation and Design* (1 ed.). Englewood Cliffs, New Jersey, 07632: Prentice-Hall, Inc.

Martinez-Botas, R., G. Lock, and T. Jones (1995). Heat Transfer Measurements in an Annular Cascade of Transonic Gas Turbine Blades Using the Transient Liquid Crystal Technique. *Journal of Turbomachinery 117*(3), 425–431.

Mattingly, G. (1996). *Empirical Formulas for Orifice Discharge Coefficients*, pp. 357–359. 1900 Frost Road, Suite 101, Bristol, PA 19007-1598: Taylor & Francis.

Mayle, R. and F. Camarata (1975). Multihole Cooling Film Effectiveness and Heat Transfer. *Journal of Heat Transfer 97*, 534–538.

Mayle, R., F. Kopper, M. Blair, and D. Bailey (1977). Effect of Streamline Curvature on Film Cooling. *Journal of Engineering for Power 99*(1), 77–82.

McGovern, K. and J. Leylek (2000). A Detailed Analysis of Film Cooling Physics: Part II - Compound-Angle Injection With Cylindrical Holes. *Journal of Turbomachinery 122*(1), 113–121.

Medic, G. and P. Durbin (2002a). Toward Improved Prediction of Heat Transfer on Turbine Blades. *Journal of Turbomachinery 124*(1), 187–192.

Medic, G. and P. Durbin (2002b). Toward Improved Film Cooling Prediction. *Journal of Turbomachinery 124*(1), 193–199.

Mee, D., P. Ireland, and S. Bather (1999). Measurement of the Temperature Field Downstream of Simulated Leading-Edge Film-Cooling Holes. *Experiments in Fluids 27*(3), 273–283.

Mehendale, A. and J. Han (1992). Influence of High Mainstream Turbulence on Leading Edge Film Cooling Heat Transfer. *Journal of Turbomachinery 114*(4), 707–715.

Meroney, R. (1974). Measurements of Turbulent Boundary Layer Growth Over a Longitudinally Curved Surface. *Project THEMIS Technology Report 25*.

Metzger, D. and D. Larson (1986). Use of Melting Point Surface Coatings for Local Convection Heat Transfer Measurements in Rectangual Channel Flows with 90-deg Turns. *Journal of Heat Transfer 108*(1), 48–54.

Metzger, D., D. Takeuchi, and P. Kuenstler (1973). Effectiveness and Heat Transfer With Full-Coverage Film Cooling. *Journal of Engineering for Power 95*(3), 180–184.

Mick, W. (1988). Stagnation Film Cooling and Heat Transfer, Including Its Effect Within the Hole Pattern. *Journal of Turbomachinery 110*(1), 66–72.

Miller, R. (1983). *Flow Measurement Engineering Handbook* (1st ed.). San Francisco, California: McGraw-Hill.

Moffat, R. (1987). Turbine Blade Cooling. *Heat Transfer and Fluid Flow in Rotating Machinery*, 3–36.

Moffat, R. (1988). Describing the Uncertainties in Experimental Results. *Experimental Thermal and Fluid Science 1*(1), 3–17.

Moffat, R. (1990). Some Experimental Methods for Heat Transfer Studies. *Experimental Thermal and Fluid Science 3*(1), 26–32.

Moffat, R., J. Eaton, and D. Mukerji (2000). General Method for Calculating the Heat Island Correction and Uncertainties for Button Gauges. *Measurement Science and Technology 11*(7), 920–932.

Molki, M. and E. Sparrow (1986). An Empirical Correlation for the Average Heat Transfer Coefficient in Circular Tubes. *Journal of Heat Transfer 108*(2), 482–484.

Moran, M. and H. Shapiro (2004). *Fundamentals of Engineering Thermodynamics* (5th ed.). Hoboken, NJ: John Wiley & Sons.

Morkovin, M. (1962). *Effects of compressibility on turbulent flows*, pp. 367–380. CNRS.

Mukerji, D. and J. Eaton (2002, March). Spatially-Resolved Measurements of Heat Transfer in Turbomachinery Applications. Technical Report TSD-145, Stanford, California 94305.

Mukerji, D., J. Eaton, R. Moffat, and C. Elkins (1999). A 2-D Numerical Study of the Heat-Island Effect for Button-Type Heat Flux Gages. *Proceedings of the 5th ASME/JSME Joint Thermal Engineering Conference, AJTE99/6186*.

Muldoon, F. and S. Acharya (1999). Dynamics of Large-Scale Structures for Jets in a Crossflow. *Journal of Turbomachinery 121*(3), 577–587.

Muska, J., R. Fish, and M. Suo (1975). Additive Nature of Film Cooling from Rows of Holes. *Journal of Engineering for Power 98*(4), 457–464.

Nirmalan, N. and L. Hylton (1990). An Experimental Study of Turbine Vane Heat Transfer with Leading Edge and Downstream Film Cooling. *Journal of Turbomachinery 112*(3), 477–487.

Ou, S. and J. Han (1992). Influenece of High Mainstream Turbulence on Leading Edge Film Cooling Heat Transfer Through Two Rows of Inclined Film Slots. *Journal of Turbomachinery 114*(4), 724–733.

Ou, S., A. Mehendale, and J. Han (1992). Influenece of High Mainstream Turbulence on Leading Edge Film Cooling Heat Transfer: Effect of Film Hole Location. *Journal of Turbomachinery 114*(4), 716–723.

Parsley, M. (1991a). An Introduction to Thermochromic Liquid Crystals. Technical report, 1820 Pickwick Ln., Glenview, Illinois, 60025, USA.

Parsley, M. (1991b). The Use of Thermochromic Liquid Crystals in Research Applications, Thermal Mapping and Non-Destructive Testing. *Proceedings of the Seventh IEEE SEMI-THERM Symposium*, 53–58.

Patankar, S. and D. Spalding (1972). A Calculation Procedure for Heat, Mass and Momentum Transfer in Three-Dimensional Parabolic Flows. *Journal of Heat and Mass Transfer 15*, 1787–1806.

Peabody, H. and T. Diller (1998). Evaluation of an Insert Heat Flux Gage in a Transonic Turbine Cascade. *HTD-Vol. 361-5, Proceedings of the ASME Heat Transfer Division 5*, 625–630.

Pedersen, D., E. Eckert, and R. Goldstein (1977). Film Cooling With Large Density Differences Between the Mainstream and the Secondary Fluid Measured by the Heat-Mass Transfer Analogy. *Journal of Heat Transfer 99*(4), 620–627.

Peterson, S. and M. Plesniak (2002). Short-Hole Jet-In-Crossflow Velocity Field and its Relationship to Film-cooling Performance. *Experiments in Fluids 33*(6), 889–898.

Peterson, S. and M. Plesniak (2004). Evolution of Jets Emanating from Short Holes into Crossflow. *Journal of Fluid Mechanics 503*(1), 57–91.

Pethukov, B. (1970). *Heat Transfer and Friction in Turbulent Pipe Flow with Variable Physical Properties*, pp. 503–564. New York, New York: Academic.

Pietrzyk, J., D. Bogard, and M. Crawford (1989). Hydrodynamic Measurements of Jets in Crossflow for Gas Turbine Film Cooling Applications. *Journal of Turbomachinery 111*(2), 139–145.

Pietrzyk, J., D. Bogard, and M. Crawford (1990). Effects Of Density Ratio On The Hydrodynamics Of Film Cooling. *Journal of Turbomachinery 112*(3), 437–443.

Pope, S. (2000). *Turbulent Flows*. 40 West 20th Street, New York, NY 10011-4211: Cambridge University Press.

Priddy, W. and F. Bayley (1988). Turbulence measurements in turbine blade passages and implications for heat transfer. *110*(1), 73–79.

Quinn, W. (1990). Mean Flow and Turbulence Measurements in a Triangular Turbulent Free Jet. *International Journal of Heat and Fluid Flow 11*(3), 220–224.

Quinn, W. (1992). Streamwise Evolution of a Square Jet Cross Section. *AIAA Journal 30*(12), 2852–2857.

Quinn, W. and J. Militzer (1989). Effects of Nonparallel Exit Flow on Round Turbulent Free Jets. *International Journal of Heat and Fluid Flow 10*(2), 139–145.

Radomsky, R. and K. Thole (2000). Flowfield measurements for a highly turbulent flow in a stator vane passage. *Journal of Turbomachinery 122*(2), 255–262.

Ramsey, J. and R. Goldstein (1971). Interaction of a Heated Jet With a Deflecting Stream. *Journal of Heat Transfer 93*(4), 365–372.

Reynolds, W. (1979). *Thermodynamic Properties in SI* (1st ed.). Stanford, California: Department of Mechanical Engineering, Stanford University.

Reynolds, W. and H. Perkins (1977). *Engineering Thermodynamics* (1st ed.). San Francisco, California: McGraw-Hill.

Rigby, M., A. Johnson, and M. Oldfield (1990). Gas Turbine Rotor Blade Film Cooling With and Without Simulated NGV Shock Waves and Wakes. *American Society of Mechanical Engineers (Paper) 90-GT-78*.

Roberts, G. and R. East (1996). Liquid Crystal Thermography for Heat Transfer Measurement in Hypersonic Flows: A Review. *Journal of Spacecraft and Rockets 33*(6), 761–768.

Sabatino, D., T. Praisner, and C. Smith (2000). A high-accuracy calibration technique for thermochromic liquid crystal measurements. *Experiments in Fluids 28*(1), 497–505.

Salcudean, M., I. Gartshore, K. Zhang, and I. McLean (1994). An Experimental Study of Film Cooling Effectiveness of Film Cooling Effectiveness Near the Leading Edge of a Turbine Blade. *Journal of Turbomachinery 116*(1), 71–79.

Saumweber, C., A. Schulz, and S. Wittig (2003). Free-Stream Turbulence Effects on Film Cooling With Shaped Holes. *Journal of Turbomachinery 125*(1), 65–73.

Schlichting, B. and K. Gersten (2000). *Boundary-Layer Theory* (8th ed.). 6: Springer-Verlag.

Schmidt, D. and D. Bogard (1995). Pressure Gradient Effects on Film Cooling. *American Society of Mechanical Engineers (Paper) 95-GT-18*.

Schmidt, D., B. Sen, and D. Bogard (1996). Film Cooling With Compound Angle Holes: Adiabatic Effectiveness. *Journal of Turbomachinery 118*(4), 807–813.

Schönung, B. and W. Rodi (1987). Prediction of Film Cooling by a Row of Holes with a Two-Dimensional Boundary-Layer Procedure. *Journal of Turbomachinery 109*(4), 579–587.

Schultz, D. and T. Jones (1973). Heat-Transfer Measurements in Short-Duration Hypersonic Facilities. *AGARDograph No. 165*.

Schulz, H. and H. Gallus (1988). Experimental Investigation of the Three-Dimensional Flow in an Annular Cascade. *Journal of Turbomachinery 110*(4), 467–478.

Schwarz, S. and R. Goldstein (1989). The Two-Dimensional Behavior of Film Cooling Jets on Concave Surfaces. *Journal of Turbomachinery 111*(2), 124–130.

Schwarz, S., R. Goldstein, and E. Eckert (1991). The Influence of Curvature on Film Cooling Performance. *Journal of Turbomachinery 113*(3), 472–478.

Sellars, J. (1963). Gaseous Film Cooling With Multiple Injection Stations. *AIAA Journal 1*(9), 2154–2156.

Sen, B., D. Schmidt, and D. Bogard (1996). Film Cooling With Compound Angle Holes: Heat Transfer. *Journal of Turbomachinery 118*(4), 800–806.

Simonich, J. and P. Bradshaw (1978). Effect of Free-Stream Turbulence on Heat Transfer Through a Turbulent Boundary Layer. *Journal of Heat Transfer 100*, 671–677.

Sinha, A., D. Bogard, and M. Crawford (1991a). Film-Cooling Effectiveness Downstream of a Single Row of Holes With Variable Density Ratio. *Journal of Turbomachinery 113*(3), 442–449.

Sinha, A., D. Bogard, and M. Crawford (1991b). Gas Turbine Film Cooling: Flowfield due to a Second Row of Holes. *Journal of Turbomachinery 113*(3), 450–456.

Smith, D., T. Praisner, and D. Sabatino (2001). Temperature sensing with thermochromic liquid crystals. *30*(2), 190–201.

Smith, S. and M. Mungal (1998). Mixing, Structure and Scaling of the Jet in Crossflow. *Journal of Fluid Mechanics 357*, 83–122.

Smits, A., K. Hayakawa, and K. Muck (1983). Constant-temperature hotwire anemometry in supersonic flows - part i: The normal wire. *Experiments in Fluids 1*, 83–92.

So, R. and G. Mellor (1973). Experiment on Convex Curvature Effects in Turbulent Boundary Layers. *Journal of Fluid Mechanics 60*(1), 43–62.

So, R. and G. Mellor (1975). Experiment on Turbulent Boundary Layers on a Concave Wall. *Aeronautical Quarterly 26*(1).

Stainback, P. and K. Nagabushana (1993). Review of Hot-Wire Anemometry Techniques and the Range of Their Applicability. *FED-Vol. 167 Thermal Anemometry - 1993*, 93–423.

Sterland, P. and M. Hollingsworth (1975). An Experimental Study of Multiple Jets Directed Normally to a Cross-flow. *Journal Mechanical Engineering Science 17*(3), 117–123.

Subramanya, K. and P. Porey (1984). Trajectory of a turbulent cross jet. *Journal of Hydraulic Research 22*(5), 343–354.

Syson, B., R. Pilbrow, and J. Owen (1996). Effect of rotation on temperature response of thermochromic liquid crystal. *International Journal of Heat and Fluid Flow 17*(5), 491–499.

Takahashi, H., C. Nuntadusit, H. Kimoto, H. Ishida, T. Ukai, and K. Takeishi (2000). Characteristics of Various Film Cooling Jets Injected in a Conduit. *Turbine 2000 International Symposium on Heat Transfer in Gas Turbine Systems Izmir, Turkey*, 76–78.

Takeishi, K., S. Aoki, T. Sato, and K. Tsukagoshi (1992). Film Cooling on a Gas Turbine Rotor Blade. *Journal of Turbomachinery 114*(4), 828–834.

Tani, I. (1962). Production of Longitudinal Vortices in the Boundary Layer Along a Concave Wall. *Journal of Geophysical Research 67*, 3075–3080.

Taylor, G. (1938). The Spectrum of Turbulence. *Proceedings of Royal Society of London, Serial A. 164*, 476–490.

Teekaram, A., C. Forth, and T. Jones (1989). The Use of Foreign Gas to Simulate the Effect of Density Ratios in Film Cooling. *Journal of Turbomachinery 111*(1), 57–62.

Teekaram, A., C. Forth, and T. Jones (1991). Film Cooling in the Presence of Mainstream Rressure Gradients. *Journal of Turbomachinery 113*(3), 484–492.

Theodoridis, G., D. Lakehal, and W. Rodi (2001). Three-Dimensional Calculations of the Flow Field around a Turbine Blade with Film Cooling Injection near the Leading Edge. *Flow, Turbulence and Combustion 66*(1), 57–83.

Thiele, A. (1994). An Improved Law of Contrast Gradient for High Definition Television. *SMPTE Journal 103*(1), 18–25.

Thole, K., M. Gritsch, A. Schulz, and S. Wittig (1998). Flowfield Measurements for Film-Cooling Holes With Expanded Exits. *Journal of Turbomachinery 120*(2), 549–556.

Thomann, H. (1968). Effect of Streamwise Curvature on Heat Transfer in a Turbulent Boundary Layer. *Journal of Fluid Mechanics 33*(2), 283–292.

Tillman, E., E. Hartel, and H. Jen (1984). The Prediction of Flow Through Leading Edge Holes in a Film Cooled Airfoil With and Without Inserts. *Journal of Engineering for Gas Turbines and Power 107*(1), 92–98.

Tillman, E. and H. Jen (1984). Cooling Airflow Studies at the Leading Edge of a Film-Cooled Airfoil. *Journal of Engineering for Gas Turbines and Power 106*(1), 214–221.

Townsend, A. (1947). . *Proceedings of the Cambridge Philosophical Society 43*, 560.

Tyagi, M. and S. Acharya (2003). Large Eddy Simulation of Film Cooling Flow From an Inclined Cylindrical Jet. *Journal of Turbomachinery 125*(4), 734–742.

Van Driest, E. (1952, January). Investigation of Laminar Boundary Layer in Compressible Fluids using the Croco Method. Technical Note NACA TN 2597, Washington, D.C., 20001.

Vantico Corporation (2001). Private Communication.

Vedula, R. and D. Metzger (1991). A Method for the Simultaneous Determination of Local Effectiveness and Heat Transfer Distributions in Three-Temperature Convection Situations. *American Society Mechanical Engineers (Paper) 91-GT-345*.

Vidal, R. (1956). Model instrumentation techniques for heat transfer and force measurements in a hypersonic shock tunnel. *Calspan Report No. AD-917-A-1*.

Vogel, G., A. Graf, J. von Wolfersdorf, and B. Weigand (2003). A Novel Transient Heater-Foil Technique for Liquid Crystal Experiments on Film-Cooled Surfaces. *Journal of Turbomachinery 125*(3), 529–537.

Walters, D. and J. Leylek (1997). A Systematic Computational Methodology Applied to a Three-Dimensional Fllm-Cooling Flowfield. *Journal of Turbomachinery 119*(4), 777–785.

Walters, D. and J. Leylek (2000a). A Detailed Analysis of Film Cooling Physics: Part I–Streamwise Injection With Cylindrical Holes. *Journal of Turbomachinery 122*(1), 102–112.

Walters, D. and J. Leylek (2000b). Impact of Film-Cooling Jets on Turbine Aerodynamic Losses. *Journal of Turbomachinery 122*(3), 537–545.

Wang, H., R. Goldstein, and S. Olson (1999). Effect of High Free-Stream Turbulence With Large Length Scale on Blade Heat/Mass Transfer. *Journal of Turbomachinery 121*(1), 217–224.

Wang, L., H. Tsang, T. Simon, and E. Eckert (1996). Measurements of Mean Flow and Eddy Transport Over a Film Cooling Surface. *HTD, National Heat Transfer Conference 327*(5), 71–79.

Wang, Z., P. Ireland, and T. Jones (1996). A Color Image Processing System for Transient Liquid Crystal Heat Transfer Experiments. *Journal of Turbomachinery 188*(3), 421–427.

Watanabe, K., M. Matsuura, K. Suenaga, and K. Takeishi (1999). An Experimental Study on the Film Cooling Effectiveness With Expanded Hole Geometry. *Proceedings of the 7th IGTC 2*, 615–622.

Whitaker, S. (1972). Forced Convection Heat Transfer Correlations for Flow in Pipes, Past Flat Plates, Single Cylinders, Single Spheres, and for Flow in Packed Beds and Tube Bundles. *AIChE Journal 18*(2), 361–371.

White, F. (1991). *Viscous Fluid Flow* (2nd ed.). San Francisco, California: McGraw-Hill.

Wiberg, R. and N. Lior (2004). Errors in thermochromic liquid crystal thermography. *Review of Scientific Instruments 75*(9), 2985–2994.

Wilcox, D. (1994). Simulation of Transition with a Two-Equation Turbulence Model. *AIAA Journal 32*, 247–255.

Wilcox, D. (2000). *Tubulence Modeling for CFD* (2nd ed.). 5354 Palm Drive, La Cañada, California, 91011: DCW Industries.

Wisler, D., R. Bauer, and T. Okiishi (1987). Secondary Flow Turbulent Diffusion and Mixing in Axial-Flow Compressor. *Journal of Turbomachinery 109*(4), 455–482.

Wittig, S., A. Schulz, M. Gritsch, and K. Thole (1996). Transonic Film Cooling Investigations: Effects of Hole Shapes and Orientations. *American Society of Mechanical Engineers (Paper) 96-GT-222*.

Wu, X. (2000). Private Communication.

Yamamoto, A., Y. Kondo, and R. Murao (1991). Cooling-Air Injection Into Secondary Flow and Loss Fields Within a Linear Turbine Cascade. *Journal of Turbomachinery 113*(2), 375–383.

Yavuzkurt, S. (1997). Effects of Free-Stream Turbulence on the Instantaneous Heat Transfer in a Wall Jet Flow. *Journal of Turbomachinery 119*(2), 359–363.

Yavuzkurt, S., R. Moffat, and W. Kays (1980). Full-Coverage Film Cooling. Part 1. Three-Dimensional Measurements of Turbulence Structure. *Journal of Fluid Mechanics 101*, 129–158.

Yu, Y. and M. Chyu (1998). Influence of Gap Leakage Downstream of the Injection Holes on Film Cooling Performance. *Journal of Turbomachinery 120*(3), 541–548.

Yu, Y., C. Yen, T. Shih, M. Chyu, and S. Gogineni (2002). Film Cooling Effectiveness and Heat Transfer Coefficient Distributions Around Diffusion Shaped Holes. *Journal of Heat Transfer 124*(4), 820–827.

Yuan, L., R. Street, and J. Ferziger (1999). Large-Eddy Simulations of a Round Jet in Crossflow. *Journal of Fluid Mechanics 379*, 71–104.

Ziegler, H. and P. Wooler (1971). Multiple Jets Exhausting into a Crossflow. *Journal of Aircraft 8*(6), 414–420.

Zucrow, M. and J. Hoffman (1976). *Gas Dynamics*, Volume 1. New York, NY: John Wiley & Sons, Inc.